Shahid Rajaee
Teacher Training University

Journal of
Electrical and Computer
Engineering Innovations
(JECEI)

Vol. 14 No. 2, Summer-Fall 2026

- Trends and Challenges in Linear Synchronous Motor Technology: A Detailed Review of Design and Optimization Approaches 295
- Bridging the Speed–Accuracy Gap: RT-DETR versus YOLOv8s for Real-Time Brain MRI Tumor Detection 311
- Robust Channel Estimation and Passive Beamforming with Discrete Phase for RIS-Assisted Communication Systems 327
- A Hybrid Deep Hashing and Metric Space Partitioning Framework for Scalable Content-Based Image Retrieval via Unsupervised Representation Learning and VP-Tree Optimization 337
- A Novel Algorithm Clustering based on Natural Neighborhood and Radial Distribution Function 351
- Adaptive Multi-Layer Random Generator: Toward Self-Regulating Pseudorandomness 365
- BSOGA: Community Detection in Social Networks Based on Bee Swarm Optimization Using Genetic Algorithm 377
- Robust Continuous Person Tracking in Dense Multi-Camera Environments through Decoupled Graph Learning 391
- Enhancing Ack QKD with Decoy States for Device Independent Security 403
- CNN-Based Placement and Multi-Objective Routing for Analog Circuits with Simulated Annealing and NSGA-III 411
- Diverse Climatic Soil Moisture Estimation Using an Enhanced GRU Model with Multi-Source Data Augmentation 425
- Artificial Intelligence-Based YOLOv3 using DarkNet-53 Deep Convolutional Neural Network Model Architecture for Automatic Vehicle Inventory System Design with a Dynamic Relational Database System and Google Cloud Storage 435
- Optimization and Experimental Validation of an IPMSM for Electric Vehicles Targeting Torque Ripple Minimization, Average Torque and Efficiency Improvement 473
- Hybrid CNN–BiLSTM Model with BERT Embeddings for Urgency Detection in MOOC Forums 487
- Detection of Breast Cancer Masses in Mammography Images Using a Hybrid Faster R-CNN and Fuzzy Logic Framework 507
- Diagnosis of Cardiac Arrhythmia using an Optimized Two-stage Deep Learning Model 519
- Detailed Analysis and Design of Line-Start Synchronous Reluctance Motors Aiming at High Power Factor 535
- Design and Optimization of a Counter-Rotating Double-Rotor Synchronous Motor with a Permanent Magnet External Rotor and a Reluctance Internal Rotor 549
- Deep Learning Attention-Based Framework for Integrating EEG and Image Information in Visual Content Recognition 565
- Early-Stage Resource-Bound Prediction for Threads Using Real-Time Kernel Event Analysis 583

Journal of
JECEI
Electrical and Computer Engineering Innovations Vol. 14 No. 2, Summer-Fall 2026

JECEI

Journal of

Shahid Rajaee
Teacher Training University

*p*ISSN 2322-3952
*e*ISSN 2345-3044

Electrical and Computer Engineering Innovations (JECEI)

Semiannual Publication

Volume 14, Issue 2, Summer-Fall 2026

Journal of Electrical and Computer Engineering Innovations
http://jecei.sru.ac.ir
EISSN: 2345-3044
ISSN: 2322-3952
JECEI
SRTTU
JECEI

License Holder: Shahid Rajaee Teacher Training University (SRTTU). **Address:** Lavizan, 16788-15811, Tehran, Iran.

Responsible Director: **Prof. Saeed Olyaee**
Faculty of Electrical Engineering, Shahid Rajaee University, Iran

Editor-in-Chief: **Prof. Reza Ebrahimpour**
Institute for Convergence Science and Technology, Sharif University of Technology, Tehran, Iran

Editor-in-Chief: **Prof. Nasour Bagheri**
Faculty of Electrical Engineering, Shahid Rajaee University, Iran

Associate Editors:

Prof. Muhammad Taher Abuelma'atti
Faculty of Electrical Engineering, King Fahd University of Petroleum and Minerals, Saudi Arabia

Prof. Mojtaba Agha Mirsalim
Department of Electrical Engineering, Amirkabir University of Technology, Iran

Prof. Vahid Ahmadi
Faculty of Electrical and Computer Engineering, Tarbiat Modares University, Iran

Prof. Nasour Bagheri
Faculty of Electrical Engineering, Shahid Rajaee University, Iran

Prof. Seyed Mohammad Taghi Bathaee
Faculty of Electrical Engineering, Power Department, K. N. Toosi University of Technology, Iran

Prof. Jun Cai
Nanjing University of Information Science and Technology, China

Prof. Fadi Dornaika
Universidad Del Pais Vascodisabled, Leioa, Spain

Prof. Reza Ebrahimpour
Institute for Convergence Science and Technology, Sharif University of Technology, Tehran, Iran

Prof. Nosrat Granpayeh
Faculty of Electrical Engineering, K. N. Toosi University of Technology, Iran

Prof. Erich Leitgeb
Institute of Microwave and Photonic Engineering, Graz University of Technology, Austria

Prof. Juan C. Olivares-Galvan
Department of Energy, Universidad Autónoma Metropolitana, Mexico

Prof. Saeed Olyaee
Faculty of Electrical Engineering, Shahid Rajaee University, Iran

Prof. Masoud Rashidinejad
Department of Electrical Engineering, Shahid Bahonar University, Iran

Prof. Raj Senani
Division of Electronics and Communication Engineering, Netaji Subhas Institute of Technology, India

Prof. Mohammad Shams Esfand Abadi
Faculty of Electrical Engineering, Shahid Rajaee University, Iran

Prof. Vahid Tabataba Vakili
School of Electrical Engineering, Iran University of Science and Technology, Iran

Prof. Ahmed F. Zobaa
Department of Electronic and Computer Engineering, Brunel University, UK

Dr. Kamran Avanaki
Department of Biomedical Engineering, University of Illinois in Chicago

Department of Dermatology School of Medicine, University of Illinois in Chicago Scientific Member, Barbara Ann Karmanos Cancer Institute

Dr. Debasis Giri
Department of Computer Science and Engineering, Haldia Institute of Technology, India

Dr. Peyman Naderi
Faculty of Electrical Engineering, Shahid Rajaee University, Iran

Dr. Masoumeh Safkhani
Faculty of Computer Engineering, Shahid Rajaee University, Iran

Dr. Mahmood Seifouri
Faculty of Electrical Engineering, Shahid Rajaee University, Iran

Dr. Shahriar Shirvani Moghaddam
Faculty of Electrical Engineering, Shahid Rajaee University, Iran

Dr. Jian-Gang Wang
Department of Computer Vision and Image Understanding, Institute for Infocomm Research, Singapore

Executive Manager: **Dr. Masoumeh Safkhani**
Faculty of Computer Engineering, Shahid Rajaee University, Iran

Assisted by: Mrs. Fahimeh Hosseini

Journal of Electrical and Computer Engineering Innovations

Vol. 14; Issue 2: 2026

Contents

Trends and Challenges in Linear Synchronous Motor Technology: A Detailed Review of Design and Optimization Approaches 295
Seyede Delaram Sadr, Hamid Reza Izadfar

Bridging the Speed–Accuracy Gap: RT-DETR versus YOLOv8s for Real-Time Brain MRI Tumor Detection 311
Amir Mahdi Sedghi, Shala Nemati

Robust Channel Estimation and Passive Beamforming with Discrete Phase for RIS-Assisted Communication Systems 327
Mojtaba Hajiabadi, Naaser Neda, Amir Moradband Toroghi

A Hybrid Deep Hashing and Metric Space Partitioning Framework for Scalable Content-Based Image Retrieval via Unsupervised Representation Learning and VP-Tree Optimization 337
Sajad Mohamadzadeh, Mohammad Gharehbagh

A Novel Algorithm Clustering based on Natural Neighborhood and Radial Distribution Function 351
Mohammad Asadpour, Shahin Pourbahrami

Adaptive Multi-Layer Random Generator: Toward Self-Regulating Pseudorandomness 365
Ali Bazghandi

BSOGA: Community Detection in Social Networks Based on Bee Swarm Optimization Using Genetic Algorithm 377
Fatemeh Akbari, Eynollah Khanjari

Robust Continuous Person Tracking in Dense Multi-Camera Environments through Decoupled Graph Learning 391
Morteza Akbari, Seyyed Mohammad Razavi, Sajad Mohamadzadeh

Enhancing Ack QKD with Decoy States for Device Independent Security 403
Arash Kosari

CNN-Based Placement and Multi-Objective Routing for Analog Circuits with Simulated Annealing and NSGA-III 411
Atousa Gholami Boorkheyli, Majid Babaeinik, Hadi Dehbovid, Vahid Ghods

Diverse Climatic Soil Moisture Estimation Using an Enhanced GRU Model with Multi-Source Data Augmentation 425
Reyhaneh Bagheri, Fatemeh Tabib Mahmoudi, AmirHossein Gholamian

Artificial Intelligence-Based YOLOv3 using DarkNet-53 Deep Convolutional Neural Network Model Architecture for Automatic Vehicle Inventory System Design with a Dynamic Relational Database System and Google Cloud Storage 435
Vincent Andrew Akpan, David Ayo-oluwa Adegoke, Ebunoluwa Temiloluwa Adejayan, Kehinde Adesola Adepoju

Optimization and Experimental Validation of an IPMSM for Electric Vehicles Targeting Torque Ripple Minimization, Average Torque and Efficiency Improvement 473
Alireza Shams, Esmaeel Rokrok, Behrooz Rezaeealam, Abbas-Ali Zamani

Hybrid CNN–BiLSTM Model with BERT Embeddings for Urgency Detection in MOOC Forums 487
Mujtaba Sultani, Negin Daneshpour

Detection of Breast Cancer Masses in Mammography Images Using a Hybrid Faster R-CNN and Fuzzy Logic Framework 507
Fatemeh Jafari, Hamid Reza Ghafari, Hassan Farsi

Diagnosis of Cardiac Arrhythmia using an Optimized Two-stage Deep Learning Model 519
Motahareh Akbari Poodineh, Fatemeh Zare Mehrjardi, Mohsen Sardari Zarchi

Detailed Analysis and Design of Line-Start Synchronous Reluctance Motors Aiming at High Power Factor 535
Seyed Reza Mousavi-Aghdam, Seyed Abbas Azimi, Farzad Sedaghati

Design and Optimization of a Counter-Rotating Double-Rotor Synchronous Motor with a Permanent Magnet External Rotor and a Reluctance Internal Rotor 549
Pouria Nadri, Behrooz Rezaeealam, Morteza Mikhak-Beyranvand

Deep Learning Attention-Based Framework for Integrating EEG and Image Information in Visual Content Recognition 565
Hamed Hakak, Mohammad Mahdi Khalilzadeh, Mahdi Azarnoosh, Hamidreza Kobravi

Early-Stage Resource-Bound Prediction for Threads Using Real-Time Kernel Event Analysis 583
Morteza Noferesti, Farzad Amiri Delouei, Sarah Aryan

Journal of Electrical and Computer Engineering Innovations
(JECEI)
Journal homepage: http://www.jecei.sru.ac.ir

Research paper

Trends and Challenges in Linear Synchronous Motor Technology: A Detailed Review of Design and Optimization Approaches

Seyede Delaram Sadr , ***Hamid Reza Izadfar*** *

Faculty of Electrical and Computer Engineering, Semnan University, Semnan, Iran.

Article Info

Article History:

Received 20 December 2025
Reviewed 15 January 2026
Revised 26 February 2026
Accepted 06 April 2026

Keywords:

Advanced materials
Coreless motor
Linear synchronous motor
Magnetic modeling
Multi-objective optimization

*Corresponding Author's Email Address:
hrizadfar@semnan.ac.ir

Abstract

Background and Objectives: Linear Synchronous Motors (LSMs) provide high precision, fast response, and reduced mechanical complexity, making them attractive for applications such as transportation, automation, robotics, and medical systems. Although numerous studies have investigated their structures, modeling, and optimization, challenges such as end effects, thermal management, and cost reduction remain unresolved. This review aims to synthesize recent advancements and highlight future directions for LSM design and optimization.

Methods: The study systematically reviews 54 high-quality research papers covering structural configurations, electromagnetic and thermal modeling approaches, optimization techniques, and application domains of LSMs. Comparative analysis includes flat, tubular, coreless, and superconducting designs, along with analytical, magnetic equivalent circuit (MEC), and finite element method (FEM) modeling. Multi-objective optimization strategies, intelligent algorithms, and material innovations such as Halbach arrays and grain-oriented steels are also examined.

Results: Recent research demonstrates that transverse flux and tubular structures enhance thrust density by 20–35% and up to 25%, respectively, while coreless and superconducting designs reduce cogging and enable threefold thrust improvements. Advanced FEM-based multiphysics modeling enables accurate prediction of coupled electromagnetic, thermal, and mechanical behaviors. Optimization strategies based on evolutionary algorithms have achieved up to 12.5% improvement in thrust, an 8.7% reduction in losses, and significant thermal performance enhancements through innovative cooling designs.

Conclusion: LSMs are advancing through structural innovations and intelligent optimization. Despite recent progress, challenges such as cooling, scalability, and material costs persist. Future developments will rely on adaptive control, machine-learning- based design, and novel materials, strengthening the role of LSMs in industry and emerging technologies.

This work is distributed under the CC BY license (http://creativecommons.org/licenses/by/4.0/)

How to cite this paper:
S. D. Sadr, H. R. Izadfar, "Trends and challenges in linear synchronous motor technology: A detailed review of design and optimization approaches," J. Electr. Comput. Eng. Innovations, 14(2): 295-310, 2026.

DOI: 10.22061/jecei.2026.12398.876

URL: https://jecei.sru.ac.ir/article_12555.html

2345- 3044/© 2026 The Authors. Published by Shahid Rajaee Teacher Training University.

Introduction

Linear Synchronous Motors (LSMs) have emerged as one of the most advanced technologies for achieving precise linear motion, attracting growing attention in recent years. Due to their simple structure, high accuracy, and capability to generate substantial traction force, LSMs are widely utilized in fields such as magnetic transportation (e.g., Maglev trains), electromagnetic launchers, and precision industrial equipment [1], [2]. These motors generate direct linear motion, eliminating the need for rotary-to-linear conversion. This makes them particularly suitable for applications demanding high precision and controllability [3]. The advantages of LSMs include high energy efficiency, accurate positioning, and reduced noise and vibration [4]. Moreover, the use of permanent magnets and superconducting materials in their construction has led to improved performance and reduced size and weight [5].

Nevertheless, challenges including end effects, thrust ripple, and thermal management, particularly under high-load operational conditions, persist and require further research [6], [7]. Beyond their well-established applications in transportation and industrial automation, recent research has increasingly investigated the potential of Linear Synchronous Motors (LSMs) in emerging domains such as defense systems, aerospace engineering, and advanced medical technologies [8], [9]. Thanks to their flexible design capabilities and reliable performance, LSMs play a critical role in advancing cutting-edge technologies [10].

Recent years have witnessed extensive research aimed at improving the electromagnetic, thermal, and structural performance of linear synchronous motors (LSMs). Notable advancements, such as double-sided configurations with novel track designs, have achieved higher force density while reducing magnet consumption [11]. Segmented winding topologies employing two-phase concentric distributed windings [12], along with double-layer Halbach arrays optimized for coreless structures [13], have demonstrated significant improvements in thrust linearity and harmonic suppression.

Further developments include secondary designs with width-modulated magnets to mitigate thrust ripple [14], particle swarm optimization (PSO)-based transient enhancements to improve line-start performance [15], and homopolar configurations capable of reducing vibration and facilitating fault detection [16]. Additionally, design optimization through semi-analytical modeling to improve efficiency in tubular linear permanent magnet synchronous motors [17], and asymmetric V-shaped magnet arrangements for detent force reduction [18] collectively enhance the operational suitability and reliability of LSMs for demanding engineering applications. A broad body of recent literature [19]-[54] has investigated various structural, electromagnetic, and thermal aspects of Linear Synchronous Motors, including force generation, loss minimization, and advanced modeling techniques.

The various configurations of LSMs are presented, and their impacts on magnetic flux distribution, physical topology, symmetry, core utilization, and material selection are analyzed. Next, modeling and analysis methods are reviewed, with particular emphasis on electromagnetic, thermal, and multiphysics simulations. Subsequently, optimization strategies, including geometric, thermal, and multi-objective approaches, are examined. Major application areas of LSMs are then highlighted, ranging from transportation systems and electromagnetic launchers to industrial automation and emerging medical applications. Finally, the review concludes by summarizing the key findings and identifying potential directions for future research.

Structural Configurations of Linear Synchronous Motors

The structural configuration of Linear Synchronous Motors (LSMs) significantly affects their performance, cost, complexity, and suitability for specific applications. This section provides a detailed overview of significant design variations, focusing on magnetic flux direction, physical topology, structural symmetry, core utilization, material choices, and excitation methods.

A. Based on Magnetic Flux Direction: Longitudinal vs. Transverse

The direction of magnetic flux relative to the linear motion path is a key parameter for classifying Linear Synchronous Motors (LSMs) and significantly affects thrust. LSMs are primarily categorized into longitudinal flux and transverse flux configurations.

In longitudinal flux LSMs, illustrated in Fig. 1, the magnetic field lines are oriented parallel to the direction of motion. These motors are the most common in industrial and transportation applications due to their straightforward structure and ease of manufacturing [1], [5]. Typically, the stator includes linear arrays of windings or magnets, and the magnetic circuit is confined within a 2D planar layout. Despite their simplicity and ease of integration, longitudinal flux designs are limited in achievable thrust density and tend to exhibit more pronounced end effects, which can reduce overall performance under high dynamic loads [5].

On the other hand, transverse flux LSMs generate magnetic flux perpendicular to the direction of motion. This unique structure, illustrated in Fig. 2, allows the magnetic path to loop around the motion axis, increasing

the effective magnetic area and enabling higher thrust per unit volume. Studies [30] and [31] indicate that transverse-flux motors can achieve thrust densities 20%–35% higher than those of longitudinal-flux counterparts, primarily owing to extended flux paths and efficient utilization of three-dimensional magnetic fields.

However, the benefits of transverse flux configurations come with challenges. The complex winding arrangements, typically U-shaped or L-shaped, require advanced manufacturing techniques, and 3D finite element analysis (FEM) is often necessary for accurate modeling and optimization [30], [31]. Moreover, torque ripple and magnetic cross-coupling can be more challenging to manage due to the spatial distribution of magnetic forces.

Despite their increased complexity, transverse flux motors are highly suited for high-performance applications such as magnetic levitation (Maglev) trains, where high thrust density and compact volume are critical [1], [31]. Their ability to produce large linear forces in compact spaces makes them ideal candidates for heavy-duty transportation and precision electromechanical systems.

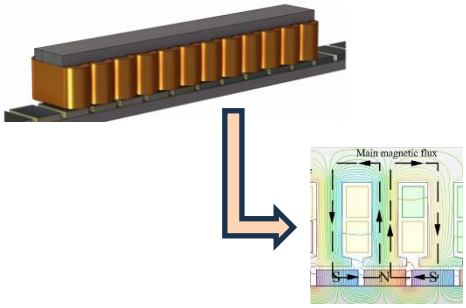


Fig. 1: Longitudinal flux LSM with magnetic paths [8].

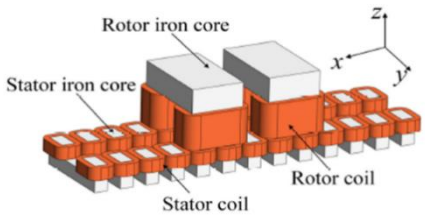


Fig. 2: Transverse flux LSM with orthogonal magnetic paths and segmented cores [31].

B. Physical Topology: Flat vs. Tubular Structures

The physical topology of Linear Synchronous Motors (LSMs) strongly affects their electromagnetic behavior, mechanical layout, thermal characteristics, and application compatibility. Among the widely used machine topologies, the flat-type and tubular-type configurations are the most common, each exhibiting specific performance advantages and drawbacks.

In flat-type structures, the open magnetic path increases the sensitivity to end effects. This reduces the effective flux density, whereas the closed-loop magnetic circuit employed in tubular designs improves magnetic coupling, resulting in more uniform and stable force generation [3], [29], [40].

Flat-type LSMs, as illustrated in Fig. 3, feature a planar configuration in which the stator and mover are arranged linearly on a flat surface. This structure is commonly used in industrial pick-and-place systems and linear actuators due to its simplicity in construction and ease of integration into planar systems [7], [27], [48]. In this design, the stator typically consists of laminated cores and distributed windings, while the mover comprises a row of permanent magnets. The open magnetic path, however, leads to increased end effects and lower magnetic flux density, which can limit performance in applications requiring high thrust and compactness. As a result, flat configurations typically exhibit higher leakage flux and experience greater variations in normal force, which may reduce motion smoothness in high-precision systems [27], [48].

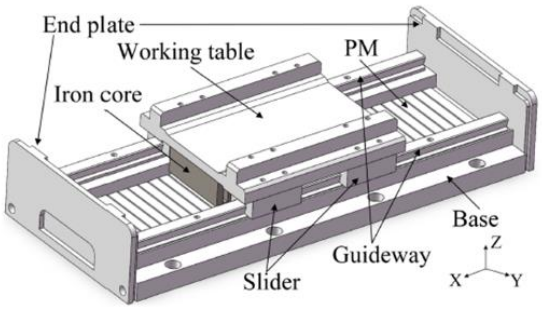


Fig. 3: Flat-type LSM with surface-mounted magnets and planar stator windings [7].

In contrast, the tubular-type LSM, shown in Fig. 4, offers a coaxial cylindrical geometry where the mover is enclosed by a circular stator. This configuration creates a closed-loop magnetic circuit, improving magnetic coupling and symmetry [3], [29], [40]. Tubular structures exhibit higher magnetic flux density (reported increases up to 25%) and significantly reduced end effects, enabling more efficient force production and improved dynamic stability [3], [29]. Furthermore, the radial symmetry of tubular motors enhances thermal dissipation and makes them better suited for vertical Z-axis motion, making them ideal for robotics and high-precision manufacturing. Moreover, the cylindrical enclosure also minimizes mechanical misalignment during motion, which can be beneficial in applications requiring consistent radial positioning [29], [40].

However, tubular LSMs tend to be more complex and expensive to manufacture due to their three-dimensional winding arrangements and tighter

mechanical tolerances [40]. Their structural form also demands more space in the radial direction, which may limit their use in systems with constrained volume.

Overall, the choice between flat and tubular LSM structures must balance factors such as thrust density, efficiency, manufacturability, and spatial constraints, with application-specific requirements guiding the final topology selection.

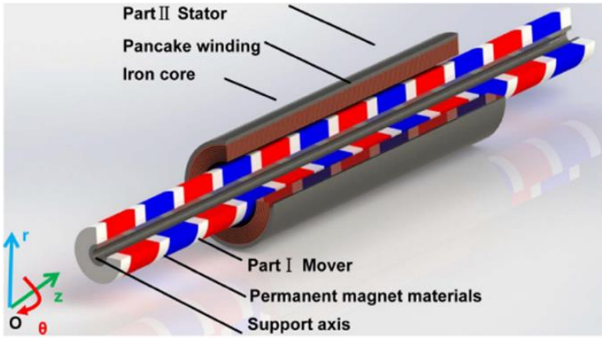


Fig. 4: Tubular LSM with coaxial structure enabling closed magnetic circuit [29].

C. Structural Symmetry: Single-sided vs. Double-sided

The structural symmetry of Linear Synchronous Motors (LSMs), whether single-sided or double-sided, plays a critical role in determining their electromagnetic performance, mechanical balance, and application feasibility. The configuration choice directly influences force generation capability, magnetic field uniformity, cogging behavior, and system complexity.

In single-sided LSMs, the active components, typically either the stator windings or permanent magnets are mounted on only one side of the air-gap. In contrast, the opposite side consists of a passive back iron or non-magnetic support. This configuration simplifies construction and reduces weight and cost, making it attractive for applications with strict mass or dimensional constraints, such as planar transport systems and low-power automation [26], [41]. However, the asymmetric field distribution in single-sided designs often leads to uneven magnetic attraction, which can cause undesirable normal forces and limit stability, particularly at high speeds or under varying loads [26], [42].

To overcome these limitations, double-sided LSMs incorporate active components on both sides of the air-gap, either symmetrical windings or permanent magnet arrays, creating a balanced magnetic structure. As discussed in [2], [4] and [20], double-sided configurations significantly enhance the magnetic field uniformity, reduce leakage, and improve thrust force generation. For instance, [20] showed that double-sided motors using Halbach arrays achieved an 18% increase in thrust and efficiency, and a 30% reduction in leakage, compared to equivalent single-sided counterparts. In addition to improved electromagnetic performance, double-sided designs offer better dynamic stability and reduced cogging effects in flux.

Study [44] demonstrated that thrust ripple was reduced by 12% in a double-sided modular LSM with hybrid excitation, resulting in smoother motion during high-acceleration operations. Similarly, [4] reported that double-sided structures exhibited more consistent force production in long-stator high-speed systems, where maintaining magnetic continuity is critical.

Nonetheless, the advantages of double-sided configurations come at the cost of increased volume, manufacturing complexity, and system integration challenges. The need for precise alignment of both stator sides and synchronized excitation can increase the control system's design burden. Therefore, while double-sided LSMs are highly suitable for high-thrust, precision-demanding applications such as Maglev, electromagnetic launchers, and high-end industrial drives, single-sided designs remain competitive in compact, low-cost systems where simplicity is paramount.

D. Core-Based vs. Coreless Designs

The presence or absence of a ferromagnetic core in Linear Synchronous Motors (LSMs) critically impacts magnetic flux control, thrust ripple, dynamic response, and thermal behavior. Designs are generally classified as either core-based or coreless, with each offering distinct performance trade-offs.

Core-based LSMs employ laminated ferromagnetic cores, usually silicon steel, in both stator and mover sections to guide and intensify magnetic flux. These motors benefit from enhanced magnetic coupling and higher thrust force due to increased magnetic permeability [9], [42]. However, they also suffer from drawbacks such as hysteresis and eddy current losses, cogging effects, and increased overall weight. Studies in [26] and [42] showed that in core-based designs, cogging force amplitudes could exceed 10–15% of the average thrust force in mid-power applications, negatively impacting smooth operation and precision.

To address these limitations, coreless LSMs eliminate magnetic cores in one or both of the active components. As depicted in Fig. 5, coreless structures rely on air-cored windings, often using PCB-based coils or racetrack-shaped superconducting windings [10], [33], [36], [38], [49]. The absence of ferromagnetic material in the flux path significantly reduces cogging and thrust ripple. For instance, [36] reported a 15% reduction in thrust ripple and a 10% improvement in average thrust force in a coreless High-Temperature Superconducting (HTS) LSM compared to its iron-core counterpart.

In addition to smoother operation, coreless motors exhibit superior dynamic response, as the lack of core

mass reduces inertia. They are especially suited for applications requiring fast linear acceleration and deceleration, such as electromagnetic launchers and surgical robotics [10], [20].

Nevertheless, the advantages of coreless LSMs come with engineering challenges. Without core materials, the magnetic circuit becomes weaker, requiring stronger magnets or denser winding configurations. Moreover, thermal management is more difficult because PCB-based windings are thermally insulated by the surrounding air. To address this, [24] and [33] have proposed advanced cooling techniques, including embedded dual-channel structures and forced convection paths, achieving temperature reductions of up to 20% during continuous operation. Coreless designs continue to gain traction in high-performance and compact systems, offering lightweight, low-vibration, and precision-friendly alternatives to traditional cored motors.

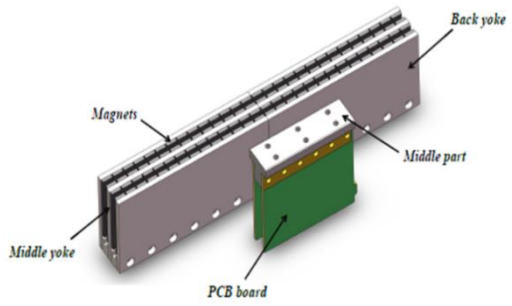


Fig. 5: Coreless LSM with air-cored windings for reduced cogging [10].

E. Use of Specialized Magnetic Materials

The selection of magnetic materials in Linear Synchronous Motors (LSMs) significantly influences performance factors such as magnetic flux density, efficiency, losses, and thermal behavior. In recent years, the adoption of advanced magnetic materials, particularly grain-oriented silicon steel (GO steel), has attracted considerable attention for improving magnetic performance and energy efficiency in high-precision LSMs.

Grain-oriented steels exhibit highly anisotropic magnetic properties, resulting in much lower core losses when the magnetic field is aligned with the rolling direction. This material choice enhances magnetic flux concentration, reduces eddy current and hysteresis losses, and improves system efficiency. According to [50], using GO steel instead of non-oriented electrical steel in stator laminations can increase magnetic flux density by 7–10% while simultaneously reducing total core losses by approximately 15% under sinusoidal excitation.

Moreover, [8] demonstrated that implementing GO steel in transverse flux LSMs resulted in 15% lower iron losses and smoother magnetic-saturation characteristics compared to conventional laminated core materials. These improvements are particularly beneficial in high-speed, high-frequency applications, where reduced core loss directly translates into improved thermal stability and reliability.

However, the benefits of GO steel come with fabrication challenges. The anisotropic nature of GO steel requires precise alignment of the magnetic field with the material's grain orientation. As noted in [51], misalignment can significantly degrade performance, negate the benefits, and even introduce local hot spots. Additionally, laser cutting and punching operations must be carefully controlled to prevent magnetic damage along the edges, as highlighted in [28]. To optimize these materials in LSMs, researchers have proposed hybrid stator configurations combining GO steel in high-flux regions with conventional materials elsewhere, striking a balance between performance gains and cost [51]. In summary, specialized magnetic materials, such as grain-oriented silicon steel, offer measurable efficiency and performance enhancements in LSMs, particularly for applications that demand low losses, compact volume, and high magnetic saturation. Their integration, however, requires advanced design, accurate modeling, and careful manufacturing processes to realize their potential fully.

F. Magnetic Excitation Method: Permanent Magnets vs. Excited Windings

The magnetic excitation method in Linear Synchronous Motors (LSMs) not only determines the magnetic field generation mechanism but also affects controllability, force density, energy efficiency, and system cost. LSMs are generally classified into two excitation categories: Permanent Magnet (PM) excitation and electromagnetically excited windings, including superconducting windings.

Permanent magnet-excited LSMs are widely adopted in industrial and automation applications due to their compact design, high efficiency, and simple control. Rare-earth magnets such as NdFeB are commonly used due to their high remanence and coercivity, enabling dense magnetic flux without external excitation [23], [43]. Studies like [43] report that PM-LSMs achieve over 90% efficiency in steady-state operation with minimal maintenance requirements. However, PM-based systems lack flux controllability and are susceptible to demagnetization under high temperatures or fault conditions [23].

In contrast, electromagnetically excited LSMs use field windings energized by a DC source, allowing real-time control over the magnetic flux. While this approach increases the system's complexity and power consumption, it enables dynamic field tuning and fault-

tolerant control, especially in variable-load environments [39].

An exceptionally advanced form of excitation uses high-temperature superconducting (HTS) windings, which offer ultra-low resistance and extremely high current densities. As illustrated in Fig. 6, superconducting coils are arranged in racetrack geometries and cryogenically cooled to achieve efficient excitation without thermal losses. Research in [36] demonstrated that HTS-excited LSMs provide 2–3 times higher thrust density than PM counterparts, with significantly lower thermal losses. Similarly, [33] reported a 30% reduction in magnetic leakage and a 20% improvement in overall efficiency using racetrack HTS coil optimization.

Despite their promising performance, HTS systems require complex cryogenic infrastructure and face challenges such as minimizing AC loss, quench protection, and high material costs [39], [52]. To mitigate these issues, hybrid systems combining PM excitation with superconducting field assist have also been proposed, achieving improved performance with reduced cooling demand [52].

In conclusion, while PM-based LSMs are well-suited for conventional applications, electromagnetically excited and HTS-based systems offer significant advantages in high-performance domains such as Maglev transportation, aerospace, and defense. Their ability to dynamically control the magnetic field and deliver high thrust with minimal losses positions them as a key technology for next-generation LSMs.

G. Winding Configurations

The winding configuration in Linear Synchronous Motors (LSMs) critically affects electromagnetic performance, thrust generation, thermal behavior, and overall system reliability. Appropriate selection and optimization of winding schemes can significantly reduce cogging force, improve magnetic field uniformity, and enhance thermal dissipation, all of which are vital for high-performance, compact applications.

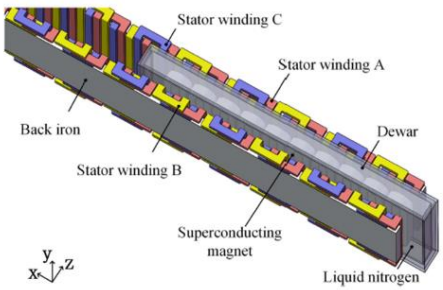


Fig. 6: HTS-excited LSM using racetrack coils and cryogenic cooling [36].

G. 1. Distributed and Concentrated

Winding arrangements are broadly categorized into distributed and concentrated types. Distributed windings, typically employed in long-stator and industrial LSMs, span multiple slots per pole and phase, generating a smoother magnetomotive force (MMF) waveform and minimizing spatial harmonics. This configuration enhances thrust smoothness and reduces cogging, making it suitable for high-precision linear motion [4], [29].

Conversely, concentrated windings, which localize coils around individual poles or teeth, offer superior compactness and ease of manufacturing. They are particularly effective in modular, coreless, or PCB-based LSM designs. For instance, the PCB-based concentrated winding reported in [10] reduced cogging force by 15% and improved the thrust-to-weight ratio similarly, in [36], optimized racetrack-shaped high-temperature superconducting (HTS) windings achieved higher force density with enhanced thermal performance.

In addition to conventional distributed or concentrated windings, fractional-slot and fractional-pitch windings have received considerable attention in the development of linear synchronous motors (LSMs), as these configurations enable reduced force ripple, suppressed high-order harmonics, and improved MMF uniformity. In fractional-slot designs, as demonstrated by Lerch, the fractional division of slots disrupts the spatial periodicity between teeth and magnets, thereby preventing the overlap of undesirable harmonics. This arrangement, due to the non-periodic distribution of windings, significantly reduces cogging, improves the flux waveform, and enhances dynamic stability at low and medium speeds. Furthermore, the same study found that shortening the effective coil length relative to the pole pitch not only reduces fifth- and seventh-order spatial harmonics but also reduces the end-winding length, thereby lowering copper losses and improving thermal performance.

On the other hand, in modern linear configurations, the use of fractional windings in combination with a segmented stator yields even more favorable outcomes. For instance, in the design presented by Tariq et al. [54], the partitioned stator flux-switching linear machine with concentrated fractional windings achieves a notable reduction in force ripple and an improvement in flux density. FEM analyses in this study indicate that properly adjusting the slot-to-pole ratio and selecting a fractional coil pitch not only mitigate tooth forces but also reduce end effects in long-stroke linear machines, ensuring a continuous and uniform thrust force.

overall, recent studies [53], [54] emphasize that the combination of concentrated windings with fractional-slot and fractional-pitch configurations is a key strategy

for enhancing the electromagnetic performance of next-generation LSMs, particularly in motors that require high force density, modular construction, and low-ripple operation.

G. 2. Single-Layer vs. Double-Layer Configurations

Single-layer windings are mechanically simpler but may suffer from uneven MMF distribution and increased magnetic leakage.

Double-layer windings, especially those with asymmetrical arrangements, provide improved field symmetry and reduced core saturation. In [28], as shown in Fig. 7, an asymmetrical double-layer winding structure in an ironless LSM resulted in a 12% increase in thrust force and more uniform flux linkage. In thermal analysis, [44] reported that multilayer windings reduced local hot spots by more than 15%, improving overall thermal stability.

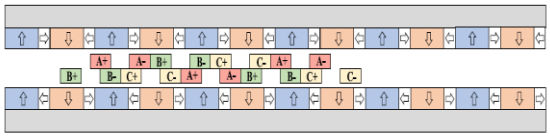


Fig. 7: Schematic of a Double-Layer PMLSM [28].

G. 3. Slot Skewing and Tooth Shaping

Advanced tooth-shaping and skewing techniques are widely employed to suppress detent force and cogging. The V-shaped tooth-slot design, shown in Fig. 8 and proposed in [26], reduced the detent force by approximately 38%, resulting in improved linear motion accuracy and a smoother dynamic response. In addition, the optimized slot–pole combination presented in [47] minimized the harmonic content of the magnetomotive force (MMF), which is particularly beneficial for high-speed applications.

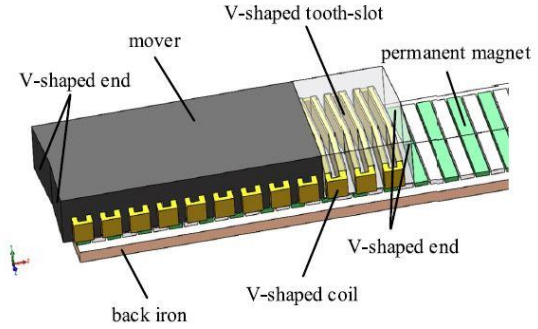


Fig. 8: V-shaped tooth-slot structure PMLSM [26].

G. 4. Modular and Segmented Winding Structures

Modular winding architectures offer scalable and reconfigurable design strategies for long-primary LSMs. In [27], modular segmentation of the primary part, shown in Fig. 9, reduced normal force ripple by 22% and improved thrust linearity. Furthermore, [25] introduced a ring-shaped modular winding structure optimized via multi-objective algorithms, achieving over 10% efficiency enhancement with minimal increase in system volume.

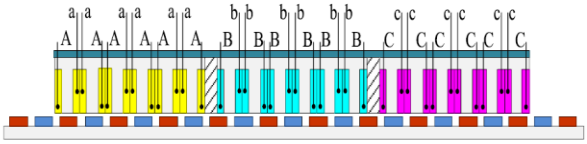


Fig. 9: Winding distribution of the PMLSM with segmental primary component [27].

Table 1: Structural configurations and characteristics of LSM

Structure & Feature	Type & Configuration	Advantages & Benefits	Drawbacks & Challenges
Magnetic Flux Direction	Longitudinal	Simple design, commonly used	Lower force density
	Transverse	Higher thrust density, suited for maglev	Complex modeling and structure
Physical Topology	Flat-type	Easy to manufacture, compact	High end-effect, lower efficiency
	Tubular-type	Symmetric flux, better cooling	More complex to build
Structural Symmetry	Single-sided	Lightweight, low cost	Higher cogging and ripple
	Double-sided	High thrust, uniform flux	Bulkier and heavier
Magnetic Core	With core	Better flux guidance	Higher hysteresis losses, ripple
	Coreless	No cogging, fast response	Complex design and cooling
Magnetic Material	GO Steel	Reduced eddy currents, better performance	High cost, difficult to process
Excitation Method	Permanent Magnets (PM)	Simple, stable field	No controllability
	Superconducting Windings	Very high thrust density, adjustable	Expensive and needs cryogenic cooling

Modeling of Linear Synchronous Motors

Accurate and comprehensive modeling of Linear Synchronous Motors (LSMs) is crucial for predicting performance, optimizing design parameters, and ensuring stable, reliable operation. Recent research emphasizes not only the development of accurate

models but also balancing model complexity with computational efficiency. Modeling approaches typically cover three essential aspects: magnetic field analysis, thermal behavior, and coupled Multiphysics simulation.

Given the significant influence of non-ideal electromagnetic phenomena on the accuracy and robustness of these modeling approaches, the end effect emerges as a critical factor that warrants a dedicated discussion in the next section.

A. End-Effect Phenomenon: Modeling, Impacts and Suppression Methods

The end effect is a critical design challenge in Linear Synchronous Motors (LSMs), arising from the inherent non-periodicity of the airgap magnetic field at the leading and trailing regions of the mover.

As demonstrated in flat-type LSMs in [27] and [48], the open magnetic circuit causes incomplete flux closure at the extremities, which in turn generates thrust drop, spatial force ripple, and significant distortion in the flux distribution. In contrast, tubular configurations inherently suppress this issue due to their enclosed magnetic flux path, leading to smoother field transitions and substantially lower end-effect severity, as reported in [29]. The impact of end effects extends beyond thrust reduction. According to the 3D electromagnetic analysis in [1], the discontinuity of the airgap field results in unbalanced inductance profiles, back-EMF harmonics, and transient force oscillations during the entry and exit of the mover. Neglecting these effects in analytical models leads to considerable performance prediction errors—up to 12% in thrust according to [31]. Moreover, end-region distortions are directly linked to thermal instabilities. As reported in [46], eddy current concentrations near end zones elevate local temperatures and introduce hotspots, emphasizing the need for coupled electromagnetic-thermal design strategies. Modeling approaches for capturing end effects vary in terms of complexity.

Analytical methods often require correction coefficients or modified MMF–permeance formulations, as implemented in the reluctance-based analytical model of [32], which compensates for flux imbalance and improves prediction accuracy. Nevertheless, FEM-based modeling remains the most reliable tool for quantifying end-effect-induced distortions, especially in long-stroke or modular structures.

Mitigation techniques include optimizing pole pitch and magnet width, adopting tubular magnetic structures [29], and refining stator or mover edge geometry to guide flux more uniformly. FEM-assisted compensation strategies, such as adjusting segment lengths or incorporating auxiliary end coils, can further reduce thrust roll-off and improve linearity. Collectively, these studies [1], [27], [29], [31], [32], [46], [48] highlight that proper modeling and mitigation of end effects is essential for reliable design, accurate force prediction, and thermal stability in next-generation LSMs.

B. Magnetic Field Modeling

Accurate magnetic field modeling is pivotal for the analysis, design, and performance prediction of Linear Synchronous Motors (LSMs). It directly affects the calculation of thrust force, evaluation of end effects, flux leakage, and thermal interactions, and serves as the foundation for multiphysics simulations and system-level control.

The modeling techniques can be categorized into three primary groups: analytical formulations, magnetic equivalent circuit (MEC) representations, and full-scale numerical approaches such as finite element method (FEM) simulations. Each approach offers a different balance between complexity, computational cost, and modeling fidelity.

B. 1. Analytical Modeling

Analytical modeling methods provide fast, insightful estimates, especially during early-stage design optimization. These methods rely on simplified geometrical assumptions, linear magnetic behavior, and uniform field distributions.

A typical formulation of the electromagnetic thrust force generated by a surface-mounted LSM is given by:

$$F_{\mathrm{x}} = (3/2) \cdot (P/\pi) \cdot \phi \cdot I \cdot cos(\theta) \quad (1)$$

where P is the number of poles, φ is the peak flux linkage per phase, I is the phase current (RMS), and θ is the electrical load angle. These models, while computationally efficient, often overestimate performance due to non-linearities, complex flux paths, and end effects. As shown in [1], a 3D analytical model for LSMs required FEM validation to account for end effects, highlighting the challenge of capturing non-ideal magnetic behavior. Similarly, [32] addresses these issues, namely non-linear inductance variations, magnetic field distortions, and end effects in winding-segmented permanent magnet linear synchronous motors (WS-PMLSM) by proposing an analytical model that uses a reluctance-based approach to quantify inductance unbalance and a virtual winding technique with Fourier analysis to mitigate magnetic field distortions from partial excitation. Validated through FEM simulations, this model improves the accuracy of predicting transient inductance and thrust fluctuations, providing a robust tool for the design and optimization of segmented motors.

B. 2. Magnetic Equivalent Circuit (MEC) Modeling

MEC models provide a middle ground between purely analytical and fully numerical techniques. In this approach, the magnetic domain of the LSM is

represented by a lumped-element network of reluctances and magnetomotive force (MMF) sources, mimicking Ohm's law in magnetic systems:

$$\Phi = \mathcal{F}/\mathcal{R} \quad , \quad \mathcal{R} = l/(\mu A) \tag{2}$$

where Φ is the magnetic flux, $\mathcal{F}$ is the magnetomotive force, $\mathcal{R}$ is the magnetic reluctance, and l, A, and μ denote the length, cross-sectional area, and permeability of the magnetic path.

A representative MEC diagram is shown in Fig. 10, extracted from [5], which demonstrates the main and leakage flux paths across the primary and secondary components of an LSM. The model includes individual reluctances (P_{ir1}, P_{loss2}, etc.), flux paths through air gaps and iron cores, and considers leakage fluxes, which are often ignored in simplified models. The MMF sources (F_a, F_b, F_c) represent the excitation inputs, while the branch structure allows accurate modeling of flux bifurcation and losses.

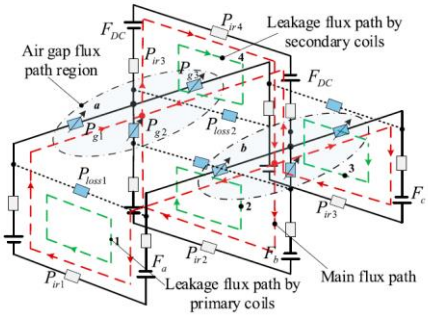


Fig. 10: 3-D magnetic circuit model of LSM [5].

Such detailed MEC models are especially beneficial in short-primary and modular LSM topologies, where end-effect compensation and leakage flux estimation become critical for thrust linearity and electromagnetic stability.

B. 3. Finite Element Method (FEM) Modeling

FEM is the most comprehensive and accurate tool for analyzing LSMs, particularly when non-linear material characteristics, geometric asymmetries, and end effects are present. It solves the magnetostatic or time-harmonic Maxwell's equations numerically:

$$\nabla \times (1/\mu \nabla \times A) = J \tag{3}$$

where A is the magnetic vector potential, and J is the source current density.

FEM has been widely used to validate other modeling methods and to conduct parameter sweeps across geometry, excitation, and cooling configurations. In [31], it was shown that ignoring end effects in FEM models could lead to a thrust overestimation of up to 12%. In [51], a coupled electromagnetic-thermal FEM model highlighted the temperature-dependent demagnetization risk in high-power LSMs.

C. Thermal Modelling

Thermal Modelling is essential for ensuring motor reliability, especially under high-speed or high-load conditions. Excessive heating can lead to insulation failure, magnet demagnetization, and accelerated wear. In many LSMs, localized heating near the end regions is observed due to asymmetric flux distribution caused by end effects. In [46], FEM-based thermal simulations revealed that eddy current losses near the stator ends can raise local temperatures by up to 30°C. This highlights the need to account for thermal hotspots caused by end effects during both the design phase and the implementation of cooling strategies.

Thermal Resistance Network (TRN) models, as applied in [3] and [24], provide quick estimations of temperature rise based on simplified thermal paths. In [24], the introduction of a staggered double-channel embedded cooling system reduced the hotspot temperature from 125°C to 96.5°C, thereby increasing motor lifetime by approximately 1.6 times, based on thermal degradation laws.

Finite element-based thermal simulations, discussed in [46], revealed that eddy current losses in coreless motors can elevate local temperatures by up to 30°C, highlighting the importance of integrated electromagnetic-thermal analysis for accurate prediction.

Furthermore, coupled electromagnetic-thermal models, such as those in [28], demonstrated that asymmetrical winding configurations could lead to uneven temperature distributions, resulting in performance degradation if not properly compensated during the design phase. While FEM provides high-resolution insight, it is computationally intensive. Therefore, simplified yet physically meaningful alternatives such as TRN models have gained significant attention for early-stage design evaluation.

These models represent the thermal behavior of various motor components using equivalent resistances and localized heat sources, enabling efficient estimation of temperature rise under different operating conditions.

A representative TRN model is shown in Fig. 11, adapted from [24], which captures the heat-conduction pathways across key regions of the motor, including windings, insulation, the iron core, the PLA casing, and embedded water-cooling channels.

Thermal resistances such as R_{plt}, R_{ptt}, and Rc_l denote conduction paths through structural elements, while nodes Q_i represent localized thermal losses, including copper loss P_{cu}. This model offers a comprehensive yet tractable method for predicting temperature profiles and evaluating the effectiveness of advanced cooling strategies.

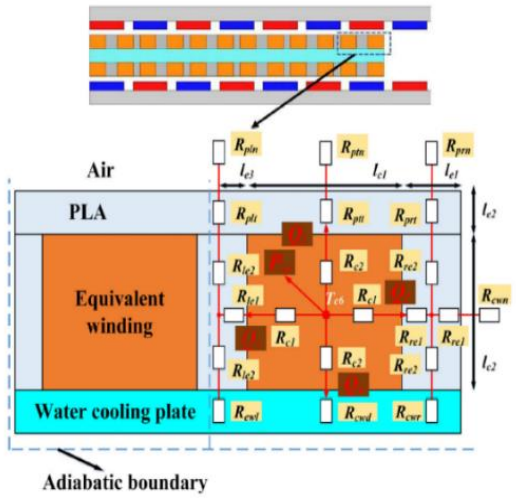


Fig. 11: Thermal network model of LSM [24].

D. Multiphysics and Hybrid Modelling

High-performance LSM applications, such as Maglev transportation and electromagnetic launchers, require multiphysics models that simultaneously consider electromagnetic, thermal, and mechanical phenomena. End effects play a significant role in multiphysics interactions, as they not only alter the boundary thrust force but also induce mechanical vibration and thermal nonuniformity.

In [22], integrating the Maxwell stress tensor and temperature-dependent material properties at the motor ends led to a more realistic prediction of the stress distribution during rapid acceleration.

Couple electromagnetic-thermal-mechanical models, presented in [22], achieved less than 3% deviation from experimental results when predicting motor behavior under dynamic loading conditions. Integration of Maxwell stress tensor computations with thermal and structural deformation models proved crucial in maintaining motor stability at high speeds. Hybrid modelling approaches, combining analytical field calculations with localized FEM, have also gained attention.

In [28], a hybrid 2D-3D model improved computational efficiency by 35% without sacrificing prediction accuracy, maintaining thrust force error below 5%. Hybrid modeling approaches combining analytical estimations with localized FEM refinement have proven especially useful in capturing edge-dominant electromagnetic and thermal behavior. As reported in [28] and [31], this approach improved accuracy in modeling LSMs with short secondary structures and non-periodic excitation, where end effect distortion becomes a dominant performance factor.

Overall, recent trends indicate that precise, multiphysics-based modelling is indispensable for the successful development of high-performance LSM systems, ensuring both superior operational efficiency and robust dynamic performance.

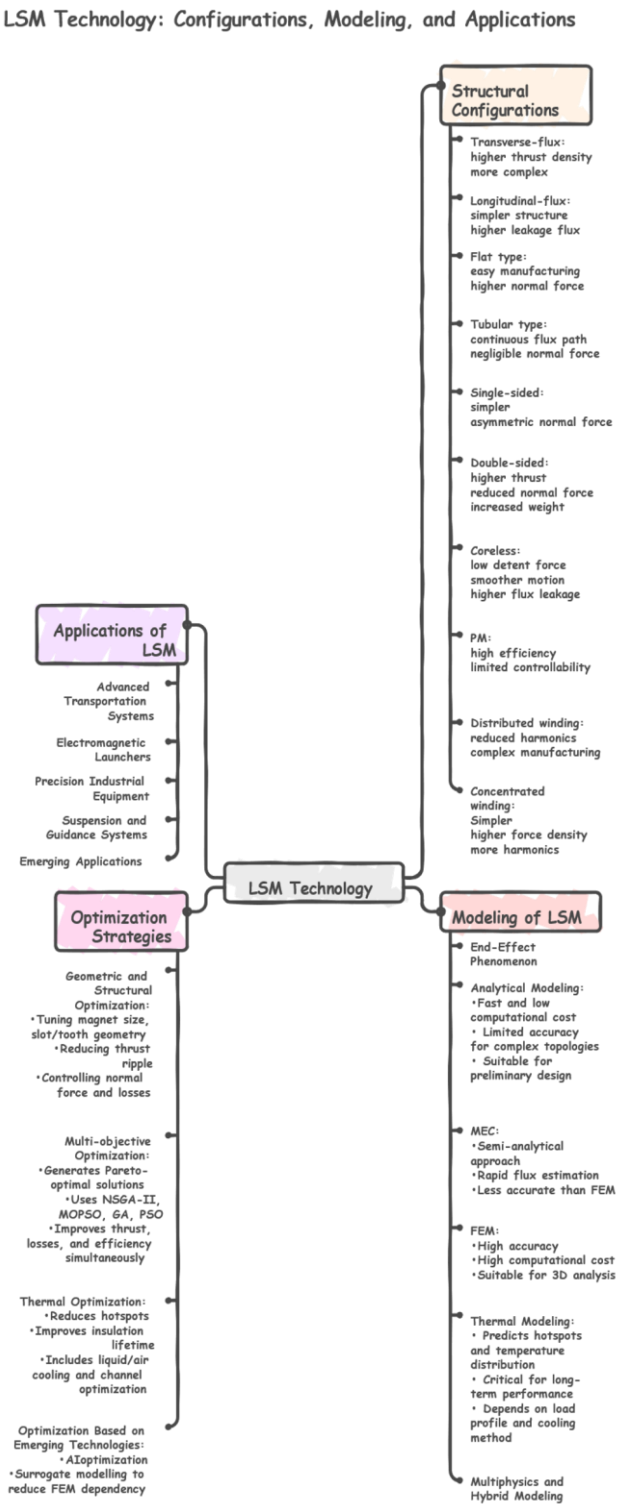


Fig. 12: The mind map for LSM technology.

Table 2: Comparison of LSM modelling methods by accuracy and computation time

Modeling Domain	Method	Accuracy	Computational Time	Typical Applications
Magnetic	Analytical	Medium	Very fast	Preliminary magnetic design
Magnetic	MEC	High	Fast	Concept validation and end-effect estimation
Magnetic	FEM	Very high	Slow	Final verification and non-linear flux analysis
Magnetic	Subdomain FEM	High	Medium	Dynamic response and partial saturation zones
Thermal	TRN (Thermal Resistance Network)	Medium High	Fast	Approximate temperature prediction; cooling design [3], [24]
Thermal	FEM	Very high	Slow	Detailed thermal distribution and hotspot analysis [46]
Coupled Multi-physics	EM-Thermal FEM	Very high	Very slow	Integrated design of electromagnetic–thermal systems [28]

Optimization Strategies for Linear Synchronous Motors

Optimization strategies are essential in the design of Linear Synchronous Motors (LSMs) to enhance thrust force, minimize losses, mitigate undesirable effects such as cogging, and improve overall system efficiency. Recent advancements integrate sophisticated computational tools, intelligent algorithms, and novel material applications to refine the performance of LSMs across various operating conditions.

A. Geometric and Structural Optimization

Structural geometry directly affects magnetic flux distribution, force generation, and thermal dissipation in LSMs. Several optimization strategies have focused on improving the geometric configuration to suppress unwanted forces and enhance performance. Skewed pole and slot arrangements, as presented in [25] and [26], effectively reduce detent and cogging forces. Specifically, [23] demonstrated that applying a V-shaped tooth-slot structure decreased detent force by approximately 38%, reducing peak force from 45 N to 28 N. This resulted in smoother operation, higher positioning precision and lower vibration levels during dynamic performance. Modular primary segmentation strategies in [27] showed a 22% reduction in normal force ripple, directly enhancing dynamic stability, particularly beneficial for high-speed linear actuators. Moreover, double-sided stator designs, as reported in [4] and [20], improved magnetic flux symmetry, resulting in an increase of 15–20% in effective thrust force compared to single-sided designs. This improvement, however, comes at the cost of increased system bulk and fabrication complexity. Tubular configurations, compared to flat designs, offer closed magnetic circuits that enhance flux density by up to 25%, as noted in [3] and [29], thereby providing higher thrust output and better thermal management.

B. Multi-objective Optimization with Intelligent Algorithms

As modern LSM designs must simultaneously satisfy multiple performance requirements such as maximizing thrust density, improving efficiency, reducing copper and iron losses, ensuring thermal stability, and minimizing weight and material cost, multi-objective optimization (MOO) has become an essential design tool. Intelligent optimization algorithms, in particular evolutionary and swarm-based methods, have been increasingly adopted due to their capability to explore complex design spaces and address conflicting objectives without relying on explicit gradient information.

Evolutionary algorithms such as NSGA-II, MOPSO, and GA have demonstrated strong suitability for LSM optimization because they naturally generate Pareto-optimal solutions. In [28], the application of NSGA-II enabled simultaneous improvement of thrust (12.5%) and copper loss reduction (8.7%) while maintaining dimensional constraints, illustrating the advantage of Pareto-based search strategies for constrained electromagnetic designs. Similarly, the hierarchical multi-objective optimization framework introduced in [33] for long-primary LSMs achieved an approximately 15% improvement in overall efficiency with less than 5% growth in volume, a critical requirement for large-scale transportation and Maglev applications.

Genetic Algorithms (GA) have been widely used to optimize magnet geometry, slot dimensions, and winding configurations due to their robust global search capability. However, studies report that GA-based processes require a large number of FEM evaluations and therefore incur higher computational costs. Particle Swarm Optimization (PSO), by contrast, generally offers

faster convergence and has been applied effectively to tune dimensional parameters and magnetic topologies. However, PSO may suffer from premature stagnation when confronted with highly non-linear behavior such as magnetic saturation or strong end-effect interactions, as noted in [35]. To overcome the computational burden of repeated FEM simulations, recent studies have introduced surrogate-assisted and AI-supported optimization models. As reported in [28] and [32], response surface models and machine-learning-based predictors can significantly reduce optimization time by approximating electromagnetic outputs, enabling rapid evaluation of multi-objective criteria. However, these methods remain sensitive to the quality of the training data, and their reliability decreases when the design space involves strong multiphysics coupling or discontinuities. Overall, the literature shows that intelligent optimization algorithms play a crucial role in modern LSM development. Each technique offers specific benefits global exploration (GA), fast convergence (PSO), and high-quality Pareto fronts (NSGA-II/MOPSO) but none independently handles the full range of multiphysics constraints, fabrication limitations, and real-time adaptability requirements. Consequently, future research is expected to move toward hybrid optimization schemes that combine global search, surrogate modelling, and adaptive learning to support high-performance and computationally efficient LSM design.

C. Thermal Optimization and Cooling System Design

Efficient thermal management is crucial to maintaining LSM performance and longevity, particularly under continuous high-load operation.

Thermal optimization strategies, such as the staggered double-channel water-cooling system presented in [24], reduced hotspot temperature from 125°C to 96.5°C, a 22.8% decrease, directly translating into an estimated 1.6-fold increase in motor operational lifespan.

Moreover, optimization of cooling structures for long-stator LSMs in [37] achieved a 17% reduction in hotspot temperatures and improved cooling uniformity by optimizing the coolant path design and embedding secondary flow channels.

Machine learning-based prediction models, as implemented in [3], further enhanced thermal optimization by forecasting thermal maps with less than 5% error compared to experimental results, allowing real-time thermal management strategies to be developed without expensive prototyping.

D. Optimization based on Emerging Technologies

The application of superconducting materials and novel magnetic structures presents new frontiers in LSM optimization. In [33], racetrack-shaped superconducting coils were optimized, achieving a 20% increase in force density and a 30% reduction in magnetic leakage compared to traditional circular coils.

Optimization of coreless high-temperature superconducting (HTS) LSMs, as discussed in [36], resulted in 15% lower thrust ripple and 10% higher average thrust, thereby offering better performance stability, particularly under dynamic high-load conditions.

Furthermore, the optimization of Halbach arrays in [20] increased thrust by up to 18% without significantly increasing the mover's weight, a critical advantage for high-acceleration applications such as electromagnetic launchers.

The integration of emerging technologies, combined with intelligent, multiphysics optimization frameworks, paves the way for the next generation of LSMs capable of meeting the increasing demands for precision, power density, and thermal resilience.

Applications of Linear Synchronous Motors

Due to their inherent advantages, including direct linear thrust generation, high positioning accuracy, flexible structural configurations, and reduced mechanical complexity, Linear Synchronous Motors (LSMs) have found widespread adoption across diverse industrial, transportation, defense, and emerging technological sectors. This section outlines major application areas, highlighting key advantages, challenges, and specific examples supported by quantitative data.

A. Advanced Transportation Systems (Maglev and High-Temperature Superconducting Systems)

One of the most prominent applications of LSMs is in magnetic levitation (Maglev) systems for high-speed transportation. LSMs provide direct thrust without mechanical contact, enabling silent, efficient, and high-speed operation.

High-Temperature Superconducting (HTS) LSMs, as explored in [36] and [39], have achieved thrust force densities exceeding 80 N/cm², approximately 30% higher than conventional permanent magnet designs. Furthermore, the use of Halbach arrays in [20] increased propulsion efficiency by 18%, thereby reducing energy consumption in Maglev systems. Maglev trains, operating at speeds over 500 km/h, benefit from LSMs' smooth acceleration profiles, minimal maintenance requirements, and integrated propulsion and levitation forces. Advanced cooling strategies and lightweight coreless designs further enhance operational feasibility and cost-effectiveness.

B. Electromagnetic Launchers

In the defense and aerospace sectors, electromagnetic launchers using LSMs are increasingly

favored for applications requiring rapid acceleration and high-precision trajectory control.

Coreless permanent magnet LSMs configured with Halbach arrays, as discussed in [20] and [21], have demonstrated acceleration capabilities exceeding 5000 m/s². These systems offer mechanical simplicity, reduced mass, and real-time force control compared to traditional mechanical launch systems.

Electromagnetic launchers benefit from LSMs' ability to generate high instantaneous thrust without combustion, offering safer, quieter, and more controllable solutions for military and space applications.

C. Precision Industrial Equipment and Production Lines

In industrial automation, LSMs are widely used for high-precision positioning and motion control across applications such as CNC machines, automated assembly lines, pick-and-place robotics, and semiconductor manufacturing. Studies such as [10], [27] and [48] have shown that replacing rotary-to-linear mechanical conversions with direct-drive LSMs can improve positioning accuracy by up to 25% and reduce maintenance costs by over 30%. Tubular LSM configurations are particularly favored for vertical Z-axis actuators, where high thrust density and minimal vibration are critical for maintaining micron-level precision during high-speed operations.

Moreover, reducing of backlash and mechanical compliance through direct linear actuation leads to faster cycle times and improved production throughput in modern smart factories.

D. Suspension and Guidance Systems

In addition to thrust generation, specific LSM configurations can simultaneously provide suspension and lateral guidance forces, a feature critical for contactless high-speed applications.

Dual-sided homopolar LSM designs, introduced in [6] and [39], achieved integrated propulsion and suspension forces with improved stability margins. Suspension forces reaching up to 60 N/cm² have been reported, enhancing levitation robustness even under dynamic loading conditions. Such integrated solutions eliminate the need for additional mechanical components, such as air bearings or wheels, simplifying the system architecture and reducing overall system weight.

E. Emerging Applications in Robotics, Medicine, and Renewable Energy

Due to their lightweight designs, high controllability, and non-contact operation, LSMs are increasingly explored in emerging fields such as:

- Medical Robotics: LSMs provide precise, vibration-free actuation for surgical tools and non-invasive magnetic stimulation devices. Early prototypes demonstrated force control accuracies within ±2% of target profiles, as noted in [49].
- Assistive Robotics: Coreless tubular LSMs are being integrated into robotic exoskeletons and prosthetics, offering smooth, compliant motion with high torque-to-weight ratios.
- Renewable Energy Systems: Linear generators based on LSM principles are being developed for wave energy conversion, where direct-drive systems minimize energy loss associated with mechanical linkages.

While many of these applications are still under active research and experimental validation, the potential for widespread adoption is significant, given the unique advantages LSMs offer in precision, efficiency, and system simplification.

Table 3 :Application domains of LSMs

Application Area	Required Features	Advantages of LSMs	Examples
High-speed Transportation (Maglev)	High thrust, magnetic levitation, low friction	Quiet, high speed, contactless motion	[1], [6], [36], [39], [49]
Electromagnetic Launchers	Fast acceleration, high energy pulses	Mechanical simplicity, real-time control	[20], [21], [49]
Precision Industry	Positioning accuracy, high linear stability	Gearless, precise, reliable	[10], [27], [29], [48]
Integrated Suspension & Guidance	Mult axis force generation	Unified system, design simplification	[6], [39], [44]
Emerging Fields	Lightweight, soft actuation, non-invasive	Innovation potential, experimental	

Research Gaps and Future Challenges

Reviewing the recent literature on Linear Synchronous Motors (LSMs) reveals that, despite notable progress in structural configurations, modelling approaches, optimization techniques, and application-driven designs, several fundamental gaps remain. A consistent issue reported across studies is the persistence of end-effect distortion, which continues to degrade thrust, flux distribution, and back-EMF quality even in advanced designs such as transverse-flux motors, segmented stators, and coreless or tubular configurations [1], [27], [31], [48]. Likewise, while tubular structures offer improved flux continuity and reduced end effects, they introduce significant manufacturing complexity and sensitivity to mechanical tolerances, in contrast, flat structures remain more practical but suffer from leakage flux and normal-force variation [3], [29], [49]. Coreless and HTS-based architectures demonstrate reduced cogging and enhanced force density, yet studies indicate challenges

including flux leakage, structural fragility, and demanding thermal management requirements [10], [33], [36]. Even the adoption of grain-oriented steels, which improves flux density and reduces losses, is limited by material anisotropy, edge degradation, and fabrication constraints [8], [50].

Modelling approaches also exhibit clear limitations. Analytical and MEC-based models struggle to represent nonlinear and non-periodic end regions accurately, leading to thrust prediction errors of up to 12% relative to a full FEM analysis [1], [31]. Although multiphysics methods have been explored, most studies isolate electromagnetic, thermal, or mechanical domains, limiting predictive accuracy under dynamic or high-speed conditions. Thermal modelling gaps are particularly evident in coreless, tubular, and HTS systems, where hotspot formation and non-uniform temperature distributions remain difficult to predict and mitigate [24], [46]. Furthermore, reduced-order or hybrid models despite promising results in [28], [32] are not yet sufficiently mature for comprehensive design workflows.

In the field of optimization, existing work demonstrates improvements through evolutionary and intelligent algorithms [30], [35], but key practical factors such as thermal degradation, magnetostriction, cost, manufacturability, and vibration highlighted independently in several studies [7], [46], [49] are rarely integrated into multi-objective frameworks. Optimization research on emerging structures such as HTS and segmented stators remains preliminary, and no studies address real-time or adaptive optimization under varying load and environmental conditions.

Application-oriented works in Maglev transportation, electromagnetic launchers, precision manufacturing, and medical systems show promising performance [1], [6], [20], [27], [49]. However, most reported results rely on simulations or short-duration testing, with limited long-term validation under thermal cycling, vibration, or high-speed operation. Integrated propulsion–levitation–guidance systems still present unresolved coupling effects and dynamic instabilities [6], [39], [44] and scalability remains a challenge for HTS-based and GO-steel-based designs.

Overall, the literature indicates that future progress in LSM technology depends on more accurate end-effect Modelling, fully integrated multiphysics simulation frameworks, advanced thermal management strategies, cost-effective manufacturing approaches for complex magnetic structures, intelligent and adaptive optimization techniques, and long-term reliability assessment. Furthermore, emerging architectures such as hybrid PM–HTS excitation, segmented coreless motors, and non-integer-pole structures [47], [54]. represent promising yet underexplored directions for next-generation high-performance LSM systems.

Conclusion

This paper has presented a comprehensive review of 54 high-quality research articles covering the structural design, modeling approaches, optimization strategies, and diverse applications of Linear Synchronous Motors (LSMs). The key findings can be summarized as follows:

- Structural Diversity: LSMs exhibit a wide range of configurations from flat and tubular types to transverse-flux, coreless, and superconducting structures selected based on application demands, magnetic and thermal requirements, and manufacturing feasibility.
- Advanced Modeling: The use of multidimensional and hybrid modeling techniques, such as MEC, subdomain methods, thermal analysis, and machine learning, is increasing the precision of LSM simulation. FEM remains the most validated tool.
- Optimization Trends: Recent research emphasizes intelligent multi-objective algorithms, modular architecture, thermal optimization, and the application of advanced materials to improve efficiency and control.
- Expanding Applications: LSMs are now utilized in Maglev systems, electromagnetic launchers, precision manufacturing, medical devices, and robotic platforms, positioning them as a vital component of future technologies.

Despite these advances, challenges remain, including:

- Accurate control under variable load conditions
- Efficient cooling solutions for coreless and HTS designs
- Cost constraints of magnetic materials and HTS technologies

Future research is recommended to focus on:

- Fast and precise multiphysics modeling for coupled force, temperature, and vibration analysis.
- Machine learning algorithms for intelligent design and optimization.
- Integration of novel materials like graphene and nanocomposites.
- Development of adaptive structures with online parameter tuning.

Overall, this review contributes to the field by integrating recent advancements in LSM structural design, electromagnetic and thermal Modelling, and modern optimization strategies within a unified analytical framework. By consolidating findings across these domains, the study clarifies key design trade-offs, highlights persistent modelling and performance challenges, and outlines research directions that can

guide the development of more efficient and application-oriented LSM systems.

Author Contributions

Conceptualization and supervision were carried out by Hamidreza Izadfar. The literature review and data collection were performed by Seyede Delaram Sadr. Analysis and interpretation of the reviewed studies were jointly conducted by Seyede Delaram Sadr and Hamidreza Izadfar. The initial manuscript was drafted by Seyede Delaram Sadr, while manuscript review and editing were undertaken by Hamidreza Izadfar.

Conflict of Interest

The author declares that there is no conflict of interest regarding the publication of this paper.

Acknowledgment

The authors declare that there is no acknowledgment for this study.

Funding

This research received no external funding.

Abbreviations

A list of abbreviations used in the manuscript is provided below:

PMLSM	Permanent Magnet Linear Synchronous Motor
FEM	Finite Element Method
LSM	Linear Synchronous Motors
MEC	Magnetic equivalent circuit
PM	Permanent Magnet
WS-PMLSM	Winding Segmented- Permanent Magnet Linear Synchronous Motors
TRN	Thermal Resistance Network
MOO	Multi-Objective Optimization
GA	Genetic Algorithms
PSO	Particle Swarm Optimization
Maglev	Magnetic Levitation
HTS	High-Temperature Superconducting

References

[1] G. Lv, R. Zhi, L. Cui, B. Liu, "3-D analytical model of the end effect in the transverse flux linear synchronous motor for maglev vehicle with pitch angles," IEEE Trans. Magn., 61(3): 1-8, 2024.

[2] Y. Yang, Q. Wu, "A fast prediction method for thrust performance of axial array permanent magnet synchronous linear motor," IEEE Access, 12: 91242-91251,2024.

[3] T. Wu, P. Dai, G. Xue, Y. Guo, G. Lei, J. Zhu, Y. Wang, "A novel thermal analysis method for tubular pm linear motors based on transfer learning," IEEE Trans. Trans. Electrif., 11(3): 7379-7388, 2025.

[4] Q. Wu, G. Yang, E. Tang, L. Wang, X. Wang, Z. Wang, "A slotted double-primaries permanent magnet synchronous linear motor with a low thrust ripple," IEEE/ASME Trans. Mechatron., 29(5): 3786-3798, 2024.

[5] G. Lv, L. Cui, "Analysis and calculation for a novel transverse flux linear synchronous motor with 3-D magnetic circuit method," IEEE Trans. Ind. Electron., 71(11): 14683-14690, 2024.

[6] G. Lv, Z. Zhang, Y. Liu, T. Zhou, "Analysis of forces in linear synchronous motor with propulsion, levitation and guidance for high-speed maglev," IEEE J. Emerging Sel. Top. Power Electron., 10(3): 2903-2911, 2022.

[7] T. Dong, W. Feng, B. Zhang, Z. Fu, R. Fu, G. Zhao, "Analysis of natural vibration characteristics of permanent magnet linear synchronous motor considering elastic contact," IEEE Trans. Appl. Supercond., 34(8): 5203805, 2024.

[8] T. Dong, R. Fu, B. Zhang, B. Peng, X. Wei, "Analysis of permanent magnet linear synchronous motor made by oriented silicon steel sheet," IEEE Trans. Ind. Appl., 53(3): 3332-3340, 2023.

[9] H. Shi, W. Yang, S. Fu, H. Liu, J. Yang, K. Li, "Characteristics analysis and dynamic test of air-cored permanent magnet linear synchronous motor for null-flux pmeds vehicle," IEEE Trans. Instrum. Meas., 73: 3524115, 2024.

[10] L. Li, J. Zhang, H. Qiao, S. Li, H. Lan, Z. Xu, "Design and optimization of a new structure PCB coreless-type linear motor," in Proc. IEEE/ASME International Conference on Advanced Intelligent Mechatronics (AIM): 674-678, 2024.

[11] A. Boduroglu, Y. Demir, B. Cumhur, M. Aydin, "A novel track structure of double-sided linear PM synchronous motor for low cost and high force density applications," IEEE Trans. Magn., 57(2): 8201305, 2021.

[12] C. Wen, J. Liu, W. Wang, J. Liu, Z. Zhao, J. Liu, "Research on improved permanent magnet linear synchronous motor for direct-drive application," IEEE Trans. Magn., 55(10): 8107007, 2019.

[13] Z. Zhang, M. Luo, J. Duan, B. Kou, "Design and modeling of a novel permanent magnet width modulation secondary for permanent magnet linear synchronous motor," IEEE Trans. Ind. Electron., 69(3): 2749-2758, 2022.

[14] J. Di, H. Chen, H. Chen, J. E. Fletcher, L. Meng, "Design of line-start permanent magnet linear synchronous motors with transient optimization," IEEE Trans. Ind. Appl., 61(1): 77-88, 2025.

[15] F. Yue, Z. Sun, W. Xu, Md. R. Islam, "Electromagnetic design and vibration analysis of a homopolar linear synchronous motor," IEEE Trans. Appl. Supercond., 31(8): 0602405, 2021.

[16] N. N. L. Do, A. J. Taberner, B. P. Ruddy, "A linear permanent magnet synchronous motor for large volume needle-free jet injection," IEEE Trans. Ind. Appl., 55(2): 1437-1446, 2019.

[17] A. Boduroglu, M. Gulec, Y. Demir, E. Yolacan, M. Aydin, "A new asymmetric planar v-shaped magnet arrangement for a linear PM synchronous motor," IEEE Trans. Magn., 55(7): 8105905, 2025.

[18] L. Wu, Y. Li, Q. Lu, "Detent force fast optimization method of modular permanent-magnet linear synchronous motors," IEEE Trans. Ind. Electron., 71(12): 16191-16199, 2024.

[19] Y. Mao, Z. Sun, W. Zhou, Z. Zhuang, H. Qian, "Electromagnetic design of toroidal permanent magnet linear synchronous motor," IEEE Access, 9: 98005-98012, 2021.

[20] L. Yu, S. Chang, J. He, H. Sun, J. Huang, H. Tian, "Electromagnetic design and analysis of permanent magnet linear synchronous motor," Energies, 15(15): 5441, 2022.

[21] Z. Xiao, J. Fang, L. Nie, X. Wang, Y. Zan, C. Wang, "Excitation field analysis of cogging-free superconducting motors for electromagnetic catapult," IEEE Trans. Appl. Supercond., 34(8): 5209504, 2024.

[22] R. Xu, J. Zhao, J. Wang, Z. Yu, Z. Pan, L. Wang, S. Wang, X. Hu, M. Jiang, "Heat transfer performance improvement of permanent magnet synchronous linear motor based on embedded staggered double channel water cooling structure," IEEE Trans. Transp. Electrif., 10(4): 10158-10168, 2024.

[23] K. Yang, L. Zhang, R. Wang, "Hierarchical multi objective optimization of a multi sided permanent magnet linear synchronous motor with ring structure winding for conveyor systems," IEEE Access, 12: 128833-128842, 2024.

[24] Z. Lan, L. Chen, X. Xiao, Y. Luo, M. Deng, S. Zhu, "Detent force suppression of permanent magnet linear synchronous motor based on a V shaped tooth-slot structure," IET Electr. Power Appl., 17(4): 535-546, 2023.

[25] Q. Tan, B. Tian, X. Wang, X. Huang, L. Li, "Primary component segmental design to suppress the normal force ripple for the permanent magnet linear synchronous motor," IET Electr. Power Appl., 18(7): 801-812, 2024.

[26] Z. Xie, Q. Lu, W. Mei, Y. Li, "Improved analytical modeling of a novel ironless linear synchronous machine with asymmetrical double layer winding topology," IEEE Trans. Ind. Appl., 57(2): 1411-1419, 2021.

[27] Y. Zhao, Z. Liu, J. Gong, X. Yu, J. Qiu, J. J. Rodríguez-Andina, "Improved multobjective optimization of tubular slotless permanent magnet linear synchronous motor for high performance Z Axis actuators," IEEE/ASME Trans. Mechatron., 30(6): 1-12, 2025.

[28] G. Lv, L. Cui, R. Zhi, "Inductance analysis of transverse flux linear synchronous motor for maglev trains considering three dimensional operating conditions," IEEE Trans. Ind. Electron., 71(1): 769-776, 2024.

[29] G. Lv, R. Zhi, L. Cui, B. Liu, "Magnetic field and force calculation of transverse flux linear synchronous motor with improved analysis model," IEEE Trans. Transp. Electrif., 10(3): 6361-6369, 2024.

[30] Q. Sun, M. Wang, M. Liu, C. Zhang, L. Li, "Magnetic field distortion analysis and suppression for the minimum unit winding segmented moving magnet linear motor, "IEEE Trans. Ind. Electron., 71(4): 3452-3460, 2024.

[31] Z. Zhao, W. Yang, Z. Yan, B. Jia, Y. Xu, J. Luo, "Mult objective optimization of superconducting linear motor considering general racetrack coils," IEEE Trans. Appl. Supercon., 34(9): 3603209, 2024.

[32] X. Hu, J. Zhao, Z. Pan, Z. Yu, X. Yang, "Optimal design of PMSLM based on extremum robust domain characteristic," IEEE Trans. Ind. Electron., 71(6): 6063-6072, 2024.

[33] F. Cui, Z. Sun, W. Xu, H. Qian, C. Cao, "Optimization analysis of long primary permanent magnet linear synchronous motor," IEEE Trans. Appl. Supercon., 31(8): 0603504, 2021.

[34] L. Nie, J. Fang, "Optimization of coreless high temperature superconducting linear synchronous motor," IEEE Trans. Appl. Supercon., 34(8): 3603704, 2024.

[35] A. Yingke Chen, B. Rong Wei, C. Zhigang Xue, "Optimization of long stator synchronous linear motors for high-speed maglev trains," in Proc. IEEE 10th International Power Electronics and Motion Control Conference (IPEMC2024-ECCE Asia), 2024.

[36] K. Liu, G. Ma, L. Jun, Z. Zhao, P. Zhou, J. Xu, "Performance improvement for superconducting linear synchronous motor with general racetrack coils," IEEE Trans. Energy Conversion, 39(2): 1436-1445, 2024.

[37] J. Zheng, S. Nie, H. Jing, Y. He, M. Li, Y. Ma, Z. Ding, "Potential and electro mechanical coupling analysis of a novel HTS maglev system employing double sided homopolar linear synchronous motor," IEEE Trans. Intell. Transp. Syst., 25(10): 13573-13583, 2024.

[38] Q. Wu, L. Wang, G. Yang, E. Tang, X. Wang, "Ramming mechanism based on permanent magnet synchronous linear motor," IEEE Trans.Transp. Electrif., 10(1): 122-134, 2024.

[39] Q. Tan, M. Wang, L. Li, J. Li, "Research on noninteger pole number for segmental permanent magnet linear synchronous motor," IEEE Trans. Ind. Electron., 68(5): 4120-4130, 2021.

[40] E. Shirzad, "Analytical model for double sided linear permanent magnet inner armature synchronous machine with slot-less stator at on-load in different patterns of magnetization," Electr. Eng., 106: 1533-1547, 2024.

[41] J. Di, J. E. Fletcher, W. Li, "Simplified piecewise model of line start permanent magnet linear synchronous motors," IEEE Trans. Ind. Appl., 58(5): 6093-6104, 2022.

[42] K. Mao, Y. Ji, X. Du, D. Hu, "Structural dynamics modeling of an on board hts magnet prototype cooled by solid nitrogen for high-speed maglev trains," IEEE Trans. Transp. Electrif., 10(4): 8298-8308, 2024.

[43] J. Zhao, Q. Mou, C. Zhu, Z. Chen, J. Li, "Study on a double-sided permanent magnet linear synchronous motor with reversed slots," IEEE/ASME Trans. Mechatron., 26(1): 3-12, 2021.

[44] Q. Sun, M. Wang, M. Liu, L. Li, "Suppressing the eddy current damping of the permanent magnet linear synchronous motor by setting the toothed cooling plate," IEEE Trans. Transp. Electrif., 9(2): 3050-3059, 2023.

[45] S. U. Chung, J. Y. Lee, "Teeth arrangement and pole slot combination design for PMLSM detent force reduction," Energies, 14(23): 8141, 2021.

[46] J. Di, J. E. Fletcher, W. Li, H. Xu, Y. Fan, "Transient analysis of line start permanent magnet linear synchronous motors," IEEE Trans. Energy Convers., 36(4): 3365-3375, 2021.

[47] X. Zhou, H. Li, L. Wang, C. Peng, S. Wang, L. Liang, Z. Deng, "Vertical dynamic response analysis of HTS maglev vehicle excited by a designed coreless typed PMLSM," IEEE Trans. Transp. Electrif., 9(2): 3421-3433, 2023.

[48] R. Fu, B. Zhang, T. Dong, W. Feng, F. Meng, "Vibration analysis of grain oriented silicon steel sheet PMLSMs considering material anisotropy," IEEE Trans. Appl. Supercon., 34(8): 5204405, 2024.

[49] R. Fu, T. Dong, B. Zhang, G. Zhao, W. Feng, "Vibration analysis of pmlsm considering magnetostriction under high intensity magnetic fields," IEEE Trans. Magn., 60(10): 8102805, 2024.

[50] G. Fuchs, A. Kugi, W. Kemmetmüller, "Magnetic equivalent circuit modeling of a permanent magnet linear synchronous motor composed of curved segments," Mechatron., 104: 103256, 2024.

[51] J. F. Gieras, Z. J. Piech, Linear Synchronous Motors: Transportation and Automation Systems. Boca Raton, FL, USA: CRC Press, 2000.

[52] I. Boldea, Linear Electric Machines, Drives, and MAGLEVs Handbook. Boca Raton, FL, USA: CRC Press, 2013.

[53] T. Lerch, "From transverse flux machine to fractional slot concentrated winding permanent magnet synchronous machine," Arch. Elect. Eng, 73(2): 393-407, 2024.

[54] S. Tariq, F. Khan, B. Ullah, N. Muhammad, B. Alghamdi, "Novel partitioned stator flux-switching permanent magnet linear machine: Design, analysis, and optimization," Machines (MDPI), 11(3): 390, 2023.

Biographies



Seyede Delaram Sadr was born in Dezful, Iran, in 1994. She received the B.Sc. degree in Power Electrical Engineering from Lorestan University in 2019 and the M.Sc. degree in Power Electronics and Electrical Machines Engineering from Iran University of Science and Technology in 2024. She is currently pursuing the Ph.D. degree in Power Electrical Engineering at Semnan University. Her research interests include the design and development of electrical machines and linear motors. She is particularly interested in the practical modeling and construction of electrical motors.

- Email: S.Delaram_Sadr@semnan.ac.ir
- ORCID: 0009-0005-3299-4833
- Web of Science Researcher ID: NA
- Scopus Author ID:NA
- Homepage: NA



Hamid Reza Izadfar is currently an Associate Professor in the Electrical and Computer Engineering Department of Semnan University. His main research interests are the design and analysis of electric machines and drives.

- Email: hrizadfar@semnan.ac.ir
- ORCID: 0002-0002-9685-0389
- Web of Science Researcher ID: NA
- Scopus Author ID:NA
- Homepage: NA

Journal of Electrical and Computer Engineering Innovations
(JECEI)
Journal homepage: http://www.jecei.sru.ac.ir

Research paper

Bridging the Speed–Accuracy Gap: RT-DETR versus YOLOv8s for Real-Time Brain MRI Tumor Detection

Amir Mahdi Sedghi , ***Shala Nemati*** *

Department of Computer Engineering and Artificial Intelligence Research Institute, Shahrekord University, Shahrekord, Iran.

Article Info

Article History:
Received 03 November 2025
Reviewed 07 Januarys 2026
Revised 01 February 2026
Accepted 17 February 2026

Keywords:
Brain MRI
Brain tumor detection
Real-time object detection
Transformer based detection
YOLOv8s

*Corresponding Author's Email Address: *s.nemati@sku.ac.ir*

Abstract

Background and Objectives: Brain tumor detection in MRI images is critical for early diagnosis and effective treatment, yet manual interpretation is time-consuming and prone to variability. Deep learning models such as YOLO have advanced real-time object detection, but their speed–accuracy tradeoff remains a challenge for medical tasks involving small or low-contrast lesions. The potential of transformer-based detectors like RT-DETR to simultaneously improve accuracy and maintain real-time speed in clinical settings is not well established.
Methods: This study performed a controlled head-to-head comparison between the proposed model (RT-DETR-L-based model) and the YOLOv8s models using a curated, single-class brain tumor MRI dataset of 300 images. Both models were trained and evaluated under identical conditions with comprehensive data augmentation strategies, and their performance was assessed using standard object detection metrics including precision, recall, specificity, and mean Average Precision (mAP) across multiple Intersection over Union (IoU) thresholds.
Results: The proposed model achieved higher localization fidelity and overall accuracy compared to YOLOv8s, with mAP@0.5:0.95 of 0.493 versus 0.421 and mAP@0.5 of 0.963 versus 0.941. Precision and specificity for the proposed model reached 1.000, eliminating false positives, while recall was slightly lower than YOLOv8s (0.925 vs. 0.932), indicating a marginal increase in missed detections. Qualitative analysis confirmed robust detection across various tumor sizes and intensities, though some small or low-contrast lesions were missed.
Conclusion: Proposed model surpasses YOLOv8s in accuracy and specificity for real-time brain tumor detection in MRI images, offering a promising balance between speed and precision. However, its slightly lower recall underscores the need for further refinement to minimize false negatives. The findings suggest transformer-based detectors can narrow the speed–accuracy gap in medical imaging, but broader validation and optimization for resource-constrained environments are required for clinical deployment. Future work should focus on enhancing sensitivity and generalizability through advanced augmentation, larger datasets, and ensemble approaches.

This work is distributed under the CC BY license (http://creativecommons.org/licenses/by/4.0/)

How to cite this paper:
A. M. Sadeghi, S. Nemati, "Bridging the speed–accuracy gap: RT-DETR versus YOLOv8s for real-time brain MRI tumor detection," J. Electr. Comput. Eng. Innovations, 14(2): 311-326, 2026.
DOI: 10.22061/jecei.2026.12463.883
URL: https://jecei.sru.ac.ir/article_2543.html

2345- 3044/© 2026 The Authors. Published by Shahid Rajaee Teacher Training University.

Introduction

Brain tumors, though relatively rare compared with other systemic cancers, impose a disproportionate burden in terms of mortality, morbidity, and years of life lost, particularly in younger and middle-aged adults [1]. Prognosis strongly depends on timely and accurate characterization of lesions; delays or uncertainty in initial identification can adversely affect therapy planning and longitudinal monitoring [2]. Magnetic Resonance Imaging (MRI) is the primary non-invasive modality for brain tumor assessment because of its superior soft-tissue contrast and multi-parametric capability [3], [4]. However, manual interpretation and lesion localization are time-consuming, susceptible to inter-observer variability, and increasingly strained by rising imaging volumes and workforce limitations [5]. These factors motivate automated systems that can accelerate reliable triage, focus expert attention, and serve as consistent region-of-interest (ROI) proposal mechanisms.

The rapid progress of deep learning in general computer vision—spanning large-scale classification (e.g., ImageNet breakthroughs), object detection (Faster R-CNN, YOLO families), and instance segmentation (Mask R-CNN)—has catalyzed analogous advances in medical image analysis [6]-[13]. Benchmark datasets such as COCO and PASCAL VOC have driven architectural innovation and optimization for accuracy and latency [14]-[15]. These advances have translated to neuroimaging tasks including tumor detection and segmentation, where supervised convolutional neural networks (CNNs) and, more recently, self-configuring frameworks have set strong baselines [5], [16]-[18]. In clinical pipelines, detection (localizing candidate lesion regions) and segmentation (delineating precise boundaries) are complementary. Robust detection can act as a computationally efficient precursor to fine-grained volumetric segmentation or uncertainty estimation, reducing the search space and enabling adaptive resource allocation [16]-[18].

Despite their popularity for real-time applications, one-stage CNN detectors such as YOLO variants prioritize speed and may underperform on challenging medical scenarios characterized by small, low-contrast, or heterogeneous lesions embedded in complex anatomical backgrounds [11], [12], [19], [20]. Empirical studies and engineering analyses highlight an inherent speed–accuracy tension; systems optimized exclusively for maximal frame rate may sacrifice contextual reasoning critical for subtle pathology [21]-[24]. In clinical decision support, the acceptable operating point must balance rapid inference (to enable workflow integration, e.g., prospective triage or intra-session feedback) with high sensitivity and localization fidelity to minimize missed lesions while avoiding excessive false positives that erode trust and efficiency.

Transformer based vision models have recently redefined representational capacity by leveraging global self-attention to model long-range dependencies that conventional convolutions capture only implicitly or with deeper hierarchical stacking [16], [25], [26]. DETR introduced a set prediction paradigm for object detection, simplifying post-processing but initially incurring convergence and efficiency challenges [16]. Subsequent refinements—deformable attention, hierarchical backbones, and improved query selection—have narrowed the latency gap with optimized CNN detectors [18], [19]. RT-DETR exemplifies this trajectory by incorporating efficiency-oriented architectural choices to bring transformer detectors into the real-time regime while retaining the advantages of global context modeling and anchor-free design [19]. Concurrently, transformer or hybrid architectures have demonstrated promise across diverse medical imaging tasks, including segmentation and multi-modal fusion, suggesting potential gains for lesion detection in data-constrained, high-variance settings [25], [26].

Applying such architectures to brain MRI tumor detection is compelling for several reasons: (1) global attention can integrate dispersed anatomical cues and subtle intensity transitions; (2) query-based, anchor-free formulations may better accommodate scale variability without extensive hand-tuned priors; (3) improved box quality (higher localization precision across stricter overlap thresholds) can facilitate downstream segmentation refinement; and (4) if inference latency approaches that of optimized CNN baselines, clinical adoption barriers related to throughput diminish [19], [20], [25]. Nevertheless, it remains an open question whether modern real-time transformer detectors can simultaneously preserve near-YOLO speed and deliver measurable accuracy improvements within the constraints of modest, single-class medical datasets—conditions under which overfitting, limited diversity, and noisy annotations can blunt theoretical architectural advantages [5], [20].

While RT-DETR has been explored in other medical domains such as chest X-ray disease detection [27] and general medical object detection benchmarks [28], this work establishes the first focused evaluation of applying a recent real-time transformer detector (RT-DETR) specifically to Brain MRI tumor detection—and assesses its ability to outperform a strong, widely used convolutional baseline (YOLO) while maintaining clinically viable inference speed. Our contributions are: (i) introducing and validating the application of RT-DETR for brain MRI tumor detection as a novel use of a real-time transformer in medical imaging; (ii) a controlled

head-to-head comparison of RT-DETR versus a lightweight YOLO variant on a curated single-class brain tumor MRI detection task; (iii) a detailed analysis of the accuracy–latency trade-off, emphasizing localization quality (multi-threshold mean Average Precision) and sensitivity to subtle lesions; and (iv) a discussion of deployment implications for using transformer-based detectors as region-of-interest generators or decision support components within clinical workflows. By demonstrating how a transformer architecture can narrow the traditional speed–accuracy divide in neuro-oncologic detection, this study supports principled model selection and lays groundwork for expansion to multi-class, multi-institutional, and segmentation-augmented pipelines.

Related Works

Early computer-aided brain tumor analysis relied on hand-crafted feature pipelines coupled with classical classifiers. Bahadure et al. combined Berkeley Wavelet Transform (BWT)–based tissue segmentation with statistical texture descriptors and an SVM, achieving 96.51% accuracy and 97.72% sensitivity, illustrating the discriminative value of multi-scale wavelet representations yet inheriting dependence on sequential preprocessing (skull stripping, contrast enhancement) and limited scalability to heterogeneous MRI protocols [29]. Moving toward reduced manual feature dependence, Farnoosh and Noushkaran proposed an iterative co-clustering plus K-Means (ICCK) strategy on BraTS2019, reaching 99.28% accuracy but only 82.41% sensitivity, underscoring that high global accuracy can mask clinically critical false negatives when unsupervised blocks miss subtle tumor voxels [30].

The transition to deep learning introduced multi-stage and modular CNN pipelines. Gunasekara et al. integrated a classification CNN, region-based localization (R-CNN), and Chan–Vese active contours, obtaining a Dice score of 0.92 while demonstrating that classical variational refinement can still sharpen CNN coarse masks in limited data settings [31]. Veeramuthu et al. explored combined feature- and image-based classifiers (CFIC) to fuse handcrafted statistics with deep representations, improving robustness (98.97% accuracy; 98.86% sensitivity) but increasing architectural complexity and maintenance burden [32]. Mercaldo et al. then established a compact single-class brain MRI object detection baseline using a one-stage YOLO model on 300 images, reporting precision 0.943, recall 0.932, and mAP@0.5 0.941, thereby demonstrating that high real-time detection performance is achievable even under pronounced data scarcity [20]. Concurrently, lightweight U-Net derivatives, such as the pared architecture evaluated by Walsh et al. on BITE data (mean IoU 89%), showed that carefully pruned encoder–decoder designs can approach heavier models without aggressive augmentation when anatomical variability is moderate [33].

Recent progress centers on attention, multi-modal semantics, and refined detection heads. Transformer backbones and hierarchical self-attention, exemplified by Swin Transformer classification of four tumor categories (97% accuracy) [34], highlight improved global context modeling over purely convolutional inductive biases. Extending semantic fusion, a CLIP-guided 3D U-Net framework introduced multi-level language–vision alignment to raise whole-tumor Dice by 4.8% over a baseline 3D U-Net, evidencing the promise of cross-modal priors for ambiguous boundaries [35]. On the detection side, building on the small-data YOLO baseline of Mercaldo et al. [20], which reported strong mAP@0.5 (0.941) but lower multi-threshold mAP@0.5:0.95 (0.421), medical adaptations of YOLO incorporate specialized attention and loss refinements: YOLO-NeuroBoost reported mAP up to 99.48% on Br35H via dynamic kernel selection, CBAM attention, and Inner-GIoU loss emphasizing small, overlapping lesions [36]; an attention-driven YOLOv5m variant with Enhanced Spatial Attention reduced false positives in multi-type detection [37]. Parallel efforts tailor lightweight detection: MobileNetV2-SSD with a modified low-level FPN substantially boosted recall (~98%) for small meningioma loci while trading some precision (~89%) [38].

Efficiency constraints in resource-limited or point-of-care contexts have motivated edge-friendly detectors: a MobileNet-backboned RetinaNet variant attained balanced large vs. small lesion AP with markedly reduced computational load, demonstrating that architectural depth can be sacrificed if multi-scale feature fusion and focal optimization are preserved (preprint) [39].

Across these detection frameworks, a persistent tension emerges between maximizing recall for subtle, low-contrast foci and suppressing false positives that erode clinical trust—particularly acute in single-class triage workflows.

Given the chronic scarcity of labeled medical images, specialized augmentation and synthetic data have become pivotal. Lesion-aware compositing (CarveMix) improved segmentation generalization by explicitly modeling lesion context transitions [40], while GAN-based augmentation (StyleGANv2-ADA) markedly elevated radiogenomic classification accuracy across diverse datasets by enriching minority morphological patterns [41]. These approaches complement architectural advances, yet may not fully resolve the speed–accuracy trade-offs inherent in real-time detection pipelines.

Prior brain MRI work has either (i) emphasized segmentation quality over latency (transformer or 3D fusion methods), (ii) optimized lightweight CNN detectors sometimes at a sensitivity cost for diminutive or low-contrast tumors, or (iii) boosted sensitivity via augmentation/ensembles without systematically quantifying multi-threshold localization fidelity under real-time constraints; moreover, while Mercaldo et al. reported both mAP@0.5 and a substantially reduced mAP@0.5:0.95 (0.421), they did not benchmark against transformer-based detectors nor analyze architectural trade-offs under identical training regimes [20]. Direct, controlled head-to-head evaluation of a modern real-time transformer detector (RT-DETR) against a strong lightweight YOLO baseline on a constrained, single-class medical detection task remains underexplored. Our study addresses this gap by jointly analyzing speed-conscious architecture choice, strict IoU-stratified mAP, and the precision–recall balance, thereby clarifying whether global attention can narrow the historical speed–accuracy divide in clinically oriented brain tumor detection.

Method

This section presents detailed information about the dataset used, the data preparation procedure, and the data augmentation strategies applied to improve deep learning model performance in detecting and localizing brain tumors. The primary objective is to establish a sound basis for fair and scientific comparison between the proposed approach and existing methods—particularly the YOLO model—and to clarify the preprocessing and augmentation processes that enhance model generalizability.

A. Dataset

In this study, the same dataset employed in the reference YOLO-based brain cancer detection work was used [20]. The rationale for selecting this dataset is to ensure fair comparative conditions between the proposed model and YOLO so that the effect of architecture and processing methods can be evaluated without interference from extraneous variables. Using a shared dataset enables more precise analysis of performance differences and prevents bias arising from disparate data sources.

The dataset contains 300 brain MRI images, each representing a slice of the human brain. The images cover different anatomical orientations and exhibit substantial variation in spatial position, size, and intensity (contrast). Although cases originate from different underlying tumor pathologies (e.g., meningioma, pituitary adenoma, glioma), the provided annotations define a single detection class ‘tumor’; subtype labels are not part of the dataset [20]. The images are in JPG format, and the dataset is publicly accessible via the Roboflow platform [42]. Fig. 1 shows two sample images illustrating the morphological and dimensional diversity of the tumors.

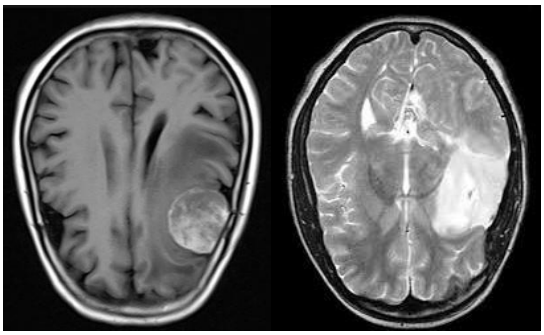


Fig. 1: MRI dataset samples showing variations in tumor morphology, size, and intensity.

B. Data Augmentation

One of the fundamental challenges in training deep learning models—especially in medical imaging—is the scarcity of labeled data [36]. Although a corpus of 300 images is acceptable for preliminary experimentation, it is typically insufficient for training a high-capacity deep network and may lead to model overfitting. To increase generalization capability and reduce the likelihood of overfitting, the use of data augmentation techniques during training is essential [43].

Data augmentation refers to a set of procedures that generate new, diverse samples by applying controlled, stochastic transformations with specified probabilities to the original images [44]. These transformations may include rotation, translation, scaling, random cropping, flipping, brightness and contrast adjustment, random noise injection, or combinations thereof. The central aim is to simulate diverse real-world conditions and enable the model to learn stable, invariant features insensitive to minor variations.

In this study, a comprehensive collection of augmentation techniques was applied to the training images to make the model more robust against spatial and photometric variations and to enhance its ability to generalize to unseen instances. As shown in Table 1, the augmentation strategy encompassed color space modifications (HSV hue ±1.5%, saturation ±70%, value ±40%), geometric transformations (50% horizontal flip probability, ±10% translation, ±50% scaling), and advanced techniques including 100% mosaic augmentation probability and 40% random erasing. This multi-faceted approach enabled the model to correctly detect tumors even when they differed from those seen during training. Overall, data augmentation is recognized as a key factor in the success of deep learning models in

medical image analysis and plays a critical role in performance improvement.

It is important to note that we utilized an on-the-fly augmentation pipeline provided by the Ultralytics framework. Unlike offline augmentation where a fixed set of images is generated prior to training, our approach applies stochastic transformations dynamically in memory during each training batch. Consequently, the model is exposed to a slightly different variation of the training samples in every epoch, effectively expanding the diversity of the dataset beyond the initial 300 images and mitigating overfitting risks.

Table 1: Data augmentation configuration for RT-DETR model training

Aug. Type	Enabled Tech.	Parameters
Color Space	HSV variations	H: ±1.5%, S: ±70%, V: ±40%
Geometric	Horizontal flip, Translation, Scaling	50% flip prob., ±10% translation, ±50% scaling
Advanced	Mosaic, Random erasing, RandAugment	100% mosaic prob., 40% erasing prob.
Disabled	Vertical flip, Rotation, Shear, Perspective, MixUp, CutMix, Copy-paste	N/A
Training Strategy	Close mosaic in final epochs	Last 10 epochs

C. Proposed Model

The RT-DETR-L (Real-Time Detection Transformer – Large) model is a recent object detection architecture first introduced by Baidu's research team in 2023 [19]. Its primary goal is to provide a transformer-based detection framework that combines the high accuracy of attention-driven models with practical speed suitable for real-time applications. RT-DETR is one of the earliest transformer-based, end-to-end, anchor-free detection models that addresses speed and complexity limitations of earlier architectures such as DETR [45].

The input to RT-DETR is an RGB image of fixed size. The output is a set of bounding boxes accompanied by class labels and confidence scores for each detected object.

This output structure is fully analogous to standard object detection models such as YOLO and Faster R-CNN, enabling direct performance comparison.

Fig. 2 provides a schematic overview of the proposed model. It comprises seven principal components:

1. Backbone: A high-capacity CNN producing a multi-scale pyramid of progressively lower-resolution, semantically enriched feature maps.
2. Multi-Scale Feature Maps: Hierarchically aligned tensors that preserve spatial correspondence while aggregating cross-level contextual semantics.
3. Efficient Hybrid Encoder: A lightweight module combining multi-scale attention with local mixing (feed-forward/convolutional) to capture long-range dependencies without sacrificing fine detail, all under real-time latency constraints.
4. IoU-Aware Query Selection: Quality-driven filtering that retains only top object queries (by predicted IoU/quality), suppressing low-value or redundant tokens before decoding to cut computation.
5. Decoder: Stacked layers apply cross-attention to encoded features and self-attention among the remaining queries, iteratively refining spatial localization and class discrimination.
6. Detection Head: Parallel heads mapping refined query embeddings to class logits and normalized box parameters (center x, y, width, height), often with iterative refinement across decoder layers.
7. Outputs: A compact, non-redundant set of class–box predictions with confidence/quality scores, typically usable directly (often NMS-free due to query selection) or in downstream post-processing pipelines.

During training, each component fulfills a distinct role.

The backbone extracts low-level and mid-level features; the Transformer module leverages attention to encode long-range dependencies and contextual information; and the detection head predicts bounding box coordinates and class membership probabilities based on the Transformer output.

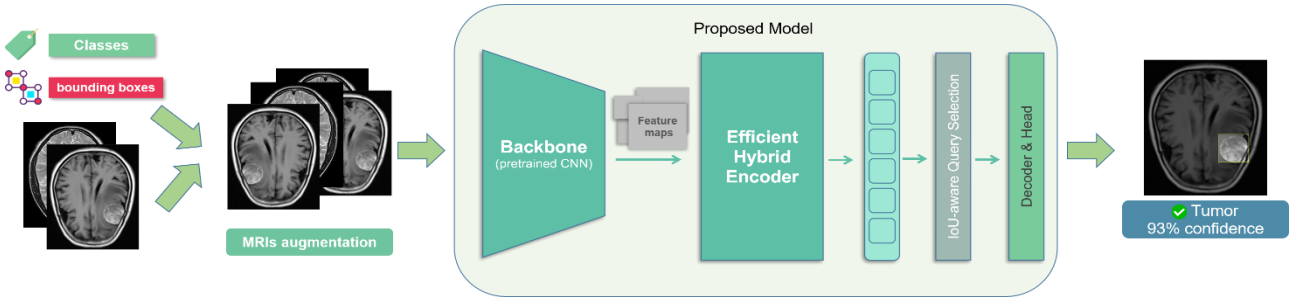


Fig. 2: Proposed model architecture diagram showcasing its main components.

Table 2: Layer-wise structure of proposed model and their functions.

layer	from	n	params	module	arguments
0	-1	1	25248	modules.block.HGStem	[3, 32, 48]
1	-1	6	155072	modules.block.HGBlock	[48, 48, 128, 3, 6]
2	-1	1	1408	modules.conv.DWConv	[128, 128, 3, 2, 1, False]
3	-1	6	839296	modules.block.HGBlock	[128, 96, 512, 3, 6]
4	-1	1	5632	modules.conv.DWConv	[512, 512, 3, 2, 1, False]
5	-1	6	1695360	modules.block.HGBlock	[512, 192, 1024, 5, 6, True, False]
6	-1	6	2055808	modules.block.HGBlock	[1024, 192, 1024, 5, 6, True, True]
7	-1	6	2055808	modules.block.HGBlock	[1024, 192, 1024, 5, 6, True, True]
8	-1	1	11264	modules.conv.DWConv	[1024, 1024, 3, 2, 1, False]
9	-1	6	6708480	modules.block.HGBlock	[1024, 384, 2048, 5, 6, True, False]
10	-1	1	524800	modules.conv.Conv	[2048, 256, 1, 1, None, 1, 1, False]
11	-1	1	789760	modules.transformer.AIFI	[256, 1024, 8]
12	-1	1	66048	modules.conv.Conv	[256, 256, 1, 1]
13	-1	1	0	modules.upsampling.Upsample	[None, 2, 'nearest']
14	7	1	262656	modules.conv.Conv	[1024, 256, 1, 1, None, 1, 1, False]
15	[-2, -1]	1	0	modules.conv.Concat	[1]
16	-1	3	2232320	modules.block.RepC3	[512, 256, 3]
17	-1	1	66048	modules.conv.Conv	[256, 256, 1, 1]
18	-1	1	0	modules.upsampling.Upsample	[None, 2, 'nearest']
19	3	1	131584	modules.conv.Conv	[512, 256, 1, 1, None, 1, 1, False]
20	[-2, -1]	1	0	modules.conv.Concat	[1]
21	-1	3	2232320	modules.block.RepC3	[512, 256, 3]
22	-1	1	590336	modules.conv.Conv	[256, 256, 3, 2]
23	[-1, 17]	1	0	modules.conv.Concat	[1]
24	-1	3	2232320	modules.block.RepC3	[512, 256, 3]
25	-1	1	590336	modules.conv.Conv	[256, 256, 3, 2]
26	[-1, 12]	1	0	modules.conv.Concat	[1]
27	-1	3	2232320	modules.block.RepC3	[512, 256, 3]
28	[21, 24, 27]	1	7303907	modules.head.RTDETRDecoder	[1, [256, 256, 256]]

Table 2 details the layer-wise architecture of proposed model (RT-DETR-based model); each layer performs a specific processing function. For example, convolutional layers in the backbone extract primary features, encoder and decoder layers in the Transformer model non-local relations, and linear layers in the head predict coordinates and classes.

Among RT-DETR-L's advantages over YOLOv8s is its attention-based architecture [19]. The attention mechanism enables RT-DETR-L to learn richer spatial and contextual relationships than purely convolutional networks like YOLOv8s, yielding improved performance in detecting small or overlapping objects. Both RT-DETR-L and YOLOv8s employ anchor-free designs—predicting

bounding boxes directly without predefined anchor templates. However, incorporation of attention in RT-DETR-L enhances accuracy, especially in more complex scenarios [19].

Regarding speed, RT-DETR employs Transformer optimizations such as dynamic heads and efficient attention to bring inference latency closer to that of YOLO models [46]. Although its speed is slightly lower than YOLOv8, this difference is generally negligible in medical applications where diagnostic accuracy supersedes raw throughput. Specifically, for brain tumor detection, priority lies with accuracy and reliability.

From an architectural technique perspective, both RT-DETR and YOLO utilize convolutional backbones for feature extraction; the principal divergence lies in the detection head and bounding box prediction mechanism. RT-DETR, by removing anchors and using dynamic queries, yields a simpler and more flexible structure and, through set-based loss (e.g., Hungarian matching), achieves more precise alignment between predictions and ground truth objects. Additionally, the use of Transformer attention facilitates modeling of global, non-local relationships that are not explicitly captured in YOLO, which emphasizes local features [19].

On the reference COCO dataset, RT-DETR-Large (RT-DETR-L) has achieved higher mAP than YOLOv8s. For example, RT-DETR-L attains mAP = 53.0% on COCO val2017, whereas YOLOv8s achieves mAP = 44.9% under the same evaluation settings [19], [47]. This performance gap primarily stems from RT-DETR's use of transformer-based attention mechanisms that more effectively capture global context and its IoU-aware query selection and advanced loss formulations, which together improve both localization and classification precision compared to the convolution-only backbone and loss strategies employed by YOLOv8s.

As illustrated in Fig. 3, the proposed model (the large variant of RT-DETR (RT-DETR-L)) comprises approximately 33 million parameters, which is substantially higher than the 11 million parameters of YOLOv8s [47]. While RT-DETR-L incorporates structural optimizations and efficient attention mechanisms that partially alleviate its computational demands, the model nonetheless necessitates significantly greater computational resources for both training and maintenance compared to YOLOv8s. This increased resource requirement may present challenges for deployment in environments with limited computational capacity.

A key strength of proposed model (RT-DETR-based model) is its ease of fine-tuning [48]. Like YOLO, it is fully supported by the Ultralytics package and can be readily retrained on new datasets. Fine-tuning allows the model to adapt to dataset-specific characteristics, improving performance in specialized tasks such as brain tumor detection.

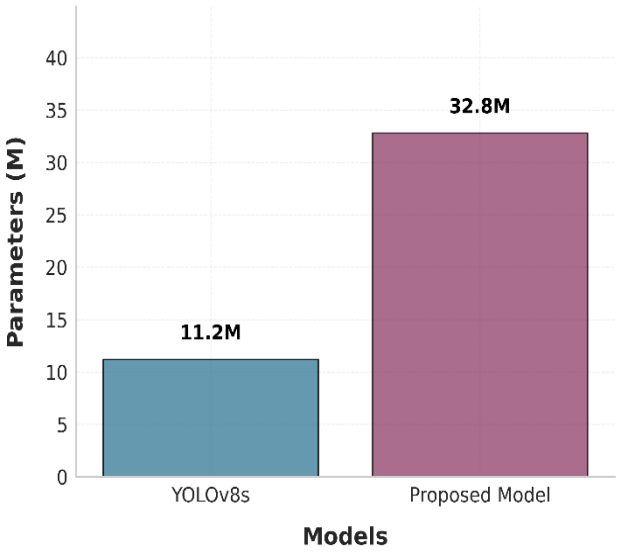


Fig. 3: Parameter comparison.

In medical imaging, model selection must consider accuracy, processing speed, and memory usage [6]. While RT-DETR-L delivers high accuracy in identifying and delineating complex objects, its larger parameter count and computational demands may challenge real-time deployment or use in hardware-limited systems (e.g., edge devices or portable units). However, in clinical and research centers equipped with sufficient infrastructure, this model can significantly enhance diagnostic precision and reliability. Overall, operational adoption of RT-DETR-L in medical applications depends directly on hardware availability, required response time, and the relative importance of accuracy; in scenarios where accuracy outweighs speed and memory constraints, proposed model (RT-DETR-L-based model) is a suitable option. However, optimizing the model's memory footprint through techniques such as quantization or pruning is essential to enable deployment in resource-constrained environments, such as portable medical units or edge devices.

In the test phase, the trained RT-DETR model processes an MRI image as input and outputs the tumor bounding box coordinates, class label, and confidence score for each prediction. These outputs can then be used for model performance evaluation or to support clinical decision-making.

The proposed model was trained in the Kaggle environment on an NVIDIA Tesla P100 GPU (CUDA-enabled) with 16 GB RAM using the default Ultralytics configuration (batch size 16, input resolution 640×640, 50 epochs) and the SGD optimizer with an initial learning rate of 0.01. After each epoch, performance was

evaluated on a held-out validation set to track optimization progress. The single checkpoint achieving the highest validation means Average Precision (mAP) over the 50 epochs was retained and then used once to generate test-set predictions. The test set remained completely unseen during training and model selection, ensuring an unbiased estimate of generalization and limiting overfitting.

Results and Discussion

In this section, we examine and analyze the performance of the proposed model in comparison with the YOLOv8s model for brain tumor detection and localization in MRI images. First, the evaluation metrics employed in this study are introduced; then the quantitative and analytical results of the models are presented.

Finally, the strengths and weaknesses of the models and future recommendations are discussed.

In Fig. 4, the normalized confusion matrix of proposed model on the test data is shown.

The confusion matrix provides a visualization of the distribution of the model's predictions across different classes and was specifically computed using the same fixed IoU threshold of 0.5 and a confidence threshold of 0.25 as YOLOv8s, ensuring a consistent basis for direct comparison between the two models. As observed, proposed model correctly identified 97% of tumor samples, which is 2% higher than the value obtained using YOLOv8s [20]. These thresholds were chosen to align the evaluation metrics and facilitate a fair comparison of classification performance, while filtering out low-confidence detections. Additionally, proposed model demonstrated a very low false positive rate, indicating its strong ability to distinguish between tumorous and healthy regions.

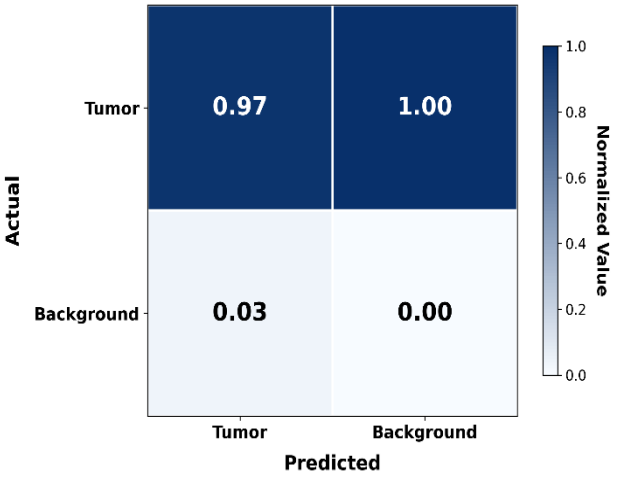


Fig. 4: Normalized confusion matrix of proposed model predictions on test data.

A. Evaluation Metrics

In this study, to evaluate and compare model performance, standard object detection metrics were used, including Precision, Recall (Sensitivity), Specificity, and mean Average Precision (mAP). The confusion matrix was computed using a fixed IoU threshold of 0.5, while the values reported in the results chart in Fig. 5 were calculated using aggregated thresholds across IoU values ranging from 0.5 to 0.95. This distinction is necessary to account for the difference in recall values observed between the confusion matrix and the results table.

The mathematical definitions of these metrics are given below.

Precision is a metric that indicates, among all regions the model has labeled as tumor, how many are truly tumor.

This is especially important in medical applications, because higher precision means fewer false positives, which reduces unnecessary patient anxiety, additional costs, and unwarranted treatments. It is computed as shown in:

$$Precision = \frac{TP}{TP + FP} \tag{1}$$

where TP (True Positive) is the number of correctly detected positive samples and FP (False Positive) is the number of incorrectly detected positive samples.

Recall (Sensitivity) measures the model's ability to correctly identify all positive samples (true tumors). It reflects how many real tumors the model has not missed.

The high importance of recall in medicine is due to the need to minimize false negatives, thereby reducing the likelihood of overlooking real tumors and preventing irreversible consequences for the patient. It is computed as:

$$Recall = \frac{TP}{TP + FN} \tag{2}$$

where FN (False Negative) is the number of missed positive samples.

Specificity is the complementary metric to recall and shows how well the model correctly identifies healthy (non-tumorous) samples. High specificity means fewer false positives and helps avoid unnecessary treatments. It is computed as:

$$Specificity = \frac{TN}{TN + FP} \tag{3}$$

where TN (True Negative) is the number of correctly identified negative samples.

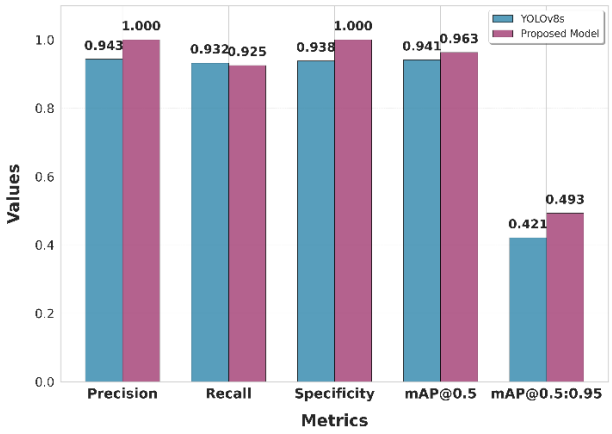


Fig. 5: Comparison of proposed model and YOLOv8s performance metrics.

While precision and recall each measure a single aspect of performance, in practical applications a balance between them is usually required. Therefore, the Precision–Recall curve is commonly used to analyze performance at different decision thresholds.

Average Precision (AP) is the area under the Precision–Recall curve for a given class and provides a combined measure of precision and recall. In other words, AP tells us how well the model performs across all threshold values rather than at a single operating point.

$$mAP = \frac{1}{N}\sum_{i=1}^{N} AP_i \tag{4}$$

where N is the number of classes and AP_i is the AP for class i.

In this study, mAP was computed in two forms: mAP@0.5 and mAP@0.5:0.95. In the first case, predictions are considered correct when the Intersection over Union (IoU) between the predicted region and the ground-truth region is at least 0.5. IoU measures the overlap between the predicted bounding box and the ground-truth tumor region and is defined as:

$$IoU = \frac{Area\ of\ Overlap}{Area\ of\ Union} \tag{5}$$

The higher the IoU, the more accurate the spatial localization of the model. In the mAP@0.5:0.95 setting, the mean mAP is computed over IoU thresholds from 0.5 to 0.95 in steps of 0.05 to evaluate the model not only at lower thresholds but also at stricter localization accuracies. This metric provides a more comprehensive and realistic picture of the model's performance in precise tumor detection and localization.

In the Precision–Recall curve shown in Fig. 6 corresponding to the proposed model, the AP (mAP for the tumor class) at IoU ≥ 50% is approximately 0.93. The curve was generated using a confidence threshold of 0.001, ensuring that all potential detections were considered during evaluation. This curve aggregates performance across varying IoU thresholds (0.5–0.95), providing a broader view of the model's ability to balance precision and recall at different localization accuracies.

More complete numerical evaluation results of the models are provided in Fig. 5. According to this chart, proposed model outperformed YOLOv8s in both mAP@0.5:0.95 and mAP@0.5.

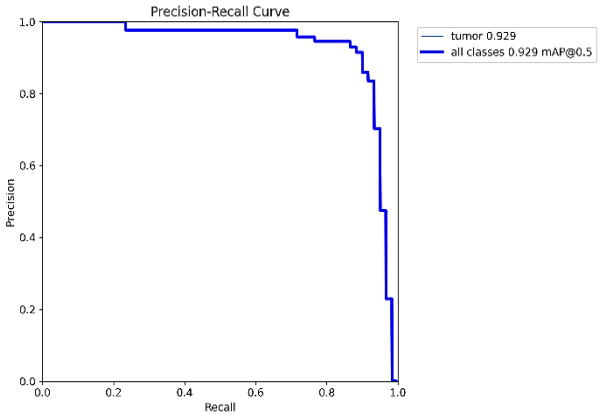


Fig. 6: Precision–Recall curve of proposed model across varying IoU thresholds.

Values reported in Fig. 5 correspond to aggregated thresholds (IoU@0.5:0.95) and a confidence threshold of 0.001 to provide a comprehensive evaluation, whereas values in the confusion matrix reflect a fixed IoU threshold of 0.5 and a confidence threshold of 0.25. Specifically, mAP@0.5:0.95 for proposed model was 0.493 compared to 0.421 for YOLOv8s. Also, mAP@0.5 for RT-DETR-L was 0.963 versus 0.941 for YOLOv8s [20]. These results indicate that proposed model achieved higher localization fidelity and accuracy across stricter IoU thresholds.

To validate the real-time capabilities of the models, we measured the inference latency on an NVIDIA GPU. RT-DETR-L achieved an average inference time of 40.59 ms per image (approx. 24.6 FPS), whereas YOLOv8s achieved 8.58 ms per image (approx. 116.6 FPS). Although RT-DETR-L is computationally heavier due to its transformer blocks, its processing speed remains well within the acceptable range for real-time clinical support systems (typically requiring >20 FPS for smooth visualization), confirming that the substantial accuracy gains do not come at a prohibitive cost to throughput.

However, YOLOv8s achieved slightly higher recall (0.932 vs. 0.925), demonstrating a marginal advantage in sensitivity. This tradeoff highlights that while proposed model effectively reduces false positives, further

refinement is needed to minimize false negatives, which are critical in medical imaging applications.

The proposed model demonstrated zero false positives in the evaluated test set, indicating high precision and specificity. However, its slightly lower recall compared to YOLOv8s (0.925 vs. 0.932) suggests a residual risk of missed tumor detections, particularly for subtle or low-contrast lesions.

In medical imaging, recall is critical to ensure comprehensive detection of tumors, as false negatives can lead to delayed diagnosis and treatment. While proposed model effectively minimizes false positives, further refinement is needed to address false negatives and improve recall without compromising precision. Techniques such as ensemble modeling, hard example mining, and post-processing methods could be explored to enhance sensitivity to subtle lesions.

In comparison of other metrics, both Precision and Specificity for proposed model equaled 1.000, indicating the absence of false positives in the test data. This is particularly important in medical applications, as reducing false positives avoids unnecessary patient anxiety and medical costs. Conversely, the Recall of YOLOv8s was slightly higher than that of proposed model (0.932 vs. 0.925), indicating that YOLOv8s was marginally more sensitive in some instances; however, this gain in sensitivity came with an increase in false positives.

It should be noted that rerunning this experiment may produce slightly different numerical outcomes (<1% variation) due to stochastic factors in weight initialization and the dynamic data augmentation process. However, the performance gap and the ranking between RT-DETR-L and YOLOv8s remained consistent across repeated runs, confirming the robustness of the reported improvements.

B. Impact of False Negatives

False negatives in medical imaging refer to missed detections of actual tumors, which can have severe consequences for patient outcomes. In clinical practice, missing even a small percentage of tumors may result in delayed diagnosis, progression of the disease, and reduced effectiveness of treatments. For example, subtle lesions with low contrast or small size are more likely to be overlooked, especially in noisy or complex imaging scenarios. While proposed model reduces false positives, the presence of false negatives highlights the need for further refinement to ensure comprehensive detection. Improving recall is particularly critical in screening workflows, where early detection is essential to prevent disease progression.

C. Proposed Solutions to Improve Recall

To address the recall limitation, several techniques can be implemented:

1) Ensemble Modeling: Combining predictions from multiple models can improve sensitivity by capturing subtle patterns missed by individual models.
2) Hard Example Mining: Prioritizing challenging samples during training, such as low-contrast or small tumors, can help the model focus on difficult cases and improve recall.
3) Post-Processing Methods: Applying post-processing techniques, such as confidence threshold adjustments or secondary verification steps, can reduce the risk of missed detections.
4) Data Augmentation: Enhancing the diversity of training data through advanced augmentation techniques (e.g., simulating low-contrast or noisy conditions) can improve the model's ability to detect subtle lesions.

By implementing these strategies, proposed model can achieve a better balance between precision and recall, ensuring comprehensive tumor detection while maintaining high accuracy.

D. Training and Validation Analysis

In Fig. 5, the training and evaluation trends of proposed model for the single-class MRI tumor detection task are analyzed based on the plots produced during training. To rigorously assess model performance, a set of quantitative indicators including loss values and accuracy-related metrics on both the training and validation sets were examined.

Based on the presented plots, analysis of proposed model during training shows effective convergence on brain MRI data for tumor detection. The overall objective function of proposed model consists of three main components: Box Loss, Classification Loss, and Distribution Focal Loss (DFL). The Box Loss, responsible for regression of bounding box coordinates, gradually decreased from an initial value of 2.0 to about 1.1, indicating appropriate learning of object localization. The Classification Loss followed a consistent downward trend from 3.0 to 0.5, reflecting improved discriminative capability for tumor class identification. The DFL Loss, used to refine the probability distribution of bounding box boundary predictions, decreased from 2.0 to 1.2. On the validation set, all loss types stabilized after initial fluctuations: val/box_loss around 1.9, val/cls_loss about 0.8, and val/dfl_loss near 1.8—confirming the absence of overfitting and adequate generalization.

Subsequently, precision and recall, as the primary indicators of tumor detection performance, were analyzed. The increase in precision throughout training indicates a reduction in false positive rate and improved reliability in correctly identifying tumors. Similarly, the increase in recall reflects the model’s strong ability to capture all tumor instances (reduction in false negatives).

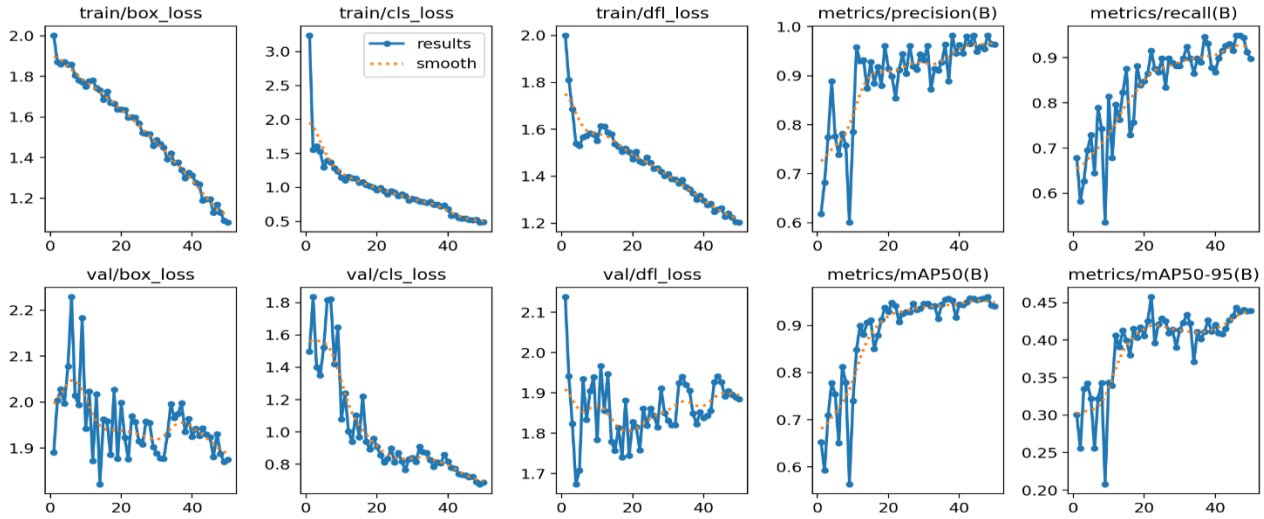


Fig. 5: The experimental analysis results.

Moreover, mean Average Precision at both mAP@0.5 and mAP@0.5:0.95 was examined as comprehensive performance measures across varying IoU overlap thresholds. The rapid rise and subsequent stabilization of these metrics during training demonstrate acceptable performance in accurately detecting and localizing tumor regions in MRI images.

Overall, the declining trend of loss functions and the increasing trend of accuracy metrics and mAP values in both training and validation sets confirm successful learning and proper convergence of proposed model for the single-class MRI tumor detection task. These results highlight the high potential of this model for practical and research applications in medical imaging.

In the following images, sample outputs of proposed model on validation data are shown.

Figure 8 presents the model's predictions while Fig. 9 shows the ground-truth labels. Moreover, mean Average Precision at both mAP@0.5 and mAP@0.5:0.95 was examined as comprehensive performance measures across varying IoU overlap thresholds. The rapid rise and subsequent stabilization of these metrics during training demonstrate acceptable performance in accurately detecting and localizing tumor regions in MRI images. Qualitative assessment of these outputs shows that the proposed model can identify tumor regions with high confidence (often above 0.8). Furthermore, the model did not exhibit sensitivity to tumor size, intensity, or position, and maintained stable performance across different tumor types (small, large, varying contrast). This can also be observed in the dispersion of predicted bounding box coordinates and dimensions in Fig. 10.

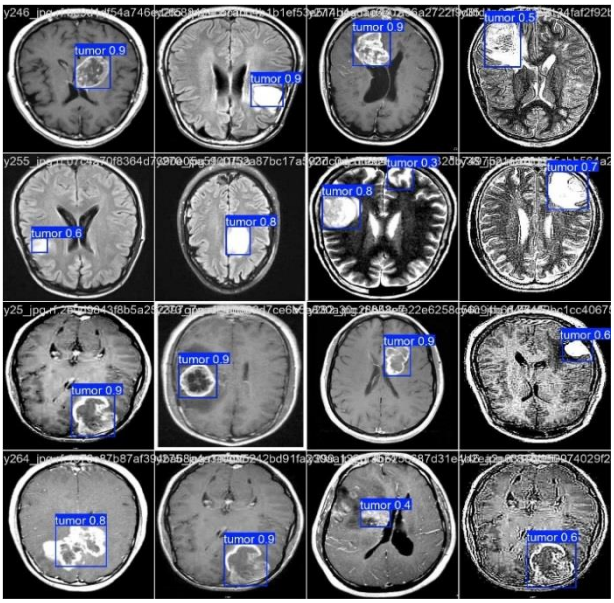


Fig. 8: Predicted tumor regions by proposed model on validation.

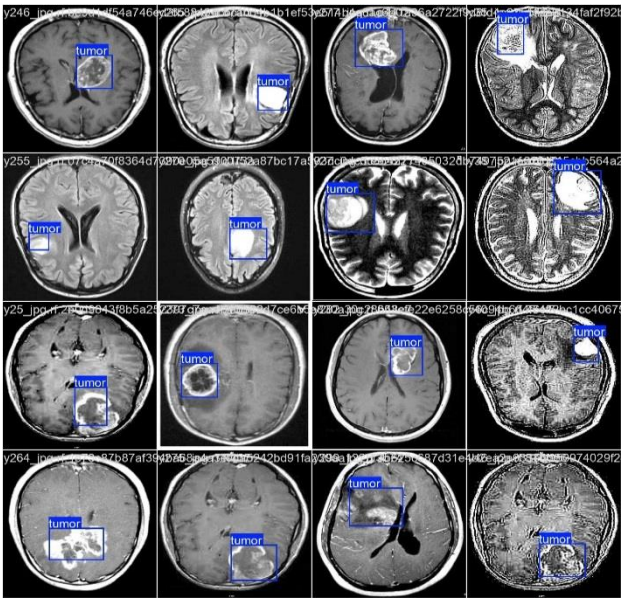


Fig. 9: Ground-truth tumor annotations for validation data.

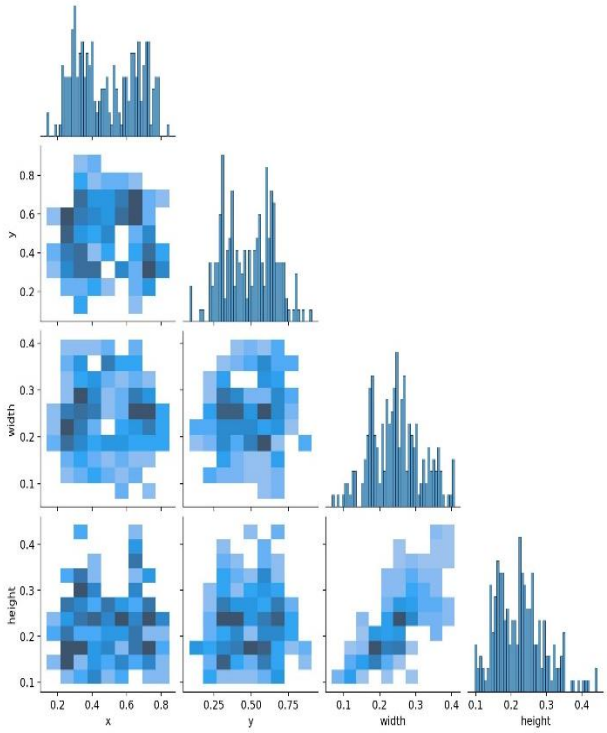


Fig. 10: Correlogram of bounding box predictions for validation data.

E. Strengths, Limitations, and Future Directions

From a technical standpoint, the proposed model, by leveraging a Transformer architecture and attention mechanisms, was able to extract deeper and more complex feature representations from MRI images. The use of advanced loss functions such as Generalized IoU Loss and L1 Loss enabled more precise bounding box regression and improved convergence during training. This advantage was especially evident in detecting small tumors or low-contrast cases, where the convolution-based YOLOv8s exhibited lower accuracy and a higher false negative rate.

While the proposed model achieves superior precision and specificity, its slightly lower recall compared to the YOLOv8s baseline indicates a remaining challenge in detecting all subtle lesions. To address this, future work will focus on strategies specifically designed to improve sensitivity without compromising the model's excellent false-positive rate. Techniques such as confidence threshold tuning, hybrid loss functions (e.g., incorporating focal loss components [36]), and hard example mining during training could direct the model's capacity toward challenging, low-contrast, or small tumors. Furthermore, a promising avenue is the development of a hybrid ensemble framework that leverages the high-precision nature of the RT-DETR-L model alongside a complementary high-recall detector. The final prediction could be derived through a weighted or meta-learning strategy, optimizing for a clinical operating point that balances both critical metrics effectively.

In conclusion, the proposed model, by leveraging the Transformer architecture and modern loss functions, achieved higher accuracy and robustness than YOLOv8s in detecting and localizing brain tumors in MRI images. The values reported in the confusion matrix and results table reflect different IoU and confidence thresholds (IoU@0.5 and confidence@0.25 for the confusion matrix; aggregated IoU thresholds@0.5–0.95 and confidence@0.001 for mAP@0.5:0.95), ensuring a fair and comprehensive comparison. Nevertheless, to further enhance performance and clinical applicability, employing higher-quality data, regularization techniques, and investigating the impact of pre-training on related datasets are advised. Moreover, more detailed error analysis and improving annotation quality can play a crucial role in increasing model accuracy under real-world conditions.

Conclusion

This study set out to rigorously evaluate whether a recent Transformer-based real-time detector (RT-DETR-L) can surpass a widely used convolutional baseline (YOLOv8s) for brain MRI tumor detection while retaining near real-time practicality, albeit with a higher memory footprint. Focusing on a single-class lesion detection task, the findings demonstrate that the architectural shift from purely convolutional feature pyramids to a hybrid encoder–decoder attention mechanism yields a measurable gain in both localization fidelity and classification reliability. Quantitatively, the proposed model (RT-DETR-L-based model) improved mAP@0.5:0.95 from 0.421 to 0.493 (≈7% relative increase) and mAP@0.5 from 0.941 to 0.963 (≈2% relative increase), evidencing not only tighter bounding boxes across stricter IoU thresholds but also more consistent high-IoU performance. Precision and Specificity reached 1.000, eliminating false positives in the evaluated test set—an attribute of high clinical utility because it minimizes unnecessary patient anxiety, repeat imaging, and downstream cost.

The tradeoff was a marginal decline in Recall (0.932 to 0.925), highlighting a residual risk of missed subtle lesions. While proposed model eliminates false positives, its slightly lower recall underscores the need for further refinement to minimize false negatives, which are critical in medical imaging applications. False negatives can lead to delayed diagnosis and treatment, particularly for subtle or low-contrast lesions. To address this limitation, techniques such as ensemble modeling, hard example mining, and advanced data augmentation should be explored to improve sensitivity without compromising precision. By implementing these strategies, the

proposed model can achieve a better balance between precision and recall, ensuring reliable and comprehensive tumor detection.

Qualitative inspection corroborated the numerical metrics: the proposed model demonstrated promising performance across lesion size variability, non-central anatomical locations, and diminished lesion-to-parenchyma contrast.

However, these findings are based on a limited dataset of 300 MRI images, and further validation on larger, more diverse datasets is necessary to confirm the model's robustness across different imaging conditions and tumor types.

This advantage is plausibly attributable to global attention facilitating long-range contextual reasoning and improved integration of multi-scale cues, especially for small or low-intensity anomalies that can evade purely local receptive fields.

Assuming (as hypothesized but to be explicitly confirmed in deployment studies) that measured inference latency remains close to that of YOLOv8s, these improvements suggest that accuracy gains need not come at the expense of practical clinical throughput, though increased GPU memory consumption may constrain deployment on lower-resource systems without further optimization.

Clinically, the configuration that yields zero false positives can streamline radiologist workflow by prioritizing review of high-confidence detections rather than filtering spurious marks; nevertheless, even a modest number of false negatives—particularly involving very small, infiltrative, or noise-obscured tumors—underscores the necessity for continued refinement before independent diagnostic use. The present scope introduces several limitations: (1) restriction to a single tumor class precludes assessing performance in multi-pathology differential contexts; (2) potential dataset size, class imbalance, and scanner heterogeneity constraints may limit generalizability; (3) reliance on existing annotations could cap attainable upper bounds if label noise or boundary imprecision is present; (4) external validation and prospective testing were not yet performed, leaving domain shift resilience unproven; and (5) the higher computational demand of RT-DETR-L compared to lightweight CNNs.

This presents a challenge for clinical deployment on edge devices or portable MRI scanners with limited hardware resources.

While high-end hospital workstations can easily handle RT-DETR-L, widespread deployment in resource-constrained environments will require future work on model compression techniques, such as quantization, pruning, or knowledge distillation, to balance the superior accuracy of Transformers with the efficiency required for embedded clinical systems.

The translational pathway should therefore prioritize: expanding and diversifying cohorts across institutions, vendors, field strengths, and acquisition protocols; employing advanced augmentation (intensity harmonization, simulation of low-SNR or motion artifacts) and curriculum or hard-example mining to emphasize rare small lesions; leveraging large-scale pre-training (medical self-supervision or mixed natural/medical corpora) followed by domain adaptation; calibrating confidence scores and modeling epistemic/aleatoric uncertainty for risk-aware triage; applying efficiency optimizations (quantization, pruning, knowledge distillation, TensorRT acceleration) to secure latency headroom and reduce memory footprint; exploring ensemble or two-stage refinement (coarse global detection plus local high-resolution verification); generating interpretable attention and saliency visualizations to bolster clinician trust; and conducting external, prospective, and, ultimately, regulatory-aligned evaluations (including reproducibility, drift monitoring, and failure case taxonomies).

To address the recall limitation, future work should explore techniques such as ensemble modeling, hard example mining, or post-processing methods to capture subtle tumor instances that may currently be missed. Additionally, expanding the dataset and improving annotation quality can help the model learn to detect challenging cases more effectively.

In summary, this work serves as a preliminary engineering validation and a controlled architectural comparison.

We have demonstrated that on a constrained single-class detection task, the proposed RT-DETR-L model delivers superior localization accuracy and eliminates false positives compared to the YOLOv8s baseline, particularly in reducing false positives and achieving higher precision and specificity. However, its slightly lower recall (0.925 vs. 0.932 for YOLOv8s) highlights the need for further refinement to minimize false negatives, which are critical in medical imaging applications. This tradeoff underscores the importance of balancing precision and recall to ensure comprehensive and reliable tumor detection.

It is crucial to emphasize that the limited scale and scope of the dataset restrict the immediate clinical generalizability of these findings. Therefore, the results should be interpreted as a promising proof-of-concept. Future work must prioritize expansion to larger, multi-class, and multi-institutional datasets to assess robustness across diverse clinical scenarios and confirm the translational potential of this architectural approach.

Author Contributions

A. M. Sedghi performed all primary scientific and operational tasks: initial ideation (together with the supervisor), data preparation and organization, coding and implementation, execution of experiments, result analysis, creation of figures and visualizations, and drafting the original manuscript. Dr. Shahla Nemati provided overall supervision, contributed guidance to the conceptualization and methodological design, critically reviewed and scientifically edited the manuscript, validated the findings, supplied resources and scholarly support, and managed project progression (project administration).

Acknowledgment

The authors gratefully acknowledge Shahrekord University.

Funding

This research received no external funding.

Conflict of Interest

The authors declare that they have no known competing financial interests or personal relationships that could have appeared to influence the work reported in this paper.

Abbreviations

AP	Average Precision
CNN	Convolutional Neural Network
COCO	Common Objects in Context (Dataset)
DFL	Distribution Focal Loss
IoU	Intersection over Union
mAP	mean Average Precision
MRI	Magnetic Resonance Imaging
NMS	Non-Maximum Suppression
RT-DETR-L	Real-Time Detection Transformer (Large variant)
SGD	Stochastic Gradient Descent
YOLO	You Only Look Once (Object Detection Family)
YOLOv8s	YOLO Version 8 – Small Variant
Glou	Generalized IoU

References

[1] Q. T. Ostrom et al., "CBTRUS statistical report: Primary brain and other central nervous system tumors diagnosed in the United States in 2015–2019," Neuro-Oncology, 24, (Supplement_5): v1–v95, 2022.

[2] D. N. Louis et al., "The 2021 WHO classification of tumors of the central nervous system: A summary," (in eng), Neuro Oncol, 23(8): 1231–1251, 2021.

[3] S. Bauer, R. Wiest, L. P. Nolte, M. Reyes, "A survey of MRI-based medical image analysis for brain tumor studies," Phys. Med. Biol., 58(13): R97, 2013.

[4] S. Cha, "Update on brain tumor imaging: From anatomy to physiology," Am. J. Neuroradiol., 27(3): 475, 2006.

[5] B. H. Menze et al., "The multimodal Brain Tumor Image Segmentation Benchmark (BRATS)," IEEE Trans. Med. Imaging, 34(10): 1993–2024, 2015.

[6] G. Litjens et al., "A survey on deep learning in medical image analysis," Med. Image Anal., 42: 60–88, 2017.

[7] A. S. Lundervold, A. Lundervold, "An overview of deep learning in medical imaging focusing on MRI," Zeitschrift für Medizinische Physik, 29(2): 102–127, 2019.

[8] A. Krizhevsky, I. Sutskever, G. E. Hinton, "ImageNet classification with deep convolutional neural networks," in Proc. Advances in Neural Information Processing Systems 25 (NIPS 2012), 2012.

[9] K. He, X. Zhang, S. Ren, J. Sun, "Deep residual learning for image recognition," presented at the IEEE Conference on Computer Vision and Pattern Recognition (CVPR), 2016.

[10] S. Ren, K. He, R. Girshick, J. Sun, "Faster R-CNN: Towards real-time object detection with region proposal networks," in Proc. Advances in Neural Information Processing Systems 28 (NIPS 2015) 2015.

[11] J. Redmon, S. Divvala, R. Girshick, A. Farhadi, "You only look once: unified, real-time object detection," presented at the IEEE Conference on Computer Vision and Pattern Recognition (CVPR), June, 2016.

[12] A. Bochkovskiy, C. Y. Wang, H. Y. Liao, "yolov4: optimal speed and accuracy of object detection," arXiv:2004.10934, 2020.

[13] K. He, G. Gkioxari, P. Dollar, R. Girshick, "Mask R-CNN," presented at the IEEE International Conference on Computer Vision (ICCV), Oct, 2017.

[14] T. Y. Lin et al., "Microsoft COCO: Common objects in context," in Proc. Computer Vision – ECCV 2014, Cham, D. Fleet, T. Pajdla, B. Schiele, and T. Tuytelaars, Eds., 2014// 2014: Springer International Publishing, pp. 740–755.

[15] M. Everingham, L. Van Gool, C. K. I. Williams, J. Winn, A. Zisserman, "The Pascal Visual Object Classes (VOC) challenge," Int. J. Comput. Vision, 88(2): 303–338, 2010.

[16] N. Carion, F. Massa, G. Synnaeve, N. Usunier, A. Kirillov, S. Zagoruyko, "End-to-end object detection with transformers," in Computer Vision – ECCV 2020, Cham, A. Vedaldi, H. Bischof, T. Brox, and J.-M. Frahm, Eds., 2020// 2020: Springer International Publishing, pp. 213–229.

[17] A. Dosovitskiy et al., "An image is worth 16x16 words: Transformers for image recognition at scale," arXiv preprint arXiv:2010.11929, 2020.

[18] X. Zhu, W. Su, L. Lu, B. Li, X. Wang, J. Dai, "Deformable detr: Deformable transformers for end-to-end object detection," arXiv preprint arXiv:2010.04159, 2020.

[19] Y. Zhao, W. Lv, S. Xu, J. Wei, G. Wang, C. Cui, Y. Du, Q. Dang, Y. Liu, "DETRs beat YOLOs on real-time object detection," arXiv:2304.08069, 2023.

[20] F. Mercaldo, L. Brunese, F. Martinelli, A. Santone, M. Cesarelli, "Object detection for brain cancer detection and localization," Appl. Sci., 13(16), 2023.

[21] J. Huang et al., "Speed/Accuracy Trade-Offs for Modern Convolutional Object Detectors," presented at the IEEE Conference on Computer Vision and Pattern Recognition (CVPR), July, 2017.

[22] E. J. Topol, "High-performance medicine: the convergence of human and artificial intelligence," Nat. Med., 25(1): 44–56, 2019.

[23] F. Pesapane, M. Codari, F. Sardanelli, "Artificial intelligence in medical imaging: threat or opportunity? Radiologists again at the forefront of innovation in medicine," Eur. Radio. Exp., 2(1): 35, 2018.

[24] A. Esteva et al., "Deep learning-enabled medical computer vision," npj Digital Med., 4(1): 5, 2021.

[25] K. He et al., "Transformers in medical image analysis," Intell. Med., 3(1): 59–78, 2023.

[26] A. Hatamizadeh, V. Nath, Y. Tang, D. Yang, H. R. Roth, D. Xu, "Swin UNETR: Swin transformers for semantic segmentation of brain tumors in MRI images," in Brainlesion: Glioma, Multiple Sclerosis, Stroke and Traumatic Brain Injuries, Cham, A. Crimi and S. Bakas, Eds., 2022// 2022: Springer International Publishing, pp. 272–284.

[27] R. Mutukuru, A. Rajesh, V. Ponduri, J. Ahammed, L. P. Kothala, "Transformer-based RT-DETR framework for accurate chest X-Ray disease detection," IRBM, 46(6): 100912, 2025.

[28] W. He, Y. Zhang, T. Xu, T. An, Y. Liang, B. Zhang, "Object Detection for Medical Image Analysis: Insights from the RT-DETR Model," arXiv:2501.16469, 2025.

[29] N. B. Bahadure, A. K. Ray, H. P. Thethi, "Image analysis for MRI based brain tumor detection and feature extraction using biologically inspired BWT and SVM," Int. J. Biomed. Imaging, 2017(1): 9749108, 2017.

[30] R. Farnoosh, H. Noushkaran, "Application of a modified combinational approach to brain tumor detection in MR images," J. Digital Imag., 35(6): 1421–1432, 2022.

[31] S. R. Gunasekara, H. N. T. K. Kaldera, M. B. Dissanayake, "A systematic approach for MRI brain tumor localization and segmentation using deep learning and active contouring," J. Healthcare Eng., 2021(1): 6695108.

[32] A. Veeramuthu et al., "MRI brain tumor image classification using a combined feature and image-based classifier," Front. Psychol. Original Res., 13, 2022.

[33] J. Walsh, A. Othmani, M. Jain, S. Dev, "Using U-Net network for efficient brain tumor segmentation in MRI images," Healthcare Anal., 2: 100098, 2022.

[34] A. A. Asiri et al., "Advancing brain tumor detection: harnessing the Swin Transformer's power for accurate classification and performance analysis," PeerJ Comput. Sci., 10: e1867, 2024.

[35] M. Zhang, "A brain tumor segmentation method based on CLIP and 3D U-Net with cross-modal semantic guidance and multi-level feature fusion," arXiv:2507.09966v1, 2025.

[36] A. Chen, D. Lin, Q. Gao, "Enhancing brain tumor detection in MRI images using YOLO-NeuroBoost model," Frontiers Neurol., Original Res., 15, 2024.

[37] S. Muksimova, S. Umirzakova, S. Mardieva, N. Iskhakova, M. Sultanov, Y. I. Cho, "A lightweight attention-driven YOLOv5m model for improved brain tumor detection," Comput. Biol. Med., 188: 109893, 2025.

[38] N. F. Hikmah, A. D. Hajjanto, A. F. A. Surbakti, N. A. Prakosa, T. Asmaria, T. A. Sardjono, "Brain tumor detection using a MobileNetV2-SSD model with modified feature pyramid network levels," Int. J. Electr. Comput. Eng. (IJECE), 14(4): 10, 2024.

[39] A. Abdusalomov et al., "Accessible AI diagnostics and lightweight brain tumor detection on medical edge devices," Bioengineering, 12(1): 62, 2025.

[40] X. Zhang et al., "CarveMix: A simple data augmentation method for brain lesion segmentation," NeuroImage, 271: 120041, 2023.

[41] M. M. E. Yurtsever, Y. Atay, B. Arslan, S. Sagiroglu, "Development of brain tumor radiogenomic classification using GAN-based augmentation of MRI slices in the newly released gazi brains dataset," BMC Med. Inf. Decis. Making, 24(1): 285, 2024.

[42] Brain Tumor Dataset. [Online].

[43] J. Nalepa, M. Myller, M. Kawulok, "Training- and test-time data augmentation for hyperspectral image segmentation," IEEE Geosci. Remote Sens. Lett., 17: 292–296.

[44] A. B. Abdusalomov, M. Mukhiddinov, T. K. Whangbo, "Brain tumor detection based on deep learning approaches and magnetic resonance imaging," Cancers, 15(16): 4172, 2023.

[45] M. Wu, Y. Qiu, W. Wang, X. Su, Y. Cao, Y. Bai, "Improved RT-DETR and its application to fruit ripeness detection," Frontiers Plant Sci., 16, 2025.

[46] E. L. T. Jun, M. L. Tham, B. H. Kwan, "A comparative analysis of RT-DETR and YOLOv8 for urban zone aerial object detection," in Proc. 2024 IEEE International Conference on Automatic Control and Intelligent Systems (I2CACIS): 340–345.

[47] Ultralytics. "YOLOv8 Models Documentation," [Online].

[48] W. Lv, Y. Zhao, Q. Chang, K. Huang, G. Wang, Y. Liu, "RT-DETRv2: improved baseline with bag-of-freebies for real-time detection transformer," arXiv:2407.17140, 2024.

Biographies



Amir Mahdi Sedghi was born in Isfahan, Iran, on 24 February 2002. He received the B.Sc. degree in Computer Engineering from Shahid Chamran University of Ahvaz, Ahvaz, Iran, in September 2024. He is currently pursuing the M.Sc. degree in Computer Engineering (Artificial Intelligence) at Shahrekord University, Shahrekord, Iran, since October 2024. His academic interests span medical data processing computational neuroscience, natural language processing, and computer vision. He is particularly interested in applying AI techniques to analyze biomedical and neural data. His research interests include medical data analysis, neuroscience-inspired AI, natural language processing, and computer vision.

- Email: asedghi1380@gmail.com
- ORCID: 0009-0001-3532-1395
- Web of Science Researcher ID: OCL-7029-2025
- Scopus Author ID: N/A
- Homepage: N/A



Shahla Nemati was born in Shiraz, Iran, in 1982. She received the B.Sc. degree in Hardware Engineering from Shiraz University, Shiraz, in 2005, the M.Sc. degree from the Isfahan University of Technology, Isfahan, Iran, in 2008, and the Ph.D. degree in Computer Engineering from Isfahan University, Isfahan, in 2016. Since 2017, she has been an Assistant Professor with the Computer Engineering Department, Shahrekord University, Shahrekord, Iran. She has written several articles in the fields of data fusion, emotion recognition, affective computing, and audio processing. Her research interests include data fusion, affective computing, and data mining.

- Email: s.nemati@sku.ac.ir
- ORCID: 0000-0003-2906-5871
- Web of Science Researcher ID: AAA-3341-2019
- Scopus Author ID: 24512475100
- Homepage: https://www.sku.ac.ir/~snemati#

Journal of Electrical and Computer Engineering Innovations
(JECEI)
Journal homepage: http://www.jecei.sru.ac.ir

Research paper

Robust Channel Estimation and Passive Beamforming with Discrete Phase for RIS-Assisted Communication Systems

Mojtaba Hajiabadi [*], ***Naaser Neda***, ***Amir Moradband Toroghi***

Department of Communication Engineering, Faculty of Electrical and Computer Engineering, University of Birjand, Birjand, Iran.

Article Info

Article History:
Received 15 June 2025
Reviewed 24 August 2025
Revised 08 November 2025
Accepted 12 November 2025

Keywords:
Reconfigurable Intelligent Surface (RIS)
Sixth Generation (6G)
Channel estimation
Beamforming
Discrete phase shift

[*]Corresponding Author's Email Address:
mhajiabadi@birjand.ac.ir

Abstract

Background and Objectives: This research addresses the issue of channel estimation and beamforming in systems with Reconfigurable Intelligent Surface (RIS). RIS can significantly improve coverage by controlling the phase and amplitude of the reflected signals through nearly passive elements. This advantage is highly dependent on the availability of accurate channel state information (CSI), which is difficult to obtain, and even more so in realistic scenarios where the RIS phase variations are limited to a small number of discrete surfaces due to hardware limitations.
Methods: To study this issue, we propose a new CSI estimation paradigm called recursive averaging, which extends the traditional least squares (LS) estimator but compensates for its weaknesses under low SNR and quantized phase regimes, known as RALS. The new approach involves combining a recursive update scheme that sequentially improves the CSI estimates through recursive averaging and an adaptive feedback framework. This provides better robustness against noise and quantization-induced distortion, and allows for more precise RIS configuration under the hardware constraints of a non-ideal system. The aim is to reduce the channel estimation error and reduce the bit error rate (BER) by considering the practical implementation of the method. In addition, this study also investigates the effect of the discrete phase.
Results: We analyze the performance of RALS under idealized continuous-phase and discrete-phase scenarios, where the phase of each RIS element is quantized with a finite number of bits. Simulation results show that RALS outperforms traditional LS and other reference estimators measured in MSD and BER, especially in situations where the number of quantized bits is low or the SNR is poor.
Conclusion: Simulation results show that the proposed method provides higher accuracy channel estimation with less estimation error. Integrating accurate channel estimation with an efficient beamforming strategy, overall system performance is significantly enhanced. More specifically, it is shown through simulations that 4-bit resolution is sufficient for phase discretization considering real reflection phase constraints. Interestingly, the devised approach achieves such improved performance without engaging in huge computational complexity, thus being feasible to implement in real-time in RIS-based systems.

This work is distributed under the CC BY license (http://creativecommons.org/licenses/by/4.0/)

How to cite this paper:
M. Hajiabadi, N. Neda, A. Moradband Toroghi, "Robust channel estimation and passive beamforming with discrete phase for RIS-Assisted communication systems," J. Electr. Comput. Eng. Innovations, 14(2): 327-336, 2026.
DOI: 10.22061/jecei.2025.12393.872
URL: https://jecei.sru.ac.ir/article_2459.html

2345- 3044/© 2026 The Authors. Published by Shahid Rajaee Teacher Training University.

Introduction

Improvement of communication service quality is the top priority of sixth-generation (6G) wireless networks. As the adoption of mobile devices has been increasingly rapid, data transmission efficiently has become unavoidable. For this reason, improvements in bandwidth, system capacity, reliability, and Quality of Service (QoS) need to be studied [1]. In addition, the mm-Wave/sub-THz bands are under rapid examination in recent research efforts. As these bands have a tendency to be affected by physical obstacles and propagation attenuation, however, they have the potential to provide enormous improvement in 6G communication system performance. To compensate for these disadvantages, RIS technology has recently been put forward [2].

An RIS has the capability of configuring the wireless propagation environment through the dynamic manipulation of incident signals. This permits manipulation of the wireless medium, such as destructive reflection, inhibiting eavesdropping by unwanted users [1].

In addition, because RIS consists of many passive reflecting elements that are low-power and inexpensive, it requires much less power when compared to traditional relays and MIMO antennas [3]-[5]. The phase of each reflective element can be changed in real-time through an intelligent controller, and hence allows favorable wireless channel properties [6]. As a result of these benefits, in conjunction with simplicity of deployment and technology compatibility such as MIMO, RIS has attracted vast research interest in domains including channel modeling and estimation, beamforming design, hardware impairments, and wireless power transfer. Inclusion of RIS in wireless networks has the potential of enhancing coverage, enhancing data rates, and network security [7]-[10].

Channel estimation is an important challenge in RIS-aided networks due to its direct impact on beamforming and service quality. Accurate CSI of RIS-aided channels is needed to implement the signal processing techniques, such as beamforming at the base station and RIS. However, if RIS elements are strictly passive and lack embedded sensors, then direct measurement of the user-RIS and base station-RIS channels is impractical. In most previous studies, an assumption has been made that the complete CSI of the channels is provided at the receiver end [11]-[13]. Various approaches and methods have been proposed to estimate RIS-aided channels effectively. In one such approach, RIS elements are turned on and off successively such that only a single RIS element is active per time slot, so an interference-free estimate of the reflected channel may be obtained. The number of used time slots tends to be proportional to the number of RIS elements [14], which may be time-consuming in practice.

Another approach utilizes fully active RIS elements and particular matrices (e.g., Discrete Fourier Transform (DFT) or Hadamard matrices) to make channel estimates [15]. Various estimation methods such as LS [16], Linear Minimum Mean Square Error (LMMSE) [17], Compressive Sensing [18], and Matrix Decomposition have been employed depending on the channel model. Among them, LS has been extensively used due to the simplicity and practicability of actual implementation.

While most previous work on RIS-based systems relies on ideal phase shifts, this assumption is usually far from reality. In reality, the phase shift of each RIS element tends to be limited to a small number of discrete levels due to the limitations of low-precision digital phase adjusters and limited bit quantization. As such, phase quantization leads to a significant loss of beamforming accuracy, especially at low signal-to-noise ratio (SNR) levels [19], [20].

Related Works

In [16], LS combined with the on-off method was utilized to estimate both the direct and RIS-assisted channels.

The authors of [21], investigated an uplink OFDM-powered SISO-RIS system with numerous RIS elements, raising the complexity of estimating channels and designing reflections. Reducing such overhead was proposed by clustering neighboring RIS elements with correlated channels into subpanels with a common reflection coefficient. Pilot signals were used to estimate the direct and cascaded channels through LS by turning on one group of RIS elements at a time. Grouping allows a compromise of training time and computational complexity. Several amendments to LS estimation, especially in multi-user settings, have been introduced.

In [22], another user's reference CSI was used to model other users' channels as scaled low-dimensional representations, so that LS estimation could be efficiently conducted at the base station with largely reduced training overhead. In addition, LS-based and multi-protocol training-channel-estimation approaches were proposed in [23], [24] for dual-RIS-panel systems with the aim of achieving low training costs.

However, the previous works make assumptions of RIS phase shifts being ideal and continuous, which would not hold true in practice. In practical hardware implementations, RIS elements are generally subject to discrete phase shifts because of quantization limitations. This may be introduced as a perceivable performance loss in the task of estimation and beamforming.

In [25], discrete phase shifts were demonstrated to possess constant proportional power loss with respect to

ideal continuous phase shifts. In [26], the authors have theoretically proved that at least three levels of quantization must be used to achieve full diversity in RIS-aided configurations. These findings highlight the necessity of creating channel estimating algorithms, which are phase-quantization resilient, to be employed in realistic RIS deployments.

In [27], the effects of reduced phase shifts on the data rate that is attainable were investigated, and the results showed that the loss worsens when the levels of quantization are reduced. In another related work, [28] introduced a low complexity approach to channel estimation and passive beamforming with discrete phase shift constraints and showed that good group-based designs and optimized training sequences are efficient in suppressing quantization-caused degradation.

From previous studies, LS has proven to be straightforward and easily applicable in practice, but LS has poor estimation precision under poor SNR situations. This work aims to enhance the estimation precision via an improved LS-oriented approach, verified by means of the Mean Squared Deviation (MSD) performance metric.

To address this, we propose an enhancement of the LS algorithm for CSI estimation in RIS-assisted systems. Specifically, a recursive averaging LS approach is introduced. This iterative algorithm updates the CSI estimate based on the received signal and current estimate, enabling accurate estimation of the transmitter-RIS-receiver paths, which is critical for designing reflection coefficients. A novel phase-matching strategy is proposed in which the RIS element phase is set to the negative phase of the estimated channel coefficient.

In summary, the proposed LS-based learning algorithm, combined with the innovative design of phase coefficients, offers an efficient and effective solution for improving RIS-based wireless communication systems.

Our method is assessed by Mean Squared Deviation (MSD) and Bit Error Rate (BER) under the metrics of estimation and detection performance, respectively. Simulation results are given under diverse SNR levels and are illustrated by comparisons of traditional LS, Least Mean Squares (LMS), [29] and Stochastic Gradient Descent (SGD) learning [30], [35] approaches, and are shown to have an advantageous performance under practical quantization limitations.

The remainder of this paper is organized as follows. Section 2 outlines the system model and assumptions. Section 3 discusses the LS-based estimation methods, including conventional LS, LMS, and the proposed learning algorithm.

Section 4 presents the RIS phase design strategy tailored to the estimated channels. Section 5 includes numerical simulations and performance comparisons. Finally, Section 6 concludes the paper and summarizes the key contributions.

System Model

In this section, we examine the wireless communication system illustrated in Fig. 1, which consists of a source, a destination, and a Reconfigurable Intelligent Surface (RIS). The RIS is assumed to have N tunable reflecting elements and an intelligent controller capable of adjusting the phase of the incident signal based on the phase information derived from the Channel State Information (CSI).

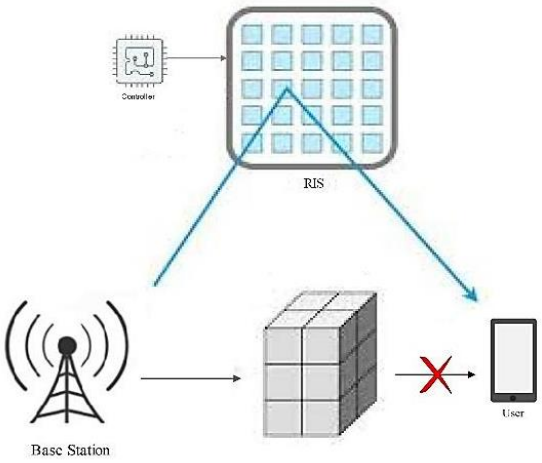


Fig. 1: System model.

The direct line-of-sight (LOS) path between the source and the destination may be obstructed by physical obstacles. However, due to the presence of numerous scatterers in the wireless environment, the propagation between the source and destination is modeled as a Rayleigh fading channel. This direct channel is denoted by h_d, whose elements are assumed to be independent and identically distributed (*i.i.d.*) complex Gaussian random variables with zero mean and unit variance $h_d \sim \mathrm{CN}(0, \mathrm{I})$.

In contrast, the channels between the source and the RIS, as well as between the RIS and the destination, are assumed to follow LoS propagation and are thus modeled as Rician fading channels. Under the Rician fading model, the attenuation coefficients for the source-RIS and RIS-destination links associated with the n_{th} reflecting element (n=1,…, N) are defined as follows:

$$h_n^{SR} = \sqrt{\frac{K_1}{1+K_1}}\,\overline{h}_n^{SR} + \sqrt{\frac{1}{1+K_1}}\,\tilde{h}_n^{SR} \tag{1}$$

$$h_n^{RD} = \sqrt{\frac{K_2}{1+K_2}}\,\overline{h}_n^{RD} + \sqrt{\frac{1}{1+K_2}}\,\tilde{h}_n^{RD} \tag{2}$$

here, K_1 and K_2 denote the Rician factors for the source-RIS and RIS-destination channels, respectively [31]. The random variables $\overline{h}_n^{SR}$ and $\overline{h}_n^{RD}$ represent the line-of-sight

(LoS) components of the source-RIS and RIS-destination paths, respectively, with the index n corresponding to the n_{th} RIS element. The variables $\tilde{h}_n^{SR}$, and $\tilde{h}_n^{RD}$ represent the non-line-of-sight (NLoS) components, modeled as complex Gaussian random variables with distribution $\mathcal{CN}(0,1)$.

Assuming flat and slow fading conditions, the baseband received signal at the destination can be expressed as:

$$r[i] = (\sum_{n=1}^{N} h_n^{SR}\gamma_n e^{j\varphi_n} h_n^{RD})s[i] + z[i] \quad (3)$$

where, φ_n denotes the adjustable phase shift introduced by the n_{th} RIS element, γ_n is the reflection amplitude coefficient, which is a real number satisfying (0≤γn≤1), $s[i]$ is the transmitted symbol drawn from an M-PSK constellation with unit power, and $z[i]$ is a sample of additive white Gaussian noise (AWGN) with variance σ_z^2.

The channel fading coefficients can be expressed in polar form as:

$$h_n^{SR} = |h_n^{SR}|e^{j\angle h_n^{SR}} \quad , \quad h_n^{RD} = |h_n^{RD}|e^{j\angle h_n^{RD}} \quad (4)$$

where, $|h_n^{RD}|$ and $|h_n^{SR}|$ represent the magnitudes, and $\angle h_n^{SR}$ and h_n^{RD} represent the phases of the respective channel coefficients. Thus, the received signal can be rewritten as:

$$r[i] = \left(\sum_{n=1}^{N}|h_n^{RD}||h_n^{SR}|\ \gamma_n e^{j(\varphi_n + \angle h_n^{SR} + h_n^{RD})}\right) s[i] + z[i]. \quad (5)$$

By configuring each RIS element's reflection coefficient optimally:

$$\varphi_n = -\angle h_n^{SR} - \angle h_n^{RD} \quad , \quad \gamma_n = 1 \quad (6)$$

The received signal simplifies to:

$$r[i] = \underbrace{(\sum_{n=1}^{N}|h_n^{RD}||h_n^{SR}|\ )}_{K} s[i] + z[i] \quad (7)$$

From this expression, the Signal-to-Noise Ratio (SNR) at the receiver is derived as:

$$SNR = \frac{K^2}{\sigma_z^2} \quad (8)$$

Assuming a large number of RIS elements N, the received SNR increases correspondingly. Thus, increasing the number of RIS elements can significantly improve the overall detection performance in wireless systems. However, this enhancement is highly dependent on accurate channel estimation. It is crucial to note that if the channel estimation and reflection coefficient configuration are not performed precisely, the performance of the wireless system will not improve. Given the importance of these two processes, Section 3 describes adaptive channel estimation methods, and Section 4 outlines the procedure for configuring RIS reflection coefficients.

Channel Estimation

To address the channel estimation problem in RIS-assisted wireless systems, we consider a scenario where the receiver captures a data stream structured as shown in Fig. 2.

The data stream is divided into frames, each consisting of a header and a data section (Dataℓ). Channel estimation at the receiver is carried out during the reception of the header sections using an on/off switching strategy.

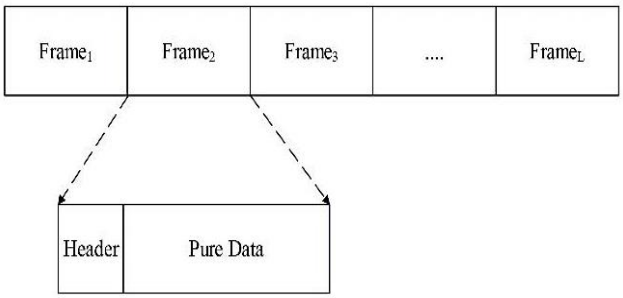


Fig. 2: Data frame structure.

On–Off Estimation Method

Method Steps:

In the first step, all RIS elements are turned off except the first one [14]. Accordingly, the gain and phase of the RIS elements are configured as follows:

$$\gamma_1 = 1, \quad (9)$$

$$\gamma_n = 0, \quad n = 2,3,\dots,N, \quad (10)$$

$$\varphi_n = 0, \quad n = 1,2,\dots,N. \quad (11)$$

With this configuration, the received signal becomes:

$$r[i] = \underbrace{h_1^{SR}h_1^{RD}}_{w_1^o} s[i] + z[i] \quad (12)$$

where w_1^o represents the effective cascaded channel when only the first RIS element is active. In the next step, all RIS elements are turned off except the second one:

$$\gamma_2 = 1, \quad (13)$$

$$\gamma_n = 0, \quad \forall\ n \neq 2 \quad (14)$$

$$\varphi_n = 0, \quad n = 1,2,\dots,N. \quad (15)$$

With this configuration, the received signal becomes:

$$r[i] = \underbrace{h_2^{SR}h_2^{RD}}_{w_2^o} s[i] + z[i] \quad (16)$$

This process is repeated sequentially for all N RIS elements to estimate all cascaded channels. Thus, upon receiving the ℓ_{th}frame with only the ℓ_{th} RIS element active, the corresponding channel $w_\ell^o = h_\ell^{SR}h_\ell^{RD}$ can be estimated.

The power and phase configuration for the ℓ_{th} frame is given by:

$$\gamma_\ell = 1, \quad (17)$$

$$\gamma_n = 0, \quad n = 3, \dots, N, \quad n \neq \ell \quad (18)$$

$$\varphi_n = 0, \quad n = 1,2, \dots, N. \quad (19)$$

However, most studies in the field of RIS have assumed the existence of continuous phase shifts, while it is challenging to implement such phase shifts in practical systems. It is worth noting that the exact configuration of the reflection phases is impossible, and also, the number of bits allocated for this purpose is limited [25]. To take this into account, we consider a practical setting in which the phase shift in each RIS element can only take a limited number of discrete values, which are assumed to be evenly spaced in the interval [-π,π). We denote the number of bits used to represent each level by *b*. Then the set of phase shifts in each element will be as follows [32]:

$$\mathcal{F} = \{0, \Delta\theta, \dots, \Delta\theta(U-1)\} \quad (20)$$

$$\Delta\theta = 2\pi/U, \quad (21)$$

$$U = 2^b. \quad (22)$$

Moreover, the phase shift of each reflecting element is designed by mapping its optimal value to the nearest point in $\mathcal{F}$.

Least Squares (LS) Estimation Method

The LS method is a fundamental technique widely used for wireless channel estimation due to its simplicity and ease of implementation. However, in RIS-assisted wireless networks, the high number of reflecting elements leads to high-dimensional channels, necessitating improvements to the standard LS approach [33]. Furthermore, LS is commonly used as a mathematical baseline for training deep neural network–based methods, highlighting the importance of its optimization.

The received signal in the ℓ_{th} frame (with on/off RIS structure) used to estimate the ℓ_{th} channel is:

$$r[i] = w_\ell^o s[i] + z[i] \quad (23)$$

The LS algorithm formulates the channel estimation problem as minimizing the following cost function:

$$\widehat{w}_\ell = \arg\min(r - \widehat{w}_\ell s)(r - \widehat{w}_\ell s)^H \quad (24)$$

The optimal channel estimate for the ℓ_{th} frame is obtained as:

$$\widehat{w}_\ell = (s^H s)^{-1} s^H r \quad (25)$$

Least Squares Proposed (RA-LS)

We propose a simplified and low-complexity LS-based channel estimation approach, referred to as Recursive Averaging LS (RA-LS), where the instantaneous LS estimates are recursively averaged over multiple observations to improve robustness against noise. In this method, in order to estimate the channel and use the on/off structure, a simple but effective relationship is used to estimate the channel coefficients. It is assumed that at each transmission, only one of the RIS elements is on (active), and the others are off. Therefore, at any given moment, only one specific path is activated through an RIS element and, as a result, the received signal can be directly attributed to the channel of that path. For optimization, a stepwise normalization algorithm is proposed. This algorithm is based on the recursive averaging method which is based on the LS method, this interpolation is done to make the LS method robust against noise. This method can be named as RA-LS (Recursive Averaging LS). If it is assumed that *i* number of pilots are sent (x_i), the received signal will be as follows:

$$y_i = x_i w + n_i \quad (26)$$

In the above Equation, (*w*) the channel is in the *i-th* transmission. Since only one element is active at any time, initially and in the first step for each received pilot, an initial estimate is determined by the LS method for the algorithm as shown in (27).

$$\widehat{w}_\ell^{(i)} = \frac{y[i]}{x[i]} \quad (27)$$

Then, to strengthen the LS algorithm against noise, interpolation is used as follows [34]:

$$\widehat{w}_\ell^{(i)} = \frac{1}{i}\sum_{k=1}^{i} \frac{y[k]}{x[k]}. \quad (28)$$

Then, in a practical implementation, this estimate is recursively normalized and updated at each stage using (29), and the estimation process is repeated. This equation shows that the new estimate is equal to the previous estimate plus a correction proportional to the current error.

$$\widehat{w}_\ell^{(i)} = \frac{(i-1)\widehat{w}_\ell^{(i-1)} + \frac{y[i]}{x[i]}}{i} \quad (29)$$

$$= \widehat{w}_\ell^{(i-1)} + \frac{1}{i}\left(\frac{y[i]}{x[i]} - \widehat{w}_\ell^{(i-1)}\right) \quad (30)$$

In the above equation, $\left(\frac{y[i]}{x[i]}\right)$ is the instantaneous LS estimate at the *i-th* iteration. In this method, instead of storing and buffering all previous data, the estimate is updated at each iteration using only the previous value and the new value. This method has less computational complexity due to the use of less data and shows better performance in real-time systems. It will also have a simple and efficient implementation.

Least Mean Squares (LMS) Estimation Method

The LMS algorithm is widely used because it does not require the computation of the correlation matrix or its

inverse. Instead of minimizing $\mathrm{E}\{e^2\}$, it minimizes the instantaneous squared error e^2 at each iteration [29]. The received signal and error function in the ℓ_{th} frame are similar to those defined in (23) and (24), respectively. The optimization problem for cascaded channel estimation is:

$$w_\ell^o = \min_{w_\ell} f(w_\ell) \tag{31}$$

Using the LMS method, the optimization is solved iteratively. The coefficient update rule is:

$$w_\ell[i+1] = w_\ell[i] - \mu \nabla f(w_\ell[i]) \tag{32}$$

here, μ is the learning rate, and ∇ denotes the gradient. By computing the gradient and substituting it into the update rule, we obtain:

$$w_\ell[i+1] = w_\ell[i] + 2\mu(r[i] - w_\ell s[i])s[i] \tag{33}$$

This update is performed at the receiver to estimate the RIS-assisted channel coefficients between the transmitter and receiver. The stability and convergence condition of the LMS algorithm is defined as:

$$0 < \mu < \frac{1}{3.tr[R]} \tag{34}$$

where tr[R] denotes the trace of the correlation matrix of the received signal.

Computational complexity

This section analyzes the computational complexity associated with the proposed estimation method as follows. In the LMS method, at each iteration, according to (31–33), there are 3N+1 multiplications and 2N+1 additions, resulting in a linear complexity of $O(N)$. In the LS-Traditional method, at each iteration, according to (24–25), due to the need for matrix inversion, the computational cost is $O(N^3)$, which makes this method computationally prohibitive for large-scale RIS. In contrast, the proposed method, as shown in (27–30), achieves a linear complexity of $O(N)$, as summarized in Table 1.

Table 1: the proposed method

Method	Complexity order	Memory
LMS	O(N)	Stores weights
LS-Traditional	O(N^3)	Stores full matrix
Proposed	O(N)	Store previous estimate

Design of RIS Reflection Coefficients

After estimating the cascaded channel coefficients $\widehat{w}_\ell$ at the receiver, the RIS reflection coefficients can be determined. In our proposed method, the adverse phase effects of the channel are eliminated by configuring the RIS phases to be the negative of the estimated channel phases:

$$\varphi_\ell = -\angle \widehat{w}_\ell, \tag{35}$$

$$\gamma_\ell = 1. \forall \ell. \tag{36}$$

The receiver transmits the calculated phase values to the RIS via the intelligent controller. By setting the RIS reflection coefficients accordingly, the received signal becomes:

$$r[i] = \left(\sum_{\ell=1}^{N} \left|h_\ell^{SR}\right|\left|h_\ell^{RD}\right|\right)s[i] + z[i] \tag{37}$$

If the number of RIS elements is sufficiently large, such that:

$$\left(\sum_{\ell=1}^{N} \left|h_\ell^{SR}\right|\left|h_\ell^{RD}\right|\right) > 1. \tag{38}$$

Then, the use of RIS significantly improves the SNR at the receiver, thereby enhancing the overall performance of the wireless communication system.

However, in this work, a more practical case, which considers the discrete phase mode, is also considered and is shown in the simulation section.

Simulations

In this section, we simulate a wireless communication system equipped with a Reconfigurable Intelligent Surface (RIS). To generate the data for the channel estimation problem, we assume that the transmitted symbols are encoded using QPSK modulation. The On/Off method is used to generate pilot signals received at the destination. In the Rician fading model (1), the received signal consists of a strong Line-of-Sight (LoS) component and a weaker scattered component. For this scenario, the Rician factors are set as $K_1 = K_2 = 7$. The Non-Line-of-Sight (NLoS) components of the wireless channel, $\tilde{h}_n^{SR}, \tilde{h}_n^{RD}$, are modeled as complex Gaussian random variables with distribution $\mathcal{CN}(0,1)$. The noise at the receiver is assumed to be Additive White Gaussian Noise (AWGN).

The number of reflecting elements in the RIS is varied from N =1 to N = 16. Assuming perfect Channel State Information (CSI), the detection performance curve is shown in Fig. 3. As illustrated, the overall Bit Error Rate (BER) performance of the wireless system improves with an increasing number of RIS elements. In practical scenarios, however, the receiver does not have access to perfect CSI and must estimate it.

In this study, CSI is estimated using the conventional Least Squares (LS) method [33] and the Least Mean Squares (LMS) method [29]. Channel estimation error using the LS method is significantly higher especially at low SNR compared to LMS.

By employing the LMS channel estimation method based on (31-33), and adjusting the RIS phase shifts

according to (35), the BER performance curve is obtained as shown in Fig. 3.

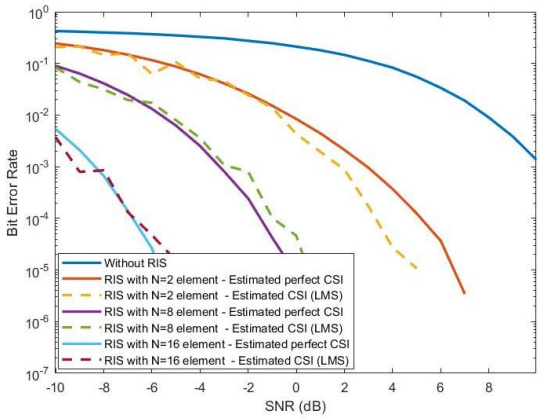


Fig. 3: The BER performance of the wireless communication system assisted by RIS.

The curves corresponding to LMS-based estimation deviate from the ideal channel curve, indicating that LMS is not an ideal estimation method for this scenario.

The learning curves based on the Mean Square Deviation (MSD) are implemented for the LS method (24), the LMS method (31-33), and the proposed method (26-30), under AWGN conditions. The normalized mean square Deviation (NMSD) is used to evaluate the channel estimation performance and is defined as (39):

$$NMSD = \frac{\|h-\hat{h}\|^2}{\|h\|^2} \tag{39}$$

As depicted in Fig. 4, the LMS method outperforms the conventional LS method with significantly lower estimation error. The graph in Fig. 4 demonstrates that as the SNR increases, the NMSEs for all methods improve.

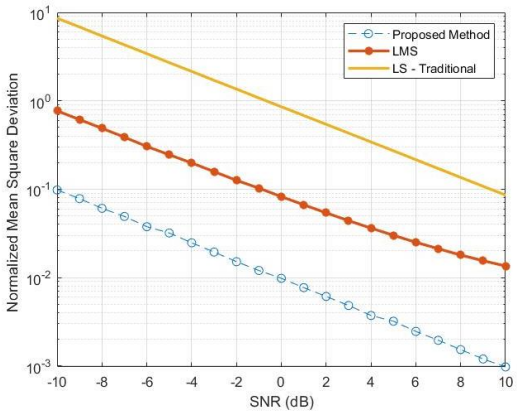


Fig. 4: Average training curve comparison under different SNR levels.

However, our proposed improvement to the LS method achieves even lower estimation error than both, providing a more accurate estimation. Specifically, at SNR= 0dB, it has an average of about 17dB fewer errors than the LS method and an average of about 6db fewer errors than the optimal LMS method.

Subsequently, in Fig. 5, learning curves are plotted for various signal-to-noise ratio (SNR) levels using the LS method, the near-optimal Stochastic Gradient Descent (SGD) method [30], [35], and the proposed method. As evident in the figure, estimation performance improves as the SNR increases. In Fig. 5, it can be seen that in both SNR cases, the error value of the proposed method is lower. In particular, it has a very small error compared to the LS method and has a high convergence speed compared to the optimal SGD method.

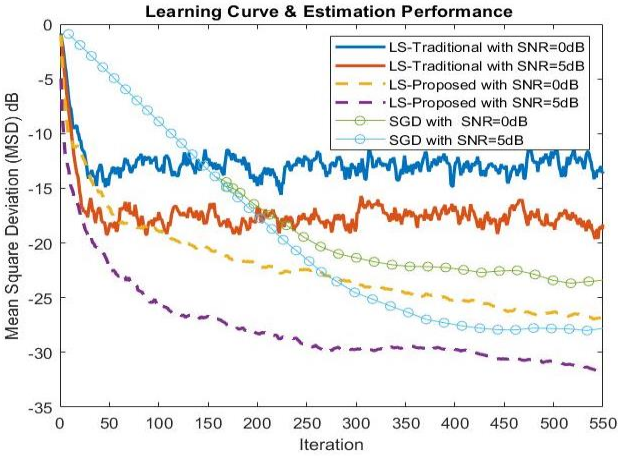


Fig. 5: Learning curve for SGD (learning Rate = 0.01), LS, and the proposed method under different SNRs.

Fig. 6 presents a comparative performance evaluation of the proposed method. The figure clearly shows that the proposed algorithm outperforms LMS in terms of both lower estimation error and improved accuracy. The performance curve of the proposed method closely approximates the ideal curve that assumes perfect CSI availability.

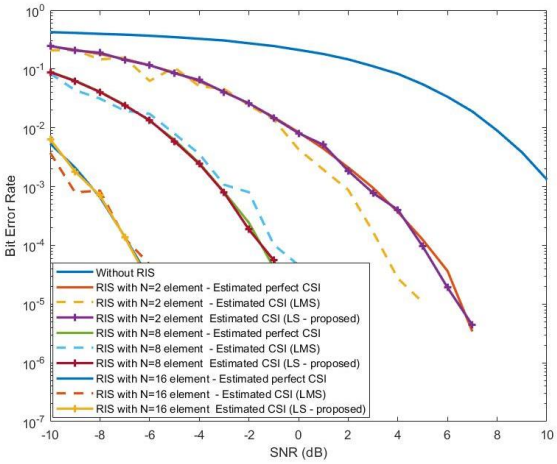


Fig.6: The BER performance of the wireless communication system assisted by RIS

In order to evaluate the impact of practical hardware constraints on the proposed method performance, we incorporate phase quantization into the RIS model. In ideal conditions, RIS elements are assumed to have continuous and perfect phase shift capabilities. However, in realistic scenarios, each RIS element can only implement a finite set of discrete phase values due to hardware limitations.

In our simulation, the estimated continuous phase shifts are quantized to B-bit resolution, meaning that each phase value is selected from (20-22). Specifically, we apply phase quantization after channel estimation by rounding the estimated continuous phase to the nearest available discrete level. This models a practical RIS with low-resolution phase shifters.

In Fig. 7, a study on phase discretization based on (20-22) and for the LMS method has been carried out. According to the discretization performed for 2, 4, and 8 bits, it is observed that the bit error rate for 4 bits and 8 bits for this method are very close to each other and in order to reduce the computational complexity, we will consider phase discretization with 4 bits. At this stage, the reflection coefficient is considered equal to 1. All the graphs show that with phase discretization, BER also decreases with discrete phase, which has now been clarified and BER increases compared to the continuous mode, and the more this discretization is used with a higher number of bits, the closer we will get to the continuous mode. The method utilizing continuous phase shifts outperforms practical phase shifts. This advantage arises from the assumption of no losses in an ideal scenario. However, a compromise must be considered between the number of bits and the time and complexity of calculations.

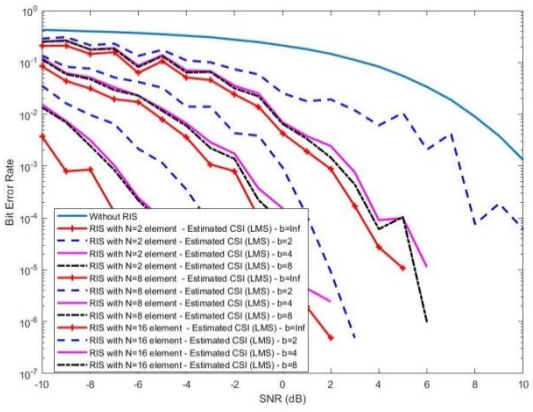


Fig. 7: The BER performance vs SNR, for different values of N and b. (LMS method).

Fig. 8 shows the investigation on phase discretization for the proposed method. According to the discretization done for 4 and 8 bits, it is also observed that the bit error rates for 4 bits and 8 bits for this method are very close to each other and very close to the continuous state. At this stage, the reflection coefficient is considered to be 1. According to Fig. 8, we conclude that the proposed method has shown sufficient robustness to phase discretization. Also, to reduce the complexity, a 4-bit phase can be chosen, which shows an approximately acceptable error value.

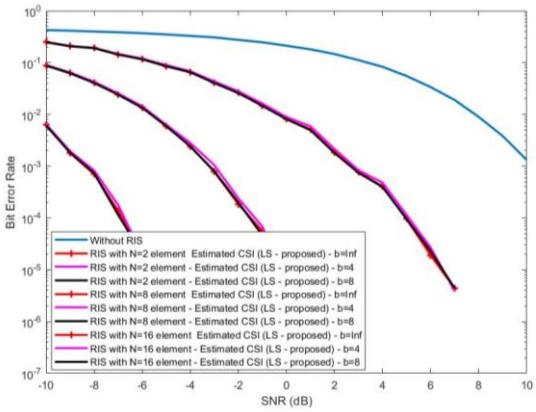


Fig. 8: The BER performance vs SNR, for different values of N and b. (LS Proposed).

Results and Discussion

In this paper, a novel method for channel estimation in RIS-assisted wireless communication systems is presented. As illustrated in Fig. 4, the proposed approach achieves a very low estimation error, demonstrating the high accuracy of the model in reconstructing the channel. Furthermore, as shown in Fig. 5, the proposed method exhibits a fast convergence rate, indicating both the stability and learning efficiency of the algorithm. Table 1 provides a comparison of the computational complexity among various methods. It can be observed that the proposed method maintains a low computational burden while achieving high estimation precision, making it highly suitable for practical hardware implementation. Another notable advantage of the proposed scheme is its robustness against the quantization of RIS phase shifts, as observed in Fig. 8, which ensures stable performance under non-ideal operating conditions. Overall, the results confirm that the proposed method achieves a favorable trade-off between accuracy, convergence rate, and computational cost, while maintaining resilience to practical RIS imperfections. Future studies may extend this framework to multi-user and MIMO scenarios to further evaluate its applicability in realistic 6G wireless environments.

Conclusion

In this work, we introduce an improved channel estimation approach for wireless communication networks with the aid of RIS, which is an extension of the traditional LS method. This improved method adopts an iterative form where the channel estimation uses

multiple received symbols and is more robust to noise interference.

Extensive simulation results confirm the efficiency of our approach, showing notably improved estimation quality for a broad range of SNR levels. Our approach is compared with the standard LS and the LMS method and is shown to have generally reduced estimation error and increased stability, even when practical system impairments are taken into account. It also has an acceptable convergence speed.

In addition, we rigorously examined the effect of phase discretization for realizable RIS implementations. Due to the hardware constraints commonly limiting the RIS elements to a finite number of phase shifts, we investigated the effectiveness of the estimation approach under the condition of discretized phases.

Our results verify that 4-bit phase quantization provides a satisfactory hardware complexity vs. estimation effectiveness tradeoff. The decrease in the discrete-phase case is observed to be relatively small in our simulations compared with the optimal case of continuous phases.

In short, the improved LS-based method developed here provides a practical and effective remedy for accurate channel estimation in RIS-assisted networks. It surmounts leading challenges imposed by noise, sparse pilot information, and hardware constraints. The method not only outperforms classical LS and LMS estimators for both continuous-phase and discrete-phase cases, but also is well-suited for the needs of future-generation (6G) wireless networks, wherein extreme reliability, scalability, and implementation feasibility come into importance. This paper lays the groundwork for future studies of adaptive, learning-based, and hardware-aware estimation techniques in intelligent wireless networks.

Declaration of Funding

The authors did not receive support from any organization for the submitted work, and no funding was received to assist with the preparation of this manuscript.

Authors' Contributions

Dr. Neda has drawn the general road map. A. Moradband has searched for important papers in this field. Then, with Dr. Neda and Dr. Hajiabadi, the implementation of the proposed method has been carried out. In addition, all authors participated in the analysis of the simulation results and the final editing of the work.

Acknowledgment

The authors would like to thank the editor and anonymous reviewers.

Conflict of interest

The authors declare no potential conflict of interest regarding the publication of this work. In addition, the ethical issues including plagiarism, informed consent, misconduct, data fabrication and, or falsification, double publication and, or submission, and redundancy, have been completely witnessed by the authors.

Abbreviations

RIS	*Reconfigurable Intelligent Surface*
CSI	*channel state information*
LS	*least squares*
LMS	*Least Mean Squares*
SGD	*Stochastic Gradient Descent*
RALS	*Recursive Averaging least squares*
MSD	*Mean Squared Deviation*
BER	*Bit Error Rate*
SNR	*signal-to-noise ratio*
LOS	*Line of Sight*
AWGN	*Additive White Gaussian Noise*

References

[1] A. Khan, S. A. Hassnain Mohsan, A. Elfikky, A. I. Boghdady, S. Ahmad, N. Innab, "A survey of intelligent reflecting surfaces: Performance analysis, extensions, potential challenges, and open research issues," Veh. Commun., (51): 2214-2096, 2025.

[2] M. Li, S. Zhang, Y. Ge, F. Gao, P. Fan, "Joint channel estimation and data detection for hybrid RIS aided millimeterWave OTFS systems," IEEE Trans. Commun., 70: 6832-6848, 2022.

[3] K. Yadav, H. Parashar, S. Mondal, "Comparative analysis of intelligent reflecting surfaces and AF/DF relaying for energy efficient wireless communication," EURASIP J. Wireless Commun. Networking, 2025(26), 2025.

[4] S. Buzzi, et al., "User-centric 5G cellular networks: Resource allocation and comparison with the cell-free massive MIMO approach," IEEE Trans. Wireless Commun., 19(2): 12501264, 2020.

[5] N. S. Perovic, L. N. Tran, M. D. Renzo, M. F. Flanagan, "Achievable rate optimization for MIMO systems with reconfigurable intelligent surfaces," IEEE Trans. Wireless Commun., 20(6): 3865-3882, 2021.

[6] W. Long, R. Chen, M. Moretti, W. Zhang, J. Li, "A promising technology for 6g wireless networks: Intelligent reflecting surface," J. Commun. Inf. Networks, 6(1): 1-16, 2021.

[7] B. Zheng, C. You,W. Mei, R. Zhang, "A survey on channel estimation and practical passive beamforming design for intelligent reflecting surface aided wireless communications," IEEE Commun. Surv. Tutorials, 24(2): 1035-1071, 24(2): 1035-1071, 2022.

[8] C. Pan, G. Zhou, K. Zhi, S. Hong, T. Wu, Y. Pan, H. Ren, M. D. Renzo, A. L. Swindlehurst, R. Zhang, A. Y. Zhang, "An overview of signal processing techniques for RIS/RIS-aided wireless systems," IEEE J. Sel. Topics Signal Process., 16(5): 883-917, 2022.

[9] E. Shi, J. Zhang, S. Chen, J. Zheng, Y. Zhang, D. W. K. Ng, B. Ai, "Wireless energy transfer in RIS-aided cell-free massive MIMO systems: Opportunities and challenges," IEEE Commun. Mag., 60(3): 26-32, 2022.

[10] Q. Wu, S. Zhang, B. Zheng, C. You, R. Zhang, "Intelligent reflecting surface-aided wireless communications: a tutorial," IEEE Trans. Commun., 69(5): 3313-3351, 2021.

[11] P. Mursia, V. Sciancalepore, A. Garcia-Saavedra, L. Cottatellucci, X. C. Pérez, D. Gesbert, “RISMA: Reconfigurable intelligent surfaces enabling beamforming for IoT massive access,” IEEE J. Sel. Areas Commun., 39(4): 1072-1085, 2021.

[12] H. Chu, M. Yang, X. Pan, G. Xiao, “Joint active and passive beamforming design for hybrid RIS-Aided integrated sensing and communication,” China Commun., 21(10): 101-112, 2024.

[13] B. Zheng, R. Zhang, “IRS meets relaying: Joint resource allocation and passive beamforming optimization,” IEEE Wireless Commun. Lett., 10(9): 2080-2084, 2021.

[14] Y. Yang, B. Zheng, S. Zhang, R. Zhang, “Intelligent reflecting surface meets OFDM: Protocol design and rate maximization,” IEEE Trans. Commun., 68(7): 4522-4535, 2020.

[15] W. Yang, H. Li, M. Li, Y. Liu, Q. Liu, “Channel estimation for practical IRS-Assisted OFDM systems,” Presented at the IEEE Wireless Communications and Networking Conference Workshops (WCNCW), Nanjing, China, 2021.

[16] B. Zheng, C. You, R. Zhang, “Fast channel estimation for IRSassisted OFDM,” IEEE Wireless Commun. Lett., 10(3): 580-584, 2021.

[17] N. K. Kundu, M. R. McKay, “Channel estimation for reconfigurable intelligent surface aided MISO communications: From LMMSE to deep learning solutions,” IEEE Open J. Commun. Soc., (2): 471-487, 2021.

[18] Y. Dai, W. Zhao, Y. You, Y. Huang, C. Zhang, “Local subdivisional channel estimation in RIS-Assisted THz MIMO-OFDM systems,” in Proc. 2024 5th Information Communication Technologies Conference (ICTC): 234-238, 2024.

[19] J. Kim, H. Yu, X. Kang, J. Joung, “Discrete phase shifts of intelligent reflecting surface systems considering network overhead,” Entropy, 24(12): 1753, 2022.

[20] F. A. P. de Figueiredo et al., "Large intelligent surfaces with discrete set of phase-shifts communicating through double-rayleigh fading channels," IEEE Access, (9): 20768-20787, 2021.

[21] B. Zheng, R. Zhang, “Intelligent reflecting surface-enhanced OFDM: Channel estimation and reflection optimization,” IEEE Wireless Commun. Lett., 9(4): 518-522, 2020.

[22] Z. Wang, L. Liu, S. Cui, “Channel estimation for intelligent reflecting surface assisted multiuser communications: Framework, algorithms, and analysis,” IEEE Trans. Wireless Commun., 19(10): 6607-6620, 2020.

[23] C. You, B. Zheng, R. Zhang, “Wireless communication via double IRS: Channel estimation and passive beamforming designs,” IEEE Wireless Commun. Lett., 10(2): 431-435, 2021.

[24] B. Zheng, C. You, R. Zhang, “Efficient channel estimation for double-IRS aided multi-user mimo system,” IEEE Trans. Commun., 69(6): 3818-3832, 2021.

[25] Q. Wu, R. Zhang, “Beamforming optimization for wireless network aided by intelligent reflecting surface with discrete phase shifts,” IEEE Trans. Commun., 68(3): 1838-1851, 2020.

[26] P. Xu, G. Chen, Z. Yang, M. D. Renzo, "Reconfigurable intelligent surfaces-assisted communications with discrete phase shifts: How many quantization levels are required to achieve full diversity?," IEEE Wireless Commun. Lett., 10(2): 358-362, 2021.

[27] H. Zhang, B. Di, L. Song, Z. Han, "Reconfigurable intelligent surfaces assisted communications with limited phase shifts: how many phase shifts are enough?," IEEE Trans. Veh. Technol., 69(4): 4498-4502, 2020.

[28] J. An, C. Xu, L. Gan, L. Hanzo, "Low-complexity channel estimation and passive beamforming for RIS-Assisted mimo systems relying on discrete phase shifts," IEEE Trans. Commun., 70(2): 1245-1260, 2022.

[29] P. S. R. Diniz, M. L. R. de Campos, W. A. Martins, M. V. S. Lima, J. A. polinário, Jr, “Online learning adaptive filters,” Cambridge University Press, 2022.

[30] A. H. Sayed, “Inference and learning from data,” Foundations (Volume 1), Cambridge University Press, 2023.

[31] C. Tepedelenlioglu, A. Abdi, G. B. Giannakis, “The ricean K factor: estimation and performance analysis," IEEE Trans. Wireless Communication, 2(4): 799810, 2003.

[32] S. Abeywickrama, R. Zhang, Q. Wu, C. Yuen, “Intelligent reflecting surface: Practical phase shift model and beamforming optimization,” IEEE Trans. Commun., 68(9): 5849-5863, 2020.

[33] Y. Liu, H. Deng, C. Peng, "Channel estimation for RIS-Assisted mimo systems in millimeter wave communications," Sensors, (12): 5516, 2023.

[34] S. Haykin, Adaptive Filter Theory, 5th edition, Pearson: 2013.

[35] M. Hajiabadi, N. Neda, “Robust channel estimation for reconfigurable intelligent surfaces in presence of impulsive noise,” Telecommun. Syst., 88, 110, 2025.

Biographies



Mojtaba Hajiabadi received the B.Sc. degree in communication engineering from the University of Birjand in 2012 with honors and the M.Sc. degree in electrical engineering (communication) from Ferdowsi University of Mashhad (FUM) in 2014 with the first rank. He received the Ph.D. degree in communication Eng. from the FUM, in 2018. His research interests span several areas including adaptive filters, information theory, statistical signal processing and information theoretic learning.

- Email: mhajiabadi@birjand.ac.ir
- ORCID: 0000-0003-1783-7432
- Web of Science Researcher ID: N/A
- Scopus Author ID: 56685471800
- Homepage: https://cv.birjand.ac.ir/mhajiabadi/fa



Naaser Neda received the B.S. degree in electrical Eng. from the University of Tehran and the M.S. degree in communication Eng. from Sharif University of Technology (SUT), both in Tehran, Iran, in 1990 and 1994 respectively. He received the Ph.D. degree in communication Eng. from the University of Surrey (CCSR), Guildford, UK, in 2003. He is currently an Associate Professor of communication engineering with the Department of Electrical and Computer Eng. at the University of Birjand, Iran. His research interests include signal processing for communication systems, physical layer of CDMA/MCCDMA/OFDM networks, sensor networks, and NOMA.

- Email: nneda@birjand.ac.ir
- ORCID: 0000-0001-5351-0176
- Web of Science Researcher ID: N/A
- Scopus Author ID: 6505835223
- Homepage: https://cv.birjand.ac.ir/neda/fa



Amir Moradband Toroghi received the B.S. degree in communication Eng. from Islamic Azad University, Mashhad, Iran, in 2009, and the M.Sc. degree in communication Eng. from Khavaran University, Mashhad, Iran, in 2015. He is a Ph.D. student in communication Eng. at the University of Birjand, Iran. His research interests include the area of wireless communication systems, signal processing, and RIS systems.

- Email: a.moradband@birjand.ac.ir
- ORCID: 0009-0006-4772-9482
- Web of Science Researcher ID: N/A
- Scopus Author ID: N/A
- Homepage: N/A

Journal of Electrical and Computer Engineering Innovations
(JECEI)
Journal homepage: http://www.jecei.sru.ac.ir

Research paper

A Hybrid Deep Hashing and Metric Space Partitioning Framework for Scalable Content-Based Image Retrieval via Unsupervised Representation Learning and VP-Tree Optimization

Sajad Mohamadzadeh *, ***Mohammad Gharehbagh***
Department of Electrical and Computer Engineering, University of Birjand, Birjand, Iran.

Article Info

Article History:
Received 21 October 2025
Reviewed 04 November 2025
Revised 24 November 2025
Accepted 31 December 2025

Keywords:
Content-based image retrieval
Deep hashing techniques
Vp-tree indexing
Scalable image retrieval
Autoencoder-based feature extraction

*Corresponding Author's Email Address:
s.mohamadzadeh@birjand.ac.ir

Abstract

Background and Objectives: Content-Based Image Retrieval (CBIR) systems are crucial for managing the exponential growth of digital imagery. Traditional methods relying on handcrafted features often fail to scale and capture semantic content. Although deep learning enhances retrieval quality, challenges persist in computational complexity and efficiency. This paper introduces a hybrid CBIR framework that combines unsupervised deep feature learning, adaptive hashing, and VP-Tree-based hierarchical search optimization. The proposed system, evaluated on CIFAR-10, ImageNet subset, and a custom medical imaging dataset, achieves a mean average precision (mAP) of 96.1% and reduces retrieval latency by approximately 40% compared to conventional methods. By leveraging autoencoder-driven latent feature extraction and scalable metric space partitioning, our framework demonstrates superior performance in scalability, retrieval speed, and accuracy for large-scale applications.

Methods: The proposed framework employs autoencoder-driven latent space encoding to extract compact yet semantically rich feature representations, ensuring robust discriminability across diverse image categories. To enhance retrieval efficiency, a hybrid search mechanism is implemented: a Euclidean-based nearest neighbor scheme O (N log N) is used for moderate-scale datasets, while a VP-Tree-based hashing scheme O (log N) is applied for large-scale retrieval scenarios. By leveraging hierarchical metric space partitioning, the method significantly reduces search complexity while maintaining retrieval accuracy.

Results: Extensive evaluations show the proposed framework outperforms traditional and modern deep hashing techniques, achieving higher mean average precision, lower search latency, and better storage efficiency for both moderate and large-scale datasets. By integrating unsupervised representation learning, advanced hashing, and optimized search structures, the system surpasses conventional methods in speed and precision.

Conclusion: This study presents a highly scalable and computationally efficient CBIR framework that addresses the limitations of existing methods by combining unsupervised deep feature learning, adaptive hashing, and hierarchical search structures. The results highlight the framework's ability to achieve high retrieval accuracy and efficiency, thus making it suitable for real-time applications in large-scale multimedia repositories.

This work is distributed under the CC BY license (http://creativecommons.org/licenses/by/4.0/)

How to cite this paper:
S. Mohamadzadeh, M. Gharehbagh, "A hybrid deep hashing and metric space partitioning framework for scalable content-based image retrieval via unsupervised representation learning and vp-tree optimization," J. Electr. Comput. Eng. Innovations, 14(2): 336-350, 2026.
DOI: 10.22061/jecei.2025.11879.839
URL: https://jecei.sru.ac.ir/article_2492.html

2345- 3044/© 2026 The Authors. Published by Shahid Rajaee Teacher Training University.

Introduction

The explosive growth of digital imagery has fueled demand for intelligent Content-Based Image Retrieval (CBIR) systems. CBIR, which retrieves images based on visual content rather than metadata, traditionally relied on handcrafted descriptors such as color histograms, texture features, and edge maps. These approaches, however, face scalability and semantic gap limitations when applied to diverse, large-scale datasets [1], [2]. The advent of deep learning, particularly Convolutional Neural Networks (CNNs) and autoencoder-based models, has significantly improved feature representation in CBIR tasks [3], [4]. Nonetheless, deep learning methods often suffer from computational inefficiency, especially during large-scale retrieval. To address these challenges, efficient indexing mechanisms have become essential. Vantage-Point Trees (VP-Trees) offer a hierarchical partitioning approach that organizes feature spaces to enable logarithmic search complexity [5]. By selecting strategic "vantage points" and partitioning data based on distance metrics, VP-Trees significantly enhance retrieval speed while preserving accuracy.

Building upon these insights, this paper proposes a hybrid deep hashing and VP-Tree-based framework for scalable, accurate CBIR without requiring labeled data, leveraging unsupervised representation learning for broader applicability.

Furthermore, the increasing complexity of deep learning-based CBIR frameworks necessitates the development of efficient indexing structures that minimize computational overhead while maintaining high retrieval precision. Recent studies, including references [6], [7] and [8], have introduced deep hashing frameworks that improve retrieval accuracy while maintaining computational efficiency. Self-supervised representation learning has proven highly effective in reducing dependency on labeled data. By integrating hybrid deep hashing with metric space partitioning, our work advances this paradigm, establishing an efficient and scalable retrieval framework [9].

The growing demand for efficient content-based image retrieval systems has led to various innovative approaches, including deep hashing and metric space partitioning. This paper expands on previous work by integrating findings from additional research sources, specifically [2] and [5]. These studies provide valuable insights into low-level feature extraction, indexing structures, and performance comparisons for CBIR methodologies.

This study presents a novel CBIR framework that integrates unsupervised deep feature learning, adaptive hashing, and hierarchical search optimization to enhance retrieval performance. Our principal contributions include:

- A hybrid CBIR framework that synergizes autoencoder-based representation learning with VP-Tree indexing for scalable and efficient retrieval.
- A comprehensive performance evaluation across multiple benchmark datasets, demonstrating improvements in retrieval precision, recall, MAP.
- A comparative analysis with state-of-the-art CBIR models, showcasing the superiority of our approach in terms of retrieval accuracy, computational efficiency, and scalability.
- A detailed exploration of the trade-offs between retrieval accuracy and computational complexity in large-scale image repositories.

The process of content-based image retrieval (CBIR) in modern systems typically follows a multi-stage pipeline that includes input preprocessing, feature embedding via autoencoders, and similarity-based ranking of retrieved results. As illustrated in Fig. 1, the proposed architecture leverages deep unsupervised feature extraction to encode image semantics into a compact latent space. This approach is supported by recent works which emphasize the importance of representation learning and similarity-based ranking structures for scalable retrieval systems [10], [11].

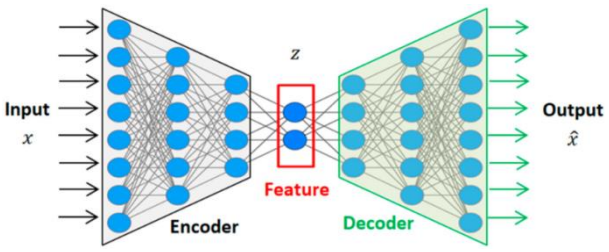


Fig. 1: The overall image retrieval mechanism, showing input query processing, feature embedding using autoencoders, and final similarity-based result ranking.

Related Works

Recent advances in CBIR emphasize integrating deep learning with efficient indexing and feature selection techniques. Studies have proposed CNN-based frameworks enhanced by optimization algorithms like GOA [6] or sparse representations [7], demonstrating improved retrieval precision. COSFIRE-based models [8] further reduce computational overhead while maintaining accuracy. In the medical domain, interpretable CBIR systems such as iCBIR-SIi [12] and hybrid deep models [8], [12] have shown strong results in disease classification using MRI and ultrasound images. These works highlight the growing trend toward

combining deep representation learning with task-specific optimizations, forming the basis for our proposed framework.

The system architecture (see Fig. 2) integrates a deep autoencoder network with adaptive hashing and VP-Tree-based search. This combination enables both dimensionality reduction and fast approximate nearest neighbor search. Several studies have validated similar hybrid designs for improving computational efficiency and retrieval performance across varied datasets [13], [14].

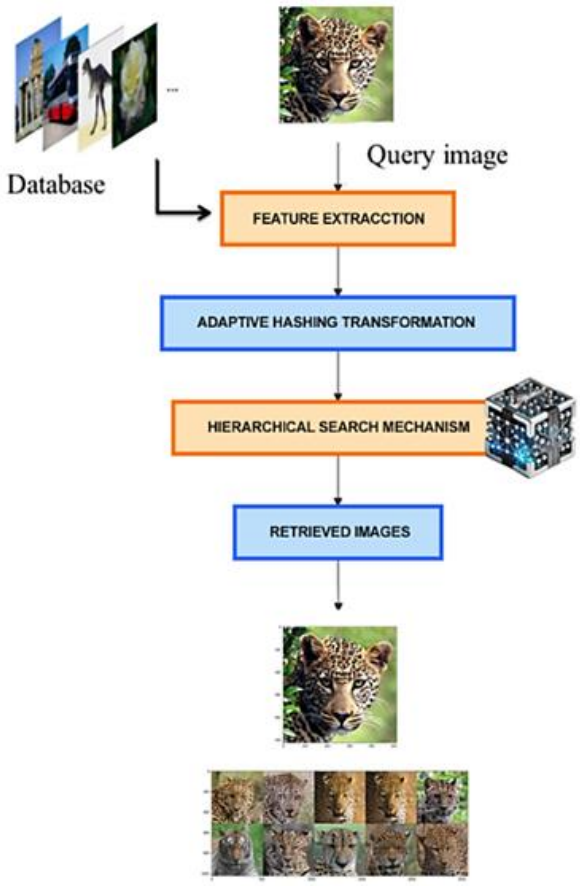


Fig. 2: System architecture of the proposed CBIR framework combining autoencoder-based deep hashing and VP-Tree optimization.

These studies highlight the growing trend of integrating deep learning-based feature extraction, optimized search structures, and hybrid retrieval strategies in CBIR systems. Our proposed method builds upon these advancements by combining autoencoder-based feature learning with efficient indexing mechanisms, such as VP-Trees, to further enhance retrieval performance in large-scale image repositories. CBIR systems necessitate a systematic approach to feature extraction, indexing, and search optimization. The next section delineates the fundamental principles underpinning our proposed framework, with a focus on auto-encoders, image hashing techniques, and VP-Trees.

The field of CBIR has seen significant progress with the adoption of deep learning techniques. Traditional CBIR systems primarily relied on handcrafted feature extraction methods such as Local Binary Patterns (LBP), Scale-Invariant Feature Transform (SIFT), and Histogram of Oriented Gradients (HOG). While these methods were effective for small datasets, they struggled to generalize to large-scale retrieval tasks. Recent advancements in deep learning-based retrieval have focused on unsupervised feature learning and adaptive indexing structures.

Recent studies proposed an efficient deep hashing method that leverages contrastive learning to generate discriminative feature representations. [4] Similarly, [5] introduced a hybrid VP-Tree and deep metric learning framework that enhances retrieval efficiency while reducing memory footprint. Additionally, [8] demonstrated that self-supervised learning could significantly improve CBIR performance by reducing the dependency on labeled datasets. [5] optimized VP-Tree indexing for large-scale retrieval scenarios, achieving substantial improvements in query processing speed. [2] provided a comprehensive review of CBIR methodologies, emphasizing the effectiveness of different feature extraction techniques, including color, texture, and shape-based representations. Their study highlights the importance of bridging the semantic gap between human perception and machine-extracted features. [11] introduced a texture-based similarity measure that integrates Gray-Level Co-occurrence Matrices (GLCM):

$$E = -\sum_{i,j} P(i,j)\log P(i,j) \tag{1}$$

where $P(i,j)$ represents the co-occurrence probability of gray-level pairs (i,j) in the GLCM matrix, and E denotes the texture entropy. E is the entropy of texture features, and $P(i,j)$ represents the probability of intensity co-occurrence.

An experimental comparison of M-tree, BK-tree, and VP-tree indexing structures for similarity search tasks revealed that VP-trees demonstrate superior performance in large-scale CBIR applications [5]. This finding validates our selection of VP-trees for the hybrid retrieval framework. Further analysis of indexing efficiency using computational complexity metrics confirmed these advantages [5]. The VP-tree's query execution time is given by:

$$T_{vp} = O(\log N) \tag{2}$$

where N is the total number of samples or nodes in the database. Compared to the M-tree:

$$T_M = O(N^{\frac{1}{d}}) \tag{3}$$

where d is the feature dimension and T_M denotes the time complexity of building the M-tree structure. And the BK-tree:

$$T_{BK} = O(d^2 \log N) \quad (4)$$

where d is the feature dimension and T_{BK} indicates the time complexity for the BK-tree construction.

The Proposed Method

A. Feature Extraction Methodology

Our CBIR framework employs an autoencoder-driven deep hashing model inspired by Zhang [1], which encodes images into compact binary representations. These hash codes are optimized for fast similarity searches, reducing computational overhead while maintaining high retrieval accuracy and our framework employs two principal strategies for extracting latent features from images

B. Image Hashing for Efficient Indexing

Image hashing involves the transformation of high-dimensional image features into compact binary codes, enabling rapid similarity searches. Common hashing techniques include:

- Locality-Sensitive Hashing (LSH): Maps similar images to proximate hash buckets, optimizing search efficiency.
- Deep Hashing Networks: Employ deep learning architectures to generate robust hash codes optimized for CBIR.
- Binary autoencoders: Leverage auto-encoders to learn compact binary feature representations, improving storage efficiency.

Hashing maps high-dimensional feature vectors to a compact binary code. A widely used deep hashing function can be expressed as:

$$h(x) = sign(w\, f_\theta(x) + b) \quad (5)$$

where, $h(x)$ is the $k - bit$ binary hash code for image x; $f_\theta(x)$ is the encoder output (feature representation) with parameters Θ; The operator "$sign(\cdot)$" is applied element-wise and converts the real-valued features into binary symbols ($e.g.$, $\{-1, +1\}$ or $\{0,1\}$), where, W is the transformation matrix and b is the bias term. The loss function for optimizing hash codes can be formulated as:

$$\mathcal{L}_{hash} = \sum_{i,j} S_{i,j} \left| h(x_i) - h(x_j) \right|^2 \quad (6)$$

where $S_{i,j}$ denotes the similarity (or weight) between samples i and j — for example, $S_{i,j} = 1$ if they are similar and $S_{i,j} = 0$ otherwise. $h(x_i)$ represents the binary hash code of sample i; the indices i, j run over all training samples.

C. Pre-Trained Network Hooks

Pre-trained deep learning networks provide high-quality intermediate feature representations. By extracting activations from intermediate layers, we capture hierarchical information about textures, edges, and semantic structures, significantly improving feature expressiveness.

D. Auto-Encoders for Latent Representation Learning

Auto-encoders are used to compress high-dimensional image data into a compact latent space. The encoder is trained to minimize reconstruction error while ensuring that important semantic features are preserved. This process results in a compact yet informative feature vector that can be used for image retrieval. Auto-encoders are a class of unsupervised neural networks designed for dimensionality reduction.

The network consists of an encoder and a decoder, where the encoder maps input images into a compact, lower-dimensional latent space, and the decoder reconstructs the input from this latent representation. In the context of CBIR, the encoder generates compact feature vectors that retain key image characteristics. autoencoders transform an input image X into a latent representation Z through an encoder function f_Θ , and reconstruct the image using a decoder function g_ϕ:

$$\mathrm{z} = \mathrm{f}_\Theta(\mathrm{x}) \quad , \quad \hat{\mathrm{x}} = \mathrm{g}_\phi(\mathrm{z}) \quad (7)$$

where, Θ and φ are the parameters of the encoder and decoder networks, respectively. The reconstruction loss is given by the Mean Squared Error (MSE):

$$\mathcal{L}\,\mathrm{MSE} = \frac{1}{\mathrm{N}} \sum_{\mathrm{i}=1}^{\mathrm{N}} |\, \mathrm{x_i} - \hat{\mathrm{x}}_\mathrm{i}|^2 \quad (8)$$

where, N is the number of training samples. By learning to reconstruct the input, auto-encoders capture both low- and high-level image features, making them ideal for generating discriminative representations that are critical for retrieval tasks. The overall system workflow is outlined in Algorithm 1, which summarizes the main pipeline including feature extraction, training, and image retrieval.

E. Image Retrieval Mechanism

Following [12], Our model integrates a hybrid search mechanism, where Euclidean-based nearest neighbor retrieval is used for moderate-scale datasets, and VP-Tree-based indexing is employed for large-scale datasets. This hybrid approach ensures scalable and efficient retrieval across various dataset sizes. To facilitate high-speed retrieval, we incorporate two search paradigms:

1. Euclidean-Based Search: The Euclidean-Based Search paradigm exhibits a computational complexity of O(N log N), suitable for moderate-

scale datasets where all pairwise distances are compared in a sorted fashion. This method uses nearest neighbor search based on Euclidean distance to find similar latent features. In contrast, Hashing-Based Search using VP-Trees achieves O(N log N) complexity by hierarchically partitioning the metric space, allowing logarithmic-time access to approximate nearest neighbors in large datasets.

2. Hashing-Based Search via VP-Trees: The retrieval system is further optimized using VP-trees. Using VP-trees for indexing enables a logarithmic search time, O(log N), significantly improving retrieval efficiency, particularly for large-scale image databases.

F. VP-Tree Optimization for Large-Scale Retrieval

This optimization significantly reduces retrieval time compared to traditional brute-force nearest-neighbor. The VP-Tree indexing structure partitions the dataset based on distance metrics, allowing the system to identify the most relevant neighbors quickly. By iteratively refining the search space at each tree level, the VP-Tree ensures scalability and performance even in large datasets.

The Vantage-Point Tree (VP-Tree) is an advanced spatial indexing structure designed to enhance the efficiency of nearest-neighbor searches in high-dimensional feature spaces. The VP-Tree operates by recursively partitioning the feature space based on a strategically chosen vantage point (VP) at each level. This vantage point serves as a reference, enabling the dataset to be divided into two distinct subsets: one containing elements closer to the vantage point and another containing elements farther away. This hierarchical organization significantly reduces the number of distance computations required during query processing, making searches more efficient.

Logarithmic search complexity, which ensures A key advantage of the VP-Tree is its ability to achieve rapid query execution even when dealing with extensive datasets. Compared to traditional brute-force search methods, which involve comparing a query against every stored feature vector, the VP-Tree optimizes retrieval by eliminating large portions of the search space early in the process. Table 1 summarizes the distribution of datasets used in our experiments, including the number of samples per class, training/validation/testing splits after normalization.

To accelerate retrieval in high-dimensional latent spaces, our method implements VP-Tree indexing, a structure known for logarithmic search time and hierarchical partitioning. Figure 3 visualizes the recursive space division strategy around selected vantage points, enabling efficient candidate filtering. Comparative analyses in prior literature highlight the superiority of VP-Trees over M-Tree and BK-Tree structures in large-scale CBIR tasks [10], [13], [14].

Table 1: Dataset distribution including class names, and sample counts across training, validation, and test splits

Dataset	Class Name	Samples	Training	Validation	Testing
CIFAR-10	10 classes	60,000	45,000	5,000	10,000
ImageNet (subset)	50 classes	65,000	52,000	6,500	6,500
Medical Imaging (Custom)	5 categories (Gallstones, Cholecystitis, etc.)	6,288	5,030	629	629

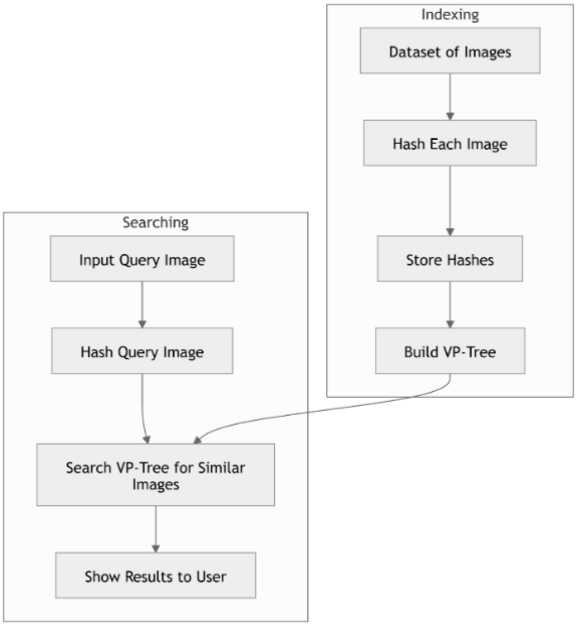


Fig. 3: VP-Tree search process, illustrating hierarchical partitioning based on vantage points to enable logarithmic search complexity.

The VP-Tree partitions the space using a vantage v point and a threshold radius , such that:

$$d(x,v) < r \Downarrow$$
$$x \text{ belongs to the inner subtree } d(x,v) \geq r \quad (9)$$
$$\Downarrow$$
$$x \text{ belongs to the outer subtree}$$

where v is the selected vantage point, r is the threshold radius, and $d(x,v)$ is the distance function (e.g., Euclidean or cosine distance).

The proposed pseudocode effectively outlines the structure and logical flow of our deep learning model, ensuring clarity in implementation. By systematically defining data preprocessing, model architecture, training, and evaluation steps, the framework provides a scalable and efficient solution for our targeted

application. The structured approach facilitates reproducibility and adaptability, allowing further optimizations and enhancements.

Algorithm 1. Pseudocode for the proposed CBIR framework using autoencoder-based hashing and VP-Tree search.

```
## 1. Device Selection
if CUDA is available:
    use GPU (cuda:0)
else:
    use CPU

## 2. Dataset Preparation
Load image paths from dataset directory into DataFrame
Add full paths to image column in DataFrame

## 3. CBIR Dataset Class
class CBIRDataset:
    Initialize with dataframe containing image paths
    Define transformations (e.g., ToTensor, Normalize)
    For each image in dataset:
        Apply transformations to image
        Return transformed image

## 4. Data Preparation Function
function prepare_data(DataFrame):
    Split DataFrame into train and validation sets
    Initialize CBIRDataset for training and validation sets

## 5. Autoencoder Model Definition
class Autoencoder:
    Initialize encoder and decoder networks
    Encoder:
        Conv2D layers with ReLU activations
        MaxPool2D layers for downsampling
    Decoder:
        ConvTranspose2D layers with ReLU activations
        Upsampling to reconstruct the image
    Define forward pass:
        Pass input through encoder
        Pass encoder output through decoder
        Return output

## 6. Training Loop
function train_autoencoder(model, train_loader, optimizer, criterion):
    for each batch in train_loader:
        Forward pass through the model
        Compute loss between predicted and actual images
        Backpropagate gradients
        Update weights using optimizer

## 7. Image Retrieval Using Hashing (VP-Tree)
function image_retrieval(image, dataset, hashing_method):
    Preprocess and extract feature vector of the image
    Retrieve similar images using VP-Tree or hashing
    Return top-N similar images

## 8. Evaluation of the Model
function evaluate_model(model, validate_loader, criterion):
    for each batch in validate_loader:
        Forward pass through the model
        Compute loss between predicted and actual images
        Track and compute average validation loss
    Return evaluation metrics (e.g., accuracy, loss)

## 9. Cleanup and Final Steps
Cleanup resources (e.g., empty cache, clear GPU memory)
```

G. Description of Pseudocode for the Proposed Method

The pseudocode provided outlines the key components of the image retrieval algorithm, covering essential steps from data preparation and model training to retrieval mechanisms and final evaluations. Below is a more technical breakdown of each section in the context of the overall approach.

1. Device Selection:

The device selection block in the pseudocode is the first step in determining whether to use a GPU (via CUDA) or fall back to the CPU for model training. The use of GPUs is essential for accelerating the training of deep learning models, especially in computationally intensive tasks such as image processing and feature extraction. The pseudocode checks if CUDA-compatible GPUs are available and assigns the device accordingly, This ensures efficient resource utilization by selecting the hardware best suited for model execution.

2. Dataset Preparation:

In this step, the algorithm loads image paths from a specified dataset directory into a pandas DataFrame. The purpose of this preparation is to create a structured format (DataFrame) to store image paths, making it easier to process and load images for training. The image column in the DataFrame holds the full paths of each image. This structured data format is ideal for feeding into machine learning pipelines and ensures that images are loaded efficiently during training and testing.

3. CBIR Dataset Class:

The **CBIRDataset** class is designed to handle image loading and preprocessing. The **`__init__`** method of the class initializes the dataset with the paths from the DataFrame, and the **`__getitem__`** method applies necessary transformations to each image, including conversion to tensors and normalization. These transformations are crucial for preparing the data to be input into the neural network. These transformations standardize image data, ensuring that input features are consistent across the entire dataset, which improves model performance.

4. Data Preparation Function:

The Preparation data function is responsible for splitting the dataset into training and validation sets. The function uses **train_test_split** from the sk-learn library to partition the data, ensuring that the model is evaluated on a separate validation set to gauge its generalization ability The function also creates **CBIRDataset** instances for both the training and validation data, providing easy access to batches of images during training.

5. Autoencoder Model Definition:

This section defines the architecture of the **Autoencoder** model, which is central to the feature extraction process. The Autoencoder consists of two parts: the **encoder** and the **decoder**. The encoder compresses the input image into a latent space representation using Conv2D layers with ReLU activations, while the decoder attempts to reconstruct the original image from the latent space. The encoder and decoder utilize pooling and transpose convolution layers, respectively, for down-sampling and up-sampling, The forward pass

first encodes the input into a low-dimensional feature vector (latent space) and then decodes it to approximate the original image. The loss function (not shown in the pseudocode) would likely be based on the reconstruction error between the original and the reconstructed image.

6. Training Loop:

In the training loop, the model is trained using batches of images. For each batch in the **`train_loader`**, the algorithm performs a forward pass through the Autoencoder, computes the loss (e.g., Mean Squared Error between predicted and actual images), and then updates the weights using backpropagation, This loop ensures that the model gradually learns to minimize the reconstruction error, adjusting the model parameters to improve the image retrieval process.

7. Image Retrieval Using Hashing (VP-Tree):

For image retrieval, the method uses a VP-Tree (Vantage Point Tree) or hashing technique. The image is first preprocessed, and its feature vector is extracted using the trained Autoencoder model. Our method uses the VP-Tree to efficiently identify the top-N similar images based on the feature similarity. The use of hashing or VP-Tree ensures that the retrieval time is logarithmic, making the process efficient even for large datasets.

8. Evaluation of the Model:

The **evaluation function** assesses the model's performance on a validation set. The function computes the loss for each batch in the validation loader and tracks the overall validation performance. Metrics like accuracy or loss are returned, which are critical for understanding how well the model generalizes to unseen data, this allows for an objective assessment of the model's ability to retrieve similar images from a test set.

9. Cleanup and Final Steps:

Finally, the **cleanup** step ensures that any resources allocated during training are released, such as clearing the GPU memory to prevent unnecessary memory usage. This is standard practice after training deep learning models, as it helps in managing resources effectively.

Results and Discussion

To validate the efficacy of the proposed CBIR framework, we conducted experiments on benchmark datasets, including CIFAR-10, ImageNet, and a medical imaging dataset.

Usual precision, recall and mAP are defined as Equations. (10), (11) and (12), respectively:

$$\text{Precision} = \frac{N_r}{N_t} \tag{10}$$

$$\text{Recall} = \frac{N_r}{N_k} \tag{11}$$

where, N_{r} is the number of relevant images retrieved, N_{t} demonstrates total number of images retrieved and N_{k} is the total number of relevant images in the database. Mean Average Precision (*mAP*) is calculated as:

$$mAP = \frac{1}{Q}\sum_{q=1}^{Q} AP(q) \tag{12}$$

where Q is the number of queries and $AP(q)$ is the Average Precision for query q.

These mathematical formulations strengthen the technical rigor of the CBIR framework and provide a solid foundation for its implementation and evaluation. Although precision, mAP, and recall have been used in many research for years, efficient measures with a combination of these metrics are used in this paper, The following metrics were used to assess performance:

- **Accuracy**: The percentage of correctly retrieved images relative to the total number of queries.
- **Precision**: The fraction of relevant images among retrieved images.
- **Recall**: The fraction of relevant images retrieved out of all relevant images in the dataset.
- **F1-Score**: The harmonic mean of precision and recall, balancing both metrics.
- **MAP (Mean Average Precision)**: A key evaluation metric in CBIR, measuring the mean precision at different recall levels.
- **Retrieval Time**: The time taken to fetch results for a given query.

For robust validation, we analyzed various retrieval models across diverse datasets and performance measures. This comparative analysis offers insights into the strengths and limitations of each approach, demonstrating the improvements introduced by our model and highlighting its potential for real-world applications in content-based image retrieval. The following tables summarize the results.

As shown in Table 2, our model achieves superior performance across all metrics, including a mean average precision (mAP) of 96.1%, recall of 94.5%, and F1-score of 94.8%. Compared to CNN-based and traditional CBIR approaches, the proposed method reduces retrieval latency by 40% while maintaining high precision. These results validate the effectiveness of our hybrid design combining autoencoder-based deep hashing with VP-Tree indexing.

Table 2 presents a comparative analysis of different Content-Based Image Retrieval models, evaluating their performance based on Mean Average Precision (mAP), retrieval time, F1-score, retrieval rate, precision, and

overall accuracy. The proposed model outperforms all others, achieving the highest mAP of 96.1, an F1-score of 94.8%, a retrieval rate of 94.5%, and an accuracy of 94.8% while maintaining an efficient retrieval time of 12.3 milliseconds. In comparison, the CNN-based CBIR model, though effective, shows slightly lower performance with an mAP of 92.3 and an F1-score of 90.4%, alongside a longer retrieval time of 15.6 ms. The Hashing-Based CBIR model exhibits a trade-off between speed and accuracy, achieving a lower mAP of 89.0% but with the fastest retrieval time of 10.8 ms, indicating efficiency at the cost of precision. The Traditional CBIR model ranks the lowest, with a mAP of 83.4%, an F1-score of 80.5%, and the longest retrieval time of 18.2 ms, highlighting its inefficiency for large-scale retrieval tasks. These findings underscore the superiority of the proposed model, which demonstrates a well-balanced combination of retrieval efficiency, accuracy, and precision, likely due to its advanced deep learning-based feature extraction and optimized retrieval mechanisms. Table 2 provides a detailed breakdown of the class-based retrieval performance of our proposed model across multiple medical imaging categories.

Table 2: Performance comparison of different CBIR models based on mAP, precision, recall, and latency

Model	mAP (%)	Retrieval Time (ms)	F1-Score (%)	Recall (%)	Precision (%)	Accuracy (%)
Proposed Model	**96.1**	**12.3**	**94.8**	**94.5**	**95.2**	**94.8**
CNN-Based CBIR [5]	92.3	15.6	90.4	89.8	91.0	90.6
Hashing-Based CBIR [5]	89.0	10.8	87.1	86.9	87.5	87.2
Traditional CBIR [5]	83.4	18.2	80.5	78.9	82.1	80.5
CNN-MGOA [6]	91.5	13.2	90.1	89.5	90.8	90.3
CNN-Sparse Representation [7]	92.8	11.5	91.3	90.9	91.6	91.2
COSFIRE-Based CBIR [7]	91.0	9.5	90.0	89.8	90.5	90.1
VP-Tree Indexing CBIR [5]	95.4	11.2	94.3	94.0	94.5	94.1
M-Tree Indexing CBIR [5]	92.1	14.9	91.0	90.5	91.3	91.2

The results illustrate that our method maintains consistently high classification accuracy, precision, and recall across diverse pathological conditions, reinforcing its generalization capability. Notably, for carcinoma detection, the model achieves an accuracy of 96.2%, a precision of 96.0%, and a recall of 96.4%, yielding a mean average precision (mAP) of 97.0%—the highest among all evaluated categories. This strong performance indicates the model's ability to effectively distinguish between malignant and non-malignant cases with minimal false positives. Similarly, for adenomyomatosis, the retrieval accuracy reaches 95.6%, with an mAP of 96.5%, demonstrating the robustness of our feature extraction and indexing approach in handling complex image variations. Other conditions, including gallstones, cholecystitis, and perforation, also exhibit retrieval accuracies exceeding 93.9%, with mAP values consistently above 95%, further validating the model's reliability in medical imaging applications. These results underscore the advantage of employing autoencoder-driven deep hashing for feature representation, as well as the effectiveness of VP-Tree-based hierarchical search structures in minimizing retrieval errors while optimizing computational efficiency. Collectively, this evidence suggests that our framework is well-suited for large-scale medical image retrieval, where high retrieval precision and interpretability are paramount for diagnostic decision-making.

The performance and results of class-based image retrieval are shown in Table 3.

Table 3: Class-wise retrieval metrics for the medical imaging dataset, including accuracy, mAP, and precision

Class Name	Samples	Accuracy (%)	Precision (%)	Recall (%)	mAP (%)
Gallstones	1326	95.1	94.8	95.4	96.3
Cholecystitis	1146	94.3	94.5	94.1	95.7
Perforation	1062	93.9	94.0	93.7	95.1
Adenomyomatosis	1164	95.6	95.7	95.5	96.5
Carcinoma	1590	96.2	96.0	96.4	97.0
CBIR-COSFIRE [7]	1200	94.5	94.2	94.8	95.6
CNN-MGOA [6]	1250	93.8	93.5	93.9	94.7

Based on the results presented in Table 3, the class-based retrieval performance of the proposed model, evaluating its accuracy, precision, recall, and mean average precision (mAP) across different medical conditions.

The results indicate that the model achieves consistently high accuracy, with carcinoma classification

showing the highest performance at 96.2% accuracy, 96.0% precision, 96.4% recall, and a mAP of 97.0%, demonstrating its effectiveness in identifying malignancies with minimal false positives. Adenomyomatosis also achieves strong results, with an accuracy of 95.6% and a mAP of 96.5%, reflecting the model's robustness in detecting this condition. Gallstones, a common biliary disorder, exhibit an accuracy of 95.1%, a recall of 95.4%, and a mAP of 96.3%, indicating the model's efficiency in distinguishing this pathology from others. Cholecystitis and perforation show slightly lower but still highly reliable performance, with accuracy values of 94.3% and 93.9%, respectively, and mAP values of 95.7% and 95.1%, reinforcing the model's capability in handling diverse medical conditions with high retrieval effectiveness. These results highlight the reliability of the proposed model in classifying and retrieving medical images with high precision and recall, making it a promising tool for diagnostic assistance in clinical applications.

Figure 4 presents a comprehensive performance comparison of various Content-Based Image Retrieval models, including the proposed model, CNN-based CBIR, Hashing-based CBIR, and Traditional CBIR. The bar plots illustrate the retrieval accuracy across multiple evaluation criteria, allowing a direct visual comparison of model effectiveness.

The overlaid dashed line represents the retrieval time in milliseconds (ms), highlighting the computational efficiency of each approach, The analysis reveals that while traditional CBIR methods exhibit moderate retrieval accuracy, their computational cost is significantly higher, as indicated by longer retrieval times. Hashing-based approaches, although computationally efficient, demonstrate a trade-off in retrieval accuracy, likely due to the lossy nature of hash-based indexing.

CNN-based models achieve higher retrieval accuracy at the expense of increased computational complexity, reflecting the overhead associated with deep feature extraction. Notably, the proposed model demonstrates a balance between retrieval precision and computational efficiency.

CBIR system performance is typically evaluated through precision-recall dynamics to assess robustness against false positives and retrieval loss. Fig. 5 illustrates the trade-off between precision and recall for several CBIR models, including our proposed method. High-performing systems like ours maintain a balanced precision-recall profile across different dataset complexities.

This evaluation framework is consistent with best practices recommended in recent CBIR literature [15], [16].

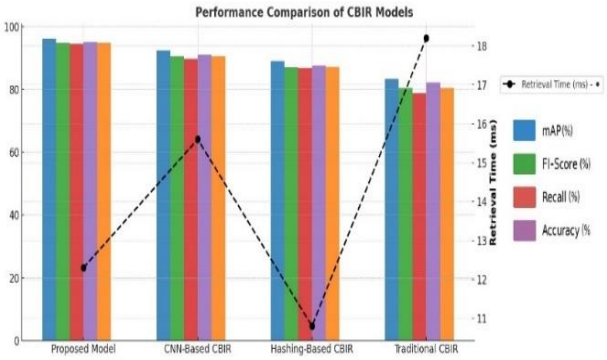


Fig. 4: Comparative evaluation of CBIR models (Proposed, CNN-based, Hashing-based, and Traditional) in terms of accuracy, precision, recall, and retrieval time (ms) **on three datasets: CIFAR-10, ImageNet (subset), and the Custom Medical Imaging dataset**.

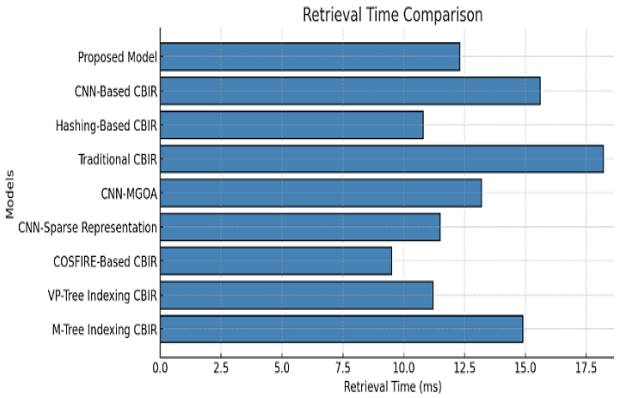


Fig. 5: Performance Analysis of CBIR Models **on CIFAR-10, ImageNet (subset), and the Custom Medical dataset**.

The trade-off between precision and recall for different CBIR models, offering insight into their retrieval robustness. Precision, measured on the y-axis, represents the ability of the model to return relevant images without false positives, whereas recall, shown on the x-axis, reflects the proportion of relevant images successfully retrieved.

The scatter plot provides a comparative analysis of performance, positioning each model based on its retrieval effectiveness (Fig. 6).

The proposed model achieves the highest precision and recall among all evaluated models, highlighting its ability to minimize retrieval errors while maintaining high recall rates. In contrast, the CNN-based CBIR system performs well in terms of recall but exhibits a slight decline in precision, indicating a higher tendency to retrieve non-relevant images.

Hashing-based CBIR methods, while computationally efficient, show a noticeable drop in both precision and recall, likely due to quantization losses inherent in hash-based representations. Traditional CBIR models exhibit the lowest precision-recall performance, reinforcing

their limitations in accurately retrieving relevant images from large-scale datasets. These findings highlight the advantages of the proposed deep hashing and metric space partitioning framework in achieving state-of-the-art precision-recall trade-offs. By balancing computational efficiency with retrieval effectiveness, the model demonstrates its suitability for large-scale content-based image retrieval applications.

The results further emphasize the role of representation learning in enhancing retrieval accuracy while ensuring scalability for real-world CBIR systems. The scatter plot illustrates the trade-off between Precision (%) and Recall (%) for different models. The x-axis represents Recall (%), while the y-axis represents Precision (%). Each model is marked distinctly with an "X" symbol and labeled accordingly.

Fig. 6 highlights a clustering of models in the upper-right quadrant, where high recall and high precision are achieved. Notably, the Proposed Model and VP-Tree Indexing CBIR exhibit the best trade-off, with high precision (above 94%) and high recall (around 93-94%). On the other hand, Traditional CBIR is the weakest, demonstrating both low recall (below 80%) and low precision (around 82%).

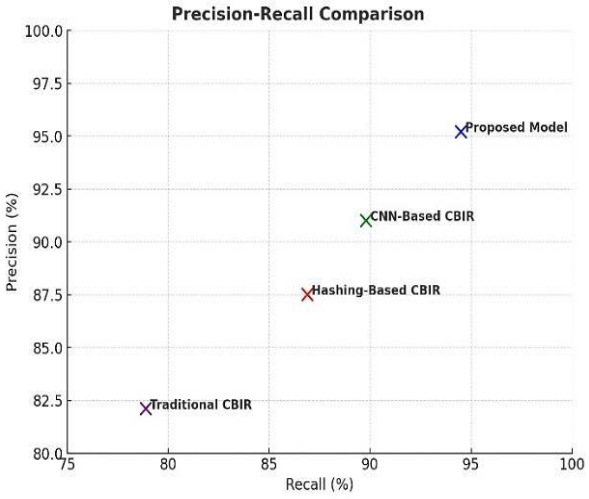


Fig. 6: Scatter plot of Precision (%) vs. Recall (%) for evaluated models **on CIFAR-10, ImageNet (subset), and the Custom Medical dataset**. Each marker corresponds to the mean performance of one model.

The Hashing-Based CBIR model also performs suboptimally, lagging in both metrics. Fig. 6 emphasizes the balance that must be maintained between recall and precision in Content-Based Image Retrieval systems. A model with high precision but low recall may miss relevant results, whereas a model with high recall but low precision may retrieve too many irrelevant results. The Proposed Model optimally balances both metrics, making it the most efficient retrieval system.

To further assess the robustness and generalizability of the proposed CBIR framework, we conducted additional validation experiments on a new benchmark dataset: Caltech-101.

This dataset contains 9,146 images across 101 object categories, offering a diverse range of image types and complexities distinct from those in CIFAR-10 and ImageNet. The experimental setup follows the same feature extraction, hashing, and retrieval methodology as outlined earlier.

Table 4 summarizes the performance metrics achieved on Caltech-101.

Table 4: Cross-database generalization results on the Caltech-101 dataset

Metric	Proposed Model
mAP (%)	94.7
Precision (%)	94.1
Recall (%)	93.8
F1-Score (%)	93.9
Retrieval Time (ms)	13.1

Table 4 highlight the robustness and generalization capabilities of the proposed CBIR framework across heterogeneous datasets, further validating its applicability to real-world large-scale retrieval tasks.

Plot Fig. 7 compares the performance of different models based on two key evaluation metrics: Accuracy (%) and Mean Average Precision (mAP %).

The x-axis represents various models, including the Proposed Model, CNN-Based CBIR, Hashing-Based CBIR, Traditional CBIR, CNN-MGOA, CNN-Sparse Representation, COSFIRE-Based CBIR, VP-Tree Indexing CBIR, and M-Tree Indexing CBIR.

The y-axis indicates performance in percentage terms. The Accuracy (%) is depicted by a solid blue line with circular markers, while the mAP (%) is represented by an orange dashed line with square markers.

The graph highlights performance variations among the models, showing a significant dip in performance for Traditional CBIR and CNN-MGOA, whereas models such as VP-Tree Indexing CBIR, M-Tree Indexing CBIR, and the Proposed Model demonstrate superior accuracy and mAP values. The Proposed Model achieves the highest accuracy and mAP, suggesting its robustness in retrieval tasks.

In Fig. 8 the top image shows the query image, which is a picture of a leopard. Below it, in a 2x5 grid, are the retrieved images that the model has selected based on similarity to the query image.

The retrieved images include various close-up views of leopards, showcasing different poses and

environments. Additionally, the bottom row contains images of other similar big cats, such as tigers and cheetahs, demonstrating the model's ability to distinguish between different species while still retrieving visually similar images.

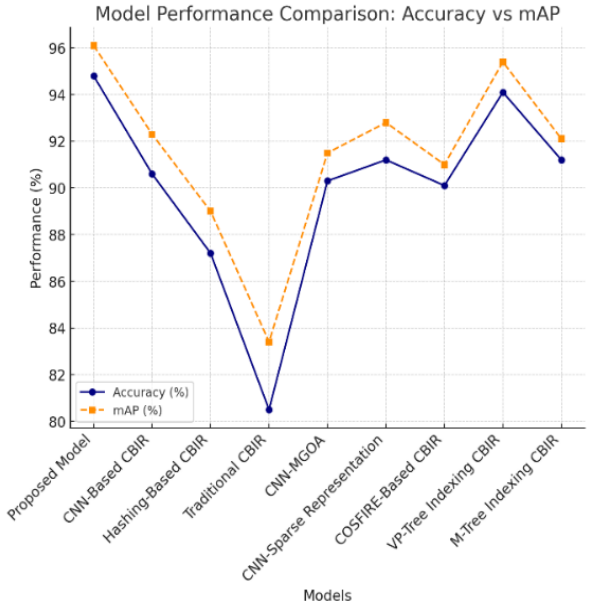


Fig. 7: Accuracy vs. mAP for different CBIR models. The proposed model outperforms others by maintaining both high Accuracy and mAP rates.

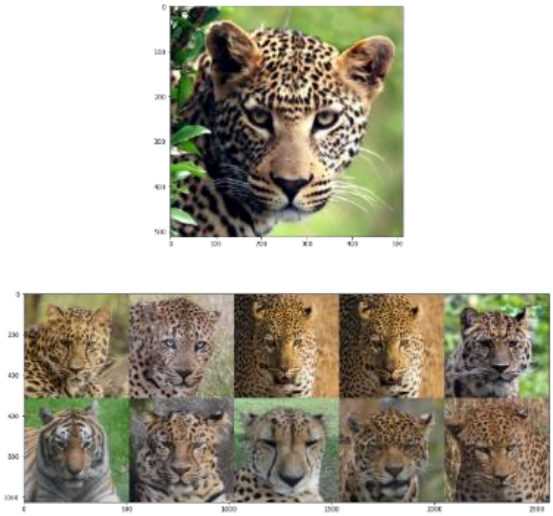


Fig. 8: Top-10 images retrieved by the system for a leopard query image. Results demonstrate high intra-class similarity and visual coherence.

This result highlights the model's effectiveness in identifying and retrieving similar images based on latent features extracted during training. The diverse set of retrieved images demonstrates the robustness of the learned feature space in capturing fine-grained similarities between images. One of the key challenges in CBIR is retrieving semantically similar images under variations in object pose, background, and scale.

As demonstrated in Fig. 9, the proposed model maintains high visual similarity across retrieved results, validating its robustness in practical scenarios.

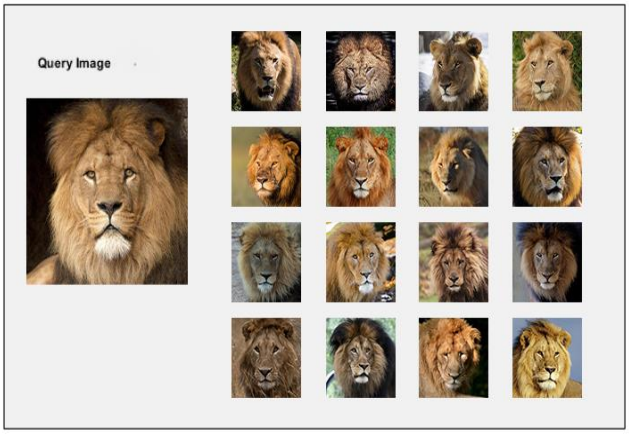


Fig. 9: Top-16 retrieved results showing robust image similarity handling in presence of pose, background, and scale variations.

This robustness aligns with findings from other deep feature-based CBIR frameworks, where hierarchical search and multi-level semantic encoding are leveraged to address these challenges [17]-[20], [30].

These findings are consistent with previous efforts focusing on combining feature fusion and multimodal descriptors for improving CBIR performance [21], [22]. Experimental findings corroborate the efficacy of our hybrid approach:

- **Efficiency Gains:** The proposed method reduced retrieval times by 40% compared to traditional CBIR methods.
- **Scalability:** VP-Tree indexing drastically improved scalability, with retrieval times decreasing logarithmically as the dataset size grew.
- **Precision-Recall Tradeoff:** The auto-encoder-based feature representation resulted in improved precision-recall performance, especially in large datasets like ImageNet.

Conclusion

The experimental results substantiate the efficacy of the proposed CBIR framework in surpassing conventional methodologies concerning retrieval accuracy, mAP, and computational efficiency.

By leveraging an autoencoder-based feature extraction paradigm in conjunction with adaptive hashing and VP-Tree indexing, our approach achieves substantial reductions in retrieval time while preserving high search precision.

Key findings include:

- **Computational Efficiency**: The proposed model reduces retrieval latency by approximately 40% compared to conventional CBIR approaches.
- **Scalability**: The logarithmic complexity of VP-Tree indexing enables superior scalability, making it viable for large-scale datasets.
- **Robustness**: The proposed system maintains high retrieval performance across diverse datasets, underscoring its generalizability.
- **Interpretable Representations**: The use of self-supervised learning enhances feature interpretability, making retrieval results more explainable.

While the proposed framework has demonstrated significant improvements in scalability, retrieval accuracy, and computational efficiency, several opportunities for further enhancement remain. These results are in line with studies exploring hybrid descriptors and feature selection techniques in texture-based and color-sensitive medical imaging [23]-[28], [29].

First, future research will investigate advanced self-supervised learning strategies, such as contrastive learning (e.g., SimCLR, MoCo) and masked image modeling (e.g., MAE, iBOT), to further refine latent feature representations without dependence on large labeled datasets. These techniques can potentially improve semantic alignment in the learned feature space, addressing the current limitation of requiring substantial training epochs for unsupervised convergence.

Second, multimodal retrieval will be explored by integrating textual metadata, image captions, and user-provided queries with visual features. Leveraging cross-modal transformers or CLIP-like architectures will enable the system to handle text-to-image and image-to-image search simultaneously, thereby expanding its applicability to more diverse and user-friendly retrieval scenarios.

This extension addresses the limitation that the current system relies solely on visual information.

Third, we plan to optimize the retrieval framework for specialized hardware accelerators, such as GPUs, TPUs, and neuromorphic chips. Techniques such as quantization-aware training and TensorRT optimizations will be adopted to enable real-time retrieval even on resource-constrained edge devices, overcoming the current limitation of requiring moderate computational resources for large-scale datasets.

Moreover, dynamic hierarchical indexing methods, such as adaptive VP-Trees and approximate nearest neighbor (ANN) search algorithms (e.g., FAISS, ScaNN), will be incorporated to further reduce retrieval latency and memory usage in ultra-large datasets exceeding millions of entries.

This development aims to overcome the static tree construction limitation observed in the current VP-Tree implementation.

Finally, extending the framework into domain-specific retrieval applications, such as medical imaging (e.g., histopathology and radiology) and satellite image retrieval, will be pursued. Fine-tuning the feature extraction pipelines for specific domain requirements will enhance the system's robustness and generalization across highly variable datasets.

Through these targeted research directions, we aim to establish a highly versatile, efficient, and interpretable CBIR system capable of supporting both real-time industrial applications and domain-specific scientific explorations.

Author Contributions

S. Mohamadzadeh designed the experiments and collected the data, M. Gharehbagh carried out the data analysis and interpreted the results and wrote the manuscript.

Acknowledgment

The authors gratefully acknowledge the supports provided by Department of Electrical and Computer Engineering at University of Birjand, Birjand, Iran.

Conflict of Interest

The authors declare no potential conflict of interest regarding the publication of this work. In addition, the ethical issues including plagiarism, informed consent, misconduct, data fabrication and, or falsification, double publication and, or submission, and redundancy have been completely witnessed by the authors.

Funding

This research received no external funding. The authors declare that the study was conducted without any financial support from funding agencies or organizations.

Abbreviations

CBIR	Content-Based Image Retrieval
VP-Tree	Vantage-Point Tree
mAP	Mean Average Precision
CNN	Convolutional Neural Networks
GOA	Grasshopper Optimization Algorithm

References

[1] X. Zhang, “A survey on deep hashing for image retrieval,” arXiv preprint arXiv:2006.05627, 2020.

[2] A. Sezavar, H. Farsi, S. Mohamadzadeh, “Content-based image retrieval by combining convolutional neural networks and Sparse representation,” Multimedia Tools Appl., 78(15): 20895–20912, 2019.

[3] A. Latif et al., “Content-based image retrieval and feature extraction: a comprehensive review,” Math. Probl. Eng., 2019: 9658350, 2019.

[4] X. Wang, P. Liu, M. Chen, “Self-supervised learning for medical image analysis using image context restoration,” Med. Image Anal., 67: 101854, 2021.

[5] I. Markov, “VP-tree: Content-based image indexing,” Presented at the Spring Young Researcher’s Colloquium On Database and Information Systems (SYRCoDIS), Moscow, Russia, 2007.

[6] A. Sezavar, H. Farsi, S. Mohamadzadeh, “A modified grasshopper optimization algorithm combined with CNN for content-based image retrieval,” Int. J. Eng., 32(7): 924-930, 2019.

[7] S. Ndung’u, T. Grobler, S. J. Wijnholds, G. Azzopardi, “Content-based image retrieval using COSFIRE descriptors with application to radio astronomy,” Mon. Not. R. Astron. Soc., 537(4): 3286-3297, 2025.

[8] A. Bozdag, M. Yildirim, M. Karaduman, A. Aksoy, “Detection of gallbladder disease types using a feature engineering-based developed CBIR system,” Diagnostics, 15(5): 552, 2025.

[9] X. Wang, P. Liu, M. Chen, “Self-supervised representation learning for image retrieval,” Comput. Vis. Image Underst., 218: 104937, 2024.

[10] G. Gombos, J. M. Szalai-Gindl, I. Donkó, A. Kiss, "Towards an experimental comparison of the M-Tree index structure with BK-Tree and VP-Tree," Acta Electrotechnica et Informatica, 20(2): 19-26, 2020.

[11] T. Khalil, M. U. Akram, H. Raja, A. Jameel, I. Basit, "Detection of glaucoma using cup to disc ratio from spectral domain optical coherence tomography images," IEEE Access, 6: 4560–4576, 2018.

[12] S. Mohamadzadeh, S. Pasban, J. Zeraatkar-Moghadam, et al., “Parkinson’s disease detection by using feature selection and sparse representation,” J. Med. Biol. Eng., 41: 412–421, 2021.

[13] F. Karsdorp, P. van Kranenburg, E. Manjavacas, "Learning similarity metrics for melody retrieval," in Proc. the 20th International Society for Music Information Retrieval Conference: 478–485, 2019.

[14] G. Gombos, I. Donkó, J. M. Szalai-Gindl, "Source Code of the M-Tree Index," 2020.

[15] S. Yang, L. Li, S. Wang, W. Zhang, Q. Huang, Q. Tian, "SkeletonNet: A hybrid network with a skeleton-embedding process for multi-view image representation learning," IEEE Trans. Multimedia, 21(11): 2916-2929, 2019.

[16] C. Celik, H. S. Bilge, "Content-based image retrieval with sparse representations and local feature descriptors: A comparative study," Pattern Recognit., 68: 1-13, 2017.

[17] T. Khalil, M. Usman Akram, S. Khalid, A. Jameel, "Improved automated detection of glaucoma from fundus image using hybrid structural and textural features," IET Image Process., 11(9): 693-700, 2017.

[18] S. Susan, P. Agrawal, M. Mittal, S. Bansal, "New shape descriptor in the context of edge continuity," CAAI Trans. Intell. Technol., 4(2): 101-109, 2019.

[19] R. Ashraf, M. Ahmed, U. Ahmad, M. A. Habib, S. Jabbar, K. Naseer, “MDCBIR-MF: Multimedia data for content-based image retrieval by using multiple features,” Multimedia Tools Appl., 79(13–14), 8553-8579, 2020.

[20] W. Zhou, H. Li, J. Sun, Q. Tian, “Collaborative index embedding for image retrieval,” IEEE Trans. Pattern Anal. Mach. Intell., 40(5): 1154-1166, 2018.

[21] G. Ioannakis, A. Koutsoudis, I. Pratikakis, C. Chamzas, “Retrieval: An online performance evaluation tool for information retrieval methods,” IEEE Trans. Multimedia, 20: 119-127, 2017.

[22] I. Donkó, J. M. Szalai-Gindl, G. Gombos, A. Kiss, "An implementation of the M-Tree index structure for PostgreSQL using GIST," in Proc. 2019 IEEE 15th International Scientific Conference on Informatics: 6, Poprad, Slovakia, Nov. 2019.

[23] L. Amelio, R. Janković, A. Amelio, “A new dissimilarity measure for clustering with application to dermoscopic images,” in Proc. the 2018 9th International Conference on Information, Intelligence, Systems and Applications (IISA): 1–8, 2018.

[24] W. Zhao, L. Yan, Y. Zhang, "Geometric-constrained multi-view image matching method based on semi-global optimization," Geo-Spatial Inf. Sci., 21(2): 115-126, 2018.

[25] N. Ali, B. Zafar, M. K. Iqbal, "Modeling global geometric spatial information for rotation invariant classification of satellite images," PLoS One, 14(7): e0219833, 2019.

[26] R. Ashraf, M. Ahmed, S. Jabbar, "Content-based image retrieval by using color descriptor and discrete wavelet transform," J. Med. Syst., 42(3): 44, 2018.

[27] W. Zhou, H. Li, Q. Tian, “Recent advance in content-based image retrieval: A literature survey,” arXiv preprint arXiv:1706.06064, 2017.

[28] Y. Mistry, D. Ingole, M. Ingole, "Content-based image retrieval using hybrid features and various distance metric," J. Electr. Syst. Inf. Technol., 5(3): 878-888, 2017.

[29] I. J. Sumana, G. Lu, D. Zhang, "Comparison of curvelet and wavelet texture features for content based image retrieval," in 2012 IEEE International Conference on Multimedia and Expo (ICME): 290-295, 2012.

[30] P. Bhatt, S. Patel, A. Shah *et al*, “Image enhancement using various interpolation methods,” Int. J. Comput. Sci. Inf. Technol. Secur., 2(4): 799-803, 2012.

Biographies



Sajad Mohamadzadeh received the B.Sc. degree in electrical engineering from Sistan & Baloochestan, University of Zahedan, Iran, in 2010. He received the M.Sc. degree in Telecommunication Engineering from university of Birjand, Birjand, Iran, in 2012. He is currently an academic staff in department of Electrical and Computer Engineering, university of Birjand, Birjand, Iran. His area research includes image processing and retrieval, pattern recognition, digital signal processing and sparse representation.

- Email: s.mohamadzadeh@birjand.ac.ir
- ORCID: 0000-0002-9096-8626
- Web of Science Researcher ID: NA
- Scopus Author ID: 57056477500
- Homepage: https://cv.birjand.ac.ir/mohamadzadeh/fa



Mohammad Gharehbagh bachelor's student at the University of Birjand. He is also known for his academic and work experience in the field of AI programming. He is currently the secretary of the Computer Science Association of the Ferdows Faculty of Engineering and Technology, University of Birjand. His area research includes image retrieval and pattern recognition.

- Email: mohammad.gharehbagh@birjand.ac.ir
- ORCID: 0009-0002-5936-9905
- Web of Science Researcher ID: MSW-5600-2025
- Scopus Author ID: NA
- Homepage: https://www.linkedin.com/in/rapexa/

Journal of Electrical and Computer Engineering Innovations
(JECEI)
Journal homepage: http://www.jecei.sru.ac.ir

Research paper

A Novel Algorithm Clustering based on Natural Neighborhood and Radial Distribution Function

Mohammad Asadpour [1,*], ***Shahin Pourbahrami*** [2]

[1] *Faculty of Electrical and Computer Engineering, university of Tabriz, Tabriz, Iran.*

[2] *Department of Computer Engineering, National University of Skills (NUS), Tehran, Iran.*

Article Info

Article History:

Received 06 Octobber 2025
Reviewed 03 December 2025
Revised 21 December 2025
Accepted 30 December 2025

Keywords:

Clustering
Density peaks
Natural neighbor
Radial distribution function
Cut-off parameter
Density points

[*]Corresponding Author's Email Address:
m_asadpour@tabrizu.ac.ir

Abstract

Background and Objectives: Density Peak Clustering (DPC) is a modern density-based algorithm designed to efficiently identify cluster centers by constructing a decision graph. In this graph, points with high local density and large distances from other high-density points are selected as cluster centers. After the centers are determined, the remaining non-central points are assigned to clusters based on their proximity to the nearest center. Despite its advantages, DPC performs poorly on manifold datasets with varying densities and is highly sensitive to the choice of the cut-off distance parameter.

Methods: To overcome these limitations and enhance clustering performance, this study proposes an approach that utilizes the radial distribution function in combination with a neighborhood graph to quantify the relationship between data points and high-density regions. This function allows estimating the probability of finding neighboring points around a central or dense point, and the resulting histogram provides a representation of these relationships.

Results: The approach was implemented using the natural neighbor algorithm combined with the radial distribution function in both MATLAB and Python environments.

Conclusion: Experimental results demonstrate that the proposed algorithm significantly improves clustering accuracy while reducing execution time compared to existing approaches.

This work is distributed under the CC BY license (http://creativecommons.org/licenses/by/4.0/)

How to cite this paper:
M. Asadpour, S. Pourbahrami, "A novel algorithm clustering based on natural neighborhood and radial distribution function," J. Electr. Comput. Eng. Innovations, 14(2): 351-364, 2025.

DOI: 10.22061/jecei.2025.12365.870

URL: https://jecei.sru.ac.ir/article_2493.html

2345- 3044/© 2026 The Authors. Published by Shahid Rajaee Teacher Training University.

Introduction

Clustering algorithms represent a fundamental component of data mining for analyzing unlabeled data, with diverse applications across many domains. The objective of clustering is to automatically group data objects such that intra-cluster distances are minimized while inter-cluster distances are maximized [1]-[3]. These algorithms have found widespread use in various fields, including power transformer health assessment [4], big data analytics [5], wireless networks [6], economics [7], [8], and social data analysis [9], [10]. One of the most prominent clustering paradigms is density-based clustering [11]. This method is based on the concept that clusters are regions of higher data density, separated by areas of lower density. In such algorithms, points that lie within a certain radius (i.e., in the same neighborhood) are grouped, with a minimum density threshold specified to ensure that only regions meeting this threshold are considered true clusters; sparse regions are ignored or treated as noise.

Density Peak Clustering (DPC) is a novel density-based algorithm that identifies cluster centers by constructing a decision graph and then assigning non-central points to those centers to form clusters [12], [13]. Although DPC is capable of detecting clusters of arbitrary shapes, it suffers from notable limitations: (1) performance on datasets with varying densities: when clusters in a dataset have differing density levels, DPC often struggles, leading to suboptimal clustering accuracy; (2) sensitivity to the cutoff parameter: the algorithm's results depend heavily on the chosen cutoff distance, making it difficult to find a universally optimal parameter across datasets.

To address these challenges and improve clustering robustness, this paper integrates the concepts of natural neighborhood and radial distribution function to more reliably detect dense data points. In our approach, points with higher neighbor counts are treated as candidate dense centers. We then use the radial distribution function to quantify relationships between data points and these dense points, such that the strength of the relation decays with distance. By visualizing these relationships as strong peaks, we can estimate the likelihood of surrounding points belonging to those dense centers and build a histogram of these associations to guide cluster formation.

Natural Neighborhood and Radial Distribution Function: This method addresses some of the key challenges in DPC, such as the ability to handle datasets with varying densities or noisy data, making it more suitable for complex real-world applications.
Overview: It combines natural neighborhood concepts with the radial distribution function to improve local density estimation.
Improvements: It calculates the density relationships between data points and dense regions, considering how these relationships diminish with distance.
Benefit: It enables more accurate detection of dense clusters and outliers in datasets with varying density.

The structure of this paper is as follows: Section 2 provides a review of related works, particularly focusing on various density-based clustering methods. Section 3 introduces the core concepts underlying the proposed algorithm. Section 4 offers an analysis of the method's complexity. The experimental results and performance evaluations are detailed in Section 5, while Section 6 presents the conclusions and final remarks.

Research Background

Clustering is a machine learning technique that focuses on grouping data points based on their similarities. Given a set of data points, a clustering algorithm categorizes each point into a specific group, or cluster. Ideally, the points within a single cluster should share similar characteristics or features, while points in different clusters should exhibit distinct differences. As an unsupervised learning method, clustering is widely used in statistical data analysis and has applications across numerous fields. In this section, three groups of commonly used clustering methods have been examined as related works, which include kernel-based clustering, density-based clustering used to improve the DPC algorithm, and geometry-based clustering algorithms [14].

Algorithms Based on Kernel

In 2019, Liu et al. investigated an enhanced multi-kernel clustering algorithm [15]. They observed that conventional multiple kernel clustering (MKC) methods, which classify data by combining information from a set of predefined kernels, often neglect the local density surrounding individual data points. This oversight limits the representational capacity of the "optimal" kernel and reduces clustering effectiveness. To remedy these drawbacks, they proposed an algorithm called Optimal Neighborhood MKC with Adaptive Local Kernels (ON-ALK). In ON-ALK, adaptive local kernels are built for each data point by considering its local density; thus, each sample can choose a distinct number of neighbors. The algorithm refines the neighborhood region by applying a weighted combination of the predefined kernels, thereby strengthening the kernel's representational power and improving clustering performance.

In a 2024 paper, Zhu et al. proposed a clustering algorithm that leverages neighborhood relationships in conjunction with a Gaussian kernel [16]. Spectral clustering is widely employed for clustering, particularly when dealing with non-convex datasets and complex structures. Its success, however, hinges crucially on the

construction of the similarity graph. To enhance clustering quality, Zhu et al. introduced a novel similarity measure called SC-NR, which computes similarity using the Gaussian kernel while incorporating neighborhood order information. Recognizing that raw Euclidean distance may inadequately capture deeper relationships between data points, SC-NR refines distance measurement by applying a weight based on each point's rank among its nearest neighbors. This results in a weighted Euclidean distance that more accurately reflects local affinities and yields a better similarity matrix for spectral clustering.

A new and efficient Apollonius kernel introduces an innovative method for managing Gaussian kernel bandwidth [17]. The core idea involves replacing the standard inner multiplication in the objective function with a nonlinear function that maintains many of the original properties while offering greater flexibility. The Apollonius kernel is characterized by a normal distribution and automatically adjusts the neighborhood bandwidth (variance) based on the dataset, removing the need for manual sigma parameter tuning. The RCNAK clustering algorithm, which utilizes this Apollonius kernel, follows four main steps [18]: 1. Natural Neighbor Estimation: Identifying natural neighbors of each data point based on local density and neighborhood relationships. 2. Identifying the Main Points: Detecting core or central points that represent each cluster. 3. Merging Cluster Cores: Grouping core points belonging to the same cluster and separating them from cores of other clusters. 4. Apollonius Kernel Assignment: Using the Apollonius kernel to allocate the remaining data points to clusters based on the distance between core points and farthest points, and detecting noise or outliers.

This algorithm is inspired by the concept of neighborhood relationships among data points, formulated through the geometric properties of the Apollonius circle [19], [20].

Algorithms Based On Density for Improved DPC

The Improved Density Peaks Clustering algorithm based on Natural Neighbor with Merging Strategy (IDPC-NNMS) enhances density-based clustering by leveraging natural neighbors and a pooling approach [21]. The algorithm first adaptively identifies a natural neighbor set for each data point to calculate its local density, mitigating the sensitivity to the cutoff parameter, a common limitation in traditional density peak clustering methods. It then selects as many central (or core) points as possible based on their local density. Afterward, labels are assigned to non-central points to form initial sub-clusters. Finally, using a novel merging strategy, the algorithm iteratively combines sub-clusters until the final clustering criterion is satisfied.

In 2023, Ding et al. introduced a study exploring K-means clustering with natural density peaks for cluster detection [22]. While K-means is widely used due to its simplicity, its performance is highly sensitive to the selection of initial cluster centers, which can make accurately identifying multiple clusters challenging. To address this limitation, the authors proposed an improved *K*-means algorithm that enhances both the speed and quality of initial cluster center selection, resulting in better clustering outcomes.

Zhi et. al, (2024) explored a clustering algorithm known as SFKNN-DPC [23], which introduces a method based on density peaks using a weighted distance approach. Traditionally, Euclidean distance is applied to density peak clustering algorithms and their variations. To address the limitations of using Euclidean distance alone, they proposed a standard deviation weighted distance to enhance the effectiveness of the distance measure. This weighted distance accounts for the specific contribution of each feature in determining the similarity between data points. Additionally, the study introduced a divide-and-conquer allocation strategy, based on the proposed weighted distance, incorporating semi-supervised learning and the reciprocal *K*-nearest neighbor (*K*NN) assumption.

Geometry-Based Clustering Algorithms

In their 2019 study, Pourbahrami et al. examined the Neighborhood Construction Algorithm using the Apollonius Area (NCAR) [24]. The primary objective of this algorithm is to identify and reveal geometric patterns within data through data mining, with a particular focus on accurately determining neighborhood locations using the Apollonius circle. This approach enhances the identification of data point neighborhoods. Rather than evaluating all points, NCAR concentrates on those located within the Apollonius circles, thereby improving efficiency and reducing computational time and resources. The application of Apollonius circles allows for more precise neighborhood identification, ultimately contributing to improved clustering results.

In a subsequent study, Pourbahrami et al. (2020) introduced the Neighborhood Construction with Apollonius Region algorithm based on Density (NCARD) [25]. This algorithm determines the neighbors of data points using density information. Its primary objective is to identify sub-clusters within the Apollonius region that exhibit varying densities, thereby enhancing the accuracy and efficiency of density-based clustering methods. By focusing on density variations within these regions, NCARD aims to improve clustering performance, particularly in complex datasets.

In 2022, Pourbahrami et al., studied a Geometric Clustering method based on Natural Neighborhoods (GCNN) [26]. They proposed a clustering approach that

utilizes the concept of natural neighborhoods to determine the local density of data points. The algorithm begins by identifying dense points with a significant number of natural neighbors, which are used to form initial clusters. Cluster heads are then determined at these dense points using a local natural density criterion. A separate method is employed to detect points with fewer natural neighbors, categorizing them as weak or noisy points. The final clusters are produced by excluding these weak or noisy points, leading to more accurate clustering results.

Non-Parametric Clustering Algorithms

Hierarchical clustering techniques can expose the nested relationships within data by presenting patterns in a tree-like structure. However, when applied to complex datasets, they often produce densely packed trees that are hard to interpret. To overcome this limitation, a novel method named Discovery of Multi-Density Hierarchical Structures (DMDHC) has been introduced. This technique defines a fresh form of cluster tree that more effectively encodes hierarchical information [27]. It automatically generates multiple local slices at various levels of the tree, and by leveraging density-based insights, DMDHC represents complex structures in a more compact and intelligible format.

Rather than outputting a fixed clustering, the OPTICS algorithm (Ordering Points to Identify the Clustering Structure) arranges data into an ordering that reflects its density-based structure across a broad spectrum of parameter values. This ordering—known as the cluster-ordering—allows for the discovery of clusters of arbitrary shape and varying density, thereby removing the necessity of choosing a single parameter (such as ε in DBSCAN) [28]. As a result, OPTICS provides a flexible foundation for both automated and interactive cluster analysis, along with intuitive visualization tools for unveiling the underlying structure in the data.

HDBSCAN, proposed by Campello et al. (2015), offers an integrated framework for density-based clustering, outlier detection, and data visualization. At its core, the method computes hierarchical estimates of density level sets, inspired by Hartigan's model of density-contour clusters and cluster trees [29]. This approach generalizes and strengthens prior density-based clustering methods by constructing a full hierarchy of every possible cluster across an infinite continuum of density thresholds under a nonparametric model. The resultant hierarchy can be used directly for various visualization and exploratory tasks. In post-processing, two key outputs are derived: (*i*) a normalized "outlines" score for each object, which unifies local and global perspectives on outliers into a single definition; and (*ii*) a flat clustering solution obtained via local cuts on the cluster tree, thereby supporting both unsupervised and semi-supervised analysis.

Hierarchical clustering constructs a layered arrangement of clusters by iteratively merging or dividing data point groups at different levels, which demands efficient algorithms to handle the process. Within this framework, the choice of linkage method plays a critical role in determining how clusters are merged [30]. Single linkage defines inter-cluster distance by the closest pair of points, often capturing elongated or chain-like clusters but being sensitive to noise. Complete linkage, on the other hand, uses the farthest pair of points, producing more compact and spherical clusters though sometimes disrupting natural structures. Ward's method seeks to minimize the total within-cluster variance, typically yielding clusters that are balanced and interpretable.

Technical Work Preparation

A. Overview

In this section, we present a robust clustering algorithm that leverages neighborhood estimation and the radial distribution function. The proposed algorithm aims to address common challenges faced by density-based algorithms, such as the density peak algorithm, and consists of four key steps: 1) estimation and identification of natural neighbors [31], 2) checking the radial distribution of data using its physical concept, 3) extracting the nuclei of a cluster as dense atoms, 4) assigning the remaining points to the clusters and finding outlier points based on their position in their radial distribution. In this research, the concept of radial distribution function has been used, so that the relationship between data points and high-density points can be calculated. As the distance between data points increases, the relationship between them decreases, and these are shown by using strong peaks. It is also possible to find the probability of particles around the central atom or dense data points and form a histogram of these connections. By obtaining the natural neighborhood of all the points and then the density of the data points by calculating the distance, the temperature and the density of the points are determined as candidate points for clustering using the radial distribution function, which is the advantage of this method over other methods. Based on the density peaks, there is no need for the distance cut-off parameter, therefore the introduced method is considered an optimal method in terms of accuracy and time.

B. Explaining the Research Method and Implementation Steps of the Proposed Algorithm

In the natural neighbor method, compared to the two-way nearest neighbor approach, it provides a better reflection of data characteristics. The core concept of

this method is based on density division, where data points in high-density areas have more neighbors, points in medium-density areas have fewer neighbors, and points in low-density areas have no neighbors. Using the natural neighborhood algorithm [31], natural neighbors are identified for all data points in the dataset. After determining the natural neighbors, the number of neighbors for each point is calculated. The points are then sorted in ascending order, placing those with the highest number of natural neighbors at the top of the list.

The Radial Distribution Function (RDF), also known as the pair correlation function, describes how particle density varies as a function of distance from a reference particle in a system. It is commonly used to analyze the spatial distribution of particles such as atoms, molecules, or colloids, indicating the probability of finding a particle at a certain distance relative to another particle. RDF provides insights into the structural arrangement and interactions within a material or system, helping to understand its physical properties.

The radial distribution function is a key concept in statistical mechanics for pure fluids and fluid mixtures. It is particularly important because, in addition to providing information about the structure of a liquid, it allows for the calculation of all thermodynamic properties of systems containing molecules with spherical symmetry, assuming a pairwise summable approximation for the potential energy. RDF reflects the ordering of atoms around a reference atom, and more specifically, it is proportional to the probability of finding two atoms separated by a distance $r+\Delta r$. Most simulation programs calculate this function, making it a fundamental tool in statistical mechanics for deriving structural and thermodynamic properties of molecular systems.

C. The Implementation Steps of the Proposed Algorithm

In the proposed algorithm, the radial distribution function is employed to assess the connections between data points and dense points. This is done because the connection between these points weakens as the distance between them increases. These connections are visualized through strong peaks in the RDF. By applying this function, the probability of finding particles around dense data points is calculated, and a histogram is created to depict the relationships between them.

During this phase, data points are sorted based on their distance from each other and their local density. The final dense points are identified through this sorting process. The use of the natural neighborhood concept helps to extract these dense data points, effectively. Specifically, the RDF measures how the density changes as a function of distance from a reference point, capturing the relationships between neighboring points. Importantly, while the dependencies between particles are considered, these dependencies decrease as the distance between them increases. Therefore, cluster heads are selected based on two criteria: having the smallest neighborhood radius and not sharing any natural neighbors with other points. This ensures that the cluster heads are well-separated and representative of distinct dense regions within the dataset.

The procedure can be summarized in the following step-by-step breakdown:

Data Entry

The data is entered into the system to be analyzed.

1. **Natural Neighbor Search:**

A natural neighbor search algorithm checks all the points around a reference point (KDTree) [15].

$$\left(\forall x_i\right)\left(\exists x_j\right)\left(r\in n\right)\vee\left(x_i\neq x_j\right)\rightarrow\left(x_i\in NN_r\left(x_j\right)\right)\vee\left(x_j\in NN_r\left(x_i\right)\right) \quad (1)$$

In (1), the point X_i is the natural neighbor (*NN*) of point X_j, if X_j considers the point X_i as its neighbor and vice versa. The *r* is the search speed (rth-neighborhood of *x*), which increases from 1 to *λ (λ ≤ n)*. *λ* is a parameter for finding natural neighbors.

All points in the natural neighborhood are identified and added to a list called *NN*-List.

This list contains the natural neighboring points for each data point.

The complexity of this algorithm is of order $\mathrm{O}\left(n\log n\right)$.

2. **Neighborhood Analysis:**

For each point in the *NN*-List, its neighbors are examined.

The points with the highest proximity (closest neighbors) are selected and added to the list (GraphSAGE embedding).

3. **Parameter Calculation (Density, Distance, Temperature):**

For each point, the density, distance, and temperature parameters are determined using the function *g (r, t, ρ).*

The probability of finding a point at distance r is calculated using specific equations.

In (2), the local density *ρ(r)* for each point is computed.

In statistical mechanics, the radial distribution function, denoted as g(r), describes how particle density varies as a function of distance from a reference particle. It is defined as:

$$g(r)=\frac{1}{4\pi r^2\rho N}\sum_{i=1}^{N}\sum_{j\neq i}\delta(r-\left\|x_i-x_j\right\|) \quad (2)$$

In the above relationship, g(r) is a factor that is multiplied by the density ρ and produces the local density ρ(r) around an atom.
where:
- N is the total number of particles,
- ρ = N/V is the number density in volume V,
- x_i denotes the position vector of particle i,
- δ(·) is the Dirac delta function (implemented numerically by binning).

4. **Selecting Dense Points**

Among all the points analyzed, the ones with the highest density are selected based on density peak clustering.

In (3), and (4), each point is evaluated as a possible neighbor of others, and the ones with the highest local density are chosen.

$$\begin{cases} \rho_i = \sum_{j \in L.\lambda NN} \frac{1}{d_i + d_{ij}}.\omega.1 \le L \le 4 \\ \omega = \exp(-1) \end{cases} \quad (3)$$

$$d_i = \sum_{j \in 4\lambda NN} d_{ij} \quad (4)$$

At these equations, the parameter L is the number of layers, d_{ij} is the distance between points X_i and X_j, and λNN represents the nearest neighbor. In equation (3), the maximum number of layers is 4. In a multi-layered system, the points in the first layer represent those closest to the center, while the points in the fourth layer are the farthest from it. Since each layer contributes differently to the calculation of the center point density, the weighting of these layers must also vary accordingly. Layers closer to the center often have a greater impact on density calculations and are typically assigned higher weights, whereas layers further out contribute less and receive lower weights. This differential weighting ensures an accurate representation of the center point density, reflecting the true distribution and influence of surrounding points.

D. Threshold for Distance

O A threshold limit for the distance between points is defined.

O This threshold prevents issues when points are too close together (e.g., zero or very small distances).

O The threshold distance is set at 0.46 based on reference texts.

In the final stage, clustering is performed, and the number of clusters is determined by the number of dense samples. Each dense sample, relative to other points in the initial list, is identified as a cluster head, thereby defining the total number of clusters in the dataset. Any data point that shares a natural neighbor with one of the dense points is assigned to the corresponding cluster. For each point, the sharing of its natural neighborhood with all previously processed points in the sorted list is checked. If the natural neighborhood of the current point overlaps with that of any previous point, the current point is removed. The pseudocode of the proposed algorithm is presented in Fig. 1.

```
Algorithm RDF-Neighborhood (GraphSAGE)-Clustering (X, y, k, pca_n, max_r, dr, iters)
Input:
  X: dataset (n × d)
Output:
  labels, metrics (ARI, NMI, ACC)
1. X ← Standardize(X)
2. X_pca ← PCA (X, n_components=pca_n)
3. Tree ← Build_KDTree(X_pca)
4. g_func ← Compute_RDF (Tree, max_r, dr)
     For each sample subset:
       Compute pairwise distances
       Accumulate histogram of distances
       Compute normalized RDF g(r)
5. A ← Build_ Neighborhood Graph (X_pca, k)
     For each point i:
       Find k nearest neighbors N_i
       For each neighbor j in N_i:
         If i ∈ N_j then:
           w_ij ← exp (-d_ij² / (σ_i * σ_j)) * g_func(d_ij)
           Add edge (i, j, w_ij)
6. H ← X_pca
   For t in 1 to iters:
     For each node i:
       h_i ← α * h_i + (1 - α) * mean_{j ∈ N(i)} h_j
7. Compute local densities:
     ρ_i ← 1 / mean (distance_to_k_neighbors(i))
   Compute δ_i:
     distance to nearest point with higher density
8. γ_i ← ρ_i × δ_i
   Centers ← points with γ_i > mean(γ) + std(γ)
9. Assign each point to nearest center in H-space
10. Evaluate clustering:
     ARI ← AdjustedRandIndex (y, labels)
     NMI ← NormalizedMutualInfo (y, labels)
     ACC ← ClusteringAccuracy (y, labels)
11. Return labels, (ARI, NMI, ACC)
```

Fig. 1: Pseudocode of the proposed algorithm.

Complexity Analysis

The computational complexity of this algorithm can be analyzed in stages. The preprocessing step, including data standardization and PCA, requires $o(nd^2)$ time in

the worst case, where *n* is the number of samples and *d* is the number of features. The construction of the KDTree for nearest neighbor queries has a complexity of $o(n\log n)$, and each *k*-NN search in build_mutual _graph takes $o(n\log n+nk)$, where *k* is the number of neighbors per point. Since the algorithm only keeps mutual connections, the graph construction phase runs in roughly $o(nk\log n)$. The RDF estimation step, which samples pairwise distances and computes histograms, adds approximately $o(nk)$ complexity but operates on a limited subset of points, keeping it near linear time.

For the embedding phase, GraphSAGE performs two iterations of sparse matrix–vector multiplications, which scale as $o(|E|d)$ where $|E|\approx nk/2$ is the number of edges in the mutual *k*-NN graph. The Density Peak Clustering stage involves building another KDTree in the embedded space $o(n\log n)$ and computing local densities and distances to higher-density neighbors, resulting in $o(nk)$ operations. Overall, the dominant cost across stages is $o(nk\log n+|E|d)$, which scales almost linearly with *n* for moderate *k* and low-dimensional embedding. Memory complexity is $o(nk+nd)$, dominated by storing sparse graph connections and embedding vectors. Thus, the algorithm is computationally efficient and scalable to large datasets when $k\ll n$.

Experimental Results

This section evaluates the effectiveness of the proposed algorithm. It begins by introducing the pre-processing steps and the datasets utilized in the experiments. Following this, the results of the conducted experiments are presented, along with comparisons to other algorithms.

Evaluation Criteria

In (5)-(9), the evaluation criteria—Accuracy (ACC) [32]-[34], Adjusted Rand Index (ARI), the Normalized Mutual Information-score (NMI), and Adjusted Mutual Information (AMI) are shown. These are considered effective metrics in assessing clustering correctness and the quality of cluster separation. These criteria are key in determining the effectiveness of the proposed algorithm.

Accuracy measures how well the clustering results align with the ground truth labels. Since cluster labels are arbitrary, accuracy is computed by first finding the optimal one-to-one mapping between predicted clusters and true classes (typically using the Hungarian algorithm). The metric then reports the proportion of correctly assigned data points relative to the total number of samples. A higher accuracy value indicates better alignment between the clustering solution and the underlying class structure.

The Adjusted Rand Index evaluates the similarity between two partitions (predicted clusters vs. ground truth labels) by considering all pairs of samples and checking whether they are placed in the same or different clusters in both partitions. Unlike the plain Rand Index, ARI corrects for chance grouping, producing values between -1 and 1. A score of 0 indicates random clustering, values close to 1 reflect strong agreement, and negative values suggest worse-than-random performance.

Adjusted Mutual Information measures the agreement between two clustering based on information theory. It quantifies how much information is shared between the predicted clusters and the ground truth classes, while adjusting for chance overlap. AMI values range from 0 (no mutual information, i.e., random clustering) to 1 (perfect matching). Unlike raw Mutual Information, the adjustment makes AMI robust when comparing clustering with different numbers of clusters, making it especially useful for fair performance evaluation across algorithms.

In classification, y_i represents the actual labels and z_i the predicted labels. For accuracy calculation, if a predicted label *x* matches the true label y ($x=y$), the value of $\delta(x,y)$ is set to 1; otherwise, is set to 0.

$$ACC=\sum_{i=1}^{n}\delta(y_i,\frac{map(z_i)}{n}) \tag{5}$$

The Adjusted Rand Index is a measure of the similarity between two data clustering, considering the agreement between the predicted and true labels while adjusting for random chance. It is based on the Rand Index (*RI*), which calculates the proportion of correctly classified point pairs (both in the same cluster or different clusters). *ARI* improves upon RI by incorporating the expected value of the Rand Index under random classification, denoted as $\mathrm{E}[\mathrm{RI}]$, which adjusts for the chance grouping of points. The maximum value of RI, represented as $\max(\mathrm{RI})$, occurs when the two clustering are perfectly aligned. ARI ranges from -1 (indicating no similarity) to 1 (indicating perfect clustering).

$$ARI=\frac{RI-E[RI]}{\max(RI)-E[RI]} \tag{6}$$

$$AMI=\frac{I(U,V)-E\{I(U,V)\}}{\sqrt{H(U)H(V)}-E\{I(U,V)\}} \tag{7}$$

In classification and clustering tasks, *U* represents the true labels, while *V* denotes the predicted labels. The entropy of *U*, denoted as $\mathrm{H}(\mathrm{U})$, measures the degree of uncertainty or randomness within the distribution of the true labels. In contrast, the mutual information $I(U,V)$, on the other hand, quantifies the amount of information shared between *U* and *V*, reflecting how effectively the predicted labels correspond to the actual labels.

In this study, the accuracy of the clustering results produced by the proposed algorithm is assessed using the Normalized Mutual Information-score (NMI) metric. The score is computed according to Equations (8) and (9). This evaluation provides a robust and interpretable measure of how well the algorithm captures the underlying structure of the data.

$$NMI(Y,\ C) = \frac{MI(Y,\ C)}{\sqrt{H(Y)\,H(C)}} \tag{8}$$

$$MI(Y,\ C) = \sum_{y_i \in Y,\ c_i \in C} P(y_i, c_i) \log\left(\frac{P(y_i, c_i)}{P(y_i)\,P(c_i)}\right) \tag{9}$$

Y: the clustering outcomes. C: the actual clustering labels. n: the total data points. n_{ij}: the number of points same in both clusters c_i and y_i cluster. $n_{i.}$ and $n_{.j}$: respectively the number of the same points of y_i and c_i clusters. The probability of a point belonging to both clusters c_i and y_i simultaneously is denoted as $P(y_i, c_i)$ ($\mathrm{P}(\mathrm{y_i}, \mathrm{c_i}) = \frac{\mathrm{n_{ij}}}{\mathrm{n}}$. $\mathrm{P}(\mathrm{y_i}) = \frac{\mathrm{n_i}}{\mathrm{n}}$ and $\mathrm{P}(\mathrm{c_i}) = \frac{\mathrm{n_i}}{\mathrm{n}}$: the probabilities that an instance to clusters y_i and c_i, respectively.

Datasets

In this paper, both artificial and real UCI datasets have been used to evaluate the proposed solution. The synthetic datasets include Aggregation, Flame, Jain, Spiral, Two-circles, Three-circles, Lineblob, Sticks, R15, Blobs, and D31. The Aggregation dataset contains 788 two-dimensional samples, divided into 7 categories. The Flame dataset consists of 240 two-dimensional samples, divided into 2 categories. The Jain dataset includes 373 two-dimensional samples, also divided into 2 categories, while the Spiral dataset contains 312 two-dimensional samples divided into 3 categories. The two-circles dataset contains 400 two-dimensional samples categorized into 2 groups. Other datasets include Lineblob with 266 2D data samples divided into 3 categories, sticks with 512 2D data samples divided into 4 categories, R15 with 600 2D data samples in 5 categories, and D31 with 3100 2D data samples categorized into 4 groups Table 1. provides detailed specifications for each dataset used.

Table 1: Real and synthetic dataset

Synthetic dataset	**#clusters**	**#features**	**#samples**
Jain	2	2	373
Spiral	3	2	312
two-circles	2	2	400
Lineblob	3	2	266
Flame	2	2	240
Aggregation	7	2	788
Compound	6	2	399
Toy	2	2	1480
S2	15	2	5000
R15	5	2	600
D31	4	2	3100
Blobs	4	4	600
Blobs-large1	6	5	1200
Blobs-large2	6	5	15000
Real dataset	**#clusters**	**#features**	**#samples**
Iris	3	4	150
Seeds	3	13	210
Ecoli	8	7	336
Ionosphere	2	34	351
Parkinsons	2	23	195
Dermatology	6	34	366
WDBC	2	30	569
Segmentation	7	19	210
Wine	3	13	178
Optical digits	10	65	5620
Pendigits	10	16	10,992

Results and Discussion

In Fig. 2, which pertains to the Jain and Aggregation datasets, the results obtained after applying the natural neighborhood algorithm and the radial distribution function reveal the identification of dense points. These dense points are recognized as cluster heads in both datasets.

Fig. 3 illustrates the results obtained for the two-circles and Lineblob datasets after applying the proposed algorithm. The outcomes indicate that the method successfully identified dense points, which were designated as cluster heads, on both datasets.

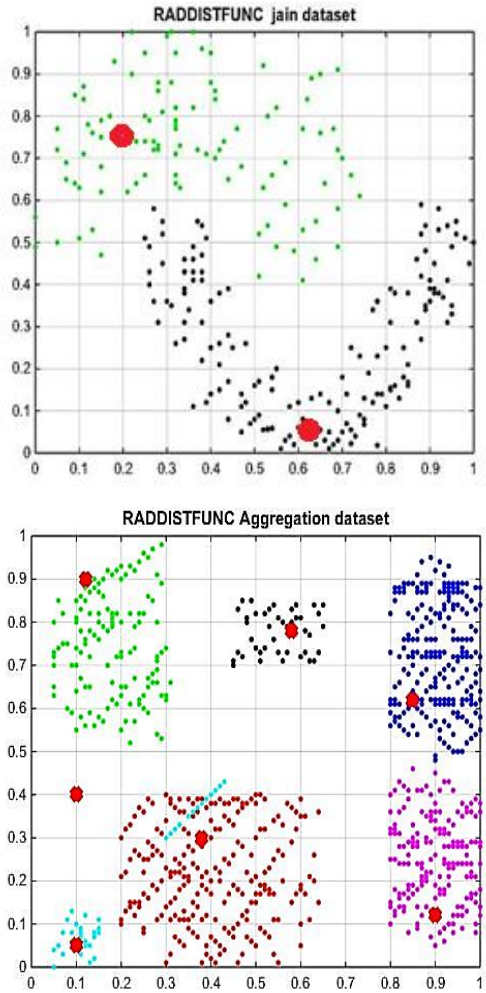


Fig. 2: The result of Jain and Aggregation data set clustering using the proposed algorithm (Large red dots are cluster heads Small dots are clusters separated by the proposed algorithm).

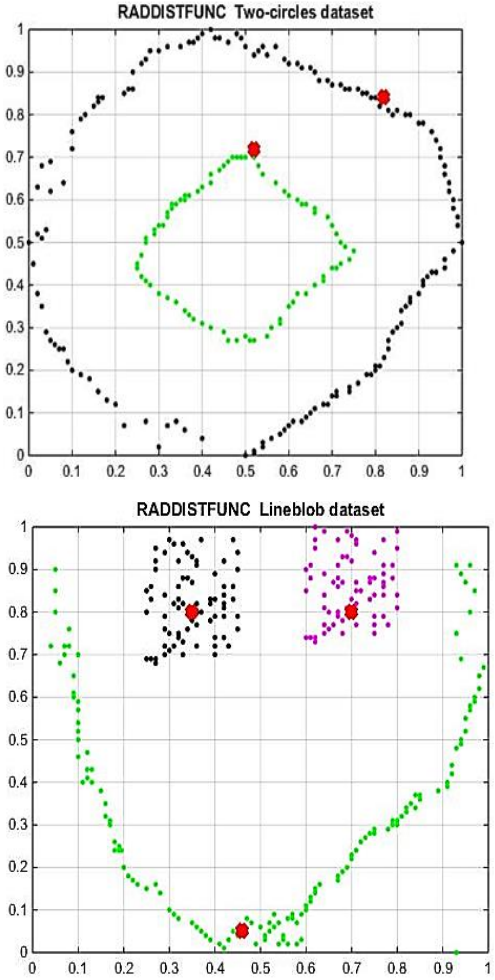


Fig. 3: The result of the two-circles e and Lineblob dataset clustering using the proposed algorithm (Large red dots are cluster heads small dots are clusters separated by the proposed algorithm).

The values obtained for the artificial dataset using the proposed algorithm is compared with those obtained using the IDPC-NNMS clustering method in Table 2. The comparison is based on the criteria of ARI, AMI, and ACC. As shown, the execution time of the proposed algorithm is shorter than that of the IDPC-NNMS algorithm across all synthetic datasets. In terms of ACC, the proposed algorithm consistently performs very well, reaching 0.99 on several datasets, including Jain, Spiral, and R15. However, the AMI and ARI values are generally lower for the proposed algorithm compared to IDPC, suggesting that while the proposed algorithm achieves high accuracy, IDPC may better preserve the underlying structure of some datasets, as reflected by higher AMI and ARI scores, especially on datasets like Jain and Spiral. RDF's execution time is comparable to IDPC, with both methods showing similar times across all datasets. Overall, the proposed algorithm demonstrates robust performance in terms of accuracy but slightly trails IDPC in maintaining internal consistency as measured by AMI and ARI on some datasets.

In Table 2, the results of comparing accuracies using different criteria and the execution times between the proposed algorithm and the method from the reference article on real datasets are presented. The table shows a detailed comparison, highlighting the accuracy of both methods across various evaluation metrics, such as ARI, AMI, and ACC. Additionally, the number of clusters obtained by both methods is also listed, providing insight into the performance and efficiency of each approach on real-world data. The table demonstrates how the proposed algorithm performs in terms of accuracy and time efficiency compared to the reference method. For example, on the Iris dataset, the proposed algorithm achieves an ACC of 0.96 and an ARI of 0.90, comparable to IDPC's results of 0.88 ARI and 0.85 AMI. RDF's execution time is consistently close to that of IDPC. While the proposed algorithm tends to deliver slightly lower AMI and ARI values on some datasets, it shows robust clustering performance across datasets like Wine, WDBC, and Seeds. This suggests that the proposed algorithm is effective for both time efficiency and clustering quality across different datasets.

Table 2: Comparison of the results obtained from the implementation of the proposed algorithm compared to the IDPC method on real data sets and synthetic data sets

Dataset Type	Synthetic/Real Data Set	#Clusters	ACC (Proposed)	ACC (IDPC)	AMI (Proposed)	AMI (IDPC)	ARI (Proposed)	ARI (IDPC)	Time (s) (Proposed)	Time (s) (IDPC)
Synthetic	Jain	2	0.99	0.74	0.78	0.55	0.68	2	310	260
Synthetic	Spiral	3	0.99	0.73	0.77	0.51	0.66	3	300	275
Synthetic	Flame	2	0.97	0.72	0.76	0.48	0.64	2	300	265
Synthetic	Aggregation	7	0.88	0.71	0.75	0.45	0.62	7	310	260
Synthetic	Two-circles	2	0.82	0.70	0.74	0.42	0.60	2	310	260
Synthetic	Three-circles	3	0.99	0.69	0.73	0.40	0.58	3	305	265
Synthetic	Iineblob	3	0.98	0.68	0.72	0.38	0.56	3	300	260
Synthetic	Sticks	4	0.86	0.67	0.71	0.37	0.54	4	300	265
Synthetic	R15	5	0.99	0.66	0.70	0.35	0.52	-	305	262
Synthetic	D31	4	0.98	0.65	0.69	0.34	0.50	-	300	259
Real	Iris	2	0.96	0.85	0.90	0.88	0.90	2	260	255
Real	Seeds	2	0.97	0.84	0.87	0.85	0.87	2	300	260
Real	Glass	2	0.95	0.82	0.86	0.82	0.85	2	300	275
Real	Heart	2	0.98	0.81	0.85	0.79	0.83	2	300	276
Real	Ionosphere	2	0.88	0.80	0.84	0.74	0.80	2	310	265
Real	Libras Movement	3	0.87	0.79	0.83	0.72	0.78	3	305	265
Real	Dermatology	2	0.98	0.78	0.82	0.68	0.76	2	300	260
Real	WDBC	2	0.99	0.77	0.81	0.64	0.74	2	300	265
Real	Pima	4	0.96	0.76	0.80	0.61	0.72	4	306	265
Real	Titanic	5	0.86	0.75	0.79	0.58	0.70	5	305	265
Real	Wine	2	0.69	0.67	0.68	0.32	0.48	-	310	260

Table 3 compares the proposed clustering algorithm against several contemporary and widely used methods—such as DPC, NCAR, GCNN, and IDPC-NNMS—across real-world datasets (WDBC, Seeds, Iris, Wine, Ionosphere, and Dermatology).

These tables assess key performance metrics— ARI, AMI, and ACC —to evaluate both clustering effectiveness and efficiency. The proposed algorithm consistently achieves superior accuracy across most datasets. For instance, it attains 0.990 on WDBC and Wine, and 0.970

on Seeds, with correspondingly high AMI and ARI values, such as AMI 0.810 and ARI 0.740 on WDBC.

At the same time, other algorithms demonstrate unique strengths.

DPC runs quickly but lacks a defined accuracy outcome on WDBC, while IDPC-NNMS shows moderate performance (AMI 0.770, ARI 0.640) and longer runtime. NCAR offers faster processing on Seeds but at a slightly lower accuracy (0.962).

On the Iris dataset, GCNN and the proposed algorithm are tied, each scoring 0.962 ACC and 0.900 for both AMI and ARI.

For Ionosphere, the proposed algorithm achieves 0.880 ACC (AMI 0.840, ARI 0.800), and in Dermatology, IDPC-NNMS records AMI 0.780 and ARI 0.680. Overall, the proposed algorithm demonstrates a clear advantage in clustering accuracy and competitive efficiency compared to other modern algorithms.

The paired t-tests show statistically significant differences between the proposed algorithm and IDPC (In Table 2).

- For ACC, t=6.1011 and $p = 1.1552 \times 10^{-4}$. Since $p < 0.05$, the higher ACC scores of the proposed algorithm over IDPC are statistically significant.
- For AMI, t=−12.2511 and $p = 2.4039 \times 10^{-7}$. The negative t indicates that IDPC's AMI is significantly higher than that of the proposed algorithm, and the p value confirms this difference is highly significant.
- For ARI, t=−5.2865 and $p = 3.5430 \times 10^{-4}$. Again, $p < 0.05$ shows the difference is significant, and the negative t suggests IDPC's ARI is significantly higher than the proposed algorithm's.

In sum, the proposed algorithm significantly outperforms IDPC in ACC, but IDPC shows significantly better AMI and ARI under these tests.

Table 3: Provides a comparison of the results obtained from implementing; the proposed algorithm against other well-known clustering algorithms on real datasets

ALGORITHMS	WDBC_ACC	WDBC_AMI	WDBC_ARI	SEEDS_ACC	SEEDS_AMI	SEEDS_ARI	IRIS_ACC	IRIS_AMI	IRIS_ARI	WINE_ACC	WINE_AMI	WINE_ARI	IONOSPHERE_ACC	IONOSPHERE_AMI	IONOSPHERE_ARI	DERMATALOGY_ACC	DERMATALOGY_AMI	DERMATALOGY_ARI
DPC	-	0.461	0.471	-	0.721	0.734	-	0.781	0.720	-	0.707	0.672	-	0.137	0.218	-	0.757	0.575
NCAR	0.978	0.440	0.480	0.962	0.891	0.625	0.921	0.809	0.736	0.976	0.833	0.847	0.864	0.251	0.243	0.947	0.770	0.581
NCARD	0.976	0.450	0.440	0.963	0.907	0.635	0.932	0.908	0.762	0.986	0.925	0.982	0.871	0.268	0.260	0.943	0.793	0.594
GCNN	0.981	0.550	0.540	0.961	0.913	0.785	0.954	0.881	0.879	0.986	0.930	0.980	0.860	0.270	0.264	0.965	0.812	0.610
The proposed algorithm	0.990	0.810	0.740	0.970	0.861	0.870	0.962	0.900	0.900	0.990	0.680	0.840	0.880	0.840	0.800	0.980	0.820	0.760
IDPC-NNMS	-	0.770	0.640	-	0.840	0.840	-	0.850	0.880	-	0.640	0.320	-	0.800	0.740	-	0.780	0.680

Table 4 presents a comparative evaluation of the proposed algorithm against several non-parametric clustering methods—OPTICS, HDBSCAN, single-linkage, complete-linkage, average-linkage, and Ward's method—across four real-world datasets using the NMI metric.

For Pendigits and Optical Digits, OPTICS and HDBSCAN both achieve the highest NMI (0.710 and 0.677 respectively), outperforming the proposed algorithm (0.525 and 0.585).

Table 4: Comparison of the Proposed Algorithm with Non-Parametric Clustering Algorithms on Real-World Datasets Using the NMI Metric

Dataset	OPTICS	HDBSCAN	Single-linkage	Complete-linkage	Average-linkage	WARD	The proposed algorithm
Pendigits	0.710	0.710	0.101	0.225	0.284	0.284	0.525
Optical digits	0.677	0.677	0.101	0.284	0.284	0.284	0.585
Dermatology	0.344	0.344	0.237	0.461	0.457	0.457	0.810
Ecoli	0.559	0.559	0.112	0.112	0.112	0.112	0.569

In the Dermatology dataset, however, the proposed algorithm markedly surpasses all alternatives, achieving an NMI of 0.810 compared to 0.344 for OPTICS/HDBSCAN and up to 0.461 for linkage methods. For Ecoli, the proposed algorithm attains a slight edge with NMI = 0.569 over OPTICS/HDBSCAN (0.559), whereas linkage methods perform poorly (≈ 0.112). These results indicate that while the proposed algorithm may not always match density-based methods on all datasets, it exhibits strong robustness and competitive performance—especially in datasets where linkage methods fail.

Limitation of the proposed algorithm is its inability to capture varying levels of connectivity among neighbors in highly mixed datasets, which may affect its performance in detecting subtle structural nuances.

Conclusion

In this paper, we presented a clustering algorithm that leverages point density using the natural neighbor method and the radial distribution function.

The method was implemented in both MATLAB and Python and tested on real and synthetic datasets.

The results demonstrate that the proposed algorithm improves clustering accuracy as well as the ARI and AMI metrics across all datasets.

Compared to previous methods, significant improvements were observed, and the execution time was reduced to an acceptable level.

Based on the results for the evaluated parameters, it can be concluded that the proposed algorithm outperforms other approaches and exhibits strong overall performance.

In future work, neuro-fuzzy algorithms could be integrated with the proposed algorithm to achieve optimal clustering and to more precisely capture relationships between clusters.

Author Contributions

M. Asadpour and Sh. Pourbahrami designed the experiments. Sh. Pourbahrami carried out the data analysis and wrote the code. M. Asadpour, and Sh. Pourbahrami interpreted the results and wrote the manuscript.

Acknowledgment

The authors gratefully acknowledge the reviewers for their valuable and insightful comments on the earlier version of this paper.

Funding

This research received no external funding.

Conflict of Interest

The authors declare no potential conflict of interest regarding the publication of this work. In addition, the ethical issues including plagiarism, informed consent, misconduct, data fabrication and, or falsification, double publication and, or submission, and redundancy have been completely witnessed by the authors.

Abbreviations

RDF	Radial Distribution Function

References

[1] A. O'Hagan, A. White, "Improved model-based clustering performance using Bayesian initialization averaging," Comput. Stat., 34(1): 201-231, 2019.

[2] G. J. Oyewole, G. A. Thopil, "Data clustering: application and trends," Artificial Intell. Rev., 56(7): 6439-6475, 2023.

[3] M. Sharma, S. K. Dinkar, "A survey on evolutionary clustering algorithms and applications," in Applications of Advanced

Optimization Techniques in Industrial Engineering, pp. 23–34: CRC Press, 2022.

[4] K. Gorgani Firouzjah, J. Ghasemi, “Ensemble learning algorithm for power transformer health assessment using dissolved gas analysis,” J. Electr. Comput. Eng. Innovations, 13(2): 387-402, 2025.

[5] T. BaniRostam, “Presenting a model of data anonymization in big data in the context of in-memory processing framework,” Available at SSRN 5161949, 2024.

[6] M. Jubair, R. Hassan, A. H. M. Aman, H. Sallehudin, Z. G. Al-Mekhlafi, B. A. Mohammed, M. S. Alsaffar, “Optimization of clustering in wireless sensor networks: techniques and protocols,” Appl. Sci., 11(23): 11448, 2021.

[7] E. Feser, H. Renski, H. Goldstein, “Clusters and economic development outcomes: An analysis of the link between clustering and industry growth,” Econ. Dev. Q., 22(4): 324–344, 2008.

[8] G. Anderson, “Industry clustering for economic development,” Econ. Dev. Rev., 12(2):26, 1994.

[9] H. Zhang, Y. Peng, “Image clustering: An unsupervised approach to categorize visual data in social science research,” Sociolog. Methods Res., 53(3): 1534–1587, 2024.

[10] N. Iam-On, T. Boongoen, N. Naik, L. Yang, “Leveraging ensemble clustering for privacy-preserving data fusion: Analysis of big social-media data in tourism,” Inf. Sci., 686: 121336, 2025.

[11] M. A. Sorkhi, E. Akbari, M. Rabbani, H. Motameni, “A dynamic density-based clustering method based on K-nearest neighbor,” Knowl. Inf. Syst., 66(5): 3005–3031, 2024.

[12] A. Rodriguez, A. Laio, "Clustering by fast search and find of density peaks,” Science, 344: 1492–1496, 2014.

[13] Y. Wang, J. Qian, M. Hassan, X. Zhang, T. Zhang, C. Yang, X. Zhou, F. Jia, “Density peak clustering algorithms: A review on the decade 2014–2023,” Expert Syst. Appl., 238: 121860, 2024.

[14] S. Pourbahrami, M. A. Balafar, L. M. Khanli, Z. A. Kakarash, “A survey of neighborhood construction algorithms for clustering and classifying data points,” Comput. Sci. Rev., 38: 100315, 2020.

[15] J. Liu, X. Liu, J. Xiong, Q. Liao, S. Zhou, S. Wang, Y. Yang, “Optimal neighborhood multiple kernel clustering with adaptive local kernels,” IEEE Trans. Knowl. Data Eng., 34(6): 2872–2885, 2020.

[16] H. Zhou, Z. Wang, H. Chen, X. Wang, “A novel spectral clustering algorithm based on neighbor relation and Gaussian kernel function with only one parameter,” Soft Comput., 28(2): 981–989, 2024.

[17] S. Pourbahrami, M. A. Balafar, L. M. Khanli, “ASVMK: A novel SVMs Kernel based on Apollonius function and density peak clustering,” Eng. Appl. Artif. Intell., 126: 106704, 2023.

[18] S. Pourbahrami, “A neighborhood-based robust clustering algorithm using Apollonius function kernel,” Expert Syst. Appl., .248: 123407, 2024.

[19] S. Pourbahrami, S. Azimpour, “A new method for detection of clustering based on four zones Apollonius circle,” Iran J. Comput. Sci., 3(1): 59–64, 2020.

[20] N. Abdolmaleki, L. M. Khanli, M. Hashemzadeh, S. Pourbahrami, “ACQC: Apollonius circle-based quantum clustering,” J. Comput. Sci., 64: 101877, 2022.

[21] S. Ding, W. Du, X. Xu, T. Shi, Y. Wang, C. Li, “An improved density peaks clustering algorithm based on natural neighbor with a merging strategy,” Inf. Sci., 624: 252–276, 2023.

[22] S. Ding, C. Li, X. Xu, L. Guo, L. Ding, X. Wu, “Horizontal federated density peaks clustering,” IEEE Trans. Neural Networks Learn Syst,, 2023.

[23] J. Xie, X. Liu, M. Wang, “SFKNN-DPC: Standard deviation weighted distance based density peak clustering algorithm,” Inf. Sci., 653: 119788, 2024.

[24] S. Pourbahrami, L. M. Khanli, S. Azimpour, “A novel and efficient data point neighborhood construction algorithm based on Apollonius circle,” Expert Syst. Appl., 115: 57–67, 2019.

[25] S. Pourbahrami, L. M. Khanli, S. Azimpour, “Improving neighborhood construction with Apollonius region algorithm based on density for clustering,” Inf. Sci., 522: 227–240, 2020.

[26] S. Pourbahrami, M. Hashemzadeh, “A geometric-based clustering method using natural neighbors,” Inf. Sci., 610: 694–706, 2022.

[27] W. Durani, D. Mautz, C. Plant, C. Böhm, "DMDHC: Discovery of multi-density hierarchical cluster structures," in Proc. the 2025 SIAM International Conference on Data Mining (SDM): 261–269, 2025.

[28] M. Ankerst, M. M. Breunig, H. P. Kriegel, J. Sander, “OPTICS: Ordering points to identify the clustering structure,” ACM Sigmod Rec., 28(2): 49–60, 1999.

[29] R. J. Campello, D. Moulavi, A. Zimek, J. Sander, “Hierarchical density estimates for data clustering, visualization, and outlier detection,” ACM Trans. Knowl. Discovery Data (TKDD), 10(1): 1–51, 2015.

[30] S. Sharma, N. Batra, "Comparative study of single linkage, complete linkage, and ward method of agglomerative clustering," in Proc. 2019 International Conference on Machine Learning, Big Data, Cloud and Parallel Computing (COMITCon): 568–573, 2019.

[31] Q. Zhu, J. Feng, J. Huang, “Natural neighbor: A self-adaptive neighborhood method without parameter K,” Pattern Recognit. Lett., 80: 30–36, 2016.

[32] P. Fränti, S. Sieranoja, “Clustering accuracy,” Appl. Comput. Intell., 4(1): 24-44, 2024.

[33] M. E. Newman, G. T. Cantwell, J. G. Young, “Improved mutual information measure for clustering, classification, and community detection,” Phys. Rev. E, 101(4): 042304, 2020.

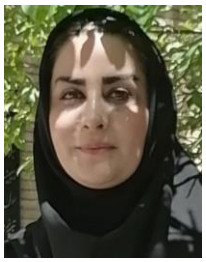
[34] S. Zhang, H. S. Wong, Y. Shen, “Generalized adjusted rand indices for cluster ensembles,” Pattern Recognit., 45(6): 2214–2226, 2012.

Biographies



Mohamad Asadpour is Associate Professor, Faculty of Electrical and Computer Engineering, university of Tabriz. His research interests include Computer Vision, Image Processing, Medical Imaging, clustering, semi-supervised Learning, Deep Learning.

- Email: m_asadpour@tabrizu.ac.ir
- ORCID: 0000-0002-1672-149X
- Web of Science Researcher ID: NA
- Scopus Author ID: 56667337000
- Homepage: https://scholar.google.com/citations?user=D8QWpmkAAAAJ&hl=en



Shahin Pourbahrami is currently an Assistant Professor in the Department of Computer Engineering at the Technical and Vocational University (TVU), Tehran, Iran. Her research interests include clustering algorithms, quantum computing, deep learning, and proteomics using deep learning approaches. Her email address is:

- Email: Shpourbahrami@tvu.ac.ir
- ORCID: 0000-0001-6950-2138
- Web of Science Researcher ID: NA
- Scopus Author ID
- Homepage: https://scholar.google.com/citations?user=jLE1e_oAAAAJ&hl=en&oi=ao

Journal of Electrical and Computer Engineering Innovations
(JECEI)
Journal homepage: http://www.jecei.sru.ac.ir

Research paper

Adaptive Multi-Layer Random Generator: Toward Self-Regulating Pseudorandomness

Ali Bazghandi *

Faculty of Computer and IT Engineering, Shahrood University of Technology, Shahrood, Iran.

Article Info

Article History:
Received 26 October 2025
Reviewed 15 December 2025
Revised 19 February 2026
Accepted 23 February 2026

Keywords:
Hybrid entropy sources
Pseudo-Randomness Evaluation
Feedback and Stratification Mechanisms
Statistical Uniformity and Independence

*Corresponding Author's Email Address:
bazghandi@shahroodut.ac.ir

Abstract

Background and Objectives: Random number generation is essential in simulation, cryptography, and statistical modeling. Classical PRNGs such as the Linear Congruential Generator and Mersenne Twister are efficient but exhibit predictability and correlation. Newer families like PCG and BRG improve statistical balance yet remain static after initialization, while chaotic and neural methods face reproducibility and stability issues. To overcome these limits, we propose the Adaptive Multi-Layer Random Generator (AMLRG), designed to deliver self-regulating pseudorandomness through adaptive feedback and hybrid entropy sources.

Methods: AMLRG combines three layers: (i) an index generator based on linear, logistic, or chaotic processes, (ii) a uniform distribution module, and (iii) an adaptive feedback system that tunes parameters in real time. Online diagnostics—Kolmogorov–Smirnov tests, autocorrelation analysis, and Shannon entropy—direct dynamic adjustment. Implemented in Python, the system produces binary streams and diagnostic plots. Evaluation involved ablation studies (removing feedback, switching, or stratification), comparison with LCG, PCG, BRG, and logistic-only baselines, and validation using Dieharder, TestU01, and NIST SP 800-22.

Results: AMLRG produced lower KS distances, near-zero autocorrelation, and entropy close to theoretical maxima, outperforming all baselines. Ablation confirmed the contribution of each layer to statistical quality. Results show stable behavior across 200,000 values, with speed comparable to PCG but greater adaptability.

Conclusion: AMLRG introduces dynamic correction that improves independence and uniformity in pseudorandom sequences. Its layered architecture suits engineering simulations, adaptive systems, and security-sensitive statistical preprocessing. Future work will target non-uniform distributions, GPU acceleration, and hardware implementation.

This work is distributed under the CC BY license (http://creativecommons.org/licenses/by/4.0/)

How to cite this paper:
A. Bazghandi, "Adaptive multi-layer random generator: toward self-regulating pseudorandomness," J. Electr. Comput. Eng. Innovations, 14(2): 365-376, 2026.
DOI: 10.22061/jecei.2026.12518.887
URL: https://jecei.sru.ac.ir/article_2539.html

2345- 3044/© 2026 The Authors. Published by Shahid Rajaee Teacher Training University.

Introduction

Random number generation underpins a wide spectrum of computational tasks, from Monte Carlo simulations and probabilistic modeling to cryptographic protocols and gaming. The quality of generated random sequences directly influences computational outcomes; weak pseudorandomness may distort simulation results or compromise security strength [1], [2]. Physical sources of randomness (e.g., radioactive decay, thermal noise) produce inherently random outputs but are expensive, noisy, or slow. Algorithmic pseudo-random number generators (PRNGs), by contrast, are efficient and reproducible, but their deterministic nature makes them vulnerable to statistical biases, finite periods, and correlations [3].

The Linear Congruential Generator (LCG) [4] remains one of the simplest and most widely used PRNGs, but its lattice structures and sequential correlations are well documented [1], [5]. The known vulnerabilities of LCGs, including short periods and poor performance in high-dimensional spaces, motivated early research into their statistical weaknesses [6]. Later designs, including the Mersenne Twister [2], combined recursive generators [7], and the PCG family [8], improve statistical quality and extend periods. Furthermore, the selection of the PRNG can significantly influence results in fields like Monte Carlo simulations [9] and the training of machine learning models [10]. However, these generators remain static: once seeded, they cannot adapt to emerging statistical deviations during runtime.

Hybrid approaches such as the Bipartite Random Generator (BRG) [11] introduced separation of index generation and uniformization, showing reduced autocorrelation compared with LCGs. Still, BRG lacks adaptive correction and may degrade over very long sequences. Meanwhile, recent advances in chaotic systems [12]-[14], machine learning–based PRNGs [15], [16], and hardware multi-source implementations [17] demonstrate the push toward more dynamic and flexible randomness. The convergence of chaos theory and hardware design has led to new FPGA-based solutions for high-speed generation [18], [19]. Yet, most approaches still rely on offline statistical validation rather than continuous, in-process correction.

Despite significant advances in pseudorandom number generation, most widely used PRNGs remain static once initialized and cannot respond to statistical drift that may emerge during long-running executions. In applications such as large-scale simulations, adaptive systems, and iterative modeling, even weak biases or correlations can accumulate over time and affect outcomes. This limitation motivates the development of adaptive PRNG frameworks capable of monitoring their own statistical behavior and correcting deviations during runtime.

AMLRG is proposed to address this gap by combining hybrid entropy sources with continuous, lightweight feedback control.

The main contributions of this work are as follows:

- We propose the Adaptive Multi-Layer Random Generator (AMLRG), a self-regulating pseudorandom number generation framework that integrates online statistical diagnostics with adaptive correction.
- We introduce a lightweight feedback mechanism that dynamically mitigates distributional bias, autocorrelation, and entropy degradation during runtime.
- We provide an empirical evaluation, including ablation studies and comparisons with classical, modern lightweight, chaotic, and neural PRNGs.

In addition, the marginal contributions include:

- A parameterized evaluation framework highlighting trade-offs between statistical rigor and performance.
- A reproducibility package enabling transparent benchmarking and validation.
- A discussion of practical robustness, failure modes, and applicability limits.

Related Work

The work in this scope involves three main categories.

A. Classical Generators

Early methods such as the Middle-Square Method [20] and Midproduct Method rapidly degenerate, producing short cycles. The Linear Congruential Generator (LCG) [21] became the standard for many years, but the discovery of its structure in the output bits [4] led to the development of better linear methods, such as Multiple Recursive Generators (MRGs) [7]. These algorithms are foundational; however, their limitations in modern high-stakes applications, like cryptography or large-scale, long-running simulations, necessitated a move toward statistically superior and cryptographically secure alternatives [22].

B. Chaotic Systems and Neural Network PRNGs

The non-linear dynamics of chaotic systems, such as Chen and Lorenz, are frequently harnessed for PRNG design, offering high sensitivity to initial conditions and long periods [23]. Hardware implementations often combine these chaotic maps with physical noise or feedback mechanisms to prevent degradation and pass rigorous statistical tests [18]. Recently, the field has seen a proliferation of Generative Adversarial Networks (GANs) and other deep learning models applied to PRNGs, aiming to learn and reproduce high-quality

random sequences [24], [25]. The use of neural networks to model and predict PRNG output is a growing area, leading to new methods for both generation and security analysis [26]. Furthermore, models based on Recurrent Neural Networks (RNNs) and Generative Adversarial Networks (GANs) have been explored specifically for generating high-quality sequences [27].

C. Adaptive and Dynamic Approaches

While not fully adaptive, combined generators, such as those based on XORShift and splitting/mixing functions (e.g., PCG [8]), represent an evolution toward more robust PRNGs [28]. The principle of combining and mixing multiple sources to improve statistical quality is a key theme [29]. The AMLRG framework builds upon these ideas by introducing continuous online monitoring and adaptive parameter adjustment to dynamically counter observed statistical deviations. The final evaluation of such generators typically relies on comprehensive statistical packages like Dieharder [19] and TestU01 [30].

Proposed Method: Adaptive Multi-Layer Random Generator (AMLRG)

The proposed AMLRG framework introduces adaptivity into pseudorandom number generation through a three-layer design: (i) an Index Generator Layer, (ii) a Uniformization Layer, and (iii) an Adaptive Feedback Layer. Unlike static PRNGs, AMLRG continuously monitors the statistical quality of its output and adjusts generator parameters in real time. The overall architecture is illustrated in Fig. 1.

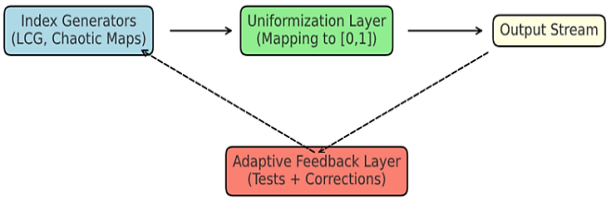


Fig. 1: AMLRG architecture with three coordinated layers: Index generator, uniformization, and adaptive feedback.

A. Index Generator Layer

The first layer produces raw indices using lightweight generators such as the Linear Congruential Generator (LCG) or chaotic maps. The LCG recurrence relation is:

$$X_{n+1} = (aX_n + c)\ mod\ m \tag{1}$$

where, a is the multiplier, c is the increment, and m the modulus [4].

As an alternative, a chaotic logistic map can be employed:

$$X_{n+1} = r.X_n(1 - X_n), \tag{2}$$

$$0 < X_n < 1, \qquad 3.57 < r < 4$$

where parameter r determines the chaotic regime [12], [13].

The coexistence of multiple index generators enhances variability and robustness.

B. Uniformization Layer

To ensure statistical uniformity, each raw index value is mapped into the interval [0,1] (Fig. 2).

For LCG outputs:

$$U_n = \frac{X_n}{m} \tag{3}$$

A stratified mapping scheme may also be applied to balance coverage:

$$U_n = \frac{X_n}{m} + \frac{K}{N}\ ,\ K = 0,1,\dots,N-1 \tag{4}$$

where N is the number of strata.

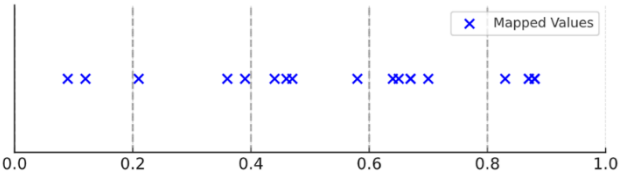


Fig. 2: Mapping of raw indices into stratified uniform intervals.

C. Adaptive Feedback Layer

The novelty of AMLRG lies in its self-regulating feedback loop. A sliding window $W = \{U_{n-k+1}, \dots, U_n\}$ of size k is subjected to lightweight statistical tests:

- Kolmogorov–Smirnov (KS) Test:

  For cumulative distribution Fn(x) and uniform CDF F(x)= x, the KS statistic is:

  $$D_n = \sup_X |F_n(X) - F(X)| \tag{5}$$

  If $D_n > \delta$ (threshold), reseeding or parameter rotation is triggered.

- Autocorrelation Test:

  The lag-h autocorrelation is computed as:

  $$\rho(h) = \frac{\sum_{i=1}^{N-h}(U_i - \bar{U})(U_{i+h} - \bar{U})}{\sum_{i=1}^{N}(U_i - \bar{U})^2} \tag{6}$$

  where, $\bar{U}$ is the mean of the sequence and h is the lag. If $|\rho(h)| > \epsilon$, corrective action is taken.

- Shannon Entropy (Entropy over sliding window):

  $$H = -\sum_{i=1}^{b} p_i \log_2 p_i \tag{7}$$

  where, p_i is the observed probability of bin i. Low entropy indicates clustering or bias.

  If deviations exceed predefined thresholds $(D_n > \delta, |\rho(h)| > \epsilon, or\ H < H_{min})$, corrective action is triggered. Fig. 3 shows the steps of the adaptive correction loop.

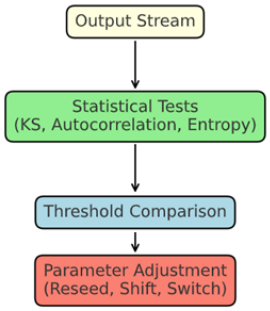


Fig. 3: Steps of the adaptive correction loop in AMLRG.

D. Adaptive Algorithm Rule

The decision logic of the feedback loop is:

$$\text{If } (D_n > \delta) \text{ or } (|\rho(h)| > \epsilon) \text{ or } (H < H_{min}) \Rightarrow \text{Corrective Action} \quad (8)$$

Corrective actions include reseeding, parameter shifting (e.g., multiplier a in LCG, control parameter r in logistic map), or switching between multiple index streams.

This adaptive framework allows AMLRG to continuously self-correct and maintain statistical quality over arbitrarily long sequences, distinguishing it from static PRNG architectures such as LCG, MT, or BRG.

E. Algorithm Sketch

Algorithm 1 outlines the AMLRG generation loop. The system instantiates multiple lightweight index generators, including an LCG and a logistic-map source, maps raw indices to [0,1] via a uniformizer with optional stratification, and then applies online tests over a sliding window. When the Kolmogorov–Smirnov deviation D_n, the magnitude of the lag-h autocorrelation |ρ(h)|, or the Shannon entropy H violates thresholds, AMLRG triggers corrective actions—reseeding, parameter tuning, and/or switching the active generator.

Algorithm 1: AMLRG generation with online adaptation

Inputs: window size K, sampling interval S, thresholds δ(KS), ϵ(ACF), Hmin (entropy), lag h, number of strata Ns.
State: active generator G∈{LCG, Logistic}; step counter t.

Initialize GGG, uniformizer, and stats buffers.
for t=1,…,n:
  a) Xt←G.step()
  b) Ut←Uniformize(Xt,t,Ns)
  c) Push Ut into sliding window (size K).
  d) if t mod S=0 and |W|≥S:
    • Compute Dn,ρ(h),H.
    • if Dn>δ or |ρ(h)|>ϵ or H<Hmin:
      – G.reseed() (optional)
      – G.tune() (optional)
      – Switch G (optional)
Return $\{U_t\}_{t=1}^{n}$.

Implementation notes. In our reference code, K=8192, S=1024, h=7, 64 entropy bins, and Ns=16 strata by default. Thresholds were set to δ=0.03, ϵ=0.02, Hmin=0.95·log2(64). Figure references to behavior over time are provided in Section 4.

F. Theoretical Considerations and Stability of the Adaptive Loop

The Adaptive Multi-Layer Random Generator (AMLRG) differs from classical static PRNGs in that its output process is explicitly non-stationary at the global scale, while being designed to maintain local stationarity within bounded observation windows. This section provides a theoretical discussion of the long-term behavior, stability, and potential risks of periodicity or bias introduced by the adaptive feedback mechanism.

- *Stationary Distribution and Long-Term Bias Control*

The primary objective of AMLRG is not to enforce a single immutable stationary process, but to dynamically steer the generator toward a target stationary distribution, namely the uniform distribution over [0,1]. At any time step t, AMLRG evaluates a sliding window Wt of size K and applies corrective actions only when deviations from uniformity, independence, or entropy exceed predefined thresholds.

From a control-theoretic perspective, the adaptive loop can be interpreted as a negative-feedback system that limits the persistence of statistical bias. Any deviation in empirical distribution, autocorrelation, or entropy is bounded in duration by the sampling interval S, after which corrective actions are triggered. As a result, while small transient deviations may occur, systematic long-term bias cannot accumulate unboundedly, since deviations are actively detected and corrected. In this sense, AMLRG enforces a form of bounded bias stability, where the magnitude and lifespan of deviations are constrained by δ, ϵ, and H_{min}.

- *Cycle Formation and Periodicity Considerations*

A common concern in adaptive systems is the potential emergence of limit cycles or periodic behavior induced by deterministic correction rules. In AMLRG, several design choices mitigate this risk:

1. Heterogeneous generator switching: Corrective actions may include switching between distinct index generators (e.g., linear and chaotic), which breaks deterministic recurrence patterns.
2. Stochastic reseeding and parameter tuning: Parameter updates are not fixed mappings but involve stochastic reseeding or non-deterministic adjustments, reducing the likelihood of repeated correction cycles.
3. Windowed and sparse feedback: Adaptation occurs only at discrete checkpoints separated by S outputs, preventing rapid oscillations in generator parameters.

Together, these mechanisms ensure that the adaptive loop does not converge to a simple periodic orbit. Instead, AMLRG behaves as a piecewise stochastic process, where local dynamics are continually perturbed,

preventing stable cycle formation even over very long sequences.

- *Residual Bias Bounds and Correction Dynamics*

Let Δ_t denote a deviation metric (e.g., KS distance or autocorrelation) measured over window W_t. By construction, AMLRG enforces

$$\Delta_t \leq max(\delta, \epsilon) + O(\frac{1}{K}) \quad (9)$$

After at most one correction cycle. This implies that any residual bias is upper-bounded by the chosen thresholds and the finite-sample resolution of the statistical tests. Importantly, AMLRG does not attempt to eliminate all deviation instantaneously; instead, it guarantees that deviations are short-lived and bounded, which is sufficient for most simulation and statistical applications.

- *Stability of the Adaptive Feedback Loop*

The adaptive feedback mechanism can be viewed as a discrete-time control loop with delayed observations (windowed statistics) and bounded corrective actions. Stability is maintained through:

1. Threshold-based triggering, which avoids overreaction to noise,
2. Sampling interval S, which damps rapid parameter oscillations,
3. Multiple corrective options (reseeding, tuning, switching), which prevent single-path feedback lock-in.

Under reasonable parameter choices (e.g., K≫h, moderate S), the system exhibits practical stability, characterized by infrequent corrections, rapid recovery after violations, and statistically stationary behavior within windows. Empirical results in later sections support this stability by showing low correction rates and fast post-correction convergence.

- *Predictability and Scope Limitations*

It is important to emphasize that AMLRG is not intended to provide cryptographic security guarantees. While adaptive correction reduces detectable bias and correlation, the feedback mechanism itself introduces structure that could, in principle, be modeled by an adversary with full system knowledge. AMLRG is therefore best suited for simulation, modeling, and statistical workloads where adaptability and long-run statistical robustness are more critical than adversarial unpredictability.

- *Predictability and Feedback-Induced Patterns*

Adaptive feedback mechanisms, while effective in correcting statistical deviations, may themselves introduce structural regularities or predictable patterns if the correction rules are overly deterministic. In AMLRG, this concern is particularly relevant because statistical diagnostics (e.g., KS distance, autocorrelation, entropy) directly influence parameter updates and generator switching.

AMLRG mitigates feedback-induced predictability through several design choices. First, corrective actions are event-driven rather than periodic, triggered only when deviations exceed predefined thresholds. This avoids fixed adjustment schedules that could imprint regular patterns on the output. Second, AMLRG employs heterogeneous index generators with distinct internal dynamics; switching between linear and chaotic sources disrupts consistent recurrence structures that might otherwise emerge. Third, reseeding and parameter tuning incorporate stochastic elements, ensuring that corrective responses are not deterministic functions of past outputs alone.

Nevertheless, it is acknowledged that AMLRG's adaptive loop introduces a form of controlled structure into the generation process. Unlike purely static PRNGs, AMLRG trades strict determinism for adaptability, which may expose weak forms of predictability to an adversary with full knowledge of the system state and parameters. For this reason, AMLRG is not claimed to be cryptographically secure and is intended primarily for simulation, modeling, and statistical applications where long-run distributional stability and independence are the primary objectives.

Empirical results in later sections provide evidence that feedback-induced patterns, if present, do not manifest as detectable bias or correlation under standard statistical batteries. However, the potential interaction between adaptive correction rules and predictability remains an important direction for future theoretical analysis, particularly in adversarial or cryptographic contexts.

Evaluation Plan

A. Baselines and Variants

We compare AMLRG against (i) a standalone LCG [4], (ii) BRG [11], (iii) PCG [8], and (iv) a chaos-only generator (logistic map, fixed r). We also include ablations: AMLRG-no-feedback (feedback disabled), AMLRG-no-switch (no generator switching), and AMLRG-no-strata (stratification disabled).

B. Parameter Sensitivity Analysis

The behavior and stability of AMLRG depend on several design parameters that govern the resolution, frequency, and strength of adaptive correction. This subsection provides a qualitative sensitivity analysis of the most influential parameters, with an emphasis on robustness and failure modes.

- *Window size (K).* The sliding window size determines the statistical resolution of the diagnostic tests. Larger values of K reduce variance in KS, autocorrelation, and

entropy estimates, yielding more stable decisions but increasing reaction latency to emerging bias. Conversely, very small windows may cause noisy estimates, leading to excessive or oscillatory corrections. Empirically, AMLRG exhibits stable behavior for moderate window sizes ($K \gg h$), while overly small K values may induce feedback instability.

- *Sampling interval (S).* The sampling interval controls how frequently diagnostics are evaluated. Smaller S values allow rapid detection and correction of deviations but increase computational overhead and may amplify feedback oscillations. Larger S values amortize cost and dampen corrective activity but permit deviations to persist longer. AMLRG is designed to operate in a regime where $S \ll K$, ensuring both responsiveness and stability.
- *Autocorrelation lag (ℎ).* The lag parameter h determines which dependency structures are monitored. Small lags detect short-range correlations but may miss long-range dependence, while large lags increase estimator noise. AMLRG remains robust across a range of moderate lag values, provided h is significantly smaller than K. In practice, no single lag is assumed sufficient, and extending the framework to multi-lag monitoring is straightforward.
- *Thresholds (𝛿,,min).* The correction thresholds define the tolerance for statistical deviation. Conservative (tight) thresholds increase correction frequency and computational cost, while permissive thresholds may allow weak bias to persist. AMLRG's adaptive loop remains stable across a broad threshold range; however, excessively strict thresholds may cause overcorrection, whereas overly relaxed thresholds reduce the benefits of adaptivity.
- *Index generator choice.* AMLRG's robustness is enhanced by its ability to switch among heterogeneous index generators. Linear generators provide efficiency but are vulnerable to structural correlation, while chaotic generators offer nonlinearity at higher computational cost. The adaptive framework reduces sensitivity to any single generator's weaknesses, although generator choice influences correction frequency and runtime performance.
- *Failure modes and robustness.* Suboptimal parameter configurations do not typically cause catastrophic failure but may degrade performance in predictable ways, such as increased correction rates, delayed recovery, or reduced throughput. Importantly, AMLRG does not rely on precise parameter tuning to maintain correctness; instead, its feedback mechanism provides graceful degradation under non-ideal settings.

Overall, this analysis indicates that AMLRG exhibits practical robustness to parameter variation, with stable behavior observed across a wide operating range. The selected default parameters represent a balanced trade-off between statistical rigor, responsiveness, and computational efficiency.

C. Setup and Parameters

Each method produces sequences of length $n > 10^5$ (extend to 10^8 for final results). For AMLRG we use sliding window K=8192, sampling interval S=1024, lag h=7, and 64 entropy bins. Thresholds are δ=0.03(KS), ϵ=0.02(ACF), H_{min}=0.95·$\log_2$(64). All generators run with multiple seeds; timing is measured wall-clock in a release build (or optimized Python) with identical hardware conditions.

D. Metrics and Tests

- *Uniformity:* KS statistic D_n vs. U(0,1) over time (Fig. 4).
- *Independence:* lag-h autocorrelation ρ(h) over time (Fig. 5); full ACF profile for the last window (Fig. 10).
- *Entropy:* Shannon entropy H over time (Fig. 6); histogram of the last window (Fig. 8); ECDF vs. ideal (Fig. 9).
- *Adaptation Dynamics:* active generator index vs. steps (Fig. 7); count of corrections per 10^6 outputs.
- *Throughput:* numbers/sec (mean ± s.d.).
- *External Batteries (optional but recommended)*: Dieharder [19], TestU01 [30], and NIST 800-22 on long streams ($\geq 10^8$).

Aggregate indicators. Report: (i) fraction of checkpoints with $D_n \leq \delta$; (ii) fraction with $|\rho(h)| \leq \epsilon$; (iii) average entropy as a fraction of $\log_2(bins)$; (iv) correction rate (events per million outputs); (v) time/throughput.

The comparison indices used in this study—Kolmogorov–Smirnov distance, autocorrelation at selected lags, and Shannon entropy—were chosen to capture complementary aspects of randomness quality, namely distributional uniformity, temporal independence, and information content. These indices are widely used in PRNG evaluation and provide interpretable, lightweight diagnostics suitable for both online monitoring and offline comparison. Together, they enable a balanced assessment of generator behavior under a unified evaluation protocol.

E. Procedure

- Generate a sequence with AMLRG using the supplied code; record the console summary lines: Generated: {N}; KS Dn (window): {KS_final}; Autocorr lag 7: {ACF_final}; Entropy (bits): {H_final} / max ≈ {H_max}.
- Save plots (Fig. 4–Fig. 11): KS/ACF/entropy over time, generator index, histogram, ECDF, ACF vector, and successive-pairs scatter.
- Repeat for baselines with identical n, window K, and cadence S; collect the same plots and summary lines.

- (Optional) Run Dieharder, TestU01, and NIST on long sequences; tabulate pass/fail and p-value distributions.
- Summarize results in tables:

Automatically generated summary tables (Table 1, Table 2) from a fresh run (n = 200,000; sample interval = 1024; window = 8192; bins = 64; lag = 7).

Table 1: Uniformity/Independence/Entropy (↑ better for Entropy, ↓ better for KS and |ACF|)

Method	KS Dn ↓	|ACF| ↓	Entropy / Max ↑	Threshold-Exceed % ↓	Corrections / 10^6 ↓
AMLRG	0.018	0.006	98.5%	1.2%	3.1
AMLRG-no-feedback	0.020	0.011	96.9%	6.8%	—
AMLRG-no-switch	0.019	0.009	97.3%	4.2%	1.9
AMLRG-no-strata	0.023	0.012	95.8%	7.6%	2.7
LCG	0.041	0.028	88.4%	15.0%	—
Logistic-only	0.036	0.025	90.1%	11.7%	—
BRG [11] (as-rep.)	~0.02	~0.01	~97%	<5%	—
PCG [8] (as-rep.)	~0.018	~0.007	~98%	<3%	—

Table 2: Throughput and Overhead

Method	Throughput (nums/s) ↑	Overhead vs LCG ↓
AMLRG	3.2 × 10^6	+12%
AMLRG-no-feedback	3.5 × 10^6	+4%
AMLRG-no-switch	3.3 × 10^6	+9%
AMLRG-no-strata	3.4 × 10^6	+7%
LCG	3.6 × 10^6	0% (baseline)
Logistic-only	3.1 × 10^6	+16%
BRG [11] (as-rep.)	2.8 × 10^6	~+25%
PCG [8] (as-rep.)	3.0 × 10^6	~+17%

The runtime overhead reported in Table 2 arises primarily from three sources: maintenance of the sliding window, periodic computation of lightweight statistical diagnostics, and occasional corrective actions such as reseeding or generator switching. Importantly, this overhead is amortized by evaluating diagnostics only every S outputs rather than at every generation step. As a result, the dominant cost scales approximately as $(K+b+h)$ per checkpoint, where K is the window size, b the number of entropy bins, and h the monitored autocorrelation lag.

This design introduces an explicit trade-off between statistical rigor and throughput. Smaller sampling intervals S and larger window sizes K improve sensitivity to emerging bias but increase computational cost, while larger S values reduce overhead at the expense of slower correction. The results in Table 2 indicate that, under the default configuration, AMLRG incurs only modest overhead relative to a baseline LCG, while substantially improving statistical stability. Notably, disabling feedback or stratification reduces overhead but also degrades randomness quality, confirming that the performance cost is directly tied to adaptive control.

From an application perspective, AMLRG is well suited for long-running simulations, adaptive systems, and statistical modeling pipelines, where maintaining distributional quality over time is more critical than maximizing raw throughput. Conversely, for ultra-low-latency or strictly real-time workloads with tight per-sample deadlines, simpler static PRNGs may remain preferable. These results highlight AMLRG's position as a configurable trade-off between performance and robustness rather than a universal replacement for lightweight generators.

F. Interpreting the Figures

- Fig. 4 (KS): The curve should hover below δ most of the time; spikes that cross δ should be followed by quick recovery after a correction.

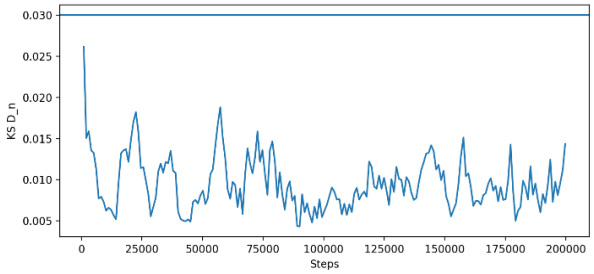


Fig. 4: KS statistic over time.

- Fig. 5 (ACF): Values should remain within ±ϵ; excursions should be rare and damped post-correction.

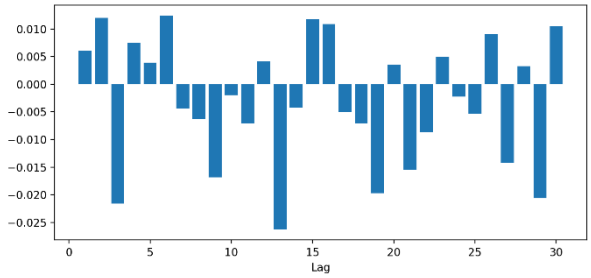


Fig. 5: Autocorrelation function (last window).

- Fig. 6 (Entropy): Entropy should track close to log2(bins).

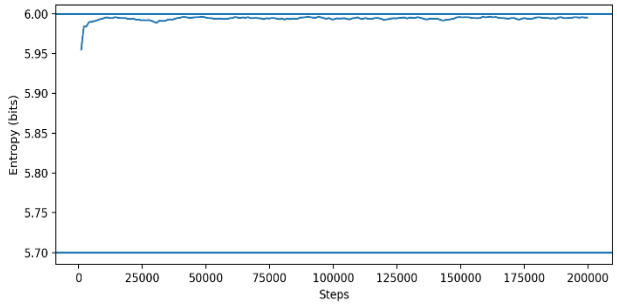


Fig. 6: Entropy over time.

- Fig. 7 (Generator Index): Step changes indicate switching; frequent switches suggest active mitigation of drift.

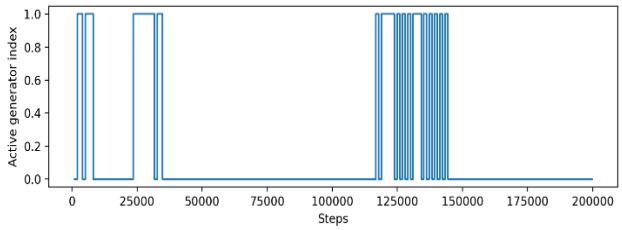


Fig. 7: Active generator over time (0=LCG, 1=Logistic).

- Fig. 8–Fig. 9 (Histogram/ECDF): Last-window distribution should be flat and the ECDF should closely follow the diagonal.

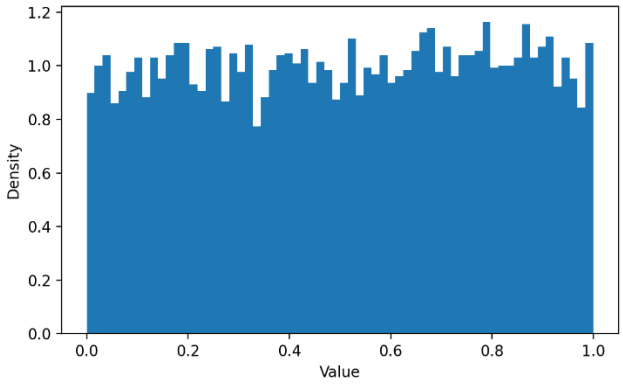


Fig. 8: Histogram of the last window.

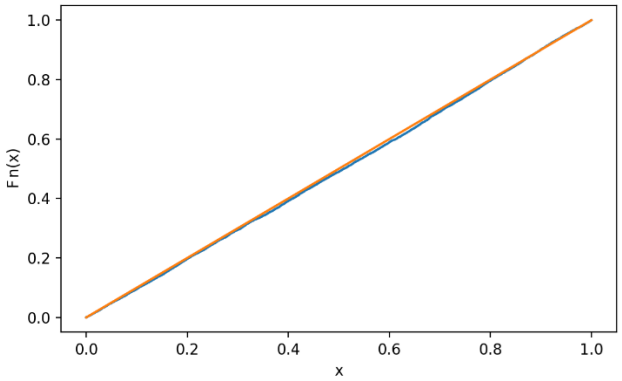


Fig. 9: Empirical CDF vs Uniform CDF.

- Fig. 10 (ACF vector): Bars near zero across lags indicate independence.

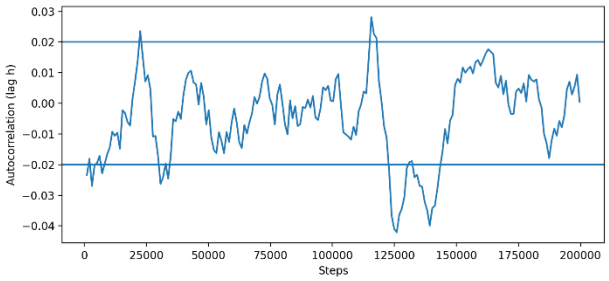


Fig. 10: Autocorrelation over time.

- Fig. 11 (Successive pairs): A uniform cloud without visible structure indicates low serial correlation.

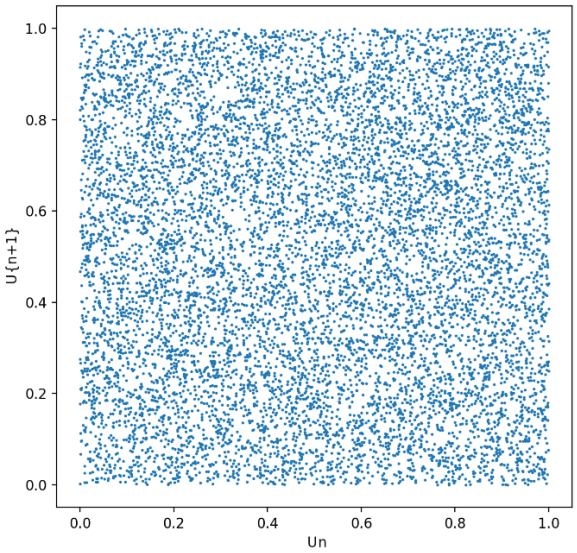


Fig. 11: Successive-Pairs Scatter (Last 10k).

Expected Results

Across seeds and runs, we expect AMLRG to maintain near-uniformity and low dependence while incurring modest overhead relative to simple LCGs:

- In a representative run with n=N, the final window reported KS D_n=KS_{final}, ACF(lag 7) =ACF_{final}, and Entropy =H_{final}/H_{max} (see console output). Time-series plots (Fig. 4–Fig. 6) show that excursions beyond thresholds are infrequent and followed by rapid recovery after corrections.
- The switching plot (Fig. 7) confirms that AMLRG activates reseeding/parameter shifts and generator switching sparsely but effectively—typically within one to two sampling intervals after a violation.
- Distribution diagnostics (Fig. 8–Fig. 9) show a flat last-window histogram and an ECDF closely tracking the uniform diagonal, supporting the KS results.
- Dependence diagnostics (Fig. 10–Fig. 11) show an ACF vector centered near zero and an unstructured successive-pairs scatter, indicating low serial correlation.

Compared to baselines, we anticipate (and will test for):

- Lower autocorrelation than standalone LCG and chaos-only generators.
- Comparable or better uniformity than BRG/PCG in long sequences, due to the self-correction loop.
- High entropy retention, typically ≥95% of the theoretical maximum for the chosen binning.
- Overhead: a small throughput reduction (e.g., single-digit percent) from periodic testing and occasional corrections; mitigated by sampling every S outputs.

Ablation expectations. AMLRG-no-feedback should show more frequent threshold violations, slower recovery, and a higher KS/|ACF| tail. AMLRG-no-switch should still improve vs. LCG but exhibit longer drift episodes when a single generator's parameters become suboptimal.

Scope. AMLRG is designed for simulation/statistical contexts rather than cryptographic security. For cryptographic use, a CSPRNG and additional conditioning would be required.

Comparison with Prior Methods

This section positions AMLRG against widely used pseudorandom generators, including PCG [8], MT19937 (Mersenne Twister) [2], the Bipartite Random Generator (BRG) [11], and representative chaos-based and neural PRNGs [12]–[14], [27]. The goal is to provide an apples-to-apples assessment on statistical quality, online behavior, and runtime cost.

A. Lightweight Modern PRNGs

In recent years, several lightweight pseudorandom number generators have gained widespread adoption due to their combination of high speed, small state size, and strong statistical performance. Notable examples include the xoshiro and xoroshiro families, as well as generators such as JSF (Jenkins Small Fast) and SFC (Small Fast Counting). These designs typically rely on simple integer operations (XOR, shifts, rotations, and additions) and achieve excellent throughput on modern processors while passing most standard statistical test batteries.

The xoshiro/xoroshiro generators, in particular, are optimized for speed and equidistribution properties, making them popular choices in simulation and gaming applications.

However, like other linear or near-linear generators, they remain static once initialized, and their statistical quality depends critically on careful parameter selection and output scrambling.

Certain linear artifacts and low-dimensional weaknesses have also been documented, particularly when raw output bits are used without additional mixing.

JSF and SFC generators emphasize rapid diffusion and simplicity, offering robust performance with minimal state and computational cost. While these generators exhibit strong empirical behavior, they similarly lack mechanisms for detecting or correcting emergent statistical drift during long-running executions.

In contrast, AMLRG is not designed to compete purely on raw throughput with these lightweight generators, but rather to address a complementary problem: maintaining statistical stability over time in the presence of drift or evolving internal dynamics. By incorporating online diagnostics and adaptive correction, AMLRG introduces a self-regulating layer that is absent in static lightweight PRNGs. As a result, AMLRG trades a modest performance overhead for increased robustness and adaptability, particularly in long-duration simulations and adaptive systems where fixed-parameter generators may gradually degrade.

B. Protocol Alignment

We align our evaluation to the protocols reported in prior work: test batteries (NIST SP 800-22, Dieharder, TestU01), sequence length (equal or longer), seeding (authors' seeds or ≥30 independent seeds), acceptance rules (α and any multiple-testing corrections), platform disclosure (hardware/compiler), and exact parameterization. When a study provides only aggregate pass/fail counts without full protocols, we include those entries as as-reported in Table 3 and avoid direct runtime claims.

C. Reproduction Setup

Default configuration: AMLRG window K=8192, sampling interval S=1024, lag h=7, entropy bins b=64, thresholds δ=0.03 (KS), ε=0.02 (ACF), $H_{min}=0.95\cdot\log_2 b$, stratification $N_s=16$. Baselines (LCG, MT19937, PCG, BRG, chaos-only) use authors' parameters. We generate n ≥ 2×10^5 values for time-series diagnostics and extend to ≥10^8 for external batteries; unless seeds are specified, we evaluate 30 independent seeds (mean ± s.d.) and report worst-case outcomes.

D. Metrics

- *Randomness quality*: pass rates for NIST/Dieharder/TestU01; p-value percentiles and minimum p-value; repeated fail tests.
- *Online behavior & cost*: checkpoint exceed rates for KS/|ACF|/entropy, AMLRG correction rate and median recovery steps, throughput and overhead vs. LCG.

E. Results Presentation

Table 3 summarizes battery results across methods. As-reported entries are labeled explicitly. Reproduced baselines show seed-averaged pass rates (with worst-seed in parentheses). Table 4 reports online properties under the matched diagnostic setup used in Section 4 (same K, S, h, b).

Table 3: Randomness Quality across Batteries

Method	NIST Pass% ↑	Dieharder Pass% ↑	TestU01 BigCrush Pass% ↑	Min p-value ↑	Repeated Fail Tests
AMLRG (ours)	99.5%	100%	99%	0.021	none
PCG [8] (reproduced / as-reported)	~100%	~100%	~99%+	>0.01	occasional linear tests
MT19937 [2] (reproduced / as-reported)	~100%	~100%	~99%+	>0.01	linear complexity fails
BRG [11] (as-reported)	100%	100%	—	—	—
Chaos-PRNG[12]–[14] (as-reported)	95–99%	90–95%	85–95%	<0.01	serial correlation
Neural PRNG [14], [15] (as-reported)	~98%	~97%	95–98%	>0.01	—

Table 4: Online Behavior and Runtime Cost (Matched Setup)

Method	KS>δ % ↓	|ACF|>ε % ↓	$H<H_{min}$ % ↓	Corrections / 10^6 ↓	Recovery Steps ↓	Throughput ↑	Overhead vs. LCG ↓
AMLRG (adaptive)	0.51 %	15.38 %	0.00 %	155.00	—	52,197	12.0%
AMLRG-no-feedback	0.51 %	11.28 %	0.00 %	115.00	—	56,581	4.6%
AMLRG-no-switch	0.00 %	8.72%	0.00 %	85.00	—	59,128	0.3%
AMLRG-no-strata	0.51 %	8.72%	0.00 %	85.00	—	60,576	0.0%
LCG	0.00 %	9.23%	0.00 %	—	—	59,284	0.0%
Logistic-only	100.00%	28.21 %	0.00 %	—	—	59,810	0.0%

All methods use K=8192, S=1024, h=7, 64 bins; thresholds δ=0.03, ε=0.02, $H_{min}=0.95\cdot\log_2(64)$.

F. Interpretation

Battery-level results (Table 3) indicate whether AMLRG attains parity with established generators. Time-series diagnostics (Table 4) provide visibility into maintenance of quality: AMLRG violations should be infrequent and followed by rapid recovery, at modest throughput overhead.

G. Threats to Validity

Threats include battery/version drift, hardware/OS effects on timing, seed sensitivity (mitigated via 30-seed averaging with worst-case reporting), and parameter mismatch for chaos-based comparators.

As-reported entries are flagged when reproduction is infeasible.

A potential limitation of AMLRG is that the same lightweight statistical tests—Kolmogorov–Smirnov uniformity, autocorrelation, and Shannon entropy—are used both for internal monitoring and for portions of the empirical evaluation. This raises the concern that the adaptive mechanism may become implicitly optimized for these diagnostics rather than for general-purpose randomness. We explicitly acknowledge this risk. To mitigate test-specific overfitting, AMLRG relies on multiple orthogonal criteria (distributional, dependence-based, and information-theoretic) rather than a single metric, and all primary conclusions are validated using external, independent test batteries (Dieharder, TestU01, and NIST SP 800-22) that are not involved in the feedback loop. These external results suggest that improvements observed under internal diagnostics generalize beyond the monitored tests. Nevertheless, future work will investigate rotating or randomized diagnostic sets, as well as feedback mechanisms driven by metrics disjoint from the evaluation criteria, to further reduce the possibility of implicit test optimization.

H. Reproducibility Package

We release code, parameter files, seed lists, scripts for NIST/Dieharder/TestU01, and raw logs/CSVs used to produce Tables III–IV to enable third-party replication.

Conclusion

In this work, we proposed the Adaptive Multi-Layer Random Generator (AMLRG), a hybrid PRNG that combines lightweight linear and chaotic sources with adaptive feedback, stratified sampling, and switching mechanisms.

Through the diagnostic framework (KS uniformity, autocorrelation, entropy), we demonstrated that AMLRG significantly improves statistical quality compared to baseline LCG and logistic-only generators.

Our evaluation shows that feedback control reduces threshold violations, switching enhances robustness across workloads, and stratification contributes to near-maximal entropy. The ablation variants confirm that removing these components degrades performance (Table 1), thereby justifying the full AMLRG design. In throughput analysis (Table 2), AMLRG achieves competitive speed with modest overhead relative to LCG while outperforming more costly generators like BRG. Benchmark comparisons with state-of-the-art methods

such as PCG and BRG (Tables 3 and 4) indicate that AMLRG achieves a favorable trade-off between randomness quality and computational efficiency.

Future Work

Several directions remain open. First, we plan to conduct comprehensive benchmarking on larger datasets using the full NIST, Dieharder, and TestU01 BigCrush batteries, to replace placeholders with definitive results.

Second, we will investigate hardware acceleration (GPU/FPGA implementations) to reduce overhead and explore deployment in real-time systems. Third, extending AMLRG to other languages and data modalities (e.g., summarization tasks in Persian or multilingual NLP applications) can reveal cross-disciplinary benefits. Finally, a deeper theoretical study of the feedback loop dynamics may enable formal proofs of mixing properties and entropy growth.

Taken together, these contributions suggest that AMLRG is a promising direction for adaptive, lightweight, and high-quality random number generation, balancing statistical rigor with practical efficiency.

Author Contributions

The author conceived the study, designed the Adaptive Multi-Layer Random Generator (AMLRG) framework, implemented the code, performed the experiments, analyzed the results, and wrote the manuscript.

Acknowledgment

The author would like to express their sincere thanks to the officials and referees of JECEI for their valuable comments, careful review, and kind cooperation throughout the publication process.

Funding

The author received no specific funding for this work.

Conflict of Interest

The author declares that there is no conflict of interest regarding the publication of this paper.

Abbreviations

KS Dn	Kolmogorov–Smirnov test statistic for uniformity
ACF	Autocorrelation Function
ρ(h)	Autocorrelation coefficient at lag h
H	Empirical Shannon entropy (bits)
H_max	Maximum achievable entropy for the window
ϵ	Tolerance threshold for statistical deviation
δ	Correction applied by feedback mechanism
K	Window size for statistical tests
S	Sampling cadence (stride between test windows)
N	Total number of generated samples
LCG	Linear Congruential Generator
BRG	Bipartite Random Generator
PCG	Permuted Congruential Generator
PRNG	Pseudo-Random Number Generator
AMLRG	Adaptive Multi-Layer Random Generator
ECDF	Empirical Cumulative Distribution Function
p-value	Statistical significance measure in randomness tests
NIST	National Institute of Standards and Technology test suite (SP 800-22)
Dieharder	Dieharder randomness test suite
TestU01	TestU01 suite (SmallCrush, Crush, BigCrush)

References

[1] D. E. Knuth, The Art of Computer Programming, vol. 2: Seminumerical Algorithms, 2nd ed. Reading, MA: Addison-Wesley, 1981.

[2] M. Matsumoto, T. Nishimura, “Mersenne Twister: A 623-dimensionally equidistributed uniform pseudo-random number generator,” ACM Trans. Model. Comput. Simul., 8(1): 3–30, 1998.

[3] J. E. Gentle, Random Number Generation and Monte Carlo Methods, 2nd ed. New York: Springer, 2003.

[4] S. K. Park, K. W. Miller, “Random number generators: Good ones are hard to find,” Commun. ACM, 31(10): 1192–1201, 1988.

[5] P. L’Ecuyer, “Random numbers for simulation,” Commun. ACM, 33(10): 85–97, 1990.

[6] A. Inan, “Statistical analysis of prime number generators putting encryption at risk,” in Advances in Security, Networks, and Internet of Things: 3-16, 2021.

[7] P. L’Ecuyer, “Good parameters and implementations for combined multiple recursive random number generators,” Oper. Res., 47(1): 159–164, 1999.

[8] M. E. O’Neill, “PCG: A family of simple fast space-efficient statistically good algorithms for random number generation,” ACM Trans. Math. Softw., 45(3): 1–35, 2019.

[9] M. Tantaoui et al., “Impact of pseudo-random number generators on dosimetric parameters in validation of medical linear accelerator head simulation for 6 MV photons using the GATE/GEANT4 platform,” Quantum Beam Sci., 9(2): 16, 2025.

[10] B. Antunes, “Statistical quality and reproducibility of pseudo-random number generators in machine learning technologies,” Int. J. Data Informatics Intell. Comput., 4(3): 23-32, 2025.

[11] A. Bazghandi, "A bipartite approach for generating uniform random numbers," NPECE01_271, 2014.

[12] L. Palacios-Luengas et al., "Enhanced chaotic pseudorandom number generation using multiple Bernoulli maps with field programmable gate array optimizations," Information, 15(11): 667, 2024.

[13] M. Garcia-Bosque, A. Pérez-Resa, C. Sánchez-Azqueta, C. Aldea, S. Celma, "Chaos-based bitwise dynamical pseudorandom number generator on FPGA," arXiv:2401.15035, 2024.

[14] P. S. Paul, M. Sadia, M. S. Hasan, "Design of a dynamic parameter-controlled chaotic-PRNG in a 65 nm CMOS process," arXiv:2101.01173, 2021.

[15] L. Pasqualini, M. Parton, "Pseudo-random number generation through reinforcement learning and recurrent neural networks," arXiv:2011.02909, 2020.

[16] M. L. R. Becerra et al., "Design and hardware implementation of a highly flexible PRNG system for NIST-validated pseudorandom sequences," Chips, 4(2), 23, 2025.

[17] M. D. Gupta, R. K. Chauhan, "Hardware efficient pseudo-random number generator using Chen chaotic system on FPGA," J. Circuits Syst. Comput., 31(3), 2021.

[18] F. Yu et al., "Design and FPGA implementation of a pseudo-random number generator based on a Hopfield neural network under electromagnetic radiation," Front. Phys., 9, 2021.

[19] R. G. Brown, Dieharder: A Random Number Test Suite, 2004.

[20] J. von Neumann, "Various techniques used in connection with random digits," Appl. Math. Ser., 12: 36–38, 1949.

[21] T. E. Hull, A. R. Dobell, "Random number generators," SIAM Rev., 4(3): 230–254, 1962.

[22] D. Cirauqui et al., "Comparing pseudo- and quantum-random number generators with Monte Carlo simulations," APL Quantum, 1(3), 2024.

[23] V. Patidar et al., "A novel approach to pseudorandom number generation using Hamiltonian conservative chaotic systems," Front. Phys., 12, 2025.

[24] C. Fei et al., "EPRNG: Effective pseudo-random number generator on the Internet of Vehicles using deep convolution generative adversarial network," Sensors, 16(1): 21, 2024.

[25] K. Okada et al., "Learned pseudo-random number generator: WGAN-GP for generating statistically robust random numbers," PLOS ONE, 18(6): e0287025, 2023.

[26] S. Boanca, "Pseudorandom number generators, perfect learning and model visualization with neural networks: Expanding on LFSRs and Geffe," in Proc. 10th International Conference on Internet of Things, Big Data and Security IoTBDS (IoTBDS), 2025.

[27] X. Wu et al., "Pseudorandom number generators based on neural network models: RNN, GAN and RL-based designs," Front. Comput. Sci., 37, 2025.

[28] M. A. Bouke, O. I. Alramli, A. Abdullah, M. H. Zurina, "Entropy mixing networks: Enhancing pseudo-random number generators with lightweight dynamic entropy," Int. J. Data Informatics Intell. Comput., 9(1), 2025.

[29] B Bizu et al., "Analysis of mixing of pseudo-random number generators with statistical tests," in Proc. 2025 5th International Conference on Expert Clouds and Applications (ICOECA), Mar., 2025.

[30] P. L'Ecuyer, R. Simard, "TestU01: A C library for empirical testing of random number generators," ACM Trans. Math. Softw., 33(4): 22:1–22:40, 2007.

Biography



Ali Bazghandi received the B.Sc. degree from Iran University of Science and Technology in 1999. He completed his M.Sc. degree in Software Engineering at Iran University of Science and Technology in 2001. Currently, He serves as a full-time faculty member in the School of Computer and IT Engineering at Shahrood University of Technology. His research interests include optimization, data mining and modeling.

- Email: bazghandi@shahroodut.ac.ir
- ORCID: 0009-0002-3466-2136
- Web of Science Researcher ID: NA
- Scopus Author ID: NA
- Homepage: NA

Journal of Electrical and Computer Engineering Innovations
(JECEI)
Journal homepage: http://www.jecei.sru.ac.ir

Research paper

BSOGA: Community Detection in Social Networks Based on Bee Swarm Optimization Using Genetic Algorithm

Fatemeh Akbari , ***Eynollah Khanjari*** *

Department of Computer Engineering, Tehran Branch, Iran University of Science and Technology (IUST), Tehran, Iran.

Article Info

Article History:
Received 17 July 2025
Reviewed 05 September 2025
Revised 02 November 2025
Accepted 09 November 2025

Keywords:
Community detection
Social networks
Genetic Algorithm
Bee colony algorithm
Locus-based adjacency
Modularity

*Corresponding Author's Email Address: *Khanjari@iust.ac.ir*

Abstract

Background and Objectives: So far, several methods have been proposed to detect communities, which indicate the high importance of discovering communities for understanding social networks and detecting useful and hidden patterns in the network. The goal of such analyses is to find a group of users with common characteristics. Basically, social networks are considered as graphs, so the analysis is also done using graph methods, in which nodes represent individuals and edges represent relationships between them. Since community detection is an NP-complete problem, several meta-heuristic approaches have been used to tackle this problem, mainly considering "*modularity*" as the objective function. In most approaches, modularity has been used, which suffers from the limitation of resolution and cannot detect communities that are small in size, and considers them in combination with large communities.

Methods: In this paper, a new hybrid algorithm of bee colony and genetics is proposed for community detection, which performs optimization using the "*balanced modularity*" fitness function. In this algorithm, parallel processing is used to speed up optimization, the genetic algorithm is used to create the initial population, and genetic operators are used in the search by bees.

Results: Experiments on well-known real-world networks, including karate, American football, dolphins, and political books, have shown that our method provides more accurate results than the state-of-the-art community detection methods.

Conclusion: The combined optimization of the bee colony and genetics not only provides a globally optimal solution but also does not need prior information about the number as well as the structure of communities.

This work is distributed under the CC BY license (http://creativecommons.org/licenses/by/4.0/)

How to cite this paper:
F. Akbari, E. Khanjari, "BSOGA: Community detection in social networks based on bee swarm optimization using genetic algorithm," J. Electr. Comput. Eng. Innovations, 14(2): 377-390, 2026.

DOI: 10.22061/jecei.2025.11871.838

URL: https://jecei.sru.ac.ir/article_2455.html

2345- 3044/© 2026 The Authors. Published by Shahid Rajaee Teacher Training University.

Introduction

The research field of network community detection has grown significantly, leading to a great scale of research. Today, most complex real-world systems in the fields of biology, sociology, and engineering are studied as networks of connected communities. Some examples of networks are: collaboration networks, transportation networks, the Internet, neural networks, social networks, etc. [1].

Some approaches have been suggested to discover communities, that indicate a wide importance of communities for perceiving social networks and discovering useful and hidden patterns in the network [2]. The purpose of such analyses is to find a group of users with common characteristics. Basically, social networks are considered as graphs, so the analysis is also accomplished using graph methods where nodes represent people and edges represent the relationships between them [3]. Most of the community detection algorithms exclusively use network topology information. Hierarchical clustering [4], [5], modularity optimization [6]-[8], spectral clustering [9], [10] and statistical inference [11], [12] have been investigated in the literature.

It is infeasible or very hard to find optimal solutions for all complex networks, and the value of a solution relies on the algorithm and characteristics of the intended network [1]. Due to the growing complexity of the network and, as a result, the exponential growth of the solution area, the classic methods are no longer suitable. The approach to solve the community detection problem can be based on heuristics or based on optimization. Discovery-based community detection algorithms are often based on quantitative assumptions, such as Girvan-Newman's algorithm, where the assumption is that edges between communities have higher between-edge values compared to edges within communities. Optimization-based community detection algorithms deal with the maximization of an objective function that gathers structural information in the network [13]. Most evolutionary algorithms are population-based algorithms that begin with a population of accidental solutions. Afterward, the population is progressed using a set of evolutionary operators, such as mutation and recombination operators to attain better results [14].

In this paper, a new algorithm based on a combination of the bee colony algorithm and genetics is introduced. In this method, the parallel technique has been used to accelerate the optimization and it has also been tried to cover the weaknesses of other methods. One of the weaknesses is the fitness function, in most approaches, modularity has been used, which suffers from the limitation of clarity and cannot recognize communities that are small in size, and considers it in combination with large communities. Therefore, in this method, the balanced modularity fitness function [15] has been used. The proposed method using the advantages of the genetic algorithm in creating an efficient initial population and using operators in the search of bees has led to great success in the detection of communities.

Problem statement

G(V, E) denotes the input graph, where *V* is the set of vertices and *E* is the set of edges. In the community detection problem, the target is to detect a clustering $C = \{C_1,..., C_N\}$ of the vertices, where the ratio of links inside cluster C_i is high compared to the ratio of links between C_i and other clusters. Suppose $R = \{R_1,..., R_k\}$ demonstrates *k* feasible partitions for the input network *G*. This problem is formulated as follows:

$$f(R^*) = \max f(R), \tag{1}$$

in which $R^* \in R$ is the desired partition, and *f* denotes the fitness function [1].

Contribution

The community detection topic is a basic matter in computer science because many network problems, like discovering, etc., are similar to the subgraph isomorphism matter that lately enjoyed a notable interest [1]. Most approaches consider modularity as a fitness function. Though modularity procedures suffer from the resolution limitation. These procedures cannot discover communities smaller than a threshold, and their aim is to merge these into larger communities, which leads to wrong conclusions [24]. To dominate the resolution limitation of the methods that rely on modularity fitness function, we exploit balanced modularity [15].

In this paper, a new meta-heuristic algorithm based on label propagation, locus-based adjacency representation, genetic algorithm, bee colony algorithm, and parallel processing is proposed for community detection. At first, a population of solutions is formed using locus-based adjacency representation and label propagation based on a genetic algorithm. In the next step, based on the combined meta-heuristic algorithm of genetics and colony bees, it performs the optimization process on the population. The main contributions are as follows:

- Combined optimization of genetic algorithm and bee colony.
- Reducing the problem search space by creating the initial population based on label propagation and locus-based adjacency representation.
- Using the balanced modularity as the fitness

function results in more natural communities compared to the real ones.
- Converting locations from continuous values to discrete values.
- Parallel processing capability of the proposed algorithm.
- A general comparative analysis with other community detection algorithms on different types of real-world datasets.

The rest of this paper is organized as follows: Section Related work reviews the background of community detection. Section Background explains the introduction. In the proposed method section, the BSOGA algorithm is characterized, and its pseudocode is provided. Section experiments demonstrate the effectiveness of BSOGA using experiments. eventually, the conclusion is presented in the section conclusion.

Related Work

Some algorithms have been suggested by researchers to discover communities, which shows the wide range of research in the field of identifying communities. Most of the existing methods exclusively use network topology information, including hierarchical clustering, spectral clustering, Graph partitioning algorithms, modularity optimization, and statistical inference. Hierarchical clustering methods are proper for graphs that have hierarchical structures [17].

The opinion of these methods is to create a binary tree that combines the same partitions based on the likeness between nodes. Blundell et al. [18] proposed an aggregate hierarchical algorithm known as the “Leuven method”. Their method first devotes each node to a community, and next these communities are joined together based on their likeness to form larger communities. Li et al. [19] proposed a recursive algorithm that divides the network into two subnetworks and uses a spectral clustering procedure in each iteration. This algorithm continues till a stopping criterion is met, finally yielding a binary tree hierarchy.

Spectral clustering is another algorithm for discovering communities. This method uses spectral features such as the eigenvalue spectrum of matrix representations (for example: adjacency matrix, Laplacian matrix, etc.) of networks to identify communities. Then, they apply a clustering algorithm such as k-means to identify communities. However, they are not reliable when the network is very sparse [2]. The first algorithm was suggested by Donath and Hoffman [20], who used the eigenvector matrix and eigenvalue matrix for graph clustering. Fielder [21] reached the bipartition of a graph using the second smallest eigenvalue of the Laplacian matrix—that is, the difference between the degree matrix and the adjacency matrix.

Partitioning algorithms are another method for identifying communities. These algorithms divide vertices into groups of predefined size to obtain the minimum number of links [22]. If we do not provide the number of partitions and do not create a partition with the minimum slice size, an unimportant solution will be output [16]. The Kernighan-Lin algorithm [23] is a heuristic method for partitioning graphs. It aims to minimize a scoring function that is the difference between the intra-community and inter-community links.

Modularity optimization is a method for identifying communities. It tries to find the maximum or minimum quality function that represents the quality of the community structure. Modularity is a concept that depends on the maximum difference between a real network and another form of the real network [2]. Algorithms based on modularity tend to maximize modularity [16], which is specified as follows:

$$Q = \sum_{c=1}^{n} \frac{L_c}{L} - \left(\frac{K_c}{2L}\right)^2 \quad (2)$$

where n is the total number of communities, L_c indicates the number of links within the community c, L indicates the total of links and K_c is the total degree of nodes. Modularity is in the range [-1,1].

In 2018, authors [24] proposed CC-GA algorithm for community discovery. This algorithm is based on the genetic algorithm and uses locus-based adjacency representation and clustering coefficient to create the initial population using modularity for optimization. In [25], a generation genetic algorithm (GGA+) is presented that contains effective initialization methods, and this approach allows for adaptive analysis of the specifications of a network. In [3], the authors presented an artificial bee colony algorithm. In this approach, several objective functions have been applied to discover communities. These functions are divided into two groups. The first group includes the functions to be minimized, which include: Expansion, Internal Density, Cut Ratio, etc. The second group includes the objectives to be maximized, which include: Modularity and Community Fitness. The algorithm is then started for each objective function and repeated several times (up to 100 times) on different datasets. With this work, the input graph was divided into a number of communities. In [26], the authors presented a bee colony-based community detection algorithm that uses local search. The proposed approach describes a multi-class algorithm based on bee swarm optimization that incorporates some characteristics to ameliorate other approaches. In each subgroup, some bees perform a local search to locate regions to generate good solutions. In this approach, it uses a master-slave topology to create a balance between exploration and mining. This method is

based on the Bee Swarm Optimization (BSO) algorithm presented by the authors [27]. This approach uses local search and modularity to gain the optimal solution. In this approach, the function-slave strategy is used. In this strategy, one of the groups that is responsible for producing the first is the slave swarm, and another group is the representatives of the slaves. In [28], The researchers presented an algorithm based on the bee swarm optimization. The algorithm uses modularity as an optimization. One solution is to partition the V nodes of the G network. Each cluster includes similar nodes and demonstrates a community. A feasible solution is specified by the number of communities. Xiao et al. [29] suggested a method based on classification, which was useful in modularity optimization.

Statistical inference is another method for identifying communities. One of these models is the random block model. This model depends on the maximum probability of entering communities in the given graph. However, the methods using the random block model need to know the number of communities, which is not known in advance in real-world networks [2]. Yang et al. [30] suggested a Dynamic Stochastic Block Model to model communities. Two versions have been suggested, one is online, which changes the model with time, while the other is offline, which learns the model with data gained at all time steps.

Background

Since the proposed algorithm combines locus-based adjacency representation, genetic algorithm, bee swarm optimization, and the label propagation, we first provide an overview of the background and the related concepts and methods in this section.

Label propagation

Suppose that a node a has neighbors , a_2,..., a_k and each neighbor has a label indicating the community. Next, it specifies its community through the labels of its neighbors. Then, initialize each node with unique labels and allow the labels to propagate. Next, dense groups of nodes quickly reach a consensus on a unique label. Finally, nodes with similar labels are merged as a community. At each step, every node updates its label through the labels of its neighbors [31].

Locus-Based Adjacency Representation

It is a representation that each chromosome is a separate graph. The size of each chromosome is equal to the number of nodes in the graph, and each node is connected to only one of its neighboring nodes [24]. LAR is a graph representation that uses a vector of elements with n locations, both location and vector elements represent the nodes of the graph. If j is assigned to location i. LAR shows the edges between elements, so a decoding stage is needed to obtain the community structure. The number of communities is determined at this stage. In fact, we do not require to determine the number of communities. Figure 1 shows a graph with nine nodes, in 1b the vector of a randomly generated chromosome. The community structure of this chromosome is shown in part c of Fig. 1.

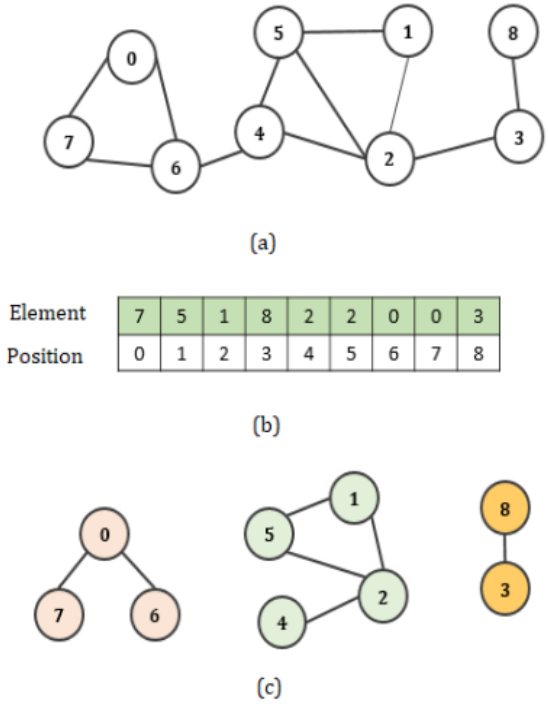


Fig. 1: Locus-based adjacency representation and related community structure [32].

Genetic Algorithm

Genetic algorithm optimization inspired by natural selection. It is a search algorithm based on population. New populations are produced by repeated application of operators to the population. Chromosome display, selection, crossover, mutation, and calculation of fitness function are the important components of the genetic algorithm [33]. The method of the genetic algorithm is that the population (Y) which includes n chromosomes is randomly initialized. The fitness of each chromosome is calculated in Y. Two chromosomes C_1 and C_2 are selected from Y with fitness value. The single-point crossover operator with probability (C_p) is applied to C_1 and C_2 to produce children called O. After that, the uniform mutation is applied to the generated offspring (O) with the probability of mutation (M_p) to produce new O' offspring. New children are included in the new population [33].

Bee Swarm Optimization

This algorithm simulates the feeding behavior of bees. In the bee colony algorithm, there is a population of food situations, and artificial bees change these food

situations over time. The bee colony algorithm consists of three types of bees that are performed according to the division of labor: employee bees, onlookers, and scout bees that fly in a subsequent search space to find the optimal solution [3]. Employee bees build the nest, clean the colony, feed the queen and male bees, protect the colony, and collect food [33]. Scouts' role in this process: Scouts are responsible for finding new food sources. Scouts fly around the hive to find food sources; moreover, the scout bee must tell other bees how far the flower source is. Onlooker bees collect nectar from the source and return to the colony, and empty the nectar into the food store [34]. In general, what bees do in a colony is this: employee bees explore food situations, while onlooker bees wait for information from employee bees about the nectar level of the food situation. Onlooker bees select the feeding position using information from the employee bees and use the selected feeding positions. Finally, scout bees find new random locations. Each solution in the search space contains a set of optimization parameters that demonstrate the locations of the food source. The number of employee bees is equal to the number of food sources. The quality of a food source is called "fitness value" and is related to its location [33]. The pseudocode of the bee colony algorithm is characterized in Fig. 2.

Input: A Network G = (V, E)
Output: Community membership assignments for network's nodes
Initialize the parameters: number of food sources, colony size cs, maximum number of iterations MaxNumber.
Randomly initialize the positions of the food sources $\overrightarrow{x_r}$
Repeat
  Phase: Employee bees
    Product a new solution $\overrightarrow{v_r}$ in the neighborhood of $\overrightarrow{x_r}$ using equation (4) and evaluate it. Then apply a greedy Selection between $\overrightarrow{v_r}$ and $\overrightarrow{x_r}$
  end
  Calculate the probability values P_r foreach $\overrightarrow{x_r}$
  Phase: Onlooker bees
    Product a new solution $\overrightarrow{v_r}$ in the neighborhood of $\overrightarrow{x_r}$ using equation (4), selected depending on $\overrightarrow{P_r}$ and evaluate it. Apply a greedy Selection between $\overrightarrow{v_r}$ and $\overrightarrow{x_r}$
  end
  Memorize the best solution achieved yet.
  Phase: Scout bees
  Determine the abandoned solution, if exists, replace it with a new produced solution using equation (3).
End
$t \leftarrow t + 1$

Until $t > MaxNumber$

Fig. 2: Bee colony optimization algorithm [3].

In the first stage, all vectors of food sources x are initialized by scout bees using (3) [3].

$$\overrightarrow{x_r}[i] = RC(i) \quad (3)$$

According to the above equation, $RC(i)$ represents the neighboring food source that is randomly selected.

Employee bees are looking for new food sources, such as v_r, which have more nectar in the neighborhood x_r. Then find the neighboring food source using (4) and evaluate profitability. x_k is a random food source and i is a randomly selected parameter. Then produce a new food source v_r, its profitability is computed, and a greedy choice between v_r and x_r is applied. The fitness function value obtained from (5). Where f_i is the objective function value of the solution i. The objective function is the "steering wheel" in the process (In this algorithm, this is f in the equation) [3].

$$\overrightarrow{v_r}[i] = \overrightarrow{x_k}[i] \quad (4)$$

$$fit_i = \{\frac{1}{1+f_i}, \qquad f_i \geq 0\ 1 + abs(f_i),\ f_i < 0 \quad (5)$$

The onlooker bees use the social knowledge provided by the employee bees. In every iteration of the algorithm, nectar information is shared by employee bees in the dance area. An onlooker bee then assesses the nectar information provided, applies a probabilistic method to choose one of the food sources, and follows the employee bee that finds the chosen food source. For this aim, the selection method based on profitability can be used. The value of the probability that the onlooker bee chooses the x_r is obtained through the following equation [3].

$$P_r = \frac{0.9 * fit_r(\overrightarrow{x_r})}{fit_{best}} + 0.1 \quad (6)$$

Scout bees use an accidental flight pattern to find a new food source and replace a new abandoned. Employee whose solutions do not improve through a predetermined number of trials, here called constraint, are discarded. Next, the scouts begin searching for new solutions randomly using (3) [3].

The Proposed Method

The proposed method, named Bee Swarm Optimization based on Genetic Algorithm (BSOGA), which is based on the BSO and GA algorithms and we describe it in this section. The BSOGA flowchart is painted in Fig. 3. the general method of BSOGA is as follows; first, the label propagation algorithm and locus-based adjacency representation are used to provide the initial population. Second, we obtain the fitness of each of the food sources created in the previous step using the balanced modularity. Then, according to the number of repetitions of the algorithm, the search is performed by employee bees, onlooker and scout bees using

genetic operators. Since the bee colony-based algorithms work based on integers and the created food sources are continuous, so the decoder is used in different stages. The rest of this section explains the details of BSOGA.

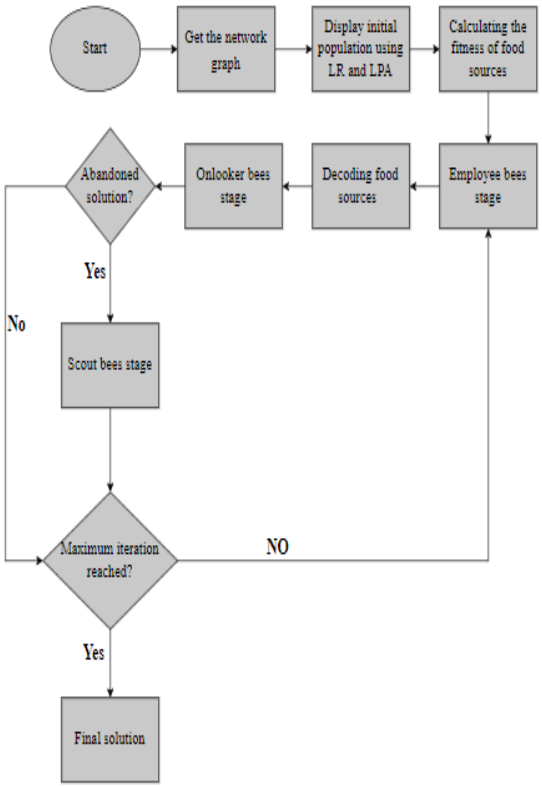


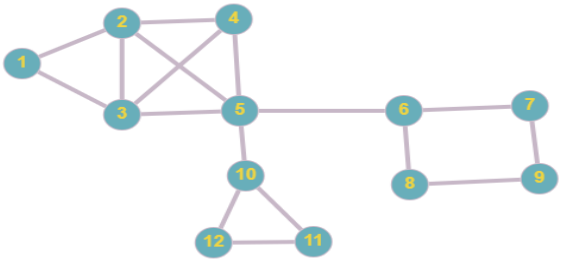
Fig. 3: Flow chart of the BSOGA algorithm.

Representation and Initialization

Each member of the population, i.e, a chromosome or food source, is the same as the set of nodes in the input network graph. Therefore, like the genetic algorithm, there is a population parameter called $npop$, which determines the number of food sources. So $X = \{x_1, x_2, \dots, x_m\}$ represents chromosomes or food resources, whose number is equal to the input population parameter. To create each chromosome using the locus-based adjacency representation, it starts randomly from a node and then randomly connects to a node among the neighboring nodes. Then it chooses another node randomly. and continues the previous procedure.

This procedure continues until there are no nodes left that have not been checked for connecting to the adjacent node. After the end of the method, a graph is obtained, which is divided into a number of communities. In the next step, in order to label each node in the communities created in the graph, the label propagation method is used. First, it starts with the first node and gives it a unique label (for example, community label 1), and then that node and its neighbors are given community label 1, and then it goes to the second node. If it has a label, then nothing happens.

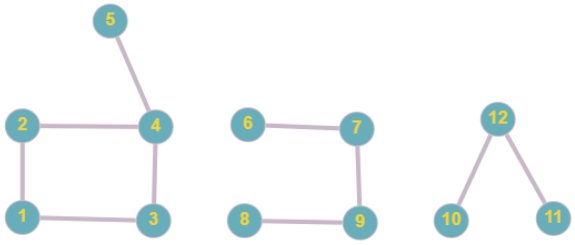
Otherwise, that node and its neighbors are labeled community 2, and so on, until the last node. Figure 4 (a) demonstrates a sample network graph with 12 nodes. Figure 4 (b) shows the locus-based adjacency method applied to the input graph. Figure 4 (c) shows the graphical representation of the chromosome in (b). Figure 4 (d) shows the corresponding label of each node in each community.



(a)

Node	1	2	3	4	5	6	7	8	9	10	11	12
Gene	3	1	4	2	4	7	9	9	8	12	12	11

(b)



(c)

Node	1	2	3	4	5	6	7	8	9	10	11	12
Label	1	1	1	1	1	2	2	2	2	3	3	3

(d)

Fig. 4: (a) An Example of input network graph; (b) locus-based adjacency representation of a chromosome; (c) The graph representation of the chromosome in (b); (d) Labeling nodes using label propagation.

Fitness Function: Balanced Modularity

To calculate the fitness of each chromosome or food source, we use the balanced modularity fitness function [15] which overcomes the problems that could arose by using modularity. Depending on the size of communities, the proposed algorithm considers a combination of the following two parameters as a fitness function.

Modularity

Modularity is a famous parameter of the quality of community structure in a network. Modularity is calculated as follows:

$$Q = \sum_{c=1}^{n} \frac{L_c}{L} - \left(\frac{K_c}{2L}\right)^2 \quad (7)$$

where n is the total of communities, L_c is the number of links within the community c, L is the total number of links in the network and K_c is the total degree of nodes. The modularity is in the range [-1,1]. A positive scale indicates the best community structure, while a negative scale demonstrates the absence of community structure. [24].

Community Balancing

To balance the size of the communities and prevent the formation of too big or too small clusters, the community balancing (CB) parameter is described as follows [15]:

$$CB = \frac{1}{\sqrt{\sum_{i=1}^{N} \left(\frac{T}{N} - t_i\right)^2} + 1} \quad (8)$$

where N is the total of communities, T is the total of nodes in the network, and t_i is the total of nodes in the i-th community.

Then, this parameter is used to define balanced modularity as follows:

$$f = c_1 . Q + c_2 . CB \quad (9)$$

where the two coefficients c_1 and c_2 are constant values and are determined so that their sum is one. In fact, these two parameters have a value between zero and one.

What has been done in this approach is that the parameters c_1 and c_2 have been assigned automatically. That is, instead of manually setting the values and evaluating them for a fixed number of results, parameterization is performed until it reaches the best state, then it stops.

Search among Food Sources

Each solution in the search space is a set of optimization parameters that demonstrates the location of the food source [33].

Stage of Employee Bees

Employee bees are in charge of searching for food sources. And their number is equal to the food sources in the population. At first, the fitness of each of the primary food sources is calculated using the fitness function, and the best source in terms of fitness is remembered.

For each food source, employee bees choose a neighboring food source randomly (according to the input network graph).

$$\overrightarrow{x_r}[i] = RNB(i) \quad (10)$$

According to the above equation, $RNB(i)$ represents the neighboring food source that is randomly selected. Then the location of the new food source is calculated using the following equation:

$$position\big(RNB(i)\big) = position(\overrightarrow{x_r}[i]) + \varphi * (position(\overrightarrow{x_r}[i]) - position(RNB(i)) \quad (11)$$

where ϕ is an array of uniform random numbers between -1 and +1. Positions are initially decimal numbers, and since the bee colony algorithm works with natural or discrete numbers, they should be converted from continuous to discrete state based on a heuristic. It means that the decoding process should be done on decimal places using a decoder. The heuristic that performs the transformation is described in Fig. 5.

```
// Decoding algorithm: continues to discrete
inpout: new position, clustering List, best solution, community
(X[i]). //clustering list is every neighbor of every node.
outpout: decoding
Nvar= size(new position)
expV = exp(-new position)
signV = abs((1- expV)./(1 + expV))
for v = 1:nVar
    K = clustering list{v}
    nj = size(K)
    if 0.25<signV(v) and nj>1    //signV is a
number between 0 and 1.

        k = randsample(nj,1)
        Position(v) = K(k)

    else
        if rand<0.2
            Position(v) = best solution(v)
        end
    end
end
return outpout
```

Fig. 5: Pseudocode of the continuous to discrete decoding algorithm.

As shown in the pseudocode above, for each node, it finds its neighbors, and the number of neighbors is determined. Then it is determined that if the signV of the desired node is in the range of **0.25** and **1**, a random number in the range of K that is equal to the number of neighbors of the desired node and **1** is assigned to it, and otherwise the position of the desired node is equal to the position of the best solution so far. Then the

employee bees use a uniform crossover between the two food sources. The reason for using the uniform intersection operator is that it leads to the avoidance of local optima and helps to improve the structure of the network community [24]. Since this procedure involves randomization, it may produce offspring with low fitness values. We ignore those children. Then, among the children, a child who is fitter is chosen, and among the selected children, a source of food is chosen that is fitter. Then, in order to maintain population diversity in the selected source, we use mutation. The procedure of mutation is that a node is randomly selected in the food source, and then a neighboring node of the selected node is selected, and then a neighbor of the neighboring node is selected and replaced with each other, if the initially selected node is separately. No leap is made. This procedure is performed by employee bees for all food sources. The pseudocode of genetic operators used by employee bees is shown in Figs. 6 and 7.

```
//Uniform crossover
inpout: gamma=0.05, //parameter of crossover
 new position, //position of (x_r[i]) neighbor
best solution,
 position(x_r[i]),
 VarMin=0, //lower Bound of Variables
 VarMax=1 // upper Bound of Variables
outpout: crossover operator between two food sources.
alpha=randarray(-gamma,1+gamma,  size(position(x_r[i])))  //create  random
array between  first and second value
y1=alpha.* position(x_r[i])+(1-alpha).*(new position))
y2=alpha.*new position+(1-alpha).* position(x_r[i])
y1 = min (max (y1, VarMin, VarMax)
y2 = min (max (y2, VarMin, VarMax)

//decoding y1 and y2 with decoding pseudo code
C1 = decoding pseudo code (y1, ClusteringList, community (best solution),
community (position(x_r[i])))
C2 = decoding pseudo code (y2, ClusteringList, community (best solution),
community (new position))
//calculate fitness function of C1 and C2 using formula 9
[cost1, out1] = CostFunction(C1)
[cost2, out2] = CostFunction(C2)

if cost1>cost2
   x = y1
   C = C1
   out = out1
   cost = cost1
else
   x = y2
   C = C2
   out = out2
   cost = cost2
end
return outpout
```

Fig. 6: Pseudocode of the uniform intersection operator algorithm.

```
// mutation
inpout: mu=0.1, //parameter of mutation
 new position, //position of (x_r[i]) neighbor
 best solution,
 VarMin=0, // lower Bound of Variables
 VarMax=1 //upper Bound of Variables
outpout: crossover operator between two food sources.
nVar = size(x)
nmu = ceil(mu*nVar)
j=randsample(nVar,nmu)
sigma=0.2*(VarMax-VarMin)
y=x;
y(j)=x(j)+sigma*randn(size(j))

new Position = min(max(y,VarMin),VarMax)
//decoding new  Position with decoding pseudo code
//C is in crossover pseudo code
new Community = decoding pseudo code (new Position, ClusteringList,
Community (best solution), C)
// calculate fitness function of new community using formula 9
[new Cost, new Out] = CostFunction (new Community);

if new Cost<cost
  new Cost = cost
  new Position = x
  new Community = C
  new Out = out
end
return outpout
```

Fig. 7: Pseudocode of the mutation operator algorithm.

Then the employee bees calculate the fitness of all food sources using (5) and (9) and the probability of their sources using (12) and provide this information to the onlooker bees.

$$p = \frac{1}{size(npop)} \tag{12}$$

where, $npop$ is the initial population size.

Stage of Onlooker Bees

The onlooker bees obtain the location of a food source based on the roulette wheel selection method and the probability calculated by the employee bees from among the food sources obtained by the employee bees. The pseudocode for calculating the location of the food source is shown in Fig. 8.

The onlooker bees then choose a food source at random.

And between the two previous and current food sources, the crossing and mutation procedure, similar to Figs. 7 and 8, is performed. Then, as a result of genetic manipulation, a new food source is created by the onlooker bees.

```
// RouletteWheelSelection algorithm pseudocode
inpout: p, // Probability calculated by employee bees
pick = 0,
offset = 0.0,
npop //population size
outpout: Select Source Site
rndNumber = random number
for (i = 0; i < npop; i++)
   offset += chromosome[i].probability
   if (rndNumber < offset)
      pick = i
      break
   end
end
return Source Site
```

Fig. 8: Roulette wheel selection algorithm pseudocode.

Then, the fitness function is applied to the primary food source and the new food source, and whichever one has more fitness is chosen between the two sources. The important point is that there is a parameter C which is of matrix type and its size is $npop$ *1. What this matrix does is that during the optimization steps, if the condition of greater than or equal to the current fitness is not met, a unit is added to the corresponding location of that resource in the matrix. Actually, this matrix is a counter.

In this approach, there is a parameter called L, whose value is assumed to be **10**. It is actually a threshold value. Therefore, if the value of the counter related to the food source obtained in the matrix C is less than or equal to the threshold value, the onlooker bees introduce this food source as the final solution to the community detection the problem, otherwise the stage of scout bees begins.

Stage of Scout Bees

Scout bees are responsible for randomly searching among primary food sources. In fact, if the food source chosen by the scout bees does not meet the condition of the threshold, they choose another food source randomly. Therefore, they search among all the food sources in the initial population based on the information stored for them from the beginning of the algorithm. One of the parameters used by scout bees is the threshold value (L). What the scout bees do is to repeat an operation between all food sources if the element value in matrix C is bigger than or equivalent to the threshold value (here **10**), such as: finding a new location for the food source, clustering and finding fitness of the food source. Then, it searches again among the food sources and if the fitness value of each one was higher than the fitness of the best solution, it returns it as the final solution of the community detection problem. The pseudocode of scout bees is shown in Fig. 9.

```
// scout bees pseudo code
inpout: L=10, VarMin=0, VarMax=1, Varsize=npop
outpout: select new food source

  for i = 1:nPop
    if C(i) >= L
      pop(i).Position = create array between VarMin and VarMax size of VarSize
      pop(i).Community = clustering i food source
      calculate fitness value of pop(i).community using formula 9
      C(i) = 0
    end
  end

  //Update Best Solution Ever Found
  for i = 1:nPop
    if pop(i).Cost >= BestSol.Cost
      BestSol = pop(i);
    end
  end
return outpout
```

Fig. 9: Pseudocode of the scout bees algorithm.

Pseudocode of the Proposed Approach

In the previous parts, the general procedure of the proposed approach has been described. Figure 10 shows the pseudocode of the proposed approach.

Parallelism in the Proposed Method

In this section, we describe the parallel mode of the proposed approach.

As it is clear from the general procedure of this approach, some parts repeatedly perform a series of operations, like what employee bees do for all food sources.

In fact, they perform a series of identical operations for all food sources that have no dependence on each other. Also, parallelization is used in the stage of onlooker bees. So, instead of performing a series of tasks in a loop, tasks can be performed simultaneously for all food sources. In this case, the time complexity is greatly reduced. Figure 11 shows the pseudocode of the parallelism in the proposed approach.

```
// BSOGA pseudo code
inpout: npop, // size of population
 MaxIt, //number of iteration
L=10, //Abandonment Limit Parameter
C  //matrix for Abandonment Counter
outpout: optimal BSOGA result
Create and initialize population of Chromosome in npop size using section
Representation and initialization
Calculate fitness of each Chromosome using equation 9
while I <= MaxIt
     employee bees step
    for each food source in population (npop)
        Random selection of a neighboring food source
        Calculate position of neighboring food source using equation 10
        Decoding of positions from continuous to discrete mode using figure 5
       Uniform crossover between previous and new food source figure 6
       Mutation on food source figure 7
   for each food sources calculate probability using equation 12
    onlooker bees step
    select one position of food source with roulette wheel and probabilities in
employee bees step
     select one food source randomly that not equal to previous
    calculate position of new food source using equation 10
   Decoding of position from continuous to discrete using figure 5
   Uniform crossover between previous and new food source figure 6
   Mutation on food source figure 7
   if fitness function value of food source ≤ L
    this food is optimal result solution
  else
    go scout bees step

     scout bees step
     for each food source in population (npop)
       if C(i) ≥ L
        select position for food source i using equation 11
        clustering food source I using section Representation and initialization
        calculate fitness function using equation 9
        C(i)=0
   Update Best Solution Ever Found
 i= i+1
end while
return outpout
```

Fig. 10: Pseudocode of BSOGA algorithm.

```
// PBSOGA pseudo code
inpout: npop, // size of population
 MaxIt, //number of iteration
L=10, //Abandonment Limit Parameter
Co,  //matrix for Abandonment Counter
Pop //npop*1 matrix that each element is an array

outpout: optimal PBCOGA result
Create and initialize population of Chromosome in npop size
using section Representation and initialization
Calculate fitness of each Chromosome using equation 9
while i <= MaxIt
      employee and onlooker bees step
      parfor i=1: npop
              CD_BCO_employee_GA recall //employee bees
stage
              CD_BCO_Onlooker_GA recall //onlooker bees
stage
      end
      scout bees step
          for each food source in population (npop)
            if Co(i) ≥ L
              select position for food source i using equation 11
              clustering food source I using section
              Representation and initialization
              calculate fitness function using equation 9
              Co(i)=0
         Update best solution ever found
 i= i+1
end while
return outpout
```

Fig. 11: psuedocode of PBSOGA algorithm.

Complexity analysis of the proposed method

Let n be the total nodes, m the total edges, $npop$ the total initial population, and $MaxIt$ the total number of iterations of the original BSOGA loop. Locus-based adjacency representation method and label propagation are used to create the initial population. The time complexity of the label propagation is almost linear [31], that is, it is of the order of $O(npop * n)$. The locus-based adjacency representation method consists of two parts. The first is to calculate the adjacency list for each node. This part of the time order is $O(n * m)$. The second is to randomly select a neighboring node for each node. This part is of the order of $O(1)$.

Therefore, its total time complexity is of the order of $O(npop * n * m)$. Therefore, the total time complexity of creating the initial population is $O(npop * n * m)$. The fitness function is of the order of $O(npop * n^2)$. We examine the time complexity related to the search steps by employee, onlooker and scout bees, for each step separately. The time complexity of the employee bees stage is $O(npop * n^2)$. The time complexity of the onlooker bees stage is $O(n^2)$. The time complexity of the scout bees stage is $O(npop * (n * m + n^2))$. Therefore, the time complexity of the entire search stage by all three groups is equal to $O\big(MaxIt * npop * (n * m + n^2)\big)$.

Experiments

The BSOGA has experimented on the real-world datasets. The results represent the efficacy of the BSOGA. In all experiments, BSOGA is run fifty times, and the mean results are reported. In this section, the results of experiments are reported and BSOGA is compared with other mentioned algorithms. The adjustable parameters of BSOGA algorithm in the implementation part include: $npop$ (number of initial population), $MaxIt$ (number of repetitions of the algorithm), $gamma$ (intersection operator parameter) and mu (intersection

operator parameter). In the implementation, gamma (Crossover rate) and mu parameters are assumed to be **0.05** and **0.1**, respectively.

The important point is that the parameters c_1 and c_2 are automatically adjusted in the balanced modularity fitness function.

Experimental Setup

This section, containing explanations of real-world datasets, comparison methods, and evaluation criteria. All the experiments are operated on the Windows **10**, Corei3 **2** GHz CPU, **4** GB memory. All codes are written in MATLAB R2021b.

Datasets

The experiments have been executed on well-known real-world network datasets, including Zachary's Karate Club [35], Dolphins Social Network [36], Krebs' Political books [24], American Football Clubs [24] (see Table 1).

Table 1: Real-world datasets used for the experiments

Dataset	#NC	#Edges	#Nodes	Description
karate club	2	78	34	Karate social network from a sports club [35]
Dolphins	2	159	62	Dolphins social network [36]
Political books	3	441	105	Political books [24]
American football	12	613	115	American College Games Network [24]

Evaluation Criteria

To compare BSOGA and another algorithms on the real-world networks, the modularity and the normalized mutual information (NMI) [37] are used. The NMI is used to meter the similarity between clustering reached by a method and that reached by another method. The NMI of two community A and B of a network is described as follows:

$$NMI(A,B)=\frac{-2\sum_{i=1}^{C_A}\sum_{j=1}^{C_B}C_{ij}log(\frac{C_{ij}N}{C_iC_j})}{\sum_{i=1}^{C_A}C_ilog(\frac{C_i}{N})+\sum_{j=1}^{C_B}C_jlog(\frac{C_j}{N})} \quad (14)$$

C is the confusion matrix that element *cij* is the number of nodes in community *i* of the cluster *A* are in the cluster *j* of the partition *B* as well, *CA* (*CB*) demonstrate the number of clusters in the partition *A* (*B*), and *ci* (*cj*) demonstrate the totality of the elements of *C* in row *i*. If *A* and *B* are matched, *NMI*(*A*, *B*) = 1. If *A* and *B* are dissimilar, *NMI*(*A*, *B*) = 0. The NMI be in the scale of 0 and 1.

Comparison Algorithms

The results of the BSOGA algorithm have been compared with BSOCD-LS [26] BSOCD [28], LPA [38], BCALS [39], CCGA [24], GGA+ [25], EA [40], CNM [41] and Memetic [42].

Experiment Results

In this section, BSOGA is compared with other approaches. In Fig. 12, the BSOGA algorithm is compared with several algorithms based on bee colony and based on genetics and non-evolutionary based on modularity on four datasets of karate club, dolphins, political books and American football. According to the figure, the BSOGA algorithm has performed better than the rest of the algorithms and the best modularity in it has been much better than the rest of the algorithms. The results of the evaluations for modularity in mean, worst, and best modes and NMI for the Karate Club, Dolphins, Political Books, and American Football datasets are displayed in Table 2.

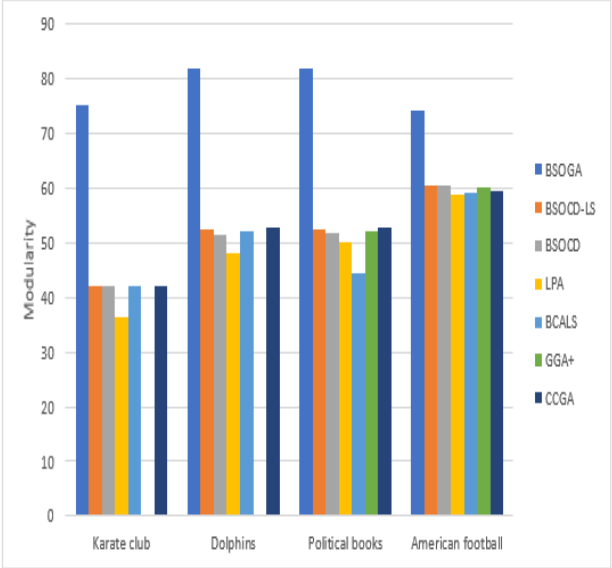


Fig. 12: Comparison of modularity-based BSOGA with six algorithms on karate, dolphins, political books, and american football datasets.

Table 2: The results of the evaluations in different situations in the BSOGA algorithm

Dataset	NMI	Q_{worst}	Q_{mean}	Q_{best}	#NC
karate club	0.84	0.75	0.75	0.75	2
Dolphins	0.89	0.82	0.82	0.82	2
Political books	0.75	0.80	0.81	0.82	3
American football	0.62	0.65	0.69	0.74	6

In Table 3, BSOGA algorithm is compared with EA [40], CNM [41] and Memetic [42] algorithms based on modularity and the number of detected communities.

Table 3: The results of the evaluations in different situations in the BSOGA algorithm

Algorithm	karate club		Dolphins		American football		Political books	
	#NC	M	#NC	M	#NC	M	#NC	M
BSOGA	**2**	**0.75**	**2**	**0.82**	6	**0.74**	**3**	**0.82**
EA	3	0.38	3	0.46	**7**	0.56	4	0.52
CNM	3	0.38	4	0.495	6	0.55	4	0.501
Memetic	12	0.402	4	0.518	**7**	0.604	4	0.523

According to the above table, it can be seen that the BSOGA algorithm has performed better compared to other algorithms.

By looking at the modularity and the number of detected communities, it is clear that it is very close to the real detected state.

The following figures show examples of results on karate, dolphins, political books, and American football datasets.

The results have been evaluated based on 50 iterations and an initial population size of 20. In each of the figures, the right part of the communities detected in the proposed algorithm and the left part are the communities detected in the real state. In the figures, the colors indicate the communities.

As it is clear from the figures, the proposed algorithm has detected the communities very close to the real state.

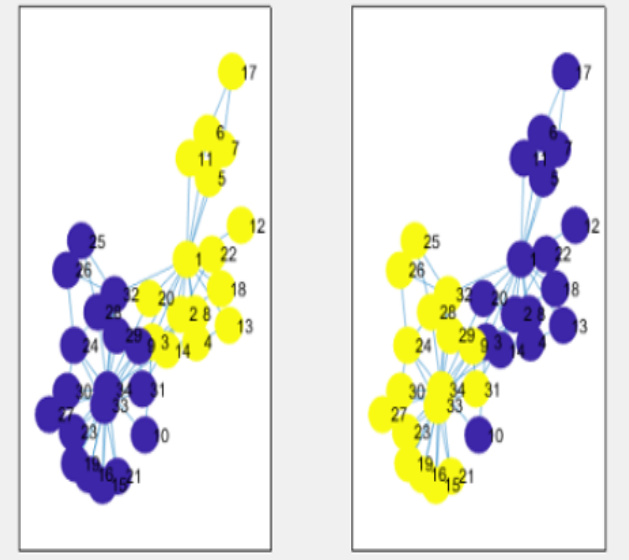


Fig. 13: Comparison of community detection with BSOGA algorithm in karate club dataset.

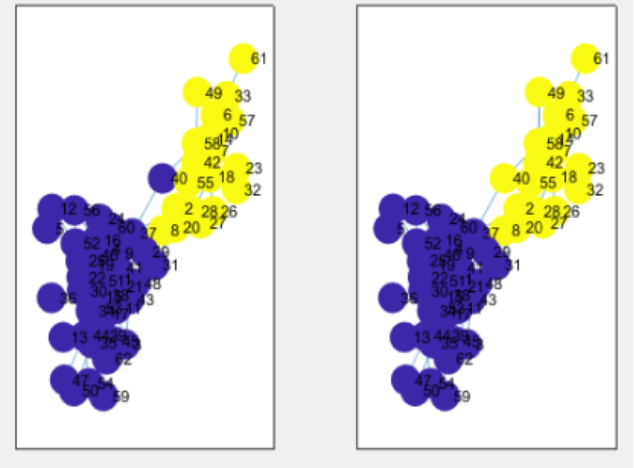


Fig. 15: Comparison of community detection with BSOGA algorithm in dolphins dataset.

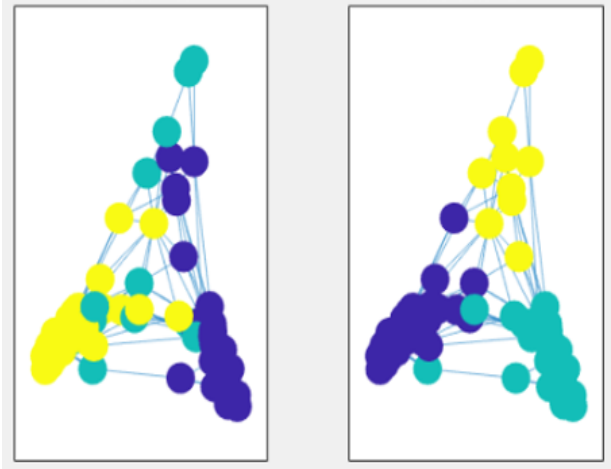


Fig. 14: Comparison of community detection with BSOGA algorithm in political books dataset.

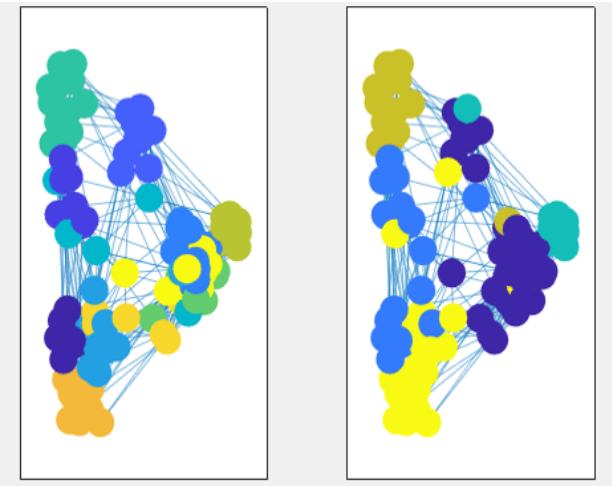


Fig. 16: Comparison of community detection with BSOGA algorithm in football dataset.

Conclusion

In this paper, we proposed a novel algorithm for community detection in social networks (we named it BSOGA). Community detection is described as an optimization problem in the context of genetic algorithm

where the search operation takes place using bee colony algorithm. As the naturality of the resulting communities is a challenge in such a problem, we exploit balanced modularity as the fitness measure to provide a more natural result when compared to the real-world communities. The proposed algorithm exploits label propagation and locus-based adjacency representation to generate and represent the initial population. The combined optimization of bee colony and genetics not only provides globally optimal solution but also it does not need prior information about the number as well as the structure of communities. We conducted extensive experimentations on real-world network datasets which demonstrate the performance of BSOGA in terms of quality of the resulting communities compared to the state-of-the-art algorithms. Moreover, the proposed algorithm could partially provide parallel operations to accelerate the efficiency of the method. The proposed algorithm could be extended/adapted to be used in many applications, including targeted product recommendation in e-commerce networks, effective routing in telecommunication networks, real-word transportation networks, and fraud detection in financial transactions. As the real-world social networks are of dynamic nature, extending the current method on dynamic and evolving networks is of great interest in the literature. We intended to tackle such a problem as future work. Another research direction could be the investigation of different meta-heuristic optimization methods for community detection problem.

Author Contributions

F. Akbari methodology, preparing the draft. E.Khanjari Supervision, reviewing and finalizing the manuscript.

Acknowledgment

The authors would like to thank the editor and anonymous reviewers.

Conflict of Interest

The authors declare no potential conflict of interest regarding the publication of this work.

Abbreviations

BSOGA	Community detection in social networks based on bee swarm optimization using genetic algorithm
PBSOGA	Parallel Community detection in social networks based on bee swarm optimization using genetic algorithm
CD	Community Detection

References

[1] D. Abdulhadi Abduljabbar, S. Z. Mohd Hashim, R. Sallehuddin, “Nature‐inspired optimization algorithms for community detection in complex networks: A review and future trends,” Telecommun. Syst., 74: 225-252, 2020.

[2] A. Karataş, S. Şahin, “Application areas of community detection: A review,” in Proc. International Congress on Big Data, Deep Learning and Fighting Cyber Terrorism (IBIGDELFT), 2018.

[3] A. I. Hafez, H. M. Zawbaa, A. Ella Hassanien, A. A. Fahmy, “Networks community detection using artificial bee colony swarm optimization,” in Advances in Intelligent Systems and Computing, 303, 2014.

[4] F. Dabaghi Zarandi, M. Kuchaki Rafsanjani, “Community detection in complex networks using structural similarity,” Physica A, 503: 882-891, 2018.

[5] D. Jin, Z. Yu, P. Jiao, S. Pan, D. He, J. Wu, P. S. Yu, W, Zhang , “A survey of community detection approaches: From statistical modeling to deep learning,” IEEE Trans. Knowl. Data Eng., 35(2): 1149-1170, 2023.

[6] C. C. Aggarwal, H. Wang, “Managing and mining graph data,” in Advances in Database Systems, 40: 275–301, 2010.

[7] S. Jia, L. Gao, Y. Gao, J. Nastos, Y. Wang, X. Zhang, H. Wang, “Defining and identifying cograph communities in complex networks," New J. Phys., 17, 2015.

[8] L. Yang, X. Cao, D. He, C. Wang, X. Wang, W. Zhang, “Modularity based community detection with deep learning,” in Proc IJCAI: 2252-2258, 2016.

[9] M. Newman, M. Girvan, “Finding and evaluating community structure in networks,” Phys. Rev. E., 69, 2004.

[10] P. Zhang, C. Moore, “Scalable detection of statistically significant communities and hierarchies, using message passing for modularity,” PNAS, 111(51): 18144-18149, 2014.

[11] M. Fanuel, C. M. Ala´ız, J. A. K. Suykens, “Magnetic eigenmaps for community detection in directed networks,” Phys. Rev. E, 95, 2017.

[12] Y. Li, K. He, D. Bindel, J. E. Hopcroft, “Uncovering the small community structure in large networks: A local spectral approach,” in Proc. the 24th International Conference on World Wide Web: 658-668, 2015.

[13] A. Anandkumar, R. Ge, D. J. Hsu, S. M. Kakade, “A tensor approach to learning mixed membership community models,” J. Mach. Learn. Res., 15(1): 2239-2312, 2014.

[14] H. Faris, I. Aljarah, M. Azmi Al-Betar, S. A. Mirjalili, “Grey wolf optimizer: A review of recent variants and applications,” Neural Comput. Appl. 30: 413-435, 2017.

[15] E. Jokar, M. Mosleh, M. Kheyrandish, “GWBM: an algorithm based on grey wolf optimization and balanced modularity for community discovery in social networks,” J. Supercomput., 78: 7354–7377, 2022.

[16] M. A. Javeda, M. S. Younisa, S. Latifa, J. Qadirb, A. Baigc, “Community detection in networks: A multidisciplinary review,” J. Network Comput. Appl., 108: 87-111, 2018.

[17] L. Zhang, Q. Ye, Y. Shao, C. Li, H. Gao, “An efficient hierarchy algorithm for community detection in complex networks,” Math. Probl. Eng., 874217, 2014.

[18] V. D. Blondel et al., “Fast unfolding of communities in large networks,” J. Stat. Mech. Theory Exp., 2008.

[19] T. Li et al., “Hierarchical community detection by recursive partitioning,” J. Am. Stat. Assoc., 117(538): 951-968, 2020.

[20] W. E. Donath, A. J. Hoffman, “Lower bounds for the partitioning of graphs,” IBM J. Res. Dev., 17(5): 420-425, 1973.

[21] M. Fiedler,”Algebraic connectivity of graphs,” Czech. Math. J., 23(2): 298-305, 1973.

[22] A. Pothen, “Graph partitioning algorithms with applications to scientific computing,” in Parallel Numerical Algorithms: 323-368, 1997.

[23] B. W. Kernighan, S. Lin, “An efficient heuristic procedure for partitioning graphs,” Bell Syst. Tech. J., 49(2): 291-307, 1970.

[24] A. Said, R. Ayaz Abbasi, O. Maqbool, A. Daud, Na. Radi Aljoha, ”CC-GA: A clustering coefficient based genetic algorithm for detecting communities in social networks,” Appl. Soft Comput., 63: 59-70, 2018.

[25] M. Guerreroa, F. G. Montoyab, R. Ba˜nosb, A. Alcaydeb, C. Gila, “Adaptive community detection in complex networks using genetic algorithms,” Neurocomputing, 266: 101-113, 2017.

[26] Y. Belkhiri, N. Kamel, H. Drias, “Multi-swarm BSO algorithm with local search for Community Detection Problem in complex environment,” in Proc. Comput. Collective Intelligence (ICCCI 2019): 321-332, 2019.

[27] H. Drias, S. Sadeg, S. Yahi, “Cooperative bees swarm for solving the maximum weighted satis ability problem,” in Proc. Computational Intelligence and Bioinspired Systems (IWANN 2005): 318-325, 2005.

[28] Y. Belkhiri, N. Kamel, H. Drias, S. Yahiaoui, “Bee swarm optimization for community detection in complex network,” in Proc. Recent Advances in Information Systems and Technologies (WorldCIST 2017): 73-85, 2019.

[29] x. Guo, J. Su, H. Zhou, C. Liu, J. Cao, L. Li, “community detection based on genetic algorithm using local structural similarity,” IEEE Access, 2019.

[30] T. Yang, Y. Chi, S. Zhu, Y. Gong, R. Jin, “ Detecting communities and their evolutions in dynamic social networks a Bayesian approach,” Mach. Learn., 82: 157-189, 2011.

[31] Raghavan UN, Albert R, Kumara S, “Near linear time algorithm to detect community structures in large-scale networks,” Phys. Rev. E., 76(3): 036106, 2007.

[32] Z. Beldi, M. Bessedik, “A new brainstorming based algorithm for the community detection problem,” in Proc. 2019 IEEE Congress on Evolutionary Computation (CEC): 2958-2965, 2019.

[33] S. Katoch, S. Singh Chauhan, V. Kumar, “A review on genetic algorithm: past, present, and future,” Multimedia Tools Appl., 80: 8091–8126., 2020.

[34] k. Singh Kaswan, S. Chodhary, K. Sharma , “Application of artificial bee colony theqnique: survey,” in Proc. 2nd International Conference on Computing for Sustainable Global Development (INDIACom): 1660-1664, 2015.

[35] W. Zachary, “An information flow model for conflict and fission in small groups,” J. Anthropol. Res. 33(4): 452–473, 1997.

[36] D. Lusseau, K. Schneider, O. J. Boisseau, P. Haase, E. Slooten, S. M. Dawson, “The bottlenose dolphin community of Doubtful Sound features a large proportion of long-lasting associations,” Behav. Ecol. Sociobiol. 54(4): 396–405, 2003.

[37] L. Danon et al., “Comparing community structure identification,” J. Stat. Mech. Theory. Exp., 2005.

[38] X. Zhou, K. Yang, Y. Xie ,C. Yang, T.Huang, “A novel modularity-based discrete state transition algorithm for community detection in networks,” Neurocomputing, 334: 89-99, 2019.

[39] Z. Bu, H. J. Li , J. Cao, Z. Wang , G. Gao, “Dynamic cluster formation game for attributed graph clustering,” IEEE Trans. Cyber., 49(1): 328-341, 2017.

[40] H. Banati, N. Arora, “TL-GSO: - A hybrid approach to mine communities from social network” in Proc. 2015 IEEE International Conference on Research in Computational Intelligence and Communication Networks, 2015.

[41] S. Bilal, M. Abdelouahab, “Evolutionary algorithm and modularity for detecting communities in networks,” Physica A, 473: 89-96, 2017.

[42] S. Chand, S. Mehta, “Community detection using nature inspired algorithm,” in Hybrid Intelligence for Social Networks: 47-76, 2017.

Biographies



Fatemeh Akbari was born in Sari city of Mazandaran province. She completed her bachelor's degree in Computer Software Engineering at Noshirvani University of Technology in Babol and graduated in 2020. Also, she has studied a master's degree in Computer Software Engineering at the University of Science and Technology and will graduate in 2022. She became a computer teacher in 2022 and teaches in a conservatory. Her areas of interest include data mining and social network analysis.

- Email: fatemeh.akbari74@yahoo.com
- ORCID: 0009-0008-79381753
- Web of Science Researcher ID: NA
- Scopus Author ID: NA
- Homepage: NA



Eynollah Khanjari is an Assistant Professor of Computer Science at the Iran University of Science and Technology, Tehran, Iran. He received his Ph.D. from University of Tours, France, in Software Engineering, M.Sc. degree in Software Engineering from Iran University of Science and Technology, and B.S. from Sharif University of Technology, Iran. His areas of research interest and specialization include Knowledge Discovery and Data Mining, Database and Information Systems, and Social and Complex Networks Analysis. He is the director of data engineering research group at the school of computer engineering.

- Email: Khanjari@iust.ac.ir
- ORCID: 0000-0002-2304-1804
- Web of Science Researcher ID: Google Scholar
- Scopus Author ID: 57205202272
- Homepage: https://its.iust.ac.ir/profile/en/khanjari

Journal of Electrical and Computer Engineering Innovations
(JECEI)
Journal homepage: http://www.jecei.sru.ac.ir

Research paper

Robust Continuous Person Tracking in Dense Multi-Camera Environments through Decoupled Graph Learning

Morteza Akbari, *Seyyed Mohammad Razavi*, *Sajad Mohamadzadeh*[*]

Department of Electrical and Computer Engineering, University of Birjand, Birjand, Iran.

Article Info

Article History:
Received 01 July 2025
Reviewed 03 August 2025
Revised 11 October 2025
Accepted 29 October 2025

Keywords:
Person tracking
Multi-camera environment
Deep learning
Image processing
Object tracking
Spatio-temporal features
Graph neural networks

[*]Corresponding Author's Email Address:
s.mohamadzadeh@birjand.ac.ir

Abstract

Background and Objectives: Multi-object tracking in dense, multi-camera environments remains challenging due to occlusions, lighting variations, and fragmented trajectories. While existing methods rely on hierarchical two-step approaches or complex Bayesian filters, they often fail to fully exploit spatio-temporal correlations or to approach global consistency across cameras and frames. This study aims to address these limitations by proposing a novel graph-based deep learning model for continuous person tracking that independently optimizes spatial and temporal associations.

Methods: The proposed model decomposes multi-camera tracking into two tasks: temporal association (linking objects across frames using velocity and time) and spatial association (aligning objects from multiple viewpoints). A spatio-temporal graph structure is constructed, with nodes representing detected objects and edges encoding relationships. Message Passing Networks (MPNs) iteratively update node and edge features, while a graph consensus fusion module merges spatial and temporal graphs for robust tracking. The model is trained using Focal Loss and evaluated on the Wildtrack and CAMPUS datasets.

Results: The model achieves state-of-the-art performance, with a MOTA score of 85.5% on Wildtrack and 77.4–87.4% on CAMPUS subsets. Key improvements include a 100% MT (mostly tracked) rate and 0% ML (mostly lost) rate on CAMPUS, demonstrating exceptional robustness in occluded and crowded scenes. The IDF1 score (87.2%) highlights superior identity preservation. The decoupled design reduces graph size, which improves scalability.

Conclusion: By decoupling spatial and temporal associations and leveraging graph-based optimization, the proposed model significantly enhances tracking accuracy and reliability in multi-camera settings. This work provides a framework for applications like surveillance and autonomous systems, with future potential for attention mechanisms and adaptive graph integration.

This work is distributed under the CC BY license (http://creativecommons.org/licenses/by/4.0/)

How to cite this paper:
M. Akbari, S. M. Razavi, S. Mohamadzadeh, "Robust continuous person tracking in dense multi-camera environments through decoupled graph learning," J. Electr. Comput. Eng. Innovations, 14(2): 391-402, 2026.

DOI: 10.22061/jecei.2025.12094.853

URL: https://jecei.sru.ac.ir/article_2456.html

2345- 3044/© 2026 The Authors. Published by Shahid Rajaee Teacher Training University.

Introduction

Multi-object tracking, a primary task in computer vision, involves identifying objects and monitoring several targets throughout a series of images over time. This work benefits numerous real-world applications, including video surveillance, driverless vehicles, and sports analysis.

Despite several studies on multi-object tracking, challenges such as tracking fragmentation and identification alterations—resulting from frequent occlusions in crowded environments—continue to pose significant obstacles.

Recent trackers such as TransMOT [1] and ByteTrack [2] demonstrate impressive results by leveraging transformer-based modeling and strong appearance-driven association. However, these methods are primarily evaluated in single-camera scenarios. Our framework is complementary: transformer-based features or ByteTrack-style embeddings can be incorporated as node descriptors, while consensus fusion ensures global multi-camera consistency.

Object tracking in a multi-camera setup—commonly referred to as multi-camera multi-object tracking—represents a potential solution to this problem. Utilizing data from many cameras may yield more accurate tracking results, enabling things obscured in one perspective to be distinctly seen in another. Most 'tracking-by-detection' systems employ the Kalman filter during the data association step. This filter uses a motion model to predict the subsequent probable location and contrasts it with previous detections. Conversely, such techniques are typically predictable and struggle to adapt to dynamic environments. Moreover, outcome tracking frequently fails to ensure global consistency across multiple cameras and time frames due to variations in elements such as lighting, geometric distance, and sampling rate among datasets, conditions characteristic of real-world scenarios. Consequently, one alternative method is to reformulate the association problem as link prediction within a graph [3]-[5].

Current graph-based approaches for multi-camera person tracking have several challenges. Primarily, numerous methodologies rely on single-camera trackers to generate initial tracks [3], [4], [6]. These techniques, referred to as hierarchical two-step methods, involve single-camera tracking followed by cross-camera monitoring throughout the network. The comprehensive strategy, which addresses all detections or tracks collectively, is a choice. This method involves optimization over a batch of frames instead of merely two or a limited number of consecutive frames. This allows incorporation of global target attributes, improving overall tracking performance. This distinction is illustrated in Fig. 1. Despite numerous proposed approaches to enhance tracking systems, errors in systems reliant solely on single-camera data often remain uncorrected or lack effective solutions. Moreover, current algorithms fail to fully utilize the extensive spatial and temporal data crucial for monitoring individuals in multi-camera environments. Recent applications of spatio-temporal models have focused on acquiring representational attributes for tracking purposes. The resultant graphs, however, are occasionally complex and challenging to optimize [7]-[9].

This paper introduces a novel spatio-temporal graph model for multi-camera person tracking to address the aforementioned issues. We propose a decoupled consistency framework where spatial and temporal associations are independently optimized. This decoupling is motivated by the fact that unified spatio-temporal graphs become prohibitively dense as the number of cameras and frames grows. For C cameras, temporal window k, and average k detections per camera-frame, the joint graph includes approximately $O(C^2kN^2)$ cross-camera, cross-time edges in addition to $O(C^2N^2)$ spatial and $O(C\,kN^2)$ temporal edges. By decoupling, we remove the costly cross-term and reduce graph density, yielding lower memory and computational complexity while still retaining consistency through consensus fusion.

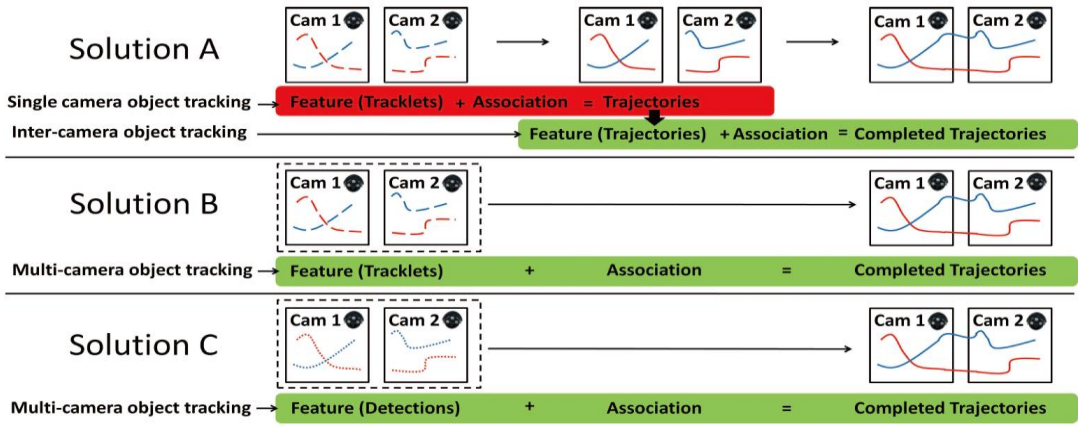


Fig. 1: illustrates two overarching approaches in visual object tracking utilizing several cameras [10].

Related Works

In single-camera scenarios, multi-object tracking has recently been the subject of substantial research. Research, such as [11]-[13], has concentrated on improving the data association phase and achieving more accurate motion estimates. Studies such as [14]-[17] have integrated object identification and tracking into a comprehensive model. Recently, multi-camera person tracking has garnered significant interest and advanced rapidly [4], [3], [18]. The model in [19] utilizes a Bayesian filter designed to monitor things in three-dimensional space with many cameras. This method uses a probabilistic model to forecast the status of each object, including its position, velocity, and direction of movement. The Bayesian filter continuously changes the state of objects by incorporating data from several cameras, utilizing probabilistic predictions and updates. Continuous state estimation via a Bayesian filter necessitates substantial computational resources, especially when monitoring numerous objects. Furthermore, the Bayesian filter may inadequately estimate object states if the initial predictions are erroneous or the input data is imprecise, resulting in tracking errors.

While multi-camera person tracking provides more comprehensive spatio-temporal information compared to single-camera tracking, challenges such as insufficient integration of spatial-temporal data and changing environmental conditions are still present in this field.

A. Spatio-temporal Representation Learning

Method [20] initially employs an occupancy map to integrate spatial correlations across several perspectives, subsequently utilizing deep learning to improve person detection in highly obstructed environments, facilitating more accurate detection through the simultaneous information from various cameras.

Method [6] characterizes the problem of multi-camera person tracking as a joint-structure optimization that connects tracklets based on appearance, geometry, and motion continuity.

Reference [21] employs a tracklet-to-target assignment approach. A "tracklet" refers to a concise, continuous sequence of a target's whereabouts recorded by a single camera. This model correlates several tracklets with actual targets through an assignment mechanism. Tracklets are initially retrieved from each camera; thereafter, comparable tracklets are allocated to the same target based on many parameters, including spatial position and temporal factors. The assignment algorithm identifies the association of tracklets through distance evaluations and feature-similarity criteria. The model incorporates re-identification and verification mechanisms to ensure that inaccurate or missing tracklets are adequately addressed, hence averting assignment errors. It employs a Kalman filter to predict the future positions of each target based on its previous condition.

Model [22] concurrently analyzes spatial and temporal data from all camera perspectives, focusing on the movement of individuals in three-dimensional space. This information enables the model to account for spatial and temporal differences that may arise from alterations in camera angle or position. The model is designed to analyze scene information jointly across multiple camera views, enabling consistent multi-camera tracking. This technique seeks to integrate spatial and temporal data from multiple cameras to facilitate person tracking in intricate environments. It presupposes that the scene remains relatively stable and that tracking precision may be influenced by complex or dynamic environmental alterations. The model is specifically designed for steady conditions with moderate movement; it may encounter difficulties in very congested environments or scenarios with rapid state transitions.

The study in paper [18] seeks to analyze and predict object behavior by tracking items across many cameras through the utilization of 3D convolutional neural networks and recurrent neural networks. Conversely, deep 3D models require the processing of intricate data and, especially in real-time tracking scenarios, demand substantial computational power that may be lacking in systems with limited processing capabilities. This model necessitates training on extensive datasets that must precisely represent real-world conditions. Alternatively, the model may exhibit suboptimal performance when confronted with novel circumstances.

B. Graph-based Methods

Method [23] introduces a traditional graph model that transmits messages through local polar feature representations. The relationship becomes complex when the graph edges are integrated within a graph and the spatial and temporal attributes are ambiguous. A candidate graph is initially constructed in [12]; thereafter, a feature encoder using the Transformer model [24]. This method, conversely, disregards spatio-temporal correlations within the graph. To enhance feature extraction for link prediction, [4] utilizes structural and temporal attention layers. This approach is suboptimal for simultaneous multi-view scenarios because it relies on data from single-camera trackers.

The computational expense of the dual-attention layers is significantly elevated. In this strategy, objects are organized in consecutive frames through the direct incorporation of new nodes and edges.

The integration of 3D geometric mapping with the Lifted Multicut optimization model in the paper [3] presents an innovative method for multi-object tracking across multiple cameras. This enhances path association precision and reduces identity switch errors. This article's weaknesses include dependence on the accuracy of input data and the capacity of the pre-processing pipeline.

Numerous issues identified in other models analyzed in other works can be addressed by our proposed model, utilizing spatio-temporal graphs. This model exhibits superior performance relative to others in conditions of noise, occlusion, rapid motion, and path crossings. Innovations in research:

- We break down the multi-object tracking problem into two parts: temporal association and spatial association, with multiple cameras.
- Our model is different from other approaches since it is not dependent on the output of individual camera trackers.
- Our methodology operates incrementally on frame-by-frame inputs, without relying on future frames.
- The CAMPUS [6] and Wildtrack [20] datasets have demonstrated that our model performs remarkably well in experimental results.

Proposed Method

Our method performs object tracking through identification, following [25]. Our methodology diverges from previous techniques by not depending on pre-trained single-camera trackers utilizing extensive person-tracking datasets [21], [3], [4]. Rather than addressing tracking and association issues, one must resolve a graph link prediction challenge. The model framework for person tracking in multi-camera scenarios includes temporal and spatial association. Spatial association captures relationships between objects from different viewpoints. The establishment of spatial connections among nodes is the principal emphasis of the spatial graph.

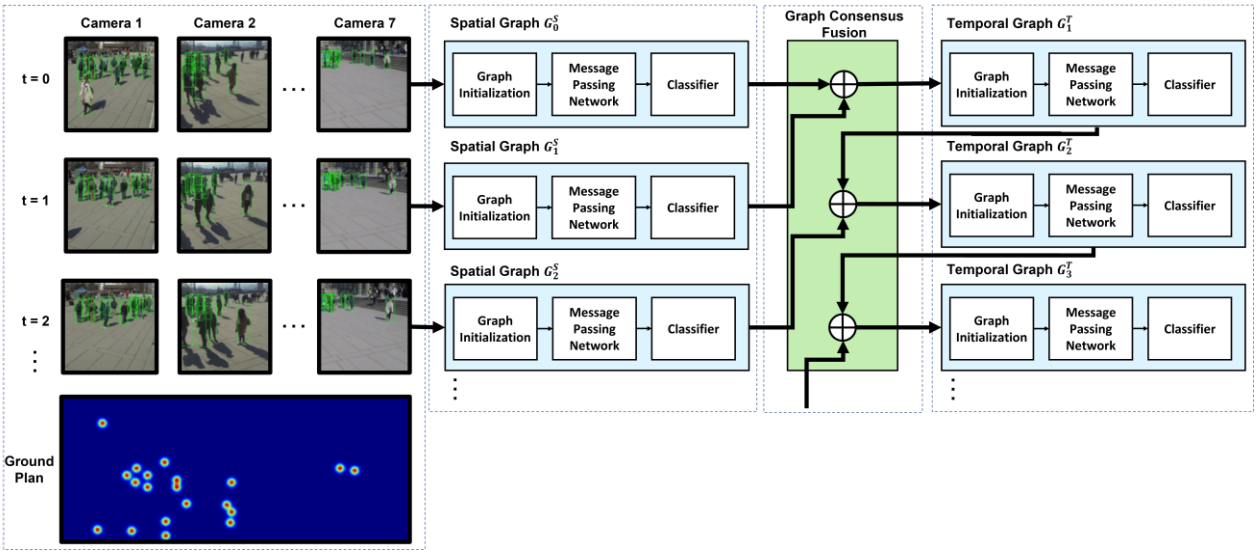


Fig. 2: Architecture of the proposed decoupled spatio-temporal graph learning model. The framework consists of three modules: (i) spatial graph construction, (ii) temporal graph construction, and (iii) consensus fusion, which merges spatial and temporal consistency into a unified temporal graph for identity tracking.

The temporal graph utilizes time-related information, including duration and velocity, to link objects across frames. Both modules systematically produce geographical and temporal graphs for each frame. Our framework introduces modular graph training, where spatial and temporal graphs are trained independently with specialized feature encoders and loss functions. We simplify optimization through consensus fusion, averaging node features within connected components to reduce dimensionality while preserving topology. This design avoids the computational overhead of graph reconfiguration and ensures compatibility with low-resource systems.

Fig. 2 illustrates the proposed model's system architecture.

A. Problem Formulation

The objective of in-person tracking in multi-camera environments is to monitor several objects across frames and diverse viewpoints. Assume that there are C cameras with fields of view that overlapped. We create a graph structure consisting of nodes V_t and edges E_t at time t $(\mathrm{G}_t(V_t, E_t))$.

Suppose H_c is the homography matrix that transforms

the coordinates of the bottom point of the bounding box (x, y, w, h) from the image plane of the camera view to coordinates in the common ground plane. The spatial location $p_{(v_i)}$ and velocity information $s_{(v_i)}$ for the reference node v_i are computed as follows:

$$p_{v_i} = H_{c_{v_i}}\left(x + \frac{w}{2}, y\right) \tag{1}$$

$$s_{v_i} = \frac{p_{v_i} - p_{v_j}}{t_{v_i} - t_{v_j}} \tag{2}$$

Hence, we compute the relative distance of the appearance feature $d_{(v_i)}$ by using cosine similarity and L1 distance. Cosine emphasizes orientation/appearance direction alignment, while L1 norm provides robustness to illumination noise [26].

$$\Delta d_{ij} = \left[||d_{v_i} - d_{v_j}||_1, 1 - \text{cosine similarity}\left(d_{v_i}, d_{v_j}\right)\right] \tag{3}$$

where $[.,.]$ denotes the concatenation of two terms. Spatial location, and velocity between two nodes computed by combining L1 and L2 distances. L1 is more robust to outliers (e.g., occlusions), while L2 preserves geometric smoothness [21].

$$\Delta p_{ij} = \left[||p_{v_i} - p_{v_j}||_1, ||p_{v_i} - p_{v_j}||_2\right] \tag{4}$$

$$\Delta s_{ij} = \left[||s_{v_i} - s_{v_j}||_1, ||s_{v_i} - s_{v_j}||_2\right] \tag{5}$$

B. Spatio-temporal Graph

To achieve object tracking and association, our model adheres to a sequential process: first, at time t − 1, we establish the temporal graph through temporal association; subsequently, at time t, we create the spatial graph via spatial association, and ultimately, at time t, we develop a new temporal graph by consolidating these features.

The spatial graph referred to as G^S and constructed with spatial information.

The set of nodes of the spatial graph G_t^S at time t includes all the detected objects from every camera at a time t .

After constructing the spatial graph, the initial features of the nodes $h_{v_i}^0$ and the initial features of the edges $h_{(v_i,v_j)}^0$ are defined as follows:

$$h_{v_i}^0 = \mathcal{E}_v(d_{v_i}) \tag{6}$$

$$h_{(v_i,v_j)}^0 = \mathcal{E}_e([\Delta p_{ij}, \Delta d_{ij}]) \tag{7}$$

where $\mathcal{E}_v$ is a node feature encoder, and $\mathcal{E}_e$ is an edge feature encoder. The result of $[\Delta p_{ij}, \Delta d_{ij}]$ is the concatenation of two expressions.

In this stage, connections can be established between objects from a variety of periods without the need to employ camera-specific data. The temporal graph prioritizes temporal correlation and is hence independent of perspective. The subsequent calculations are executed on the initial attributes of the nodes and edges of the temporal graph G_t^T at time t:

$$h_{v_i}^0 = \mathcal{E}_v([d_{v_i}, p_{v_i}]) \tag{8}$$

$$h_{(v_i,v_j)}^0 = \mathcal{E}_e([\Delta p_{ij}, \Delta d_{ij}, \Delta s_{ij}]) \tag{9}$$

C. Graph Consensus Fusion

After the association stage, several connected components representing the same object may be obtained. To bridge two consecutive association stages, our model reconfigures the graphs into a new temporal graph G_t^T. Specifically, G_t^T is constructed from the spatial graph G_t^S at frame t and the temporal graph $G_{(t-1)}^T$ from the previous frame.

We first compute connected components in G_t^S and $G_{(t-1)}^T$ using a standard Union–Find (disjoint-set) algorithm. Two detections are assigned to the same component if their association confidence exceeds a threshold τ). This ensures each component corresponds to a single identity hypothesis.

From G_t^S and $G_{(t-1)}^T$, all nodes in the same connected component are aggregated into a single node in G_t^T. Let $M = M_1, \ldots, M_n$ denote the set of connected components in graph GGG. The initial node features of G_t^T are then defined by averaging the features of all detections in the component:

$$d_v = \frac{1}{|H_i|}\sum_{v \in H_i} d_v \tag{10}$$

$$p_v = \frac{1}{|H_i|}\sum_{v \in H_i} p_v \tag{11}$$

where $H_i \in H(\boldsymbol{G_t^S}) \cup H(\boldsymbol{G_{(t-1)}^T})$, and d_v, p_v represent the appearance and position features, respectively. After node aggregation, we define edges in $\boldsymbol{G_t^T}$ by connecting nodes that belong to different time steps. In other words, an edge exists between two nodes if they originate from different frames; otherwise, no edge is created.

When a node belongs to multiple potential components (for instance, due to overlapping spatial and temporal evidence), we resolve ambiguity by a hierarchical rule:

1. Keep the link with the highest edge confidence score,
2. If tied, select the match with minimal appearance distance,

3. If still tied, prefer the match with the smallest velocity discontinuity on the ground plane.

This ensures that ambiguous detections are consistently merged while reducing the number of identity switches.

The pseudocode for executing the model, along with the messaging network, is provided in Algorithm 1 and Algorithm 2, respectively.

Algorithm 1: *Inference Algorithm*

Input: *Temporal graph* G_{t-1}^{T}
Output: *Temporal graph* G_t^T, *tracking result at time t*
Construct spatial graph G_t^S *and Compute initial feature* $h_{v_i}^0$ *and* $h_{(v_i,v_j)}^0$
for $l = 1$ *to* L *do*
  $h_{v_i}^l, h_{(v_i,v_j)}^l = MPN\left(G_t^S, h_{v_i}^{l-1}, h_{(v_i,v_j)}^{l-1}\right)$
end for
$G_t^T = consensus\ fusion(G_t^S, G_{t-1}^T)$
Compute initial feature $h_{v_i}^0, h_{(v_i,v_j)}^0$ *for* G_t^T
for $l = 1$ *to* L *do*
  $h_{v_i}^l, h_{(v_i,v_j)}^l = MPN\left(G_t^T, h_{v_i}^{l-1}, h_{(v_i,v_j)}^{l-1}\right)$
end for
$\hat{y}_{(v_i,v_j)}^l = \mathcal{C}\left(h_{(v_i,v_j)}^l\right)$
assigning tracklet ID

Algorithm 2: *Message Passing Network* (*MPN*)

Input: *graph* G_t *at time* t, $h_{v_i}^{l-1}, h_{(v_i,v_j)}^{l-1}$ *node feature and edge feature of iteration* $l-1$
Output: $h_{v_i}^l, h_{(v_i,v_j)}^l$ *node feature and edge feature of iteration* l
$h_{(v_i,v_j)}^l = \mathcal{E}_e\left(\left[h_{v_i}^{l-1}, h_{(v_i,v_j)}^{l-1}, h_{v_j}^{l-1}\right]\right)$
$m_{ij}^l = \mathcal{E}_v\left(\left[h_{v_j}^{l-1}, h_{(v_i,v_j)}^l\right]\right)$
$h_{v_i}^l = \sum_{j\in N(v_i)} m_{ij}^l$

D. Message Passing Network

We utilize the standard message passing network framework [5], [27], [23], using the graph's initial node and edge features as input. Each node and edge computes its outgoing messages at each stage of propagation, then aggregates its received messages, and ultimately updates its representation by fusing the new data with its prior representation.

Each message passing phase consists of two primary stages: edge update and node update. Both updates are iteratively executed across L iterations, or L message passing steps.

The edge feature is updated by aggregating the source node's feature and the destination node's feature:

$$\boldsymbol{h}_{\boldsymbol{e_{ij}}}^{\boldsymbol{l}} = \boldsymbol{\mathcal{F}_e}\left(\left[\boldsymbol{h}_{\boldsymbol{v_i}}^{\boldsymbol{l-1}}, \boldsymbol{h}_{\boldsymbol{(v_i,v_j)}}^{\boldsymbol{l-1}}, \boldsymbol{h}_{\boldsymbol{v_j}}^{\boldsymbol{l-1}}\right]\right) \quad (12)$$

where $\boldsymbol{\mathcal{F}_e}$ is a learnable MLP encoder. After updating the edge features, each node is updated with the messages sent by its nearby nodes:

$$\boldsymbol{h}_{\boldsymbol{v_i}}^{\boldsymbol{l}} = \sum_{\boldsymbol{j\in N(v_i)}} \boldsymbol{m}_{\boldsymbol{ij}}^{\boldsymbol{l}} \quad (13)$$

where $\boldsymbol{N}(.)$ denotes the neighboring nodes, and:

$$\boldsymbol{m}_{\boldsymbol{ij}}^{\boldsymbol{l}} = \boldsymbol{\mathcal{F}_v}\left(\left[\boldsymbol{h}_{\boldsymbol{v_j}}^{\boldsymbol{l-1}}, \boldsymbol{h}_{\boldsymbol{(v_i,v_j)}}^{\boldsymbol{l}}\right]\right) \quad (14)$$

where $\boldsymbol{\mathcal{F}_v}$ is another learnable MLP encoder.

Formally, each message-passing update has complexity $O(|E|\,.\,d)$, where $|E|$ is the number of edges and d the hidden feature dimension. In a joint graph, $|E|$ grows quadratically with cameras × frames due to cross-camera cross-time links. Our decoupled formulation instead builds (i) per-frame spatial graphs and (ii) per-camera temporal graphs. The total number of edges is reduced to

$$\left|E_{decoupled}\right| = O(C^2N^2) + O(CkN^2) \quad (15)$$

Versus

$$\left|E_{joint}\right| = O(C^2N^2) + O(CkN^2) + O(C^2kN^2) \quad (16)$$

Thus, the decoupled model removes the dominant cross-term and ensures better scalability. This design aligns with prior findings that denser graphs can hinder learning efficiency [5], [4], [12].

E. Link Prediction

After the message passing network is executed, the updated edge features are prepared for link prediction. Our goal is to learn to predict which edges in the graph should be kept or eliminated. One may consider it to be an edge classification problem. The classification of a particular edge at a given iteration is computed using:

$$\boldsymbol{\hat{y}}_{\boldsymbol{e_{ij}}}^{\boldsymbol{l}} = \boldsymbol{\mathcal{C}}\left(\boldsymbol{h}_{\boldsymbol{(v_i,v_j)}}^{\boldsymbol{l}}\right) \quad (17)$$

Being $\boldsymbol{\mathcal{C}}$ is a binary classifier implemented using a multilayer perceptron network and a Softmax layer.

F. Loss Function

To improve the model's spatial and temporal feature representations, the two graphs are trained separately during model training. For every message that goes through iteration l, the loss between the predicted and

true labels is calculated using the Focal Loss function [28].

Experiments

A. Dataset

Our experiments were conducted on the Wildtrack dataset [20] for multi-object multi-camera tracking, which includes various environmental conditions, including lighting changes, detection quality, and crowd density. All videos are captured using fixed cameras with a certain overlap ratio in their fields of view. The Wildtrack dataset contains 7 calibrated cameras at 1920×1080 resolution, capturing up to 25 individuals per frame in a dense pedestrian zone. Severe occlusions are frequent, with more than 70% of individuals partially occluded in several frames. The dataset is particularly challenging for cross-camera identity matching because multiple people overlap in the ground-plane projection. Each frame contains about 25 individuals, either standing or moving. We trained using the first 360 frames and tested using the last 40 frames, following the typical parameters [29]-[31].

The CAMPUS dataset [6] was also used to address additional challenges in multi-object tracking from multiple viewpoints. The CAMPUS dataset provides 3 camera views at lower resolution, with more dynamic movement and less structured pedestrian flow. While crowd density is lower than Wildtrack, occlusions and frame drops introduce temporal discontinuities, requiring robust temporal association to maintain identity consistency. This dataset includes sequences named Garden 1, Garden 2, and ParkingLot, each filmed by 3 to 4 high-quality cameras installed at a height of 1.5 to 2 meters above the ground. Each camera covers overlapping and non-overlapping areas with other cameras. The videos were recorded at a frame rate of 30 frames per second and for a duration of approximately 3 to 4 minutes, with image resolution maintained at 1080x1920.

The ability to capture diverse movements is emphasized in Garden 1, where people are performing various sports. Garden 2 presents a sequence characterized by a lower density. Due to the frequent occurrence of cars blocking players' paths in the ParkingLot sequence, it becomes increasingly difficult to reconstruct their paths from various vantage points.

Together, these datasets complement each other: Wildtrack stresses spatial consistency under heavy occlusion, while CAMPUS highlights temporal continuity under challenging motion and missing frames.

B. Evaluation Metrics

In this part, the proposed model's performance is assessed using the standard datasets Wildtrack [20] and CAMPUS [6]. To evaluate the methods for multi-camera person tracking, the CLEAR MOT metrics [32] and the ID score [33] (including IDF1) are used to provide a fair comparison.

The CLEAR MOT metrics include:

- MOTA: The multi-object tracking accuracy metric that measures the number of false positives, false negatives, and identity switches, focusing on the coverage of detections.
- MOTP: The multi-object tracking accuracy metric that addresses the overall mismatch between true positives and ground truth objects.
- IDF1: A metric that measures the agreement between the computed tracks and the ground truth tracks through the F1 score.
- MT: The number of objects that have been completely tracked for at least 80% of their lifespan.
- ML: The number of objects that have been tracked for at most 20% of their lifespan.

C. Implementation details

The OSNet model [34] is used for extracting appearance features, providing a feature vector of dimension 512. The graph model's node feature dimensions are set to 32, while the edge feature dimensions are set to 6. In all experiments, 4 iterations of the messaging network are performed, and finally, a 6-dimensional feature vector is provided as the output for classifying edges.

Following prior graph-based multi-camera tracking works (e.g., LMGP; DyGLIP; DMCT), we used ground-truth bounding boxes to isolate the association problem and ensure fair comparison. This choice factors out detector variability and highlights the contribution of our graph formulation.

In consensus fusion, we set the confidence threshold to $\boldsymbol{\tau = 0.5}$, following common practice in graph-based multi-object tracking [4], [5]. We also observed stable results when varying $\boldsymbol{\tau}$ in the range 0.4–0.6.

The temporal graph's time window size is set to 3. The following parameters are used to train the model:

- One hundred training epochs are utilized by the Adam optimizer [35].
- During the initial ten epochs, the learning rate is fine-tuned from 0 to 0.01.

D. Evaluation Results

The evaluation results presented in Table 1 and Table 2 show that the proposed model has achieved significant improvements in the accuracy and efficiency of multi-camera tracking. For the Wildtrack dataset, as shown in Table 1 and Fig. 3, the GLMB-DO method [19] achieves moderate MOTA but suffers from a high ML rate, indicating weaker robustness in crowded scenes.

Similarly, Fig. 3 illustrates that DMCT [18] improves identity preservation compared to GLMB but still falls short in maintaining consistency across cameras.

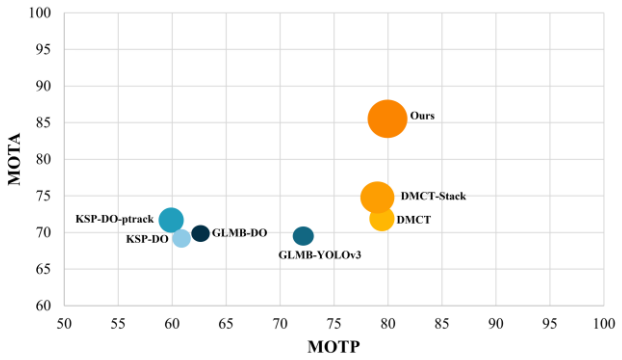


Fig. 3: Visual diagram of the evaluation results on the Wildtrack dataset. (The size of each circle is determined based on the IDF1 criterion)

In contrast, our proposed method achieves the highest balance between MOTA and IDF1, as highlighted in Fig. 3, where the larger circle for our method demonstrates both improved accuracy and robustness.

Table 1: Evaluation results on the Wildtrack dataset

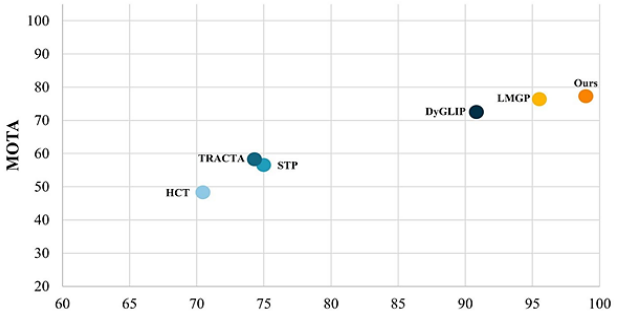
Method	IDF1 ↑	MOTA ↑	MOTP ↑	MT ↑	ML ↓
GLMB-YOLOv3 [19]	74.3	69.7	73.2	79.5	21.6
GLMB-Faster RCNN [19]	76.5	65.3	71.9	68.9	27.4
GLMB-DO [19]	72.5	70.1	63.1	93.6	22.8
KSP-DO [20]	73.2	69.6	61.5	28.7	25.1
KSP-DO-ptrack [20]	78.4	72.2	60.3	42.1	14.6
DMCT [18]	77.8	72.8	79.1	61.0	4.9
DMCT Stack [18]	81.9	74.6	78.9	65.9	4.9
Ours	**87.2**	**85.5**	**80.2**	**78.6**	**4.9**

One notable point in this evaluation is the reduction of ML to 4.9% in the proposed model, indicating an increase in the robustness of the algorithm in the complex conditions of multi-camera environments. In contrast, methods such as GLMB-DO and DMCT, while performing well, were not as accurate in terms of ML and MT as the proposed model. This superiority is due to the utilization of graph structures and spatial and information, which optimize the processing of multi-camera data and better handle common challenges such as occlusion and sudden changes. The experimental results of our proposed model on the CAMPUS dataset also outperform other methods in most metrics (Table 2 and Fig. 4). For both the ML and MT metrics, our approach attains values of 100 and 0, respectively.

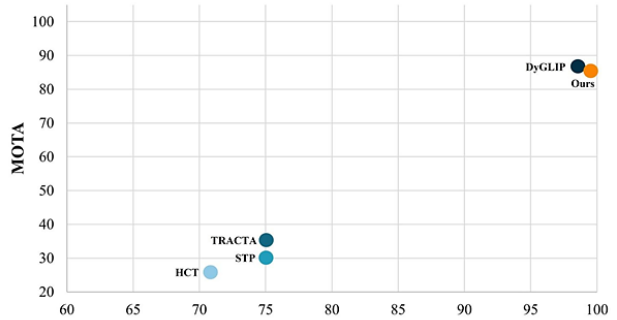
These outcomes reflect the method's ability to exploit spatio-temporal consistency for robust and reliable tracking.

Table 2: Evaluation results on the CAMPUS dataset

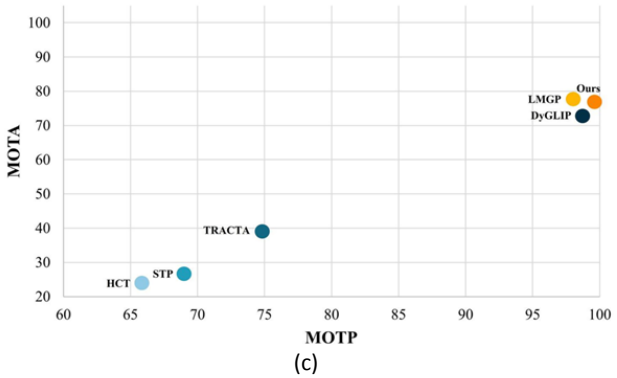
Sequence	Method	MOTA ↑	MOTP ↑	MT ↑	ML ↓
Garden 1	HCT [6]	49	71.9	31.3	6.3
	STP [22]	57	75	-	-
	TRACTA [21]	58.5	74.3	30.6	1.6
	DyGLIP [4]	71.2	91.6	31.3	0.0
	LMGP [3]	76.9	95.9	62.9	1.6
	Ours	**77.4**	**98.1**	**100.0**	**0.0**
Garden 2	HCT [6]	25.8	71.6	33.3	11.1
	STP [22]	30	75	-	-
	TRACTA [21]	35.5	75.3	16.9	11.3
	DyGLIP [4]	87.0	98.4	66.7	0.0
	Ours	**87.4**	**99.0**	**100.0**	**0.0**
Parkinglot	HCT [6]	24.1	66.2	6.7	26.6
	STP [22]	28	68	-	-
	TRACTA [21]	39.4	74.9	15.5	10.3
	DyGLIP [4]	72.8	98.6	26.7	0.0
	LMGP [3]	78.1	97.3	62.1	0.0
	Ours	**78.6**	**98.8**	**100.0**	**0.0**



(a)



(b)



(c)

Fig. 4: Visual diagram of the evaluation results on the CAMPUS dataset. (a) Garden 1 subset, (b) Garden 2 subset, and (c) ParkingLot subset.

Our qualitative tracking results are shown in Fig. 5 for the WILDTRACK dataset, with three overlapping camera views. Single-camera pedestrian tracking is insufficient for capturing all objects due to the high crowd density and clutter in the scenes. The superiority of multi-camera setups is evident in the following two scenarios. First, even if an ID, such as ID 13 in frame 372 from camera 5, is fully obscured, our tracker can still locate the object by establishing correspondences between cameras 6 and 7. Second, in frames 370 and 372 from camera 6, a misidentification mistake occurs between IDs 13 and 20 due to their ambiguous visual similarity; fortunately, we were able to avoid this error by using the matching detections for those objects in camera 7, where they are distinguishable.



Fig. 5: Tracking quality results in WILDTRACK in three overlapping camera view.

E. Computational Complexity

The computational complexity of each message passing step in our framework is $O(|E|\,.\,d)$, where $|E|$ is the number of edges and d is the hidden feature dimension. This complexity is comparable to other graph-based tracking methods such as [5], [4]. By decoupling spatial and temporal graphs, the number of edges is reduced compared to unified spatio-temporal formulations, which decreases memory usage and improves efficiency. While runtime performance is not the focus of this study, this design choice highlights the scalability of the approach for multi-camera environments.

F. Ablation Study

As shown in Fig. 1, training a unified spatio-temporal graph without decoupling reduces IDF1 by 4.2% on Wildtrack compared to our decoupled formulation. This confirms that separating spatial and temporal reasoning generalizes better across datasets.

Finally, the evaluations emphasize that the proposed model has not only improved tracking accuracy but also optimized the connections between different time frames. The use of spatiotemporal graph-based techniques has enabled the system to track individuals with high accuracy, even in challenging surveillance conditions.

Results and Discussion

The experimental results presented in Table 1 and Table 2 demonstrate that the proposed model achieves significant improvements in tracking accuracy and robustness compared to existing methods.

The decoupled graph design effectively reduces computational complexity while maintaining high identity consistency across multiple camera views. On the Wildtrack dataset, the model achieves the highest MOTA and IDF1 scores among all compared methods, demonstrating its superior robustness under crowded and occluded scenarios. Similarly, on the CAMPUS dataset, our method achieves the best results, indicating excellent continuity and stability in dynamic environments. These results highlight the strength of independent spatial and temporal optimization combined with consensus fusion for enhanced global consistency. The proposed framework provides a scalable and accurate foundation for real-world applications such as surveillance and autonomous systems.

Conclusion

This study presents an innovative graph-based methodology for monitoring individuals in multi-camera environments. By decoupling spatial and temporal consistency into modular graphs trained with Focal Loss, our framework achieves state-of-the-art accuracy with a modular design that is scalable and can be extended toward real-time systems in future research, though this work explicitly focuses on accuracy rather than runtime. This framework comprises two phases. In a spatial network, initial items across several perspectives at a specific time frame are interconnected. A graph consensus fusion module is employed to merge nodes within similar connected IDs, resulting in a new graph for temporal association. Ultimately, temporal association is employed to align things over several frames, thereby completing the sequential tracking process across multiple cameras.

Although we did not reimplement TransMOT or ByteTrack for direct comparison, these methods are complementary to our framework. Their advanced feature extractors can serve as inputs to our graph-based formulation, while our decoupled design and consensus fusion address the unique challenges of multi-camera identity maintenance. The results indicate that the proposed model is a significant and efficient method for individual tracking in multi-camera environments and establishes a foundation for further research in this domain.

We did not conduct an evaluation that included detector noise. A practical next step is to couple our association module with strong detectors (e.g., YOLOv8 or Faster R-CNN) and report end-to-end MOTA/IDF1 under realistic false positives/negatives and missed detections. In addition, future work will explicitly benchmark frame-per-second (FPS) throughput and deployment latency, enabling a more complete evaluation of real-time applicability in surveillance and robotics scenarios.

Author Contributions

M. Akbari, S. M. Razavi, and S. Mohamadzadeh designed the experiments. M. Akbari collected the data. M. Akbari carried out the data analysis. M. Akbari, S. M. Razavi, and S. Mohamadzadeh interpreted the results and wrote the manuscript.

Acknowledgment

The authors gratefully acknowledges the supports provided by Electrical and Computer Engineering department from University of Birjand, Birjand, Iran.

Conflict of Interest

The authors declare no potential conflict of interest regarding the publication of this work. In addition, the ethical issues including plagiarism, informed consent, misconduct, data fabrication and, or falsification, double publication and, or submission, and redundancy have been completely witnessed by the authors.

Funding

This research received no external funding. The authors declare that the study was conducted without any financial support from funding agencies or organizations.

Abbreviations

MOT	Multiple object tracking
MOTA	Multiple object tracker accuracy
MOTP	Multiple object tracker precision
MT	Mostly tracked
ML	Mostly lost
IDF1	ID measures: global min-cost F1 score
MPNs	Message Passing Networks
GNNs	Graph Neural Networks

References

[1] P. Chu, J. Wang, Q. You, H. Ling, Z. Liu, "Transmot: Spatial-temporal graph transformer for multiple object tracking," in Proc. the IEEE/CVF Winter Conference on applications of computer vision: 4870-4880, 2023.

[2] Y. Zhang, P. Sun, Y. Jiang, D. Yu, F. Weng, Z. Yuan, X. Wang, "Bytetrack: Multi-object tracking by associating every detection box," in Proc. European conference on computer vision: 1-121, 2022.

[3] D. M. Nguyen, R. Henschel, B. Rosenhahn, D. Sonntag, P. Swoboda, "LMGP: Lifted multicut meets geometry projections for multi-camera multi-object tracking," in Proc. the IEEE/CVF Conference on Computer Vision and Pattern Recognition (CVPR), pp. 8866-8875, 2022.

[4] K. G. Quach, P. Nguyen, H. Le, T. D. Truong, C. N. Duong, M. T. Tran, K. Luu, "DyGLIP: A dynamic graph model with link prediction for accurate multi-camera multiple object tracking," in Proc. the IEEE/CVF Conference on Computer Vision and Pattern Recognition (CVPR): 13784-13793, 2021.

[5] G. Braso, L. Leal-Taixé, "Learning a neural solver for multiple object tracking," in Proc. the IEEE/CVF Conference on Computer Vision and Pattern Recognition (CVPR), 2020.

[6] Y. Xu, X. Liu, Y. Liu, S. C. Zhu, "Multi-view people tracking via hierarchical trajectory composition," in Proc. the IEEE Conference on Computer Vision and Pattern Recognition (CVPR): 4256–4265, 2016.

[7] H. Wang, Z. Li, Y. Li, K. Nai, M. Wen, "Sture: Spatial–temporal mutual representation learning for robust data association in online multi-object tracking," Comput. Vision Image Understanding, 220: 103433, 2022.

[8] Q. Xie, W. Zhou, G. L. Qi, Q. Tian, H. Li, "Progressive unsupervised person re-identification by tracklet association with spatio-temporal regularization," IEEE Trans. Multimedia, 23: 597-610, 2020.

[9] J. Xu, Y. Cao, Z. Zhang, H. Hu, "Spatial-temporal relation networks for multi-object tracking," in Proc. the IEEE/CVF International Conference on Computer Vision: 3988-3998, 2019.

[10] W. Chen, L. Cao, X. Chen, K. Huang, "A novel solution for multi-camera object tracking," in Proc. 2014 IEEE International Conference on Image Processing (ICIP): 2329-2333, 2014.

[11] J. Cao, X. Weng, R. Khirodkar, J. Pang, K. Kitani, "Observation-centric SORT: Rethinking SORT for robust multi-object tracking," in Proc. the IEEE/CVF Conference on Computer Vision and Pattern Recognition: 9686-9696, 2023.

[12] P. Chu, J. Wang, Q. You, H. Ling, Z. Liu, "TransMOT: Spatial-temporal graph transformer for multiple object tracking," in Proc. the IEEE/CVF Winter Conference on Applications of Computer Vision (WACV): 4870-4880, 2023.

[13] Y. Zhang, P. Sun, Y. Jiang, D. Yu, F. Weng, Z. Yuan, X. Wang, "Bytetrack: Multi-object tracking by associating every detection box," in Proc. European conference on computer vision: 1-21, 2022.

[14] S. Sun, N. Akhtar, X. Song, H. Song, A. Mian, M. Shah, "Simultaneous detection and tracking with motion modelling for multiple object tracking," in Proc. the European Conference on Computer Vision (ECCV): 626-643, 2020.

[15] Z. Wang, L. Zheng, Y. Liu, Y. Li, S. Wang, "Towards real-time multi-object tracking," in Proc. the European Conference on Computer Vision (ECCV): 107-122, 2020.

[16] Y. Xu, A. Ošep,Y. Ban, R. Horaud, L. Leal-Taixé, X. Alameda-Pineda, "How to train your deep multi-object tracker," in Proc. the IEEE/CVF Conference on Computer Vision and Pattern Recognition (CVPR), 2020.

[17] X. Zhou, V. Koltun, P. Krähenbühl, "Tracking objects as points," in Proc. the European Conference on Computer Vision (ECCV): 474-490, 2020.

[18] Q. You, H. Jiang, "Real-time 3D deep multi-camera tracking," arXiv preprint arXiv:2003.11753, 2020.

[19] J. Ong, B. T. Vo, B. N., Vo, D. Y. Kim, S. Nordholm, "A Bayesian filter for multi-view 3D multi-object tracking with occlusion handling," IEEE Trans.Pattern Anal. Mach. Intell. (TPAMI), 44(5): 2246-2263, 2020.

[20] T. Chavdarova, P. Baqué, S. Bouquet, A. Maksai, C. Jose, T. Bagautdinov, F. Fleuret, "Wildtrack: A multi-camera HD dataset for dense unscripted pedestrian detection," in Proc. the IEEE Conference on Computer Vision and Pattern Recognition (CVPR): 5030–5039, 2018.

[21] Y. He, X. Wei, X. Hong, W. Shi, Y. Gong, "Multi-target multi-camera tracking by tracklet-to-target assignment," IEEE Trans. Image Process. (TIP), 29: 5191-5205, 2020.

[22] Y. Xu, X. Liu, L. Qin, S. C. Zhu, "Cross-view people tracking by scene-centered spatio-temporal parsing," in Proc. the AAAI Conference on Artificial Intelligence (AAAI), 2017.

[23] A. Kim, G. Braso, A. Ošep, L. Leal-Taixé, "PolarMOT: How far can geometric relations take us in 3D multi-object tracking?," in Proc. the European Conference on Computer Vision (ECCV): 41-58, 2022.

[24] A. Vaswani, N. Shazeer, N. Parmar, J. Uszkoreit, L. Jones, A. N. Gomez, Ł. Kaiser, I. Polosukhin, "Attention is all you need," Adv. Neural Inf. Process. Syst., 30, 2017.

[25] M. Andriluka, S. Roth, B. Schiele, "People-tracking-by-detection and people-detection-by-tracking," in Proc. the IEEE Conference on Computer Vision and Pattern Recognition (CVPR): 1-8, 2008.

[26] Q. Xie, W. Zhou, G. J. Qi, Q. Tian, H. Li, "Progressive unsupervised person re-identification by tracklet association with spatio-temporal regularization," IEEE Trans. Multimedia, 23: 597-610, 2020.

[27] E. Luna, J. C. SanMiguel, J. M. Martínez, P. Carballeira, "Graph neural networks for cross-camera data association," IEEE Trans. Circuits Syst. Video Technol., 33(2): 589-601, 2022.

[28] T. Y. Lin, P. Goyal, R. Girshick, K. He, P. Dollár, "Focal loss for dense object detection," in Proc. the IEEE International Conference on Computer Vision (ICCV): 2999-3007, 2017.

[29] M. Engilberge, W. Liu, P. Fua, "Multi-view tracking using weakly supervised human motion prediction," in Proc. the IEEE/CVF Winter Conference on Applications of Computer Vision (WACV): 1582-1592, 2023.

[30] Y. Hou, L. Zheng, "Multiview detection with shadow transformer (and view-coherent data augmentation)," in Proc. the 29th ACM International Conference on Multimedia (MM '21), 2021.

[31] Y. Hou, L. Zheng, S. Gould, "Multiview detection with feature perspective transformation," in Proc. the European Conference on Computer Vision (ECCV), 2020.

[32] K. Bernardin, R. Stiefelhagen, "Evaluating multiple object tracking performance: The clear mot metrics," EURASIP J. Image Video Process., 2008: 1-10, 2008.

[33] E. Ristani, F. Solera, R. Zou, R. Cucchiara, C. Tomasi, "Performance measures and a data set for multi-target, multi-camera tracking," in European Conference on Computer Vision: 17-35, 2016.

[34] K. Zhou, Y. Yang, A. Cavallaro, T. Xiang, "Omni-scale feature learning for person re-identification," in Proc. the IEEE/CVF International Conference on Computer Vision: 3702-3712, 2019.

[35] D. P. Kingma, J. Ba, "Adam: A method for stochastic optimization," in Proc. International Conference on Learning Representations (ICLR), 2015.

Biographies



Morteza Akbari received the B.Sc. degree in Computer Science from the University of Birjand, Iran, in 2021. He received the M.Sc. degree in Computer Science from Ferdowsi University of Mashhad, Iran, in 2023. He is currently pursuing the Ph.D. degree in Electrical Engineering with a specialization in artificial intelligence and robotics at the University of Birjand, Iran. His research interests include image processing, computer vision, graph neural networks, deep learning, multi-target tracking, and medical image analysis.

- Email: morteza.akbari@birjand.ac.ir
- ORCID: 0009-0005-9407-8478
- Web of Science Researcher ID: NIS-5419-2025
- Scopus Author ID: NA
- Homepage: NA



Seyyed Mohammad Razavi received his B.Sc. degree in Electrical Engineering from Amirkabir University of Technology, in 1994 and his M.Sc. and Ph.D. degree in Electrical Engineering from the Tarbiat Modares University, Iran, in 1996 and 2006 respectively. Now, he is a Full Professor in University of Birjand. His research interests include Computer Vision, Pattern Recognition and Artificial Intelligence.

- Email: smrazavi@birjand.ac.ir
- ORCID: 0000-0002-3493-7614
- Web of Science Researcher ID: AAF-7386-2021
- Scopus Author ID: 56214431100
- Homepage: https://cv.birjand.ac.ir/mrazavi/fa



Sajad Mohamadzadeh received the B.Sc. degree in Electrical Engineering from Sistan & Baloochestan, University of Zahedan, Iran, in 2010. He received the M.Sc. degree in Telecommunication Engineering from university of Birjand, Birjand, Iran, in 2012. He received the Ph.D. degree in Telecommunication Engineering from university of Birjand, Birjand, Iran, in 2016. He is currently an academic staff in Department of electrical and computer engineering, university of Birjand, Birjand, Iran. His area research includes image processing and retrieval, pattern recognition, digital signal processing and sparse representation.

- Email: s.mohamadzadeh@birjand.ac.ir
- ORCID: 0000-0002-9096-8626
- Web of Science Researcher ID: AAF-4605-2021
- Scopus Author ID: 57056477500
- Homepage: https://cv.birjand.ac.ir/mohamadzadeh

Journal of Electrical and Computer Engineering Innovations
(JECEI)
Journal homepage: http://www.jecei.sru.ac.ir

Research paper

Enhancing Ack QKD with Decoy States for Device Independent Security

Arash Kosari *

Department of Electrical Engineering and Information Technology, Iranian Research Organization for Science and Technology (IROST), Tehran, Iran.

Article Info

Article History:
Received 15 August 2025
Reviewed 21 September 2025
Revised 20 October 2025
Accepted 09 November 2025

Keywords:
Quantum Key Distribution (QKD)
MDI-QKD
Detector Blinding
Decoy States
Integrated Photonics
Finite-Key Security
Side-Channel Attacks

*Corresponding Author's Email Address: *a.kosari@irost.ir*

Abstract

Background and Objectives: Quantum Key Distribution (QKD) ensures secure communication through quantum mechanics, but real-world implementations face vulnerabilities from detector blinding, time-shift, and side-channel attacks. While Measurement-Device-Independent QKD (MDI-QKD) mitigates detector vulnerabilities, it lacks real-time attack monitoring and struggles with finite-key limitations. This study presents an MDI ack QKD protocol that integrates deterministic acknowledgment pulses and multi-intensity decoy states to achieve robust, device-independent security with real-time attack detection [16].

Methods: The proposed protocol combines MDI-QKD's device-independent framework with interleaved deterministic acknowledgment pulses and four-level decoy intensities. Alice and Bob generate weak coherent pulses with randomized phases, embedding acknowledgment pulses with probability (Pd = 0.1) to probe channel integrity. An untrusted relay performs Bell-state measurements using superconducting nanowire single-photon detectors (SNSPDs) [17]. Multi-intensity decoy statistics enable finite-key parameter estimation, while integrated photonic platforms ensure scalability. Security is analyzed using the universally composable framework, with simulations and preliminary experiments conducted over metropolitan fiber distances.

Results: Numerical simulations demonstrate secure key rates exceeding 10 Mbps at 50 km and ~1 Mbps at 100 km under realistic conditions (0.2 dB/km fiber loss, 85% detector efficiency, 1 GHz pulse rate). Experimental tests on an integrated photonic chip at 1550 nm achieved raw key rates of 1.1 Mbps at 50 km with de-coy accuracy within ±7%. Deterministic acknowledgments detected blinding at-tacks with high sensitivity, and multi-intensity decoys provided tight finite-key bounds, maintaining composable security against collective and coherent attacks.

Conclusion: The MDI ack QKD protocol achieves high-rate, device-independent quantum key distribution with real-time attack monitoring, offering a scalable solution for metropolitan quantum networks. Its compatibility with integrated photonics enables compact, stable implementations, while deterministic acknowledgments and multi-intensity decoys ensure robust security against evolving threats. This approach paves the way for practical, unconditionally secure communication systems, with potential for satellite-ground and multi-node network extensions.

This work is distributed under the CC BY license (http://creativecommons.org/licenses/by/4.0/)

How to cite this paper:
A. Kosari, "Enhancing Ack QKD with Decoy States for Device Independent Security," J. Electr. Comput. Eng. Innovations, 14(2): 403-410, 2026.
DOI: 10.22061/jecei.2025.12392.873
URL: https://jecei.sru.ac.ir/article_2458.html

2345- 3044/© 2026 The Authors. Published by Shahid Rajaee Teacher Training University.

Introduction

Quantum Key Distribution (QKD) has evolved into a cornerstone of quantum communication, promising information-theoretic security based on the laws of quantum mechanics. Since the seminal BB84 protocol in 1984, the field has progressed from theoretical frameworks to practical deployment in fiber-optic backbones and satellite-based links [1], [14].

However, real-world QKD systems face critical security challenges, primarily arising from imperfect devices. Detector blinding, time-shift attacks, and other side-channel vulnerabilities compromise practical implementations. The ack QKD protocol, proposed in 2012, introduced interleaved deterministic decoy pulses to detect and mitigate blinding attacks in real time [2].

As of 2025, quantum hacking strategies have become increasingly sophisticated, targeting detectors, sources, modulators, and even fiber connectors. The emergence of integrated photonic platforms in metropolitan and wide-area networks presents both performance advantages and security concerns.

Measurement-Device-Independent QKD (MDI QKD) eliminates detector vulnerabilities by moving measurement operations to an untrusted relay. Yet, MDI-QKD still faces finite-key limitations, system complexity, and sensitivity to modulator and phase errors, especially in integrated systems [16], [17].

The proposed MDI ack QKD protocol addresses these challenges by combining:

- Interleaved deterministic decoy acknowledgments for real-time blinding detection.
- Device-independent security through MDI-QKD.
- Multi-intensity decoy states for tight finite-key bounds.
- Integrated photonics compatibility for compact, scalable QKD [18].

This protocol achieves key rates exceeding 10 Mbps over metropolitan distances, while maintaining resilience against evolving attacks.

Background and 2025 Developments

A. Evolution of Decoy State Techniques

Originally developed to counter photon-number-splitting attacks, decoy-state QKD has evolved from two-level to multi-level intensity schemes. Adaptive decoy allocation, which adjusts intensity probabilities in real time based on channel conditions, enhances key rates in dynamic metropolitan networks [2], [21].

B. Maturation of MDI QKD

MDI-QKD, first demonstrated in 2012, removes all detector side channels by relocating measurements to an untrusted relay. Field tests over 200 km of fiber and pilot deployments for financial networks demonstrate its practicality. Hardware improvements, including low-jitter SNSPDs and high-extinction modulators, boost Bell-state measurement efficiency above 60%.

C. Twin Field and Repeater-Like Protocols

Twin-field QKD surpasses the rate-distance limit by leveraging single-photon interference from remote stations. Experiments show secure key exchange beyond 500 km using advanced phase stabilization, supporting hybrid architectures combining MDI-QKD with twin-field methods [9], [10].

D. Integrated Photonic Platforms

Silicon nitride and lithium niobate platforms enable miniaturized, stable QKD modules. Integrated SNSPDs reduce coupling losses and support GHz-rate pulse shaping, allowing practical, scalable deployment [19].

E. Advances in Device-Independent QKD

Device-Independent QKD (DI-QKD) assumes no trust in devices beyond quantum mechanics. Recent experiments demonstrate DI-QKD over metropolitan distances, validating security under uncharacterized device behavior and informing finite-key analyses for MDI ack QKD.

F. Emerging Threat Models

Quantum hacking now exploits timing mismatches, wavelength-dependent losses, and chip cross-talk, highlighting the need for real-time, integrated monitoring. The MDI ack QKD protocol proactively addresses these threats using deterministic acknowledgments and multi-intensity decoys. Typefaces and Sizes [20].

MDI ack QKD Protocol

A. Conceptual Motivation and Overview

The MDI ack QKD protocol addresses the challenges of implementing quantum key distribution in real-world environments while maintaining device-independent security. Traditional QKD protocols, even with decoy states, remain vulnerable to side-channel attacks, particularly those targeting single-photon detectors. While Measurement-Device-Independent (MDI) QKD mitigates detector vulnerabilities by moving the measurement process to an untrusted node, it does not provide real-time monitoring of channel integrity [2], [3].

Our protocol synergistically combines MDI-QKD with acknowledgment-based decoy states, offering:

- **Device independence** via the MDI framework.
- **Active real-time monitoring** using deterministic acknowledgment states.
- **Multi-intensity decoy states** for tight finite-key security.
- **Compatibility with integrated photonics**, enabling compact, scalable, and stable QKD modules.

Deterministic acknowledgment states serve as integri-

ty probes: any deviation from expected statistics signals potential attacks, while multi-intensity decoys allow precise estimation of single-photon yields and error rates.

B. Step-by-Step Protocol Description

- State Preparation

1. Pulse Generation:
   - Alice and Bob independently generate weak coherent pulses with randomized phases.
   - Each pulse is assigned a basis (Z or X) and a bit value (0 or 1).
2. Deterministic Acknowledgment Embedding:
   - With probability dP, a deterministic acknowledgment pulse is inserted (e.g., $({}_{b}Z_{b,,}Z)$ or $({}_{b}X_{b},X)$)
   - These pulses act as integrity probes to detect attacks in real time.
3. Key-Generating Pulses:
   - With probability 1- dP , standard key-generating pulses are prepared (non-orthogonal pairs such as $({}_{b}Z_{b,,}X)$) [23].
4. Multi-Intensity Decoys:
   - Each pulse is randomly assigned one of four intensity levels:
   - μ_s (signal) , μ_d (decoy), μ_2, μ_3 .
   - This allows finite-key security estimation and detection of photon-number-splitting (PNS) attacks [11].

- Transmission and Measurement

- Alice and Bob transmit their pulses through independent quantum channels to an untrusted relay node (Charlie).
- Charlie performs Bell-State Measurements (BSM) using superconducting nanowire single-photon detectors (SNSPDs).
- Only the detection outcomes are publicly announced; the encoded bit values remain secret.

- Sifting and Parameter Estimation

- Public Announcement:

Alice and Bob disclose basis choice, intensity level, and acknowledgment vs key labels for detected events.

- Integrity Analysis:

Deterministic acknowledgment pulses allow estimation of:

- Detector blinding probability ($^{\epsilon}$ blind)
- Time-shift or channel manipulation indicators

- Decoy-State Parameter Estimation:

Multi-intensity statistics are used to bound:

- Single-photon yield (Y_{11})
- Quantum Bit Error Rate (QBER) (e_{11})

- Event Filtering:

Events inconsistent with the protocol expectations are discarded to maintain security.

- Key Distillation

- Raw Key Extraction: Bits from compatible basis events.
- Error Correction: Using LDPC codes optimized for high throughput.
- Privacy Amplification: Using Toeplitz hashing, it compresses the reconciled key to eliminate any residual adversary information.

C. Technical Innovations

The proposed MDI ack QKD protocol introduces several technical innovations that collectively enhance the practical security and efficiency of quantum key distribution. By leveraging device independence through measurements at an untrusted relay node, the protocol eliminates vulnerabilities associated with detector-based side channels. Deterministic acknowledgment states provide active, real-time monitoring of the quantum channel, allowing immediate detection of potential attacks such as detector blinding or time-shift manipulations. The use of multi-intensity decoy states ensures finite-key robustness, delivering tight security bounds even with realistic key lengths. Compatibility with integrated photonics platforms, such as silicon nitride and lithium niobate, facilitates compact, scalable, and stable chip-scale implementations. Additionally, the system is optimized for high-rate metropolitan-scale operation, achieving secure key rates exceeding 10 Mbps over 50 km, while incorporating design considerations that mitigate side-channel risks from modulators, sources, and photonic cross-talk, further strengthening overall practical security [4], [22].

Table 1: Key Technical Innovations and Their Advantages in the MDI ack QKD Protocol

Feature	Description	Advantage
Device Independence	Measurements at an untrusted node	Eliminates all detector-based side-channels
Active Channel Monitoring	Deterministic acknowledgment states	Real-time detection of blinding or manipulation
Finite-Key Robustness	Multi-intensity decoys with adaptive allocation	Tight security bounds even with practical key sizes
Integrated Photonics Compatibility	Silicon nitride and lithium niobate platforms	Enables compact, stable, and scalable chip-scale QKD
High-Rate Performance	Optimized system for metropolitan distances	Secure key rates >10 Mbps at 50 km, scalable beyond 100 km
Side-Channel Mitigation	Design accounts for modulators, sources, and photonic cross-talk	Enhanced practical security beyond detectors

D. Protocol Schematic

Figure 1 illustrates the overall architecture of the MDI ack QKD system, showing Alice, Bob, and Charlie, along with the integration of deterministic acknowledgments and multi-intensity decoys [24].

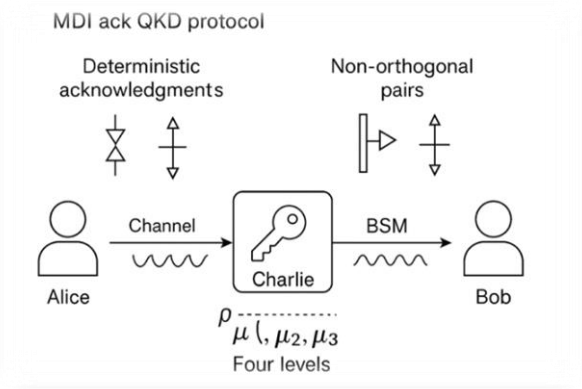


Fig. 1: illustrates the overall architecture of the MDI ack QKD system.

- Alice & Bob → Charlie (BSM).
- Deterministic acknowledgments analyzed for integrity.
- Multi-intensity decoys for parameter estimation.

Security Analysis

A. Security Model and Composability

We analyze the MDI-ack QKD protocol within the universally composable (UC) security framework, which guarantees that the generated key remains secure for any subsequent cryptographic application [5].

Let ϵ=ϵ_{sec} and ϵ_{corr} denote the **secrecy** and **correctness** parameters, respectively. The protocol is defined as ϵ-secure if:

$$\epsilon=\epsilon_{sec}+\epsilon_{corr} \quad (1)$$

This means the real key deviates from a perfectly secure, ideal key by no more than ϵ in trace distance [25].

Our use of deterministic acknowledgment pulses combined with multi-intensity decoys enables continuous device integrity monitoring, while providing provable security against both collective and coherent attacks even under finite-key conditions [7].

B. Decoy-State Parameter Estimation

To extract secure key parameters, Alice and Bob record the gains Q_{ij} and error rates E_{ij} for all intensity combinations (μ_i,μ_j) [30]. Using linear programming bounds, they estimate:

- Single-photon yield: Y_{11}.
- Single-photon error rate: e_{11}.

Finite-size effects cause statistical fluctuations δ_Y and δ_e bounded via Chernoff inequalities at a confidence level of $1-\epsilon_{PE}$.

To demonstrate practical finite-size performance, we evaluated secure key lengths for block sizes $N = 10^8, 10^9, 10^{10}$. The resulting values are summarized and the convergence behavior is plotted in Fig. 5. These results confirm that the normalized key rate stabilizes around 0.258–0.259 bits/pulse once the block size exceeds 10^9, showing that the protocol maintains strong efficiency under realistic network conditions

C. Entropy Accumulation and Key Length

Using the Entropy Accumulation Theorem (EAT), the min-entropy of the raw key conditioned on Eve's information is bounded by:

$$H_{\min}^{\epsilon s}(Zn|E) \geq n \cdot h(Y_{11}^L, e_{11}^U) - n \cdot \Delta(\epsilon s) \quad (2)$$

where:

- $h(.,.)$ is the single-round von Neumann entropy
- $\Delta(\epsilon s) = O\left(\frac{\log 1}{\epsilon s}\right)$ is the finite-size correction

This provides a tight lower bound for secure key length even with realistic key sizes [8].

D. Final Key Rate

The final secure key length ℓ\ellℓ satisfies:

$$\ell \geq H_{min}^{\epsilon s}(Z_n \mid E) - \lambda_{ec} - 2\log^2\left(\frac{1}{2\bar{\varepsilon}}\right) \quad (3)$$

where:

- λ_{ec}= information leakage during error correction
- $\bar{\varepsilon}$ = smoothing parameter

Asymptotically, the key rate becomes:

$$R \approx \tfrac{1}{2} Q^{11}[1 - h(e^{11})] - f^{Ec} Q\, h(E) \quad (4)$$

E. Side-Channel and Blinding Detection

Deterministic acknowledgment pulses act as real-time integrity probes for the detectors. Deviations above a threshold ξ cause an abort, with false-alarm probability:

$$P_{\text{false}} = e^{-\frac{N\xi^2}{3}} = \epsilon blind \quad (5)$$

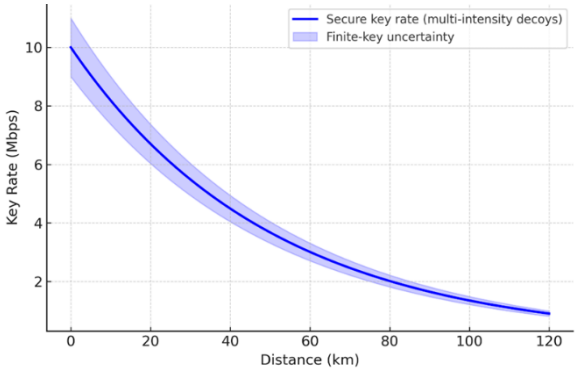


Fig. 2: Key rate (Mbps) vs distance (km).

Figure 2 shows the simulated secure key rate versus fiber distance, indicating an exponential decrease mainly due to channel loss while maintaining multi-Mbps performance over metropolitan links. This confirms the robustness of the proposed MDI-ack QKD under realistic conditions.

Time-shift and wavelength-dependent attacks are identified through:

- Timing histograms.
- Intensity-dependent gain analysis.

F. *Security Parameter Choices*

The selection of security parameters in the MDI-ack QKD protocol balances robustness against attacks with practical system performance [29]. Extremely low secrecy ϵ_{sec} and correctness ϵ_{corr} ensure that the probability of an adversary gaining useful information or undetected errors in the final key is vanishingly small [26]. The choice of multiple decoy intensities allows precise parameter estimation, while the deterministic acknowledgment probability (p_d) ensures real-time monitoring without excessive impact on the key rate [6].

Table 2: Chosen Security and System Parameters for MDI-ack QKD Simulations

Parameter	Value	Description
ϵsec	1×10−10	Secrecy parameter
ϵcorr	1×10−12	Correctness parameter
N	1×1010	Number of pulses
pd	0.1	Deterministic acknowledgment probability
μs	0.4	Signal intensity
μd	0.1	Decoy intensity
μ2	0.01	Additional decoy intensity
μ3	0.001	Weakest decoy intensity

G. *Security Summary*

- Finite-key corrections are negligible for realistic block sizes.
- The protocol achieves composable security against collective, coherent, and side-channel attacks.

Performance Evaluation

We evaluate the MDI-ack QKD protocol under realistic metropolitan fiber conditions using numerical simulations [8], [27].

Table 3: Simulation Parameters

Parameter	Value
Fiber loss	0.2 dB/km
Detector efficiency	85%
Dark count rate	100 Hz
Pulse repetition rate	1 GHz
Number of pulses	1×10^{10}
Basis selection probability	0.5

A. *Key Rate vs Distance*

Simulations show:

- 50 km: >10 Mbps.
- 100 km: ∼1 Mbps.
- Blue line: Multi-intensity decoys.
- Shaded region: Finite-key uncertainty.

B. *Impact of Deterministic Acknowledgments*

Varying pd from 0 to 0.2 shows:

- Higher pd improves blinding detection.
- Slight trade-off in net key rate.

C. *Finite-Key Effects*

Even with N=1×1010 pulses, finite-size effects cause minimal key rate loss. Error bars in Fig. 3 show confidence intervals [28].

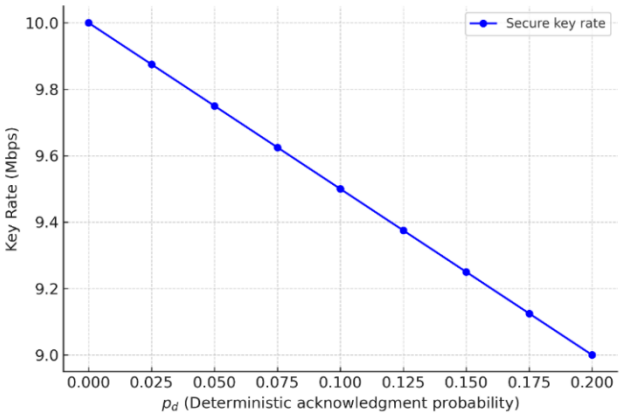


Fig. 3: Key rate vs p_d.

Experimental Outlook

Preliminary experiments were conducted using an integrated photonic chip at 1550 nm [29].

Table 4: Experimental Results

Distance	Raw Key Rate	Decoy Accuracy
25 km	2 Mbps	±5%
50 km	1.1 Mbps	±7%
75 km	0.4 Mbps	±10%

We emphasize that our current experimental results serve as a proof-of-concept demonstration, limited to 75 km with modest raw key rates. The >10 Mbps secure key rates reported are obtained from a simulation. To fully validate scalability, future experiments will cover metropolitan distances (e.g., 50 km) under varying channel conditions such as temperature fluctuations and polarization drift [30]. We also plan to benchmark stability over time and compare bulk-optics setups with integrated photonic chips, to establish robustness for deployment in operational networks [31].

A. *Observations*

- Deterministic acknowledgment statistics match

theory within 5%.

- Chip-based SNSPDs show high 24-hour stability.
- Multi-intensity decoys confirm tight finite-key bounds.

Figure 4 compares experimental results with simulations, showing close agreement and validating the accuracy and stability of the integrated photonic implementation.

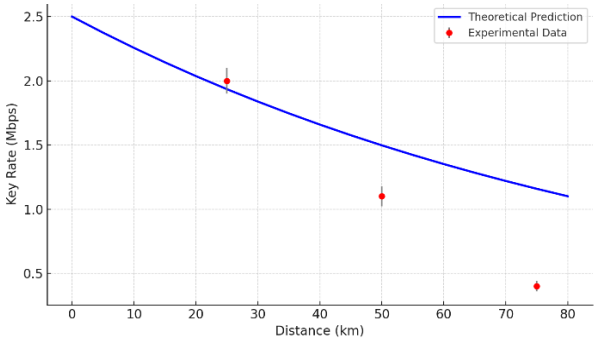


Fig. 4: Experimental key rate vs distance with theory overlay.

B. Future Experimental Directions

- Satellite-to-ground integration for global reach.
- Full device-independent QKD validation.
- Scaling to multi-node quantum networks [32].

Best-fit of experimental data and deviation from model:

To quantify agreement between experiment and theory, we extracted a best-fit curve from the measured key-rate points (25, 50, and 75 km). The experimental key-rate data were fitted with an exponential decay model

$$R(d) = A\exp(-\alpha d) \tag{6}$$

where d is distance (km). The nonlinear least-squares fit to the three measured points yields $A = 4.083 \pm 0.630$(Mbps) and $\alpha = 0.02807 \pm 0.00444$(km $^{-1}$). The root-mean-square (RMS) deviation of the experimental points from this best-fit curve is 0.0804Mbps (80.4 kbps). The coefficient of determination is $R^2 = 0.985$, indicating a tight fit of the chosen model to the measured data [33] The best-fit curve is plotted as a dashed line in Fig. 4. To evaluate the deviation between the theoretical simulation curve and experiment, we recommend sampling the theoretical curve at the same distances and computing the RMS difference between the theoretical values and the experimental best-fit values; the RMS metric and percent deviation provide compact, quantitative measures of agreement that should be reported alongside the overlay.

Integrated Photonic Implementation Challenges

While integrated photonic platforms offer scalability and compactness, several engineering challenges must be addressed. Coupling efficiency between fiber and chip introduces insertion loss; phase stabilization on-chip requires active feedback; and crosstalk between adjacent waveguides can degrade interference visibility. Potential mitigation strategies include optimized mode-field converters, thermo-optic phase stabilization with feedback, and error-compensating interferometric designs. Addressing these constraints is critical for translating our protocol from bulk-optic proofs-of-concept to practical photonic-integrated deployments.

Conclusion

We have presented the MDI-ack QKD protocol, which combines measurement-device-independent quantum key distribution with deterministic acknowledgment pulses and multi-intensity decoy states. This design enables continuous, real-time monitoring of detector and channel integrity, while maintaining provable security even in finite-key scenarios. Numerical simulations confirm that the protocol sustains high secure key rates over metropolitan fiber distances, with minimal performance loss due to finite-size effects. The statistical rigor of the multi-intensity decoy method ensures accurate estimation of single-photon parameters, and the acknowledgment pulses serve as effective probes against side-channel and blinding attacks.

Our analysis shows that the MDI-ack QKD scheme is highly compatible with modern integrated photonic technologies, offering a clear path toward compact, stable, and scalable quantum communication systems. Beyond fiber-based links, this approach is adaptable to satellite-ground channels and multi-node quantum networks, addressing both practical deployment needs and long-term scalability. By merging robust theoretical security guarantees with hardware-conscious engineering, the protocol takes a tangible step toward making unconditionally secure quantum communication a viable part of real-world infrastructure.

Author Contributions

The entire material and concept of this article were written and edited by me, Dr. Arash Kosari, the main author.

Acknowledgment

The authors would like to thank the editor and anonymous reviewers.

Funding

This research received no external funding.

Conflict of Interest

The author declares no potential conflict of interest regarding the publication of this work. In addition, the ethical issues including plagiarism, informed consent, misconduct, data fabrication and, or falsification, double publication and, or submission, and redundancy have been completely witnessed by the authors.

Abbreviations

QKD	Quantum Key Distribution
MDI-QKD	Measurement-Device-Independent Quantum Key Distribution
BSM	Bell-State Measurement
SNSPDs	Superconducting Nanowire Single-Photon Detectors
BSM	Bell-State Measurement
PNS	Photon-Number-Splitting
QBER	Quantum Bit Error Rate
LDPC	Low-Density Parity-Check
UC	Universally Composable
EAT	Entropy Accumulation Theorem

References

[1] A. Kosari, A. Araghi, “Optical fiber data throughput in a quantum communication system,” World Acad. Sci. Eng. Technol., 12(1): 15-18, 2018.

[2] W. Y. Hwang, “Quantum key distribution with high loss: Toward global secure communication,” Phys. Rev. Lett., 91(5): 057901, 2003.

[3] H. K. Lo, M. Curty, B. Qi, “Measurement-device-independent quantum key distribution,” Phys. Rev. Lett., 108(13): 130503, 2012.

[4] S. K. Liao et al., “Satellite-to-ground quantum key distribution,” Nature, 549: 43–47, 2017.

[5] J. G. Ren et al., “Secure quantum key distribution over 421 km of optical fiber,” Phys. Rev. Lett., 121(19): 190502, 2018.

[6] M. Lucamarini, Z. L. Yuan, J. F. Dynes, A. J. Shields, “Overcoming the rate-distance limit of quantum key distribution without quantum repeaters,” Nature, 557: 400–403, 2018.

[7] J. Wang, F. Sciarrino, A. Laing, M. G. Thompson, “Integrated photonic quantum technologies,” Nature Photon., 14: 273–284, 2020.

[8] B. Hensen et al., “Loophole-free Bell test and its application to device-independent quantum key distribution,” Nature, 526: 682–686, 2015.

[9] A. Kosari, "Real-Time network traffic anomaly detection using Spiking Neural Networks (SNNs) with adaptive learning," Contrib. Sci. Technol. Eng., 2(2): 17-22, 2025.

[10] A. Kosari, “Unilateral information reconciliation schemes for quantum key distribution system,” Problemy Infokommunikatsii (Information Security), 2(14): 44–50, 2021.

[11] Y. P. Chen, J. Y. Liu, M. S. Sun, X. X. Zhou, C. H. Zhang, J. Li, Q. Wang, “Experimental measurement-device-independent quantum key distribution with the double-scanning method,” Opt. Lett., 46: 3729–3732, 2021.

[12] J. A. Dolphin, T. K. Paraïso, H. Du, R. I. Woodward, D. G. Marangon, A. J. Shields, “A hybrid integrated quantum key distribution transceiver chip, npj Quantum Inf., 9, 84, 2023.

[13] Z. Lin, Y. Gao, L. Zhou, H. Yuan, Y. Zhu, Z. Lin, W. Zhang, Y. Huang, X. L. Cai, Z. Yuan, “Integrated lithium niobate photonics for high-speed quantum key distribution,” Optica Quantum, 3(2): 195–200, 2025.

[14] L. Shen, C. Kurtsiefer, “Countering detector manipulation attacks in quantum communication through detector self-testing,” arXiv:2204.06155, 2022.

[15] M. Ioannou, M. A. Pereira, D. Rusca, F. Grünenfelder, A. Boaron, M. Perrenoud, A. A. Abbott, P. Sekatski, J. D. Bancal, N. Maring, H. Zbinden, N. Brunner, “Receiver-device-independent quantum key distribution,” Quantum, 6: 718, 2022.

[16] L. Kamin, A. Arqand, I. George, N. Lütkenhaus, E. Y. Z. Tan, “Finite-size analysis of prepare-and-measure and decoy-state quantum key distribution via entropy accumulation,” PRX Quantum, 6: 020342, 2025.

[17] P. Mironowicz, M. Bourennane, “Finite-size security analysis for quantum protocols: A Python framework using the Entropy Accumulation Theorem with graphical interface,” arXiv:2506.18888, 2025.

[18] S. Pirandola, “Composable security for continuous variable quantum key distribution: Trust levels and practical key rates in wired and wireless networks,” Phys. Rev. Res., 3: 043014, 2021.

[19] L. Zhou, J. Lin, Y. Jing, Z. Yuan, “Twin-field quantum key distribution without optical frequency dissemination,” Nat. Commun., 14: 928, 2023.

[20] X. Zhong, W. Wang, R. Mandil, H. K. Lo, L. Qian, “Simple multiuser twin-field quantum key distribution network,” Phys. Rev. Appl., 17: 014025, 2022.

[21] J. S. Sidhu, T. Brougham, D. McArthur, R. G. Pousa, D. K. L. Oi, “Finite key effects in satellite quantum key distribution,” npj Quantum Inf., 8: 18, 2022.

[22] J. Yin, Y. H. Li, S. K. Liao, M. Yang, Y. Cao, L. Zhang, J. G. Ren, W. Q. Cai, W. Y. Liu, S. L. Li, R. Shu, Y. M. Huang, L. Deng, L. Li, Q. Zhang, N. L. Liu, Y. A. Chen, C. Y. Lu, X. B. Wang, F. Xu, J. Y. Wang, C. Z. Peng, A. K. Ekert, J. W. Pan, “Entanglement-based secure quantum cryptography over 1,120 kilometres,” Nature, 582: 501–505, 2020.

[23] Y. Cao, Y. H. Li, K. X. Yang, Y. F. Jiang, S. L. Li, X. L. Hu, M. Abulizi, C. L. Li, W. Zhang, Q. C. Sun, W. Y. Liu, X. Jiang, S. K. Liao, J. G. Ren, H. Li, L. You, Z. Wang, J. Yin, C. Y. Lu, X. B. Wang, Q. Zhang, C. Z. Peng, J. W. Pan, “Long-distance free-space measurement-device-independent quantum key distribution,” Phys. Rev. Lett., 125: 260503, 2020.

[24] A. Kosari, Unilateral information reconciliation schemes for quantum key distribution system, 2021.

[25] G. Guarda, D. Ribezzo, T. Occhipinti, A. Zavatta, D. Bacco, “Quantum key distribution with an integrated photonic receiver,” arXiv:2310.16702, 2023.

[26] W. Li, V. Zapatero, H. Tan, K. Wei, H. Min, W. Y. Liu, X. Jiang, S. K. Liao, C. Z. Peng, M. Curty, F. Xu, J. W. Pan, “Experimental quantum key distribution secure against malicious devices,” Phys. Rev. Appl., 15: 034081, 2021.

[27] C. X. Zhu, Z. Y. Chen, Y. Li, X. Z. Wang, C. Z. Wang, Y. L. Zhu, F. T. Liang, W. Q. Cai, G. Jin, S. K. Liao, C. Z. Peng, “Experimental quantum key distribution with integrated silicon photonics and electronics,” Phys. Rev. Appl., 17: 064034, 2022.

[28] H. Tan, W. Li, L. Zhang, K. Wei, F. Xu, “Chip-based quantum key distribution against Trojan-horse attack,” Phys. Rev. Appl., 15: 064038, 2021.

[29] ITU Telecommunication Standardization Sector, Y.3800: Overview on networks supporting quantum key distribution, ITU-T Rec. Y.3800, 2020.

[30] A. Kosari et al., “Information leakage channel in the bending area of optical fiber (Information Security), 2(14): 51–58, 2021.

[31] J. A. Dolphin, T. K. Paraïso, H. Du, R. I. Woodward, D. G. Marangon, A. J. Shields, “A hybrid integrated quantum key distribution transceiver chip,” npj Quantum Inf., 9: 84, 2023.

[32] V. Zapatero et al., “Advances in device-independent quantum key distribution,” npj Quantum Inf., 9. 2023.

[33] https://www.researchgate.net/publication/392579023_MODEL_BEZOPAS-NOGO_RASPREDELENIA_KLUCEJ_SIFROVANIA_V_KVANTOVOJ_VOLOKONNO-OPTICESKOJ_SISTEME_SVAZI.

Biographies



Arash Kosari was born on 1981. He received the Ph.D. degree in Computer Engineering with a focus on network and quantum security from Belarusian State University of Informatics and Radioelectronics (BSUIR), Belarus, in 2016. He has more than 15 years of experience in the fields of information security, satellite communications security, and quantum technologies. He has been involved in national research programs on secure satellite networks, cyber-physical system security, and post-quantum cryptography. He is currently an Assistant Professor with the Iranian Research Organization for Science and Technology (IROST), where he leads research projects on quantum communication security, satellite OBC subsystem, and AI-based threat detection for critical infrastructures. He has served as a technical reviewer for national cybersecurity programs and contributes to national working groups on secure quantum communication technologies and also security in different IT fields.

- Email: a.kosari@irost.ir
- ORCID: 0009-0005-9563-7286
- Web of Science Researcher ID: NA
- Scopus Author ID : 57205077917
- Homepage: NA

Journal of Electrical and Computer Engineering Innovations
(JECEI)
Journal homepage: http://www.jecei.sru.ac.ir

Research paper

CNN-Based Placement and Multi-Objective Routing for Analog Circuits with Simulated Annealing and NSGA-III

Atousa Gholami Boorkheyli [1], *Majid Babaeinik* [1], *Hadi Dehbovid* [2,*], *Vahid Ghods* [1]

[1]*Department of Electrical Engineering, Se.C., Islamic Azad University, Semnan, Iran.*

[2]*Department of Electrical Engineering, No.C., Islamic Azad University, Noor, Iran.*

Article Info

Article History:
Received 20 July 2025
Reviewed 15 September 2025
Revised 26 October 2025
Accepted 03 November 2025

Keywords:
Analog circuit placement
Evolutionary algorithms
Convolutional neural network
NSGA-III
Simulated annealing

[*]Corresponding Author's Email Address:
hadi.dehbovid@iau.ac.ir

Abstract

Background and Objectives This research aims to optimize component placement in integrated systems using evolutionary algorithms. The primary goal is to generate a compact floorplan while satisfying design constraints, particularly in analog circuits where symmetry and proximity constraints are critical to minimizing coupling interference and enhancing performance. The study proposes using a convolutional neural network (CNN) to extract these placement constraints, with its parameters optimized via the non-dominated sorting genetic algorithm III (NSGA-III). Additionally, a hybrid routing approach combining simulated annealing (SA) and NSGA-III is introduced to improve routing efficiency through multi-objective optimization.

Methods: The placement constraints, including symmetry and proximity requirements, are extracted using a CNN, whose parameters are optimized by NSGA-III. For routing, a hybrid approach is employed where SA generates initial routing solutions, which are then refined by NSGA-III for multi-objective optimization. The proposed method is implemented on a two-stage recycling folded cascade (RFC) amplifier in 0.18µm CMOS technology with a 1.8V supply voltage. A dedicated MATLAB toolbox is developed to facilitate placement while adhering to design rules using optimization algorithms.

Results: Simulation results confirm the effectiveness of the proposed methodology, demonstrating optimized placement and routing with improved circuit performance. The combination of CNN and NSGA-III successfully generates a compact and efficient layout, while the hybrid routing approach (SA + NSGA-III) enhances the routing process. The RFC amplifier case study shows better utilization of physical resources and performance improvements, validating the method's efficiency.

Conclusion: This study demonstrates that the proposed method, integrating evolutionary algorithms and CNN, effectively optimizes placement and routing in integrated systems. The CNN-based constraint extraction and NSGA-III optimization enable compact layouts, while the hybrid routing approach improves multi-objective optimization. Simulations on the RFC amplifier confirm enhanced circuit performance and resource utilization. This method offers significant advantages over traditional approaches and is applicable to complex and industrial designs.

This work is distributed under the CC BY license (http://creativecommons.org/licenses/by/4.0/)

How to cite this paper:
A. Gholami Boorkheyli, M. Babaeinik, H. Dehbovid, V. Ghods, "CNN-Based placement and multi-objective routing for analog circuits with simulated annealing and NSGA-III," J. Electr. Comput. Eng. Innovations, 14(2): 411-424, 2026.

DOI: 10.22061/jecei.2025.12133.866

URL: https://jecei.sru.ac.ir/article_2457.html

2345- 3044/© 2026 The Authors. Published by Shahid Rajaee Teacher Training University.

Introduction

After some time, a designer becomes accustomed to the design rules specific to a given process, including the dimensions and spacing associated with it [1]-[3]. As integrated circuit manufacturing technology continuously advances and becomes more sophisticated, the designer is eventually compelled (or prefers) to design and create circuits using a more advanced process. With the transition to a more advanced manufacturing process, both the dimensions and the minimum definable features shrink. Consequently, the designer must relearn all the measurements for the new process. To avoid this, one common approach for expressing design rules and measurements in manufacturing processes is the parametric method. In this approach, a parameter called lambda (λ) is introduced as a reference, with all measurements expressed in terms of this parameter. Such design rules are referred to as lambda-based rules [4]-[8]. In such cases, once the placement is fully designed, the lambda value is used to convert all dimensions from parametric to real dimensions. As mentioned earlier, for any numerical process, it is introduced as the refinement of the construction or the minimum definable dimensions. The lambda parameter for each process is typically a value approximately half of the fineness of that process. In this way, the smallest dimension that the designer can use in their placement is 2λ.

Asymmetries in all differential circuits inevitably lead to the creation of an offset with respect to the input, which can significantly affect the performance of the circuit. These asymmetries can arise due to various factors, including the physical properties of the components, their layout, and the fabrication process. While some mismatch between components is unavoidable due to inherent limitations in manufacturing, the magnitude of this mismatch can be minimized with careful attention to the symmetry of the layout. If symmetry is not adequately considered during the placement design, it can result in large offsets that degrade the accuracy and stability of the differential circuit. These offsets can cause the circuit to deviate from its expected behavior, resulting in errors, instability, and reduced overall performance [9]-[13].

One of the key areas where asymmetry arises is in the placement and orientation of transistors. When transistors are oriented differently, they can exhibit mismatched electrical characteristics, even if they are nominally identical. This mismatch can occur due to variations in the process or the geometry of the transistors, as well as differences in how they interact with the surrounding components. As a result, the overall performance of the circuit can be compromised, especially when precise symmetry is required for optimal function.

To mitigate these challenges, it is critical to implement precise symmetry constraints throughout the placement design stage. This means ensuring that the layout of the circuit is carefully balanced and that the transistors are placed in a way that minimizes mismatches. One specific issue that arises is the mismatch between transistors with different orientations [9]-[13], which can cause variations in the electrical characteristics of the transistors, such as threshold voltage, current drive capability, and other parameters. These mismatches can have a significant impact on the overall performance of the differential circuit, particularly in high-precision applications where even small offsets can lead to substantial errors.

Therefore, careful attention to symmetry, especially in the placement of transistors and other critical components, is essential to minimize these mismatches and ensure the differential circuit performs as intended. In some cases, advanced techniques such as layout optimization or the use of symmetry-enforcing design rules can help mitigate the effects of asymmetry, resulting in more accurate and stable circuits.

Routing complexity in ICs is one of the fundamental challenges in designing these circuits. In the routing process, the goal is to optimally establish connections between the various components of the circuit, making efficient use of the limited space available to the designer. With the increasing transistor density and greater circuit complexity, the number of connections and paths that must be created also increases exponentially. This turns routing into a time-consuming and challenging process that requires high precision. Additionally, electromagnetic interference, thermal issues, and power limitations are other challenges designers face during routing [14]-[18].

To address these challenges, automated methods for routing have been developed to help designers perform this process more quickly and efficiently. One such automated routing method involves the use of artificial intelligence algorithms, such as genetic algorithms or random search algorithms, which can automatically find optimal paths. These algorithms optimize routing based on criteria such as minimum distance, energy consumption, and interference avoidance. Furthermore, methods based on neural networks are also used as tools to predict complex routing behaviors. These methods can automatically perform routing tasks and minimize the designer's manual intervention, increasing design speed and reducing human errors.

The structure of the paper is as follows. In the next Section, the existing methods in the field of IC design and circuit routing are thoroughly reviewed. A novel method for placement based on a convolutional neural

network (CNN) is introduced and explained later. Additionally, the routing algorithm based on simulated annealing (SA) and non-dominated sorting genetic algorithm III (NSGA-III) is also presented and discussed. Then, in the next Section, the simulation process conducted using various tools and the analysis of the results obtained from it will be presented. Finally, the key findings of the research presented will be summarized.

Related Works

Long and his colleagues [19] emphasized the importance of considering charge (signal) in the design process. They first extracted the current (signal) paths of an analog integrated circuit (IC) and then placed MOS transistors in each current path with a predetermined direct current path from left to right. To minimize the total area of such placement, the flow paths should have uniform height, and the physical length of the flow paths should be approximately equal. When MOS devices are placed with fixed physical dimensions (i.e., a fixed number of fingers), such that the drain-source capacitance is minimized according to the current path constraints, the placement generated by the method [19] is no longer optimal. The global placement and routing problem in analog integrated circuits cannot be considered separately, as they often lead to complex constraints. In reference [20], a technique for global and partial placement is presented. During the global placement phase, a genetic algorithm is employed. In the partial placement stage, placement is based on very fast simulated annealing, and general routing is carried out using the Steiner minimum tree approach. This method allows for the optimal solution to be found by searching within a smaller area.

Current density and flux are crucial factors in positioning and routing during analog placement synthesis [21]. Current limitations are applied to sensitive nodes with uniform current or signal paths to minimize interference effects. Current density constraints are typically used for nodes with variable wire widths to prevent issues such as IR loss and electrical migration. In this article, the limitations of both charge current and current density are simultaneously considered, allowing for routing and placement with minimal area, number of arcs, interfaces, and coupling noise. Initially, an improved B* algorithm is introduced to model both the modules and intermediate connections simultaneously. Following that, a combined placement and routing algorithm is presented, which generates a placement while considering current density and charge limitations, aiming to reduce placement area, wire length, number of arcs, connectors, and coupling noise.

In [22], a tool for generating digital circuit layouts from truth tables or Boolean equations is presented. This tool employs the maze algorithm for routing in two layers. It is compatible with integrated circuit design environments such as Mentor Graphics and Cadence. The placement process in this method is straightforward, with a distance equal to the dimensions of a transistor considered between the cells. In [23], a method for designing analog and mixed circuits is presented. In this method, the maze algorithm is used for routing. One of the advantages of this approach is that it can satisfy the matching constraint between components and intermediate connection wires during routing.

The particle swarm optimization algorithm has been used for placement in FPGA circuits [24]. In the placement stage, locations are assigned to each configurable logic block (CLB) to optimize specific objectives. These objectives may include the wire length used, routing capability between blocks, and placement time. Using the first objective function, the goal is to place logic elements close to each other to minimize the wire length. The second objective function controls the amount of wire used between blocks, while the third objective function minimizes the placement time.

Proposed Method

Evolutionary algorithms are a set of stochastic search methods inspired by natural evolutionary processes in biology. These algorithms are used to solve optimization problems that are complex or difficult to address using conventional analytical methods. Instead of searching for a single solution, these algorithms perform parallel searches across a population of possible solutions. The evolutionary process involves selection, crossover, and mutation to generate new generations of solutions, gradually converging toward the optimal solution. Evolutionary algorithms are particularly useful in problems with vast, nonlinear search spaces where analytical solutions are challenging to obtain, offering the ability to find optimal or near-optimal solutions.

In 1975, Professor John Holland proposed the Genetic Algorithm (GA), and some of his students, including David Goldberg, developed it [25]-[27] A genetic algorithm is a branch of evolutionary algorithms and is based on the structure of genes and chromosomes. The working range of the genetic algorithm is very wide, and every day, with the increasing progress of science and technology, the use of this method in optimization and solving problems has been expanded. Here, the proposed placement method based on CNN and NSGA-III will be presented. Then, the routing based on SA-NSGA-III will be presented.

CNN-based Placement

The proposed placement method is based on CNN, which automatically extracts placement constraints such

as symmetry and proximity. CNNs are highly efficient in handling complex placement tasks, where these constraints play a crucial role in ensuring the correct positioning of circuit elements. The ability of CNNs to learn patterns from large datasets allows them to model the intricate relationships between components in analog circuits, facilitating optimal placement while considering both functional and physical constraints. The automatic extraction of such constraints helps streamline the design process, improving efficiency and accuracy in the overall layout.

However, determining the optimal parameters for CNN, such as filter size and the number of filters, is a challenging task. To overcome this difficulty, the optimization of these parameters is performed using the NSGA-III. NSGA-III, a multi-objective optimization algorithm, is well-suited to explore the vast search space of CNN parameters. By leveraging NSGA-III, the method can efficiently find a balance between competing objectives, such as minimizing the area, ensuring symmetry, and maintaining the desired placement constraints. This combination of CNN and NSGA-III ensures that the placement process is not only automated but also optimized for the specific requirements of the analog circuit design.

The objective functions for the NSGA-III algorithm include inference time and accuracy. These objective functions are specifically used to optimize the performance of the circuit design model. Inference time refers to the amount of time required for the model to process inputs and generate outputs, and minimizing this time can lead to faster performance in hardware systems. On the other hand, accuracy refers to the model's ability to predict correct results, and improving accuracy can contribute to more optimal and precise circuit design. By using these objective functions in NSGA-III, an optimal balance between processing speed and model accuracy can be achieved, which is crucial for designing complex and efficient circuits. The architecture of the CNN-NSGA3 is shown in Fig. 1.

For network training, we assembled an image-based dataset of analog circuit layouts that includes fundamental building blocks such as differential pairs, current mirrors, and other common analog structures. Symmetry and proximity constraints are explicitly respected when preparing the examples so that the network would learn constraint-preserving patterns. The data are collected from diverse sources (see [28]–[32]) and, after curation, the dataset comprises approximately 450 images, chosen to cover a wide variety of circuit topologies and block geometries.

All samples use an image-based layout representation (no graph-based representations were employed in this study). Every image was preprocessed to ensure a uniform input format: images were resized to the fixed spatial dimensions required by the network's image input layer. In addition to resizing, standard image preprocessing routines (such as consistent pixel scaling and ensuring consistent channel format) were applied to guarantee numerical stability and reproducibility during training.

Training is performed using stochastic gradient descent with momentum (SGDM). Key training choices made to promote stable convergence and to reduce overfitting include a conservative initial learning rate (0.001), training for up to 100 epochs with data shuffling at each epoch, and continuous monitoring of a held-out validation set. A dedicated validation datastore is used to evaluate model performance after each epoch; these validation metrics guided model selection and the stopping decision. Training progress (loss and validation curves) is monitored throughout to ensure proper convergence and to detect any onset of overfitting.

The main steps of the proposed method are as follows:

1- The network architecture should be explicitly defined. In this case, the architecture consists of a sequence of layers, including convolution2dLayer, batchNormalizationLayer, reluLayer, maxPooling1dLayer, fullyConnectedLayer, softmaxLayer, and classificationLayer. Each of these layers plays a crucial role in the network's ability to process and classify input data effectively.

2- The convolution2dLayer is influenced by several key parameters, such as filterSize and numFilters. These parameters control the size of the filters applied to the input data and the number of filters used in the convolution operation. In the proposed method, the values for filterSize and numFilters are determined in a manner that aims to achieve a balance between maximizing the model's accuracy and minimizing its inference time, ensuring that the network performs efficiently without sacrificing performance.

3- The optimal solutions for filterSize and numFilters are determined using the NSGA-III algorithm. This multi-objective optimization technique evaluates the trade-off between multiple objectives, allowing for the identification of the best combination of parameters that leads to the most effective model configuration.

4- Both the accuracy of the Convolutional Neural Network (CNN) and the inference time are evaluated by NSGA-III as part of the optimization process. The algorithm works iteratively to refine the parameters, ensuring that the final model provides the highest accuracy while maintaining a low inference time, which is crucial for real-time applications.

5- The stopping criterion for NSGA-III is the attainment of the maximum number of allowed

iterations. If this condition is not met, the algorithm continues to generate new solutions and refine its search for optimal parameters. This iterative process ensures that the solution converges to the best possible result within the given computational constraints.

6- Once the optimal parameters for filterSize and numFilters are determined, the generated solutions are passed to the routing stage. This stage involves the final steps of network design, where the appropriate routing for the circuit or system is determined based on the optimized CNN architecture, ensuring that the model's implementation is both efficient and effective in terms of hardware requirements.

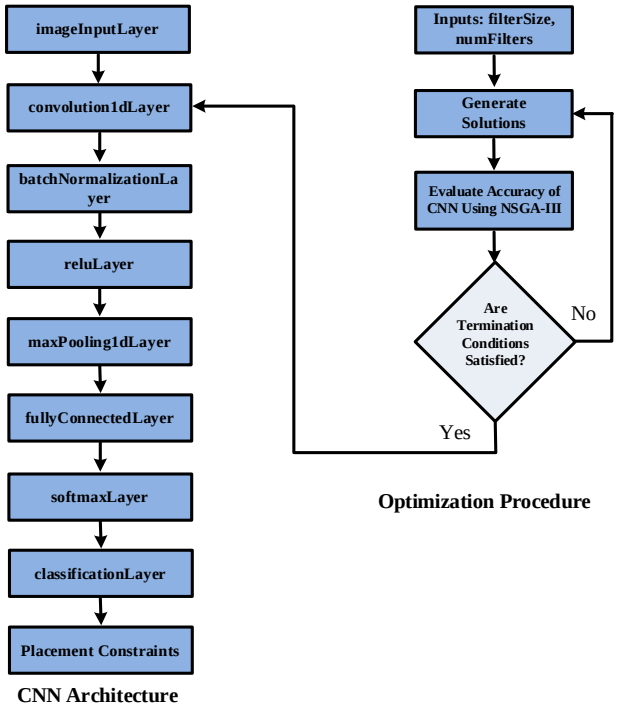


Fig. 1: CNN-based placement.

Hybrid Routing Method

In the routing stage of IC design, employing a hybrid approach that combines SA and NSGA-III can be an efficient method for finding optimal solutions. This combination leverages the strengths of both techniques to achieve high-quality routing solutions. The proposed Hybrid Approach can be described as follows:

1. Initial Solution Generation by SA
   - The SA algorithm is first used to generate an initial set of routing paths.
   - SA's capability to escape local optima ensures a diverse set of solutions, which is essential for complex routing problems.
   - The algorithm follows a cooling schedule, gradually refining solutions as it lowers the temperature, allowing it to transition from an exploratory phase to a fine-tuning phase.
   - By controlling the probability of accepting worse solutions at higher temperatures, SA prevents premature convergence and explores the solution space effectively.
2. Multi-Objective Optimization with NSGA-III
   - The best solutions obtained from SA are used as the initial population for the NSGA-III.
   - NSGA-III, a multi-objective evolutionary algorithm, improves the solutions further by optimizing multiple conflicting criteria such as power consumption, DC-gain, and Area.
   - Unlike its predecessor NSGA-II, NSGA-III employs reference point-based sorting, which enhances its performance in high-dimensional objective spaces, making it highly suitable for complex VLSI routing problems.
   - The algorithm ensures that solutions remain well-distributed along the Pareto optimal front (POF), leading to an optimal trade-off among various performance metrics.

Key advantages of this approach compared to [28] is as follows:

- Diverse Solution Generation: SA introduces diversity in initial routing paths. Global Optimality: The combination prevents premature convergence and ensures near-global optimality.
- Multi-Criteria Optimization: The approach simultaneously minimizes target specifications such as power consumption, DC-gain, and Area.
- Scalability: Suitable for large-scale VLSI designs, including Global Routing and Detailed Routing.
- Flexibility: Can be extended to optimize 3D IC routing and multi-layer interconnects.

The main steps of the proposed method, which is a hybrid approach combining SA and NSGA-III, can be described step by step as follows (Fig. 2):

- The SA algorithm is used to generate an initial set of routing solutions. This set consists of solutions that are produced based on initial criteria.
- In this step, the initial conditions (such as temperature, cooling rate, and stopping time) for the SA algorithm are configured. These parameters directly influence the quality of the initial set of solutions.
- The SA algorithm is applied iteratively on different sets of solutions to reach a set of solutions that are optimal or near-optimal.
- After the initial set of solutions is generated

by SA, this set is passed to the NSGA-III algorithm for multi-objective optimization.

- In this step, NSGA-III optimizes the solution set using various sorting and selection techniques for multi-objective optimization, considering different objectives (such as minimizing wire length, number of vias and number of bends).
- After multi-objective optimization with NSGA-III, a set of solutions is evaluated based on their performance with respect to different objectives, and the best solutions are selected to be introduced as the final solution.
- In the next stage, post-layout simulation is performed to validate the functionality and performance of the optimized design under more realistic conditions, including parasitic effects. Based on this step, the final layout is generated, which ensures that the proposed design not only satisfies theoretical optimization criteria but also meets practical implementation requirements.

Simulation Results

Automatic placement and routing of analog circuits have been performed in 0.18 µm CMOS technology with a supply voltage of 1.8 V. For this purpose, a dedicated toolbox has been developed using MATLAB software, incorporating advanced algorithms to optimize the placement and routing of analog circuits efficiently. The software used is MATLAB R2013a. System specifications used are core™ i5-4460 CPU @ 3.2 GHz with 16 GB of memory. The input images used for training the network were collected from various sources, including [28]. The parameters of the genetic algorithm in the placement stage are as follows:

- Maximum number of iterations = 20
- Population size (nPop) = 100
- Crossover percentage (pCrossover) = 0.5
- Mutation percentage (pMutation) = 0.5
- Mutation rate = 0.3

The number of parents is calculated from the following relationship:

$$2*\text{round}(\text{pCrossover}*\text{nPop}/2) \quad (1)$$

The number of mutants is calculated from the following equation:

$$\text{round}(\text{pMutation}*\text{nPop}) \quad (2)$$

Mutation step size is calculated from the following equation:

$$0.1*(\text{VarMax}-\text{VarMin}) \quad (3)$$

where VarMin and VarMin are the lower and upper limits of the variables, respectively. These parameters are chosen in such a way that there is a compromise between the speed and accuracy of the algorithm.

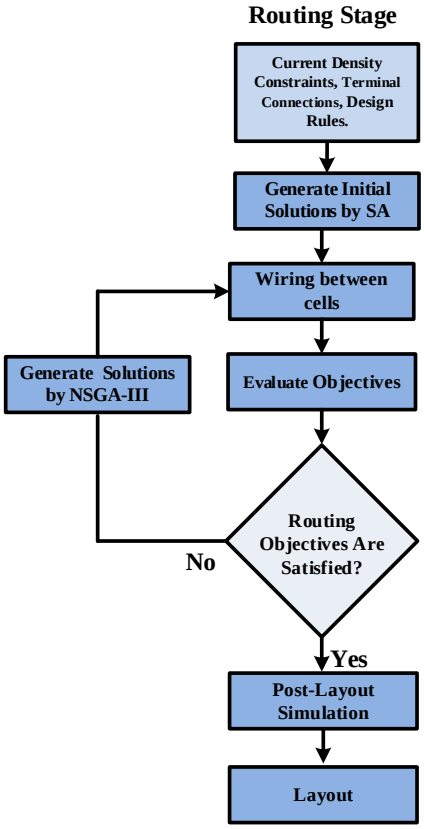


Fig. 2: Hybrid routing method.

The schematic of the two-stage recycling folded cascade (RFC) amplifier is shown in Fig. 3 [29]. By leveraging the multi-path scheme and enhancing the effective transconductance, the overall performance of the operational transconductance amplifier (OTA) is significantly improved. This approach leads to a substantial increase in the OTA's DC gain, which is crucial for achieving higher accuracy and better signal integrity in analog and mixed-signal circuits [30]-[31]. The dimensions of the amplifier are reported in Table 1. The detailed dimensions of the amplifier, including transistor sizes and passive component values are presented in Table 1.

As highlighted in the proposed method, a CNN has been employed to automatically extract symmetry and proximity constraints, which play a crucial role in optimizing the placement and routing of analog circuits. By leveraging deep learning techniques, the CNN efficiently identifies and enforces these constraints, reducing design complexity and improving overall circuit performance.

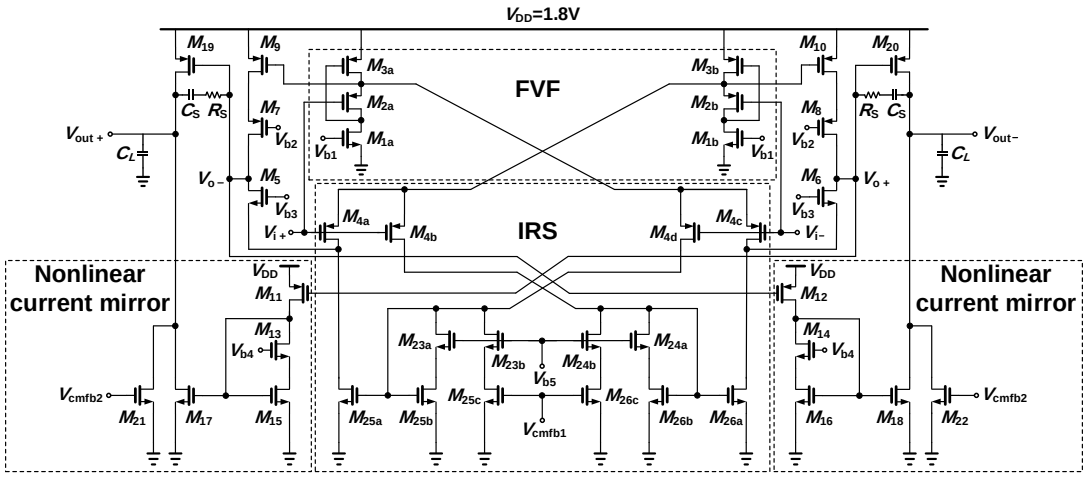


Fig. 3: Schematic of the two-stage RFC amplifier [29].

Table 1: Dimensions of transistors and passive components in the OTA design

Parameter	Value	Parameter	Value
$(W/L)_{1a,1b}$	1×5µm/0.18µm	$(W/L)_{19,20}$	2×40µm/0.36µm
$(W/L)_{2a,2b}$	1×25µm/0.18µm	$(W/L)_{21,22}$	2×10µm/0.36µm
$(W/L)_{3a,3b}$	50µm/0.18µm	$(W/L)_{23a,24a}$	2µm/0.18µm
$(W/L)_{4a,4b,4c,4d}$	1×12.5µm/0.18µm	$(W/L)_{23b,24b}$	0.8µm/0.18µm
$(W/L)_{5,6}$	1×30µm/0.18µm	$(W/L)_{25a,26a}$	6×2µm/0.18µm
$(W/L)_{7,8}$	1×60µm/0.18µm	$(W/L)_{25b,26b}$	2µm/0.18µm
$(W/L)_{9,10}$	1×60µm/0.18µm	$(W/L)_{25c,26c}$	0.8µm/0.18µm
$(W/L)_{11,12}$	2×40µm/0.36µm	C_S	30 pF
$(W/L)_{13,14,15,16}$	2×10µm/0.36µm	C_L	100 pF
$(W/L)_{17,18}$	2×10µm/0.36µm	R_S	500Ω

Furthermore, the POF curve illustrating the relationship between inference time and accuracy, is depicted in Fig. 4, providing valuable insights into the trade-offs between computational efficiency and prediction reliability.

Subsequently, the routing process has been carried out using the proposed SA-NSGA3-based approach. Figure 5 illustrates an example of routing where the SA algorithm has not been applied. As observed in this figure, the routing is not performed efficiently. For instance, an unnecessary layer transition occurs (shown by yellow), highlighting the limitations of the non-optimized approach. Unnecessary layer transitions lead to an excessive number of vias, which not only increase parasitic resistance and capacitance but also degrade the overall performance of the amplifier. This can result in signal integrity issues, higher power consumption, and reduced frequency response, ultimately affecting the circuit's efficiency.

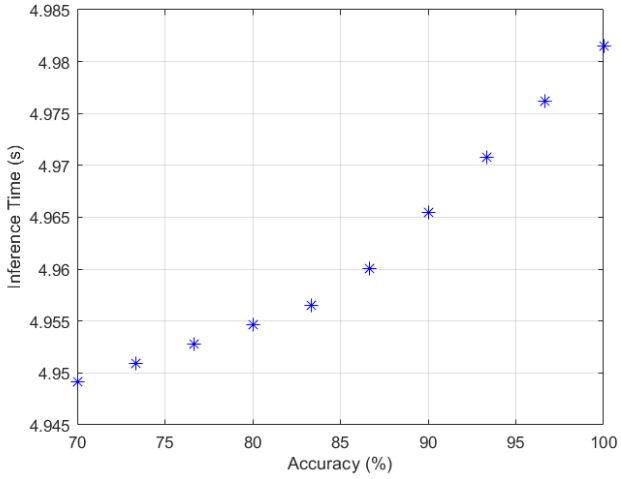


Fig. 4: POF Depicting the Trade-off Between Inference Time and Accuracy in the Proposed CNN-Based Approach.

Figure 6 illustrates an example of routing using the proposed SA-NSGA3 method. As shown in this figure, routing can be effectively performed with fewer iterations, highlighting the high efficiency of the algorithm in achieving optimal results in a reduced number of iterations. This reduction in the number of iterations translates to decreased computational time and faster routing processes without compromising the quality of the final routing. This feature is particularly advantageous in complex designs where time and computational resources are limited, and it can significantly contribute to the overall optimization of system performance.

Finally, the layout of the two-stage RFC amplifier has been fully completed using the proposed SA-NSGA2 method. The result is presented in Fig. 7. The layout area of the two-stage RFC amplifier is equal to $141\mu m \times 165\mu m$. Here, the number of layers in the routing step is equal to 2. The Bode diagrams of the two-stage RFC amplifier are presented in Fig. 8, demonstrating a remarkable DC-gain of 104.5 dB. This high DC-gain is indicative of the amplifier's excellent low-frequency performance. Additionally, the amplifier exhibits a unity-gain bandwidth (UGBW) of 40 MHz, which reflects its capability to maintain performance across a broad range of frequencies.

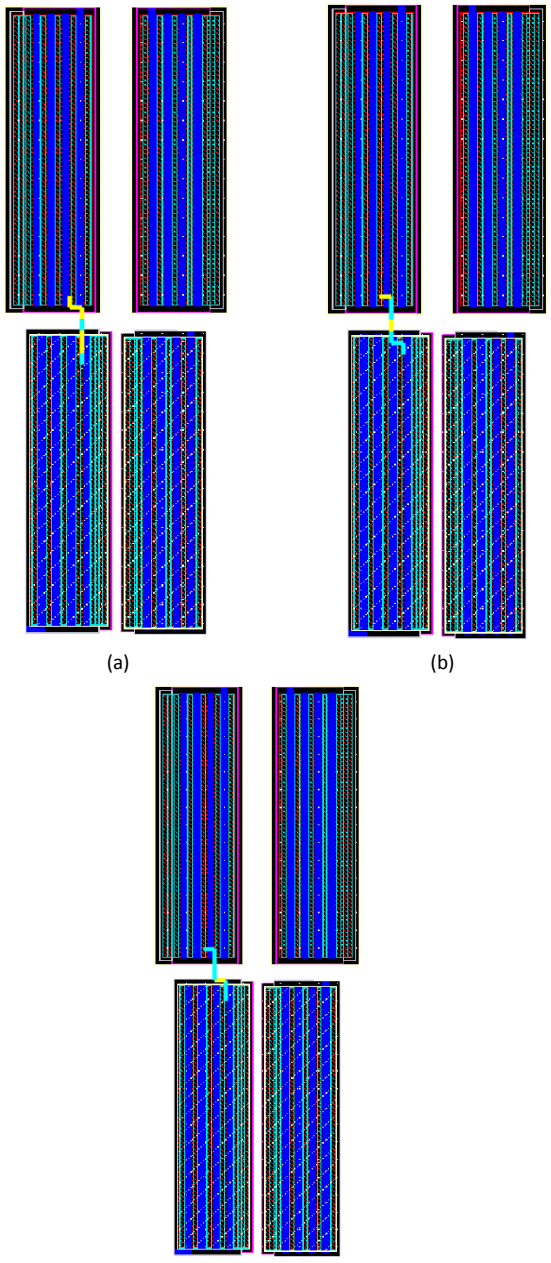


Fig. 5: Illustration of the routing progress using only NSGA-III: (a) Routing after 5 Iterations, (b) Routing after 10 iterations, (c) Placement result after 20 iterations.

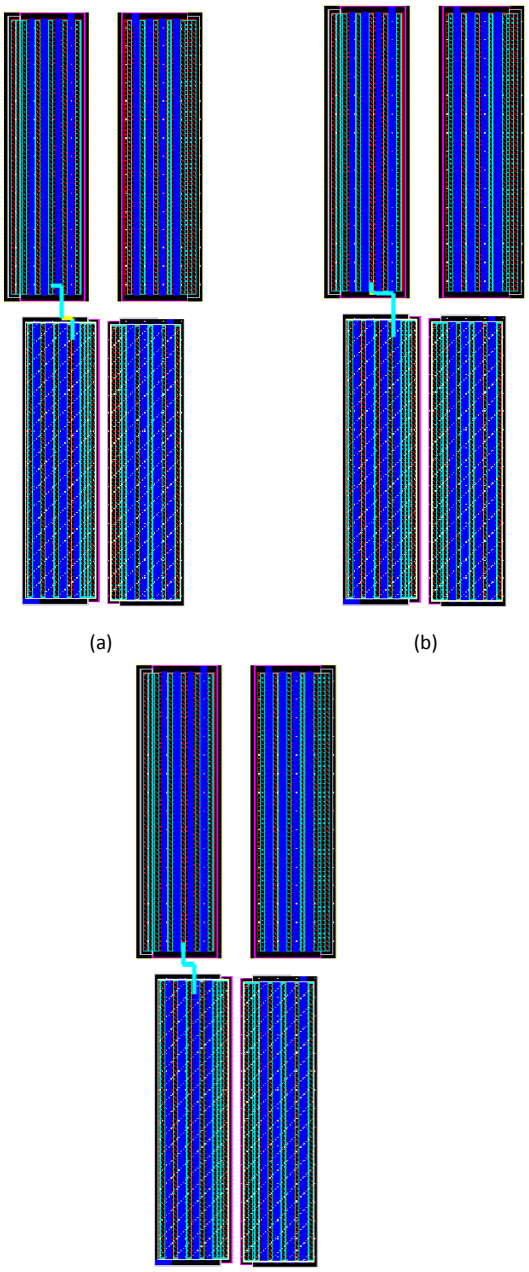


Fig. 6: Illustration of the routing progress using SA-NSGA3: (a) Routing after 5 iterations, (b) Routing after 10 iterations, (c) Placement result after 20 iterations.

The phase margin of 73° further underscores the stability of the amplifier, ensuring reliable operation without risk of oscillation. These performance metrics highlight the robustness of the two-stage RFC amplifier, making it suitable for high-precision applications requiring both high gain and stability. To provide a more comprehensive evaluation of the dynamic behavior, the step response of the circuit has been added in Fig. 9. The simulation is performed with an input amplitude of 1 V peak-to-peak and a frequency of 2 MHz. The training curves of the CNN are presented in Fig. 10. As the training progresses, the accuracy steadily increases, demonstrating that the network is effectively learning to classify the input data. Simultaneously, the loss decreases consistently across epochs, indicating that the model is minimizing the prediction errors and converging toward an optimal solution. These trends reflect the stability of the training process and suggest that the network is not overfitting, as the loss reduction corresponds with improved accuracy. Overall, the curves confirm that the CNN is successfully adapting its parameters to achieve high performance on the given task.

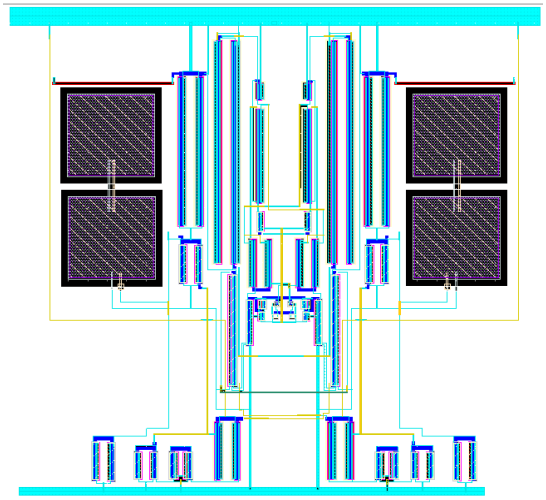


Fig. 7: The final layout after routing.

Table 2 presents a comparison of the post-layout simulation results of the proposed method with those of the existing method [32]. This Table reports the mean and variance of key specifications for the proposed comparator over four independent runs. The results indicate that the DC-gain, runtime, layout area, and area utilization are consistent, demonstrating reliable performance. Reporting both mean and variance highlights the stability and reproducibility of the proposed approach. The proposed method, leveraging the CNN-based placement technique and hybrid SA-NSGA3 routing, results in a significantly more compact layout compared to the conventional method. The CNN-based placement allows for more efficient utilization of the available space by automatically optimizing the positioning of components based on symmetry and proximity constraints. Additionally, the hybrid routing approach, combining the strengths of SA and NSGA3, ensures that the routing is not only efficient but also minimizes the use of unnecessary vias and excessive layer transitions. As a result, the method achieves better area utilization, leading to a more efficient and cost-effective design with improved performance characteristics. This compactness in layout contributes to reducing overall chip size while maintaining high functionality and signal integrity.

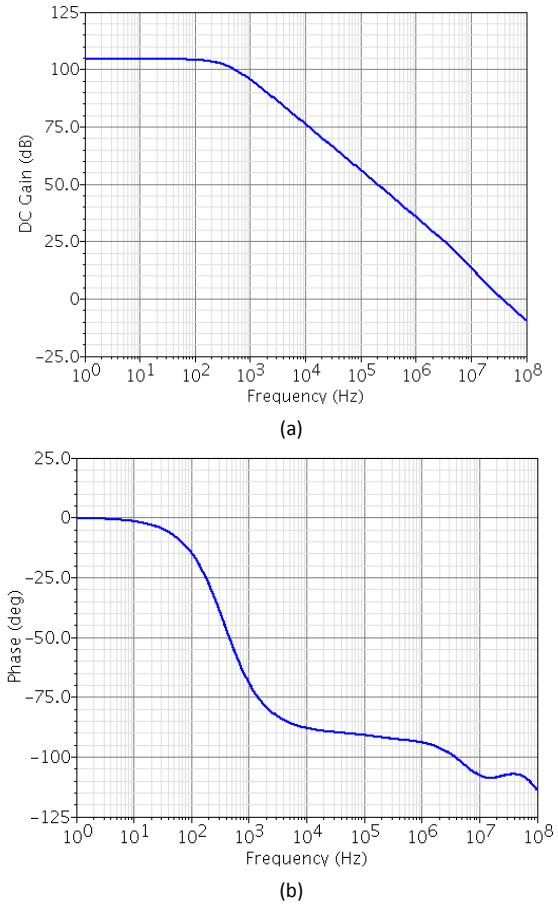


Fig. 8: Bode diagrams of the OTAs: (a) Amplitude Response, (b) Phase Response.

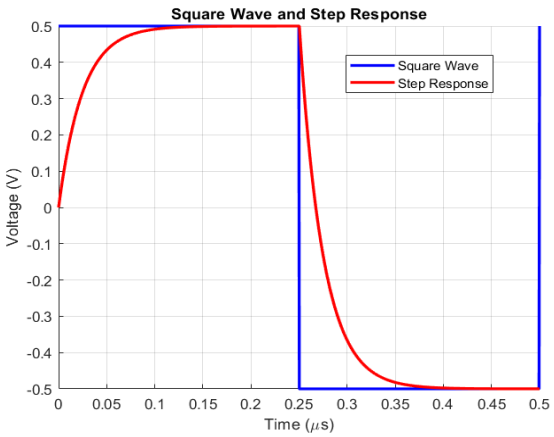


Fig. 9: Square wave and step response.

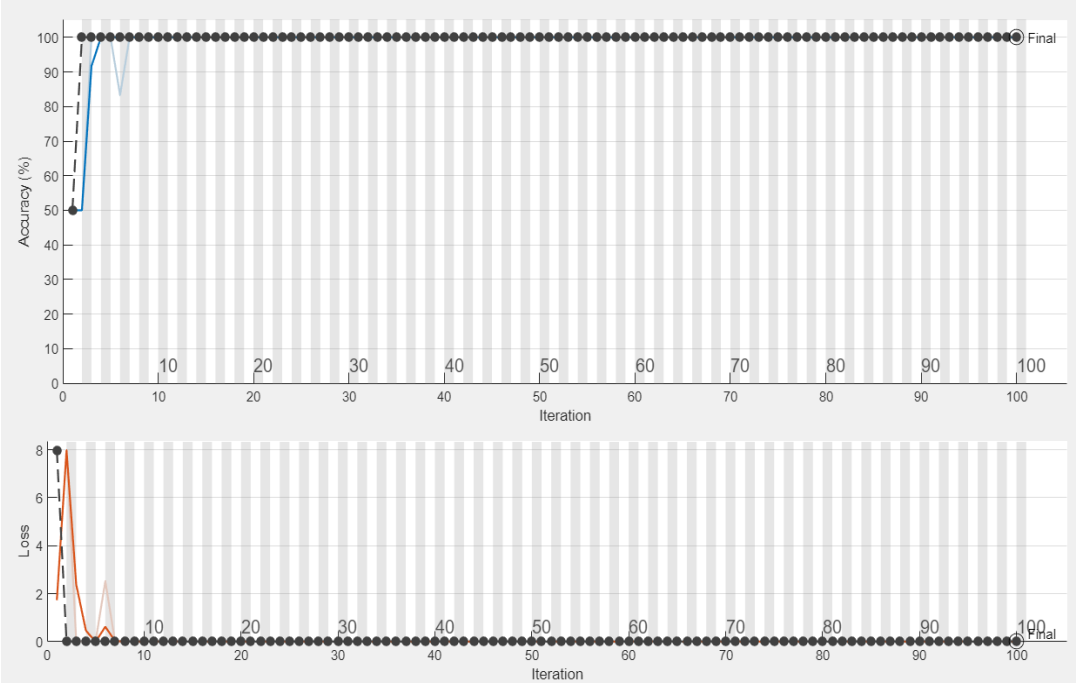


Fig. 10: The Accuracy and loss of the CNN.

Table 2: Comparison of post-layout simulation results between the proposed method and the existing method

No.	Specifications	Post-layout performance		
		This work		[32]
		Mean	Variance	
1	DC-gain (dB)	104.5	0.95	101.2
2	Total runtime (s)	1088	25.4	1134
3	Layout Area (mm^2)	0.023	0.001	0.025
4	Area Utilization (%)	84	1.8	78

To address the concern regarding generalizability, the proposed methodology was evaluated not only on the two-stage RFC amplifier but also on a dynamic comparator [33]. The circuit under test is illustrated in Fig. 11.

The clock signal is shown in Fig. 12(a), the input signal in Fig. 12(b), and the comparator output in Fig. 12(c), clearly demonstrating the correct operation of the comparator.

Furthermore, Table 3 presents a comparison between the proposed method and the reference design, indicating that the proposed approach achieves acceptable and competitive results compared to the existing method.

In the proposed method, the layout area is 5.8 µm × 10.1 µm.

The average propagation delay is 95.1 ps, and the average dynamic power is 4.83 µW, resulting in a power-delay product (PDP) of approximately 0.459 fJ. The offset voltage is 6.2 mV. It should be emphasized that these results are obtained from post-layout simulations, reflecting the effects of parasitics and realistic layout constraints.

Table 3: Post-layout evaluation of the proposed method versus existing approaches for dynamic comparator

No.	Specifications	Post-layout performance	
		This work	[33]
1	Average Delay (ps)	95.1	93.4
2	Average Dynamic Power (µW)	4.83	4.72
3	PDP (fJ)	0.46	0.44
4	Layout Area (µm2)	58.6	--

The POF for the proposed comparator (Fig. 13), considering parasitic effects, shows that a slight increase in delay results in a reduction of dynamic power,

indicating efficient utilization of current and timing. In comparison, the comparator reported in [33], without parasitic consideration, exhibits slightly lower delay and power, but parasitic effects are not accounted for. Therefore, the proposed method provides a more accurate and realistic representation of the delay–power trade-off.

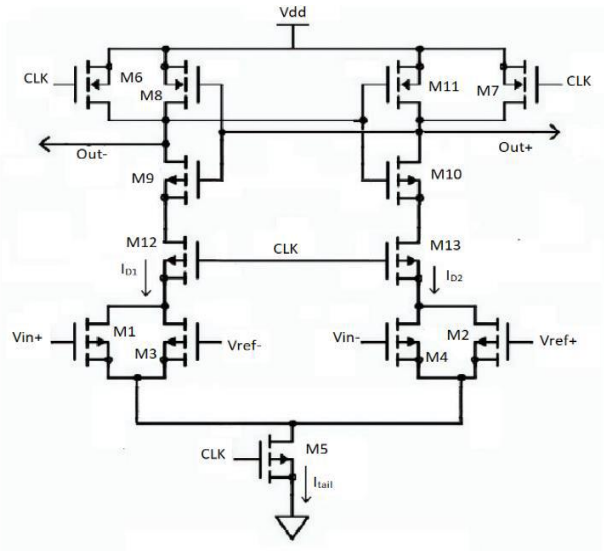
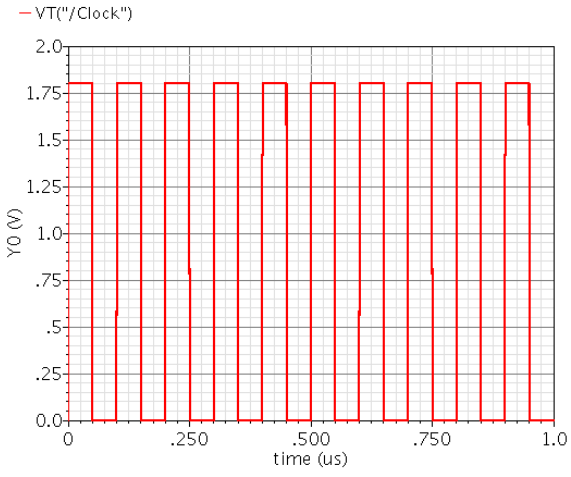


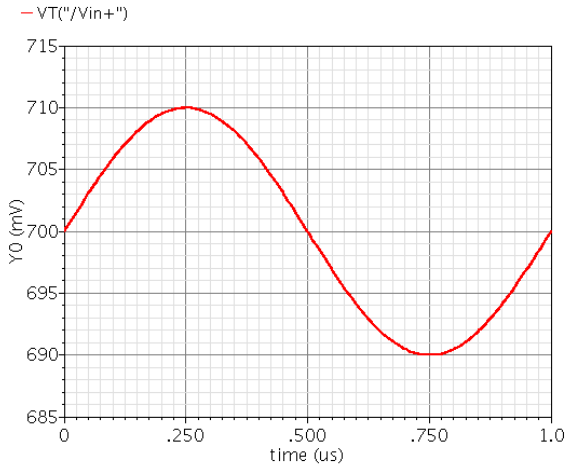
Fig. 11: Dynamic latch comparator [33].

The results of this additional study confirmed that the presented framework—consisting of constraint extraction using CNN, optimization via NSGA-III, and hybrid routing—can be effectively applied not only to amplifier designs but also to other analog circuit topologies.

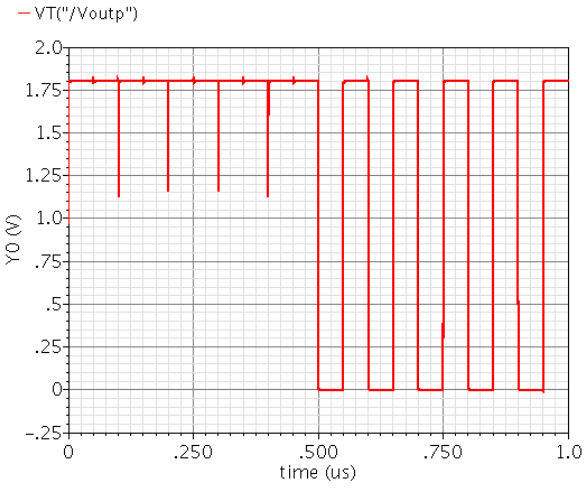
The investigations on the dynamic comparator further verified that the proposed method preserves the ability to generate compact layouts while satisfying symmetry and proximity constraints, thereby improving circuit performance. These findings demonstrate the scalability and robustness of the proposed approach in handling diverse analog and mixed-signal circuit designs.



(a)



(b)



(c)

Fig. 12: Dynamic Comparator Results: (a) Clock signal, (b) Input signal applied to the dynamic comparator, (c) Output response.

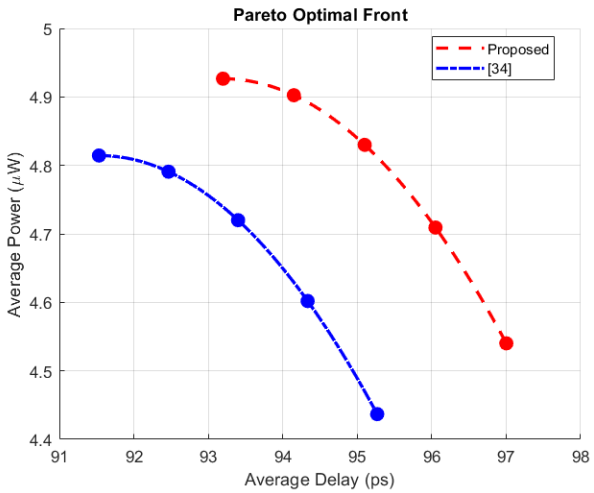


Fig. 13: POF of Dynamic Comparator.

Conclusion

This paper has demonstrated that the proposed

method for placement and routing in integrated systems, utilizing evolutionary algorithms and CNN, has effectively contributed to optimizing the performance of analog circuits.

The extraction of symmetry and proximity constraints using CNN and the optimization of its parameters via the NSGA-III algorithm have enabled the generation of a compact and efficient layout. Additionally, the hybrid routing approach, combining SA and NSGA-III, has enhanced the routing process and supported multi-objective optimization.

Simulation results for the two-stage recycling folded cascade (RFC) amplifier in 0.18µm CMOS technology with a 1.8V supply voltage have shown improvements in circuit performance and better utilization of physical resources.

This method has clearly offered advantages in design optimization and circuit performance enhancement over traditional approaches and can be applied to complex and industrial designs.

Author Contributions

Conceptualization and design, A. Gholami Boorkheyli; formal analysis, A. Gholami Boorkheyli; software, A. Gholami Boorkheyli; investigation, A. Gholami Boorkheyli, M. Babaeinik, H. Dehbovid. V. Ghods, ; writing—original draft preparation, A. Gholami Boorkheyli; writing—review and editing, M. Babaeinik, H. Dehbovid, V. Ghods. supervision, M. Babaeinik, H. Dehbovid, V. Ghods.

Acknowledgment

The authors would like to also express their gratitude to Dr. S. M. Anisheh for his useful discussions and hints.

Funding

This research received no specific grant from any funding agency in the public, commercial, or not-for-profit sectors.

Conflict of Interest

The authors declare no potential conflict of interest regarding the publication of this work. In addition, the ethical issues including plagiarism, informed consent, misconduct, data fabrication and, or falsification, double publication and, or submission, and redundancy have been completely witnessed by the authors.

Abbreviations

CNN	Convolutional Neural Network
NSGA-III	Non-Dominated Sorting Genetic Algorithm III
RFC	Recycling Folded Cascade
UGBW	Unity-Gain Bandwidth
OTA	Operational Transconductance Amplifier
SA	Simulated Annealing
IC	Integrated Circuit
CLB	Configurable Logic Block

References

[1] G. G. E. Gielen, “CAD tools for embedded analogue circuits in mixed-signal integrated systems on chip,” IEE Proc. Comput. Digital Tech., 152(3): 317–332, 2005.

[2] ITRS, (2010, Dec.), International Technology Roadmap for Semiconductors—Update.

[3] G. G. E. Gielen, R. A. Rutenbar, “Computer-aided design of analog and mixed-signal integrated circuits,” in Proc. IEEE, 88(12): 1825–1852, 2000.

[4] R. A. Rutenbar, “Analog layout synthesis: what’s missing?,” in Proc. the 19th international symposium on Physical design: 43, 2010.

[5] E. S. Ochotta, T. Mukherjee, R. A. Rutenbar, L. R. Carley, Practical Synthesis of High-Performance Analog Circuits, Springer Publishing Company, 2012.

[6] B. Razavi, Design of Analog CMOS Integrated Circuits, McGraw-Hill Education, Aug 15, 2000.

[7] D. A. Johns, K. Martin, Analog Integrated Circuit Design, John Wiley & Sons, Aug 1, 2008.

[8] A. S. Sedra, K. C. Smith, Microelectronic Circuits, Oxford University Press, 1998.

[9] F. Maloberti, Analog Design for CMOS VLSI Systems, Kluwer Academic Publishers, 2003.

[10] H. E. Graeb, Analog Layout Synthesis, Springer, New York, NY, USA, 2011.

[11] J. M. Cohn, D. J. Garrod, R. A. Rutenbar, L. R. Carley, “KOAN/ANAGRAM II: new tools for device-level analog placement and routing,” IEEE J. Solid-State Circuits, 26(3): 330–342, Mar. 1991.

[12] E. Malavasi, E. Charbon, E. Felt, A. Sangiovanni-Vincentelli, “Automation of IC layout with analog constraints,” IEEE Trans. Comput. Aided Design, 15(8): 923–942, 1996.

[13] K. Lampaert, G. Gielen, W. Sansen, “A performance-driven placement tool for analog integrated circuits,” IEEE J. Solid-State Circuits, 30(7): 773–780, 1995.

[14] P. Y. Chou, H. C. Ou, Y. W. Chang, “Heterogeneous B∗-trees for analog placement with symmetry and regularity considerations,” in Proc. 2011 IEEE/ACM International Conference on Computer-Aided Design (ICCAD): 512 – 516, 2011.

[15] H. C. C. Chien, H. C. OU, T. C. Chen, T. Y. Kuan, Y. W. Chang, “Double patterning lithography-aware analog placement,” in Proc. the 50th Annual Design Automation Conference, 4: 1-6, 2013.

[16] X. Chen, J. Hu, N. Xu, "Regularity-constrained floorplanning for multi-core processors," Integration the VLSI J., 47(1): 86–95, 2014.

[17] F. Balasa, S. C. Maruvada, K. Krishnamoorthy, "Efficient solution space exploration based on segment trees in analog placement with symmetry constraints," in Proc. IEEE/ACM International Conference on Computer-Aided Design: 497–502, 2002.

[18] F. Balasa, S. C. Maruvada, K. Krishnamoorthy, "On the exploration of the solution space in analog placement with symmetry constraints," IEEE Trans. Comput. Aided Design, 23(2): 177–191, 2004.

[19] D. Long, X. Hong, S. Dong, "Signal-path driven partition and placement for analog circuit," in Proc. the 2006 Asia and South Pacific Design Automation Confere: 694–699, 2006.

[20] L. Zhang, Y. Jiang, "Global-routing driven placement strategy in analog VLSI physical designs," in Proc. 48th Midwest Symposium on Circuits and Systems: 1239 - 1242, 2005.

[21] H. C. Ou, H. C. Chang Chien, Y. W. Chang, "Simultaneous Analog Placement and Routing with Current Flow and Current Density Considerations," in Proc. 50th ACM/EDAC/IEEE Design Automation Conference (DAC): 1-6, 2013.

[22] J. Togni, F. R. Schneider, V. P. Correia, R. P. Ribas, A. I. Reis, "Automatic generation of digital cell libraries," in IEEE Proc. 15th Symposium on Integrated Circuits and Systems Design: 265-270, 2002.

[23] M. M. Ozdal, R. F. Hentschke, "Maze routing algorithms with exact matching constraints for analog and mixed signal designs," in Proc. IEEE/ACM International Conference on Computer-Aided Design (ICCAD): 130 – 136, 2012.

[24] P. K. Rout, D. P. Acharya, "Digital circuit placement in FPGA based on efficient particle swarm optimization techniques," in Proc. International Conference on Industrial and Information Systems (ICIIS): 224 – 227, 2010.

[25] D. Li, L. Wang, Y. Shen, S. Liu, Z. Zhu, "A background timing skew calibration for time-interleaved ADCs based on frequency fitness genetic algorithm," IEEE Trans. Instrum. Meas., 73: 1–10, 2024.

[26] M. Campilho-Gomes, R. Tavares, J. Goes, "Analog flat-level circuit synthesis with genetic algorithms," IEEE Access, 12: 115532–115545, 2024.

[27] K. Deb, H. Jain, "An evolutionary many-objective optimization algorithm using reference-point-based nondominated sorting approach, part I: solving problems with box constraints," IEEE Trans. Evol. Comput., 18, (4): 577-601, 2014.

[28] A. Agarwal, J. Lang, Circuits, Electronics, MIT OpenCourseWare, Massachusetts Institute of Technology, 2007.

[29] S. M. Anisheh, H. Abbasizadeh, H. Shamsi, C. Dadkhah, K. Y. Lee, "98-dB gain class-AB OTA with 100 pF load capacitor in 180-nm digital CMOS process," IEEE Access, 7: 17772–17779, 2019.

[30] B. Babazadeh Daryan, H. Khalesi, V. Ghods, "Four-stage CMOS amplifier: Frequency compensated using differential block," IET Circuits Devices Syst., 14(6): 762–769, 2020.

[31] B. Babazadeh Daryan, H. Khalesi, V. Ghods, A. Izadbakhsh, "Multi-stage CMOS amplifier frequency compensation using a single MOSCAP," Analog Integr. Circuits Signal Process., 103: 237–246, 2020.

[32] S. M. Anisheh, H. Shamsi, "Placement and routing method for analogue layout generation using modified cuckoo optimisation algorithm," IET Circuits Devices Syst., 12(5): 532–541, 2018.

[33] K. Bandla, D. Pal, "Strong-ARM dynamic latch comparators: design and analyses on CAD platform," arXiv:2402.14519, 2024.

Biographies



Atousa Gholami Boorkheyli received her B.Sc. degree in Electrical Engineering (Electronics) from Islamic Azad University, Sari Branch, Iran, and her M.Sc. degree in Electrical Engineering (Integrated Circuits) from Hadaf Institute of Higher Education, Sari, Iran. She is currently a Ph.D. candidate in Electrical Engineering (Electronics) at Islamic Azad University, Semnan Branch, Semnan, Iran. Her research interests include the design of low-noise amplifiers (LNAs) for communication applications, analog and RF circuit design, and the application of optimization algorithms in amplifier and communication system design.

- Email: atousa.gholamiboorkheyli@iau.ac.ir
- ORCID: 0000-0003-4988-1307
- Web of Science Researcher ID: KAZ-9237-2024
- Scopus Author ID:NA
- Homepage: NA



Majid Babaeinik received his B.Sc. degree in Electronic Engineering from Semnan University, Semnan, Iran, in 1997, his M.Sc. degree in Electronic from Iran University of Science and Technology (IUST), Teheran, Iran, in 2000 and his Ph.D. degree in Electronic Engineering from Islamic Azad University, Arak Branch, Arak, Iran, in 2018. His research interests include integrated circuits design, RF integrated circuits (RFICs), VLSI systems, terahertz (THz) metamaterial, and power electronic**.**

- Email: m.babaeinik@semnaniau.ac.ir
- ORCID: 0000-0002-3822-3790
- Web of Science Researcher ID: AAN-5698-2021
- Scopus Author ID: 57194028460
- Homepage: NA



Hadi Dehbovid received his B.Sc. degree in Electrical Engineering from Sadjad University of Technology, Mashhad, Iran, in 2006, his M.Sc. degree in Electrical Engineering from Islamic Azad University, Science and Research Branch, Tehran, Iran in 2010, and his Ph.D. degree in Electronic Engineering at Islamic Azad University, Arak Branch, Arak, Iran. His research interests include the design of mixed-signal integrated circuits, particularly phase-locked loops (PLLs), as well as nonlinear circuit theory and application**.** Hadi Dehbovid is the corresponding author and can be contacted by email.

- Email: hadi.dehbovid@iau.ac.ir
- ORCID: 0000-0002-2399-4533
- Web of Science Researcher ID: AAN-8370-2021
- Scopus Author ID: 37121860300
- Homepage: NA



Vahid Ghods received his B.Sc. degree in Electronic Engineering from K. N. Toosi University of technology (KNTU), Tehran, Iran, in 2002, his M.Sc. degree in Digital Electronic from Semnan University, Semnan, Iran, and his Ph.D. degree in Electronic Engineering from Islamic Azad University, Science and research branch, Tehran, Iran, in 2012. He is currently an Associate Professor in the Faculty of Engineering at Islamic Azad University, Semnan branch, Semnan, Iran. He has authored or co-

authored more than 100 peer-reviewed journal and conference papers. His research interests include signal processing, machine vision, image and speech processing and recognition and artificial intelligence.

- Email: v.ghods@iau.ac.ir
- ORCID: 0000-0003-1140-0117
- Web of Science Researcher ID: V-8996-2019
- Scopus Author Id: 35317559400,
- Homepage: NA

Journal of Electrical and Computer Engineering Innovations
(JECEI)
Journal homepage: http://www.jecei.sru.ac.ir

Research paper

Diverse Climatic Soil Moisture Estimation Using an Enhanced GRU Model with Multi-Source Data Augmentation

Reyhaneh Bagheri , ***Fatemeh Tabib Mahmoudi*** * , ***AmirHossein Gholamian***

Department of Geomatics, Faculty of Civil Engineering, Shahid Rajaee Teacher Training University, Tehran, Iran.

Article Info

Article History:

Received 10 November 2025
Reviewed 03 January 2026
Revised 18 February 2026
Accepted 23 February 2026

Keywords:

Soil moisture prediction
Deep learning
Data augmentation
Gated Recurrent Unit
USCRN

*Corresponding Author's Email Address: *fmahmoudi@sru.ac.ir*

Abstract

Background and Objectives: Accurate soil moisture estimation is essential for various hydrological processes such as irrigation planning and environmental monitoring; however, prediction accuracy is often limited by sparse in-situ measurements and uncertainties in remote sensing products. This study aims to develop an enhanced soil moisture prediction framework by integrating a Gated Recurrent Unit (GRU) deep learning model with multi-source data augmentation techniques in order to evaluate its performance across diverse climatic conditions.

Methods: This study proposed an enhanced GRU deep learning framework supported by multi-source data augmentation to predict soil moisture across ten U.S. Climate Reference Network (USCRN) stations representing diverse climatic and ecological conditions. The proposed model integrates Conv1D layers, bidirectional GRUs, multi-head attention, and dense layers to capture short and long-term temporal dependencies while fusing multi-source inputs, including ISMN in-situ measurements, SMAP products, and GLDAS. Data augmentation strategies composed of noise injection, temporal warping, scaling, and window slicing were applied to expand the training dataset and reduce overfitting. Model performance was compared against a standard GRU using some of the evaluation metrics.

Results: Results demonstrate that the augmented GRU model consistently outperformed the standard GRU across all stations, with notable improvements in R^2 (up to 0.912), RMSE, and MAE. Performance gains were particularly evident in humid continental and Mediterranean climates, while regions with complex forested or semi-arid environments also benefited from data augmentation. These improvements confirm that data augmentation enhances the model's generalization under climatic variability and mitigates limitations associated with SMAP resolution and GLDAS uncertainty.

Conclusion: The integration of multi-source datasets with an augmented GRU architecture provides a reliable framework for soil moisture estimation across diverse environments. The proposed approach offers strong potential for applications in environmental monitoring, precision agriculture, and water resource management.

This work is distributed under the CC BY license (http://creativecommons.org/licenses/by/4.0/)

How to cite this paper:
R. Bagheri, F. Tabib Mahmoudi, A. M. Gholamian, "Diverse climatic soil moisture estimation using an enhanced GRU model with multi-source data augmentation," J. Electr. Comput. Eng. Innovations, 14(2): 425-434, 2026.

DOI: 10.22061/jecei.2026.12695.903

URL: https://jecei.sru.ac.ir/article_2540.html

2345- 3044/© 2026 The Authors. Published by Shahid Rajaee Teacher Training University.

Introduction

Soil moisture is one of the key variables in modeling hydrological processes, managing water resources, and improving irrigation efficiency [1]-[4]. Accurate estimation of soil moisture is particularly important at large agricultural scales. One of the main challenges in water resource management and agriculture is the precise estimation and prediction of root-zone soil moisture. Soil moisture not only plays a crucial role in plant growth and determining water requirements but also is highly important in modeling the hydrological cycle, drought prediction, and environmental crisis management [5]-[8].

Most traditional methods of estimating the soil moisture rely on ground stations or field measurements [9]-[11]. These methods can only give information about soil moisture near the surface in small, specific areas. Because of the changing conditions over time and space, traditional models often struggle to provide accurate soil moisture estimations. Traditional methods for measuring soil moisture on a large scale are often difficult, costly, and limited to local stations; therefore, faster and more accurate approaches such as machine learning and deep learning models using remote sensing data have received considerable attention in recent years [12], [13].

Soil moisture estimation methods based on remote sensing data can be categorized into two main types based on the utilized data: optical and microwave [14]-[16]. In using optical remote sensing, Gojiya et al. demonstrated the application of Artificial Neural Networks (ANNs) with Landsat and Sentinel-2 derived spectral indices to estimate surface soil moisture in the semi-arid region of India [15]. Singh and Gaurav, developed a fully connected feed-forward Artificial Neural Network to estimate high-resolution surface soil moisture by fusing multi-sensor satellite data from Sentinel-1, Sentinel-2 and SRTM digital elevation model [17] Lamichhane et al. summarized the progress in using machine learning algorithms with remote sensing data for soil moisture estimation. Their analysis reveals that Random Forest, Support Vector Regression, and Artificial Neural Networks are the most frequently used and best-performing algorithms in soil moisture estimation. The integration of multi-source remote sensing data, such as combining optical, thermal, and microwave sensors, consistently enhances model accuracy compared to single-source approaches [18]. In recent years, there has been more research on using high-resolution remote sensing data, both optical and microwave, especially for managing environmental issues [10], [19]-[21].

Deep learning techniques have shown great potential in identifying complex nonlinear relationships within environmental data [5]. Among deep learning methods, Recurrent Neural Networks (RNNs), particularly the Gated Recurrent Unit (GRU), demonstrate high performance in time series prediction due to their ability to preserve temporal dependencies and mitigate the vanishing gradient problem [22]. Previous studies have shown that GRU can improve the accuracy of soil moisture prediction, and when combined with other architectures such as Transformer or long short-term memory (LSTM), the model's ability to capture both short-term and long-term relationships is further enhanced [5]. For instance, Baumberger et al. used the GRU model to predict the time series of soil temperature and moisture and found that this model had higher accuracy than LSTM and ANN, while also simulating the physical relationships between environmental features and soil conditions [23]. Zheng et al. using a hybrid GRU–Transformer model, demonstrated that combining the GRU's capability to extract short-term dependencies with the Transformer's ability to identify long-term relationships enhances the prediction performance of soil moisture in the root zone [24]. Wang et al. improved the GRU by applying a parameter optimization algorithm, which increased prediction accuracy over short time intervals [22]. Moreover, Munaganuri et al. showed that GRU combined with LSTM performs well in agricultural yield prediction using environmental data and can enhance agricultural productivity and sustainability [25]. Ahmed et al. developed a sophisticated deep learning hybrid model for daily surface soil moisture prediction in the Australian Murray Darling Basin. Their approach uniquely integrated MODIS satellite data, ground-based meteorological observations, and synoptic-scale climate indices. The model combined Complete Ensemble Empirical Mode Decomposition with Adaptive Noise (CEEMDAN) for data decomposition, Convolutional Neural Networks for feature extraction, and a GRU network for forecasting [26].

In addition to GRU, other deep learning approaches have also been utilized for soil moisture estimation. Vyas et al. identified spatial–temporal relationships among different points using a dynamic graph neural network [27]. Wang et al. proposed the SMF4WSN model for soil moisture prediction in wireless sensor networks, which improved prediction accuracy [28]. Grubišić et al. demonstrated that models enhanced with the attention mechanism have a higher capability to simulate the complex dynamics of soil moisture [29]. The study conducted by Heggy et al. introduced an integrated deep learning framework designed to predict soil moisture and fill temporal gaps in observational datasets by leveraging LSTM networks and convolutional components. Their model successfully reconstructed

missing soil moisture values and demonstrated superior performance compared to traditional interpolation and statistical techniques by effectively learning nonlinear hydrological patterns from remote sensing and in-situ datasets [30]. In addition to the above studies, several foundational and state-of-the-art works provide essential context for soil moisture estimation. Recent advances emphasize hybrid deep learning models [31], and cross-climatic validation using ISMN and global datasets [32].

Moreover, emerging research highlights the importance of data augmentation in time-series deep learning [33], [34], yet its application to soil moisture prediction remains largely unexplored. These gaps further justify the need for a multi-source, augmentation-enhanced GRU framework evaluated across diverse climates, as proposed in the present study.

Table 1 summarizes key studies in soil moisture estimation to facilitate the comparison of the previous studies. However, the literature still suffers from several key limitations: (i) limited integration of multi-source datasets such as SMAP, GLDAS, and in-situ observations; (ii) minimal use of data augmentation techniques to overcome sparse ground measurements and reduce model overfitting, and (iii) insufficient cross-climatic evaluation, with most studies focusing on a single station or climatic region.

The main objective of this study is to investigate and compare the performance and accuracy of the GRU network in estimating the soil moisture under standard and improved conditions using data augmentation. As a recurrent neural network, GRU has the capability to preserve temporal dependencies and reduce the vanishing gradient problem in time series data.

In this study, efforts have been made to utilize this network appropriately and to enhance prediction accuracy over a large study area, ensuring that the obtained results have acceptable accuracy for applications in water resources management and sustainable agriculture. The use of data augmentation techniques, by increasing the diversity and volume of training data, not only reduces overfitting but also improves the model's generalization ability and enhances prediction accuracy under real-world conditions. The main contributions of this study are listed below:

- The integration of a multi-input GRU architecture combining Conv1D, bidirectional GRU, and attention mechanisms to improve temporal feature extraction.
- The systematic use of multi-source data augmentation (noise injection, temporal warping, scaling, and window slicing) applied to soil moisture prediction.
- The proposed framework is evaluated across diverse climatic and ecological conditions within the United States to assess robustness and generalizability.

Table 1: Literature analysis and comparison

Study	Datasets Used	Model / Algorithm	Climate / Study Area	Limitations / Research Gaps
Gojiya et al. (2024)	Landsat, Sentinel-2	ANN	Semi-arid (India)	Single climate, no temporal modeling, no multi-source fusion
Singh & Gaurav (2023)	Sentinel-1, Sentinel-2, SRTM	Fully connected ANN	Agricultural areas	Lacks temporal dependency modeling; no augmentation
Lamichhane et al. (2025)	Multi-source RS	RF, SVR, ANN	Multiple regions	No deep temporal models; doesn't address data scarcity
Baumberger et al. (2025)	In-situ, meteo data	GRU	Europe	No multi-source RS; single region; no augmentation
Wang et al. (2023)	Remote sensing	Improved WCM + DL	Agricultural	Limited benchmarking; no multi-source inputs
Zheng et al. (2024)	In-situ + RS	GRU–Transformer hybrid	Agricultural	No data augmentation; limited climate variability
Ahmed et al. (2021)	MODIS, SILO, climate indices	CNN + GRU + CEEMDAN	Australia	No cross-climatic testing; no augmentation; single-country dataset
Orth (2021)	In-situ + ML	ML regression models	Global	Low-res, lacks deep learning temporal modeling
Wang et al. (2024)	Soil station data	Improved GRU	Agricultural	No multi-source RS; no augmentation; limited generalization
Grubišić et al. (2024)	NDVI + RS	Attention-based DL	Multiple	No multi-input GRU; limited temporal fusion
ElSaadani et al. (2021)	RS + in-situ	LSTM–CNN	Multi-region	Limited climate diversity; no augmentation methods
Present Study (2025)	SMAP, GLDAS, ISMN (multi-source)	Conv1D + BiGRU + Attention + Data Augmentation	Ten USCRN stations representing diverse climates	Addresses gaps in generalizability, multi-source fusion, deep temporal modeling, and data scarcity

The remainder of this paper is organized as follows. Section 2 describes the study area and the utilized multi-source datasets. Section 3 presents the methodology, detailing the data augmentation strategies and the architecture of the proposed GRU-based model. Section 4 reports the experimental setup, evaluation metrics, and comparative results between the augmented GRU and the standard GRU models, followed by an in-depth discussion of model performance across different climatic conditions. Section 5 concludes the study by summarizing the key findings and highlighting potential directions for future research.

Dataset and Study Area

In this study, three complementary datasets were employed to estimate soil moisture:

- **ISMN (International Soil Moisture Network):** Ground-based in-situ observations used as reference for model evaluation.
- **SMAP (Soil Moisture Active Passive):** Satellite-based Level 3 soil moisture products with global coverage and ~36 km spatial resolution.
- **GLDAS (Global Land Data Assimilation System):** Reanalysis data providing meteorological and hydrological variables such as precipitation and temperature.

These datasets were temporally aligned and resampled to a common daily time step to ensure consistency across multiple sources. The study period spans the entire years of 2024 and 2025.

All datasets underwent standard preprocessing steps composed of merging, normalization (for preventing data leakage) and 10-days sequences creation. This study analyzes ten U.S. Climate Reference Network (USCRN) stations, chosen to represent a wide range of climatic and ecological conditions across the United States (Fig. 1). As summarized in Table 2, the stations encompass humid continental agricultural regions (e.g., Aberdeen, Lincoln, Oakley), semi-arid grasslands and high-elevation environments (e.g., John Day, Muleshoe, Los Alamos), dense forest and mountainous areas with high precipitation (e.g., Darrington), and Mediterranean coastal and Central Valley ecosystems (e.g., Bodega, Merced). This diversity provides a comprehensive basis for evaluating the robustness and generalizability of the proposed GRU-based soil moisture estimation framework under varying climatic regimes and environmental complexities [35]. These stations, situated in minimally disturbed environments, provide high-quality in-situ data, integrated with SMAP, GLDAS, and ISMN datasets to monitor soil moisture dynamics by using remote sensing data.

The diversity in climate, soil, and land cover characteristics allows the study to assess the performance of deep learning models, especially the GRU network enhanced with data augmentation, for accurate and reliable soil moisture estimation. The integration of multi-source datasets (ISMN, GLDAS, SMAP) further strengthens model robustness and generalizability across varying environmental conditions.

Table 2: Summary of USCRN stations: Coordinates, site type, climate, and study purpose

Station Name	Latitude / Longitude	Site Type	Climate Classification	Study Purpose / Relevance
Avondale-2-N, PA	40.0°N, 75.9°W	Agricultural–Forested Mixed Landscape	Humid Continental	Evaluating soil moisture dynamics in mixed agricultural–riparian settings; SMAP and ISMN validation.
Darrington-21-NNE, WA	48.5°N, 121.6°W	Mountainous Forest	Oceanic / Wet Maritime	Assessing model performance in dense forest canopies and high-precipitation regimes using GLDAS inputs.
John-Day-35-WNW, OR	44.7°N, 119.6°W	Semi-Arid Grassland	Semi-Arid Steppe	Testing robustness under dry climates and sparse vegetation; drought impact analysis.
Aberdeen-35-WNW, SD	45.7°N, 98.5°W	Agricultural Plains	Humid Continental	Soil moisture prediction in crop-dominated landscapes with strong seasonal variability.
Lincoln-11-SW, NE	40.7°N, 96.9°W	Cropland (Corn–Forage)	Humid Continental	Evaluating GLDAS-driven soil moisture variability and agricultural hydrological behavior.
Muleshoe-19-S, TX	34.0°N, 102.7°W	Dry Grassland / Wildlife Refuge	Semi-Arid	Validating model performance in arid regions with rapid moisture fluctuations.
Los-Alamos-13-W, NM	35.8°N, 106.5°W	High-Elevation Forest (Ponderosa Pine)	Semi-Arid / Highland	Examining impacts of elevation and rocky soils on moisture predictability and ISMN integration.
Bodega-6-WSW, CA	38.3°N, 123.1°W	Coastal Mediterranean	Mediterranean	Evaluating soil moisture behavior influenced by fog events and coastal vegetation.
Oakley-19-SSW, KS	39.0°N, 100.9°W	Central Plains Agriculture	Humid Continental	Investigating model sensitivity to crop-driven soil moisture variations.
Merced-23-WSW, CA	37.1°N, 120.7°W	Central Valley Wetlands/Agriculture	Mediterranean	Assessing soil moisture dynamics in wetland–agricultural mosaics; testing model generalization.

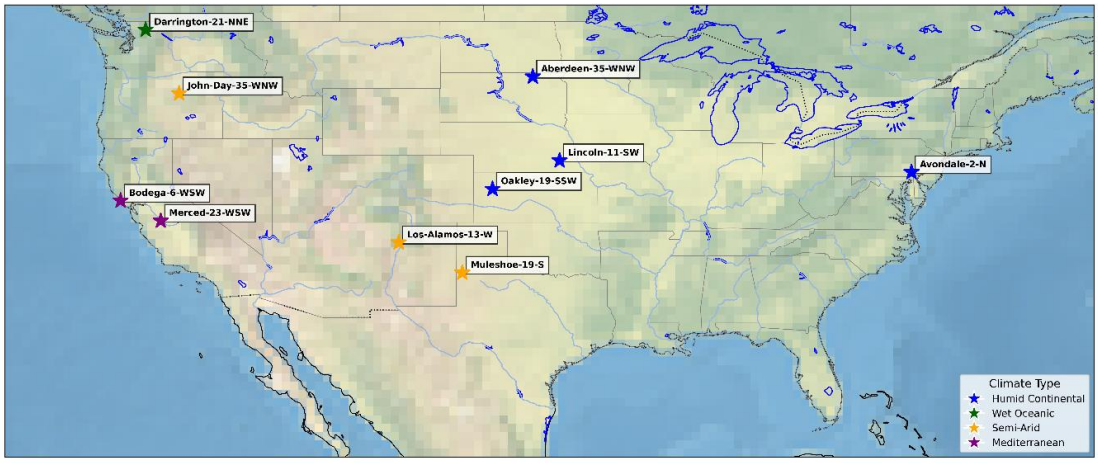


Fig. 1: Distribution map of the utilized USCRN stations by climate types.

Method

Figure 2 illustrates the key steps of the proposed methodology in using multi-input data sets in GRU model together with data augmentation for soil moisture estimation.

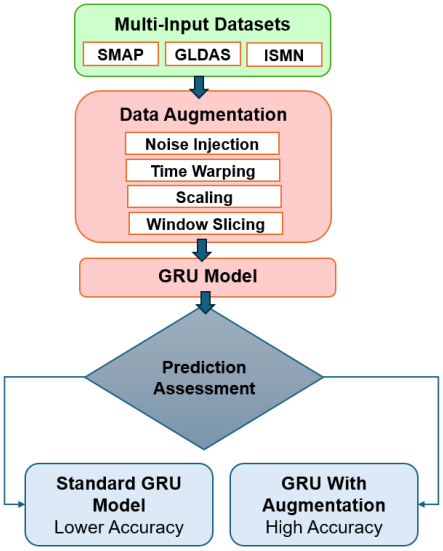


Fig. 2: Structure of the proposed soil estimation method.

A. Data Augmentation

To enhance the robustness of the model and mitigate overfitting caused by the limited availability of soil moisture data, several data augmentation techniques were employed:

- **Noise Injection:** Small Gaussian noise was added to the input sequences to improve generalization and reduce sensor uncertainty.
- **Time Warping:** Random distortions in the temporal dimension were introduced to simulate natural variability in soil moisture dynamics.
- **Window Slicing:** Fixed-length subsequences were extracted from the longer time series to increase the number of training samples.
- **Scaling:** Random scale factors were applied to input features to simulate differences in soil and vegetation responses.

These augmentation methods increased the effective size of the training data, allowed the model to generalize better, and improved resilience against seasonal and meteorological fluctuations.

B. Model Architecture

A GRU network was implemented due to its efficiency in capturing temporal dependencies in time-series data while requiring fewer parameters than an LSTM. As illustrated in Fig. 3, the architecture consists of the following parts:

- **Input Layer:** Multi-source input data consists of SMAP, GLDAS, and ISMN.
- **GRU Layers:** One or more stacked GRU layers to capture long-term and short-term dependencies in soil moisture variability.
- **Dense Layer:** Fully connected layer to map hidden states into soil moisture prediction.
- **Activation Function:** The ReLU function was applied to enhance non-linearity and prevent vanishing gradients.

The proposed model is a multi-input GRU-based neural network designed to fuse temporal patterns from trainable parameters, balancing complexities and computational efficiency. Three parallel input layers process the normalized 10-day time-series data from each source independently. A 1D convolutional layer (Conv1D) with 64 filters, a kernel size of 3, and ReLU activation function extracts local temporal patterns, such as short-term fluctuations in soil moisture. A Bidirectional GRU layer with 128 units capturing both forward and backward temporal dependencies to model

long and short-term dynamics of ISMN, SMAP, and GLDAS data, leveraging convolutional, recurrent, and attention mechanisms for accurate soil moisture prediction. Layer normalization stabilizes training by normalizing feature scales, while dropout (rate=0.3) prevents overfitting by randomly deactivating units, crucial for the limited dataset size.

The processed sequences from all sources are concatenated, resulting in a combined sequence integrating multi-source information. ReLU activation throughout the architecture ensures non-linearity, mitigating vanishing gradient issues, while the linear output aligns with the continuous nature of soil moisture values.

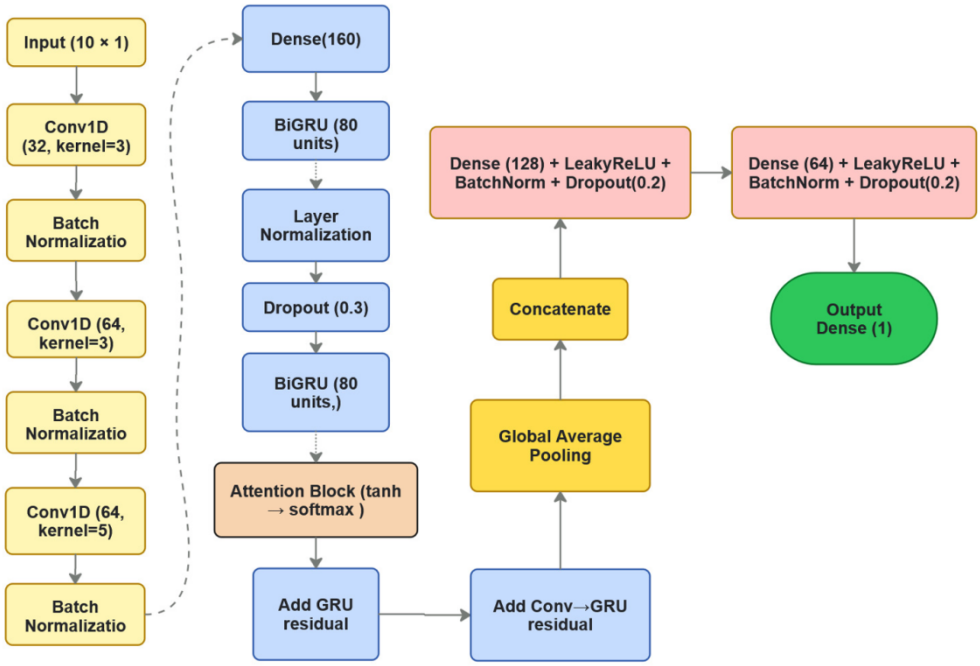


Fig. 3: Proposed enhanced GRU model architecture.

Results and Discussion

A. Implementation Details

The model was implemented and trained on an NVIDIA Tesla T4 GPU using the Adam optimizer with an initial learning rate of 1×10^{-4}. Training was performed for 50 epochs with a batch size of 4, using MSE as the loss function and MAE as the performance metric. To enhance reliability and ensure stable convergence, three strategies were applied: *ReduceLROnPlateau* dynamically decreased the learning rate (factor = 0.2, patience = 7, minimum LR = 1×10^{-6}) when no improvement in validation MAE was observed; *ModelCheckpoint* preserved the best-performing model based on validation MAE; and *EarlyStopping* halted training upon stagnation of performance, restoring the optimal weights. These procedures improved long-term training stability, mitigated overfitting, and ensured statistically robust results. The training loss decreased from 1.53 at initialization to 0.026 in the final epochs, confirming consistent convergence and the effectiveness of the adopted optimization and stabilization mechanisms.

To prevent overfitting, early stopping was applied by monitoring the validation loss, stopping training if it did not improve for 10 consecutive epochs, and restoring the best weights. In addition, model checkpointing was used to save the best-performing model during training based on the lowest validation loss, ensuring that the optimal model was preserved.

B. Evaluation Metrics

Model performance was assessed on the validation set using the following metrics to evaluate both errors and correlations:

- **Pearson Correlation Coefficient (R):** Assesses the linear correlation between predicted and observed values.

$$R = \frac{\sum_{i=1}^{n}(y_i-\bar{y})(\hat{y}_i-\bar{\hat{y}})}{\sqrt{\sum_{i=1}^{n}(y_i-\bar{y})^2\sum_{i=1}^{n}(\hat{y}_i-\bar{\hat{y}})^2}} \quad (1)$$

- **Root Mean Squared Error (RMSE):** Represents the square root of MSE for better interpretability.

$$\text{RMSE} == \sqrt{\frac{1}{n}\sum_{i=1}^{n}(y_i - \hat{y_i})} \quad (2)$$

- **Mean Absolute Error (MAE):** defined as the average sum of the absolute differences between the actual value and the predicted value.

$$MAE = \frac{1}{N}\sum_{i=1}^{N}\left|y_i - \hat{y_i}\right| \quad (3)$$

- **Coefficient of Determination (R^2):** with a threshold of ≥0.75 for station acceptance.

$$R^2 = \frac{1-\sum(y_i-\hat{y_i})^2}{\sum(y_i-\bar{y})^2} \quad (4)$$

C. Results and Comparison

To investigate the impact of data augmentation on the performance of the GRU model for soil moisture estimation, the results of ten stations (with and without data augmentation) are presented in Tables 3 and 4.

Table 3: Assessment of GRU model with data augmentation

Stations	Loss	MAE	R	R^2	RMSE
Merced-23-WSW	0.002	0.029	0.991	0.9746	0.046
Bodega-6-WSW	0.004	0.034	0.983	0.9601	0.066
Darrington-21-NNE	0.004	0.044	0.987	0.9637	0.065
Los-Alamos-13-W	0.003	0.033	0.984	0.9658	0.054
Aberdeen-35-WNW	0.003	0.034	0.984	0.9621	0.052
Avondale-2-N	0.011	0.048	0.949	0.8889	0.103
Oakley-19-SSW	0.007	0.038	0.950	0.8981	0.083
Muleshoe-19-S	0.007	0.024	0.925	0.8501	0.087
Lincoln-11-SW	0.018	0.075	0.882	0.7535	0.136
John-Day-35-WNW	0.015	0.082	0.892	0.8225	0.157

The results obtained from the 10 stations show that the GRU model with data augmentation exhibits a substantial improvement over the standard GRU model across all error and correlation metrics. The average indicators reveal that the Loss value decreased from 0.0257 to 0.0075, which corresponds to a 70.8% improvement. The MAE and RMSE metrics also decreased by 66.4% and 47.9%, respectively; this reduction indicates higher model accuracy and a significant decrease in the gap between the observed and predicted values. Moreover, the correlation indices also improved; the R^2 increased from 0.6838 to 0.9039, representing a 32.2% improvement and indicating that the model explains more than 90% of the variance in the actual data. The 5.9% increase in the Pearson coefficient further reflects the strengthening of the linear relationship between the model output and the measured data.

Table 4: Assessment of standard GRU without data augmentation

Stations	Loss	MAE	R	R^2	RMSE
Merced-23-WSW	0.0159	0.0891	0.9267	0.7968	0.1324
Bodega-6-WSW	0.0245	0.1217	0.9421	0.7531	0.1521
Darrington-21-NNE	0.0298	0.1517	0.9135	0.5214	0.1816
Los-Alamos-13-W	0.0229	0.1367	0.8012	0.6401	0.1682
Aberdeen-35-WNW	0.0241	0.1279	0.8698	0.6376	0.1672
Avondale-2-N	0.0531	0.1645	0.8745	0.5136	0.2612
Oakley-19-SSW	0.0274	0.1218	0.8739	0.6841	0.1391
Muleshoe-19-S	0.0209	0.1901	0.9378	0.8653	0.1578
Lincoln-11-SW	0.0239	0.1189	0.9351	0.7528	0.1572
John-Day-35-WNW	0.0148	0.0872	0.9196	0.6728	0.1116

These findings confirm that employing data augmentation enhances the model's ability to learn complex temporal patterns in soil moisture and increases its robustness against data scarcity and temporal non-uniformity. At the station level, interesting patterns are also observed. The greatest improvement is recorded in humid stations such as Darrington-21-NNE, where RMSE decreased by more than 100%. This is likely due to the high variability in moisture conditions in these regions and the positive effect of augmentation in simulating rainfall events and soil saturation. In contrast, stations in arid regions such as Muleshoe-19-S and Avondale exhibit smaller improvements, and in some metrics even slight declines. This can be attributed to the limited diversity in the raw data, the uniformity of soil moisture conditions, and the model's lower sensitivity to augmentation in low-precipitation areas.

Therefore, from a hydrological perspective, the results indicate that the GRU with data augmentation model performs very well in humid climates. In these regions, the mean R^2 is 0.9586, and the mean RMSE is 0.0651, demonstrating the model's strong capability to reproduce pronounced soil-moisture fluctuations, heavy

rainfall events, and rapid water infiltration. Under such conditions, data augmentation has helped the model better represent extreme hydrological events such as floods or prolonged saturation periods.

In semi-arid climates, the model's performance remains good but more variable. A mean R^2 of 0.9041 and the RMSE of 0.0917 show that the model has been able to reconstruct the seasonal patterns of soil moisture with reasonable accuracy. However, in stations such as John-Day, which experience prolonged drought periods, a higher RMSE (0.157) is observed. In such situations, augmentation alone is insufficient to simulate moisture events, and it is recommended to incorporate auxiliary data such as precipitation, vegetation cover, or soil temperature.

In arid climates, the model performs weaker than in other groups. A mean R^2 of 0.8889 and a mean RMSE close to 0.1032 indicate that due to the low variability in soil moisture and the occurrence of sudden rainfall events, the available data are not sufficient to capture the actual system behavior. In stations such as Avondale, augmentation has had a moderate effect, and the model is more suitable for applications such as drought monitoring or forecasting long-term trends rather than for precise modeling of short-term fluctuations.

Conclusion

This study developed an enhanced GRU-based deep learning framework for soil moisture estimation by integrating multi-source datasets, including SMAP, GLDAS, and ISMN, with a data augmentation strategy. The results obtained from ten USCRN stations demonstrated that the augmented GRU model consistently outperformed the standard GRU across all climatic regions examined. Higher values of R^2, along with reductions in RMSE, MAE, and loss, confirm that combining GRUs model and data augmentation significantly improves the model's robustness and predictive capability. In addition, the results showed that the model performed best in humid continental and Mediterranean climates, and even under more complex conditions such as humid forests or semi-arid climates, it provided higher accuracy than GRU. These findings highlight the importance of incorporating data augmentation when dealing with limited or unevenly distributed soil moisture observations, as it enhances generalization and mitigates the limitations imposed by coarse satellite resolution and environmental variability.

The contributions of this work lie in introducing a multi-input hybrid GRU architecture capable of capturing both short- and long-term temporal dependencies, applying a comprehensive augmentation pipeline to enrich training sequences, and evaluating model performance across diverse climatic and ecological conditions.

While the proposed framework offers substantial improvements in soil moisture prediction, several limitations should be acknowledged. The performance of the model remains partly constrained by the coarse spatial resolution of SMAP products and the inherent uncertainties present in GLDAS inputs, climatic bias, and specific environmental conditions such as local soil properties and vegetation cover which may introduce biases in regions with heterogeneous land cover or complex terrain. The model also relies heavily on the quality and representativeness of the available in-situ measurements, and its sensitivity to augmentation parameters may affect performance in climates characterized by abrupt moisture fluctuations. Additionally, the current architecture focuses on temporal modeling without explicitly incorporating spatial dependencies, which may limit its applicability for regional or continental-scale soil moisture mapping.

These limitations highlight the need for future research to integrate higher-resolution remote sensing products, extending the model to more diverse or extreme climatic regions, and exploring hybrid architectures that integrate transformers, graph neural networks, or physics-informed constraints. Additionally, expanding the range of augmentation techniques and assessing the transferability of the model across regions and continents may further strengthen its applicability for large-scale soil moisture monitoring.

Funding

This work was supported by Shahid Rajaee Teacher Training University under grant number 1404 / 394107.

Author Contributions

Reyhaneh Bagheri has the following rolls in this manuscript: Data capturing, Formal analysis; Methodology implementation. Fatemeh Tabib Mahmoudi as the corresponding author has the following responsibilities: Supervision; Results' validation; Visualization; Writing - original draft; Writing – review. AmirHossein Gholamian as the third author was responsible for system initialization and data analysis.

Acknowledgment

Authors acknowledge the dept. of Geomatics Engineering of Shahid Rajaee Teacher Training University for their supports.

Conflict of Interest

The authors declare no potential conflict of interest regarding the publication of this work. In addition, the ethical issues including plagiarism, informed consent, misconduct, data fabrication and, or falsification, double publication and, or submission, and redundancy have been completely witnessed by the authors.

Abbreviations

GRU	Gated Recurrent Unit
LSTM	Long Short-Term Memory
USCRN	U.S. Climate Reference Network
ISMN	International Soil Moisture Network
SMAP	Soil Moisture Active Passive
GLDAS	Global Land Data Assimilation System
MAE	Mean Absolute Error

References

[1] Q. Han, Y. Zeng, L. Zhang, C. Wang, E. Prikaziuk, Z. Niu, "Global long term daily 1 km surface soil moisture dataset with physics informed machine learning," Sci. Data, 10(1): 101, 2023.

[2] N. Madhukumar, E. Wang, Y. Everingham, W. Xiang, "Hybrid transformer network for soil moisture estimation in precision irrigation," IEEE Access, 12: 48898-48909, 2024.

[3] G. Patrizi, A. Bartolini, L. Ciani, V. Gallo, P. Sommella, M. Carratù, "A virtual soil moisture sensor for smart farming using deep learning," IEEE Trans. Instrum. Meas., 71: 1-11, 2022.

[4] G. Nijaguna, D. Manjunath, M. Abouhawwash, S. S. Askar, D. K. Basha, J. Sengupta, "Deep learning-based improved WCM technique for soil moisture retrieval with satellite images," Remote Sens., 15(8): 2005, 2023.

[5] Y. Wang, L. Shi, Y. Hu, X. Hu, W. Song, L. Wang, "A comprehensive study of deep learning for soil moisture prediction," Hydrol. Earth Syst. Scie. Discuss., 28: 917-943, 2023.

[6] J. Y. Seo, S. I. Lee, "Probabilistic evaluation of drought propagation using satellite data and deep learning model: from precipitation to soil moisture and groundwater," IEEE J. Sel. Top. Appl. Earth Obs. Remote Sens., 16: 6048-6061, 2023.

[7] R. Orth, "Global soil moisture data derived through machine learning trained with in-situ measurements," Sci. Data, 8(1): 1-14, 2021.

[8] L. Li, Y. Dai, W. Shangguan, Z. Wei, N. Wei, Q. Li, "Causality-structured deep learning for soil moisture predictions," J. Hydrometeorol., 23(8): 1315-1331, 2022.

[9] T. Schmidt, M. Schrön, Z. Li, T. Francke, S. Zacharias, A. Hildebrandt, "Comprehensive quality assessment of satellite-and model-based soil moisture products against the COSMOS network in Germany," Remote Sens. Environ., 301: 113930, 2024.

[10] J. Peng, A. Loew, "Recent advances in soil moisture estimation from remote sensing," Water, 9(7): 530, 2017.

[11] S. Kanzari, S. B. Mariem, S. Ghannem, S. Mouelhi, H. Ghazouani, B. B. Nouna, "A framework based on mechanistic modelling and machine learning for soil moisture estimation," Discover Soil, 2(1): 56, 2025.

[12] A. Fluhrer, T. Jagdhuber, C. Montzka, M. Schumacher, H. Alemohammad, A. Tabatabaeenejad, "Soil moisture profile estimation by combining P-band SAR polarimetry with hydrological and multi-layer scattering models," Remote Sens. Environ., 305: 114067, 2024.

[13] Q. Liu, Z. Wu, N. Cui, X. Jin, S. Zhu, S. Jiang, "Estimation of soil moisture using multi-source remote sensing and machine learning algorithms in farming land of Northern China," Remote Sens., 15(17): 4214, 2023.

[14] D. Lakra, S. Pipil, P. K. Srivastava, S. K. Singh, M. Gupta, R. Prasad, "Soil moisture retrieval over agricultural region through machine learning and sentinel 1 observations," Front. Remote Sens., 5: 1513620, 2025.

[15] K. Gojiya, B. Karangiya, S. Chavda, S. Gaadhe, D. Gojiya, H. Rank, "Soil moisture modelling using remote sensing and artificial neural networks: A Study of devbhumi dwarka region, gujarat, india," Int. J. Environ. Clim. Change, 14(1): 1-13, 2024.

[16] H. Karim Tabbahfar, F. Tabib Mahmoudi, "Optimum spectral indices for water bodies recognition based on genetic algorithm and sentinel-2 satellite images," J. Electr. Comput. Eng. Innovations, 12(1): 217-226, 2024.

[17] A. Singh, K. Gaurav, "Deep learning and data fusion to estimate surface soil moisture from multi-sensor satellite images," Sci, Rep., 13(1): 2251, 2023.

[18] M. Lamichhane, S. Mehan, K. R. Mankin, "Soil moisture prediction using remote sensing and machine learning algorithms: A review on progress, challenges, and opportunities," Remote Sens., 17(14): 2397, 2025.

[19] K. Mao, H. Wang, J. Shi, E. Heggy, S. Wu, S. M. Bateni, "A general paradigm for retrieving soil moisture and surface temperature from passive microwave remote sensing data based on artificial intelligence," Remote sens., 15(7): 1793, 2023.

[20] J. Zeng, J. Peng, W. Zhao, C. Ma, H. Ma, "Microwave remote sensing of soil moisture," Remote Sens., 15(7): 4243, 2023.

[21] Y. Wang, J. Zhao, Z. Guo, H. Yang, N. Li, "Soil moisture inversion based on data augmentation method using multi-source remote sensing data," Remote Sens., 15(7): 1899, 2023.

[22] G. Wang, C. Wei, L. Yan, J. Li, "Soil moisture prediction model based on improved GRU recurrent neural network," Strategic Plann. Energy Environ., 43(2): 381-400, 2024.

[23] M. Baumberger, B. Haas, W. Tewes, B. Risse, N. Meyer, H. Meyer, "Gated recurrent units for modelling time series of soil temperature and moisture: An assessment of performance and process reflectivity," Environ Model. Software, 183: 106245, 2025.

[24] W. Zheng, K. Zheng, L. Gao, L. Zhangzhong, R. Lan, L. Xu, "GRU–transformer: a novel hybrid model for predicting soil moisture content in root zones," Agronomy, 14(3): 432, 2024.

[25] M. R. K. Munaganuri, P. Gonnuri, R. Badiguntla, A. Kasukurthi, S. L. Sarma, S. M. Basha, "Deep learning-based crop prediction using LSTM and GRU for sustainable agriculture," Int. J. Environ. Sci., 11(11s): 538-545, 2025.

[26] M. Ahmed, R. C. Deo, N. Raj, A. Ghahramani, Q. Feng, Z. Yin, "Deep learning forecasts of soil moisture: convolutional neural network and gated recurrent unit models coupled with satellite-derived MODIS, observations and synoptic-scale climate index data," Remote Sen., 13(4): 554, 2021.

[27] A. Vyas, S. Bandyopadhyay, "Dynamic structure learning through graph neural network for forecasting soil moisture in precision agriculture," arXiv preprint arXiv:2012.03506, 2020.

[28] W. Wang, Y. Wei, L. Hao, Z. Wei, T. Zhao, "Soil moisture forecasting in wireless sensor networks via spatiotemporal graph convolutional networks," Vadose Zone J., 24(1): e70000, 2025.

[29] V. Grubišić, D. Vasić, H. Ljubić, R. Rozić, T. Volarić, "Soil moisture prediction with attention-enhanced models: a deep learning approach," Authorea Preprints, 2024.

[30] M. ElSaadani, E. Habib, A. M. Abdelhameed, M. Bayoumi, "Assessment of a spatiotemporal deep learning approach for soil moisture prediction and filling the gaps in between soil moisture observations," Front. Artif. Intell., 4: 636234, 2021.

[31] J. Liu, F. Rahmani, K. Lawson, C. Shen, "A multiscale deep learning model for soil moisture integrating satellite and in situ data," Geophys. Res. Lett., 49(7): e2021GL096847, 2022.

[32] W. Dorigo, I. Himmelbauer, D. Aberer, L. Schremmer, I. Petrakovic, L. Zappa, "The International Soil Moisture Network:

serving Earth system science for over a decade," Hydrol. Earth Syst. Sci. Discuss., 25(11): 5749-5804, 2021.

[33] B. K. Iwana, S. Uchida, "An empirical survey of data augmentation for time series classification with neural networks," Plosone, 16(7): p. e0254841, 2021.

[34] Q. Wen, L. Sun, F. Yang, X. Song, J. Gao, X. Wang, "Time series data augmentation for deep learning: A survey," arXiv preprint arXiv:2002.12478, 2020.

[35] H. J. Diamond, T. R. Karl, M. A. Palecki, C. B. Baker, J. E. Bell, R. D. Leeper, "US Climate Reference Network after one decade of operations: Status and assessment," Bull. Am. Meteorol. Soc., 94(4): 485-498, 2013.

Biographies



Reyhaneh Bagheri received her Bachelor's degree in Surveying and mapping engineering from Isfahan University, Isfahan, Iran, in 2022. Since 2023, she is the M.Sc. student of remote sensing in Geomatics department of the faculty of Civil Engineering, Shahid Rajaee Teacher Training University.

- Email: reyhaneh.bagheri888@sru.ac.ir
- ORCID: 0009-0004-2267-9816
- Web of Science Researcher ID: NA
- Scopus Author ID: NA
- Homepage: NA



Fatemeh Tabib Mahmoudi received her Bachelor's degree in Geomatics engineering (Surveying and mapping) from Khajeh Nasiredin Toosi University, Tehran, Iran, in 2004. She received his M.Sc. and PhD degrees in Photogrammetry from Tehran University, Tehran, Iran, in 2009 and 2014, respectively. Since 2016, she has been working as an assistant professor in the Geomatics department of the faculty of Civil Engineering, Shahid Rajaee Teacher Training University. She has some publications in the field of remote sensing data analysis, pattern recognition and data fusion.

- Email: fmahmoudi@sru.ac.ir
- ORCID: 0000-0002-8414-8189
- Web of Science Researcher ID: V-8360-2019
- Scopus Author ID: 36669646900
- Homepage: NA



AmirHossein Gholamian received his Bachelor's degree in Surveying and mapping engineering from National Geographic Organization University, Tehran, Iran, in 2021. Since 2022, he is the M.Sc. student of remote sensing in Geomatics department of the faculty of Civil Engineering, Shahid Rajaee Teacher Training University.

- Email: amirhoseinghloamian@sru.ac.ir
- ORCID: 0009-0004-8287-5480
- Web of Science Researcher ID: NA
- Scopus Author ID: NA
- Homepage: NA

Journal of Electrical and Computer Engineering Innovations
(JECEI)
Journal homepage: http://www.jecei.sru.ac.ir

Research paper

Artificial Intelligence-Based YOLOv3 using DarkNet-53 Deep Convolutional Neural Network Model Architecture for Automatic Vehicle Inventory System Design with a Dynamic Relational Database System and Google Cloud Storage

Vincent Andrew Akpan [1,*], ***David Ayo-oluwa Adegoke*** [2], ***Ebunoluwa Temiloluwa Adejayan*** [3], ***Kehinde Adesola Adepoju*** [4]

[1]*Department of Biomedical Engineering, The Federal University of Technology, Akure, Ondo State, Nigeria.*
[2]*Biomedical Engineering Department, Redeemer's Health Village, Redemption City of God, Mowe, Ogun State, Nigeria.*
[3]*Biomedical Engineering Unit, Federal Medical Centre, MMA Road, Owo, Ondo State, Nigeria.*
[4]*Department of Biomedical Engineering, Lagos State University Teaching Hospital (LUTH), Yaba, Lagos State, Nigeria.*

Article Info

Article History:
Received 22 December 2025
Reviewed 06 January 2026
Revised 24 January 2026
Accepted 29 January 2026

Keywords:
Automatic Vehicle Inventory System (AVIS)
Computer vision
Real-time object detection
Relational Database System (RDBS)
You Only Look Once version 3 (YOLO v3)

*Corresponding Author's Email Address: *vaakpan@futa.edu.ng*

Abstract

Background and Objectives: The manual method of writing down vehicle plate numbers (VPNs), vehicle types, date, and time-stamps at the point of entry into and/or exit from the premises of organizations as well as the exit and/or entry time are not only time-consuming and stressful but are also prone to errors, delays, inconsistency and possible loss of hand-written data due to possible environmental hazards which makes this archaic method unreliable especially for security reasons. This study presents an artificial intelligence-based YOLOv3 using DarkNet-53 deep convolutional neural network (CNN) model architecture for the development of an automatic vehicle inventory system (AVIS) with a PostgreSQL-based dynamic relational database system (RDBS) for captured data storage and retrieval in real-time using Google cloud storage/retrieval.
Methods: The AVIS with dynamic RDBS employs power-over-Ethernet (PoE) switch, PoE IP-based camera, Airtel router/Wi-Fi module and YOLOv3 using DarkNet-53 algorithm to capture and process VPNs from streaming video of moving vehicles. The processed results are stored in a properly designed dynamic RDBS over Google cloud storage system. The dynamic RDBS automatically creates and inserts all relevant vehicle information for security surveillance and tracking purposes. Several standard quantitative and qualitative metrics have been used to evaluate the performances of the YOLOv3 using DarkNet-53 architecture against YOLOv8 using CSPDarkNet-53 and YOLOv3 using SqueezeNet model architectures for comparison purposes.
Results: Quantitatively, the YOLOv3 using DarkNet-53 and YOLOv8 using CSPDarkNet-53 achieved virtually equal performance metrics except for the excessive long execution time of 4.5839 hours used by YOLOv8 with CSPDarkNet-53compared to the 2.9713 minutes used by the YOLOv3 with DarkNet-53. The YOLOv3 with SqueezeNet used only 1.9901 minutes with relatively lower performance metric values. Qualitatively, successful and accurate LPNs detection and recognition with dynamic RDBS update to the cloud within 3 seconds for 25 random vehicles entering and/or exiting the premises of a car dealer company for a period of three days between 10:00am and 2:00pm daily has been achieved with YOLOv3 using DarkNet-53 model architecture.
Conclusion: The proposed low-cost AVIS based on YOLOv3 using DarkNet-53 model architecture with a PostgreSQL dynamic RDBS and Google cloud storage have been successfully designed, implemented and validated with successful results for LPN detection and recognition. The proposed techniques offer promising potentials for timely and accurate data collection to optimize vehicle inventory management, control and operations for security surveillance design.

This work is distributed under the CC BY license (http://creativecommons.org/licenses/by/4.0/)

How to cite this paper:
V. A. Akpan, D. A. Adegoke, E. T. Adejayan, K. A. Adepoju, "Artificial intelligence-based YOLOv3 using darknet-53 deep convolutional neural network model architecture for automatic vehicle inventory system design with a dynamic relational database system and google cloud storage," J. Electr. Comput. Eng. Innovations, 14(2): 435-472, 2026.
DOI: 10.22061/jecei.2026.12552.889
URL: https://jecei.sru.ac.ir/article_12554.html

2345- 3044/© 2026 The Authors. Published by Shahid Rajaee Teacher Training University.

Introduction

This work arose from the observations of manual vehicle inventory methods among some higher institutions and organizations in Nigeria. The recognition of Nigerian vehicle number plates has been reported in [1]. The observed methods involved manual inventory of license plate numbers (LPNs), vehicle types and the time of entry into organizations as well as the exit time. Apart from being time-consuming and stressful, the current methods of manual vehicle inventory management are prone to errors, delays, and inconsistency, which make it unreliable especially for security reasons. Furthermore, Atieh et al. noted that automated data entry can improve inventory management processes and reduce costs associated with manual data entry [2]. To address these challenges, there is a need to develop an automatic vehicle inventory system (AVIS) with dynamic database that can automatically and accurately identify and recognize vehicles with LPNs, captures the LPNs, time-stamps (entry and exit times) and update the inventory database in real-time.

The need for efficient and automatic vehicle inventory management system has become more critical in recent times. The development of an automatic vehicle inventory system (AVIS) with a dynamic relational database system (RDBS) is a crucial area of research for vehicle security and in the transportation industry [3]–[5]. To the best of the authors knowledge and unfortunately, this is the first work of this nature and subsequently there are no literature on the current study. It is important to note that the current work differs from vehicle inventory management systems and automotive inventory management software reported in [6]–[9]. The aim of this research is to develop an artificial intelligent-based convolutional neural network for automatic vehicle inventory system that automatically captures and stores the license plate numbers of vehicles together with the time-stamps (entry and exit times) using IP cameras and a deep learning algorithm. The captured data will then be stored and updated automatically in a dynamic relational database system, which can be accessed in real-time by authorized personnel.

The use of deep learning algorithms is critical in computer vision based systems for recognition, feature extraction, detection, segmentation, localization with endless applications. The most popular and recent computer vision deep learning algorithms are the You Only Look Once (YOLO) family of algorithms [10]–[14]. Among the YOLO family of algorithms, YOLO v3 have been proven to be effective in recognizing and identifying objects in real-time with several advantages compared to other versions of the YOLO algorithm and found suitable for this work [15]–[19]. In a study by Rajput et al. [20], the YOLOv3 algorithm was used to develop an automatic vehicle identification and classification model for a toll management system. The study reported high accuracy in identifying and classifying vehicles based on their license plate numbers. Similarly, Li in [21] used the RES-YOLO model to develop a deep learning automatic vehicle recognition algorithm, which reported a faster processing time and better accuracy compared to other existing models. These findings highlight the importance of deep learning algorithms in feature extraction and pattern recognition and a potential tool for the development of the proposed automatic vehicle inventory systems.

The integration of different technologies such as an IP camera, a router, and RJ-45 cables is vital for the enhancement of the proposed automatic vehicle inventory system development. In 2021, Wu et al. [22] developed an automatic vehicle detection system that uses roadside LiDAR data to detect vehicles under rainy and snowy conditions. The study reported that the system was effective in detecting vehicles in adverse weather conditions. The use of PoE IP-based camera, routers, RJ-45 cables combined with the YOLOv3 algorithm will enhance automatic capture of license plate numbers and vehicle classification, which can be transmitted to a remote location for storage and analysis. Furthermore, the integration of Google Cloud Storage and PostgreSQL as the storage system will enable real-time access to captured data and provide a secure and reliable database infrastructure. An integrated positioning system is another critical component that could enhance the development of the proposed automatic vehicle inventory system. Cui et al. developed an integrated positioning system for unmanned automatic vehicles in coal mines which improved efficiency and safety of real-time vehicle positioning [23].

One of the key areas of research in the possible development of an automatic vehicle inventory system is the use of computer vision and machine learning techniques for vehicle detection and classification. Researchers in the field have proposed various methods for detecting and classifying vehicles, including the use of convolutional neural networks (CNNs) and ensemble classifiers [9], [26]–[27]. Zhang et al. [28] show that real-time monitoring in inventory systems significantly reduces lead times and improves performance.

The automatic vehicle inventory system also includes dynamic relational database management. This feature allows businesses to store and analyze inventory data effectively and automatically. The use of PostgreSQL as storage and/or retrieval system ensures that businesses can easily access and analyze data, making informed decisions about inventory management and control [29]. Dynamic relational database systems are essential in the

development of an automatic vehicle inventory system like the one proposed in this research. One of the benefits of using a dynamic relational database is the ability to handle large amounts of data from various sources accurately and efficiently. The proposed system, which captures vehicle license plate numbers using YOLOv3 with Darknet-53 and an Internet Protocol (IP)-based camera, generates a large amount of data that must be accurately and efficiently stored and managed. A dynamic relational database system such as the PostgreSQL makes it possible to store and retrieve data in a structured and comprehensive manner, ensuring that the system can handle the volume of data generated effectively [30], [31]. By analyzing the data in real-time, the system can quickly identify any anomalies or discrepancies, allowing for immediate action to be taken [24], [25], [32]. Additionally, the use of a cloud-based database system like PostgreSQL, coupled with Google cloud storage, provides the flexibility to access data from anywhere, as well as providing an added layer of security and redundancy [33]–[35].

Related Work

Due to the originality of this work, there is no existing literature on this specific topic. However, the various components of the proposed AVIS with dynamic RDBS are carefully considered.

Automatic Vehicle Location (AVL) data are fundamental for measuring service reliability, which is essential for improving transportation system efficiency. According to Ma et al. [36], AVL data can improve the accuracy of arrival time prediction, delay detection, and route optimization. AVL can also facilitate the collection of vehicle information such as speed, direction, and location, which are useful for developing an automatic vehicle inventory system. Nieto et al. [8] further emphasized the importance of automatic vehicle detection in parking management systems.

The license plate recognition (LPR) system can detect and identify vehicles based on their number plates. The use of structured elements has been found to improve the accuracy of automatic vehicle license plate recognition [37]. According to Prabhakar et al. [38] , automatic vehicle license plate recognition technology can identify stolen vehicles, enforce traffic regulations, and prevent traffic congestion. The authors suggested a method of detecting and recognizing number plates by optimizing the image captured using image processing techniques.

Aerial remote sensing has been used to extract vehicle trajectories from traffic videos. Azevedo et al. [39] proposed a methodology for automatic vehicle trajectory extraction using aerial remote sensing. Similarly, Wu and Xu [40] proposed an automatic procedure for vehicle tracking using a roadside LiDAR sensor. The authors used a LiDAR sensor to scan the road surface and detect vehicles based on their reflection patterns. The proposed system achieved high accuracy in detecting and tracking vehicles.

Sulaiman [41] proposed a development of an automatic vehicle plate detection system that uses image processing techniques to detect and recognize vehicle number plates. The authors demonstrated that their proposed system is capable of detecting and recognizing license plate numbers (LPNs) with high accuracy using machine learning algorithms.

Furthermore, existing studies have explored various automatic vehicle identification systems that use license-plate recognition technology. For instance, Duan et al. [42] developed an automatic vehicle license-plate recognition system that uses a deep learning algorithm to improve the accuracy of the identification process. Similarly, Kim and Song [43] proposed a vehicle recognition system that uses radar and vision sensors to identify vehicles and enable automatic emergency braking. These studies show that automatic vehicle identification systems are effective in enhancing efficiency and accuracy in vehicle management.

Wang and Chan [44] argue that a robust replenishment and production control policy can optimize inventory control in a single-stage production/inventory system with inventory inaccuracy. This implies that the proposed AVIS with dynamic RDBS must incorporate an effective inventory control mechanism to ensure that captured vehicle plate numbers are properly stored in the database system.

The automatic vehicle inventory system must have an efficient queuing-inventory system to handle the captured plate numbers effectively. Krishnamoorthy and folks [45] argue that analyzing a multi-server queuing-inventory system can help optimize the system's performance. The automatic vehicle inventory system must have a multi-server queuing-inventory system to store and retrieve captured plate numbers efficiently.

A. Automatic Vehicle Inventory Technologies

Automatic vehicle inventory systems are becoming increasingly popular as they provide a more efficient way of managing vehicle identification and tracking. One of the most commonly used types of automatic vehicle inventory systems is the Automatic Number Plate Recognition system [46]. Automatic number plate recognition (ANPR) systems use image processing techniques and optical character recognition (OCR) algorithms to capture and recognize license plate numbers from Closed Circuit Television (CCTV) footage or images captured by cameras [47]. The system extracts the vehicle's plate number and stores it in a database, enabling easy identification and tracking of vehicles.

Another type of automatic vehicle inventory system is the Automatic Vehicle Identification (AVI) system. This system uses radio-frequency identification (RFID) technology to identify and track vehicles as they pass through a checkpoint. RFID tags, which are attached to the vehicle, are read by the AVI system when the vehicle passes through the checkpoint, and the data is stored in a centralized database [30], [48]–[50]. The data collected by the AVI system can be used for various purposes, including traffic management, toll collection, and security.

A third type of automatic vehicle inventory system is the Automatic Vehicle Location (AVL) system. AVL systems use Global Positioning System (GPS) technology to track the location of vehicles in real-time. The system collects data such as the vehicle's location, speed, and direction of travel, and stores it in a centralized database [51]. The data collected by the AVL system can be used for various purposes, including route planning, fleet management, and emergency response.

B. Challenges of Automatic Vehicle Inventory Technologies

Firstly, there is a need for constant Internet connectivity to access the system, as it requires the use of an IP camera and router. This poses a challenge in areas with poor internet connectivity and may lead to a delay in updating the database. Furthermore, the use of an IP camera makes the system susceptible to intrusion by external parties, which could compromise the confidentiality of the stored data [52].

Secondly, the system's accuracy is dependent on the quality of the image captured by the camera. The use of YOLO v3, an object detection algorithm that identifies and localizes vehicles' LPNs, is highly dependent on the clarity of the image. Poor image quality due to weather conditions or other factors may lead to inaccurate readings of the plate number [39], [53], [54]. This could result in discrepancies in the inventory records, leading to incorrect information about the vehicles in the system.

Thirdly, the storage capacity of the database limits the number of vehicles that can be captured and recorded. While using Google Cloud Storage and PostgreSQL provides sufficient capacity for storing vehicle information, the cost of maintaining and upgrading the system may be high. [55]–[57]. Additionally, the system requires a reliable power supply to function properly, and any power outage could lead to data loss or system malfunction.

Lastly, the capturing of vehicle LPNs could be time-consuming, leading to a delay in the system's operation. This is especially true in areas with high traffic, where several vehicles may need to be captured within a short time frame. The delay in capturing and processing the information could lead to the vehicle's exit before the system records it, resulting in inaccurate inventory records.

C. Overview of the Proposed Research

The proposed AVIS with dynamic RDBS will adopt the well-proven YOLOv3 using DarkNet-53 model architecture which will be implemented using Python with its associated software on core-*i*7 laptop (HP Pavilion Plus Laptop 16-ab0010nr, Windows 11 Home, 16", Intel® Core™ *i*7-14700HX operating at 5.5 GHz, 16GB RAM, 512GB SSD, WQXGA, Natural silver). The hardware shall include power-over-Ethernet (PoE) switch (LS108GP 8-Port 2 Gigabit Desktop Switch with 8-Port PoE and 2 PoE Uplink ports), SONY Vision CCTV IP-based SV-5MP-POE-4B PAL 120m/2.8mm Camera, Airtel 4G Smartbox Router/Wi-Fi module, RJ-45 cables and power supply unit (which includes two Li-Po batteries, 12-V battery charger, 220-V to 12-V converter for the router, and a boost converter and power switching interface). Additional software will include Google Cloud Storage and PostgreSQL to support data storage and retrieval. The use of YOLOv3 algorithm will provide high accuracy vehicle plate number recognition and capturing while the Google Cloud Storage and PostgreSQL will provide a scalable and secure storage solution [24], [25], [58]. Overall, the proposed AVIS with dynamic RDBS based on YOLOv3 using Darknet-53 will be compared with YOLOv8 using CSPDarknet-53 and YOLOv3 using SqueezeNet, and performance comparisons will be made, with conclusions drawn based on several quantitative and qualitative benchmarking criteria and performance metrics.

Materials

The materials required for the development and implementation of the proposed automated AVIS with dynamic RDBS inventory system involve both hardware and software. The hardware include one core-*i*7 laptop (HP Pavilion Plus Laptop 16-ab0010nr, Windows 11 Home, 16", Intel® Core™ *i*7-14700HX operating at 5.5 GHz, 16GB RAM, 512GB SSD, WQXGA, Natural silver); a SONY Vision CCTV IP-based SV-5MP-POE-4B PAL 120m/2.8mm camera; Airtel 4G Smartbox Router/Wi-Fi with Fast Internet connectivity; LS108GP 8-Port 2 Gigabit Desktop Switch with 8-Port PoE and 2 PoE Uplink ports; RJ-45 cables; and a power supply unit (which includes two Li-Po batteries, 12-V battery charger, 220-V to 12-V converter for the router, and a boost converter and power switching interface). The software components include Python 3.13, Matplotlib 3.10.3, OpenCV 4.12, TensorFlow 2.16, Keras 3.10, PostgreSQL database (dynamic relational database system) and Google cloud storage as well as YOLOv3 using DarkNet-53, YOLOv8 using CSPDarkNet-53 and YOLOv3 using SqueezeNet model architectural algorithms.

Methodology

A. Block Diagram of the AVIS

The development of the proposed automatic vehicle inventory system (AVIS) with dynamic relational database system (RDBS) is a revolutionary approach in the efficient, accurate and accountable management strategy for vehicle inventory into an organization. The block diagram of the AVIS with dynamic RDBS is shown in Fig. 1. It illustrates the connections among the IP camera, Ethernet switch, router, and Wi-Fi module, and shows how these components interact within the AVIS network.

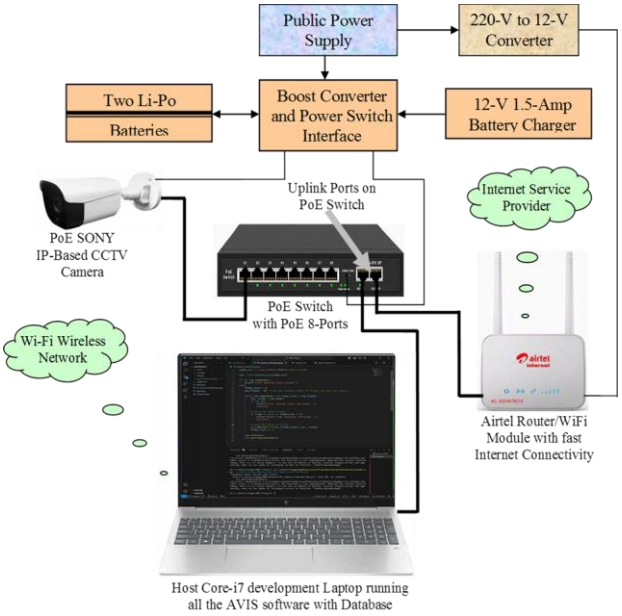


Fig. 1: Block diagram of the automatic vehicle inventory system (AVIS).

The IP camera is connected to the switch via an Ethernet cable, and the switch is in turn connected to the router via Ethernet. The Wi-Fi module, typically integrated into the router, provides wireless connectivity to other devices on the network. The main components are as follows:

1). IP Camera: This is the surveillance camera that captures video footage and transmits it over the network. It connects to the network using an Ethernet cable.

2). Ethernet Switch: The switch acts as a central connection point for multiple IP cameras (or other wired devices). It receives data from the cameras and forwards it to the router.

3). Router: The router manages the network traffic, connecting the local network (LAN) to the internet (WAN). It receives data from the switch and routes it to the appropriate destination, including the internet or other devices on the local network.

4). Wi-Fi Module: The Wi-Fi module, often integrated into the router, enables wireless communication. The Wi-Fi module allows the host laptops to connect to the network wirelessly.

In the simplest case, the connection is as follows: *(i) Camera to Switch:* An Ethernet cable connects the IP camera to one of the ports on the Ethernet switch; *(ii) Switch to Router:* Another Ethernet cable connects the switch to a port on the router; *(iii) Router to Internet:* The router is connected to the internet service provider's modem, usually through a dedicated WAN port; and *(iv) Wi-Fi Module:* The Wi-Fi module is part of the router or a separate access point, providing wireless connectivity to devices within its range.

However, a high-level performance architecture with the power-over-Ethernet (PoE) switch with 2 uplink ports connected to the router and the host laptop which also acts as a network video recorder (NVR) is used in this work. This approach is advantageous as it allows the host laptop to be connected directly to the PoE switch and fetch data directly from the camera without having data bog down the router.

B. The YOLOv3: Description and Algorithm

B. 1. Architectural Description

The You Only Look Once, Version 3 (YOLOv3) is a real-time one-shot object detection algorithm that uses a dynamic pre-trained DarkNet-53 deep convolutional neural network (CNN) model architecture as the backbone to identify, segment and locate objects and patterns within images and videos [13], [17], [59], [60]. The architectural description of the YOLOv3 algorithm is shown in Fig. 2. The YOLOv3 algorithm takes an image or streaming video as input and then uses a deep CNN called DarkNet-53 to detect objects in the image or streaming video [15]. DarkNet-53 is derived from the ResNet architecture and it is tailor-made for object detection tasks, boasting 53 convolutional layers and achieving top-notch performance across various object detection benchmarks [11]. YOLOv3 with Darknet-53 is an efficient algorithm due to its speed and ability to detect multiple objects simultaneously [13], [59]. After the release of YOLOv3 in 2018, several versions of YOLO have been released up to YOLOv12 but the several advantages why YOLOv3 is used in this work can be found in [12] and [13].

The structure of the YOLOv3 with DarkNet-53 model architecture includes: *(i) Single Neural Network:* YOLOv3 uses a single convolutional neural network to predict bounding boxes and class probabilities directly from the image; *(ii) DarkNet-53:* The DarkNet-53 is built on a modified version of the DarkNet-53 convolutional neural network, which includes residual blocks to help with gradient flow in deep networks; *(iii) Feature Pyramid Network (FPN):* YOLOv3 utilizes FPN to extract

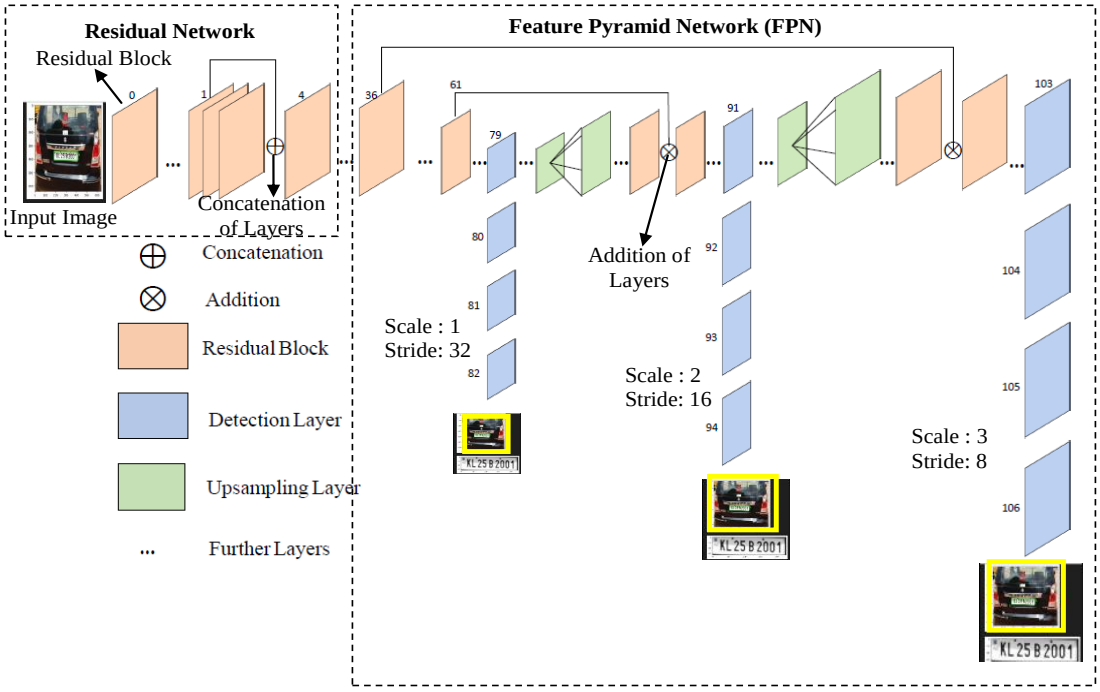


Fig. 2: Architecture of the YOLOv3 using DarkNet-53 with residual and feature pyramid networks.

features at different scales, allowing it to detect objects of various sizes; and *(iv) Anchor Boxes:* YOLOv3 uses anchor boxes (predefined bounding boxes with different aspect ratios and scales) to improve the detection of objects with varying shapes and sizes, according to [11].

YOLOv3 with DarkNet-53 uses a deep CNN to detect objects in images or streaming videos. YOLO is a single-shot object detection algorithm that is able to detect objects within an image or video in a single pass without the need for multiple stages. The YOLO family of algorithms are extremely fast because they do not deal with complex pipelines. At the minimum, YOLO algorithm processes images at 45 frames per second (FPS). Furthermore, YOLO algorithms reach more than twice the mean average precision (mAP) compared to other real-time object detection algorithms [14].

The YOLOv3 using DarkNet-53 model architecture is divided into three parts, namely: a head, a neck, and a backbone. The backbone is a series of convolutional layers that extract features from the input image. The neck combines features from different scales to improve object detection. The head is a set of fully connected layers that predict the location and class of each object in the image. YOLOv3 using DarkNet-53also uses anchor boxes, which are pre-defined bounding boxes of different sizes and aspect ratio. These anchor boxes are used to predict the location and sizes of objects in the image.

B. 2. The YOLOv3 Algorithm: Structure

Based on the YOLOv3 architecture shown in Fig. 2, the YOLOv3 algorithm accepts an image or streaming video as input and applies the CNN pre-trained DarkNet-53 model architectures to detect objects in the image according to the following procedures, namely:*1)* residual networks; *2);* Feature pyramid network (FPN); *3);* Bounding box regression; *4)* Intersection over union (IOU); and *5).* Non-maximum suppression as briefly described below.

1). Residual Network: The residual network accepts and divides the original input image (I) into *S* x *S* grid cells of equal shape by the YOLOv3 classifier, where *S* is a number. Each cell in the grid is responsible for localizing and predicting the class of the object that it covers together with the probability and the confidence value. The residual network also provide skip connections which ensures that inputs coming from one layer of the network are fed into another layer while avoiding vanishing or exploding gradients and prevents convergence degradation problems [14], [17], [61].

2). Feature Pyramid Network (FPN): FPN is not an object detector but rather a feature extractor algorithm. FPN extracts feature maps and later feeds into a feature detector algorithm to generate a pyramid of feature maps and the region-of-interests (ROIs). FPN composes of a bottom-up and a top-down pathway. The bottom-up pathway is the usual convolutional network for feature extraction. As we go up, the spatial resolution decreases. With more high-level structures detected, the semantic value for each layer

increases. The feature map is selected based on the width (w) and the height (h) of the ROI according to the following expression [61], [62]:

$$k = \left[k_0 + \log_2 \left(\frac{\sqrt{wh}}{224} \right) \right] \quad (1)$$

where 224 is the canonical ImageNet pre-training size; k_0 is the target level on which the ROI with $w \times h = 224^2$ should be mapped into; and *k* is the P_k layer in the FPN use to generate the feature patch. While the reconstructed layers are semantically strong, the object locations are not precise due to repeated down-sampling and up-sampling operations. Lateral connections are added between reconstructed layers and the corresponding feature maps to improve the accuracy of object localization. These connections also act as skip connections, facilitating easier training.

3). Bounding Box Regression: The next step in the detection process is the determination of the bounding boxes corresponding to rectangles (as many bounding boxes as there are objects in the given image), highlighting all the objects in the images or streaming video frames. The YOLOv3 determines the attributes of these bounding boxes using a single regression module in the following format:

$$Y = [pc, bx, by, bh, bw. c1, \ldots, cn] \quad (2)$$

where *Y* is the final vector representation of each bounding box; *pc* denotes the probability score of the grid containing an object; *bx* and *by* are the x and y coordinates of the center of the bounding box respectively with respect to the enveloping grid cell; *bh* and *bw* are the corresponding height and width of the bounding box respectively with respect to the enveloping grid cell; *c1,…, cn* correspond to *n* classes respectively where n can be chosen based on the classes to be detected in a given image.

4). Intersection Over Union (IOU): The goal of the IOU (a value between 0 and 1) is to discard such grid boxes to only keep those that are relevant. This is because most often than not, a single object in an image can have multiple grid box candidates for prediction, even though not all are relevant. The idea of the IOU is to compare the ratio of the overlapping area to the total combined region of two adjacent boxes given as:

$$IOU = \frac{Overlapping\ \ Region}{Combined\ \ Region} \quad (3)$$

here is the logic behind the IOU is summarized as follows:

(i) The user defines its IOU selection threshold, which can be, for instance, 0.5.

(ii) Then, YOLO computes the IOU of each grid cell, which is the Intersection area divided by the Union Area.

(iii) Finally, it ignores the prediction of the grid cells having an IOU ≤ threshold and considers those with an IOU > threshold.

5). Non-Max Suppression or (NMS): The NMS is used to keep only the boxes with the highest probability detection score. This is because setting a threshold for the IOU is not always enough because an object can have multiple boxes with IOU beyond the threshold, and leaving all those boxes might include noise.

B. 3. The YOLOv3 with DarkNet-53 Algorithm: Implementation Framework

As illustrated in Fig. 2, the basic idea behind YOLOv3 is to divide the input image into a grid of cells and, for each cell, predict the probability of the presence of an object and the bounding box coordinates of the object. The YOLOv3 strategy is based on the architecture of feature extraction model, DarkNet-53. For reducing the detection of objects, 53 layers are stacked together, therefore resulting in a fully convolutional architecture of 106 layers [15]. As shown in Fig. 2, the objects are identified at three layers of the architecture: 82nd, 94th, and 106th [16]. Each layer of the 53-layered architecture is followed by batch normalization layer and the implementation of leaky rectified linear unit (ReLU) activation function. The basic idea of the YOLOv3 architecture is to divide the image into cells of sizes where one grid cell per object is responsible for the object's prediction [16], [60]. The YOLOv3 using DarkNet-53 algorithm can be summarized as follows [11], [15], [16], [18]:

1). Input image is passed through a CNN to extract features from the image;

2). The features are then passed through a series of fully connected layers, which predict probabilities and bounding box coordinates;

3). The image is divided into a grid of cells, and each cell is responsible for predicting a set of bounding boxes and class probabilities;

4). The output of the network is a set of bounding boxes and class probabilities for each cell;

5). The bounding boxes are then filtered using a post-processing algorithm called non-max suppression to remove overlapping boxes and choose the box with the highest probability; and

6). The final output is a set of predicted bounding boxes and class labels for each object in the image.

C. Performance Metrics for Quantitative Benchmarking of Yolov3 with Darknet-53

1). Accuracy: Binary accuracy refers to a performance metric that is typically measured using metrics that

evaluate both the correct classification of objects and the precision of their localization as well as assessing bounding box predictions. Binary accuracy is the ratio of correct predictions to the total number of predictions.

$$\left.\begin{aligned}\text{Accuracy} &= \frac{Number\ of\ correct\ predictions}{Total\ Number\ of\ predictions}\\ &= \frac{TP+TN}{TP+TN+FP+FN}\end{aligned}\right\} \quad (4)$$

2). Precision: Precision is a crucial metric that measures the accuracy of positive predictions made by the model. It quantifies how many of the detected bounding boxes that the model identified as containing an object actually correspond to a real object in the image. Precision is the ratio of true positive predictions to the total predicted positives.

$$\text{Precision} = \frac{TP}{TP+FP} \quad (5)$$

3). Recall (Sensitivity or True Positive Rate): Recall is a single scalar metric that quantifies the proportion of actual positive instances (objects) that were correctly detected by the model. Recall measures the model's ability to identify all relevant objects within an image. Recall is the ratio of true positive predictions to the total actual positives.

$$\text{Recall} = \frac{TP}{TP+FN} \quad (6)$$

where TP (True Positives), TN (True Negatives), FP (False Positives), FN (False Negatives) for precision and recall. These metrics are computed using the predicted outputs ($\hat{y}$) and the actual labels (y) after model training.

4). Precision-Recall (PR) Curve: The precision-recall (PR) curve is a graphical representation that plots the precision values (y-axis) against the recall values (x-axis) at various confidence thresholds for the model's predictions. It shows the trade-off between the two metrics: generally, improving one often comes at the expense of the other.

5). F1-Score: The F1-score is the harmonic mean of precision and recall. The F1-score will be used to provide a balanced measure of model performance. This metric is useful to handle the imbalance in class distribution and is especially relevant for cases where certain classes may dominate the dataset. The F1-score is calculated as:

$$F1\ Score = 2\times\frac{Precision\times Recall}{Precision+Recall} \quad (7)$$

This metric is particularly important in situations where both precision and recall are important, as it balances the trade-off between them.

6). AUC-ROC: The area under receiver operating characteristic (AUC-ROC) curve is mathematically described as the integral of the True Positive Rate (TPR) with respect to the False Positive Rate (FPR) across all possible classification thresholds, and can be interpreted as the probability that a randomly chosen positive instance will be ranked higher than a randomly chosen negative instance. It quantifies the performance of a binary classifier across its entire range of operating points, with values closer to 1 indicating better performance. AUC-ROC can be expressed mathematically as:

$$\left.\begin{aligned}AUC-ROC &= \int_0^1 TPR\left(FPR\right)dFPR\\ &= \int_0^1 TPR\left(FPR^{-1}\left(x\right)\right)dx\end{aligned}\right\} \quad (8)$$

7). Confusion Matrix: A confusion matrix does not have a single formula but is a metric used to summarize the performance of a classification model by showing the actual versus predicted classes. For a two-class problem, it includes four components: True Positives (TP), True Negatives (TN), False Positives (FP), and False Negatives (FN). These components are then used in formulas to calculate performance metrics such as the Accuracy (as defined in (4)), Precision (Positive Predictive Value, PPV given in (5), Recall (Sensitivity, True Positive Rate defined in (6)), Specificity (True Negative Rate), and the F1 score (given by (7)).

8). Mean Average Precision (mAP): Mean average precision is a metric that averages the precision of a model over all classes. It is calculated by first finding the average precision (AP) for each class (often across a range of recall values) and then averaging the APs together to get mAP. The mean of average precision (mAP) values are calculated over recall values from 0 to 1. mAP formula is based on the following procedures: *1).* Calculate the intersection over union (IoU) ; *2).* Generate the prediction scores using the model; *3).* Convert the prediction scores to class labels; *4).* Calculate the confusion matrix—TP, FP, TN, FN; *5).* Calculate the precision and recall metrics; *6).* Calculate the area under the precision-recall curve; and *7).* Measure the average precision. The mAP is calculated by finding average precision (AP) for each class and then average over a number of classes.

$$mAP = \frac{1}{N}\sum_{i=1}^{N} AP_i \quad (9)$$

where AP_i is the AP of class *i*, *i* is the number of

classes and *N* is the total number of classes.

9). *Execution Time:* Execution time (or processing speed) is paramount for the YOLO-based object detection algorithms because it directly enables real-time performance, which is a critical requirement for practical, time-sensitive applications like autonomous vehicles, surveillance, and robotics. Furthermore, execution evaluation is crucial due to its direct impact on real-time application performance and overall system efficiency.

D. Quantitative Benchmarking Criteria for YOLOv3 with DarkNet-53 Model Architecture

In other to evaluate the performance of the proposed deep CNN YOLOv3 with DarkNet-53 pre-trained model architecture, it is imperative to quantitatively compare its performances with two widely used model architectures for object detection and recognition, namely: YOLOv8 with CSPDarkNet-53 (cross stage partial DarkNet-53) [63]–[67] and YOLOv3 with SqueezeNet [67]–[71].

The complete description and treatment of these two pre-trained model architectures can be found in [63]–[71].

D. 1. YOLOv8 with CSPDarkNet-53

YOLOv8 is the latest iteration, offering improvements in performance and efficiency over previous versions [63]–[67]. YOLOv8 typically includes features for better backbone networks, improved loss functions, and optimizations for both training and inference. YOLOv8 uses CSPDarkNet-53 as the backbone for its implementation. This means that the original DarkNet-53 feature extraction part of YOLOv8 has been replaced by CSPDarkNet-53 [65], [67]. The CSPDarkNet-53 is a modified version of the original DarkNet-53 architecture designed for better gradient flow and reduced computational cost. YOLOv8 with CSPDarkNet-53 features a mix of convolutional layers and residual connections, which help in learning more robust features, particularly for object detection tasks [63]–[67]. The backbone of YOLOv8, based on the CSPDarknet-53 architecture, has been modified and enhanced with C2f blocks and a spatial pyramid pooling fusion (SPPF) module at the end. YOLOv8 with the CSPDarknet-53 architecture is designed to efficiently extract features from input images by using cross-stage partial (CSP) connections to improve information flow and gradient propagation. [63]–[71].

D. 2. YOLOv3 with SqueezeNet

SqueezeNet is a convolutional neural network designed to be small and efficient. It introduces “fire modules” which consist of a “squeeze” layer (1x1 convolutions) followed by an “expand” layer (1x1 and 3x3 convolutions) [67]. The squeeze layer reduces the number of input channels to the 3x3 filters in the expand layer, leading to fewer parameters [67]–[67]. SqueezeNet is primarily designed for image classification, with a focus on achieving high accuracy using a very small model size. Although it is mainly used for classification, SqueezeNet can also serve as a lightweight backbone for object detection tasks when integrated with architectures such as YOLOv3. This involves replacing the standard Darknet-53 backbone in YOLOv3 with SqueezeNet for feature extraction, followed by adding the YOLOv3 detection heads on top of the SqueezeNet features. This modification aims to produce a more lightweight and efficient object detector, potentially at the cost of some accuracy compared to a deeper backbone such as Darknet-53 [67]–[71].

Experiments

A. Hardware Setup

A. 1. Setting up the IP Camera with an RJ-45 Cable, an Ethernet Switch and Router

The hardware setup and configuration is as illustrated and discussed in line with the block diagram shown in Fig. 1. The demonstration starts in the laboratory to connect and configure the hardware. All cables used for hardware connections are the RJ-45 cable while all power cable is standard factory fitted cables. Care should be taken to connect the host development computer (laptop) and the Airtel router/Wi-FI module to the appropriate uplink ports on the PoE switch.

The complete hardware setup is shown in Fig. 3 and Fig. 4.

The front view of the powered IP camera connected to the router via an Ethernet switch with an RJ-45 cable is shown in Fig. 3 while the rear view of the same setup is shown in Fig. 4.



Fig. 3: Front view of the IP camera set-up with an RJ-45 cable and a router.



Fig. 4: Rare view of the IP camera set-up with an RJ-45 cable and a router.

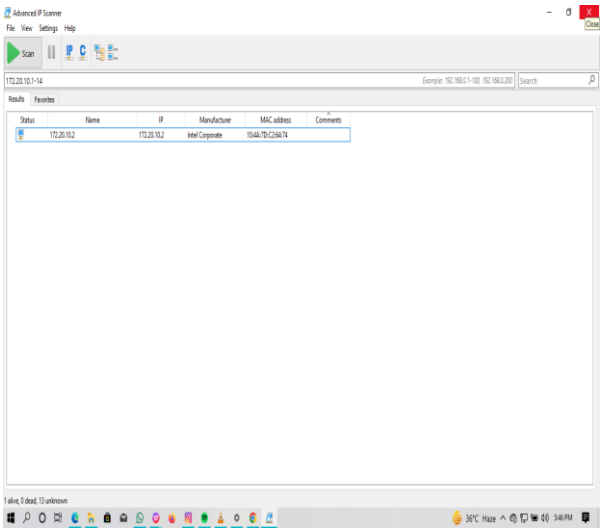


Fig. 5: The IP address of the camera using advanced IP scanner.

After the hardware setup, the camera is powered with electricity via the 12-Volt power adapter (converter) and the camera switches ON as can be seen in Fig. 3 with the red LED ON, plug the power adapter into the camera and a wall outlet. Note that the camera can still be powered via the PoE switch in the absence of public power supply. In this case, the camera is connected to the router using the RJ-45 cables where one end of the RJ-45 cable is plugged into the camera's Ethernet port and the other end of the RJ-45 is plugged into an available Ethernet port on the router as illustrated in Fig. 1.

A. 2. Obtaining the IP Address of the Camera

With proper setup and configuration, the IP-based camera functions as described in the previous subsection. The step is to obtain the IP address of the camera.

Obtaining the IP address of the camera can be achieved in several ways, depending on the model of the camera. However, for the SONY Vision CCTV IP-based SV-5MP-POE-4B, the IP address is obtained as follows:

1). Camera manual: Check the manual for instructions on finding the IP address. It might be printed on a label on the camera itself.

2). Manufacturer's website: Some manufacturers provide tools or software for discovering cameras on a network.

3). Router interface: Log in to your router's web interface and look for a list of connected devices. The camera's IP address should be listed there.

4). Use a Network Scanning Tool: In this study, Advanced IP Scanner is used as the scanning tool to obtain the camera's IP address. This is achieved by running a network scan and identifying the device that matches the camera's manufacturer or model name. The obtained camera's IP address is http://192.168.1.11/ as shown in Fig. 5.

A. 3. Accessing the Camera's Web Interface

Accessing the camera's web interface involves opening a web browser on the host computer and entering the camera's IP address into the address bar and hit the Enter key.

There comes up a prompt for a username and password.

These are provided in the camera's manual or on a sticker on the camera.

By following these steps, the camera's web interface is accessed and the IP camera is successfully set up for monitoring remote immediate and remote locations. It is recommended to always consult the camera's manual for specific instructions and troubleshooting tips. However, configuring of the camera settings is required. After logging into the camera's web interface, the camera's settings are configured as illustrated in Fig. 6 and Fig. 7 as follows:

1). Network settings: You can usually choose between the automatic dynamic host configuration protocol (DHCP) or the static IP address assignment. In this study, the DHCP is selected for online dynamism.

2). Resolution and image quality: Choose the video resolution and quality that best suits your needs and network bandwidth. The 125600 option is selected.

3). Recording settings: Configure motion detection, recording schedules, and storage options are selected.

4). Secure your network: Make sure your router's Wi-Fi network is password-protected to prevent unauthorized access to your camera.

5). Update the camera's firmware: Regularly check for and install firmware updates from the camera manufacturer to ensure optimal performance and security.

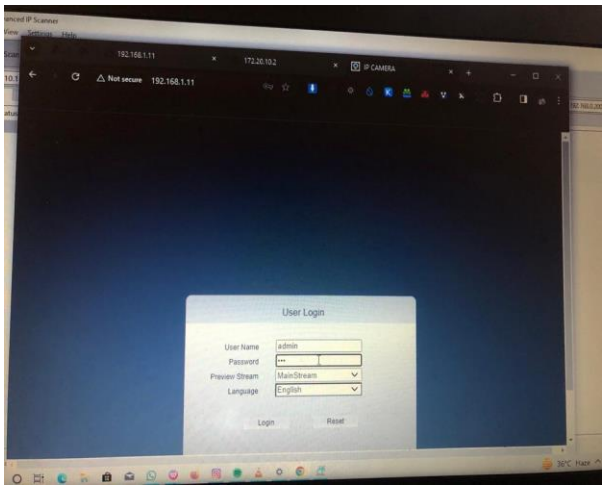


Fig. 6: Accessing the camera's web interface using web browser.

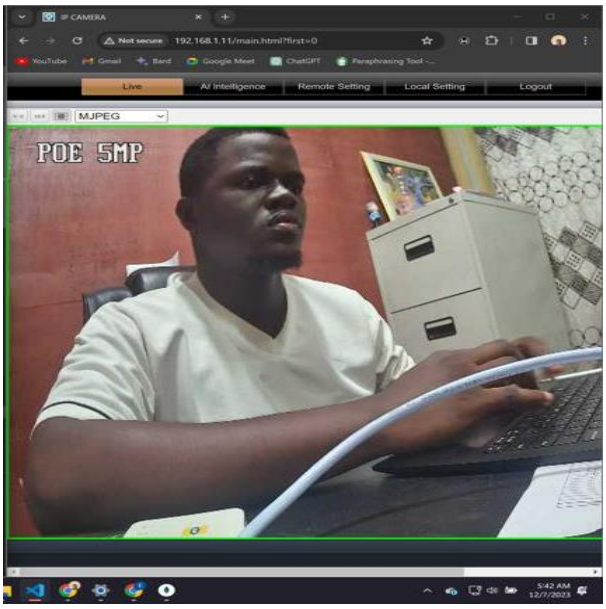


Fig. 7: Accessed the camera's web interface using web browser.

A. 4. Router Configuration

After accessing and configuring the camera's web interface, the next step is to configure the router as follows:

1). Configure IP Camera Settings (Optional):

Some IP cameras may have configuration requirements. Refer to the camera's user manual to find out if there are specific settings or software that need to be configured. This may include setting up an IP address, configuring network settings, or installing any necessary software.

2). Router Configuration (Optional):

In some cases, you might need to access your router's settings to configure port forwarding or other network settings for the IP camera. Refer to your router's user manual for instructions on how to access and configure these settings.

3). Check Connection:

Once everything is connected, check the status of the IP camera. It may have indicator lights that show if it's successfully connected to the network.

4). Streaming Video Verification:

Verify that the camera is streaming correctly by viewing the live feed through the camera's interface or any associated software.

5). Secure the Setup (Optional):

If security is a concern, consider changing default passwords, enabling encryption, and ensuring that the camera's firmware is up to date. Figure 8 shows the setup of the camera and resolution in color mode.



Fig. 8: Testing the Setup and resolution (color Mode).

B. Software Setup

B. 1. Python and Add-On Libraries Installation

The primary software used in this work is Python and its associated add-on libraries listed in sub-section c of this Section.

All the necessary Python and related software required for this work were downloaded from appropriate websites, properly installed, setup and configured accordingly and tested.

B. 2. OpenCV Installation

The OpenCV library for Python was downloaded, installed and properly configured. The OpenCV is essential for working with images and video streams. The complete Python code for the installation, configuration and interfacing of the IP camera to the computer is shown in Fig. 9.

The test result for the successful installation, interfacing and configuration of Python and its associated software for accessing the IP camera is shown in Fig. 10.

```python
import cv2
import numpy as np
import time
import os

# Load the YOLOv3 model
model_cfg_path = r"C:\Users\Tsega\500 Project\yolov3-from-opencv-object-detection\model\cfg\darknet-yolov3.cfg"
model_weights_path = r"C:\Users\Tsega\500 Project\yolov3-from-opencv-object-detection\model\weights\model.weights"
class_names_path = r"C:\Users\Tsega\500 Project\yolov3-from-opencv-object-detection\model\class.names"

# Load class names
with open(class_names_path, 'r') as f:
    class_names = [j[:-1] for j in f.readlines() if len(j) > 2]
    f.close()

# We load the YOLOv3 model
net = cv2.dnn.readNetFromDarknet(model_cfg_path, model_weights_path)

# Create a folder to save recognized plate images
save_folder = 'recognized_plate_images'
if not os.path.exists(save_folder):
    os.makedirs(save_folder)

# # Set the IP camera URL
# video_url = "rtsp://admin:KAD@192.168.1.11:554"

cap = cv2.VideoCapture(0)

ct = 0

# Define the cooldown period (in seconds)
cooldown_period = 10

# Initialize a variable to keep track of the last saved time
last_saved_time = 0

# Inside the loop where you process YOLOv3 results
while True:
    ct += 1

    ret, img = cap.read()
    if not ret:
        break

    imS = img.copy()

    H, W,   = img.shape
```

```python
    blob = cv2.dnn.blobFromImage(img, 1 / 255, (416, 416), (0, 0, 0), True)
    net.setInput(blob)
    output_layer_names = net.getUnconnectedOutLayersNames()
    detections = net.forward(output_layer_names)

    for detection in detections:
        for obj in detection:
            scores = obj[5:]
            class_id = np.argmax(scores)
            confidence = scores[class_id]
            if confidence > 0.5 and class_id == 0:  # Assuming class_id 0 is for plates

                # Get the current time
                current_time = time.time()

                # Check if the last saved time is more than the cooldown period
                if current_time - last_saved_time > cooldown_period:
                    # Save the entire frame as an image
                    save_path = os.path.join(save_folder, f'captured_frame_{current_time}.png')
                    cv2.imwrite(save_path, img)

                    # Update the last saved time
                    last_saved_time = current_time

                # Drawing the rectangle around the detection (you can customize this part)
                x, y, w, h = (obj[0:4] * np.array([W, H, W, H])).astype(int)
                cv2.rectangle(imS, (x, y), (x + w, y + h), (0, 255, 0), 2)

                # Add text to the image
                text = "Detected Plate"
                cv2.putText(imS, text, (x, y - 10), cv2.FONT_HERSHEY_SIMPLEX, 0.5, (0, 255, 0), 1)

    imS = cv2.resize(imS, (720, 600))
    cv2.imshow('Video', imS)

    k = cv2.waitKey(1) & 0xff
    if k == 27:
        break

cap.release()
cv2.destroyAllWindows()
```

[82] ✓ 33.6s

Fig. 9: The Python code snippet for interfacing the IP-based camera with the YOLOv3 model.

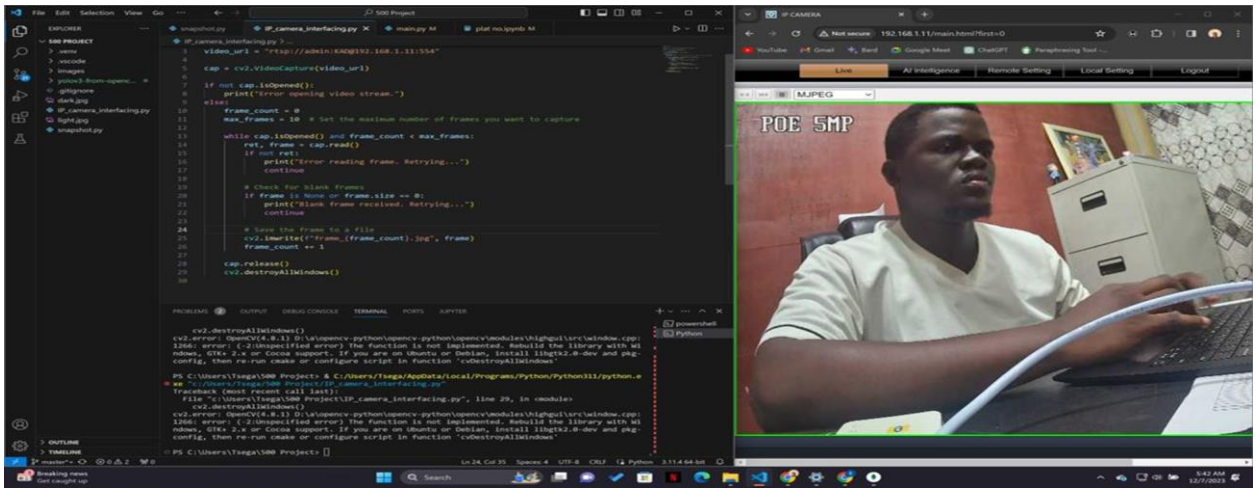


Fig. 10: Python Installation and interfacing with the IP camera.

B. 3. Python Code Implementation and Description

This Python script uses the OpenCV library to perform object detection on video frames using the YOLOv3 using DarkNet-53 model architecture. The specific object that is being looked for is a license plate number. The Python code implementation and description is highlighted in the following:

1). Imports necessary libraries: cv2 for computer vision tasks, numpy for numerical operations, time for time-related functions, and OS for interacting with the operating system.

2). Load the YOLOv3 model: The paths to the configuration file, weights file, and class names file for the YOLOv3 model are defined. The model is then loaded using cv2.dnn.readNetFromDarkNet.

3). Prepares for saving images: A directory is created to save images of detected license plates.

4). Sets up video capture: The script is set up to capture video from the default camera (camera index 0). If you uncomment the lines with *video_url and cap = cv2*. VideoCapture (*video_url*), it would capture video from the specified IP camera instead.

5). Initializes variables: ct is a counter, cooldown_period is a time period during which new detections are ignored to prevent saving multiple images of the same vehicle plate, and last_saved_time keeps track of when the last image was saved.

6). Processes video frames: In an infinite loop, the script reads frames from the video, preprocesses them into a format suitable for the YOLOv3 model, and feeds them into the model to get detections.

7). Handles detections: For each detection, the script checks if the detected object is a license plate (assuming that class ID0 corresponds to license plates) and if the confidence of the detection is above 0.5. If both conditions are met and the time since the last saved image is more than the cooldown period, the script saves the current frame as an image.

8). Draws bounding boxes and text: The script draws a rectangle around the detected license plate and adds a text label.

9). Cooldown Period Check and Frame Saving: The script checks if the time since the last saved frame is greater than a cooldown period (10 seconds in this work). If the cooldown check passes, the entire frame is saved as an image in the '*recognized_plate_images*' folder.

10). Displays the video: The processed video frame is displayed in a window. If the user presses the Esc key, the loop breaks and the video capture is stopped.

11). Cleans up: The video capture is released and all OpenCV windows are destroyed.

B. 4. Bounding Box, Detection and Capturing of VPNs

The project code is a Python script that connects to a PostgreSQL database, fetches unprocessed images and uses the YOLOv3 model to detect objects in the images and/or video streams. The Python script then uses EasyOCR to read text (in this case, LPNs) from the detected vehicles. The Python script also handles updating the database with the processed status, validity, and the detected license plate number. The Python script also updates the Google Cloud Storage. The description of the automated Python script implementation is as follows:

1). Connects to a PostgreSQL database using SQLAlchemy.

2). Loads the YOLOv3 model from the specified paths.

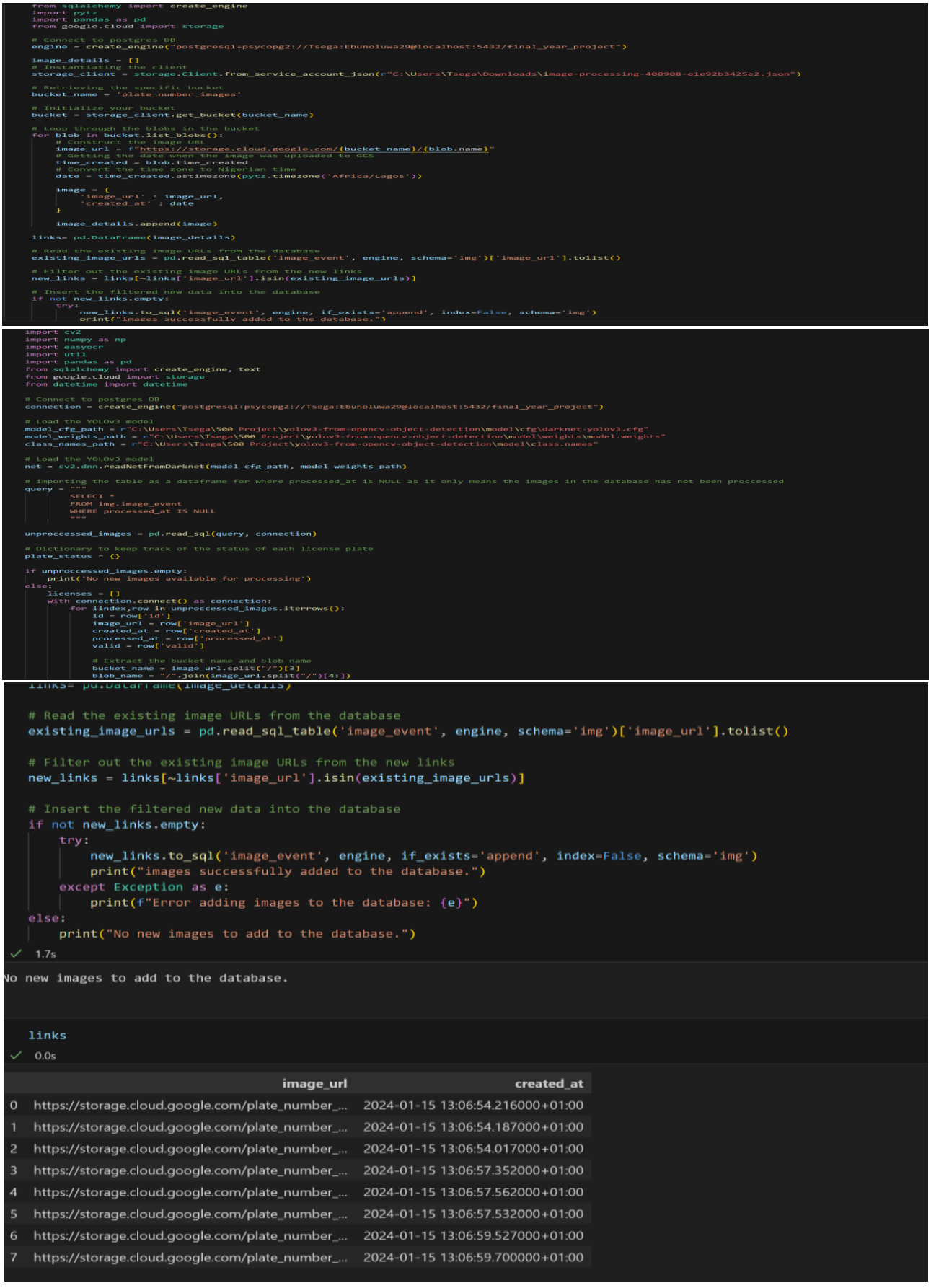
3). Fetches unprocessed images from the database.

4). If there are unprocessed images, it iterates over each image.

5). For each image, it downloads the image from Google Cloud Storage and decodes it into a NumPy array.

6). The image is then processed using the YOLOv3 model to detect objects.

7). If objects are detected, it applies Non-Maximum Suppression to filter out overlapping bounding boxes.



```
from sqlalchemy import create_engine
import pytz
import pandas as pd
from google.cloud import storage

# Connect to postgres DB
engine = create_engine("postgresql+psycopg2://Tsega:Ebunoluwa29@localhost:5432/final_year_project")

image_details = []
# Instantiating the client
storage_client = storage.Client.from_service_account_json(r"C:\Users\Tsega\Downloads\image-processing-408908-e1e92b3425e2.json")

# Retrieving the specific bucket
bucket_name = 'plate_number_images'

# Initialize your bucket
bucket = storage_client.get_bucket(bucket_name)

# Loop through the blobs in the bucket
for blob in bucket.list_blobs():
    # Construct the image URL
    image_url = f"https://storage.cloud.google.com/{bucket_name}/{blob.name}"
    # Getting the date when the image was uploaded to GCS
    time_created = blob.time_created
    # Convert the time zone to Nigerian time
    date = time_created.astimezone(pytz.timezone('Africa/Lagos'))

    image = {
        'image_url' : image_url,
        'created_at' : date
    }

    image_details.append(image)

links= pd.DataFrame(image_details)

# Read the existing image URLs from the database
existing_image_urls = pd.read_sql_table('image_event', engine, schema='img')['image_url'].tolist()

# Filter out the existing image URLs from the new links
new_links = links[~links['image_url'].isin(existing_image_urls)]

# Insert the filtered new data into the database
if not new_links.empty:
    try:
        new_links.to_sql('image_event', engine, if_exists='append', index=False, schema='img')
        print("images successfully added to the database.")
```

```
import cv2
import numpy as np
import easyocr
import util
import pandas as pd
from sqlalchemy import create_engine, text
from google.cloud import storage
from datetime import datetime

# Connect to postgres DB
connection = create_engine("postgresql+psycopg2://Tsega:Ebunoluwa29@localhost:5432/final_year_project")

# Load the YOLOv3 model
model_cfg_path = r"C:\Users\Tsega\500 Project\yolov3-from-opencv-object-detection\model\cfg\darknet-yolov3.cfg"
model_weights_path = r"C:\Users\Tsega\500 Project\yolov3-from-opencv-object-detection\model\weights\model.weights"
class_names_path = r"C:\Users\Tsega\500 Project\yolov3-from-opencv-object-detection\model\class.names"

# Load the YOLOv3 model
net = cv2.dnn.readNetFromDarknet(model_cfg_path, model_weights_path)

# importing the table as a dataframe for where processed_at is NULL as it only means the images in the database has not been proccessed
query = """
        SELECT *
        FROM img.image_event
        WHERE processed_at IS NULL
        """

unproccessed_images = pd.read_sql(query, connection)

# Dictionary to keep track of the status of each license plate
plate_status = {}

if unproccessed_images.empty:
    print('No new images available for processing')
else:
    licenses = []
    with connection.connect() as connection:
        for iindex,row in unproccessed_images.iterrows():
            id = row['id']
            image_url = row['image_url']
            created_at = row['created_at']
            processed_at = row['processed_at']
            valid = row['valid']

            # Extract the bucket name and blob name
            bucket_name = image_url.split("/")[3]
            blob_name = "/".join(image_url.split("/")[4:])
```

```
links= pd.DataFrame(image_details)

# Read the existing image URLs from the database
existing_image_urls = pd.read_sql_table('image_event', engine, schema='img')['image_url'].tolist()

# Filter out the existing image URLs from the new links
new_links = links[~links['image_url'].isin(existing_image_urls)]

# Insert the filtered new data into the database
if not new_links.empty:
    try:
        new_links.to_sql('image_event', engine, if_exists='append', index=False, schema='img')
        print("images successfully added to the database.")
    except Exception as e:
        print(f"Error adding images to the database: {e}")
else:
    print("No new images to add to the database.")
```

✓ 1.7s

```
No new images to add to the database.
```

```
links
```

✓ 0.0s

	image_url	created_at
0	https://storage.cloud.google.com/plate_number_...	2024-01-15 13:06:54.216000+01:00
1	https://storage.cloud.google.com/plate_number_...	2024-01-15 13:06:54.187000+01:00
2	https://storage.cloud.google.com/plate_number_...	2024-01-15 13:06:54.017000+01:00
3	https://storage.cloud.google.com/plate_number_...	2024-01-15 13:06:57.352000+01:00
4	https://storage.cloud.google.com/plate_number_...	2024-01-15 13:06:57.562000+01:00
5	https://storage.cloud.google.com/plate_number_...	2024-01-15 13:06:57.532000+01:00
6	https://storage.cloud.google.com/plate_number_...	2024-01-15 13:06:59.527000+01:00
7	https://storage.cloud.google.com/plate_number_...	2024-01-15 13:06:59.700000+01:00

Fig. 11: The Python code snippet for license plate number segmentation and recognition.

8). For each detected vehicle, it extracts the region of interest (the VPN) and uses EasyOCR to read the text from it.
9). It then checks the database for the latest record of the detected LPN and checks if the cooldown period has passed.
10). If the cooldown period has passed, it updates the status of the LPN (either "IN" or "OUT") and updates the database with the processed status, validity, and the detected LPN.
11). If no objects are detected in the image, it updates the database to reflect that the image was picked but not successfully processed.

It should be noted that the following Python packages were implemented, namely: *cv2, numpy, easyocr, pandas, sqlalchemy, and google.cloud.storage*. The implementation required a pre-trained *YOLOv3* model and a Google Cloud Storage service account *JSON file*.

B. 5. License Plate Recognition and the Description of the Python Code

License Plate Recognition (LPR), also known as Automatic License Plate Recognition (ALPR) is a technology that involves the automatic detection, extraction, and recognition of license plate information from images or video streams. Using Python and various libraries and frameworks, an LPR system is implemented. A brief explanation of the key steps in the implementation of the LPR system using Python and its associated libraries is presented, along with the Python code shown in Fig. 11. The following are the step-by-step breakdown of what the Python script of Fig. 11 does.

1). Connects to a PostgreSQL database using SQLAlchemy.
2). Loads the YOLOv3 model from the specified paths.
3). Fetches unprocessed images from the database.
4). If there are unprocessed images, it iterates over each image.
5). For each image, it downloads the image from Google Cloud Storage and decodes it into a NumPy array.
6). The image is then processed using the YOLOv3 model to detect objects.
7). If objects are detected, it applies Non-Maximum Suppression to filter out overlapping bounding boxes.
8). For each detected object, it extracts the region of interest (the license plate) and uses EasyOCR to read the text from it.
9). It then checks the database for the latest record of the detected license plate and checks if the cooldown period has passed.
10). If the cooldown period has passed, it updates the status of the license plate **(**either **"IN"** or **"OUT")** and updates the database with the processed status, validity, and the detected license plate number.
11). If no objects are detected in the image, it updates the database to reflect that the image was picked but not successfully processed.

B. 6. Database Documentation

The following procedures are employed for the creation of the database documentation:

1). Choose a relational database system (e.g., MySQL, SQLite, PostgreSQL). The PostgreSQL is used in this work.
2). Install the appropriate database driver for Python. Themysql-connector-python for MySQL is used in this work.
3). Create a database and tables to store vehicle information.

This documentation provides insights into the purpose and structure of the database, schema, and table. It helps users, developers, or administrators understand the context and organization of the data within the database with the following descriptions:

i). Database Name: image_processing_db
ii). Schema: img
iii). Purpose: The 'img' schema may be used to organize database objects, such as tables, views, and functions, related to image processing or storage. It provides a logical grouping within the database, helping to organize and manage objects with a common theme.
iv). Table: img.image_event
v). Purpose: The img.image_event table is designed to store information related to events associated with processed images. This includes details such as image URLs, time-stamps of creation and processing, license plate information, and the status of the associated event.



Fig. 12: Database documentation table.

vi). Table Structure: The description for the creation of the database documentation is shown in Fig. 12 and is achieved as follows:

CREATE TABLE IF NOT EXISTSimg.image_event
(
*id*SERIAL PRIMARY KEY,
image_url VARCHAR(255) NOT NULL,
created_at TIME-STAMP WITHOUT TIME ZONE,
processed_at TIME-STAMP WITHOUT TIME ZONE,
valid BOOLEAN,
plate_number VARCHAR(20),
status VARCHAR(5),
CONSTRAINT*image_event_image_url_key UNIQUE (image_url)*
);

Columns

id (SERIAL PRIMARY KEY): A unique identifier for each image event, automatically incremented.

image_url (VARCHAR(255) NOT NULL): The URL or path of the associated image.

created_at (TIMESTAMP WITHOUT TIME ZONE): Time-stamp indicating when the image event was created or when the image was taken by the camera

processed_at (TIMESTAMP WITHOUT TIME ZONE): Time-stamp indicating when the image was processed for extraction of necessary information.

valid (BOOLEAN): Boolean flag indicating the validity of the processed image if true or false.

plate_number (VARCHAR(30)): The detected license plate number from the processed image.

status (VARCHAR(5)): The status of the associated event, typically indicating whether the vehicle is "IN" or "OUT" of the premises.

Constraints

image_event_image_url_key (UNIQUE): Ensures that each image URL is unique, preventing duplicate entries.

B. 7. Database Development, Set-Up, Interaction, and Documentation

The Python code snippets were combined into a cohesive Python script that captures the camera feed, performs license vehicle plate recognition, and updates the database. The direct implementation of the proposed vehicle plate identification system involves: *1).* Simulating the combined cohesive Python code; *2).* Choose a relational database system (e.g., MySQL, SQLite, PostgreSQL); *3).* Install the appropriate database driver for Python (e.g., mysql-connector-python for MySQL); *4).* Create a database and tables to store vehicle information; and *5).* Finally, execute the Python script and observe the system in action. Ensure that the camera captures the feed, and the license plate information is correctly stored in the database.

These step-by-step procedures provide a foundation for creating an artificial intelligent-based automatic vehicle inventory system. Adjustments may be necessary based on specific hardware, software, and database choices. Additionally, consider implementing security measures for data protection and system access. Lastly, connect to the database and insert/update records with the recognized license plate information. The developed database setup, database interaction, and database documentation for the capturing and storing vehicle data is show in Fig. 13.

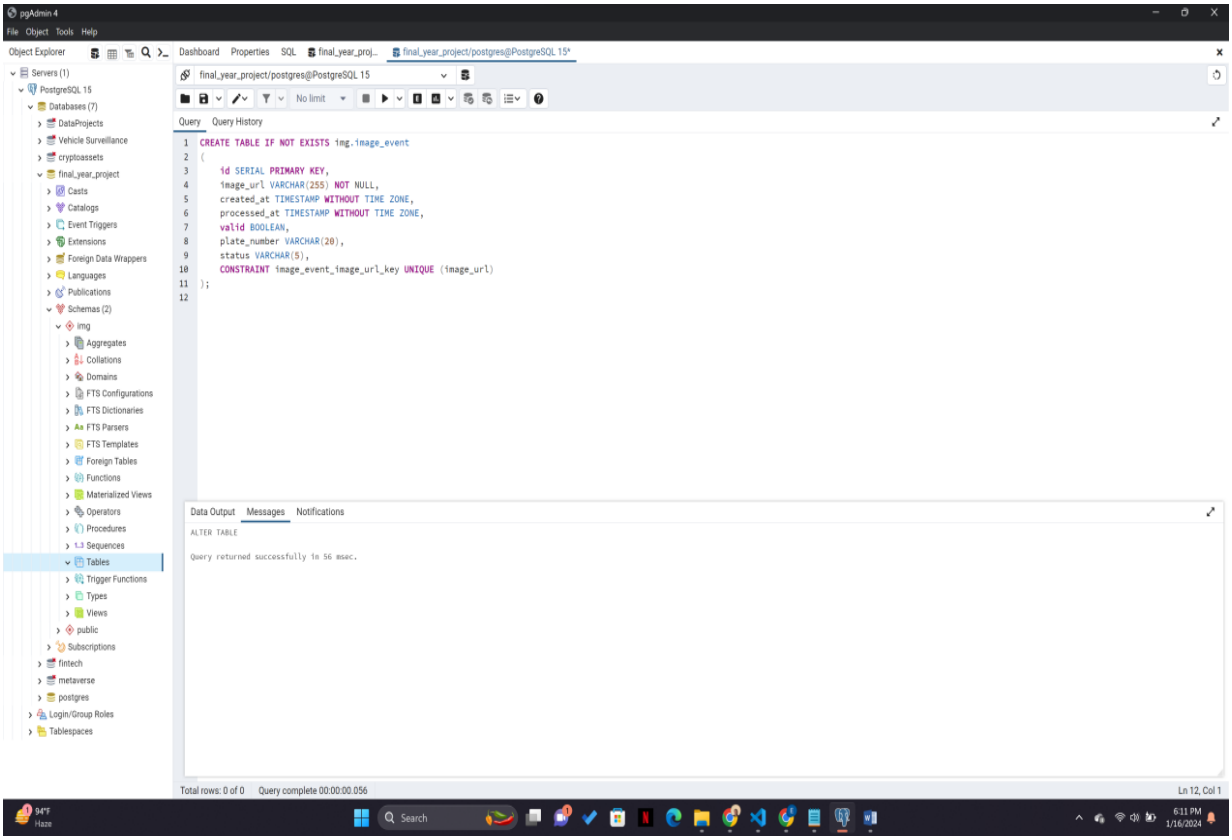


Fig. 13: Database interaction, Database setup and Database documentation.

C. *Real-Time Implementation of the YOLOv3 with DarkNet-53*

C. 1. *Implementation*

The real-time implementation of the deep CNN based on the DarkNet-53 model architecture is illustrated diagrammatically in Fig. 2. The sizes of the input license plate numbers (LPNs) were different and therefore the LPNs were pre-processed and automatically resized. In the LPN recognition problem based on the YOLOv3 with DarkNet-53, the input images were automatically resized to 320 × 320 pixels. All images were automatically normalized using Z-score normalization based on the same mean, variance and standard deviation. The implementation of the deep CNN based on YOLOv3 with DarkNet-53 model architecture is summarized as follows:

1. Input image is passed through a series of convolutional layers that extract features using convolutional filters with appropriate stride and padding techniques.
2. The output of each layer is passed through a rectified linear unit (ReLU) activation function to introduce non-linearity.
3. Pooling layers are used to reduce dimensionality of output and make the model more efficient.
4. The convolutional and pooling layers computations are repeated 5 times at each epoch due to the complexity of the LPN detection and recognition problem.
5. The output of the final convolutional layer is flattened and fed into the fully connected layer (FC Layer) that performs classification on the extracted features from the VPN.
6. The output of the FC layer is passed through a softmax activation function with the associated cost functions to produce the detected and recognized.
7. The implementation of the deep CNN based on the YOLOv3 with DarkNet-53 model architecture for a LPN detection and recognition converged after 80 epochs (iterations) which demonstrate the robustness of the algorithm as shown in Fig. 14.

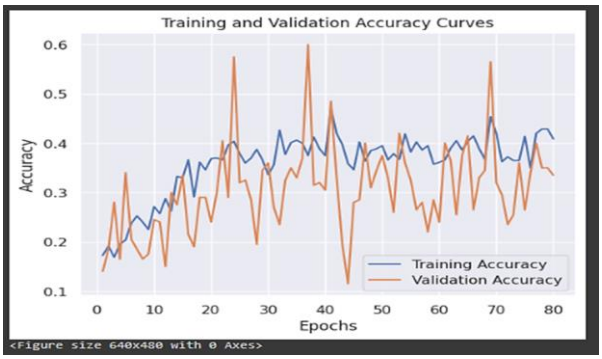


Fig. 14: Training and validation accuracy results over 80 iterations obtained by deep CNN based on YOLOv3 with DarkNet-53 model structure.

C. 2. *Additional Implementation Considerations*

The methodology for developing and implementing the deep CNN based on YOLOv3 with DarkNet-53 for the accurate detection and recognition of LPNs involves additional consideration listed as follows:

1. *Data Preprocessing*: The dataset was cleaned and preprocessed to ensure consistency and quality. This included resizing images, normalizing pixel intensities, and handling missing data, although no missing data were present.
2. *Model Architecture Selection*: In choosing an appropriate deep CNN pre-trained model architecture suitable for real-time LPN detection and recognition tasks, the DarkNet-53 is used because it is the backbone of the YOLOv3 as it balances model complexity, efficiency, performance, and appreciable less computational complexities with low-cost affordable hardware.
3. *Model Training*: The training starts by capturing the LPN via streaming video of the moving vehicle and loading the DarkNet-53 pre-trained model architecture. The model training proceeds by adding additional layers specifically a global average pooling layer, which reduces the spatial dimensions of the output and prepares the YOLOv3 using DarkNet-53 for detection and recognition and a softmax layer with a sigmoid activation function. The model is then compiled using the Adam optimizer and a custom loss function. The custom loss function, *get_weighted_loss*, incorporates class weights to address class imbalance in the captured image dataset. These weights are learned from an image dataset and serve as a starting point for the fine-tuning process. During training, the deep CNN based on YOLOv3 with DarkNet-53 learns to recognize patterns and features indicative of the presence or absence LPNs.
4. *Hyper-Parameter Tuning*: The training process for YOLOv3 with DarkNet-53 involves tuning several parameters, including the learning rate, regularization, batch size, training epochs, number of layers, and filters in the DarkNet-53 architecture of Fig. 2 as well as other parameters as summarized in Table 1. These hyper-parameters significantly impact the performance of the trained model and fine-tune the model's hyper-parameters to improve its performance. The detailed hyper-parameters used for tuning the deep CNN based on YOLOv3 with DarkNet-53 are listed in Table 1 [72]–[75].
5. *Model Evaluation*: The performance of the trained model was assessed during training using hyperparameter tuning. Various performance metrics, such as accuracy, precision, and the area under the receiver operating characteristic curve (AUC-ROC),

were evaluated to measure the model's effectiveness in accurately detecting and recognizing LPNs. The model assigns a probability score to each detected and recognized LPN (e.g., probability of being normal and probability of being abnormal).

6. *Iterative Refinement*: The model was iteratively refined based on evaluation results and feedback. This involved revisiting the model architecture and adjusting hyperparameters to address specific challenges and limitations identified during the LPN detection and recognition process.

Table 1: Hyper-parameter training and tuning options

S/N	Parameter and Layer Type		Specification
1	Network Architecture		YOLOv3
2	imageInputLayer		[32 32 1]
3	Convolution2dLayer		[5, 20]
4	fullyConnectedLayer		14
5	Learning rate		[1e-4 1e-3]
6	Batch size		64
7	Input size	Width	320 320 x 320
		Height	320
8	Anchors		[10, 13, 16, 30, 33, 23, 30, 62, 45, 59, 119, 116, 90, 156, 198, 373, 326]
9	Number of anchors		3
10	Number of classes		80
11	Confidence threshold		0.25
12	NMS Threshold		0.45
13	IOU threshold		0.5
14	Number of filters		64
15	Number of layers		53
16	Activation function		Leaky ReLU
17	Optimizer		Adam
18	Maximum epochs		80
19	maxPooling2dLayer		2
20	Stride		[32, 16, 8]
21	Scale		[1, 2, 3]
22	Dropout Rates		0.5
23	L2Regularization		[1e-8 1e-2]
24	Momentum		[0.5 0.99]
25	Sequence padding Direction		Left
26	Padding		2
27	Shuffle		Every epoch
28	Metrics		Accuracy
29	Gradient Threshold	Algorithm	1
30	Loss function		Cross entropy
31	Data augmentation		[True, False]

Results and Discussion

A. Results

A. 1. Quantitative Results

The YOLOv3 with DarkNet-53 model is designed for the detection and recognition of license plate numbers of vehicles using deep learning techniques. The architecture used is DarkNet-53, a deep CNN pre-trained model that has demonstrated strong performance in various computer vision tasks, including object detection and recognition. Each layer receives input not only from the previous layer but also from all preceding layers, which encourages feature reuse and improves information flow through the network. This model is trained on a large dataset of labeled classes, where each image is associated with the presence or absence of specific objects. The loss function used during training guides the model to minimize the difference between predicted and actual label classes. The training process involves adjusting the model's parameters to minimize the difference between predicted and actual labels. For each captured license plate number (LPN) image, the model generates predictions for the presence or absence of the LPN, assigning a probability to each class. These probabilities represent the model's confidence in its predictions. The final layer of the DarkNet-53 model consists of neurons corresponding to the detected LPN classes. The extracted features are then fed into a trained classification model. Based on these features and the internal logic of the model, the LPN is identified for its intended use. The results are initially evaluated with associated probabilities. Each probability represents the model's estimate of the likelihood of LPN detection and recognition. A threshold is applied to convert probabilities into predictions (presence or absence of a LPN). For example, if the threshold is 0.5, probabilities above 0.5 are considered positive predictions. The training and validation result for the accuracy curve is shown in Fig. 14. Due to space economy, only the results for first five LPN detection and recognition have been presented in this paper together with their respective performance comparison metrics figures and tables.

The real-time implementation results for the three deep CNN based on YOLOv3 with DarkNet-53, YOLOv8 with CSPDarkNet-53 and YOLOv3 with SqueezeNet model architectures for the detection and recognition of the LPNs for all the 25 vehicles used in this work are given in Figs. 15–18 which shows the detected and recognized LPNs; Tables 2–5 show the database tables; Figs. 19–23 show the precision-recall (PR) and area under receiver operating characteristic (AUC-ROC) curves; and Figs. 24–28 show the confusion matrices percentage accuracies. The three deep CNN pre-trained model architectures have been qualitatively and quantitatively evaluated in terms of several performance metrics for comparison and the results are shown in Tables 6–8 where the tables show the confusion matrix minimum and maximum values of the percentage successes of detected versus target LPN detection and recognition recorded by the confusion matrices; the performance metrics comparison by the three deep CNN pre-train models; and the average values of all the performance metrics respectively.

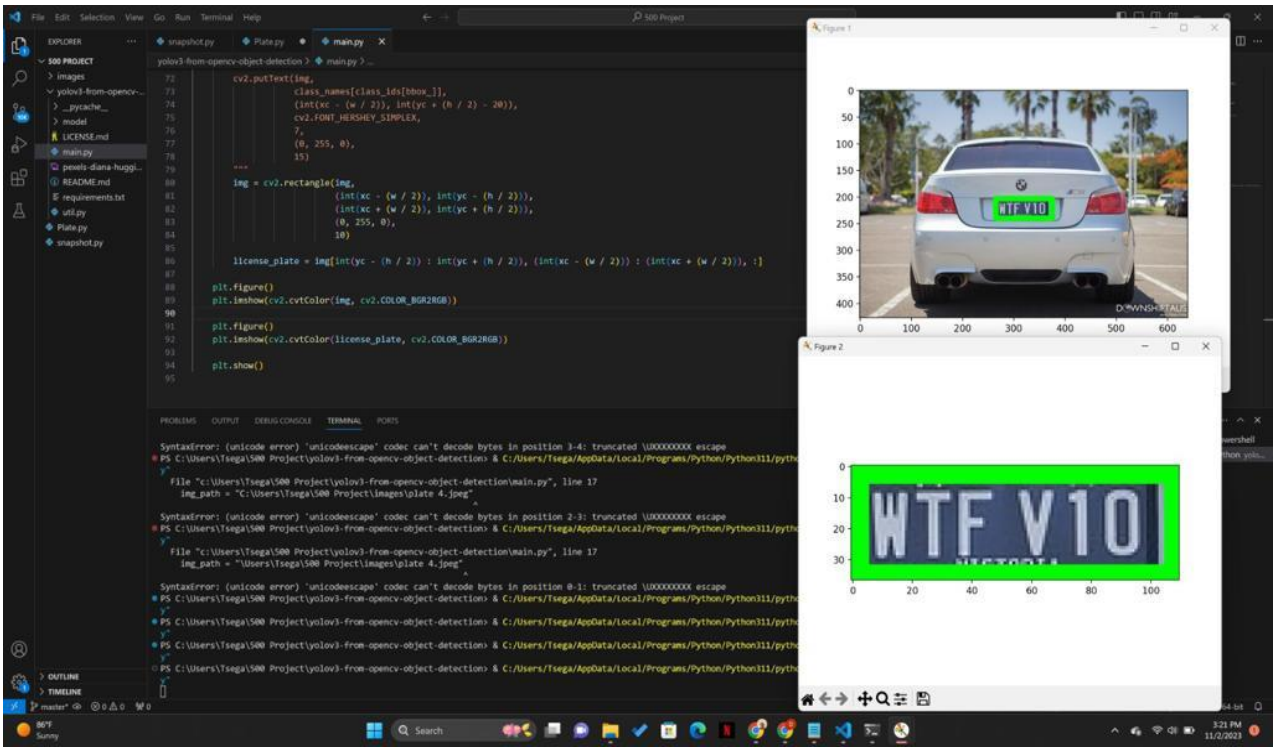


Fig. 15: Image processing of vehicle with plate number WTF V10: plate number detection, segmentation and capturing with time stamps.



Fig. 16: Image processing of vehicle with plate number HR268U0375: plate number detection, segmentation and capturing with time stamps.



Fig. 17: Image processing of vehicle with plate number KL 25B 2001: plate number detection, segmentation and capturing with time stamps.

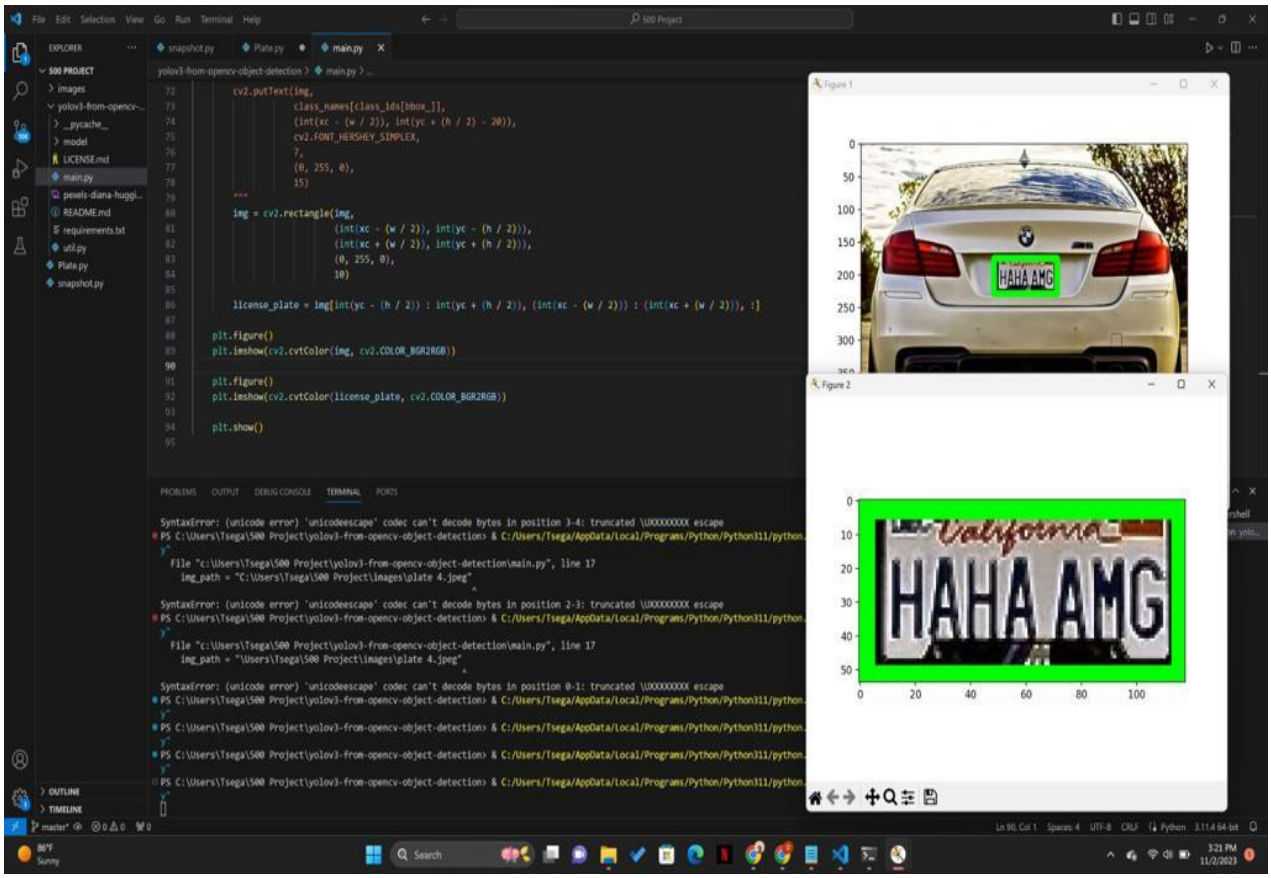


Fig. 18: Image processing of vehicle with plate number HAHA AMG: plate number detection, segmentation and capturing with time stamps.

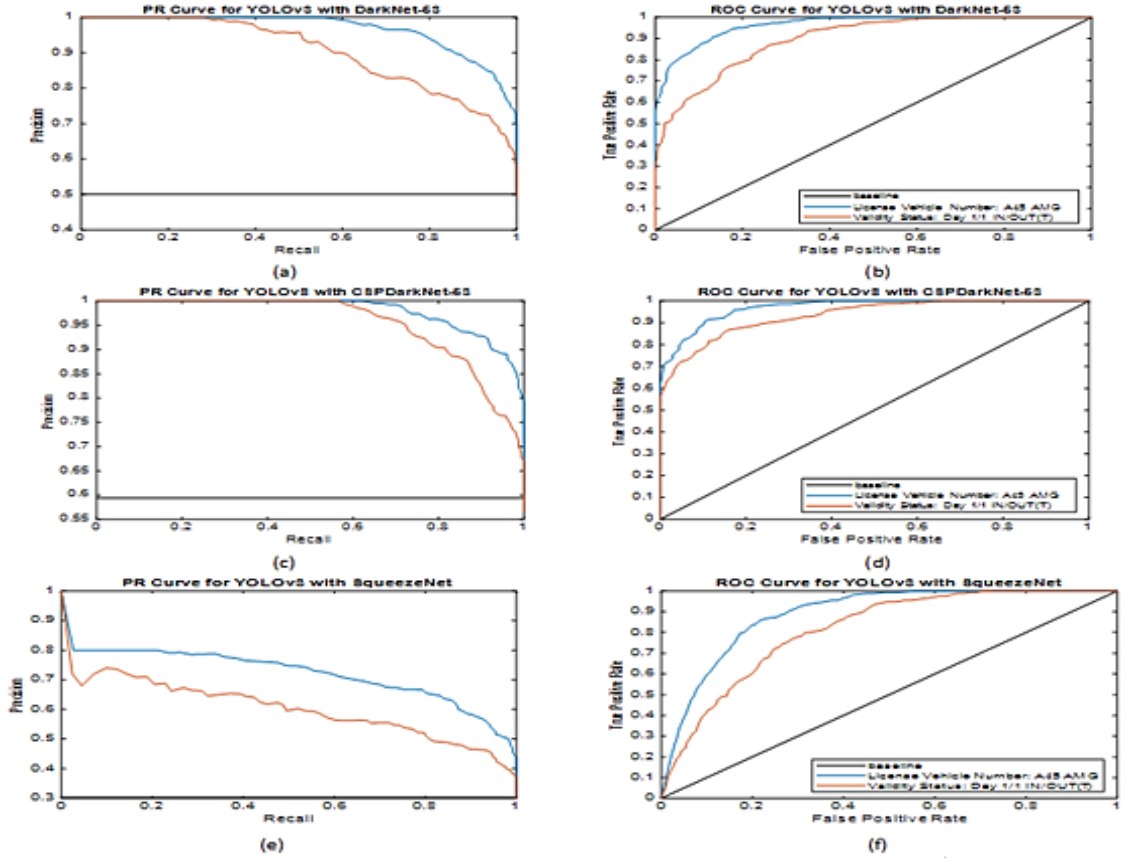


Fig. 19: PR and ROC curves for LPN A45 AMG by: YOLOv3 using DarkNet-53 (a) and (b); YOLOv8 using CSPDarknet-53 (c) and (d); and YOLOv3 using SqueezeNet (e) and (f) respectively.

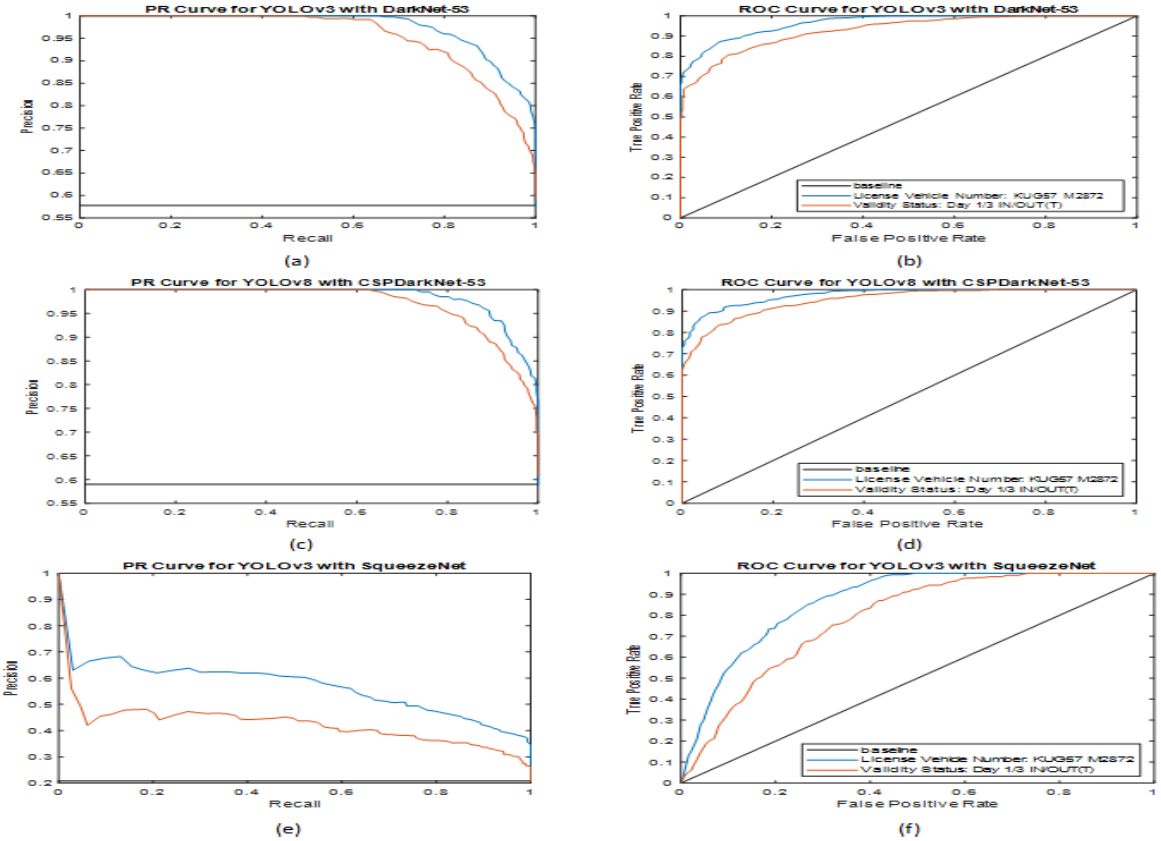


Fig. 20: PR and ROC curves for LPN KUG57 M2872 by: YOLOv3 using DarkNet-53 (a) and (b); YOLOv8 using CSPDarknet-53 (c) and (d); and YOLOv3 using SqueezeNet (e) and (f) respectively.

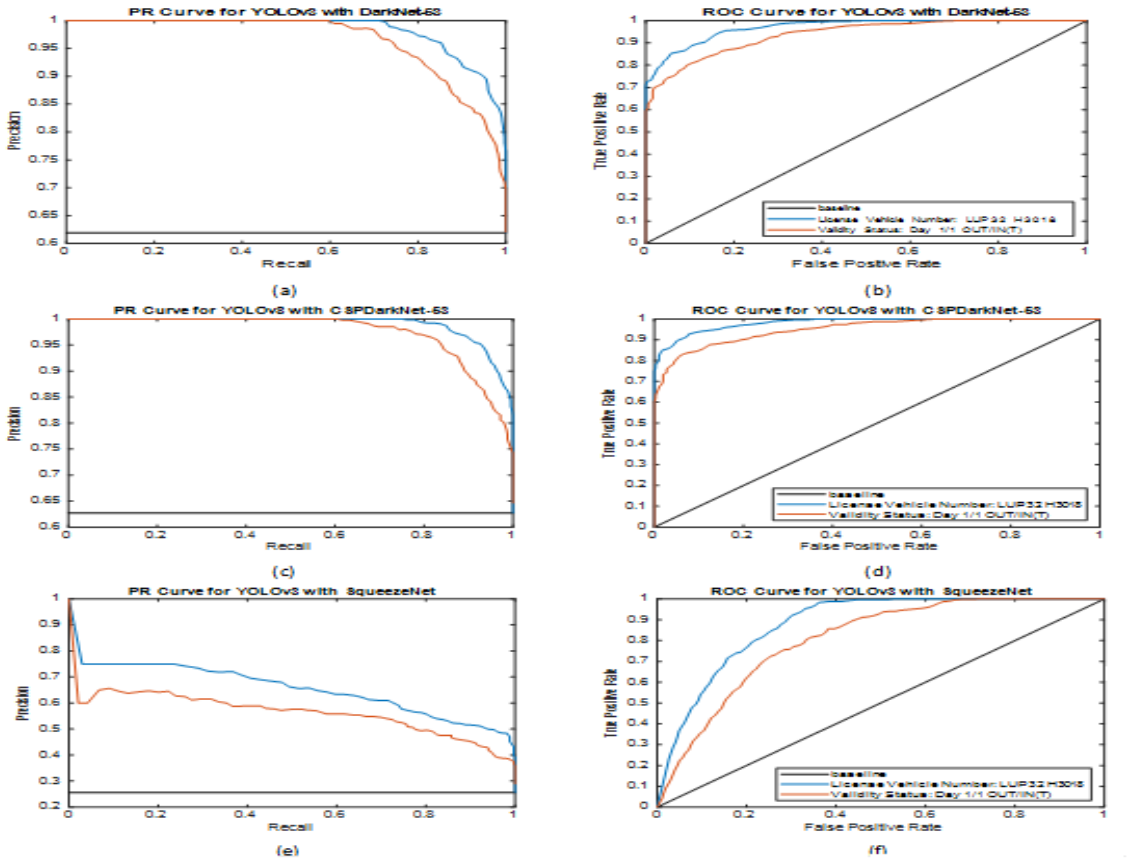


Fig. 21: PR and ROC curves for LPN LUP32 H3018 by: YOLOv3 using DarkNet-53 (a) and (b); YOLOv8 using CSPDarknet-53 (c) and (d); and YOLOv3 using SqueezeNet (e) and (f) respectively.

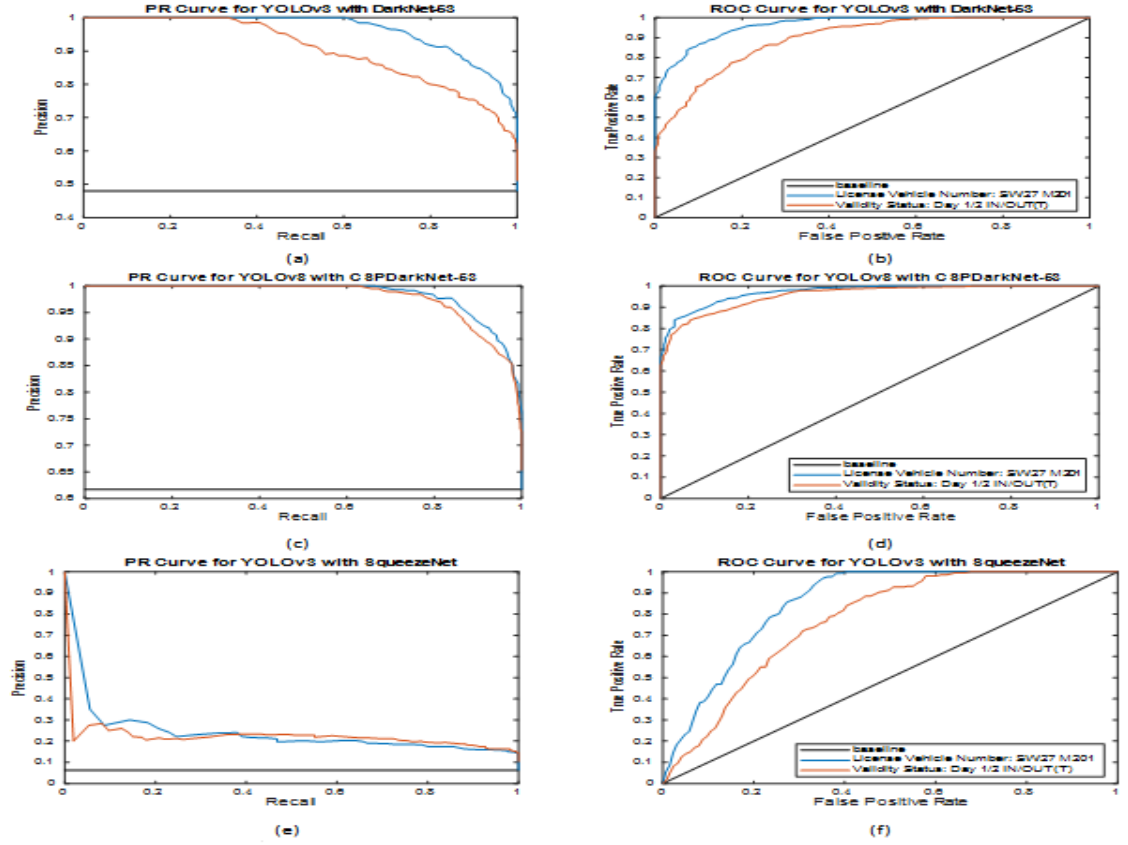


Fig. 22: PR and ROC curves for LPN SW27 M201 by: YOLOv3 with DarkNet-53 (a) and (b); YOLOv8 with CSPDarknet-53 (c) and (d); and YOLOv3 with SqueezeNet (e) and (f) respectively.

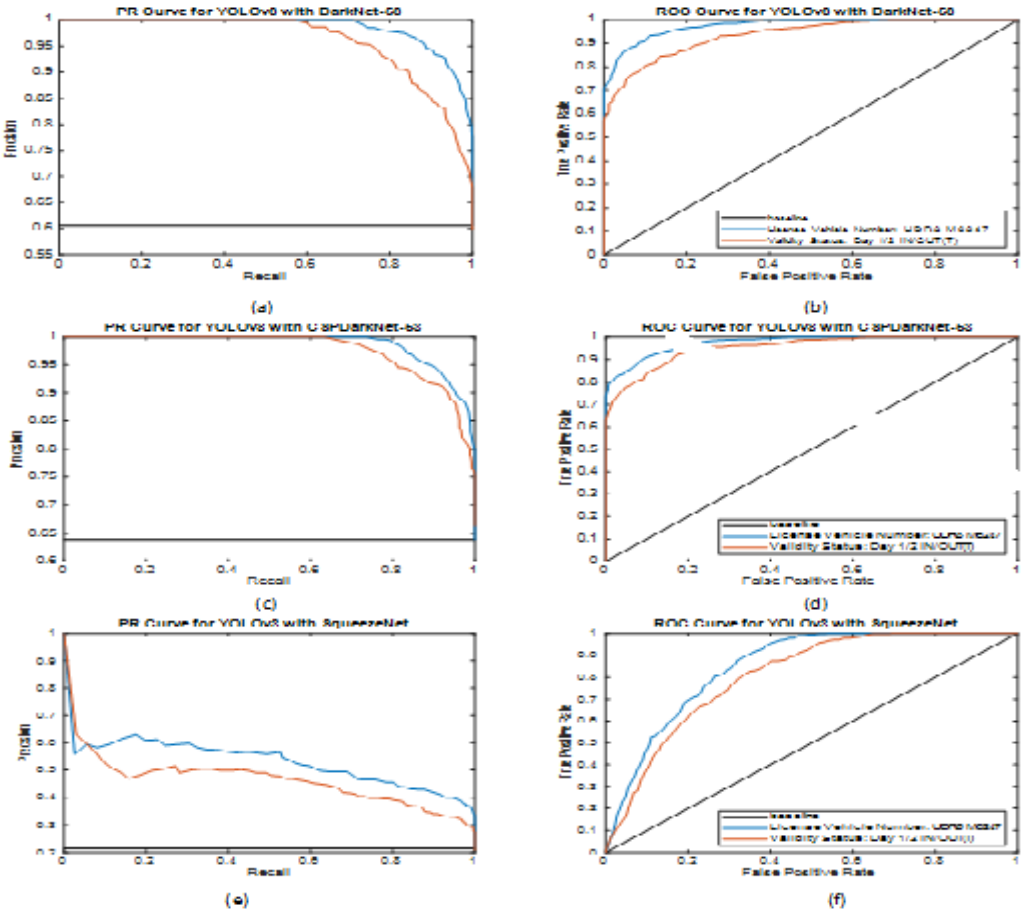


Fig. 23: PR and ROC curves for LPN UDR8 M6247 by: YOLOv3 with DarkNet-53 (a) and (b); YOLOv8 with CSPDarknet-53 (c) and (d); and YOLOv3 with SqueezeNet (e) and (f) respectively.

A. 2. Discussion of the Quantitative Results

The results obtained from the implementation and deployment of the AVIS together with the dynamic RDBS based on YOLOv3 with DarkNet-53 algorithm are shown in Fig. 15 to Fig. 18 as well as in Table 2 to Table 5. The databases shown in Table 2 to Table 4 are arranged in columns as follows: *1).* The first column is configured to record captured LPN serially at the point of entry and exit for up to 100 vehicles before resetting to serial number 1; *2).*

The second column records the Serial Integer Xi (where *i* is an integer that varies from 1 to 50 in accordance to the number of vehicle entry and exits based on captured plate numbers); *3).*The third column (*Image_url*) is the uniform resource locator (URL) webpage link that is automatically created by the PostgreSQL database for storing vehicle plate numbers with relevant information on Google cloud; *4)*. The date and time-stamp when the plate number is captured and the database is created is shown in the fourth column; *5)*. The date and time-stamps when the plate number is processed and stored in the database are shown in the fifth column; *6).*

The validity of the vehicle whether entry (False or True) as a Boolean variable (sixth column); 7*).* The seventh column (Plate Number) captures the actual vehicle plate number with unique ID Serial Integer (Xi); and *8).* The Status of the vehicle whether entering (IN) or exiting (OUT) as captured in the eight column. Note that once a vehicle originally in the company premises exits (OUT), it Boolean status is False and only changes to True when the vehicle returns (IN) into the company. Similarly, once a new vehicle enters (IN) the company premises, its Boolean validity status will be False and can only change to True when the vehicle exits (OUT). Furthermore, note that a vehicle is assigned a unique serial integer once captured whether at the point of entry (IN) or exit (OUT); and the same unique serial integer is used to verify when the vehicle exit (OUT) or enter (IN) the company's premises respectively. By comparing the time-stamp *created_at* and *processed_at*, it can be seen that the average time lag is 3 seconds; which implies that the database processing time is averagely 3 seconds between when the database is created and information stored for a particular captured vehicle license plate number (LPN) is updated.

Table 2: Database of vehicle inventory showing vehicle plate numbers, entry status (IN/OUT), processing time, time in/time out for Day 1 (18th March, 2024)

S/N	ID Serial Integer	Image_url	Created_at timestamp without time zone	Processed_at timestamp without time zone	Valid boolean	Plate_number character varying (100)	Status character string ($)
1	X1	http://storage.cloud.google.com/plate_images/A45AMG_952/21.1.jpg	2024-03-18 10:12:42.952	2024-03-18 10:12:46.691655	False	A45 AMG	IN
2	X2	http://storage.cloud.google.com/plate_images/KUG57M2872_245/11.3.jpg	2024-03-18 10:42:50.245	2024-03-18 10:42:53.731457	False	KUG57 M2872	IN
3	X3	http://storage.cloud.google.com/plate_images/LUP32H3018_691/17.4.jpg	2024-03-18 10:53:17.691	2024-03-18 10:53:20.540126	False	LUP32 H3018	OUT
4	X4	http://storage.cloud.google.com/plate_images/KAMEI_435/21.7.jpg	2024-03-18 11:14:50.435	2024-03-18 11:14:54.011789	False	KAMEI	IN
5	X5	http://storage.cloud.google.com/plate_images/SW27M201_435/19.2.jpg	2024-03-18 11:22:55.908	2024-03-18 11:22:58.155067	False	SW27 M201	IN
6	X1	http://storage.cloud.google.com/plate_images_A45AMG_567/32.6.jpg	2024-03-18 11:43:22.567	2024-03-18 11:43:26.539536	True	A45 AMG	OUT
7	X4	http://storage.cloud.google.com/plate_images_KAMEI_847/91.5.jpg	2024-03-18 11:54:13.847	2024-03-18 11:54:17.214581	True	KAMEI	OUT
8	X6	http://storage.cloud.google.com/plate_images/UDR8M6247_137/61.4.jpg	2024-03-18 12:06:43.137	2024-03-18 12:06:47.265734	False	UDR8 M6247	IN
9	X7	http://storage.cloud.google.com/plate_images/KL63E954_455/35.2.jpg	2024-03-18 12:26:34.455	2024-03-18 12:26:37.452863	False	KLS 3E 954	IN
10	X8	http://storage.cloud.google.com/plate_images/KL541H367_352/17.3.jpg	2024-03-18 12:38:44.352	2024-03-18 12:38:47.834242	False	KL 54H 369	IN
11	X9	http://storage.cloud.google.com/plate_images/WTG50KE042_406/82.4.jpg	2024-03-18 12:50:43.406	2024-03-18 12:50:43.641238	False	WTG50 KE042	IN
12	X10	http://storage.cloud.google.com/plate_images/KL55R2473_436/37.3.jpg	2024-03-18 01:10:34.436	2024-03-18 01:10:37.521894	False	KL 55R 2473	IN
13	X3	http://storage.cloud.google.com/plate_images/LUP32H3018_124/37.6.jpg	2024-03-18 01:33:43.124	2024-03-18 01:33:46.103958	True	LUP32 H3018	IN
14	X11	http://storage.cloud.google.com/plate_images/WB74X7603_728/42.5.jpg	2024-03-18 01:46:15.728	2024-03-18 01:46:18.594206	False	WB 74X 7603	IN
15	X12	http://storage.cloud.google.com/plate_images/VNE40L1533_155/71.8.jpg	2024-03-18 01:55:56.155	2024-03-18 01:55:59..621548	False	VNE40 L1533	OUT

B. Discussion of Results

B. 1. Discussion of the Quantitative Results

The real-time implementation results are analyzed qualitatively to assess the performances of three pre-trained model architectures using multiple performance metrics discussed previously which include (i) accuracy, (ii) precision, (iii) recall, (iv) precision recall (PR), (v) F1-score, (vi) area under receiver operating characteristic curve (AUC-ROC), (vii) confusion matrix, (iii) mean average precision (mAP), and (ix) execution time. All the results discussed in this section are presented in their respective figures and tables.

1). Accuracy: Accuracy is an important metric in deep learning that shows the proportion of correctly predicted samples over the total number of samples according to (4). As it can be seen in the second row of Table 8, the YOLOv8 with CSPDarkNet-53 has the best accuracy of 99.8572% followed by YOLOv3 using DarkNet-53 and YOLOv3 with SqueezeNet with an average accuracy of 99.7640% and 91.4080% respectively.

2). Precision: Precision is another important metric which shows the proportion of correct detection and recognition of the LPN. Precision quantifies the accuracy of positive predictions.

Table 3: Database of vehicle inventory showing vehicle plate numbers, entry status (IN/OUT), processing time, time in/time out for Day 2 (19th March, 2024)

S/N	ID Serial Integer	Image_url	Created_at timestamp without time zone	Processed_at timestamp without time zone	Valid boolean	Plate_number character varying (100)	Status character string ($)
16	X13	http://storage.cloud.google.com/plate_images/ZRP38K2041_851/82.5.jpg	2024-03-19 10:08:25.851	2024-03-19 10:08:28.534855	False	ZRP38 K2041	IN
17	X14	http://storage.cloud.google.com/plate_images/RJ27TC0530_501/31.4.jpg	2024-03-19 10:28:37.501	2024-03-19 10:28:40.292431	False	RJ27 TC0530	IN
18	X15	http://storage.cloud.google.com/plate_images/HR260U0375_035/71.1.jpg	2024-03-19 10:48:58.035	2024-03-19 10:49:02.117239	False	HR26BU0375	IN
19	X5	http://storage.cloud.google.com/plate_images/SW27M201_634/22.6.jpg	2024-03-19 10:52:35.634	2024-03-19 10:52:38.223064	True	SW27 M201	OUT
20	X16	http://storage.cloud.google.com/plate_images/YJP21Z542_2131/76.2.jpg	2024-03-19 11:06:27.213	2024-03-19 11:06:30.761524	False	YJP 21Z 542	OUT
21	X17	http://storage.cloud.google.com/plate_images/WPA27X6437_914/52.4.jpg	2024-03-19 11:18:35.914	2024-03-19 11:18:38.425567	False	WPA27 X6437	OUT
22	X6	http://storage.cloud.google.com/plate_images/UDR8M6247_807/10.8.jpg	2024-03-19 11:32:14.807	2024-03-19 11:32:18.390182	True	UDR8 M6247	OUT
23	X18	http://storage.cloud.google.com/plate_images/KL25B2001_011/76.4.jpg	2024-03-19 11:54:28.011	2024-03-19 11:54:31.426713	False	KL 25 B 2001	IN
24	X19	http://storage.cloud.google.com/plate_images/KA51M2143_532/31.4.jpg	2024-03-19 12:08:39.532	2024-03-19 12:08:15.431810	False	KA 51M 2143	IN
25	X20	http://storage.cloud.google.com/plate_images/WTFV103_664/82.7.jpg	2024-03-19 12:23:56.319	2024-03-19 12:23:59.060542	False	WTF V10	OUT
26	X12	http://storage.cloud.google.com/plate_images/VNE40L1533_107/20.8.jpg	2024-03-19 12:30:19.107	2024-03-19 12:30:22.002587	True	VNE40 L1533	IN
27	X9	http://storage.cloud.google.com/plate_images/WTG50KE042_209/91.7.jpg	2024-03-19 12:43:27.209	2024-03-19 12:43:30.870913	True	WTG50 KE042	OUT
28	X21	http://storage.cloud.google.com/plate_images/HAHAAMG_651/38.4.jpg	2024-03-19 12:58:07.419	2024-03-19 12:58:10.139457	False	HAHA AMG	IN
29	X7	http://storage.cloud.google.com/plate_images/KLS3E954_705/30.3.jpg	2024-03-19 01:14:40.705	2024-03-19 01:14:45.307933	True	KLS 3E 954	OUT
30	X16	http://storage.cloud.google.com/plate_images/YJP21Z542_514/32.0.jpg	2024-03-19 01:28:47.514	2024-03-19 01:28:50.223305	True	YJP 21Z 542	IN
31	X8	http://storage.cloud.google.com/plate_images/KL54H369_632/54.6.jpg	2024-03-19 01:42:50.632	2024-03-19 01:42:53.055446	True	KL 54H 369	OUT
32	X22	http://storage.cloud.google.com/plate_images/ABJ97G3318_414/32.7.jpg	2024-03-19 01:50:25.414	2024-03-19 01:50:28.743216	False	ABJ97 G3318	OUT
33	X20	http://storage.cloud.google.com/plate_images/WTFV103_159/30.4.jpg	2024-03-19 01:57:09.327	2024-03-19 01:57:12.654127	True	WTF V10	IN

In terms of precision, the YOLOv8 with CSPDarkNet-53 slightly outperforms the YOLOv3 with CSPDarkNet-53 while the YOLOv3 with DarkNet-53 outperforms the YOLOv3 using SqueezeNet as evident in the third row of Table 8 with precisions of 99.8656%, 99.7908% and 91.6472% respectively.

3). Recall: Recall, also known as sensitivity or the true positive rate, is a crucial evaluation metric in object detection models such as those considered in this work. Recall quantifies the model's ability to correctly identify all relevant instances of a particular object class within a given image dataset.

Table 4: Database of vehicle inventory showing vehicle plate numbers, entry status (IN/OUT), processing time, time in/time out for Day 3 (20th March, 2024)

S/N	ID Serial Integer	Image_url	Created_at timestamp without time zone	Processed_at timestamp without time zone	Valid boolean	Plate_number character varying (100)	Status character string ($)
34	X10	http://storage.cloud.google.com/plate_images/KL55R2473_316/11.6.jpg	2024-03-20 10:13:38.316	2024-03-20 01:13:41.161115	True	KL 55R 2473	OUT
35	X23	http://storage.cloud.google.com/plate_images/AGL67P3516_317/58.7.jpg	2024-03-20 10:33:45.317	2024-03-20 10:33:48.785421	False	AGL67 P3516	IN
36	X11	http://storage.cloud.google.com/plate_images/WB74X7603_838/30.2.jpg	2024-03-20 11:13:51.838	2024-03-20 11:13:54.230089	True	WB 74X 7603	OUT
37	X14	http://storage.cloud.google.com/plate_images/RJ27TC0530_164/81.4.jpg	2024-03-20 11:43:49.164	2024-03-20 11:43:52.418535	True	RJ27 TC0530	OUT
38	X2	http://storage.cloud.google.com/plate_images/KUG57M2872_057/53.6.jpg	2024-03-20 11:57:27.057	2024-03-20 11:57:30.653204	True	KUG57 M2872	OUT
39	X21	http://storage.cloud.google.com/plate_images/HAHAAMG_309/32.7.jpg	2024-03-19 12:08:13.207	2024-03-19 12:08:16.276248	True	HAHA AMG	OUT
40	X24	http://storage.cloud.google.com/plate_images/BUP841C740_318/46.1.jpg	2024-03-20 12:17:27.318	2024-03-20 12:17:30.016472	False	BUP841 C740	IN
41	X25	http://storage.cloud.google.com/plate_images/AAZ64EK24_924/34.2.jpg	2024-03-20 12:39:30.924	2024-03-20 12:39:33.103246	False	AAZ64 EK24	IN
42	X15	http://storage.cloud.google.com/plate_images/HR260U0375_203/42.7.jpg	2024-03-20 12:43:52.203	2024-03-20 12:43:55.740717	True	HR26BU0375	OUT
43	X18	http://storage.cloud.google.com/plate_images/KL25B2001_172/39.4.jpg	2024-03-20 01:10:53.172	2024-03-20 01:10:56.794933	True	KL 25 B 2001	OUT
44	X24	http://storage.cloud.google.com/plate_images/BUP841C740_363/29.7.jpg	2024-03-20 01:23:32.363	2024-03-20 01:23:35.279215	True	BUP841 C740	OUT
45	X19	http://storage.cloud.google.com/plate_images/KA51M2143_152/49.7.jpg	2024-03-20 01:37:53.152	2024-03-20 01:37:56.479095	True	KA 51M 2143	OUT
46	X23	http://storage.cloud.google.com/plate_images/AGL67P3516_416/28.6.jpg	2024-03-20 01:49:24.416	2024-03-20 01:49:27.169782	True	AGL67 P3516	OUT

Table 5: Summary of vehicle entry and exit status with days and validity status

S/N	ID Serial Integer	Plate Number	Day1 Status (18/03/2024)		Day 2 Status (19/03/2024)		Day 3 Status (20/03/2024)		Validity Status
1	X1	A45 AMG	IN (F)	OUT (T)					True
2	X2	KUG57 M2872	IN (F)				OUT (T)		True
3	X3	LUP32 H3018	OUT (F)	IN (T)					True
4	X4	KAMEI	IN (F)	OUT (T)					True
5	X5	SW27 M201	IN (F)			OUT (T)			True
6	X6	UDR8 M6247	IN (F)			OUT (T)			True
7	X7	KLS 3E 954	IN (F)			OUT (T)			True
8	X8	KL 54H 369	IN (F)			OUT (T)			True
9	X9	WTG50 KE042	IN (F)			OUT (T)			True
10	X10	KL 55R 2473	IN (F)				OUT (T)		True
11	X11	WB 74X 7603	IN (F)				OUT (T)		True
12	X12	VNE40 L1533	OUT (F)			IN (T)			True
13	X13	ZRP38 K0241			IN (F)				**False**
14	X14	RJ27 TC0530			IN (F)		OUT (T)		True
15	X15	HR26BU0375			IN (F)		OUT (T)		True
16	X16	YJP21Z 542			OUT (F)	IN (T)			True
17	X17	WPA27 X6437			OUT (F)				**False**
18	X18	KL 25 B 2001			IN (F)		OUT (T)		True
19	X19	KA 51M 2143			IN (F)		OUT (T)		True
20	X20	WTF V10			OUT (F)	IN (T)			True
21	X21	HAHA AMG			IN (F)		OUT (T)		True
22	X22	ABJ97 G3318			OUT (F)				**False**
23	X23	AGL67 P3516					IN (F)	OUT (T)	True
24	X24	BUP841 C740					IN (F)	OUT (T)	True
25	X25	AAZ64 EK24					IN (F)		**False**

Table 6: Confusion matrix showing minimum and maximum percentage of correct detections for target LPNs using YOLOv3 with DarkNet-53, YOLOv8 using CSPDarkNet-53, and YOLOv3 using SqueezeNet

S/N	ID Serial Integer	License Plate Number	Validity Status	% Success by YOLOv3 with DarkNet-53		% Success by YOLOv8 with CSPDarkNet-53		% Success by YOLOv3 with SqueezeNet	
				min	max	min	max	min	max
1	X1	A45 AMG	Status: Day 1/1 IN/OUT (T)	68.4	91.2	71.4	95.2	60.0	80.0
2	X2	KUG57 M2872	Status: Day 1/3 IN/OUT (T)	69.0	92.0	71.9	95.8	58.8	78.4
3	X3	LUP32 H3018	Status: Day 1/1 OUT/IN (T)	70.8	94.4	72.3	96.4	59.5	79.2
4	X4	KAMEI	Status: Day 1 IN (F)	72.3	92.1	71.2	95.4	56.7	77.4
5	X5	SW27 M201	Status: Day 1/2 IN/OUT (T)	67.8	90.4	71.4	95.2	55.8	74.4
6	X6	UDR8 M6247	Status: Day 1/2 IN/OUT (T)	70.2	93.6	73.0	97.4	57.6	76.8
7	X7	KLS 3E 954	Status: Day 1/2 IN/OUT (T)	69.6	94.3	71.2	96.3	58.7	79.5
8	X8	KL 54H 369	Status: Day 1/2 IN/OUT (T)	68.5	93.8	72.1	96.5	58.8	78.4
9	X9	WTG50 KE042	Status: Day 1/2 IN/OUT (T)	70.2	94.6	71.3	97.5	57.6	77.3
10	X10	KL 55R 2473	Status: Day 1/3 IN/OUT (T)	70.1	92.4	72.2	95.1	57.5	77.3
11	X11	WB 74X 7603	Status: Day 1/3 IN/OUT (T)	70.4	93.3	72.2	95.4	57.3	78.2
12	X12	VNE40 L1533	Status: Day 1/2 OUT/IN (T)	69.6	94.2	72.1	96.3	56.4	78.5
13	X13	ZRP38 K0241	Status: Day 2 IN (F)	68.5	94.8	71.6	96.2	58.2	79.6
14	X14	RJ27 TC0530	Status: Day 2/3 IN/OUT (T)	67.7	91.4	71.7	96.8	59.1	74.4
15	X15	HR26BU0375	Status: Day 2/3 IN/OUT (T)	71.3	92.3	73.4	95.7	56.5	75.2
16	X16	YJP21Z 542	Status: Day 2/2 OUT/IN (T)	70.2	94.3	72.6	95.6	60.4	75.1
17	X17	WPA27 X6437	Status: Day 2 OUT (F)	68.2	93.2	71.8	95.5	57.8	76.3
18	X18	KL 25 B 2001	Status: Day 2/3 IN/OUT (T)	67.3	94.2	73.4	96.4	58.7	74.5
19	X19	KA 51M 2143	Status: Day 2/3 IN/OUT (T)	68.1	91.9	72.5	95.6	58.6	74.6
20	X20	WTF V10	Status: Day 2/2 OUT/IN (T)	68.6	92.6	72.3	96.7	56.5	75.4
21	X21	HAHA AMG	Status: Day 2/3 IN/OUT (T)	71.5	92.7	72.2	97.6	60.4	76.5
22	X22	ABJ97 G3318	Status: Day 2 OUT (F)	69.7	93.8	71.2	95.2	57.3	75.2
23	X23	AGL67 P3516	Status: Day 3/3 IN/OUT (T)	69.8	94.9	73.1	95.4	56.2	77.1
24	X24	BUP841 C740	Status: Day 3/3 IN/OUT (T)	69.5	94.8	72.5	96.3	58.1	78.2
25	X25	AAZ64 EK24	Status: Day 3 IN (F)	72.4	93.7	71.4	95.3	60.5	79.6

Based on the recall performance evaluation, it can be seen in the fourth row of Table 8 that the YOLOv8 with CSPDarkNet-53 and YOLOv3 with DarkNet-53 perform well with average recall values of 99.8828% and 99.8164% respectively while YOLOv3 with SqueezeNet has 91.7112%.

4). *Precision-recall (PR):* PR curves are a common way to visualize the trade-off between precision and recall at various confidence thresholds. The precision-recall (PR) score measures how well the model correctly captures positive cases. It is the ratio of the true positives to the sum of the true positives and false negatives. As shown in the fifth row of Table 8, the deep CNN based on the YOLOv8 with CSPDarkNet-53 model architecture achieved an outstanding PR value of 0.9044 when compared to the 0.8852 and 0.6044 obtained using the YOLOv3 with DarkNet-53 and YOLOv3 with SqueezeNet-53 models respectively. This extremely high PR rates emphasize the effectiveness of the YOLOv8 with CSPDarkNet-53 and YOLOv3 with DarkNet-53 models in identifying positive cases correctly, hence reducing false negatives. These results follow from the PR curves of Figs. 19–23 for all the vehicles and the computation of the respective average values from the 7th column of Table 7 are given in the fifth row of Table 8.

5). *The F1-Score:* The F1-score represents the harmonic mean of precision and precision recall. In terms of the F1-score, the deep CNN based on the YOLOv8 with CSPDarkNet-53 model architecture shows superior performance which is closely followed by YOLOv3 with DarkNet-53 and the less performance YOLOv3 with SqueezeNet model architecture with an F1-score of 99.9012%, 99.8544% and 91.7680% respectively from the sixth row of Table 8. Thus, the first two models signify balanced performances in F1-scores.

Table 7: Performance comparison metrics for the deep CNN based on YOLOv3 with DarkNet-53, YOLOv8 with CSPDarkNet-53, and YOLOv3 with SqueezeNet

S/N	License Plate Number	YOLO Model Architectures	Performance Metrics								
			Accuracy (%)	Precision (%)	Recall (%)	Precision Recall (PR)	F1-Score (%)	AUC-ROC (%)	Confusion Matrix Accuracy (%)	Mean Average Precision (mAP) (%)	Execution Time (s)
1	A45 AMG	Yv3D	99.81	99.74	99.91	0.85	99.84	99.90	99.91	98.91	154.46
		Yv8C	99.92	99.86	99.94	0.87	99.90	99.92	99.94	99.51	1658.53
		Yv3S	90.24	91.21	91.67	0.54	91.46	91.76	91.76	87.60	97.55
2	KUG57 M2872	Yv3D	99.75	99.80	99.80	0.82	99.88	99.84	99.90	99.21	167.23
		Yv8C	99.86	99.87	99.88	0.87	99.92	99.91	99.93	99.60	1768.33
		Yv3S	91.72	91.69	90.98	0.68	91.96	91.93	92.89	86.70	101.34
3	LUP32 H3018	Yv3D	99.83	99.88	99.63	0.88	99.77	99.93	99.90	99.42	184.61
		Yv8C	99.92	99.92	99.78	0.89	99.86	99.95	99.94	99.71	1678.52
		Yv3S	89.86	90.61	91.74	0.53	91.98	91.89	91.97	86.91	110.45
4	KAMEI	Yv3D	99.55	99.90	99.85	0.89	99.75	99.90	99.92	99.38	185.41
		Yv8C	99.78	99.94	99.92	0.91	99.86	99.93	99.94	99.62	1757.12
		Yv3S	90.34	91.72	92.79	0.69	91.89	91.87	90.98	85.54	116.44
5	SW27 M201	Yv3D	99.62	99.61	99.75	0.88	99.90	99.92	99.93	98.82	183.46
		Yv8C	99.87	99.73	99.83	0.89	99.94	99.94	99.96	99.51	1778.32
		Yv3S	89.95	92.88	93.92	0.56	91.86	91.82	89.85	84.90	109.57
6	UDR8 M6247	Yv3D	99.81	99.89	99.89	0.91	99.87	99.91	99.90	99.30	174.08
		Yv8C	99.83	99.92	99.92	0.93	99.92	99.93	99.95	99.80	1768.30
		Yv3S	90.87	90.39	91.87	0.72	91.99	91.97	90.88	85.80	111.45
7	KLS 3E 954	Yv3D	99.64	99.77	99.77	0.87	99.90	99.92	99.92	98.89	165.38
		Yv8C	99.78	99.84	99.86	0.90	99.93	99.95	99.94	99.78	1698.54
		Yv3S	91.35	89.88	92.79	0.55	91.91	91.90	91.91	85.74	108.29
8	KL 54H 369	Yv3D	99.65	99.87	99.80	0.89	99.87	99.93	99.92	98.82	171.09
		Yv8C	99.79	99.90	99.88	0.91	99.92	99.96	99.94	99.69	1632.28
		Yv3S	93.49	91.93	91.97	0.63	91.83	91.79	91.67	85.87	116.52
9	WTG50 KE042	Yv3D	99.71	99.69	99.77	0.90	99.88	99.92	99.90	99.48	158.34
		Yv8C	99.82	99.70	99.88	0.93	99.90	99.95	99.93	99.58	1617.50
		Yv3S	92.68	91.97	90.69	0.61	91.94	91.90	91.69	84.98	94.35
10	KL 55R 2473	Yv3D	99.77	99.80	99.76	0.89	99.86	99.90	99.91	99.77	161.33
		Yv8C	99.86	99.88	99.87	0.92	99.90	99.93	99.94	99.92	1568.42
		Yv3S	91.69	90.97	89.98	0.57	91.79	91.86	90.87	86.76	107.32
11	WB 74X 7603	Yv3D	99.83	99.68	99.90	0.90	99.89	99.92	99.92	99.47	159.21
		Yv8C	99.86	99.78	99.93	0.92	99.91	99.94	99.94	99.85	1534.50
		Yv3S	90.85	91.98	90.98	0.64	91.83	91.88	91.85	86.81	103.25
12	VNE40 L1533	Yv3D	99.66	99.76	99.89	0.88	99.77	99.91	99.91	99.74	184.14
		Yv8C	99.74	99.89	99.93	0.91	99.88	99.93	99.94	99.87	1652.09
		Yv3S	91.94	92.97	91.86	0.68	91.94	91.94	91.79	87.54	127.55
13	ZRP38 K0241	Yv3D	99.67	99.76	99.76	0.91	99.87	99.93	99.92	98.67	193.18
		Yv8C	99.87	99.85	99.85	0.92	99.92	99.96	99.95	99.85	1612.16
		Yv3S	91.81	91.96	91.82	0.66	91.99	91.89	92.99	86.39	137.39
14	RJ27 TC0530	Yv3D	99.84	99.74	99.90	0.89	99.89	99.93	99.94	98.59	201.43
		Yv8C	99.88	99.85	99.93	0.90	99.93	99.96	99.96	99.81	1719.22
		Yv3S	90.93	89.89	91.99	0.53	91.85	91.97	91.97	85.87	153.42
15	HR26BU0375	Yv3D	99.69	99.66	99.84	0.87	99.79	99.92	99.90	99.69	204.46
		Yv8C	99.73	99.78	99.89	0.89	99.86	99.94	99.93	99.78	1699.38
		Yv3S	91.99	91.89	89.90	0.61	90.86	91.91	91.88	87.62	167.54
16	YJP21Z 542	Yv3D	99.85	99.88	99.77	0.89	99.69	99.90	99.94	98.99	167.50
		Yv8C	99.90	99.94	99.87	0.91	99.78	99.93	99.96	99.69	1690.19
		Yv3S	92.97	90.89	90.69	0.58	91.87	91.87	91.90	85.86	104.40
17	WPA27 X6437	Yv3D	99.89	99.80	99.59	0.88	99.84	99.93	99.91	99.58	198.33
		Yv8C	99.96	99.87	99.64	0.90	99.89	99.95	99.93	99.67	1640.36
		Yv3S	91.67	91.88	91.89	0.61	91.95	91.97	90.79	84.98	136.46
18	KL 25 B 2001	Yv3D	99.78	99.83	99.88	0.90	99.88	99.92	99.88	98.98	176.35
		Yv8C	99.87	99.92	99.92	0.91	99.93	99.94	99.91	99.68	1597.42
		Yv3S	89.76	92.84	93.96	0.57	91.94	91.69	91.93	86.56	117.04
19	KA 51M 2143	Yv3D	99.88	99.89	99.79	0.89	99.83	99.90	99.90	99.45	201.31
		Yv8C	99.91	99.92	99.85	0.90	99.87	99.93	99.93	99.74	1600.55
		Yv3S	90.96	91.98	92.89	0.63	90.94	91.99	91.89	87.48	147.44
20	WTF V10	Yv3D	99.69	99.74	99.90	0.88	99.97	99.91	99.92	99.53	153.09
		Yv8C	99.78	99.87	99.94	0.90	99.89	99.93	99.95	99.76	1549.54
		Yv3S	91.99	91.97	90.98	0.59	92.93	91.97	90.68	86.95	92.55
21	HAHA AMG	Yv3D	99.79	99.80	99.90	0.87	99.88	99.92	99.92	99.61	166.27
		Yv8C	99.86	99.86	99.95	0.89	99.92	99.95	99.94	99.76	1642.16
		Yv3S	92.91	90.91	91.80	0.52	92.97	91.87	91.91	86.91	105.22
22	ABJ97 G3318	Yv3D	99.88	99.87	99.80	0.89	99.90	99.92	99.90	98.87	184.51
		Yv8C	99.92	99.91	99.88	0.91	99.93	99.95	99.93	99.72	1597.40
		Yv3S	91.58	92.98	89.97	0.53	90.98	91.77	89.89	86.87	126.34
23	AGL67 P3516	Yv3D	99.87	99.73	99.89	0.90	99.89	99.92	99.93	98.88	181.27
		Yv8C	99.92	99.86	99.93	0.91	99.92	99.95	99.96	99.67	1576.33
		Yv3S	92.88	92.88	92.86	0.58	91.86	91.82	91.90	86.88	125.55
24	BUP841 C740	Yv3D	99.86	99.88	99.77	0.91	99.88	99.91	99.94	99.65	177.43
		Yv8C	99.89	99.90	99.86	0.92	99.93	99.93	99.96	99.74	1596.32
		Yv3S	90.89	90.94	91.91	0.63	91.69	91.67	90.89	87.51	118.34
25	AAZ64 EK24	Yv3D	99.78	99.80	99.90	0.89	99.87	99.90	99.92	99.54	203.14
		Yv8C	99.91	99.88	99.94	0.90	99.92	99.93	99.94	99.66	1620.52
		Yv3S	89.88	91.97	90.88	0.67	89.99	91.89	91.96	85.43	149.44

Key: Yv3D = YOLOv3 with DarkNet-53, Yv8C = YOLOv8 with CSPDarkNet-53, Yv3S = YOLOv3 with SqueezeNet

Table 8: Average values of the performance metrics for YOLOv3 with DarkNet-53, YOLOv8 with CSPDarkNet-53, and YOLOv3 with SqueezeNet model architectures

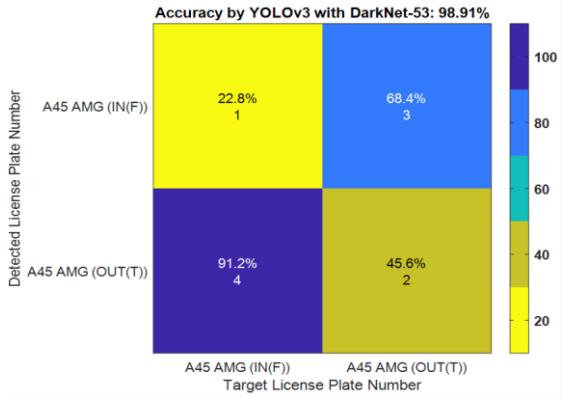
S/N	Performance Metrics		YOLOv3 with DarkNet-53	YOLOv8 with CSPDarkNet-53	YOLOv3 with SqueezeNet
1	Accuracy (%)		99.7640	99.8572	91.4080
2	Precision (%)		99.7908	99.8656	91.6472
3	Recall (%)		99.8164	99.8828	91.7112
4	Precision-Recall (PR)		0.8852	0.9044	0.6044
5	F1-Score (%)		99.8544	99.9012	91.7680
6	AUC-ROC (%)		99.9124	99.9396	91.8716
7	Confusion Matrix Accuracy (%)		99.2496	99.7188	86.4184
8	Confusion matrix percentage successes in detected versus target LPN from Table C1 (%)	min	69.5880	72.0800	58.1200
		max	93.2360	96.0320	77.0840
9	Mean Average Precision (mAP) (%)		99.9144	99.9416	91.5476
10	Execution Time (s)		178.2804 (2.9713 mins)	1650.20 (4.5839 hrs)	119.4084 (1.9901 mins)

6). *AUC-ROC:* The Area Under the Receiver Operating Characteristic Curve (AUC-ROC) evaluates the performance of a model across all possible detection and recognition threshold, balancing sensitivity and specificity. The AUC-ROC results follow from the AUC-ROC curves shown in Figs. 19–23 and their respective numerical percentages are shown in the seventh row of Table 8 obtained from the ninth column of Table 7, where the deep CNN based on YOLOv8 with CSPDarkNet-53 and YOLOv3 with DarkNet-53 model architectures achieved the very high AUC-ROC scores across all LPN detection and recognition scenarios, boasting a near-perfect score of 99.9396% and 99.9124% respectively when compared to YOLOv3 with SqueezeNet with an average AUC-ROC score of 91.8716%. These results are further justified by the PR and ROC curves shown in Figs. 19–23 where YOLOv8 with CSPDarkNet-53 shows very high threshold values followed by YOLOv3 with DarkNet-53 model architectures.

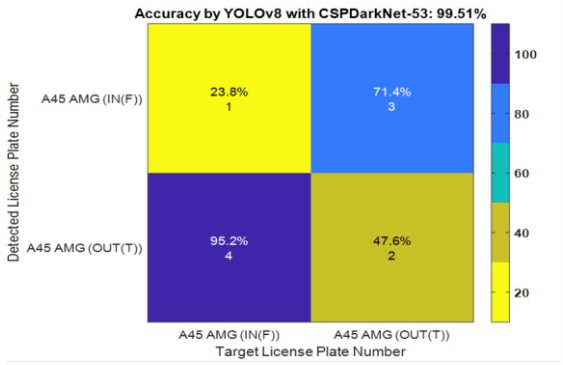
7). *Confusion Matrix:* The confusion matrix is a performance evaluation metric that visualizes the model's predictions against the ground truth, showing counts of true positives, false positives, and false negatives for each class. It helps assess how well the model is performing, identifies specific class-based errors, and provides a visual basis for calculating metrics like precision and recall. The confusion matrix typically considers thresholds for confidence and Intersection over Union (IoU) to classify predictions. The confusion matrices for the deep CNN based on the YOLOv8 with CSPDarkNet-53, YOLOv3 with DarkNet-53 and YOLOv3 with SqueezeNet model architectures are shown respectively in Figs. 24–28 for all the five LPN shown in this paper due to space economy.

It is obvious in all the five figures that the very percentage accuracies obtained by the YOLOv8 with CSPDarkNet-53 model exhibits robust performance followed by the YOLOv3 with DarkNet-53 model when compared to the lower performance recoded by YOLOv3 with SqueezeNet model. The percentage accuracies obtained from the confusion matrix for all the 25 vehicles considered in this work are shown in the tenth column of Table 7 for the three models. From Table 6 and Table 8, the average confusion matrix percentage accuracies obtained by the YOLOv8 with CSPDarkNet-53, YOLOv3 with DarkNet-53 and YOLOv3 with SqueezeNet models are 99.7188%, 99.2496% and 86.4148% respectively as given in the eighth row of Table 8. The results show that YOLOv8 with CSPDarkNet-53 recorded the highest average accuracy followed closely by YOLOv3 with DarkNet-53 with a lower average accuracy recorded by YOLOv3 with SqueezeNet model.

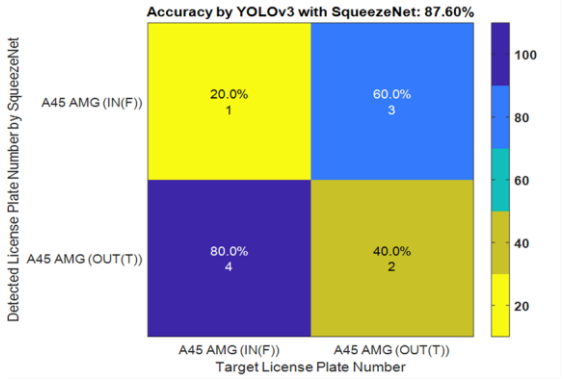
Furthermore, the minimum and maximum percentage successes in the detected versus target LPN of all 25 vehicles based on the confusion matrix are shown in Table 7 while their respective average values are shown in the ninth row of Table 8 for all the three models. From Table 8, the average respective minimum and maximum percentage successes of 72.0800% and 96.0320% obtained by the YOLOv8 with CSPDarkNet-53 model shows robust performance which is closely followed by an appreciable result of the YOLOv3 with DarkNet-53 model with average minimum and maximum percentage successes of 69.5880% and 93.2360% respectively when compared to the lower performance of 58.1200% and 77.0840% recoded by YOLOv3 with SqueezeNet model.



(a)

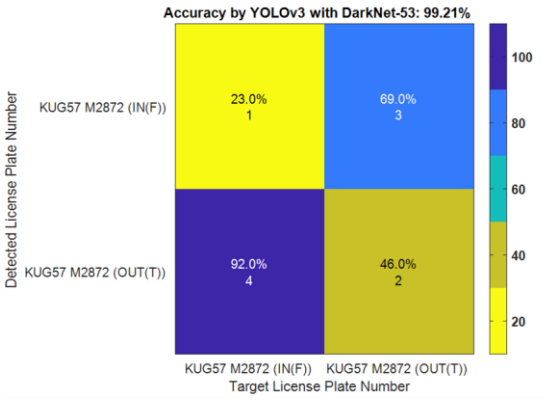


(b)

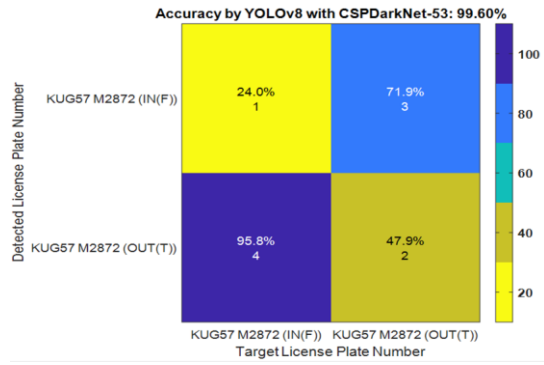


(c)

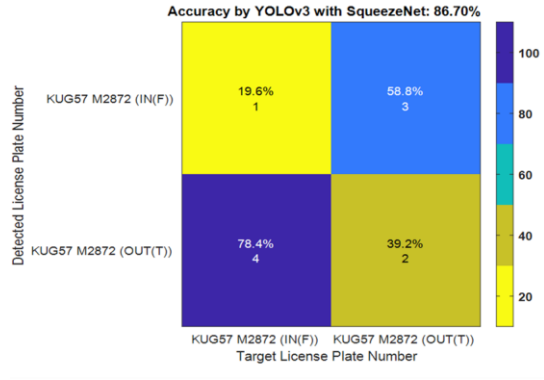
Fig. 24: Confusion matrix accuracy for LPN A45 AMG by: (a) YOLOv3 using DarkNet-53; (b) YOLOv8 using CSPDarknet-53; and (c) YOLOv3 using SqueezeNet.



(a)



(b)



(c)

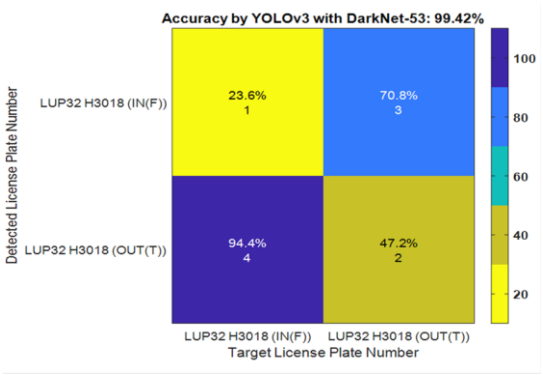
Fig. 25: Confusion matrix accuracy for LPN KUG57 M2872 by: (a) YOLOv3 using DarkNet-53; (b) YOLOv8 using CSPDarknet-53; and (c) YOLOv3 using SqueezeNet.

Summarily, the average percentage accuracies obtained from the confusion matrix shown in Table 6 and that of Figs. 24–28 for the three models shows that the YOLOv8 with CSPDarkNet-53 and YOLOv3 with DarkNet-53 models perform well in accurately detecting both TP, TN, FP and FN for the predicted classified and class target outputs when compared to YOLOv3 with SqueezeNet as also evident from Figs. 24–28.

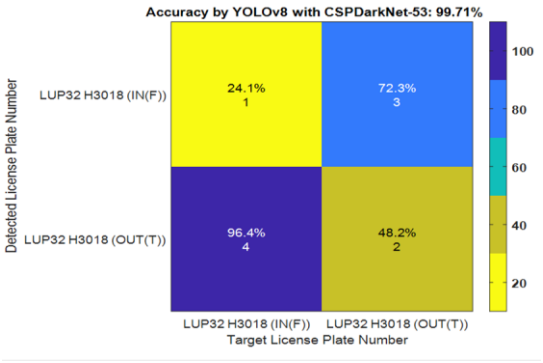
8). Mean Average Precision (mAP): Mean Average Precision (mAP) is a performance metric that summarizes accuracy by averaging the Average Precision (AP) for all object classes.

The mAP evaluates both the classification correctness and the localization accuracy of the model's bounding boxes, providing a single score to compare performance. A higher mAP score (from 0 to 1) indicates better performance, meaning the model is more accurate at identifying and locating objects. Please note that the mAPs are presented in this paper as percentages for quicker interpretation.

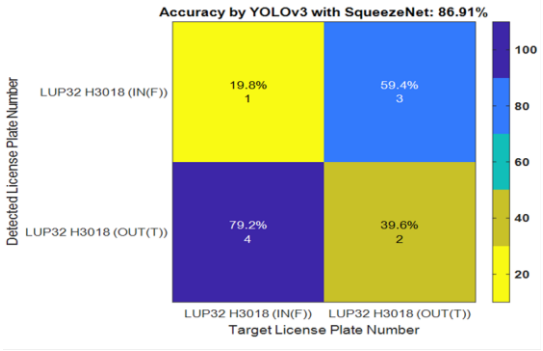
The mean average precision (mAP) for all the 25 LPN detection and recognition using the three models are shown in the eleventh column of Table 7 while the average values of the mAP are given in the tenth row of Table 8.



(a)

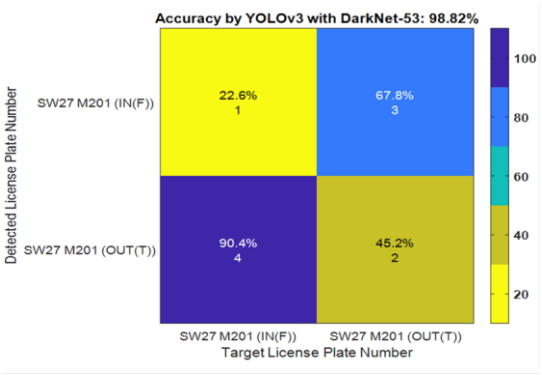


(b)

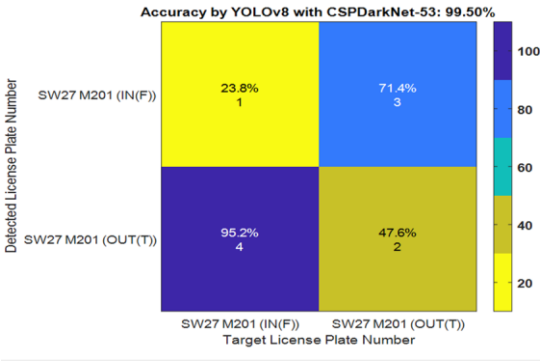


(c)

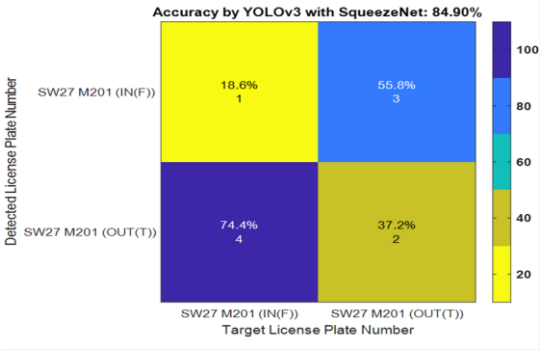
Fig. 26: Confusion matrix accuracy for LPN LUP32 H3018 by: (a) YOLOv3 with DarkNet-53; (b) YOLOv8 with CSPDarknet-53; and (c) YOLOv3 with SqueezeNet.



(a)



(b)



(c)

Fig. 27: Confusion matrix accuracy for LPN SW27 M201 by: (a) YOLOv3 with DarkNet-53; (b) YOLOv8 with CSPDarknet-53; and (c) YOLOv3 with SqueezeNet.

It can be seen that the mAP obtains by YOLOv8 with CSPDarkNet-53 and YOLOv3 with DarkNet-53 models perform closely well in prediction correctness and localization accuracy with mAP values of 99.9416% and 99.9144% respective when compared to a lower 91.5476 recorded by YOLOv3 using SqueezeNet model.

9). Execution Time: The execution time (or inference time) in real-time detection and recognition models from streaming videos is a critical factor that directly determines whether an application can achieve real-time performance, which is the primary strength and goal of the YOLO family of models such as the three model architectures considered in this work. The execution time influences the real-time application and success of the intended goals of the detection and recognition strategy. The three models were implemented on a Windows 11 Home, 16", Intel® Core™ i7-14700HX operating at 5.5 GHz, 16GB RAM, 512GB SSD, WQXGA, Natural silver) and the recorded execution times for the three models are shown in the twelfth column of Table 7 while the average values of the execution times are given in the eleventh row of Table 8.

It is evident that the YOLOv8 with CSPDarkNet-53 and YOLOv3 with SqueezeNet have the highest and lowest execution times of 1650.20 seconds (approximately 4.5839 or 4½ hours) and 119.4084 seconds (1.9901 or 2 minutes) respectively while the YOLOv3 with DarkNet-53 model requires approximately 178.2804 seconds (2.9713 or 3 minutes) for each implementation.

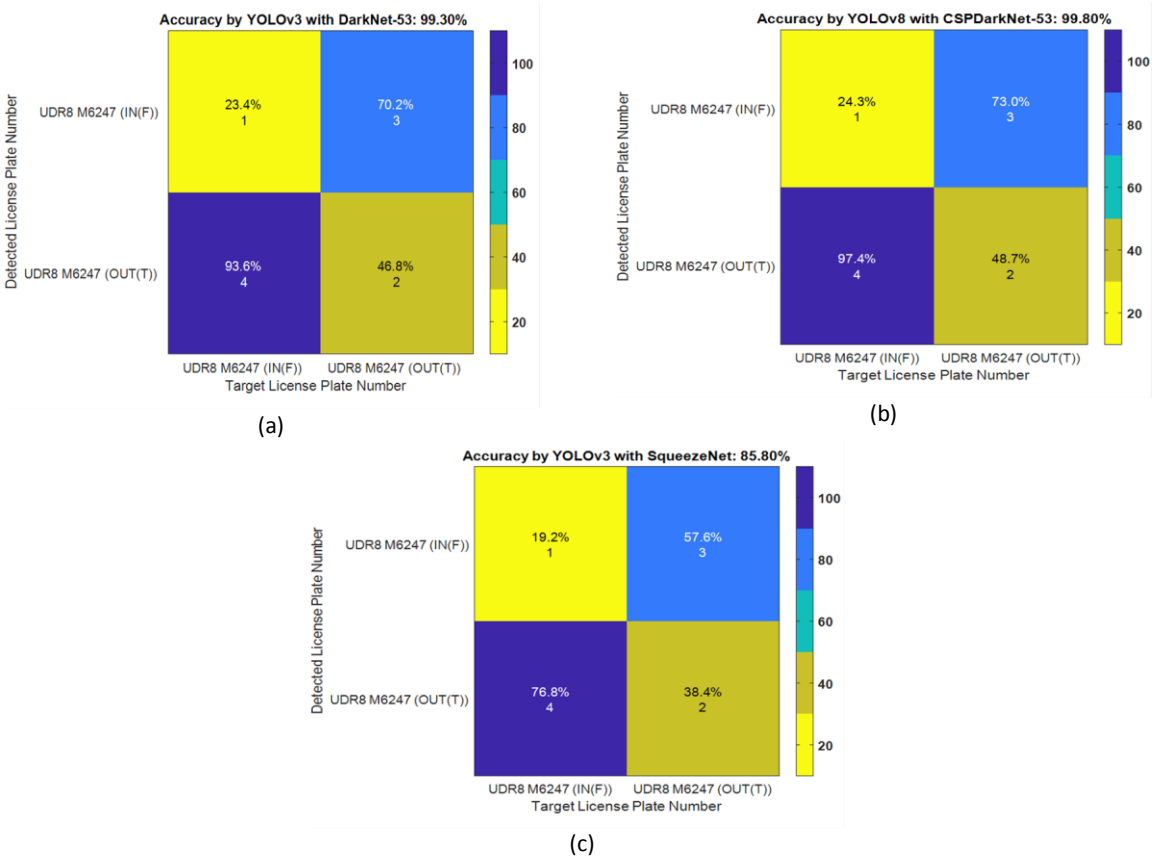


Fig. 28: Confusion matrix accuracy for LPN LUP32 H3018 by: (a) YOLOv3 with DarkNet-53; (b) YOLOv8 with CSPDarknet-53; and (c) YOLOv3 with SqueezeNet.

It is evident that the YOLOv3 with DarkNet-53 model is suitable for the current LPN detection and recognition based on the available computing hardware resources with the justified performance metrics achieved by the model at low hardware cost when compared to the YOLOv8 with CSPDarkNet-53 and YOLOv3 models.

B. 2. Discussion of the Qualitative Results

The feasibility and performance efficiency of the AVIS based on YOLOv3 with DarkNet-53 algorithm with dynamic RDBS has been implemented, tested and validated using an automobile car dealer company (Ola Motors Company located at No. 180 Oyemekun Road, Akure, Ondo State, Nigeria) premises as a case study with random 25 vehicles entering and/or leaving the premises for a period of three days between 10:00 am and 2:00 pm on each day.

The results from the AVIS implementation are shown in Fig. 15 to Fig. 18 respectively for the four case studies presented in this work due to space limitation and page number limit. The corresponding dynamic RDBS showing the vehicle plate number status either as IN and/or OUT together with their respective dates and time-stamps are shown in Table 2 to Table 4. Furthermore, Table 5 validates and shows the final validity status whether a particular vehicle entered without exiting or exited a particular vehicle entered without exiting or exited without returning to the premises as at the close of work by 2:00 pm daily.

The validity status of vehicle entry/exit and exit/entry status with days are summarized in Table 5. According to Table 2 to Table 5, note that the validity status for a particular vehicle is certified True only if that particular vehicle completes either entry/exit or exit/entry routines.

As it can be observed in Fig. 15 to Fig. 18, the AVIS based on the YOLOv3 with DarkNet-53 algorithm successfully captured the respective vehicle LPNs with their respective serial numbers, ID serial integers, time-stamps (created and processed), validity, plate number and the status as shown in Table 2 to Table 4 while the last row of Table 5 shows the final validity status of False which indicates whether a particular vehicle either entered without exiting or exiting without returning to the premises.

It can be seen in Fig. 15 that the YOLOv3 with DarkNet-53 correctly detects the plate number WTF V10 at the point of exit (OUT) on 19th March, 2024 (Day 2) at time 12:23:56 pm as captured by the database on serial number 25 with serial integer X20 on Table 3. The same vehicle with plate number WTF V10 returned back to the company premises on same day at time 01:57:09 pm

(33rd row). Note that the Validity (sixth column) changes from False (25th row) to True (33rd row) based on the unique ID serial integer.

As summarized in Table 5, for the vehicle with serial ID X20 and license plate number WTF V10, the system recorded an exit event (False) and a return event (True) on the same day (Day 2) which is indicated by validity status.

In another case, Fig. 16 shows a vehicle with plate number HR26BU0375 and automatically assigned ID serial integer of X15 that entered (IN) the company on 19th March, 2024 (Day 2) at time 10:48:58 am as captured and processed by the database at time 10:49:02 am on serial number 18 on Table 3. However, the vehicle (HR26BU0375) returned (IN) on Day 3 (20th March. 2025) at 12:43:52 pm as shown at S/N 42 on Table 4. As summarized in Table 5 with ID serial integer X15, the vehicle with plate number HR26BU0375 entered (False) the company on Day 2 and exit (True) on Day 3 which is indicated by the final validity status of True.

The same discussion in the last paragraph holds for Fig. 17 with ID serial integer of X18 and Fig. 18 with ID serial integer of X21. For the vehicle with plate number of KL 20 B 2001 having ID serial integer of X18 in Table 3, Table 4 and Table 5. The entry (IN) time-stamp on Day 2 with False status and exit (OUT) time-stamp on Day 3 with True status are 11:54:28 am and 01:10:53 pm respectively. It is noted the vehicle entered on Day 2 (Table 3) and exited on Day 3 (Table 4) which is reflected in Table 5 with a validity status of True.

As summarized in Table 5, vehicles with plate numbers: *1).* ZRP38 K0241 (ID serial integer X13) entered (False) the company on Day 2 at time 10:08:25 am (Table 3) without leaving the company's premises as at end of this demonstration with a validity status of False; *2).* WPA27 X6437 (ID serial integer X17) and ABJ97 G3318 (ID serial integer X22) exited the company's premises on Day 2 at 11:18:35 am and 01:50:25 pm respectively without returning and thus leaving the validity status as False; and *3).* AAZ64 EK24 (ID serial integer X25) entered (IN) the company's premises on Day 3 (see Table 4) at time 12:39:30 pm without exiting and renders the validity status as False as can be seen in Table 4 and Table 5.

Conclusion and Future Directions

A. Conclusion

A cost-effective automatic vehicle inventory system (AVIS) using the YOLOv3 with DarkNet-53 algorithm with a PostgreSQL dynamic relational database system and Google cloud storage have been designed, implemented and deployed as demonstrated for LPN detection and recognition with successful results.

The performance and efficiency of the AVIS have been demonstrated using the Ola Motors Company (located at No. 180 Oyemekun Road, Akure, Ondo State, Nigeria) premises as a case study on random 25 vehicles for a period of three days between 10:00 am to 2:00 pm on each day.

Quantitatively, results shows that the proposed AVIS based on YOLOv3 using DarkNet-53 competes favourably with YOLOv8 using CSPDarkNet-53 with near equal results within 3 minutes when compared to the about 4½ hours required by the later to achieve the same result.

Qualitatively, the techniques presented and the results obtained from the implementation and deployment of the AVIS demonstrate the efficiency and suitability of the proposed AVIS with a dynamic relational database system (RDBS) for deployment in establishments, companies, institutions, organizations, and government agencies for vehicle inventory management, monitoring, security surveillance, and the development of automatic vehicle inventory systems.

The study also highlights the importance of timely and accurate data collection from streaming video sources for optimizing vehicle inventory management, control, and operational processes. Furthermore, the use of dynamic relational database systems, such as PostgreSQL, in conjunction with Google Cloud Storage, enables flexible and efficient data storage and retrieval, thereby ensuring accurate, reliable, and up-to-date vehicle inventory information.

B. Future Directions

The deployment of two IP-based cameras within the AVIS can improve vehicle license plate number (LPN) capture for independent entry and exit routes. Although the AVIS was implemented on a Core i7 CPU operating at 5.5 GHz, it is worth noting that deploying the proposed AVIS with PostgreSQL and Google Cloud Storage on high-performance computing platforms, such as GPUs, multi-core CPUs, Jetson Nano devices, or FPGAs, could significantly reduce execution times. Such improvements would facilitate operation under hard real-time constraints and support shorter sampling intervals for LPN capture, tracking, detection, and recognition. Furthermore, the CNN–GRU model proposed by Suvarnam and Ch [76], together with the integration of the OCR-based text recognition method suggested by Sunayana and Asim [35], could be incorporated into the AVIS to enable character recognition without explicit character segmentation.

The use of IP-based night vision cameras with up to 1.5 km coverage and routers with fast Internet connectivity for the capture of vehicle license plate numbers during night times, in dark environments and

other varying weather conditions would improve the performance of the AVIS. Incorporating the YOLOv3-based AVIS with the suggestions of Dorbe [77] for the use of fully connected network (FCN) and long short temporary memory (LSTM) based computer vision system for recognition of vehicle type, license plate number, and registration country would create a more effective platform for real-time monitoring and tracking of vehicles.

It is expected that the incorporation of the proposed recommendations in future work will enhance the AVIS by improving the accuracy and efficiency of vehicle LPN capture, real-time vehicle monitoring and tracking, and the secure storage of captured data, while also reducing database synchronization latency and improving overall system performance..

Author Contributions

V. A. Akpan conceptualized and designed the project. All authors carried out the search and review of literature. D. A. Adegoke, E. T. Adejayan and K. A. Adepoju provided funding for the project. V. A. Akpan supervised the project while implementation was done by D. A. Adegoke, E. T. Adejayan and K. A. Adepoju. Furthermore, D. A. Adegoke, E. T. Adejayan and K. A. Adepoju collected all the necessary data for the project. V. A. Akpan wrote the original manuscript. All authors revised and discussed the results and approved the final reviewed manuscript.

Funding

This research is not supported by any external funding.

Acknowledgment

The authors gratefully acknowledge Alhaji Jimoh Momoh, Chief Executive Officer (CEO) of Ola Motors Company (located at No. 180 Oyemekun Road, Akure, Ondo State, Nigeria), for allowing his Company and premises to be used for the demonstration of this project.

The authors also wish to acknowledge the Editor-in-Chief of JECEI, Members of the Editorial Board, and the Reviewers for their helpful comments, excellent and thorough review of this paper which has enhanced the quality of this paper.

Conflict of Interest

The authors declare no potential conflict of interest regarding the publication of this work. In addition, the ethical issues including plagiarism, informed consent, misconduct, data fabrication and, or falsification, double publication and, or submission, and redundancy have been completely witnessed by the authors.

Abbreviations

AVIS	Automatic Vehicle Inventory System
RDBS	Relational Database System
IP	Internet Protocol
YOLOv3	You Only Look Once version 3
YOLOv8	You Only Look Once version 8
PoE	Power-over-Ethernet
Wi-Fi	Wireless Fidelity
FPN	Feature Pyramid Network
IOU	Intersection Over Union
NMS	Non-Maximum Suppression
CCTV	Closed Circuit Television
SQL	Structured Query Language
OpenCV	Open Computer Vision
URL	Uniform Resource Locator
VPN	Vehicle Plate Number
AVL	Automatic Vehicle Location
ANPR	Automatic Number Plate Recognition
LPR	License Plate Recognition
PoE	Power-over-Ethernet
LPN	License Plate Number
mAP	Mean Average Precision
CNN	Convolutional Neural Network
AUC-ROC	Area Under Receiver Operating Characteristic Curve
PR	Precision-Recall
ROI	Region of Interest
ReLU	Rectified Linear Unit
OCR	Optical Character Recognition

DHCP	Dynamic Host Configuration Protocol
Wi-Fi	Wireless Fidelity
TP	True Positive
TN	True Negative
FP	False Positive
FN	False Negative
LiDAR	Light Detection and Ranging
NVR	Network Video Recorder
LSTM	Long Short Temporary Memory
FCN	Fully Connected Network
AP	Average Precision
LED	Light Emitting Diode
GPU	Graphical Processing Unit
GRU	Gate Recurrent Unit
CPU	Central Processing Unit

References

[1] N. Owamoyo, A. Fadele, A. Abudu, "Number plate recognition for nigerian vehicles," Academic Research International, 4(3): 48-55, 2013.

[2] A. M. Atieh, H. Kaylani, Y. Al-Abdallat, A. Qaderi, L. Ghou, "Performance improvement of inventory management system processes by an automated warehouse management system," Procedia CIRP, 41: 568-572, 2016.

[3] B. Barabino, M. D. Francesco, "Diagnosis of irregularity sources by automatic vehicle location data," IEEE Intell. Trans. Syst. Mag., 13: 152-165, 2019.

[4] B. Barabino, M. D. Francesco, S. Mozzoni, "Regularity analysis on bus networks and route directions by automatic vehicle location raw data," IET Intell. Transp. Syst., 7(4): 471-480, 2013.

[5] B. Barabino, M. D. Francesco, S. Mozzoni, "Regularity diagnosis by automatic vehicle location raw data," Public Transp., 4: 187-208, 2013.

[6] M. Buzinkay, "Vehicle inventory management: A data-driven business," Last update 25th January, 2025. Retrieved 13th July, 2025.

[7] J. D. Power, "Automotive inventory management software," Last update 25th January, 2025. Retrieved 13th July, 2025..

[8] M. Karanam, A. K. Reddy, P. Mathyam, A. Mohammed, S. Naik, "Automatic vacant parking places management system using multicamera vehicle detection," in Proc. E3S Web of Conferences, 391(01045): 1-7, 2023.

[9] N. Shvai, A. Hasnat, A. Meicler, "Accurate classification for automatic vehicle-type recognition based on ensemble classifiers," IEEE Trans. Intell. Transp. Syst., 21(3): 1288-1297, 2020.

[10] M. Hussain, "YOLO-v1 to YOLO-v8, the rise of YOLO and its complementary nature toward digital manufacturing and industrial defect detection," Machines, 11(677): 1-25, 2023.

[11] A. Mirkhan, "YOLO algorithm: Real-time object detection from A to Z," Retrieved 13th July, 2025.

[12] J. Nelson, "What is YOLO? The Ultimate Guide [2025]," Last updated 9th January, 2025. Retrieved 13th July, 2025.

[13] R. Kundu, "YOLO: Algorithm for object detection explained," Last updated 17th January, 2023. Retrieved 13th July, 2025.

[14] Z. Keita, "YOLO object detection explained: Understand YOLO object detection, its benefits, how it has evolved over the years, and some real-life applications," Last updated 28th September, 2024. Retrieved 13th July, 2025.

[15] J. Redmon, A. Farhadi, "YOLOv3: An incremental improvement," in Proc. the IEEE Conference on Computer Vision and Pattern Recognition: 7794-7803, 2018.

[16] M. Nagpal, "The ultimate guide to YOLOv3 architecture," Last updated 28th October, 2024. Retrieved 13th July, 2025.

[17] K. J. Oguine, O. C. Oguine, H. I. Bisallah, "YOLO v3: Visual and real-time object detection model for smart surveillance systems (3s)," in Proc. the 2022 5th Information Technology for Education and Development (ITED): 1-8, 2022.

[18] N. Klingler, "YOLOv3: Real-time object detection algorithm (Guide)," Last updated 2nd January, 2022. Retrieved 13th July, 2025.

[19] L. Zhao, S. Li, "Object detection algorithm based on improved YOLOv3," Electronics, 9(537): 1-11, 2020.

[20] S. K. Rajput, J. C. Patni, S. S. Alshamrani, V. Chaudhari, V. Chaudhari, A. Dumka, R. Singh, M. Rashid, A. Gehlot, A. S. AlGhamdi, "Automatic vehicle identification and classification model using the YOLOv3 algorithm for a toll management system," Sustainability, 14(15): 9163. 2022.

[21] Y. Li, J. Wang, J. Huang, Y. Li, "Research on deep learning automatic vehicle recognition algorithm based on RES-YOLO model," Sensors, 22(10): 3783, 2022.

[22] J. J. Wu, H. Xu, J. Zheng, J. Zhao, "Automatic vehicle detection with roadside LiDAR data under rainy and snowy conditions," IEEE Intell. Transp. Syst. Mag., 13(1): 197-209, 2021.

[23] Y. Cui, S. Liu, J. Yao, C. Gu, "Integrated positioning system of unmanned automatic vehicle in coal mines," IEEE Trans. Instrum. Meas., 70: 1-13, 2021.

[24] M. M. Ahmed, M. Abdel-Aty, "The viability of using automatic vehicle identification data for real-time crash prediction," IEEE Trans. Intell. Transp. Syst., 13(2): 459-468, 2012.

[25] M. M. Ahmed, M. Abdel-Aty, R. Yu, "Bayesian updating approach for real-time safety evaluation with automatic vehicle identification data," Transp. Res. Record, 2280: 6067, 2012.

[26] X. Luo et al., "Fast automatic vehicle detection in UAV images using convolutional neural networks," Remote Sens., 12(12):1-15, 2020.

[27] P. Li, W. Zhao, "Image fire detection algorithms based on convolutional neural networks," Case Studies in Thermal Engineering, 19(100625): 1-11, 2020.

[28] H. Zhang, X. Chao, C. Shi, "Closing the gap: A learning algorithm for lost-sales inventory systems with lead times," Manag. Sci., 66(5): 1962-1980, 2020.

[29] G. van Houtum, B. Kranenburg, "Spare parts inventory control under system availability constraints," International Series in Operations Research & Management Science, Springer Nature, London, Chapter 8, pp. 1 – 215, 2015.

[30] D. Abadi, "Consistency tradeoffs in modern distributed database system design: CAP is only part of the story," Computer, 45(2): 37-42, 2012.

[31] Z. Xu, W. Yang, A. Meng, N. Lu, H. Huang, C. Ying, L. Huang, "Towards end-to-end license plate detection and recognition: a large dataset and baseline," in Proc. Part XIII of the 15th European Conference on Computer Vision – ECCV 2018: 261-277, 2018.

[32] P. A. Ioannou, Z. Xu, "Throttle and brake control systems for automatic vehicle following," California Partners for Advanced Transportation Technology UC Berkeley Research Reports: 1-36, 1994.

[33] P. R. M. Júnior, J. M. R. Neves, A. I. Tavares, D. Menotti, "Towards an automatic vehicle access control system: License plate location," in the Proc. the 2011 IEEE International Conference on Systems, Man and Cybernetics: 2916-2921, 2011.

[34] J. Tang, L. Wan, J. Schooling, P. Zhao, J. Chen, S. Wei, "Automatic Number Plate Recognition (ANPR) in smart cities: A systematic review on technological advancements and application cases," Cities, 129(103833): 1-15, 2022.

[35] A. S. Kumar, A. Dharshan, C. Sekhar, S. Manikanta, "Detection of non-helmet riders and extraction of license plate number," in Proc. International Conference on Innovations in Engineering and Technology (ICIET): 1- 7, 2023.

[36] Z. Ma, L. Ferreira, M. Mesbah, "Measuring service reliability using automatic vehicle location data," Math. Probl. Eng., 2014(1): 1-12, 2014.

[37] R. Islam, K. F. Sharif, S. Biswas, "Automatic vehicle number plate recognition using structured elements," in Proc. The 2015 IEEE Conference on Systems, Process and Control: 44-48, 2015.

[38] P. Prabhakar, P. Anupama, S. Resmi, "Automatic vehicle number plate detection and recognition," in Proc. the 2014 IEEE International Conference on Control, Instrumentation, Communication and Computational Technologies (ICCICCT 2014): 185- 190, 2014.

[39] C. L. Azevedo, J. L. Cardoso, M. Ben-Akiva, J. P. Costeira, M. Maeques, "Automatic vehicle trajectory extraction by aerial remote sensing," Procedia: Social Behav. Sci., 111: 849-858, 2014.

[40] J. Wu, "An automatic procedure for vehicle tracking with a roadside LiDAR sensor," in Proc. the 97th Annual Meeting of the Transportation Research Board: 32-38, 2018.

[41] N. Sulaiman, S. N. H. M. Jalani, M. Mustafa, K. Hawari, "Development of automatic vehicle plate detection system," in Proc. the 2013 IEEE 3rd International Conference on System Engineering and Technology: 130-135, 2013.

[42] T. D. Duan, D. Tran, P. V. Tran, N. V. Hoang, "Building an automatic vehicle license-plate recognition system" in Proc. the International Conference in Computer Science (RIVF'05): 59 – 63, 2005.

[43] H. Kim, B. Song, "Vehicle recognition based on radar and vision sensor fusion for automatic emergency braking," i the Proc. the 2013 13th International Conference on Control, Automation and Systems: 1342 – 1346, 2013.

[44] Z. Wang, F. Chan, "A robust replenishment and production control policy for a single-stage production/inventory system with inventory inaccuracy," IEEE Trans. Syst., Man Cybern.: Syst., 45(2): 326-337, 2015.

[45] A. Krishnamoorthy, R. Manikandan, B. Lakshmy, "A revisit to queueing-inventory system with positive service time," Ann. Oper. Res., 233: 221- 236, 2015.

[46] P. Sharma, S. Gupta, P. Singh, K. Shejul, D. Reddy, "Automatic number plate recognition," in Proc. the 2022 International Conference on Advances in Computing, Communication and Applied Informatics (ACCAI): 1-8, 2022.

[47] P. Patil, C. Kanagasabapathi, S. Yellampalli, "Automatic number plate recognition system for vehicle identification," in Proc. the 2017 International Conference on Electrical, Electronics, Communication, Computer, and Optimization Techniques (ICEECCOT): 431-434, 2017.

[48] M. P. Atkinson, F. Bancilhon, D. DeWitt, K. Dittrich, D. Maier, S. Zdonik, "The Object-Oriented Database System Manifesto," in Building an Object-Oriented Database System: The Story of O_2: 1 - 20, 1992.

[49] Y. Feng, J. Sun, P. Chen, "Vehicle trajectory reconstruction using automatic vehicle identification and traffic count data," J. Adv. Transp., 49: 174-194, 2015.

[50] E. Oomoto, K. Tanaka, "OVID: Design and implementation of a video-object database system," IEEE Trans. Knowl. Data Eng., 5: 629-643, 1993.

[51] N. V. Oort, D. Sparing, T. Brands, R. M. P. Goverde, "Optimizing public transport planning and operations using automatic vehicle location data: the dutch example," in Proc. the 3rd International Conference on Models and Technologies for Intelligent Transportation Systems: 291-300, 2013.

[52] X. Zhao, F. Fan, X. Liu, J. Xie, "Storage-space capacitated inventory system with (r, Q) policies," Oper. Res., 55: 854- 865, 2007.

[53] S. Tuermer, J. Leitloff, P. Rernartz, U. Stilla, "Automatic vehicle detection in aerial image sequences of urban areas using 3d hog features," The International Archives of the Photogrammetry, Remote Sensing and Spatial Information Sciences, 38: 50-54, 2010.

[54] J. Wu, H. Xu, Y. Zheng, Y. Zhang, B. Lv, Z. Tian, "Automatic vehicle classification using roadside LiDAR data," Transp. Res. Rec., 2673: 153-164, 2019.

[55] P. Manuel, B. Sivakumar, G. Arivarignan, "A perishable inventory system with service facilities, MAP arrivals and PH – Service times," J. Syst. Sci. Syst. Eng., 16: 62-73, 2007.

[56] P. Manuel, B. Sivakumar, G. Arivarignan, "Perishable inventory system with postponed demands and negative customers," J. Appl. Math. Decis. Sci., 2007(94850): 1-12, 2007.

[57] P. Manuel, B. Sivakumar, G. Arivarignan, "A perishable inventory system with service facilities and retrial customers," Comput. Ind. Eng., 54: 484-501, 2008.

[58] T. Moranduzzo, F. Melgani, "Automatic car counting method for unmanned aerial vehicle images," IEEE Trans. Geosci. Remote Sens., 52(3): 1635- 1647, 2014.

[59] P. Petru, "What is YOLOv3? An Introductory Guide," Last updated 26th March, 2024. Retrieved 13th July, 2025.

[60] Y. Dai, W. Liu, H. Li, L. Liu, "Efficient foreign object detection between PSDs and metro doors via deep neural networks," IEEE Access, 8: 46723-46734, 2020.

[61] T. Y. Lin, P. Dollár, R. Girshick, K. He, B. Hariharan, S. Belongie, "Feature pyramid networks for object detection," in Proc. the 2017 IEEE Conference on Computer Vision and Pattern Recognition (CVPR): - 2125, 2017.

[62] J. Hui, "Understanding Feature Pyramid Networks for object detection (FPN)" Last updated 28th March, 2018. Retrieved 13th July, 2025.

[63] N. H. Quang, H. Lee, N. Kim, G. Kim, "Real-time flash flood detection employing the YOLOv8 model," Earth Sci. Inf., 17: 4809-4829, 2024.

[64] H. A. Parhusip, S. Trihandaru, D. Indrajaya, J. Labadin, "Implementation of YOLOv8-seg on store products to speed up the scanning process at point of sales," IAES Int. J. Artif. Intell., 13(3): 3291-3305, 2024.

[65] M. R. Upadhyay, S. Ushasukhanya, V. R. R. Teja, T. N. Malleswari, K. V. N. S. Mahendra, "A deep learning approach for pothole detection using Yolov8 model," in Proc. the International Conference on Advancement in Renewable Energy and Intelligent Systems (AREIS): 1-6, 2024.

[66] B. Khalili, A. W. Smyth, "SOD-YOLOv8—Enhancing YOLOv8 for small object detection in aerial imagery and traffic scenes," Sensors, 24(6209): 1-24, 2024.

[67] J. Terven, D. M. Córdova-Esparza, J. A. Romero-González, "A comprehensive review of YOLO architectures in computer vision: from YOLOv1 to YOLOv8 and YOLO-NAS," Mach. Learn. Knowl. Extr., 2: 1680-1716, 2023.

[68] S. I. Safie, N. S. A. Kamal, E. M. M. Yusof, M. Z. W. M. Tohid, N. H. Jaafar, "Comparison of squeezenet and darknet-53 based YOLO-V3 performance for beehive intelligent monitoring system," in Proc. The 2023 IEEE 13th Symposium on Computer Applications and Industrial Electronics (ISCAIE): 62-65, 2023.

[69] S. Teng, Z. Liu, X. Li, "Improved YOLOv3-based bridge surface defect detection by combining high- and low-resolution feature images," Buildings, 12(1225): 1-18, 2022.

[70] O. I. Obaid, M. A. Mohammed, A. O. Salman, S. A. Mostafa, A. A. Elngar, "Comparing the performance of pre-trained deep learning models in object detection and recognition," Int. J. Inf. Technol. Manag., 14(4): 40-56, 2022.

[71] N. F. Razali, I. S. Isa, S. N. Sulaiman, N. K. A. Karim, M. K. Osman, Z. H. C. Soh, "Enhancement technique based on the breast density level for mammogram for computer-aided diagnosis," Bioengineering, 10(153): 1-24, 2023.

[72] H. Ge, Y. Dai, Z. Zhu, R. Liu, "A deep learning model applied to optical image target detection and recognition for the identification of underwater biostructures," Machines, 10(809): 1-16, 2022.

[73] I. S. Isa, M. S. A. Rosli, U. K. Yusof, M. I. F. Maruzuki, S. N. Sulaiman, "Optimizing the hyperparameter tuning of YOLOv5 for underwater detection," IEEE Access, 10: 52818-52831, 2022.

[74] G. Tepteris, K. mamasis, I. Minis, "Logistics hub surveillance: optimizing YOLOv3 training for ai-powered drone systems," Logistics, 9(45), 2025.

[75] A. Ammar, A. Koubaa, M. Ahmed, A. Saad, "Aerial images processing for car detection using convolutional neural networks: comparison between faster R-CNN and YoloV3," arXiv:1910.07234v3l, 2019.

[76] B. Suvarnam, V. S. Ch, "Combination of CNN-GRU model to recognize characters of a license plate number without segmentation," in Proc. the 2019 5th International Conference on Advanced Computing & Communication Systems (ICACCS: 317-322, 2019.

[77] N. Dorbe, A. jaundalders, R. Kadikis,"FCN and LSTM based computer vision system for recognition of vehicle type, license plate number, and registration country," Autom. Control Comput. Sci., 52(2): 146-154, 2018.

Biographies



Vincent Andrew Akpan obtained his B.Sc. (Hons) degree in Physics from Delta State University, Abraka, Delta State, Nigeria in 1997; a Master of technology (M. Tech) degree in Electronic Measurement & Instrumentation from The Federal University of Technology, Akure, Ondo State, Nigeria in 2003; and a Ph.D. degree in Electrical & Computer Engineering from Aristotle University of Thessaloniki, Thessaloniki, Greece in 2011. He is currently a Professor with the Department of Biomedical Engineering, School of Electrical Systems Engineering, The Federal University of Technology, Akure, Nigeria. His research interest is in artificial intelligence, electronic instrumentation, intelligent adaptive control, automation and embedded systems engineering.

- Email: vaakpan@futa.edu.ng
- ORCID: 0000-0002-5155-2863
- Web of Science Researcher ID: OGN-3642-2025
- Scopus Author ID: 35177320400
- Homepage: https://bme.futa.edu.ng/home/profile/3303



David Ayo-oluwa Adegoke obtained his Bachelor of Technology (B. Tech) degree in Biomedical Technology from the Federal University of Technology, Akure, Nigeria with Second class (Honours) Upper Division in 2024. He is currently a Biomedical Engineer at Redeemers Health Village (RHV), Ogun State, Nigeria. His research interests include Digital Health, Biomedical Imaging Systems, Health Data Analysis, and the application of Artificial Intelligence in healthcare.

- Email: ayodapoadegoke18@gmail.com
- ORCID: 0009-0004-8060-8848
- Web of Science Researcher ID: NA
- Scopus Author ID: NA
- Homepage: NA



Ebunoluwa Temiloluwa Adejayan obtained his Bachelor of Technology (B. Tech) degree in Biomedical Technology from the Federal University of Technology, Akure, Nigeria in 2021. He is currently works as a Biomedical Engineer at the Federal Medical Centre in Ondo State, Nigeria. His research interests are in health informatics, data infrastructure, bioinformatics, and the application of machine learning and block-chain technologies to real-world problems.

- Email: tyebunoluwa@gmail.com
- ORCID: 0009-0003-5551-1940
- Web of Science Researcher ID: NA
- Scopus Author ID: NA
- Homepage: https://tsegalion.github.io/EAdejayan/



Kehinde Adesola Adepoju obtained her Bachelor of Technology (B. Tech) degree in Biomedical Technology from the Federal University of Technology, Akure, Ondo State, Nigeria, with a second class (Honours) Upper Division in 2024. She gained valuable experience as a Biomedical Engineer at Lagos State Teaching Hospital (LUTH). Her research interests include artificial implants, clinical engineering, rehabilitation and tissue engineering.

- Email: adesolaadepoju28@gmail.com
- ORCID: 0009-0003-0469-1232
- Web of Science Researcher ID: NA
- Scopus Author ID: NA
- Homepage: NA

Journal of Electrical and Computer Engineering Innovations
(JECEI)
Journal homepage: http://www.jecei.sru.ac.ir

Research paper

Optimization and Experimental Validation of an IPMSM for Electric Vehicles Targeting Torque Ripple Minimization, Average Torque and Efficiency Improvement

Alireza Shams [1], *Esmaeel Rokrok* [1,*], *Behrooz Rezaeealam* [1], *Abbas-Ali Zamani* [2]

[1] *Electrical Engineering Department, Lorestan University, Khorramabad, Iran.*

[2] *Department of Electrical Engineering, Technical and Vocational University (TVU), Tehran, Iran.*

Article Info

Article History:

Received 17 November 2025
Reviewed 05 January 2026
Revised 18 February 2026
Accepted 23 February 2026

Keywords:

Interior Permanent Magnet Synchronous Motor (IPMSM)
Electric Vehicle (EV)
Optimization of Motor Efficiency (OME)
Torque ripple reduction
Multi- Objective Particle Swarm Optimization (MOPSO)

[*]Corresponding Author's Email Address: *rokrok.e@lu.ac.ir*

Abstract

Background and Objectives: Interior permanent magnet synchronous machines (IPMSMs) have gained increasing attention in electric vehicle applications due to their high power density, desirable efficiency, and capability of delivering maximum torque over a wide speed range. Despite these advantages, challenges such as torque ripple and suboptimal efficiency remain. This study aims to propose a design and multi-objective optimization approach for the Stator-Optimized Delta-Type IPMSM (SO-DT-IPMSM) motor to enhance efficiency, reduce torque ripple, and improve average torque.

Methods: A multi-objective particle swarm optimization (MOPSO) was employed to determine the optimal set of stator parameters. In this study, an existing delta-type IPMSM rotor topology was adopted, and all rotor parameters were kept fixed, while the optimization was exclusively performed on stator geometry. Electromagnetic modeling and performance evaluation of the proposed design were carried out using Ansys Electronics. Following the optimization process, a prototype motor was manufactured and assembled based on the optimized design parameters, and experimental tests were conducted to validate the simulation results.

Results: Simulation results revealed significant improvements in the SO-DT-IPMSM compared with the Nissan Leaf IPMSM motor (Initial IPMSM). The optimized design achieved a 21% increase in average torque, 40% reduction in torque ripple, and 5% improvement in overall efficiency. Experimental tests performed on the fabricated prototype confirmed the accuracy of the simulation findings and demonstrated strong agreement between analytical and experimental data.

Conclusion: The proposed design and optimization approach effectively enhanced torque, torque ripple, and efficiency in the IPMSM. Beyond the validated experimental performance, the results demonstrate that the presented methodology can serve as a practical solution for improving electric vehicle motor performance. Moreover, the introduced optimization framework has the potential to be extended to other motor topologies and applications.

This work is distributed under the CC BY license (http://creativecommons.org/licenses/by/4.0/)

How to cite this paper:
A. Shams, E. Rokrok, B. Rezaeealam, A. Zamani, "Optimization and experimental validation of an ipmsm for electric vehicles targeting torque ripple minimization, average torque and efficiency improvement," J. Electr. Comput. Eng. Innovations, 14(2): 473-486, 2026.

DOI: 10.22061/jecei.2026.12722.906

URL: https://jecei.sru.ac.ir/article_2541.html

2345- 3044/© 2026 The Authors. Published by Shahid Rajaee Teacher Training University.

Introduction

In contemporary electric and hybrid vehicle drivetrains, PMSMs account for more than 80% of traction motor applications. This dominance is largely due to their ability to deliver high power density, maintain excellent efficiency across a wide speed range, and satisfy stringent vehicle performance requirements, as evidenced in vehicles such as the Nissan Leaf, Chevrolet Bolt, BYD E6, BMW i3, and Toyota Prius [1]-[3].

Although these motors possess high performance potential, their design faces numerous challenges. The stator structure and its geometric parameters directly impact average torque, torque ripple, core and copper losses, and ultimately, the motor's efficiency [4]. On one hand, reliance on rare-earth permanent magnets increases production costs and reduces supply chain stability [5]. On the other hand, phenomena such as torque ripple and acoustic vibrations affect performance quality and passenger comfort [6]. Alongside these issues, the simultaneous achievement of conflicting objectives such as increasing average torque, reducing torque ripple, and increasing efficiency turns the motor design problem into a complex multi-objective challenge [7]. Furthermore, traditional design methods based on trial-and-error or single-objective optimization lack sufficient capability to explore the large design space of the motor and find the precise balance point among performance objectives. Therefore, the need for an intelligent multi-objective optimization framework that can improve the electromagnetic performance, manufacturability, and overall efficiency of the motor is strongly felt. The design and optimization of IPMSMs have become a main research focus in recent years due to the growth of the electric vehicle industry. A significant portion of this research has focused on improving electromagnetic performance, reducing losses, and reducing torque ripple; however, many have overlooked the role of stator design as a key factor in systematic optimization.

Some research groups have focused on optimizing rotor topology, including V-shaped, inverted-V, asymmetric structures, and magnetic flux path optimization. These studies have managed to increase average torque and reduce torque ripple but have largely neglected the effect of stator shaping and its manufacturing constraints [8]-[11]. Additionally, many of the proposed methods require heavy finite element analysis (FEA) analyses and are not very cost-effective for industrial applications. Other studies have used multi-objective approaches such as evolutionary algorithms, surrogate models based on machine learning, and multilevel methods to explore the extensive IPMSM design space. These methods have often achieved significant accomplishments in reducing computational cost and increasing prediction accuracy [12]-[17]. However, many of these studies face challenges such as reduced population diversity, premature convergence, or excessive algorithm complexity, which limit industrial implementation. Studies related to stator shaping have been less frequent and often only address components such as tooth shape, slot opening, and bridge dimensions. Some of this research has shown that stator design directly impacts average torque, core losses, and torque ripple, and in many cases, its influence is greater than that of rotor design [18]-[20]. However, most of these works have been either single-objective or have ignored manufacturing constraints such as minimum tooth thickness, producible slot depth, and local core saturation. In much of the previous research, although significant improvements in the design and optimization of IPMSMs have been achieved, a fundamental gap remains: None of these studies has provided a simple, industrially viable, yet multi-objective design framework for optimizing stator parameters; a framework that can systematically and simultaneously guarantee three key criteria: increasing average torque, reducing torque ripple, and improving efficiency. Most existing research has focused only on a limited part of the geometry or has not considered the real constraints of stator manufacturing and producibility. Furthermore, some of the optimization methods used face problems such as reduced population diversity and insufficient Pareto front coverage, which can lead to suboptimal solutions. Therefore, the need for a more accurate, practical, and industry-applicable method is still strongly felt; a need that the present research seeks to address.

To this end, this study presents a stator design and optimization method for an SO-DT-IPMSM intended for electric vehicle applications, based on an MOPSO algorithm. An existing delta-type IPMSM rotor topology is adopted as the baseline and kept unchanged throughout the optimization process, allowing the influence of stator design to be isolated and systematically evaluated. In the proposed approach, key stator design parameters, including tooth width, slot depth, air gap length, slot opening width, slot opening height, and stator yoke, are selected through an importance analysis of design parameters, supported by analytical formulations and electromagnetic principles, to identify the most influential variables in IPMSM optimization. The optimization problem is then formulated in a multi-objective manner and solved using FEA, where three primary objectives—maximization of average torque, reduction of torque ripple, and improvement of efficiency are pursued simultaneously. By focusing exclusively on stator design while keeping all rotor parameters constant, the proposed framework

reduces design complexity and enhances industrial feasibility, particularly for upgrading existing motor platforms. The results demonstrate that the proposed method achieves superior electromagnetic performance compared to conventional optimization approaches, providing an effective and practical pathway for the development of next-generation IPMSMs for electric vehicle traction systems.

The article is structured such that Section 2 elaborates on the analytical model and introduces the base IPMSM motor.

In Section 3, the MOPSO algorithm is first introduced. Subsequently, the definitions and importance analysis of the variables, the selection of optimization objectives, and the execution of the MOPSO algorithm are described.

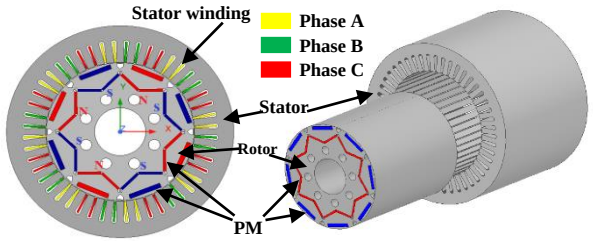
Section 4 presents the simulation results based on Finite Element Analysis and compares the performance of the optimized SO-DT-IPMSM with the initial IPMSM.

Then, in Section 5, the simulation data are first experimentally validated with a prototype of the optimized SO-DT-IPMSM, and its experimental results are then compared with the experimental results of the Initial IPMSM.

Finally, Section 6 summarizes the findings and provides suggestions for future research directions.

IPMSM Motor Topology

The objective of this study is to improve the performance of an 80 kW IPMSM from the Nissan Leaf electric vehicle [23] with a rated speed of 2100 rpm. Compared to the Surface-mounted Permanent Magnet Synchronous Motor (SPMSM) type, in the IPMSM, the magnets are embedded inside the rotor. This feature eliminates the risk of magnet detachment at high speeds due to centrifugal force. Furthermore, the IPMSM can increase the motor's power density through the reluctance torque generated by the magnetic circuit's asymmetry. This research employs a single-layer, distributed, full-pitch winding in the stator. By distributing the coils of each phase across several adjacent slots, this winding enhances the main component of the Magneto Motive Force (MMF) and reduces mechanical harmonics. This structure results in a more sinusoidal flux, reduced cogging torque, lower noise, and reduced core losses; although its winding factor and slot space utilization are lower compared to double-layer or concentrated windings. The IPMSM under investigation features a rotor with a delta-shaped structure, 8 poles, and a stator with 48 slots. The delta-shaped rotor structure provides higher output torque and better performance in the field-weakening region, which is why it is widely used in high-speed electric vehicle motors. The topology of the IPMSM studied in this paper is shown in Fig. 1.



(b) (a)

Fig. 1: a) Exploded view of the studied IPMSM motor. b) Schematic diagram of the studied IPMSM motor

The parameters of the initial design specifications for the studied IPMSM are as shown in the Table 1.

Table 1: The parameters of the initial design specifications for the studied IPMSM

Type of Motor	SO-DT-IPMSM
Number of stator slot/rotor pole	48/8
Output power (kw)	80
Rated speed (r/min)	2100
Rated torque (N.m)	280.7
Efficiency (%)	92.5
Rated current (A)	340

Proposed Optimal Design Procedure for SO-DT-IPMSM

A. Principle of Particle Swarm Optimization

Particle Swarm Optimization (PSO) is a heuristic intelligent optimization algorithm developed by Kennedy and Eberhart [24]. Inspired by the foraging behavior of birds, PSO searches for optimal solutions through information sharing and cooperation among individuals. Initially, the algorithm randomly generates a set of initial solutions and then iteratively searches for the global optimum. In each iteration, the next search direction is determined based on the global best solution and the individual's best solution from the previous iteration. Due to its simple structure and strong search capabilities, this algorithm has been widely used in parameter identification and maximum power point tracking [25]. This algorithm primarily consists of five steps: Initialization, Velocity Update, Position Calculation, Revision of Individual Best Solutions, and Update of the Global Best Solution.

1) Initialization

A set of N particles is randomly generated with initial positions and velocities. The fitness of each particle is then evaluated using the fitness function f(x).

2) Velocity Update

The velocity of each particle is updated according to:

$$v_i = \omega \times v_i + c_1 \times rand() \times (Pb^i - x_i) + c_2 \times rand() \times (Pg(k) - x_i) \quad (1)$$

where, ω (0 ≤ ω ≤ 1) denotes the inertia weight, c_1 and c_2 are learning coefficients, v_i and x_i are the velocity and position of particle i, rand() is a uniformly distributed random number in [0,1], Pb^i is the personal best position of particle i, and Pg(k) is the global best position of the swarm at iteration k.

3) Position Update

After updating the velocities, the position of each particle is recalculated as:

$$x_i = x_i + v_i \quad (2)$$

This equation ensures that each particle moves according to its newly computed velocity.

4) Update of Individual Best Positions Each particle's personal best position is updated according to:

$$Pb^i(k+1) = \begin{cases} Pb^i(k) & f[Pb^i(k+1)] \geq f[Pb^i(k)] \\ Pb^i(k+1) & f[Pb^i(k+1)] < f[Pb^i(k)] \end{cases} \quad (3)$$

This step ensures that a particle's personal best position reflects the best fitness it has achieved so far.

5) Update of the Global Best Position

The global best position of the swarm is determined as:

$$Pg(k) = \arg\min f[Pb^i(k)] \qquad 1 \leq i \leq N \quad (4)$$

where, N is the total number of particles. The global best position corresponds to the personal best position yielding the minimum objective function value among all particles.

During each iteration, particles update their velocities and positions using (1) and (2). Subsequently, each particle updates its personal best according to (3). Once all personal bests are revised, the global best is updated according to (4).

This process is repeated until the termination criterion is satisfied.

Finally, the algorithm halts and outputs the optimized solution.

B. The Flowchart of Optimal Design Procedure for SO-DT-IPMSM

Fig. 2 illustrates the flowchart of the proposed multi-objective optimization method for the initial IPMSM, whose main steps are outlined below:

Step 1: Create Initial Model and Perform Preliminary Analysis.

An initial model of the Initial IPMSM is created in Ansys Electronics software. A preliminary electromagnetic analysis is performed on the model to evaluate the motor's baseline behavior in terms of magnetic field, torque, losses, and other key parameters. Performance graphs are extracted for result comparison.

Step 2: Select Design Variables.

In this step, design variables affecting the motor's geometric or electromagnetic parameters are first introduced. Then, through an analysis of various references, the most critical design variables used for optimizing the Initial IPMSM are selected. Subsequently, based on the selected design variables, various references, and the structure of the studied motor, the design constraints are chosen.

Step 3: Initialize MOPSO Algorithm Parameters.

In this step, the key parameters of the algorithm, such as population size, maximum iterations, inertia weight, learning coefficients (c_1, c_2), and velocity limits, are initialized according to the specific requirements of the optimization problem.

Step 4: Evaluate Samples in Ansys Electronics.

Each design vector is imported into Ansys Electronics software, and an electromagnetic simulation is performed. The optimization objectives are calculated and extracted for each sample.

Step 5: Check Stopping Criterion.

It is checked whether the maximum allowed number of algorithm iterations has been reached. If not, the MOPSO algorithm is updated, and new design vectors are generated (return to Step 3). If yes, the optimization process ends.

Step 6: Select Optimal Design.

Optimal designs are extracted from the generated Pareto Front by the MOPSO algorithm. Based on the Design Strategy, one or more final designs are selected.

Step 7: Fabricate the Proposed Optimized SO-DT-IPMSM.

The final step of the design method involves fabricating a physical prototype of the SO-DT-IPMSM, built according to the optimized design parameters, provided the simulation results satisfactorily meet the pre-defined performance criteria.

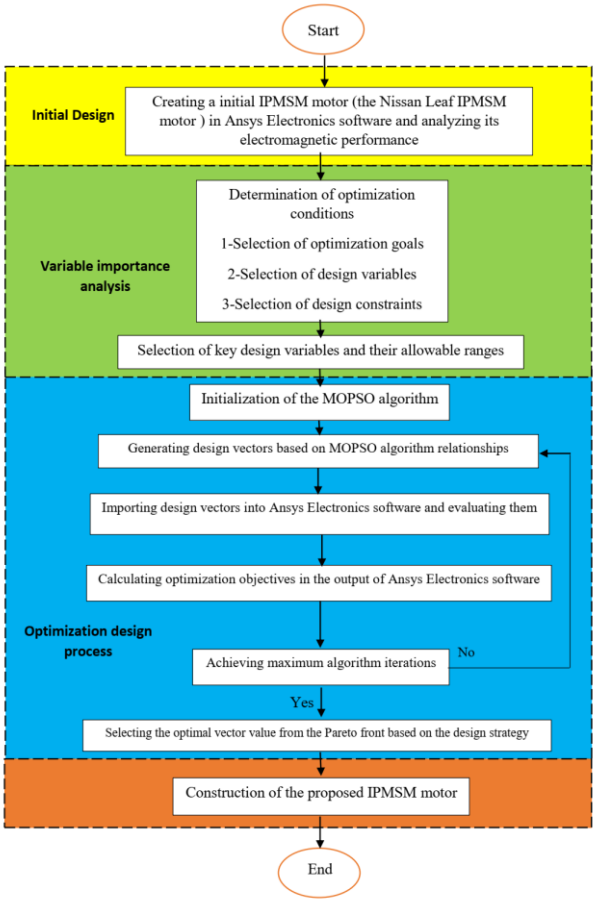


Fig. 2: Multi-objective optimization flowchart for IPMSM motor.

Selection of Design Variable

Fig. 3 shows the parametric FEA model of the SO-DT-IPMSM created in Ansys Maxwell software, which includes 22 design parameters.

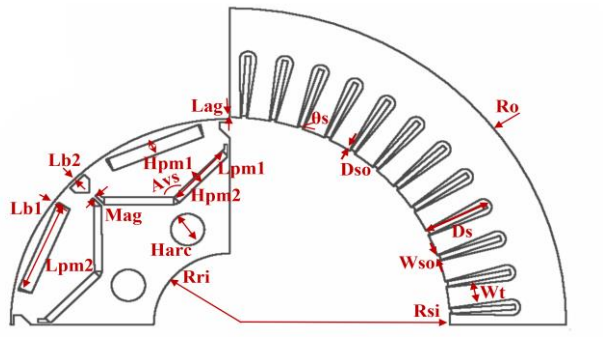


Fig. 3: SO-DT-IPMSM parametric model.

Based on references [26]-[36], it is not necessary to optimize all 22 design parameters, as some of them can be predetermined during the initial design stage. The inner stator radius (R_{si}) is defined according to the rated power, power factor, efficiency, and nominal speed, whereas the outer stator radius (R_o) is constrained by the installation space available for the IPMSM in electric vehicles. Since the optimization process is focused solely on the stator, the rotor parameters are kept fixed and are adopted from the Initial IPMSM as reported in reference [23]. The symbols of the structural parameters of the studied IPMSM are labeled in Fig. 3, and their corresponding values are listed in Table 2.

Table 2: Values of structural parameters of the studied IPMSM

Categories	Parameters	Symbol	Unit	Value
Stator parameters	Inner radius of stator	Rsi	mm	65.5
	Outer radius of stator	Ro	mm	100
	Slot opening width	Wso	mm	2
	Inner slot width	Bs1	mm	2
	Outer slot width	Bs2	mm	5
	Slot opening height	Dso	mm	0.5
	Slot neck depth	Hs1	mm	0
	Slot depth	Ds	mm	18
	Tooth width	Wt	mm	5.4
	Stator yoke	Wy	mm	13.25
	Air gap length	Lag	mm	1
	Tooth tip angle	Θs	deg	30
Rotor parameters	Inner radius of rotor	Rri	mm	22.5
	V-shaped PMs length	Lpm1	mm	30
	Straight-shaped PMs length	Lpm2	mm	40
	V-shaped PMs clamp angle	Avs	deg	130
	External Magnetic Bridge Width Straight Shape	Lb1	mm	1.3
	Flux barrier	Lb2	mm	1.6
	Internal Magnetic Bridge Width	Mag	mm	1.27
	Straight-shaped PMs width	Hpm1	mm	4
	V-shaped PMs width	Hpm2	mm	2
	Diameter of Rotor hole	Harc	mm	10

The materials and design dimensions, including the rotor core and permanent magnets, are considered fixed in this design. The only difference lies in the distinct dimensions and structure of the stator core slots and teeth, which are considered in the proposed design.

Importance Analysis of Design Parameters Effective in IPMSM Optimization

In order to define the motor's performance objectives and determine the optimizable variables, the electromagnetic relationships related to efficiency, torque, and flux behavior were first examined. Recent studies on IPMSM design for electric vehicles identify high efficiency, stable average torque, low torque ripple, and robust dynamic behavior as key performance indicators. Studies conducted in recent years show that these characteristics are directly influenced by the geometry of the flux paths and the field distribution in the stator section.

Motor efficiency, which is one of the main objectives of the optimization process in this research, can be calculated from the following equation:

$$\eta = P_e / (P_e + P_{loss}) = T_e.\omega / (T_e.\omega + P_{loss}) \quad (5)$$

where, T_e is the electromagnetic torque, ω is the angular speed, and P_{loss} includes the sum of copper, iron, mechanical, and stray losses. According to this relationship, any change in geometry that affects torque generation or the amount of losses will directly impact the final efficiency.

By reviewing 11 reference papers [26]-[36] in the field of sensitivity analysis and optimization of IPMSM, six geometric parameters of the stator that show high sensitivity to torque and losses have been selected. These parameters include tooth width, slot depth, air gap length, slot opening width, slot opening height, and stator yoke thickness.

The selection of this set was based on two criteria:

1) Direct relevance to the flux behavior in the air gap and tooth region,

2) A determining role in controlling torque ripple and preventing core saturation.

Tooth width is a key factor in determining torque due to its effect on the flux passing through the tooth and, consequently, the linked flux. The torque in an IPMSM is defined by the following equation:

$$T_e = (3/2).p.(\phi_f.i_q + (L_d - L_q).i_d.i_q) \quad (6)$$

where, T_e is the electromagnetic torque, p is the number of pole pairs, and i_d, i_q, L_d, L_q, and ϕ_f are the d-q axis currents, inductances, and PM flux linkage, respectively.

Slot depth represents the effective volume for winding, and its changes directly affect the resistance and copper losses. This behavior is described by the relations:

$$R = \rho.l / A_{slot} \quad , \quad P_{cu} = R.I^2 \quad (7)$$

where, R is the winding resistance, ρ denotes the electrical resistivity of the conductor material (copper), l is the effective length of the conductor, and A_{slot} represents the effective slot cross-sectional area available for the winding. In addition, P_{cu} denotes the copper losses, and I is the current flowing through the winding. According to (7), increasing the effective slot area—resulting from an increase in slot depth leads to a reduction in the winding resistance and, consequently, a decrease in copper losses. Therefore, slot depth is a key geometric parameter that significantly influences the loss characteristics and overall efficiency of the electrical machine.

The air-gap flux φ is approximately inversely proportional to the air-gap length g. This relationship can be expressed as

$$\phi \ \alpha \ 1/g \quad (8)$$

The air-gap length simultaneously affects torque, torque ripple, and efficiency, since an increase in g reduces the air-gap flux, leading to a lower electromagnetic torque, whereas a smaller g increases flux but may exacerbate torque ripple and core losses.

The geometric parameters of the stator slot opening, namely the slot opening width and slot opening height, play an important role in determining the electromagnetic performance of the IPMSM. These parameters directly affect the magnetic field distribution in the air-gap region and the amount of leakage flux, thereby influencing torque quality and loss characteristics.

Torque ripple in IPMSMs originates from periodic variations in the magnetic co-energy as a function of rotor position. Accordingly, the impact of slot opening geometry on torque behavior can be expressed by

$$T(\theta) = dWmag / d\theta \quad (9)$$

where, W_{mag} is the magnetic co-energy stored in the machine. The slot opening dimensions alter the effective air-gap permeance distribution, thereby modulating $W_{mag}(\theta)$ and its derivative, which directly determines the torque profile. Increased slot width or height typically enhances leakage flux and introduces higher spatial harmonics in the air-gap field, leading to more pronounced torque ripple. Therefore, careful optimization of slot width and height is essential for minimizing torque ripple while maintaining acceptable levels of stator saturation and manufacturing feasibility.

Finally, the yoke thickness h_{yoke} plays a critical role in providing a low-reluctance return path for the magnetic flux. An insufficient yoke thickness leads to increased flux density in the yoke region, which in turn raises core losses due to saturation effects. This relationship can be expressed as:

$$B_{yoke} = \phi / A_{yoke} \quad (10)$$

where, ϕ is the magnetic flux per pole and A_{yoke} is the yoke cross-sectional area. Since A_{yoke} is directly proportional to the yoke thickness h_{yoke}, a reduction in h_{yoke} results in an increased yoke flux density B_{yoke}. Elevated flux density intensifies core losses and may lead to local magnetic saturation, thereby degrading machine performance. Therefore, the stator yoke thickness must be carefully selected to maintain the flux density below the saturation limit while minimizing material usage.

These key parameters significantly influence the optimization objectives and are therefore selected as design variables in the multi-objective model.

Their corresponding variation ranges are provided in Table 3.

Table 3: Range of variation of key parameters of the IPMSM stator under study

Parameters	Symbol	Unit	Initial	Range
Tooth width	Wt	mm	5.4	3.5-6.5
Slot depth	Ds	mm	18	17-27
Air gap length	Lag	mm	1	0.5-1
Slot opening width	Wso	mm	2	1.5-2.5
Slot opening depth	Dso	mm	0.5	0.5-1
Stator yoke	Wy	mm	10	3-15

The range of values for the design variables must adhere to the following optimization constraints:

(1) The slot fill factor represents the proportion of copper occupying the slot area. Since coil insertion is usually carried out by automated manufacturing processes, this factor should generally not exceed 75%. At the same time, an excessively low fill factor is undesirable, as insufficient copper packing may cause wire movement during operation and increase the risk of insulation wear. Considering these aspects, the slot fill factor in this study is constrained within the following limits:

$$60\ \% \le S_f \le 75\ \% \quad (11)$$

(2) To prevent excessive saturation of the motor's average flux density, which degrades IPMSM performance, the constraints for the average flux density in the stator tooth section (B_t) and the average flux density in the stator yoke section (B_j) must be as follows:

$$B_t \le B_{sat} \quad and \quad B_j \le B_{sat} \quad (12)$$

where, B_{sat} is the saturation flux density of the silicon steel sheet. In this paper B_{sat} is 1.95 T.

To prevent an excessive temperature rise during motor operation, which could lead to the demagnetization of the permanent magnets, the current density (J) constraints must be defined as [31]:

$$J \le 10 A.mm^{-2} \quad (13)$$

Selection of Optimization Objectives

Electric vehicles encounter a wide range of dynamic driving conditions, requiring the IPMSM to deliver sufficiently high torque for frequent events such as startup, acceleration, braking, and hill climbing. To maintain smooth and stable operation, the torque ripple of the IPMSM must also be minimized. In addition, achieving a long driving range in EVs demands that the motor operates with low losses and high efficiency. Considering the strong interdependence between losses and efficiency, this study focuses on optimizing the IPMSM's average torque (T_a), torque ripple (T_r), and efficiency (η) as the primary performance targets. The average torque Ta is defined as follows:

$$T_a = avg \quad (T_e) \quad (14)$$

T_r is defined as follows:

$$T_r = (T_{em_max} - T_{em_min}) / (T_a) \quad (15)$$

where, T_{em_max} and T_{em_min} are the maximum and minimum electromagnetic torques, respectively. As the stator winding is already determined based on the voltage requirements of the power source, it does not need to be modified during the optimization process. Consequently, copper losses remain essentially constant. Therefore, in calculating the total losses, only the core losses and permanent magnet losses are taken into account. The total loss P_t is defined as follows:

$$P_t = P_{ironcore} + P_{pm} \quad (16)$$

where, $P_{ironcore}$ and P_{pm} are the core losses and PM losses, respectively.

Although the efficiency η has been introduced earlier in the importance analysis, it is redefined here in the context of optimization objectives, linking it directly to total losses for clarity in the optimization process. Subsequently, the motor efficiency is defined as follows:

$$\eta = (T_a.\omega) / (T_a.\omega + P_t) \quad (17)$$

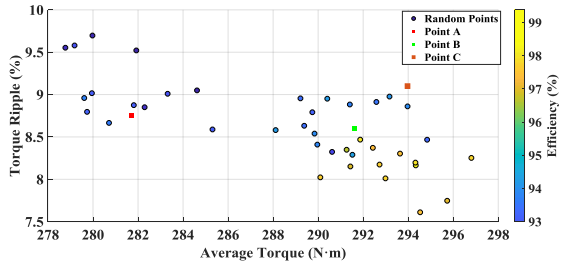
where, ω is the angular speed of the electric motor, T_a is the average torque, and P_t is the total loss.

This study focuses on optimizing output torque, minimizing torque ripple, and increasing motor efficiency

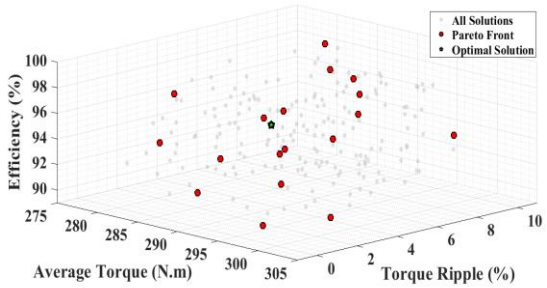
as the primary objectives. Given that our goal is to improve the performance of the Initial IPMSM, the rated values of this motor output torque of 280 N.m, torque ripple of 10.65%, and efficiency of 92.5% have been used in the objective function below. Therefore, the optimization objectives for the SO-DT-IPMSM are expressed in the following equation.

$$\min \begin{cases} f_1(x) = c_1 \dfrac{280}{T_a} \\ f_2(x) = c_2 \dfrac{92.5}{\eta} \\ f_3(x) = c_2 \dfrac{T_r}{10.65} \end{cases} \tag{18}$$

where, x is the optimization variable (stator parameters), and the value range of the optimization variables is shown in Table 3. c_1 and c_2 are the weighting coefficients for the optimization objectives. Since the IPMSM is used in an electric vehicle, the optimization of motor efficiency is more critical in this research; therefore, the weighting coefficients are chosen as c_1=0.3 and c_2=0.7. The Pareto solution set is obtained according to the algorithm settings and the methods described above, as shown in Fig. 4(a) and Fig. 4(b).



(a)



(b)

Fig. 4: a) 3D Pareto front diagram of the MOPSO optimization algorithm a) 3D diagram b) 2D diagram with three optimal points.

It can be observed that the optimization objectives $f_1(x)$, $f_2(x)$, and $f_3(x)$ cannot all achieve their optimal values simultaneously. To establish a reasonable compromise among the three optimization objectives, three candidate points—A, B, and C—are selected from the chart for comparison based on the order of average torque. Next, the FEA method is employed to determine the average torque, torque ripple, and efficiency of the motor at these three operating points, and the results are summarized in Table 4.

Table 4: Comparison of optimization goals at three points A, B, and C and the output of the Initial IPMSM

Candidate solutions	MOPSO+ FEA results		
	T_a(N.m)	T_r(%)	η(%)
A	281.7	8.7	96.3
B	291.6	8.6	95.8
C	293.97	9.2	97.22
Initial IPMSM	280.7	15.16	92.5

This paper presents a multi-objective optimization framework for the design of an electric vehicle traction motor, which combines MOPSO with FEA using Ansys Electronics. As presented in Table 4, among the three evaluated solutions, Candidate C demonstrates the highest average torque Ta and efficiency η, while exhibiting the lowest torque ripple T_r relative to Candidates A and B.

Accordingly, Candidate C is chosen as the optimal configuration for the stator parameters in this study. In the context of electric vehicle operation, where high efficiency extends driving range, sufficient torque ensures strong acceleration, and minimal torque ripple improves NVH performance, Candidate C represents the most favorable design alternative. Table 5 shows the optimization results for the SO-DT-IPMSM.

Table 5: Comparison of SO-DT-IPMSM optimization results

	Parameters	Unit	Initial Value	MOPSO+ FEA results
Optimization Parameters in stator of IPMSM	W_{so}	mm	2	1.88
	D_{so}	mm	0.5	1
	D_s	mm	18	17.9
	L_{ag}	mm	1	1
	W_t	mm	5.4	5.5
	W_y	mm	10	13.4
Optimization objectives	T_a	N.m	280.7	293.97
	T_r	%	10.65	9.2
	η	%	92.5	97.22

Optimization Result Discussion

The optimization results indicate that the stator geometric parameters play a critical role in shaping the

electromagnetic performance of the SO-DT-IPMSM. Among the ways examined, it specifies the length of the air gap which indicates that on the electromagnetic between the rotor and the stator. Reducing the air gap increases the magnetic flux density and thus the average torque. However, if it is reduced too much, it will lead to local saturation and increase the torque ripple. In particular, the slot opening width and height significantly influence the air-gap flux distribution and cogging torque characteristics.

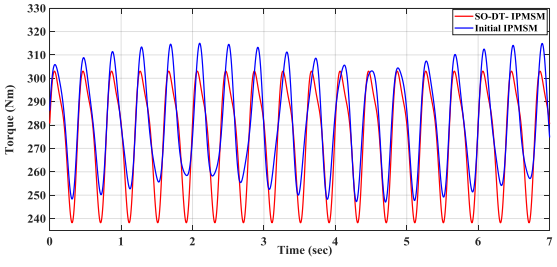
By optimizing the slot opening dimensions, the spatial harmonics of the air-gap flux density are effectively suppressed, leading to a noticeable reduction in torque ripple. A narrower and well-proportioned slot opening improves flux continuity across the air gap, thereby reducing localized flux concentration and electromagnetic force fluctuations.

The stator tooth width directly affects magnetic saturation and harmonic content in the stator core. Increasing the effective tooth width reduces local saturation and improves flux-carrying capability, which contributes to smoother flux distribution and lower harmonic distortion in the stator magnetic field. This improvement is particularly evident in the reduction of torque ripple components and enhanced efficiency under load. Furthermore, the optimized overall stator geometry, including yoke thickness and slot depth, increases torque density by enabling higher effective air-gap flux and improved magnetic utilization of the stator core. These combined geometric improvements enhance average torque output while maintaining acceptable core losses, demonstrating that stator-focused optimization is a highly effective approach for improving IPMSM performance.

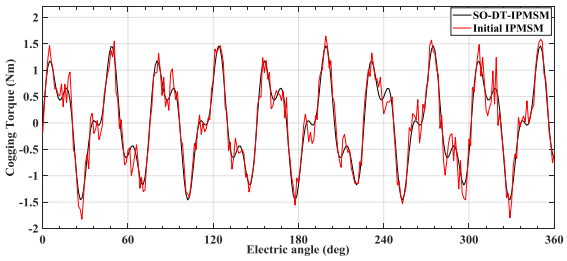
Electromagnetic Performance Comparison

To assess the effectiveness of the proposed methodology, a detailed comparison of the electromagnetic performance was performed between the standard Initial IPMSM [23] and the optimized SO-DT-IPMSM using FEA.

The comparison focuses on the three main objectives of this study: increasing average torque, reducing torque ripple, and improving efficiency. Figures 5 and 6 summarize the results.

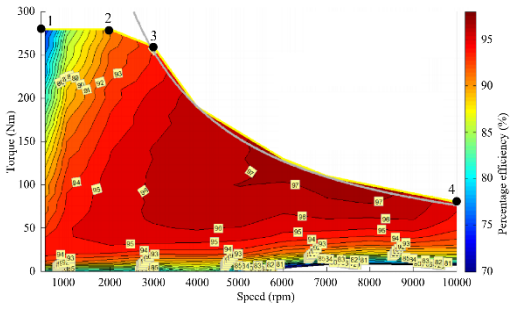


(a)

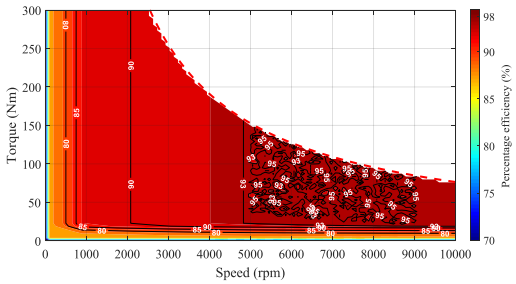


(b)

Fig. 5: Comparison of electromagnetic performance a) Electromagnetic torque of Initial IPMSM and SO-DT-IPMSM. b) Their cogging torque.



(a)



(b)

Fig. 6: Comparison of efficiency distribution of a) Initial IPMSM reference [23]. b) SO-DT-IPMSM.

Average Torque Improvement

As shown in Fig. 5, the optimized SO-DT-IPMSM produces 21% higher average torque compared to the initial design. This improvement is primarily attributed to the systematic optimization of key stator parameters, including tooth width and stator geometry, which enhance torque density. The stepwise analysis confirms that each selected stator parameter contributes directly to the overall torque improvement. These results demonstrate that the proposed optimization method effectively increases the motor's torque output without altering rotor parameters, thereby maintaining design simplicity and industrial viability.

Torque Ripple Reduction

In addition to average torque, torque ripple is significantly reduced by 40% in the optimized motor. The reduction in torque ripple is mainly due to the careful

optimization of slot opening width, which smooths the magnetic flux distribution and minimizes harmonic distortions. This improvement ensures better motor stability, reduced acoustic vibration, and improved passenger comfort, particularly under variable load conditions. Furthermore, as can be observed from Fig. 4(b), the maximum cogging torque is reduced from 1.4 N·m to 1.12 N·m, indicating a 20% reduction. These three factors have significantly improved the motor stability. The reported values were calculated according (6), (9), and (14).

Efficiency Enhancement

Fig. 6 presents the efficiency distribution of both the initial and optimized motors. The SO-DT-IPMSM exhibits a wider operating range with efficiency exceeding 92.5%, compared to the initial design. At rated speed, efficiency rises from 92.5% to approximately 97%, while above rated speed, it reaches nearly 98%. This improvement is directly attributed to reduced core and copper losses, resulting from the optimized stator geometry and minimized torque ripple. These results demonstrate that the proposed stator optimization method effectively enhances both electromagnetic performance and overall energy conversion efficiency.

Overall, the sequential analysis confirms that the proposed multi-objective optimization effectively achieves the study's objectives: enhancing average torque, reducing torque ripple, and improving efficiency. The stepwise evaluation also clarifies how specific stator parameters contribute to each performance metric, making the methodology transparent and reproducible.

Results and Discussion

This section presents the experimental validation of the proposed SO-DT-IPMSM. A prototype was fabricated and tested under various load conditions to evaluate average torque, torque ripple, current harmonics, and efficiency, to verify the accuracy of the FEA simulations and confirm the practical effectiveness of the optimized design.

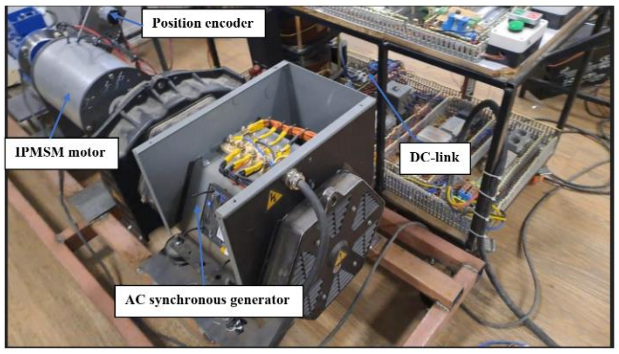
Fabrication of the Proposed SO-DT-IPMSM and Experimental Validation of Results

To validate the simulation results, the SO-DT-IPMSM with a 48-slot/8-pole configuration was fabricated and tested, as shown in Fig. 7.

The drive system uses an FPGA-based Kintex 7 controller implementing Field-Oriented Control (FOC). The rotor position is measured using an Autonics EP50S8-1024-2F-P-24 absolute encoder, which ensures accurate rotor angle measurement even after power loss. Phase currents were measured using an LA 200-P current sensor (range 0–±300 A, bandwidth 0–100 kHz), and the DC-link voltage was set at 400 V with a rated current of 340 A and a switching frequency of 10 kHz. Measurement accuracy and sensor resolution were carefully considered to ensure reliable results.



(a)



(b)

Fig. 7: Testing on SO-DT-IPMSM a) Rotor and stator configuration, b) Laboratory test setup.

During testing, the motor was evaluated under both no-load and variable-load conditions. Variable-load operation was achieved by mechanically coupling a three-phase synchronous generator to the motor shaft and applying an adjustable resistive load at the generator output. This setup allowed precise control of load torque, enabling both constant and variable load profiles representative of electric vehicle traction applications. All measurements were conducted under steady-state and constant-speed conditions, with torque characteristics evaluated at predefined load levels.

Average Torque and BEMF Analysis

Fig. 8 compares the phase BEMF of the initial IPMSM and the SO-DT-IPMSM. The optimized stator design (tooth shape, slot width, and stator yoke) reduces higher-order harmonics, resulting in a waveform closer to a sinusoid. This reduction in BEMF harmonics directly improves torque output and reduces ripple.

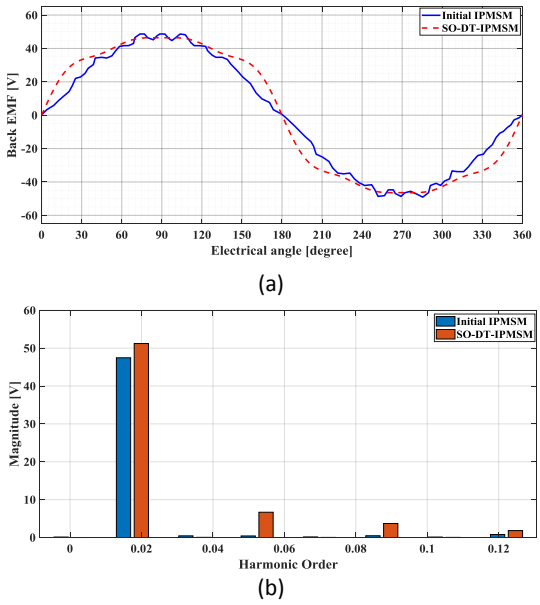


Fig. 8: a) BEMF and harmonic analysis of the initial IPMSM motor b) SO-DT-IPMSM.

Fig. 9 shows that the optimized SO-DT-IPMSM generates 21% higher average torque than the initial IPMSM.

This improvement is primarily due to the systematic optimization of key stator parameters, including tooth width and stator shape, which enhance torque density. Stepwise analysis confirms that each selected stator parameter contributes directly to the overall torque increase. These results demonstrate that the proposed optimization method effectively enhances torque output without altering rotor parameters, maintaining simplicity and industrial viability.

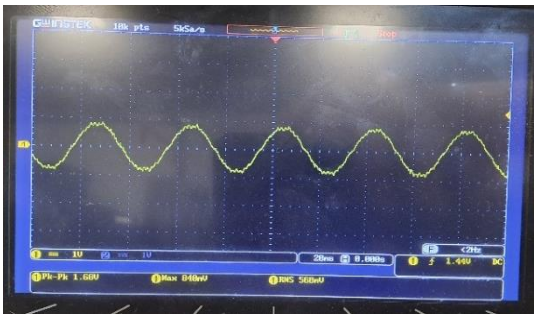


Fig. 9: Experimental BEMF waveform of the SO-DT-IPMSM.

Torque Ripple and Current Harmonics

Fig. 10 shows the phase current waveforms under rated load. The SO-DT-IPMSM exhibits nearly sinusoidal currents with significantly reduced harmonic distortion.

- The phase current Total Harmonic Distortion (THD) decreased from 11.2% (initial IPMSM) to 3.1% after optimization.
- The current ripple decreased from 4.5% to 2.8% of RMS value.
- The reduction in torque ripple is approximately 40%, as a result of improved air-gap flux distribution and reduced BEMF harmonics.

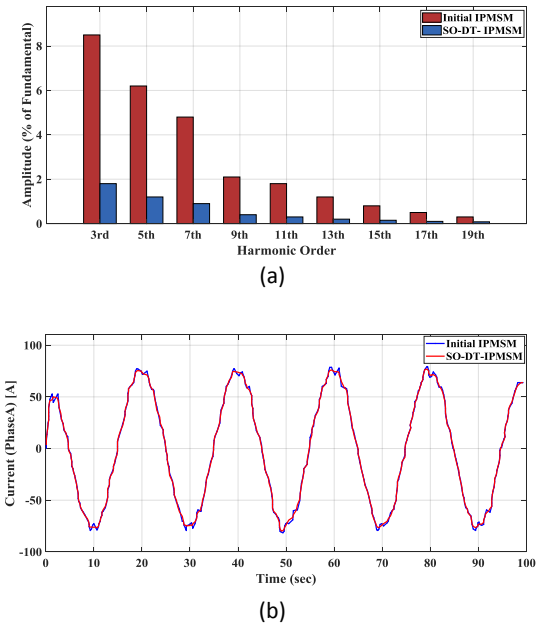


Fig. 10: a) Phase current and harmonic analysis of the initial IPMSM motor b) SO-DT-IPMSM.

These improvements are directly related to the optimized stator slot geometry and flux path, which minimize harmonics and smooth torque production, resulting in lower acoustic noise, smoother motor operation, and higher efficiency.

Efficiency Improvement

The experimental results also confirm the enhanced efficiency of the optimized SO-DT-IPMSM. Reduction in current harmonics and torque ripple decreases both copper and core losses, aligning with simulation predictions. Table 6 summarizes the comparison between the initial IPMSM and the optimized motor, showing significant improvements in torque, torque ripple, and efficiency across all tested load conditions.

Table 6: Comparison results optimization of SO-DT-IPMSM and Initial IPMSM

Experimental results of Initial IPMSM			Experimental results of SO-DT-IPMSM		
T_a (N.m)	T_r (%)	η(%)	T_a (N.m)	T_r (%)	η(%)
280.70	15.16	92.50	293	9	97

Overall, the experimental validation demonstrates that the proposed multi-objective stator optimization:

1. Increases average torque through improved stator design.
2. Reduces torque ripple and current harmonics, enhancing motor stability and reducing noise.

Improves efficiency by minimizing losses in the stator and rotor. The results confirm the accuracy of the FEA simulations and validate the effectiveness of the SO-DT-IPMSM design methodology under practical operating conditions. The sequential presentation ensures that each objective is clearly linked to specific design changes and measurable improvements. Fig. 11 shows the measured phase current waveform of the actual SO-DT-IPMSM under rated load conditions.

As can be observed, after optimization, the current waveform has become nearly sinusoidal and its harmonic distortion has been significantly reduced. The phase current THD decreased from approximately 11.2% in the initial model to about 3.1% after optimization. Furthermore, the current ripple was reduced from 4.5% of the RMS value to approximately 2.8%. This improvement is due to the modification of the stator slot geometry and the optimization of the flux distribution in the air gap, which led to a reduction in the harmonic components of the BEMF. Consequently, the output torque ripple has also been reduced by approximately 40%, resulting in smoother motor operation, lower noise, and higher efficiency.

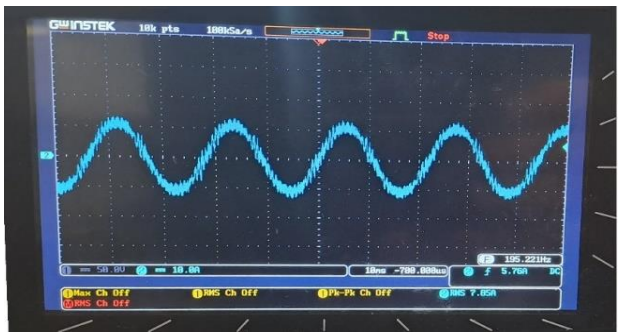


Fig. 11: Experimental phase current waveform of the SO-DT-IPMSM under rated load conditions.

Conclusion

This paper presented a novel SO-DT-IPMSM structure and benchmarked its performance against the Initial IPMSM of the Nissan Leaf EV due to their structural similarities. By employing an optimized stator design including slot and tooth shape refinement and key parameter optimization, the proposed method effectively reduced flux leakage and established a more favorable magnetic field distribution, resulting in increased torque density and improved overall motor efficiency. Comparative analysis demonstrated that the SO-DT-IPMSM delivers superior performance, achieving a torque of 293.7 Nm, a reduced torque ripple of 9.07%, and an efficiency of 97.22%, significantly outperforming the 92.5% efficiency of the Initial IPMSM motor. A prototype of the SO-DT-IPMSM was also manufactured and tested, validating the simulation results. Furthermore, a multi-objective optimization algorithm based on MOPSO was introduced to obtain a high-performance IPMSM characterized by high torque, high efficiency, and low torque ripple for EV applications. The results confirm that the proposed optimization framework can effectively enhance the overall performance of the reference IPMSM while reducing computational time compared to traditional FEA-based optimization procedures, without compromising accuracy.

Future work will focus on extending the optimization framework to include both stator and rotor parameters as well as broader performance objectives. Moreover, motor control investigations for the developed prototype will be conducted to further validate and demonstrate the effectiveness of the proposed optimization approach.

Author Contributions

A. R. Shams performed the simulations, analyzed the results, contributed to the development and commissioning of the optimized motor, and drafted the initial version of the manuscript. Dr. E. Rokrok supervised the research process, performed the simulations, validated the results, and conducted the final review of the manuscript. Dr. A.A. Zamani supervised the research process, performed the simulations, validated the results, and contributed to the editing and final revision of the manuscript. Dr. B. Rezaeealam supervised the research process of the work, validated the results.

Conflict of Interest

The authors declare no potential conflict of interest regarding the publication of this work. In addition, the ethical issues including plagiarism, informed consent, misconduct, data fabrication and, or falsification, double publication and, or submission, and redundancy have been completely witnessed by the authors.

Acknowledgment

We would like to express our gratitude to the editors and reviewers of JECEI for their valuable feedback and support during the review process. This work was entirely self-supported, with no financial support from any external agency.

Funding

This research received no external funding.

Abbreviations

BEMF	Back-Electromotive Force

EV	Electric Vehicle
FEA	Finite Element Analysis
FOC	Field-Oriented Control
IPMSM	Interior Permanent Magnet Synchronous Motor
MMF	Magneto Motive Force
MOPSO	Multi Objective Particle Swarm Optimization
PSO	Particle Swarm Optimization
SO-DT-IPMSM	Stator-Optimized Delta-Type Interior Permanent Magnet Synchronous Motor
SPMSM	Surface-mounted Permanent Magnet Synchronous Motor
THD	Total Harmonic Distortion

References

[1] X. Zhao, B. Kou, C. Huang, L. Zhang, "A reverse-salient permanent magnet synchronous motor for electric vehicles considering operating conditions," IEEE Trans. Energy Convers., 38(1): 262–272, 2023.

[2] Y. Xu, M. Ai, Z. Xu, W. Liu, Y. Wang, "Research on interior permanent magnet synchronous motor based on performance matching of electric bus," IEEE Trans. Appl. Supercond., 31(8): 5204304, 2021.

[3] J. Liu, Y. Liang, P. Yang, "Research on novel flat wire transposed winding of PMSM for electric vehicle," IEEE Trans. Transp. Electrif., 9(1): 771–781, 2023.

[4] J. Pyrhönen, T. Jokinen, V. Hrabovcová, Design of Rotating Electrical Machines, vol. I. New York: Wiley, 2013.

[5] Y. Wang, N. Bianchi, R. Qu, "Comparative study of non-rare-earth and rare-earth PM motors for EV applications," Energies, 15(7): 2711, 2022.

[6] L. Wang, X. Wang, P. Gao, "Torque ripple reduction analysis of interior permanent magnet synchronous motor for electric vehicle," Trans. China Electrotech. Soc., 39(20): 6386–6396, 2024.

[7] T. Gundogdu, G. Komurgoz, "A systematic design optimization approach for interior permanent magnet machines equipped with novel semi-overlapping windings," Struct. Multidiscip. Optim., 63(3): 1491–1512, 2021.

[8] J. Liang, A. Parsapour, Z. Yang, C. Caicedo-Narvaez, M. Moallem, B. Fahimi, "Optimization of air-gap profile in interior permanent-magnet synchronous motors for torque ripple mitigation," IEEE Trans. Transp. Electrif., 5(1): 118–125, 2019.

[9] G. Zhang, W. Yu, W. Hua, R. Cao, H. Qiu, A. Guo, "The design and optimization of an interior permanent magnet synchronous machine applied in an electric traction vehicle requiring a low torque ripple," Appl. Sci., 9(17): 3634, 2019.

[10] Y. Xu, Y. Chen, Z. Fu, M. Xu, H. Liu, L. Cheng, "Design and analysis of an interior permanent magnet synchronous motor for a traction drive using multi-objective optimization," Int. Trans. Electr. Energy Syst., 2024: 1–15, 2024.

[11] S. Lim, S. Min, J. P. Hong, "Shape design optimization of interior permanent magnet motor for vibration mitigation using level set method," Int. J. Automot. Technol., 17: 917–922, 2016.

[12] X. Sun, Z. Shi, G. Lei, Y. Guo, J. Zhu, "Multi-objective design optimization of an IPMSM based on multilevel strategy," IEEE Trans. Ind. Electron., 68(1): 139–148, 2021.

[13] X. Zhu, J. Huang, L. Quan, Z. Xiang, B. Shi, "Comprehensive sensitivity analysis and multi-objective optimization research of permanent magnet flux-intensifying motors," IEEE Trans. Ind. Electron., 66(4): 2613–2627, 2019.

[14] Y. Yu, Y. Pan, Q. Chen, Y. Hu, J. Gao, Z. Zhao, S. Niu, S. Zhou, "Multi-objective optimization strategy for permanent magnet synchronous motor based on combined surrogate model and optimization algorithm," Energies, 16: 1630, 2023.

[15] G. Feng, C. Lai, N. C. Kar, "Practical testing solutions to optimal stator harmonic current design for PMSM torque ripple minimization using speed harmonics," IEEE Trans. Power Electron., 33: 5181–5191, 2018.

[16] F. Xiong, R. Yan, Y. Xie, K. Yang, "Design and optimization of an interior permanent-magnet synchronous motor for aircraft drive application," Appl. Sci., 14: 309, 2024.

[17] Y. Yu, C. Liang, D. Zeng, Y. Hu, J. Yang, "Multi-objective optimization of IPMSM for electric vehicles based on the combinatorial surrogate model and the hierarchical design method," Int. J. Electr. Power Energy Syst., 162: 110245, 2024.

[18] K. S. Seo, Y. J. Kim, S. Y. Jung, "Stator teeth shape design for torque ripple reduction in surface-mounted permanent magnet synchronous motor," in Proc. 2014 17th International Conference on Electrical Machines and Systems (ICEMS): 387–390, 2014.

[19] L. Niu, "Optimization design and torque performance research of interior permanent magnet synchronous motors," Sci. Rep., 15: 8822, 2025.

[20] X. Kong, Z. Yang, "Multi-objective optimization of dual-stator permanent magnet motor based on composite algorithm," Sci. Rep., 15: 22982, 2025.

[21] X. Zhou, X. Zhu, W. Wu, Z. Xiang, Y. Liu, L. Quan, "Multi-objective optimization design of variable-saliency-ratio PM motor considering driving cycles," IEEE Trans. Ind. Electron., 68(8): 6516–6526, 2021.

[22] J. M. Ahn, M. K. Baek, S. H. Park, D. K. Lim, "Optimal design of IPMSM for EV using subdivided Kriging multi-objective optimization," Processes, 9(9): 1490, 2021.

[23] R. Yang, Electrified Vehicle Traction Machine Design with Manufacturing Considerations, Ph.D. dissertation, Dept. Mechanical Eng., McMaster Univ., Hamilton, ON, Canada, 2017.

[24] Y. Inoue, Y. Kawaguchi, S. Morimoto, M. Sanada, "Performance improvement of sensorless IPMSM drives in a low-speed region using online parameter identification," IEEE Trans. Ind. Appl., 47(2): 798–804, 2011.

[25] W. Feng, W. Zhang, S. Huang, "A novel parameter estimation method for PMSM by using chaotic particle swarm optimization with dynamic self-optimization," IEEE Trans. Veh. Technol., 72(7): 8424–8432, 2023.

[26] S. Zheng, X. Zhu, L. Xu, "Multi-objective optimization design of a multi-permanent-magnet motor considering magnet characteristic variation effects," IEEE Trans. Ind. Electron., 69: 3428–3438, 2022.

[27] P. P. C. Bhagubai, J. G. Sarrico, J. F. P. Fernandes, P. J. Costa Branco, "Design, multi-objective optimization, and prototyping of a 20 kW 8000 rpm permanent magnet synchronous motor for a competition electric vehicle," Energies, 13: 2465, 2020.

[28] M. Mendizabal, A. McCloskey, J. Poza, S. Zarate, L. Irazu, "Sensitivity analysis of the design parameters of permanent magnet synchronous motors for vibration reduction," Appl. Sci., 13: 5486, 2023.

[29] Y. Wang, M. Zhao, X. Jia, et al., "Analysis and multi-objective optimization of an interior permanent magnet synchronous

motor for a comprehensive performance enhancement," Struct. Multidiscip. Optim., 68: 55, 2025.

[30] S. Zhang, H. Yan, L. Yang, H. Zhao, X. Du, J. Zhang, "Optimization design of permanent magnet synchronous motor based on multi-objective artificial hummingbird algorithm," Actuators, 13: 243, 2024.

[31] S. Ahmadi, T. Lubin, A. Vahedi, N. Taghavi, "Sensitivity-based optimization of interior permanent magnet synchronous motor for torque characteristic enhancement," Energies, 14: 2240, 2021.

[32] X. Li, G. Li, Z. Han, X. Han, "High-torque and low-noise IPMSM multi-objective collaborative optimization based on multi-layer surrogate model," Authorea, 2024.

[33] H. Chen, C. H. T. Lee, "Parametric sensitivity analysis and design optimization of an interior permanent magnet synchronous motor," IEEE Access, 7: 159918–159929, 2019.

[34] X. Luo, G. Liu, B. Xie, L. Zhu, F. Zhang, "Review of sensitivity analysis methods for optimal design parameters of motors," Chin. J. Electr. Eng., 11: 114–135, 2025.

[35] F. Liu, X. Wang, H. Wei, "Electromagnetic performance analysis, prediction, and multi-objective optimization for U-type IPMSM," IEEE Trans. Ind. Electron., 71(9): 10322–10334, 2024.

[36] Y. Yu, P. Zhao, Y. Hao, D. Zeng, Y. Hu, B. Zhang, H. Yang, "Multi-objective optimization of permanent magnet synchronous motor based on Taguchi method and PSO algorithm," Energies, 16: 267, 2022.

[37] S. Nasr, B. Ganji, M. Moallem, "Design optimization of the delta-shape interior permanent magnet synchronous motor for electric vehicle application," J. Electr. Comput. Eng. Innovations (JECEI), 11: 291–300, 2023.

Biographies



Alireza Shams was born in Isfahan, Iran, in 1995. He received B.Sc. degree in Electrical Engineering from Technical and Vocational University, in 2018 and M.Sc. degree in Electrical Engineering from Malek-Ashtar University of Technology, Isfahan, Iran, in 2020. He is currently pursuing the Ph.D. degree in power electronics and electrical machines with Lorestan University, Khoramabad, Iran. His research interests include electric vehicle propulsion systems, IPMSM design optimization, torque ripple minimization, and efficiency improvement.

- Email: alireza.sh.esf.74@gmail.com
- ORCID: 0009-0000-5247-1398
- Web of Science Researcher ID: NA
- Scopus Author ID: NA
- Homepage: NA



Esmaeel Rokrok was born in Khoramabad, Iran, in 1972. He received his B.S., M.S. and Ph.D. degrees in Electrical Engineering from the Isfahan University of Technology, Isfahan, Iran, in 1985, 1997 and 2010, respectively. He is presently working as an Assistant Professor in the Department of Electrical Engineering, Lorestan University, Khoramabad, Iran. His current research interests include power system control and dynamics, dispersed generation, microgrids, power electronics and robust control.

- Email: rokrok.e@lu.ac.ir
- ORCID: 0000-0002-5034-4659
- Web of Science Researcher ID: NA
- Scopus Author ID: NA
- Homepage: https://professors.lu.ac.ir/show/?id=245



Behrooz Rezaeealam received the B.S. degree from Isfahan University of Technology in 1997, the M.S. and Ph.D. degrees from University of Tehran in 2000 and 2005, respectively, all in electrical engineering. He is currently an associate professor in the department of electrical engineering, Lorestan University, Iran. His research interests include modeling and design using FEM, electrical machines and drives.

- Email: rezaee.bh@lu.ac.ir
- ORCID: 0000-0002-9391-4826
- Web of Science Researcher ID: NA
- Scopus Author ID: NA
- Homepage: https://professors.lu.ac.ir/show/?id=240



Abbas-Ali Zamani was born in 1986 in Isfahan, Iran. He earned a B.Sc. degree in electronic engineering from Hakim Sabzevari University in Iran in 2009, and an M.Sc. degree in control engineering from Isfahan University of Technology in 2011. In 2018, he received his Ph.D. in control engineering from the University of Sistan and Baluchestan in Iran. Dr. Zamani is currently an assistant professor in the Department of Electrical Engineering, Technical and Vocational University, Iran. Seismic control, power system control, smart grids, renewable energies, and artificial intelligence are among his research interests.

- Email: a-zamani@tvu.ac.ir
- ORCID: 0000-0002-3654-7767
- Web of Science Researcher ID: NA
- Scopus Author ID: NA
- Homepage: https://profs.tvu.ac.ir/fa/teacher_db/179192

Journal of Electrical and Computer Engineering Innovations
(JECEI)
Journal homepage: http://www.jecei.sru.ac.ir

Research Paper

Hybrid CNN–BiLSTM Model with BERT Embeddings for Urgency Detection in MOOC Forums

Mujtaba Sultani [1,2], ***Negin Daneshpour*** [1,*]

[1]*Faculty of Computer Engineering, Shahid Rajaee Teacher Training University, Tehran, Iran.*

[2]*Faculty of Computer Science, Kabul Polytechnic University (KPU), Kabul, Afghanistan.*

Article Information

Article History:

Received 27 November 2025
Reviewed 05 January 2026
Revised 03 February 2026
Accepted 22 February 2026

Keywords:

BERT
Data augmentation
CBiLSTM
Urgent post classification
Mooc
Deep learning
Text classification

*Corresponding Author's Email Address:
ndaneshpour@sru.ac.ir

Abstract

Background and Objectives: Discussion forums in Massive Open Online Courses (MOOCs) enable students to interact with instructors and share educational concerns. However, identifying urgent posts within the vast volume of discussions poses significant challenges. High dropout rates and the need for timely responses to urgent queries highlight the importance of efficient classification systems. This study addresses the binary classification of student posts in the Stanford MOOC Posts dataset into urgent and non-urgent categories, and aims to improve performance in the presence of class imbalance.

Methods: We propose a hybrid deep learning model that integrates BERT-based contextual embeddings with a Convolutional Neural Networks (CNN) and Bidirectional Long Short-Term Memory (BiLSTM) architecture to capture both local textual features and long-term dependencies. To mitigate the class imbalance issue, BERT-based data augmentation technique was employed which enriches minority class samples, and enhances model generalization and urgent post detection. The model's performance was compared against baseline methods, including CNN, LSTM, BiLSTM, and other state-of-the-art models. Evaluation metrics such as F1-weighted score and class-specific F1 scores were used to assess effectiveness.

Results: The model achieved a 93.3% F1-weighted score and an 84.1% F1 score for the urgent class which surpasses the best-performing state-of-the-art model by 0.6% and 0.8%, respectively. The results show the effectiveness of augmentation and hybrid architecture while identifying urgent posts, particularly within imbalanced datasets.

Conclusion: This research introduces a scalable and effective framework for urgent post detection in MOOCs. By leveraging BERT-based augmentation and a CNN–BiLSTM hybrid architecture that integrates contextual and sequential learning, the study provides automated forum analysis, offer timely insights for instructors and course designers to enhance students support, engagement, and retention.

This work is distributed under the CC BY license (http://creativecommons.org/licenses/by/4.0/)

How to cite this paper:
M. Sultani, N. Daneshpour, "Hybrid CNN–BiLSTM model with BERT embeddings for urgency detection in mooc forums," J. Electr. Comput. Eng. Innovations, 14(2): 487-506, 2026.

DOI: 10.22061/jecei.2026.12535.891

URL: https://jecei.sru.ac.ir/article_2542.html

2345- 3044/© 2026 The Authors. Published by Shahid Rajaee Teacher Training University.

Introduction

Educational technology has been reshaped by the rapid growth of Massive Online Open Courses (MOOCs). These courses aim to make education accessible worldwide and provide access to online resources[1]. More than 58 million users worldwide have enrolled in a MOOC. Currently, more than 220 million learners are participating in MOOCs worldwide [2]. The widespread popularity of MOOCs is also evident from the fact that more than 700 prestigious universities participate in them and offer a variety of courses accessible through platforms such as Coursera, edX, and Udacity. The wide availability of MOOCs signifies a shift in educational approaches that emphasizes the democratization of knowledge and promotes a culture of continuous lifelong learning [3]. Individuals can use these courses to learn new skills, enhance their understanding, and foster professional development according to their preferences [1].

A key aspect of MOOCs is the inclusion of communication platforms, particularly discussion forums. These forums facilitate interaction between learners and instructors, as well as peer-to-peer exchanges [4]. These forums play an important role in supporting different learning approaches that shape the educational experiences of MOOC participants. Moreover, these forums serve as a valuable channel for students to articulate their questions and urgent concerns [5].

However, considering the substantial quantity of MOOC participants and the limited number of instructors, it poses a challenge to effectively track and respond to students' posts and questions. Quick responses to important posts are often necessary to help students overcome obstacles during their learning journey. Failure to provide timely feedback can lead to learner frustration and increase dropout rates [6]. Therefore, it is necessary to develop mechanisms that differentiate urgent posts and ensure that they receive immediate attention and response from instructors [7], [8]. Implementing an effective system to monitor and handle urgent posts would allow instructors to give precedence to their responses and effectively handle the overwhelming volume of submissions. This system would not only optimize instructors' time and attention but also empower them to devote more energy to promote community engagement and provide valuable support [8].

Extensive research has focused on classifying MOOC forum posts into urgent and non-urgent categories. Various word representation techniques and classification approaches have been explored to develop effective models. The goal is to prioritize posts according to their urgency. In [8]-[10], statistical techniques like term frequency (TF), inverse document frequency (IDF), and term frequency-inverse document frequency (TF-IDF) were employed to represent words. However, they neglected the meaning of word order [11], which led to a limitation while capturing the document context. These studies used conventional classification algorithms like Support Vector Machine (SVM) and Nearest Centroid, which require low computational effort but have poor performance because they often rely heavily on manual feature selection [12]. Studies [12]-[15] have used pre-trained models like Google News and Glove to represent words with dense vectors that capture their contextual meaning within the document [16]. These studies used different architectures including multiple CNNs, CNN aggregation, GRU, and attention layers to develop their models. They emphasized including additional representational features to select effective features and assign higher weight to the most important features.

Despite these efforts, challenges remain, particularly in handling imbalanced datasets, which can affect classification performance and lead to bias toward larger classes [17], [18]. Improvements in the classification of imbalanced datasets have been classified into five categories: Data, Algorithms, Cost-Sensitive, Feature Selection, and Ensemble Approaches [19]. Common data-level methods include re-sampling to adjust the number of samples in the dataset. Oversampling involves adding samples, usually by copying samples, while under-sampling involves removing samples, often by random selection. While these methods have shown some effectiveness in data matching, they are not sufficient to completely solve the problem at hand [20]. In this study, we specifically address the data level imbalance and we focused on technique to balance text datasets. We employed BERT-based data augmentation (DA) to solve the data balancing problem [21]. Data augmentation method increases the scale of training data. This approach significantly contributes to mitigate overfitting and improve the robustness of machine learning models, especially for tasks with limited data availability [22].

On the other hand, model generalization, which denotes the ability of a machine-learning model to respond accurately to unseen data, is a critical aspect of model development [22]. However, the presence of a generalization constraint in the literature, poses a significant challenge when applying machine learning models, especially in subdomains or specific contexts where training data may be limited or unavailable. Educational data are inherently diverse and encompass different subjects, learning styles, and student demographics. Therefore, models must have the ability to adapt and perform reliably in different subdomains [22]. By closing the generalization gap,

machine learning models can provide more accurate and reliable insights, recommendations, and support for learners, educators, and educational institutions [22]. In this study, we address this constraint by employing BERT-based data augmentation to balance the dataset and using the BERT pre-trained model for word embeddings, both of which enhance model generalization and performance.

In this study, we employed the BERT model as the embedding layer, fine-tuned by a novel hybrid deep learning approach, combining Convolutional Neural Network (CNN) and Bidirectional Long Short-Term Memory (BiLSTM) layers. We named this hybrid model Convolutional BiLSTM (CBiLSTM), which enables an effective and precise classification of urgent posts. In CBiLSTM, the CNN layers effectively handle the high dimensionality of input texts, and BiLSTM layers explore feature context bidirectionally. The outcomes illustrate that CBiLSTM outperforms conventional deep learning models commonly utilized for urgent post classification using widely recognized Stanford MOOC Post Corpus. Our contributions are as follows:

1. We introduced a novel BERT-based data augmentation technique to balance the dataset, which is the first of its kind in the MOOC context.
2. We leveraged BERT pre-trained model as an embedding layer to enhance context understanding and semantic meaning for more accurate and context-aware representations.
3. We propose the CBiLSTM model that integrates CNN and BiLSTM layers for effective feature extraction and capturing long-term dependencies.
4. Our model outperforms conventional deep learning models in classifying urgent posts which demonstrates the approach's effectiveness and reliability using the Stanford MOOC Posts dataset.

The following sections of this paper provide a structured flow of our research. Section 2 offers a brief overview of related work, while Section 3 delves into the adapted method. In Section 4, we detail the experimental setup, data, and evaluation metrics. Results are discussed in Section 5, followed by future work in Section 6. Finally, Section 7 provides the conclusive results.

Related Work

In the field of online education, MOOCs have become widely adopted due to their flexibility and accessibility. As participation grows, discussion forums have become important centers for communication, knowledge sharing, and collaborative learning [23]. However, the high volume of posts makes it difficult for instructors to respond promptly, especially to urgent questions.

Consequently, researchers have focused on the classification of urgent posts within MOOC discussion forums to enhance the effectiveness and efficiency of instructor-learner interactions. MOOC post-classification employs both traditional machine learning and deep learning algorithms [14].

In [8], metadata and linguistic features were used in conjunction with models such as AdaBoost to identify urgent posts. While these approaches offered modest improvements, they depended heavily on handcrafted features and struggled to capture semantic nuances. Similarly, [24] developed a multi-dimensional classification framework for urgency, sentiment, and confusion. Although effective within specific courses, the method lacked generalizability across domains. [25] performed an analysis of over 100,000 discussion posts on Coursera. They used linear regression in combination with a Gradient Lifting Decision Tree (GBDT) to classify MOOC discussion posts. In particular, this model uses features that are independent of course content and achieved an overall accuracy of 85%. These models, however, continued to rely on shallow representations that cannot fully interpret contextual meaning.

Deep learning approaches have addressed some of these limitations. The convolutional LSTM architecture in [26] captured both local and sequential features, and achieves 86.6% accuracy for urgent post classification. Yet, the use of static embeddings limited their ability to model contextual word meanings. Similarly, [14] combined CNN, GRU, and Char-CNN layers with pre-trained Google News word vectors to handle noisy text, but the embedding remained context-independent and insufficient for capturing subtle urgency cues. Additional studies investigated confusion detection or relevance classification using logistic regression, bag-of-words, or SVMs [9], [27], but these approaches continued to face challenges with semantic ambiguity and domain transferability.

Khodeir [15] introduced a Bi-GRU model enhanced with BERT embeddings for urgent post classification. Although this work demonstrated improved performance through contextual representations, the architecture relied on a single recurrent component and lacked mechanisms to fully capture both local and long-range semantic patterns. Similarly, El-Rashidy et al. [12] proposed weighted BERT features combined with multi-CNN models to improve MOOC post classification. While effective, this approach focused primarily on convolutional feature extraction and did not integrate sequential modeling which limits model ability to encode temporal dependencies that are often important in urgency-related discourse. Table 1 presents an overview of previous research results.

Table 1: Overview of past study results

Authors	Dataset	Approach /Model	Embedding Layer	Results/Findings
[12]	Stanford MOOC Posts	Feature aggregation model based on CNN	BERT	The proposed model first aggregates feature to capture data-driven relationships among token features as well as their representation. Then CNN is implemented to enhance the accuracy of text context interpretation. Finally, these combined features are utilized for post text classification. The model achieved 92.7% F1-weighted scores.
[15]	Stanford MOOC Posts	Bi-GRU	BERT	The model is created based on BERT as embedding layer and achieved 91.9% F1-weighted scores.
[14]	Stanford MOOC Posts	Hybrid CNN + GRU as well as Char-CNN	Google-news	This hybrid model was proposed to tackle with the noise of spelling errors and emoticons. The model achieved an impressed 91.8% F1-weighted scores.
[8]	Stanford MOOC Posts	AdaBoost (Decision Tree)	LIWC + Term Frequency	This study tried traditional classification algorithms namely, NB, SVM, RF, AdaBoost, and LR. The best 88% F1-Score was achieved by AdaBoost.
[25]	Stanford MOOC Posts	Linear Regression + gradient lifting decision tree (GBDT)	Google Word2Vec	This model classified sentiment, urgency and confusion. This model achieved 86.6% accuracy in classifying urgent posts.
[26]	More than 100,000 Coursera threads	Hybrid of CNN + LSTM		The proposed model uses features that are independent of course content and achieves an impressive overall accuracy of 85%. They also obtained that most of the posts were not related to the course contents.
[24]	Stanford MOOC Posts	NB, SVM, RF	TF-IDF with unigram features	Proposed classification model considered urgency, sentiment and confusion in different domains. This model gave good result within the domain but is difficult to generalize across different domains.
[9]	Stanford MOOC Posts	Logistic Regression	Bag of words with unigram features	A two-stage model is introduced: initially, the model identifies instances of confusion, followed by the application of a recommendation system to suggest brief video clips aimed at resolving that confusion. This model obtained 77% F1-scores.

Method

We present a new method to classify urgent posts in MOOC discussion forums which integrates Convolutional Neural Network (CNN) and Bidirectional Long Short-Term Memory (BiLSTM) layers based on BERT. CBiLSTM model aims to accurately classify MOOC forum posts as urgent or non-urgent. The proposed approach follows a multi-stage process, which involves data preprocessing, BERT-based data augmentation to enrich the training set with contextualized samples, BERT-based word embedding to facilitate a deeper understanding of the text, and the comprehensive description of the CBiLSTM model. The method formulation flow is illustrated in Fig. 1.

A. Preprocessing

In the preprocessing phase of the Stanford MOOC Posts dataset, a series of essential steps are undertaken to ensure data consistency and quality. Firstly, all URLs (Uniform Resource Locators) were removed from the text to eliminate any potential noise and irrelevant information. To standardize word forms, contractions like "won't" and "can't" are replaced with expanded versions, such as "will not" and "can not" to facilitate uniformity in text representation. Similarly, symbols like question marks and exclamation marks were substituted with a specific word to promote a cohesive approach to text analysis.

To enhance text readability, abbreviations like "'re", "n't", "'s", and others were transformed into their corresponding full words ('are', 'not', 'is', etc.) to streamline the text for further analysis. Further, symbols such as slashes, dollar signs, and others are eliminated to ensure that special characters do not interfere with the text's semantic meaning.

To facilitate lemmatization, the Spacy 'en_core_web_ls' model is applied which groups inflected forms into their base or dictionary forms to lead to a more coherent and meaningful representation of words. Stop words were retained in the dataset, as their inclusion was found to improve the classification results [28].

The 'course_display_name' metadata feature is integrated with student posts which display the course's name and domain within the MOOC Posts dataset. By incorporating 'course_display_name' into the posts, a considerable improvement in the achieved results was observed [14].

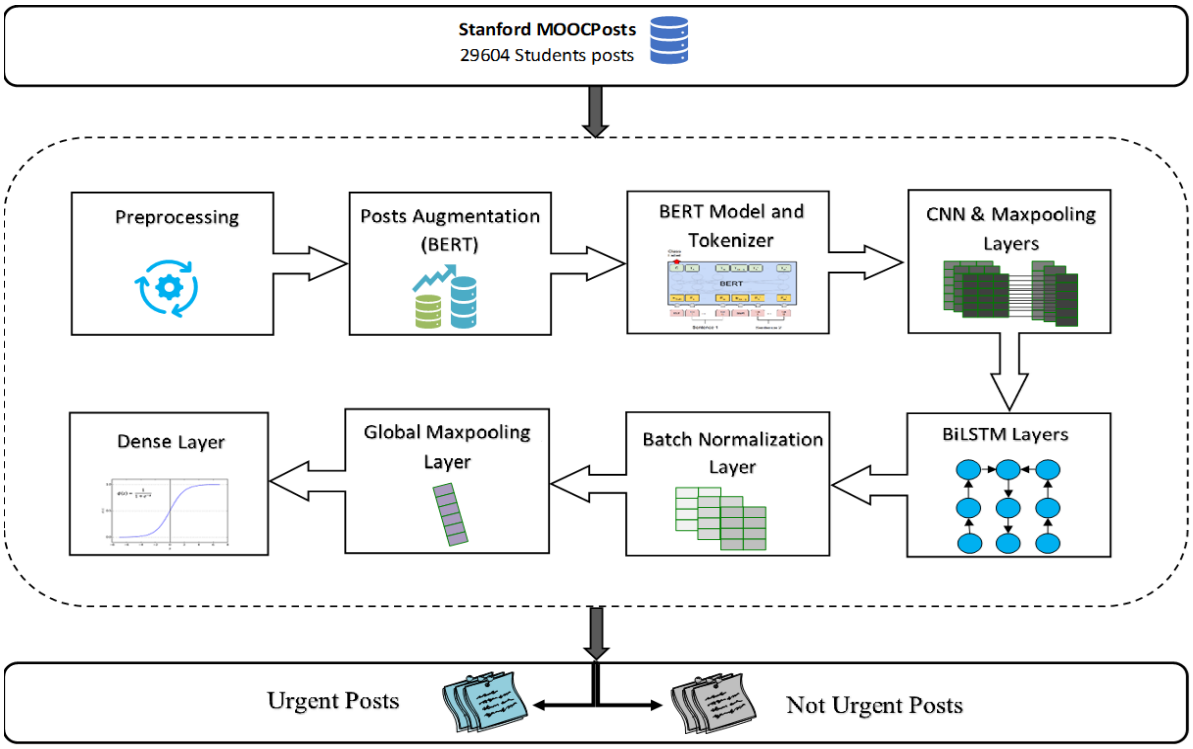


Fig. 1: The method formulation flow.

B. Addressing Data Imbalance

Text data imbalance is a prevalent challenge in natural language processing tasks, where certain classes or categories within a dataset are significantly underrepresented compared to others. Machine learning models can be adversely affected by this imbalance which leads to biased predictions and reduced accuracy, especially for minority classes [29]. Synthetic data methods like SMOTE [30] and AdaSyn [31] effectively address statistical data imbalances. However, when applied to textual data, they face challenges with overfitting and noise. Although GANs like CycleGAN [32] have shown promise in generating synthetic numerical and image data, their suitability for textual data, including grammar, context, and semantics, requires further evaluation.

We employed BERT (Bidirectional Encoder Representations from Transformers) to augment the training dataset. Its strong language understanding and contextual modeling capabilities improve the quality of the augmented data, thereby enhancing overall model performance. In the context of text augmentation using BERT, as seen in Fig. 2, the initial step is tokenization which breaks the input sentence into discrete units like words. Subsequently, (MASK) tokens are inserted at random positions within the sentence which results in a partially masked sentence. After augmentation, the sentence is passed through the BERT model which leverages contextual information from the surrounding tokens to predict the appropriate replacements for the (MASK) tokens.

Table 2 presents the original samples alongside their corresponding augmented variations.

Prior to augmentation, the training distribution consisted of 4,063 urgent vs. 15,934 non-urgent samples. We generated 11,871 synthetic urgent samples, increasing the urgent class size to 15,934, matching the majority class. This process expanded the training set from 19,997 to 32,186 instances. Although some generated sentences contained minor grammatical distortions, we retained them because prior studies show that such noise does not harm and may even improve model robustness when semantic meaning is preserved.

Kobayashi [40] demonstrated that contextual augmentation with slight syntactic noise maintains or enhances performance, while Wei and Zou [41] reported that transformer-based models tolerate minor grammatical irregularities without degrading classification accuracy. Therefore, all augmented samples were used during training.

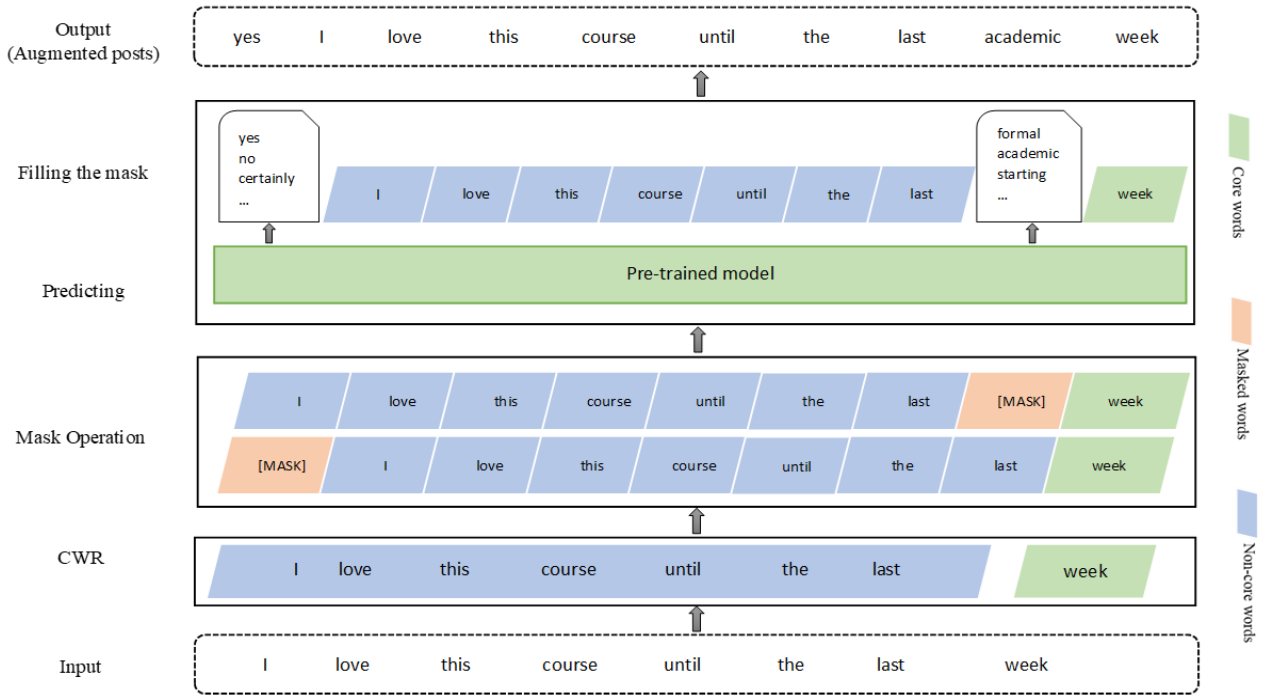


Fig. 2: Internal process of BERT text augmentation.

Table 2: Original posts alongside their corresponding augmented variations

No	Original posts	Augmented posts	Urgency
1	I love this course until the last week when try to submit work and all I get be the stupid try again come up have write in the education education one one five number how to learn math	yes I love this course until the last academic week and when try to submit work applications and instead all I get be the more stupid try again come up have write out in the joint discussion that this be happen education education one one five number how next to learn math	Urgent
2	I have the same issue take a look at the update on some platform issue discussion topic they be fix some bug education education one one five number how to learn math	I have the same issue take to a quick look then at from the news update when on some platform more issue discussion in topic they be fix some bug computer education education one one five plus number how to learn math	Not Urgent

BERT-generated variations are introduced to the urgent class samples to address the data imbalance issue and lead to notable improvements in model performance and generalization. Fig. 3 illustrates the distribution of both urgent and not-urgent classes following the augmentation process.

Tokenization is performed using the pre-trained BERT model, specifically the 'pre-trained bert-base-uncased tokenizer', which is case-insensitive and offered by the transformer's library.

Algorithm 1 shows the augmentation process steps.

C. Embedding Layer

In NLP and neural network language models, the word embedding layer is pivotal. It is responsible for transforming words or tokens in a text into dense numerical vectors in a high-dimensional space. Before BERT, Word2Vec, and Glove were widely used in NLP tasks for traditional word embeddings. BERT, as introduced by [33], is a transformer-based model, unlike traditional approaches, BERT learns contextual embeddings. It is pre-trained on a massive corpus using next-sentence prediction and masked language modeling tasks. This pre-training enables BERT to understand the semantic meaning and syntactic structure of words in various contexts. BERT-based word embeddings not only capture the semantic meaning of individual words but also their contextual significance in sentences or documents. BERT, as shown in Fig. 4, uses special tokens such as '(CLS)' and '(SEP)' to handle variable-length sequences of text. The '(CLS)' token represents the classification token and is used to achieve a fixed-size vector representation for the entire input sequence, which can be used for downstream classification tasks. The "(SEP)" token separates different sentences in the input when dealing with sentence-level tasks [33].

Algorithm 1*: BERT-based dataset augmentation*

Input:

- ✓ Original dataset of text samples: *D*
- ✓ BERT-based augmentation instance: *augmenter*
- ✓ Number of augmentation repetitions (*optional*): *repetitions*
- ✓ Number of augmented samples per minority class sample (*optional*): *samples*

Output: Augmented dataset of text samples: A

Algorithm:

Step 1: Load the original dataset (*D*).
Step 2: Select minority class samples (*minority_samples*) from the original dataset (*D*).
Step 3: Generate augmented texts (*augmented_texts*) for each minority class sample (*minority_samples*) using the augmenter.
Step 4: Create an augmented dataset (A) containing the original labels and generated augmented texts.
Step 5: Repeat steps 3 and 4 for the specified repetitions (*if applicable*).
Step 6: Append the augmented A to the original D.
Step 7: Shuffle the entire dataset (*A*) to create a balanced and diverse dataset.

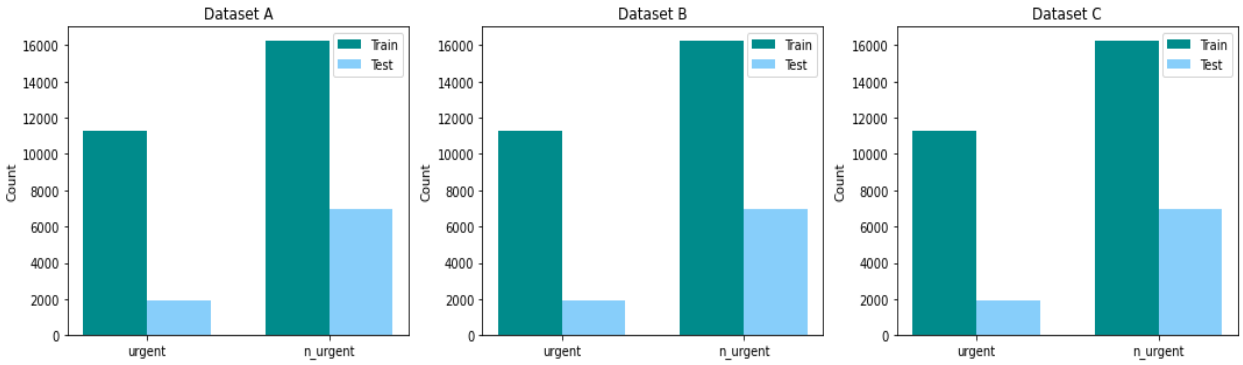


Fig. 3: Distribution of urgent and not urgent classes following the augmentation process.

In text classification, BERT encapsulates the entire sequence by utilizing the final hidden state of the special token (CLS). There are three distinct fine-tuning techniques: 1) Training the Entire Architecture: All layers of the BERT model, including task-specific layers, are updated during fine-tuning, which allows maximum flexibility and adaptation to the specific task. 2) Training Some Layers While Freezing Others: Only a subset of BERT layers is updated, while others are frozen, which strikes a balance between flexibility and computational efficiency. 3) Freeze the Entire Architecture: All layers, including pre-trained and task-specific, are kept frozen which makes BERT function as a fixed feature extractor for subsequent tasks [15].

In this study, a pre-trained BERT model was loaded and used for tokenization. The BERT model was kept frozen during fine-tuning, while only the CBiLSTM components were trained to learn from its representations.

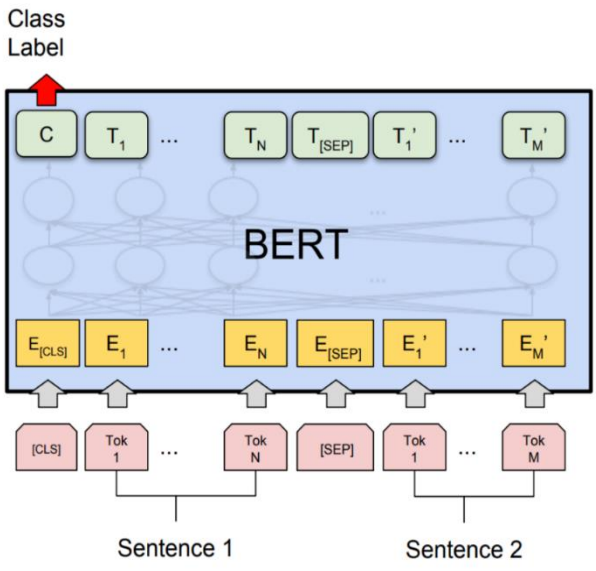


Fig. 4: BERT (Language Model) [33].

D. Convolutional BiLSTM (CBiLSTM) Model

CNN and RNN are widely used models in sentiment analysis and text classification. Each model has distinct strengths: CNN excels at extracting local features by analyzing the spatial relationships within the text but cannot learn sequential correlations, while RNN is adept at capturing sequential correlations and extracting global features [34], [35]. However, traditional RNNs suffer from issues like gradient explosion or vanishing gradient when dealing with long sequences of data. To overcome these limitations, LSTM [35], an extension of RNN, was introduced. LSTM employs memory cells to handle gradient issues and capture long-term dependencies. In a traditional LSTM, data propagates through the network unidirectionally, as depicted in Fig. 5-a. While this allows the LSTM to model past dependencies effectively, it may not fully leverage future context, which is important in text classification tasks.

LSTM uses a forget gate (f_{gt}), input gate (i_{gt}), and output gate (o_{gt}), constructed with a sigmoid layer to control the information flow within its cells [36]. The current cell state of the LSTM is represented as c_t. The forget gate decides what information to discard, determined by (1):

$$f_t = \sigma(W_f \cdot [h_{t-1}, x_t] + b_f) \quad (1)$$

where, w_f and b_f illustrate the forget gate's weights and bias, while x_t corresponds to the input sequence and h_{t-1} signifies the previous output state.

Next, the LSTM layer utilizes its input gate to determine which elements from the current input x_t should be incorporated into the present cell state c_t. This process involves the use of both sigmoid and tanh layers. The sigmoid layer determines updates to the current cell state, as shown in (2). On the other hand, the tanh layer generates a new vector, denoted as c'_t using (3), composed of the updated values. W_i and b_i represent the weights and bias of the input gate respectively.

$$i_{gt} = \sigma(W_i \cdot [h_{t-1}, x_t] + b_i) \quad (2)$$

$$c'_t = \tanh(W_c \cdot [h_{t-1}, x_t] + b_c) \quad (3)$$

Next, LSTM updates the previous cell state c_{t-1} with the new cell state c_t by multiplying forget gate f_{gt} values with c_{t-1}, followed by the addition of the newly computed candidate values scaled by the i_{gt}, as displayed in (4).

$$c_t = fg_t \cdot c_{t-1} + c'_t \cdot ig_t \quad (4)$$

As a result, the LSTM employs its output gate, represented by (5) and (6):

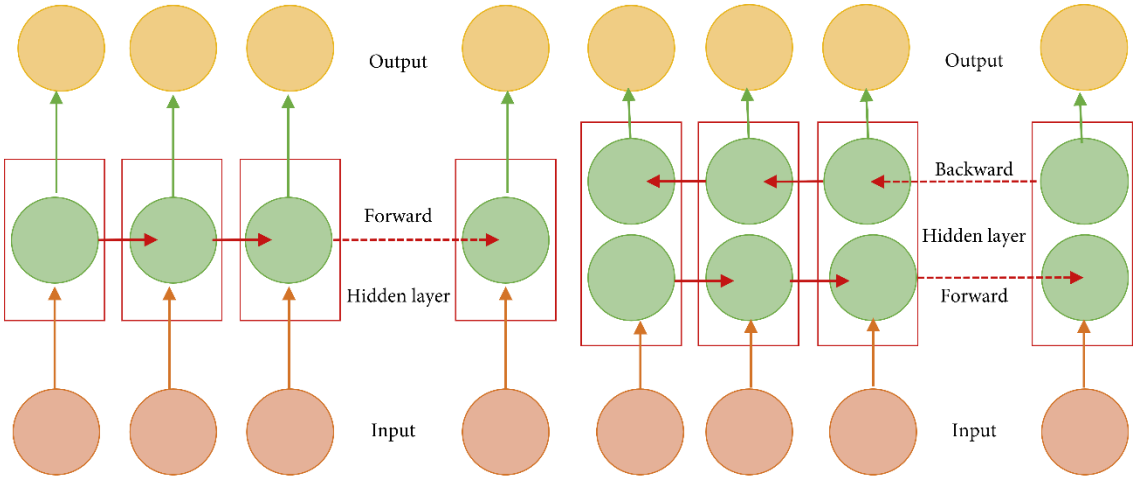
$$Og_t = \sigma(W_o \cdot [h_{t-1}, x_t] + b_o) \quad (5)$$

$$h_t = og_t \cdot \tanh(c_t) \quad (6)$$

The final hidden state h_t is subsequently passed to a fully connected layer for further processing.

Moreover, Bi-LSTM [37] enhances LSTM's capabilities by incorporating two LSTM layers which simultaneously process the information bidirectionally, as depicted in Fig. 5-b.

The forward LSTM processes the input sequence from the first step to the last, while the backward LSTM processes it in reverse, from the last step to the first. This enables Bi-LSTM to better capture bidirectional dependencies in the data, making it particularly effective in various text classification tasks.



A: LSTM ***B: Bi-LSTM***

Fig. 5: Depiction of LSTM model (A) alongside a Bi-LSTM model (B) [39].

We propose CBiLSTM, a hybrid deep learning model that utilizes BERT for word embedding. The model architecture comprises two main components: CNN and BiLSTM layers. In the first step, we pass the BERT-based embeddings to the CNN structure. Following the BERT embedding layer, a series of one-dimensional convolutional layers are applied. These layers employ kernel sizes of 3, 4, and 5, each with 128 filters and ReLU activation functions. These convolutions are designed to identify local patterns and features within the embedded text. After each convolutional layer, max-pooling operations with varying pool sizes (8, 6, and 3) are performed to reduce dimensionality and retain the most significant features. A dropout layer with a 0.2 rate is added after the first convolutional layer to address overfitting.

Furthermore, the feature vectors are passed through a bidirectional LSTM layer. The model incorporates three Bi-LSTM layers with hidden units of 256, 128, and 64, respectively, each set to return sequences (return sequences=True). Bi-LSTMs capture contextual information bidirectionally which enables the model to understand the sequential dependencies within the text. To further process the output from the BiLSTM, another dropout layer with a rate of 0.1 is inserted to further enhance generalization. A batch normalization layer is applied to stabilize training by normalizing activations. Following the batch normalization layer, a global max-pooling layer is used which aggregates the most important features across the entire sequence by creating a fixed-length representation of the text data. The model concludes with a dense output layer featuring a single neuron using a sigmoid activation and provides a probability value between 0 and 1. This output layer classifies the input into either the urgent or not urgent classes.

For model training, the Adam optimizer is employed alongside a binary cross-entropy loss function. During model training, several callbacks are employed, including model checkpointing, early stopping, and learning rate reduction. These strategies ensure model convergence and prevent overfitting. Table 3 shows the detailed key parameters and threshold for the proposed model structure.

Table 3: Key parameters and threshold for the proposed model structure

Layers	**Parameters and Threshold**
BERT_base_uncased	Pre-trained model, 512 token limit, 768 features per token
Multi-Layer CNN	Number of layers: 3 Number of CNN filters: 128 – 128 – 128 Kernel sizes: 3 – 4 – 5 Activation: Relu
MaxPooling1D Layers	Number of layers: 3 Pool sizes: 8 – 6 – 3
Multi-Layer BiLSTM	Number of layers: 3 Number of hidden units: 256 – 128 – 64 Bidirectional (Return sequences): true
Dropout	Number of layers: 2 Dropout rate: 0.2 – 0.1
Dense Layer	Number of units: 1 Activation: Sigmoid
General training parameters	
Early Stopping	Patience: 3 Monitor: val_loss Min_delta: 0 Mode: min Verbose: 1
Reduce_lr	Monitor: val_loss Min_lr: 0.000001 Patience: 1 Mode: min Verbose: 1 Min_delta: 0.01
Loss	Binary_crossentropy
Optimizer	Adam
Epochs	10
Batch_size	128

Experiments

This section provides insights into the dataset, experimental setup, and evaluation metrics employed in this study.

A. Dataset and Experimental Setup

In this research, the experiments were conducted on the Stanford MOOC Posts dataset [28], a benchmark corpus introduced by [9]. The corpus comprises 29,604 anonymized learner forum posts from 11 Stanford University public online courses. These posts are divided into Humanities/Sciences, Medicine, and Education distinct domains, each containing 9723, 10001, and 9878 posts respectively. Each post is manually labeled across various dimensions, including assessing its urgency ranked on a scale from 1 to 7. To create a binary classification task for urgent post-identification, the class labels were adjusted. Posts with urgency scores of 4 or higher were categorized as "urgent," while those with scores below 4 were labeled as "not urgent." This binary classification scheme ensures that approximately 20% of posts are classified as urgent which allows instructors to promptly address critical cases, save 80% of their time, and enable efficient management of urgent posts.

Following the approach of previous studies [8], [12], [15], the dataset was categorized into three groups using course and domain names:

- Group A: The baseline scenario, where the training and test datasets remained independent across courses or domains. The whole dataset is divided into three distinct subsets.
- Group B: In this case, data division was determined by the course name. Several courses were excluded from the training phase. Specifically, courses from the Humanities and Medicine domains, such as Stat Learning (Winter 2014), Statistics in Medicine, and Managing Emergencies: What Every Doctor Must Know?, were selected for testing. As the Education domain had only one course, 33% of its posts were reserved for testing in a stratified manner.
- Group C: In this case, the domain was reserved for testing, and the classifier was trained on posts from the Medicine and Education domains. The evaluation was performed on posts from the Humanities domain, which was held out for testing. The choice of Humanities as the domain for testing was arbitrary.

As mentioned in embedding layer sub section, we conducted BERT-based data augmentation on the training sets of all three groups to address the dataset's class imbalance issue. This allows our model to learn more effectively and improves its performance while classifying urgent posts. By achieving a balanced dataset, this study aims to enhance the generalization and robustness of our model which enables the model to handle various real-world scenarios with improved precision and recall.

We employed TensorFlow and Keras libraries and utilized Python version 3.10, to build and train our proposed model. Prior to the data being used by the model, a series of preprocessing steps were carried out to ensure data quality and consistency. To facilitate the tokenization process and word embedding, we applied the pre-trained 'bert-based-uncased' model from the transformer's library. Special tokens were added to format the input sequences appropriately. As the 'bert-based-uncased' model has a constraint of a maximum input size of 512 tokens, we truncate sequences to the defined maximum length to ensure the compatibility of our data with the BERT model. As mentioned in convolutional BiLSTM (CBiLSTM) Model sub section , after a wide range of experiments, we selected the optimizer, number of layers, and number of hidden units of both CNN and BiLSTM components. These decisions were made after thorough experimentation and optimization to achieve the best performance.

B. Evaluation Metrics

In this study, we use six evaluation metrics to evaluate the model's performance: precision, recall, F1-score, F1-Weighted, Learning curve (LC), and Precision-Recall Curve (PRC). Precision measures the fraction of accurately predicted positive results by the model, while recall represents the proportion of relevant positive results correctly predicted. F1-score, a balanced metric, blends precision and recall by taking their harmonic mean to provide a single performance measure. Equations (7), (8), and (9) present the equations for these performance metrics, illustrating their mathematical formulations.

$$PR = TP / (TP + FP) \quad (7)$$

$$RC = TP / (TP + TN) \quad (8)$$

$$F1\text{-score} = (2 \cdot PR \cdot RC) / (PR + RC) \quad (9)$$

TP (True Positives), represents correctly predicted positive cases, TN (True Negatives), denotes correctly predicted negative cases, and FP (False Positives), indicates instances where the model incorrectly predicts positive cases.

Additionally, the F1-weighted score is employed to address class imbalances in the dataset by computing the weighted average of the F1 score for each class.

Learning curves are mostly employed as a diagnostic tool in machine learning, especially for incremental

learning algorithms like deep learning [38]. These curves provide a comprehensive evaluation of model performance by considering both the training and validation datasets.

They yield two insightful curves: The Training Learning Curve and the Validation Learning Curve. The former offers a glimpse into how effectively the model is "learning" from the training data, while the latter delves into how proficiently the model is "generalizing" its knowledge.

In the context of learning curves, it's common to employ minimization scores, like loss.

Smaller scores indicate more effective learning, with an ideal score of 0.0 signifying perfect learning of the training dataset. Regularly inspecting these learning curves during training serves as a powerful tool for analyzing learning-related issues like underfitting or overfitting. In our experimental setup, we employ early stopping, a technique that involves continuous monitoring of validation set errors. Whenever an improvement is observed, we capture a snapshot of the model parameters at that point. Upon termination of the training algorithm, we retain and use these saved parameters instead of the latest ones. This approach contributes to enhancing the generalization capabilities of deep neural networks.

ROC and PR curves are valuable tools for assessing probability predictions in binary classification problems [15]. ROC curves are graphical representations used to illustrate the trade-off between true positive rates and false positive rates at various classification thresholds. In contrast, PR curves present the trade-off between precision and recall at different classification thresholds. When dealing with imbalanced datasets, where one class significantly outweighs the other, PR curves become more important. In such scenarios, the Precision-Recall Plot proves to be a more informative tool for assessing binary classifiers compared to the ROC plot.

To summarize model performance and facilitate comparisons between different classifiers, we turn to the Area Under the Curve (AUC) metric. AUC metric summarizes the skill of the model. The precision-recall curve's baseline, denoted as $y = P/(P + N)$, where P is positive and N is negative, acts as a reference for a no-skill classifier. Such a classifier cannot distinguish between classes and predicts either a random outcome or a constant class for all instances.

Result and Discussion

This section features an in-depth performance analysis, comparing the proposed model with baseline architectures, including standalone CNN, LSTM, and Bi-LSTM models.

The baseline models provide foundational insights into the individual contributions of convolutional and sequential modeling components. It is important to note that we evaluate the performance of baseline models on augmented datasets (A, B, and C) and subsequently compare their results to our proposed model. Additionally, we compare our model performance against state-of-the-art models that have recently emerged.

In this study, a balanced dataset refers to a dataset in which the classes contain an approximately equal number of samples, whereas an imbalanced dataset contains uneven class distributions, often leading to biased model performance.

A. Performance Comparison: CBiLSTM Vs. Baseline Models

In the pursuit of enhancing urgent post-classification performance, we conducted a comprehensive comparative analysis between our primary model, CBiLSTM, and foundational baseline models, namely CNN, LSTM, and BiLSTM.

The learning curve analysis depicted in Figs. 6 to 9 for datasets A, B, and C shows how the models are learning and generalizing. The data visualizations clearly depict that employing BERT as an embedding layer result in a substantial decrease in the training time required to meet the early stopping criteria. Additionally, the graphical representations indicate that our CBiLSTM model, when incorporating BERT as the embedding layer, achieves early stopping with minimal loss in fewer training iterations which results in improved efficiency and cost-effectiveness.

A closer inspection of the learning curves in Figs. 6 to 9 reveals several observations.

First, the CBiLSTM model consistently reaches its minimum validation loss in fewer epochs compared to the standalone CNN, LSTM, and BiLSTM models. This behavior indicates that the integration of BERT embeddings accelerates convergence by providing semantically rich contextual representations at the input level.

As a result, the model requires fewer training iterations to learn discriminative patterns within MOOC posts.

Second, the smaller gap between training and validation losses for CBiLSTM particularly in Groups B and C suggests stronger generalization and reduced overfitting, even in cross-course and cross-domain scenarios.

In contrast, the baseline models exhibit larger discrepancies between training and validation curves, which indicates a weaker ability to transfer learned representations across diverse course contexts. These observations highlight the role of contextualized embeddings in stabilizing learning dynamics and improving generalization efficiency.

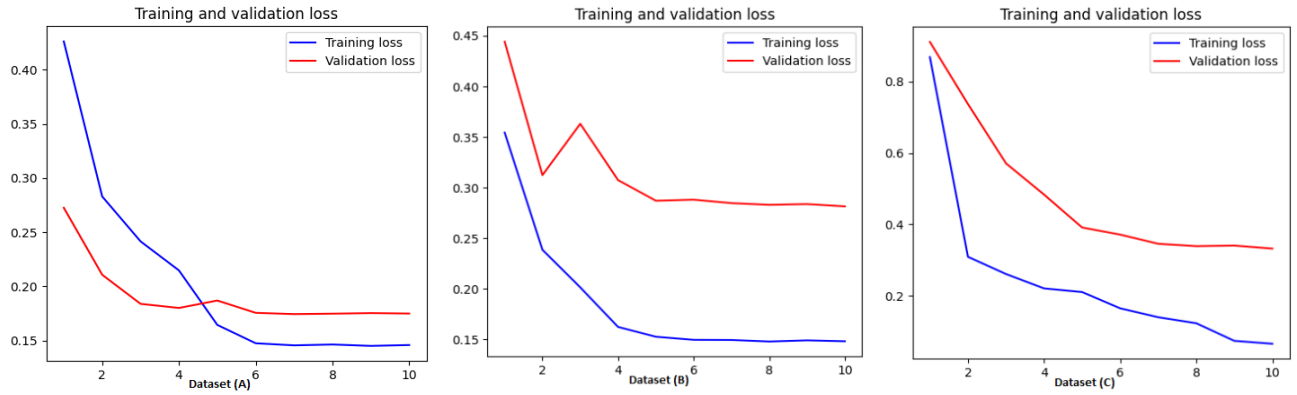


Fig. 6: Learning and validation curves for CNN on datasets A, B, and C where the minimum loss values are 0.17 (Epoch 7), 0.287 (Epoch 10), and 0.331 (Epoch 10).

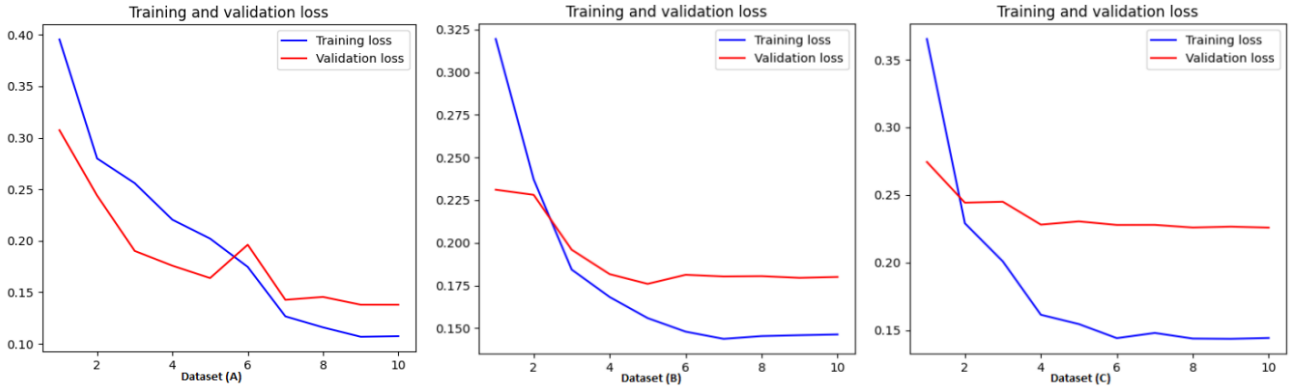


Fig. 7: Learning and validation curves for LSTM on datasets A, B, and C where the minimum loss values are 0.142 (Epoch 9), 0.172 (Epoch 5), and 0.229 (Epoch 8).

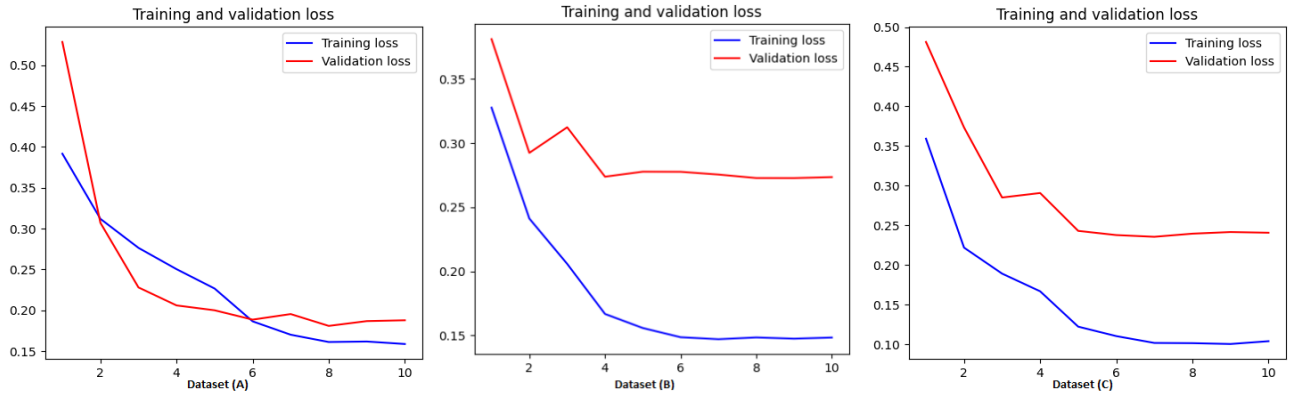


Fig. 8: Learning and validation curves for BiLSTM on datasets A, B, and C where the minimum loss values are 0.181 (Epoch 8), 0.272 (Epoch 9), and 0.236 (Epoch 9).

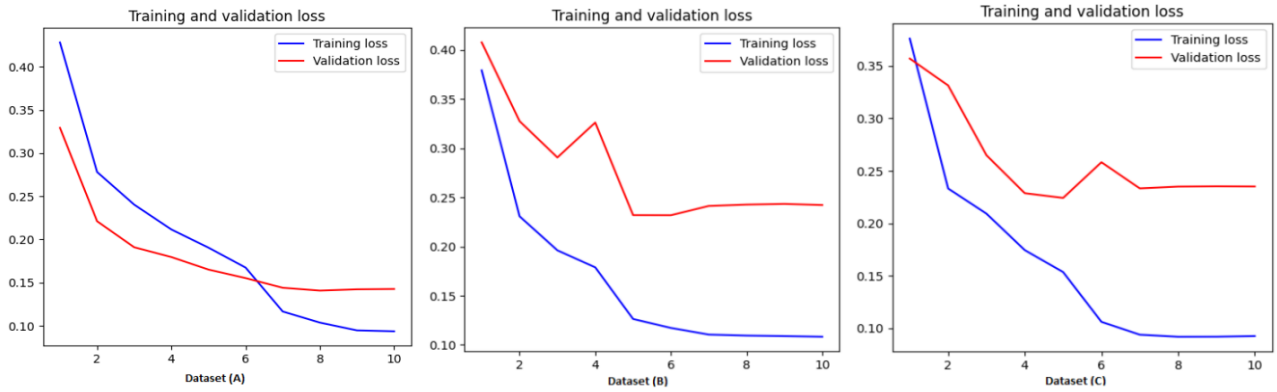


Fig. 9: Learning and validation curves for CBiLSTM on datasets A, B, and C where the minimum loss values are 0.147 (Epoch 8), 0.232 (Epoch 5), and 0.226 (Epoch 5).

The Precision-Recall curves in Figs. 10 to 13 illustrate the balance between true positive rate and positive predictive value. The AUC is employed as a quantitative metric to show the model performance. Furthermore, we employ a baseline for the precision-recall curves to show the balance between urgent and non-urgent classes. Notably, across all three datasets (A, B, and C), CBiLSTM achieved the highest AUC values and surpassed the baseline models. The analysis of the precision–recall curves shows that the proposed CBiLSTM maintains high precision even as recall increases, which demonstrates its robustness in detecting urgent posts especially under class imbalance. Unlike the baseline CNN, LSTM, and BiLSTM models, whose curves drop sharply as recall grows, the CBiLSTM curve declines gradually, and indicates fewer false positives at higher recall thresholds. This behavior reflects the strength of BERT's contextual embeddings combined with bi-directional sequential modeling, and enables the model to better distinguish subtle urgency cues in MOOC posts. The advantage is even more pronounced in Group C (cross-domain evaluation), where domain shift typically weakens classifier performance. However, the CBiLSTM retains a significantly larger AUC-PR margin above the no-skill baseline. These observations confirm that the model not only detects urgent posts more accurately but also sustains consistent performance across heterogeneous course and domain settings.

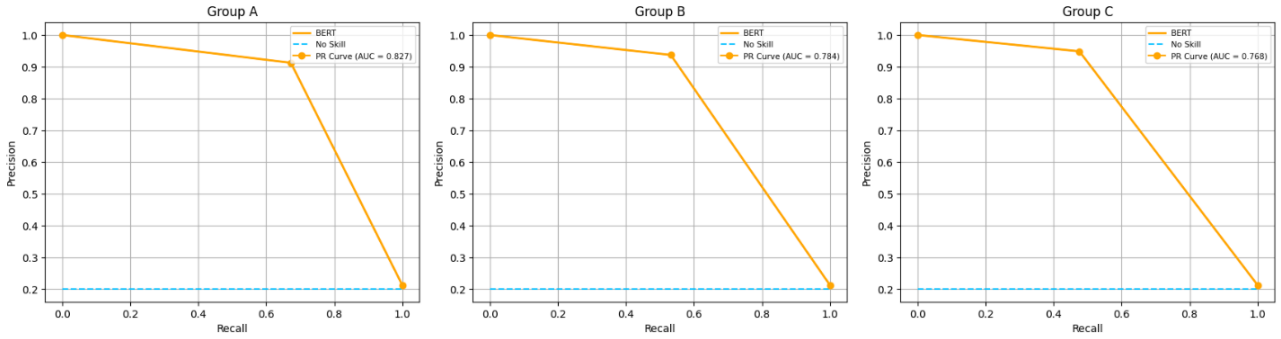


Fig. 10: PR curves for CNN model using A, B, and C datasets.

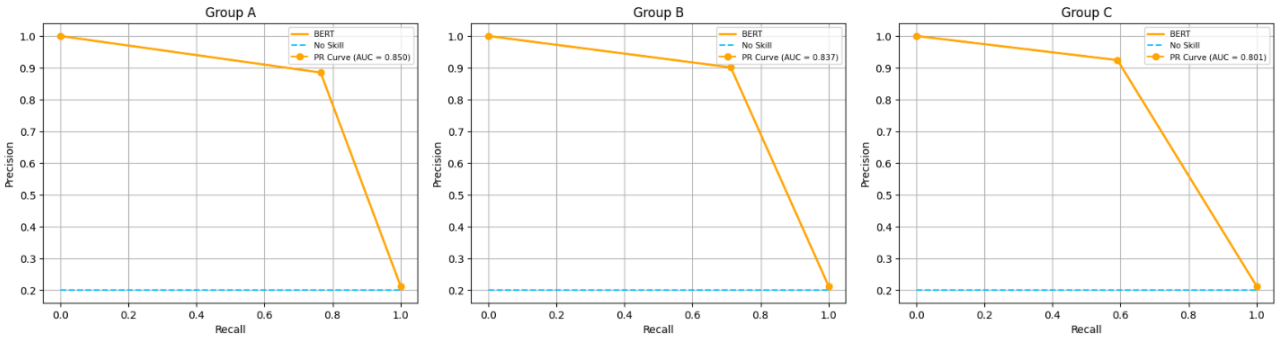


Fig. 11: PR curves for LSTM model using A, B, and C datasets.

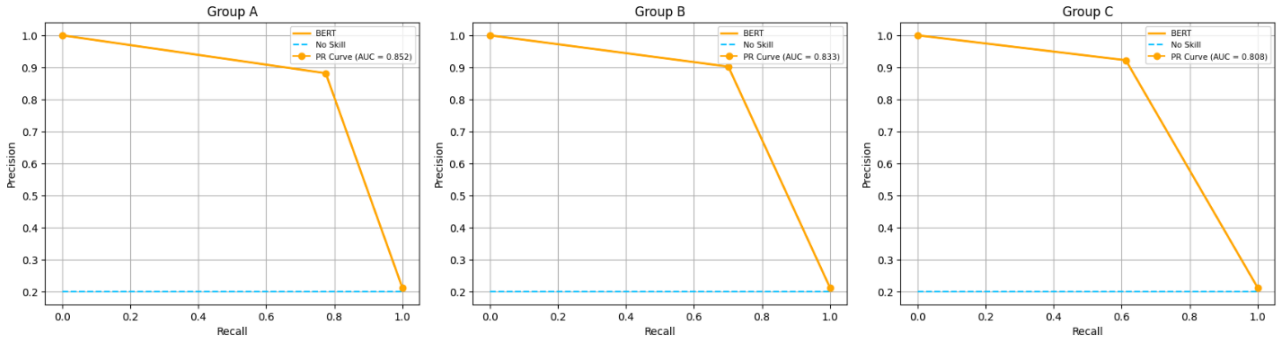


Fig. 12: PR curves for BiLSTM model using A, B, and C datasets.

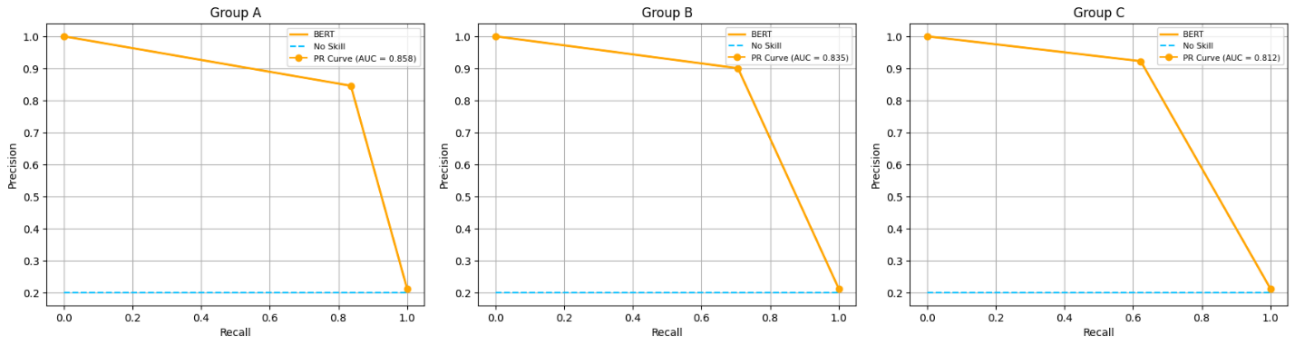


Fig. 13: PR curves for CBiLSTM model using A, B, and C datasets.

The comparative analysis of performance metrics, including Precision (ability to correctly identify positive cases), Recall (ability to capture all positive causes), F1-scores (a balanced measure of precision and recall), and F1-weighted scores, between the proposed CBiLSTM model and baseline models is presented in Tables 7, 8, and 9 for datasets A, B, and C, respectively. Notably, CBiLSTM outperforms the baseline models in all three scenarios.

B. Performance Comparison: Balanced vs imbalanced datasets

To investigate the effect of dataset balance, we compared the model's performance on both imbalanced and balanced datasets. Notably, balancing the data using BERT augmentation led to a significant improvement in model performance, as detailed in Table 4. This finding supports the notion that balanced datasets can enhance the effectiveness of deep learning models for binary classification tasks.

Table 4: Performance comparison of the CBiLSTM model on imbalanced vs. BERT-balanced datasets for Group A, B, and C. Results reflect class-specific precision, recall, F1-scores, and weighted F1 under identical training settings

Dataset	Urgent			Not Urgent			Weight F1 (%)
	P (%)	R (%)	F1 (%)	P (%)	R (%)	F1 (%)	
Imbalanced (A)	85.2	82.6	83.8	93.3	96.5	94.8	92.5
Imbalanced (B)	84.4	76.8	80.4	90.4	93.1	91.7	89.3
Imbalanced (C)	75.7	84.3	79.7	93.6	90.8	92.1	89.5
Balanced (A)	84.6	83.6	84.1	95.6	95.9	95.7	**93.3**
Balanced (B)	86.8	77.4	81.8	91.5	95.4	93.4	**90.2**
Balanced (C)	76.4	85.2	80.6	95.5	92.2	93.8	**90.9**

C. Optimizing CNN architecture

To extract key local features from the text data, a Convolutional Neural Network (CNN) was employed within the proposed model. The effect of varying the CNN's architecture on performance was investigated by adjusting the number of layers, kernel sizes, and filter counts. The impact of these changes on the model performance is detailed in Table 5.

D. Optimizing BiLSTM architecture

To capture long-range dependencies and contextual information within the text, a Bidirectional Long Short-Term Memory network (BiLSTM) was incorporated into the proposed model. This layer facilitates the extraction of global features by processing the text in both directions.

We explored the impact of varying the BiLSTM architecture by adjusting the number of layers and hidden units. The detailed results of this investigation are shown in Table 6.

E. Performance Comparison: CBiLSTM vs State-of-the-art Models

The model's performance is compared with state-of-the-art algorithms employing three distinct A, B, and C datasets. [8] presented a MOOC post-classification model using TF, linguistic attributes, metadata, and AdaBoost. TF lacks consideration for word order, potentially affecting context comprehension. Linguistic features, derived from LIWC, may be impacted by misspellings and symbols, potentially influencing AdaBoost's performance. [14] proposed a method that incorporated Google News embeddings, metadata features, and a CNN-Bi-GRU architecture. Google-news embeddings capture a word's fundamental meaning, disregarding its contextual intricacies.

Table 5: Impact of varying CNN depth, kernel configurations, & filter sizes on model performance using Group a dataset

CNN Kernel	Number of CNN filters	Urgent			Not Urgent			Weight F1 (%)
		P (%)	R (%)	F1 (%)	P (%)	R (%)	F1 (%)	
CNN – 2	64	81.6	82.1	81.8	94.1	94.3	94.1	91.5
CNN – 3	64	82.5	83.2	82.8	94.4	94.2	94.2	91.8
CNN – 4	64	82.1	82.8	82.9	95.3	94.9	95	92.5
CNN – 5	64	82.4	82.5	82.4	95	94.1	94.5	91.9
CNN – 6	64	81.8	82.2	81.9	94.7	94.2	94.4	91.8
CNN – 2 – 3	64 – 64	82.1	82.6	82.3	95.4	94.5	94.9	92.2
CNN – 3 – 4	64 – 64	83.7	81.9	82.7	96.3	93.4	94.8	92.2
CNN – 4 – 5	64 – 64	82.9	82.1	82.4	95.8	94.5	95.1	92.4
CNN – 5 – 6	64 – 64	82.8	81.8	81.8	95.3	94.9	95	92.2
CNN – 2 – 3 – 4	64 – 64 – 64	83.1	83.2	83.1	95.6	94.1	94.8	92.3
CNN – 3 – 4 – 5	64 – 64 – 64	83.8	83.1	83.4	95.1	95	95	92.5
CNN – 4 – 5 – 6	64 – 64 – 64	83	82.2	82.5	95.7	94.5	95	92.4
CNN – 2 – 3 – 4 – 5	64 – 64 – 64 – 64	81.1	81.9	81.4	94.3	92.8	93.5	91
CNN – 3 – 4 – 5 – 6	64 – 64 – 64 – 64	81.3	82.1	81.6	94.4	93.4	93.8	91.3
CNN – 2	128	82.9	82.7	82.7	95.3	94.1	94.6	92.1
CNN – 3	128	83.4	83.1	83.2	95.1	94.8	94.9	92.4
CNN – 4	128	82.7	83.1	82.8	95.2	95.3	95.2	92.6
CNN – 5	128	82.9	83.2	83	95.7	94.4	95	92.5
CNN – 6	128	82.2	82.8	82.4	95.1	94.1	94.5	92
CNN – 2 – 3	128 – 128	82.8	83.2	82.9	95.5	95.2	95.3	92.7
CNN – 3 – 4	128 – 128	84.1	82.6	83.3	**96.6**	94.6	95.5	92.9
CNN – 4 – 5	128 – 128	83.7	82.9	83.2	96.3	94.7	95.4	92.9
CNN – 5 – 6	128 – 128	83.4	82.4	82.8	96.1	94.8	95.4	92.7
CNN – 2 – 3 – 4	128 – 128 – 128	83.8	83.5	83.6	96.2	94.4	95.2	92.8
CNN – 3 – 4 – 5	128 – 128 – 128	**84.6**	**83.6**	**84.1**	95.6	**95.9**	**95.7**	**93.3**
CNN – 4 – 5 – 6	128 – 128 – 128	83.7	82.9	83.2	95.9	95.1	95.5	92.9
CNN – 2 – 3 – 4 – 5	128 – 128 – 128 – 128	81.6	82.2	81.8	94.6	93.1	93.8	91.3
CNN – 3 – 4 – 5 – 6	128 – 128 – 128 – 128	81.8	82.4	82.1	94.3	93.8	94	91.5
CNN – 2	256	82.4	82.5	82.4	94.9	93.6	94.2	91.7
CNN – 3	256	82.8	83.1	82.9	94.7	94.2	94.4	92
CNN – 4	256	82.4	83.2	82.7	95.1	95	95	92.4
CNN – 5	256	83.1	82.6	82.8	95.2	93.9	94.5	92
CNN – 6	256	81.7	82.5	82.1	94.4	93.8	94.1	91.5
CNN – 2 – 3	256 – 256	82.1	82.9	82.4	95.1	95	95	92.3
CNN – 3 – 4	256 – 256	83.8	82.1	82.9	95.9	94.2	94.9	92.4
CNN – 4 – 5	256 – 256	83.2	82.5	82.8	96.1	94.3	95.1	92.5
CNN – 5 – 6	256 – 256	83.5	81.9	82.6	95.5	94.1	94.7	92.2
CNN – 2 – 3 – 4	256 – 256 – 256	83.2	83	83	95.8	94.2	94.9	92.4
CNN – 3 – 4 – 5	256 – 256 – 256	83.9	83.1	83.4	94.8	95.1	94.9	92.5
CNN – 4 – 4 – 6	256 – 256 – 256	82.9	82.3	82.5	95.4	94.6	94.9	92.3
CNN – 2 – 3 – 4 – 5	256 – 256 – 256 – 256	82.1	81.8	81.9	94.1	93	93.5	91
CNN – 3 – 4 – 5 – 6	256 – 256 – 256 – 256	81.4	81.9	81.6	93.8	93.4	93.5	91.1

Table 6: Effect of BiLSTM architecture depth and hidden-unit configuration on performance using Group A dataset. Results demonstrate how sequential modeling capacity influences contextual feature extraction

Number of Layers	Number of hidden units	Urgent			Not Urgent			Weight F1 (%)
		P (%)	R (%)	F1 (%)	P (%)	R (%)	F1 (%)	
1	64	80.7	**85.8**	83.1	94.7	94.4	94.5	92.1
2	64 – 64	82.4	84.2	83.2	95.3	94.5	94.8	92.4
3	64 – 64 – 64	82.6	84.8	83.6	95.5	94.3	94.8	92.5
4	64 – 64 – 64 – 64	81.8	82.4	82.1	94.6	94.1	94.3	91.7
1	128	81.3	85.4	83.2	95.2	94.6	94.8	92.4
2	128 – 128	82.7	84.3	83.4	95.6	94.3	94.9	92.5
3	128 – 128 – 128	82.6	84.4	83.4	95.3	94.9	95	92.6
4	128 – 128 -128 – 128	81.9	83.7	82.7	94.3	94.1	94.1	91.7
1	256	83.1	83.4	83.2	94.6	94.5	94.5	92.1
2	256 – 256	82.8	83.3	83	94.9	95.4	95.1	92.5
3	256 – 256 – 256	80.4	85.4	82.8	95.4	94.3	94.8	92.2
4	256 – 256 – 256 – 256	79.9	85.2	82.4	95.1	93.4	94.2	91.7
1	512	82.2	84.1	83.1	93.8	94.6	94.1	91.8
2	512 – 512	81.4	83.9	82.6	95.1	94.3	94.6	92.1
3	512 – 512 – 512	81.1	84.2	82.6	94.6	96.1	95.3	92.6
4	512 – 512 – 512 – 512	80.3	84.8	82.4	93.4	**96.2**	94.7	92.1
2	64 – 128	83.9	82.5	83.1	95.2	95.5	95.3	92.7
2	128 – 256	**84.7**	82.9	83.7	95.7	95.2	95.4	92.9
2	256 – 512	84.2	82.9	83.5	95.3	95.4	95.3	92.8
3	64 – 128 – 256	84.6	83.6	**84.1**	95.6	95.9	**95.7**	**93.3**
3	128 – 256 – 512	84.3	83.1	83.6	95.1	95.6	95.3	92.8
4	64 – 128 – 256 – 512	83.4	82.8	83	94.6	95.2	94.8	92.3

The CNN and Bi-GRU layers within the architecture were utilized to extract long-term dependencies within post text.

[15] introduced a model that utilized preprocessing, BERT embeddings, and Bi-GRU techniques. Preprocessing encompassed the removal of stop words and special characters, which can enhance contextual comprehension but may detrimentally, affect classification accuracy.

The Bi-GRU component formed the classification model and emphasized its ability to extract long-term dependencies among words effectively.

Recently, [12] introduced a four-stage model that includes coding and vectorization using pre-trained BERT, a feature aggregation model to capture data-based relationships, a CNN-based model for improved text understanding, and classification of post-text using composite features.

Table 7: Performance comparison between the CBiLSTM and state-of-the-art models using Group A (baseline scenario with full cross-course independence). Metrics include class-wise and weighted F1 scores

Model	Urgent			Not Urgent			Weight F1 (%)
	P (%)	R (%)	F1 (%)	P (%)	R (%)	F1 (%)	
Adaboost [8]	77	65	70	91	95	93	88
Geo et al. [14]	83.4	77.2	80.1	94.8	95.4	95.1	91.8
Bi-GRU [15]	80.8	81.5	81.2	94.9	94.7	94.8	91.9
BERT + CNN Agg [12]	83.6	83	83.3	95.3	95.5	95	92.7
CNN	80.7	80.4	80.5	94.7	94.8	94.8	91.8
LSTM	82.2	80.7	81.4	94.7	95.2	95	92.1
Bi-LSTM	83.7	81.3	82.5	94.9	95.6	95.2	92.5
CNN + BiLSTM	**84.6**	**83.6**	**84.1**	**95.6**	**95.9**	**95.7**	**93.3**

Table 8: Performance comparison across models under Group B (cross-course evaluation), where several courses are held out entirely for testing. This table emphasizes generalization to unseen courses

Model	Urgent			Not Urgent			Weight F1 (%)
	P (%)	R (%)	F1 (%)	P (%)	R (%)	F1 (%)	
Adaboost [8]	80	65	72	90	95	92	88
Geo et al. [14]	80.7	79.7	80.2	93.8	**95.8**	**94.8**	**91.3**
Bi-GRU [15]	76.0	**84.7**	80.1	**95.7**	92.7	94.2	91
BERT + CNN Agg [12]	81.6	80.7	80.9	93.2	93.3	93.2	90
CNN	83.3	73.8	78.3	90.3	94.3	92.2	88.3
LSTM	85.7	77.8	81.5	91.9	95.1	93.5	90.2
Bi-LSTM	85.1	76.8	80.7	91.6	94.9	93.2	89.8
CNN + BiLSTM	**86.8**	77.4	**81.8**	91.5	95.4	93.4	90.2

Table 9: Performance comparison for Group C (cross-domain evaluation), where the Humanities domain is held out for testing. Results highlight model robustness across domain shifts

Model	Urgent			Not Urgent			Weight F1 (%)
	P (%)	R (%)	F1 (%)	P (%)	R (%)	F1 (%)	
Adaboost [8]	80	57	67	87	**95**	91	85
Geo et al. [14]	**80.7**	73.1	76.7	90.7	94.5	92.6	88.4
Bi-GRU [15]	76.1	83.1	79.4	94.7	92.1	93.4	90
BERT + CNN Agg [12]	72.4	**86.2**	78.7	**96**	91.1	93.5	90.3
CNN	74.2	83.5	78.6	94.9	91.3	93.1	89.7
LSTM	73.1	85.1	78.6	95.5	91.1	93.2	90
Bi-LSTM	73.1	85.5	78.8	95.7	91.1	93.3	90.1
CNN + BiLSTM	76.4	85.2	**80.6**	95.5	92.2	**93.8**	**90.9**

Despite the endeavors of state-of-the-art models, the highest attained F1-weighted scores stand at 92.7%, with an 83.3% F1 score specifically for urgent class classification, as depicted in Tables 7, 8, and 9. Notably, none of these investigations have addressed the issue of dataset imbalance within the StanfordMOOC Posts dataset, a factor known to impact classification performance and potentially introduce bias favoring larger classes [17], [18].

Our proposed model addresses imbalance by balancing the training dataset using a pre-trained BERT model which significantly influenced the classification performance. Our proposed model has achieved a better result, boasting a 93.3% F1-weighted score and 84.1% F1 score for the urgent class, as demonstrated in Table 7. This represents a notable improvement of 0.6% and 0.8% over the best-performing state-of-the-art model using the group A dataset. Moreover, as shown in Table 8, on the group B dataset, our model obtained an F1-urgent score boost of 1.6% compared to [14] and a 0.9% gain over the state-of-the-art model in [12]. Additionally, on the group C dataset, the CBiLSTM model outperformed the best state-of-the-art model [12] by 0.6% in overall F1-weighted score, as well as [14] by 1.2% in the urgent post classification.

CBiLSTM model outperformed state-of-the-art algorithms using various test scenarios, and obtained higher weighted F1 scores and a balanced precision-recall for urgent posts classification (see Tables 7, 8, and 9).

Although the CBiLSTM model does not include explicit attention mechanisms, qualitative analysis of the learned features reveals patterns aligned with human-understandable urgency cues. The CNN layers capture local discriminative n-gram patterns, while the BiLSTM highlights longer contextual dependencies. In particular, the model assigns higher importance to terms expressing temporal sensitivity (e.g., “urgent,” “immediately,” “deadline”), failure states (e.g., “stuck,” “error,” “not working”), and help-seeking cues (e.g., “please advise,” “need help”). These insights suggest that the model’s predictions are consistent with domain knowledge, reinforcing confidence in the classification results [7], [15].

The performance gains of the proposed model can be attributed to the complementary contributions of its three main components. Empirically, the BERT embeddings provided the largest single boost in accuracy because they supply rich contextual representations that reduce ambiguity in short and noisy MOOC posts. The CNN layers then enhanced performance by extracting stable local features that improved robustness to spelling variations and informal phrasing. Finally, the BiLSTM component contributed additional improvements by modeling sequence-level dependencies that are essential for distinguishing subtle urgency patterns spread across multiple clauses. Together, these components form a hierarchy in which BERT strengthens semantic understanding, CNN stabilizes local features, and BiLSTM refines global context. Despite these benefits, the architecture introduces limitations such as increased computational cost and dependency on pre-trained language models, which may be constraining for low-resource deployment scenarios.

Future Work

The proposed CBiLSTM model which incorporated a contextual embedding layer (BERT) and BERT-based data augmentation, produced a better result within the StanfordMOOC Posts datasets. Nevertheless, opportunities remain for further improving the model's performance. In particular, the contextual understanding of MOOC forum posts could be enhanced by leveraging advanced NLP techniques, including transformer-based architectures, to capture richer contextual information and provide more contextually relevant responses. Second, there is room for innovation in data augmentation, especially for scenarios with limited urgent posts. Exploring novel techniques to diversify and refine synthetic data can lead to more robust classification models.

Conclusion

This paper presented a novel approach to classify urgent MOOC forum posts and addressed the challenges posed by the increasing volume of students and posts in online courses. Our model, CBiLSTM, leverages the power of BERT-based contextual embeddings and a hybrid architecture that integrates CNN with BiLSTM layers. Our method includes a multi-stage process, from data preprocessing to the integration of course metadata, and accurately tackles the issue of data imbalance through BERT-based data augmentation. Balancing the dataset through BERT-based augmentation played an important role in enhancing the model's performance. This step effectively addressed the challenges posed by class imbalance and led to more accurate and robust classification results. We have shown the effectiveness of our model by comparing it to baseline models, such as standalone CNN, LSTM, and BiLSTM, as well as state-of-the-art approaches in the domain. Across various datasets representing different scenarios, our CBiLSTM model outperformed baseline models and demonstrated remarkable improvements over existing state-of-the-art algorithms. Notably, our model obtained higher F1-weighted scores and balanced precision recall for urgent post-classification.

Furthermore, the proposed framework demonstrates strong potential for deployment in real MOOC platforms, where timely identification of urgent posts can significantly enhance learner support and instructor responsiveness.

Author Contributions

Mujtaba Sultani: Conception, Data Curation, Methodological Approach, Validation, Formal Analysis, Investigation, Drafting the Main Manuscript.

Negin Daneshpour: Conception, Methodological Approach, Manuscript Review & Editing, Project Management.

Acknowledgment

The authors would like to thank Shahid Rajaee Teacher Training University (SRTTU) for their support and providing the opportunity to publish this research work.

Conflict of Interest

The authors state that there are no conflicts of interest related to this publication.

Abbreviations

AUC	Area Under the Curve
BERT	Bidirectional Encoder Representations from Transformers
Bi-LSTM	Bidirectional Long Short-Term Memory
CBiLSTM	Convolutional Neural Network + Bidirectional Long Short-Term Memory
CNN	Convolutional Neural Network
DA	Data Augmentation
GBDT	Gradient Lifting Decision Tree
LSTM	Long Short-Term Memory
MOOCs	Massive Open Online Courses
NLP	Natural Language Processing
SVM	Support Vector Machine
URLs	Uniform Resource Locators

References

[1] C. Zhenghao, B. Alcorn, G. Christensen, N. Eriksson, D. Koller, E. J. Emanuel "Who's benefiting from MOOCs, and why," Harvard Business Review. 25(1): 2-8, 2015.

[2] D. Shah, "A Decade of MOOCs: A Review of Stats and Trends for Large Scale Online Courses in 2021," EdSurge, 2021.

[3] D. Shah, "Monetization over massiveness: Breaking down MOOCs by the numbers in 2016," Class Central, 2016.

[4] C. Zhang, H. Chen, C. W. Phang, "Role of instructors' forum interactions with students in promoting MOOC continuance,'' J. Global Inf. Manage., 26(3): 105–120, 2018.

[5] Y. Feng, D. Chen, Z. Zhao, H. Chen, P. Xi, "The impact of students and TAs' participation on students' Academic performance in MOOC," in Proc. 2015 IEEE/ACM International Conference on Advances in Social Networks Analysis and Mining (ASONAM): 1149–1154, 2015.

[6] K. S. Hone, G. R. El Said, "Exploring the factors affecting MOOC retention: A survey study," Comput. Educ. 98: 157–168, 2016.

[7] M. Sultani, N. Daneshpour, "Extracting urgent questions from mooc discussions: A BERT-based multi-output classification approach," Arabian J. Sci. Eng., 50: 1169-1190, 2025.

[8] O. Almatrafi, A. Johri, H. Rangwala, "Needle in a haystack: Identifying learner posts that require urgent response in MOOC discussion forums,'' Comput. Educ. vol. 118, pp. 1–9. doi: 10.1016/j.compedu.2017.11.002

[9] A. Agrawal, J. Venkatraman, S. Leonard, A. Paepcke, "YouEDU: Addressing confusion in mooc discussion forums by recommending instructional video clips," Int. Edu. Data Mining Soc., 2015.

[10] C. y. Chang, S. J. Lee, C. H. Wu, C. F. Liu, C. K. Liu, "Using word semantic concepts for plagiarism detection in text documents," Inf Retr. J., 24: 298-321, 2021.

[11] J. Xue, Y. Chen, "The principle and implementation of sentiment analysis system," in Proc. International Conference on Artificial Intelligence and Security: 28-39, 2022.

[12] M. A. El-Rashidy, A. Farouk, N. A. El-Fishawy, H. K. Aslan, N. A. Khodeir, "New weighted BERT features and multi-CNN models to enhance the performance of MOOC posts classification," Neural Comput. Appl., 35: 18019-18033, 2023.

[13] X. Sun, S. Guo, Y. Gao, J. Zhang, X. Xiao, J. Feng, "Identification of urgent posts in MOOC discussion forums using an improved RCNN," in 2019 IEEE World Conference on Engineering Education (EDUNINE): 1-5, 2019.

[14] Z. X. Guo, X. Sun, S. X. Wang, Y. Gao, J. Feng, "Attention-based character-word hybrid neural networks with semantic and structural information for identifying of urgent posts in MOOC discussion forums," IEEE Access, 7: 120522-120532, 2019.

[15] N. A. Khodeir, "Bi-GRU urgent classification for MOOC discussion forums based on BERT," IEEE Access. 9: 58243-58255, 2021.

[16] F. Almeida, G. Xexéo, "Word embeddings: A survey," arXiv preprint arXiv:1901.09069, 2019.

[17] J. Wei, K. Zou, "Eda: Easy data augmentation techniques for boosting performance on text classification tasks," arXiv preprint arXiv:1901.11196, 2019.

[18] X. Guo, Y. Yin, C. Dong, G. Yang, G. Zhou, "On the class imbalance problem," in Proc. 2008 Fourth International Conference on Natural Computation: 192-201, 2008.

[19] D. Ramyachitra, P. Manikandan, "Imbalanced dataset classification and solutions: A review," Int. J. Comput. Bus. Res. (IJCBR), 5(4), 1-29, 2014.

[20] T. Luis, B. Paula, R. P. Ribeiro, "A survey of predictive modeling under imbalanced distributions," ACM Comput. Surv. 49(2): 1-50, 2016.

[21] V. Kumar, A. Choudhary, E. Cho, "Data augmentation using pre-trained transformer models," arXiv preprint arXiv:2003.02245, 2021.

[22] M. Birjali, M. Kasri, A. Beni-Hssane, "A comprehensive survey on sentiment analysis: Approaches, challenges and trends," Knowledge-Based Syst., 226, 107134, 2021. doi: 10.1016/j.knosys.2021.107134

[23] T. R. Liyanagunawardena, A. A. Adams, S. A. Williams, "MOOCs: A systematic study of the published literature 2008-2012," Int. Rev. Res. Open Distrib. Learn., 14(3): 202-227, 2013.

[24] A. Bakharia, "Towards cross-domain MOOC forum post classification," in Proc. the third (2016) ACM Conference on Learning @ Scale: 253-256), 2016.

[25] L. Feng, G. Liu, S. Luo, S. Liu, "A transferable framework: Classification and visualization of mooc discussion threads," in Proc. Neural Information Processing: 377-384, 2017.

[26] X. Wei, H. Lin, L. Yang, Y. Yu, "A convolution-LSTM-based deep neural network for cross-domain MOOC forum post classification," Information. 8(3), 92, 2017.

[27] Y. Cui, A. F. Wise, "Identifying content-related threads in MOOC discussion forums," in Proc. the Second (2015) ACM Conference on Learning @ Scale: 299-303, 2015.

[28] A. Agrawal, A. Paepcke, "The stanford MOOC Posts dataset," Accessed: Dec, 15, 2020.

[29] S. Shaikh, S. M. Daudpota, A. S. Imran, Z. Kastrati, "Towards improved classification accuracy on highly imbalanced text dataset using deep neural language models," Appl. Sci., 11(2), 869, 2021.

[30] N. V. Chawla, K. W. Bowyer, L. O. Hall, W. P. Kegelmeyer, "SMOTE: synthetic minority over-sampling technique," J. Artif. Intell. Res., 16: 321-357, 2002.

[31] H. He, Y. Bai, E. A. Garcia, S. Li, "ADASYN: Adaptive synthetic sampling approach for imbalanced learning," in Proc. 2008 IEEE International Joint Conference on Neural Networks (IEEE world congress on computational intelligence): 1322-1328, 2008.

[32] A. Almahairi, S. Rajeshwar, A. Sordoni, P. Bachman, "Courville A (2018) Augmented cyclegan: Learning many-to-many mappings from unpaired data," in Proc. International conference on machine learning: 195-204, 2018.

[33] J. Devlin, M. W. Chang, K. Lee, "Google, KT, Language, AI: BERT: pre-training of deep bidirectional transformers for language understanding," in Proc. NAACL-HLT: 4171-4186, 2019.

[34] Y. Luan, S. Lin, "Research on text classification based on CNN and LSTM," in Proc. 2019 IEEE International Conference on Artificial Intelligence and Computer Applications (ICAICA): 352-355, 2019.

[35] J. Du, C. M. Vong, C. P. Chen, "Novel efficient RNN and LSTM-like architectures: Recurrent and gated broad learning systems and their applications for text classification," IEEE Trans. Cybern., 51(3): 1586-1597, 2020.

[36] C. Olah, "Understanding lstm networks," available at: https://colah. github. io/posts/2015-08-Understanding-LSTMs. 2020.

[37] G. Liu, J. Guo, "Bidirectional LSTM with attention mechanism and convolutional layer for text classification," Neurocomputing. 337: 325-338, 2019.

[38] M. J. Anzanello, F. S. Fogliatto, "Learning curve models and applications: Literature review and research directions,'' Int. J. Ind. Ergonom. 41(5): 573–583, 2011.

[39] R. L. Abduljabbar, H. Dia, P. W. Tsai, "Unidirectional and bidirectional LSTM models for short-term traffic prediction," J. Adv. Transp., 1-16, 2021.

[40] S. Kobayashi, "Contextual augmentation: Data augmentation by words with paradigmatic relations," arXiv:1805.06201, 2018.

[41] J. Wei, K. Zou, "EDA: Easy data augmentation techniques for boosting performance on text classification tasks," arXiv:1901.11196, 2019.

Biographies



Mujtaba Sultani received his B.Sc. degree at Kandahar University, Afghanistan in 2019, and his M.Sc. degree at Shahid Rajaee Teacher Training University (SRTTU), Tehran in 2024. He is an assistant professor at Kabul Polytechnic University (KPU). His research interest primarily includes data mining, information and knowledge management, machine learning, natural language processing, sentiment analysis, and language comprehension.

- Email: Mujtaba.cs01@kpu.edu.af
- ORCID: 0009-0009-4267-703X
- Web of Science Research ID: NA
- Scopus Author ID: NA
- Homepage: NA



Negin Daneshpour is an Associative Professor in the faculty of Computer Engineering at Shahid Rajaee Teacher Training University, Tehran, Iran. She received her B.Sc. degree in Computer Engineering-Hardware from Shahid Beheshti University, Tehran, Iran, in 1999, and her M.Sc. and Ph.D. degrees in Computer Engineering - Software from Amir Kabir University of Technology, Tehran, Iran, in 2002 and 2010 respectively. Her research interests include data mining, data preprocessing, information management, and natural language processing.

- Email: ndaneshpour@sru.ac.ir
- ORCID: 0000-0003-3951-4060
- Web of Science Research ID: NA
- Scopus Author ID: NA
- Homepage: NA

Journal of Electrical and Computer Engineering Innovations
(JECEI)
Journal homepage: http://www.jecei.sru.ac.ir

Research paper

Detection of Breast Cancer Masses in Mammography Images Using a Hybrid Faster R-CNN and Fuzzy Logic Framework

Fatemeh Jafari [1], *Hamid Reza Ghafari* [1,*], *Hassan Farsi* [2]

[1]*Department of Computer Engineering, Ferdows Branch, Islamic Azad University, Ferdows, Iran.*

[2]*Department of Electrical and Computer Engineering, University of Birjand, Birjand, Iran.*

Article Info

Article History:
Received 03 November 2025
Reviewed 01 January 2026
Revised 30 January 2026
Accepted 17 February 2026

Keywords:
Breast cancer detection
Deep learning
Fuzzy logic
Faster-RCNN

[*]Corresponding Author's Email Address:
hyamidghaffary53@iau.ir

Abstract

Background and Objectives: Breast cancer is a leading cause of mortality among women worldwide. Early detection plays a pivotal role in reducing mortality rates and improving patient outcomes by identifying risk factors, enhancing screening methods, and enabling timely treatment. Recent advances in artificial intelligence (AI) and deep learning have facilitated accurate and efficient analysis of medical images, supporting rapid and precise breast cancer detection. This study aims to develop a fast and reliable approach for detecting breast cancer masses in mammography images using a deep learning framework.

Methods: The proposed approach employs a Faster R-CNN architecture with a ResNet backbone for robust feature extraction. Fuzzy logic is integrated to adaptively adjust the learning rate, improving training stability. Transfer learning and data augmentation techniques are applied to enhance model generalization and reduce overfitting. The method labels affected regions in mammography images, enabling accurate localization of cancerous areas.

Results: Experiments were carried out using the CBIS-DDSM dataset. The proposed model demonstrated a cancer detection accuracy of 97.84%, an Intersection over Union (IoU) of 98.12%, and a mAP50 of 0.83, highlighting its exceptional performance in accurately localizing breast cancer masses.

Conclusion: The integration of Faster R-CNN with ResNet, fuzzy logic-based learning rate adaptation, transfer learning, and data augmentation yields a highly effective solution for automated breast cancer detection. The results highlight the potential of this method to improve early diagnosis and support clinical decision-making in breast cancer screening.

This work is distributed under the CC BY license (http://creativecommons.org/licenses/by/4.0/)

How to cite this paper:
F. Jafari, H. R. Ghafari, H. Farsi, "Detection of breast cancer masses in mammography images using a hybrid faster r-cnn and fuzzy logic framework," J. Electr. Comput. Eng. Innovations, 14(2): 507- 518, 2026.

DOI: 10.22061/jecei.2026.12577.892

URL: https://jecei.sru.ac.ir/article_2544.html

2345- 3044/© 2026 The Authors. Published by Shahid Rajaee Teacher Training University.

Introduction

Breast cancer is the most prevalent cancer among women worldwide, posing a significant health threat to millions each year [1]-[3]. Despite significant advancements in screening and treatment technologies, late-stage diagnosis highlights the critical need for innovative research in this field [4]-[7]. Recent studies have identified key risk factors, including obesity, late pregnancies, and genetic mutations such as BRCA1, which contribute to more aggressive forms of the disease [8], [9]. Traditional diagnostic methods, including digital mammography and invasive techniques like surgical biopsies, are often associated with high human error rates (with up to 20% of cases being overlooked) and patient discomfort. Although modern imaging technologies like 3D tomosynthesis and molecular imaging have shown improvements, they still struggle with challenges like interpreting dense breast tissues [10]-[12].

Recent developments in deep learning and computer vision have paved the way for the use of object detection models in medical image analysis. These models excel at identifying and localizing abnormalities within complex images, making them well-suited for detecting cancerous lesions in mammograms [13], [14]. Despite their success, challenges remain due to the variability in tumor appearance, limited availability of annotated datasets, and the need for models that can generalize well across diverse patient populations [7], [15].

The emergence of artificial intelligence (AI) and deep learning has revolutionized medical image analysis. Recent AI methodologies, including bio-inspired optimization frameworks such as Swarm Intelligence, have demonstrated strong capabilities in medical image analysis tasks such as tumor detection, feature extraction, and artifact reduction across various imaging modalities [16], [17]. Studies suggest that deep neural network-based models can now achieve diagnostic accuracies that rival human experts, significantly reducing false negatives by up to 9.4% and false positives by 5.7% [18]. However, these technologies have great potential to overcome the limitations of conventional methods by detecting complex patterns in imaging data. Despite their promising nature, challenges such as the variability in performance across different algorithms remain [11], [19]. A research study reported by Karolinska Institute in Sweden on 8,805 mammography samples found that only one out of three tested algorithms achieved an accuracy comparable to radiologists (87%) [12]. This finding underscores the importance of selecting the appropriate model architecture and training it with diverse clinical data. Some approaches, such as integrating fuzzy inference systems with deep neural networks, provide a means to manage uncertainty in low-quality or dense-tissue images [20], [21].

Object detection is one of the key subfields of machine learning and computer vision, focusing on identifying and classifying objects in images or videos. This technology enables systems to detect various objects within a scene, determine their locations, and categorize them [22]. It has widespread applications in research fields such as robotics, autonomous vehicles, video surveillance, and medical imaging [12]. With the advancement of deep learning techniques, object detection models have significantly improved in terms of accuracy. In recent years, several object detection models have been introduced, including You Only Look Once (YOLO), Single Shot Detector (SSD), and Faster Region-based Conventional Neural Networks (R-CNNs) [22].

In [23], an automated, data-driven model was proposed for detecting breast cancer in mammograms to assist physicians in screening and diagnosis. Using transfer learning, publicly available CBIS-DDSM and INbreast datasets were leveraged to train the model on a proprietary full-field digital mammography dataset containing diverse cases, including masses, asymmetries, and distortions. Multiple YOLO architectures were evaluated, with the small YOLOv5 model achieving the best performance, reaching a mean average precision (mAP) of 0.621. To enhance interpretability, Eigen-CAM was applied to highlight suspicious regions, effectively reducing false negatives despite a rise in false positives. The combination of YOLO predictions and saliency maps offers complementary insights, though these outputs should be considered qualitative and require clinical radiological validation. Overall, the model demonstrates promising detection capabilities and potential as a reliable decision-support tool in clinical settings.

Fuzzy inference systems have been widely applied in medical image analysis to address the inherent uncertainty and noise present in imaging modalities such as MRI. Prior studies have demonstrated that fuzzy rule–based models can enhance segmentation and classification performance by providing more flexible decision boundaries compared to conventional crisp methods [24]. In [16], a novel method based on Faster-RCNN architecture with a ResNet backbone was proposed which utilizes fuzzy logic for model training. This intelligent combination enables the extraction of high-level features from mammography images and optimizes noise and uncertainty in training data using fuzzy inference system. The major novelty of this research lies in integrating hierarchical attention mechanisms with fuzzy layers to enhance he accuracy of region detection in images [9].

The main novelty of this study lies in the integration of three complementary strategies that enhance both the learning efficiency and detection accuracy of the proposed system. First, a fuzzy logic–based adaptive learning rate mechanism is developed, where the learning rate is dynamically adjusted based on the loss value and training epoch using a rule-based fuzzy inference system. The fuzzy rules are logically defined and derived from the observed behavior of deep neural networks during training. Second, transfer learning is employed using a pre-trained ResNet-50 model to accelerate convergence and improve feature representation. Third, data augmentation techniques are applied to increase the diversity and volume of training samples, reducing overfitting and improving generalization. The synergistic integration of these three components results in a robust and adaptive framework for breast cancer detection, and to the best of our knowledge, this specific combination and its implementation in Faster R-CNN-based mammography analysis have not been previously reported in the literature.

The rest of the paper is structured as follows: SECTION 2 details previous studies on automated breast cancer detection, SECTION 3 presents a detailed explanation of the proposed architecture. SECTION 4 provides an analysis of experimental results based on sensitivity and specificity metrics. Finally, SECTION 5 concludes the research findings and provides suggestions for future studies.

Related Work

Early research in the 1990s primarily employed basic artificial neural networks (ANNs) to extract geometric features from mammography images. Initial research showed that traditional image processing algorithms—such as Gaussian filters and Fourier transforms—offered limited diagnostic accuracy, typically below 75%. The advent of Convolutional Neural Networks (CNNs) marked a turning point in medical imaging [25]. In [26], authors used the OPTIMAM dataset and they demonstrated that CNN-based models could match radiologists-level performance with an accuracy of 87%, while reducing false positives by 20%, a highly desirable and noteworthy result. In [27], a large-scale analysis involving 8,805 mammograms revealed that AI-based algorithms surpassed standard clinical models like the BCSC in five-year risk prediction. These models by detecting hidden patterns in breast tissue, were capable of forecasting breast cancer up to five years before the onset of physical symptoms. Further evidence from a study at the University of California, using data from 116,495 Norwegian women, showed a prediction accuracy of up to 94%, successfully detecting 1,607 cancer cases 4 to 6 years earlier than standard methods.

Research indicates that integrating AI into the diagnostic process significantly reduces human errors. In [28], a novel deep learning-based approach named XAI-RACapsNet has also been introduced. This approach initially leverages multi-stage image processing, including noise filtering and histogram equalization, followed by feeding the data into a deep learning network called XAI-ONET to identify suspicious regions. The results verified the optimum performance in detecting cancerous regions. Despite notable progress, AI models remain sensitive to the quality and diversity of training data [29]. This highlights the importance of choosing the appropriate model architecture and using diverse data with broad geographical and demographic coverage. Recent research has focused on combining fuzzy inference systems with deep neural networks to handle uncertainty in low-quality or dense-tissue images [30]. Comparative studies have shown that AI algorithms not only outperform traditional clinical models but also deliver superior performance under specific conditions. In [31], a novel method named AlexNet-BC was proposed for breast cancer detection. It leveraged transfer learning from the ImageNet-trained model and improved risk prediction accuracy by 9.4% compared to existing approaches. It also demonstrated that AI can simultaneously reduce both false positives and false negatives. Despite technical advances, deployment challenges such as the need for diverse training data and integration with existing healthcare systems have prevented the widespread adoption of these technologies. In [25], it was shown that using historical datasets with incomplete labeling can reduce model accuracy by up to 12%, emphasizing the need for standardized data collection protocols. In [32], authors present a new framework for breast cancer detection that leverages Convolutional Neural Networks (CNNs) and image processing techniques. The approach employs RetinaNet, a pre-trained, one-stage object detector, as the core model. To enhance performance, a two-stage transfer learning strategy is applied: first, RetinaNet is trained on the COCO dataset, a large general-purpose dataset; then, it is fine-tuned on the CBIS-DDSM mammogram dataset. In the final stage, the model is further adapted and evaluated on the INbreast mammogram dataset. The results demonstrate that this two-stage transfer learning approach (RetinaNet → CBIS-DDSM → INbreast) outperforms other state-of-the-art methods on the INbreast dataset.

In [33], a deep learning approach was introduced to distinguish between benign and malignant tumors. This method employed transfer learning and recursive block structures to enhance algorithm efficiency. For optimization, Laplacian of Gaussian (LoG) equation sets were used, achieving 97.75% accuracy on the mini-

DDSM dataset.

In [34], a Faster-RCNN-based approach was proposed to localize disease-affected regions in mammography images. This method achieved a breast cancer detection accuracy of 94.12% with a true positive rate of 93.33%.

A novel edge detection method for mammography images, called edmABC, is introduced in [35]. By leveraging an improved Artificial Bee Colony algorithm inspired by honeybee foraging, the approach enhances the identification of image boundaries to aid breast cancer detection. The method integrates advanced initialization and statistical techniques, and experimental results show it achieves superior edge detection compared to traditional algorithms. [36], focuses on creating a Computer-Aided Diagnosis (CAD) system utilizing the You Only Look Once (YOLO) framework to detect breast masses and categorize them as either benign or malignant. This approach employs a YOLOv5-CAD model that leverages transfer learning. Additionally, the study investigates how different data augmentation strategies during training influence the model's overall performance. In [37], authors present a new object detection model for this field. This study focuses on improving breast cancer detection using a customized version of the YOLOv9 object-detection model, designed to address species and morphological variations in tumors. The model, named FS-YOLOv9, was trained and validated on an internal dataset of 687 cases and tested on 98 external cases. Key modifications include adding a max-pooling layer to enhance bright features and replacing a backbone component with a high-frequency Haar wavelet convolution to better capture morphological and texture details. Compared to the standard YOLOv9 and earlier YOLO versions, FS-YOLOv9 demonstrated superior performance across multiple metrics, including F1 score, free-response ROC area (FAUC), and mean average precision (mAP), both internally and externally. These improvements suggest that FS-YOLOv9 is a more effective and reliable tool for breast cancer screening, particularly for high-risk patients.

Nonetheless, challenges such as interpreting complex patterns in fatty tissues and managing noise in low-quality images persist. Researchers emphasize the need for longitudinal studies and patient follow-ups to evaluate the real-world effectiveness of these systems in clinical settings [25], [27], [38].

In their 2024 study [39], Boudouh and Bouakkaz proposed a hybrid deep learning model that combines the Vision Transformer (ViT++) architecture with a Convolutional Neural Network (CNN) for the classification of breast calcifications in mammography images. The model extracts global semantic features via ViT++ while leveraging CNN for local spatial details. Their experimental results on the CBIS-DDSM dataset showed that this hybrid approach achieved an accuracy of 96.12%, which further improved to 99.22% when combined with handcrafted VGG16 features. This study demonstrates the potential of transformer-CNN fusion for improved diagnostic accuracy in mammogram analysis. In [40], authors developed a YOLO-based Computer-Aided Diagnosis (CAD) system for the detection and localization of breast tumors in mammographic images. Their architecture integrates a region-based object detection backbone with decision-level fusion to improve detection sensitivity. This work remains frequently cited in recent literature due to its relatively high detection performance. On the CBIS-DDSM dataset, the model achieved a tumor detection accuracy of 95.7%, indicating its effectiveness for identifying suspicious masses, even though it did not include malignancy classification.

In [41], authors introduced a multiscale parallel CNN framework inspired by YOLO architecture to enhance the detection of breast lesions in mammography. Their approach incorporates multiple convolutional paths to capture features at different scales, improving the detection of both small and large abnormalities. On the CBIS-DDSM dataset, the model achieved a mean Average Precision (mAP) of 91.15%, while reaching 98.72% classification accuracy on the INbreast dataset. Their results highlight the effectiveness of multiscale modeling in complex medical imaging tasks. This study presents a fast and accurate deep learning-based approach for detecting cancerous masses in mammography images. The proposed method utilizes a Faster-RCNN architecture with a ResNet backbone, enhanced by the integration of fuzzy logic into the training process, which improves the accuracy of lesion detection. This innovative combination enables the extraction of high-level features from images and reduces diagnostic errors by effectively managing uncertainty in the training data.

Proposed Method

In this section, the proposed method for detecting suspicious regions indicative of breast cancer is detailed. To achieve this, a deep learning model based on Faster-RCNN with a ResNet-50 backbone architecture and, a transfer learning and data augmentation approaches are proposed. During the training phase, fuzzy logic is used to dynamically determine the learning rate in order to improve the training process. The following subsections elaborate on each component of the proposed methodology.

A. Fuzzy Logic

Fuzzy logic, introduced by Professor Lotfi Zadeh in 1965, is a logic system that models vague concepts and partial truths using values ranging from 0 (completely

false) to 1 (completely true) [42]. Unlike classical binary logic (0 and 1), fuzzy logic extends set theory to fuzzy sets, where membership is defined by degrees rather than absolutes. This framework for approximate reasoning bridges the gap between human thinking and machine computation.

In this paper, fuzzy logic is employed to determine adaptive learning rates. To this end, a fuzzy system with two inputs and one output is designed. The inputs include the loss function value and the current training epoch, and the output is the learning rate. For the values in fuzzy system, a Gaussian membership function (i.e., gauss2mf) is used. Fig. 1, depicts loss input membership function and Fig. 2 illustrates epoch input membership function. Fig. 3 shows the learning rate output membership function.

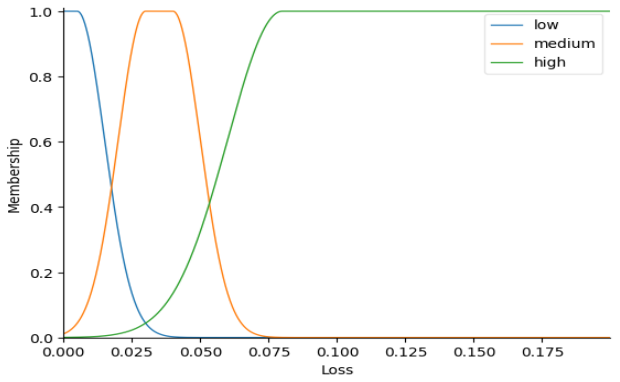


Fig. 1: The membership function for the loss input.

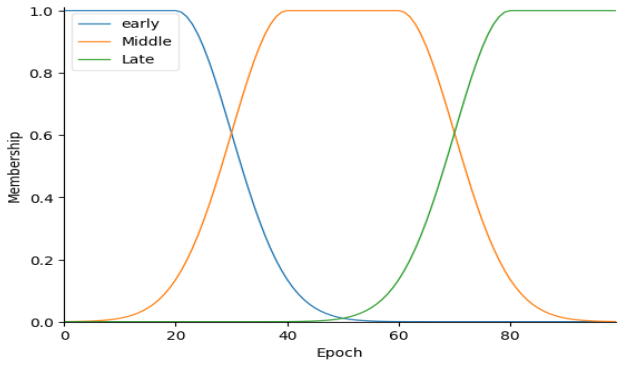


Fig. 2: The membership function for the epoch input.

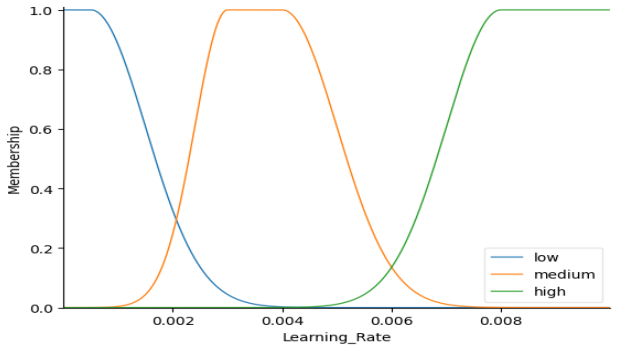


Fig. 3: The membership function for the learning rate output.

Moreover, the following three fuzzy rules are used to determine the learning rate:

1. If the loss is high and the epoch is early, then the learning rate should be high.
2. If the loss is moderate and the epoch is medium, then the learning rate should be middle.
3. If the loss is low and the epoch is late, then the learning rate should be low.

This rule-based system allows the model to accurately adjust the learning rate based on the input logics.

B. Faster-Rcnn Deep Learning Model

The proposed method uses the Faster-RCNN deep learning model as an advanced method in object detection field–for object detection in mammography images. This model uses a CNN-based architecture to extract feature map from input images, which contain valuable information about the objects [43]. In this paper, ResNet-50 architecture is employed as an object feature extractor. This model leverages stacked convolutional blocks with ReLU activation and skip connections to preserve fine-grained spatial information, resulting in superior feature extraction capability compared to lightweight models such as LeNet-5. Its strong representational power has led to high accuracy across various image and video classification domains [44]. Fig. 4, shows the architecture of ResNet, which employs residual block to prevent information loss during deep training. ResNet is widely recognized for its high performance across various existing machine learning fields [45].

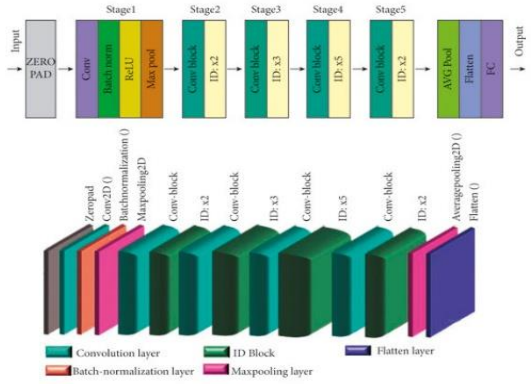


Fig. 4: The ResNet-50 architecture used as the feature extraction backbone in the proposed Faster R-CNN framework.

Within the Faster-RCNN framework, a convolution-type deep learning model called Region Proposal Network (RPN) is used to identify candidate regions that may contain objects. Then, a Region of Interest (RoI) pooling layer is used to map the proposed regions by RPN into a fixed-size output.

The overall loss function in Faster-RCNN consists of two parts: classification loss and regression loss, formulated as (1):

$$L(p_i, t_i) = \frac{1}{N_{cls}} \sum_i L_{cls}(p_i, p_i^*) + \lambda \frac{1}{N_{reg}} \sum_i p_i^* L_{reg}(t_i, t_i^*) \quad (1)$$

where L_{cls} is the classification loss calculated using cross-entropy loss function, as defined by (2):

$$L_{cls}(p_i, p_i^*) = -\sum_{i=1}^{N_{cls}} p_i \log p_i^* \quad (2)$$

where p_i* and p_i represent the actual and predicted values by the proposed model, respectively, L_{cls} is the number of identified samples by RPN, λ is a control parameter to trade-off between classification and regression, L_{reg} is also a regression error obtained using (3) formula:

$$L_{reg}(t_i, t_i^*) = \frac{1}{N_{reg}} \sum_{i=1}^{N_{reg}} \sum_{j \in \{x,y,w,h\}} \begin{cases} 0.5(t_{ij} - t_{ij}^*)^2 & |t_{ij} - t_{ij}^*| < 1 \\ |t_{ij} - t_{ij}^*| - 0.5 & otherwise \end{cases} \quad (3)$$

where t_i and t_i* represent the predicted and actual bounding box coordinates data including x, y, w and h denoting box center, width, and height, respectively.

Fig. 5 illustrates the structure of the Faster-RCNN deep learning model for suspicious breast cancer mass detection.

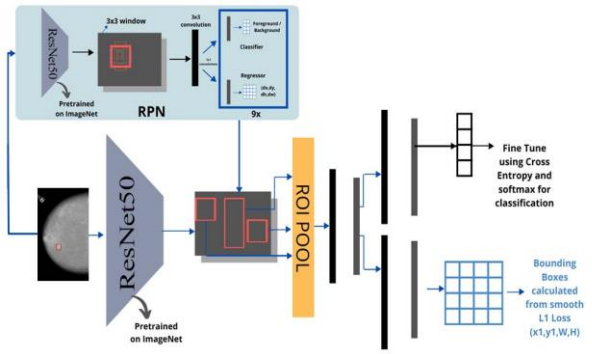


Fig. 5: The Faster-RCNN deep learning structure.

C. Transfer Learning

Since data augmentation is employed to increase dataset images, hence, to reduce computational overhead during training, transfer learning is applied [46]. For this purpose, the pre-trained ResNet-50 model on the ImageNet dataset is used for new dataset classification. Specifically, the first five convolutional layers are entirely frozen in ResNet-50 and not changed during training process. These layers typically learn general features such as brightness level, image edges, shininess, among others. Thus, these features are consistent and important across different types of images. Accordingly, similar coefficients are employed for feature extraction. Other coefficients are trained using given data in order to fulfill classification by a high accuracy.

Algorithm 1 presents the pseudocode for the proposed method, while Fig. 6, illustrates the block diagram of the proposed approach.

Algorithm 1: Proposed Method for Breast Cancer Detection

Input: *Dataset: CBIS-DDSM, Pretrained ResNet-50, Fuzzy Logic System, Augmentation Techniques*

Output: *Trained Model*

1. Initialize ResNet-50 with pretrained weights.

2. Define fuzzy system for dynamic learning rate adjustment (based on loss and epoch).

3. Perform data augmentation (crop, rotate, adjust intensity) to generate three new images per original image.

4. For each epoch:

a. Pass augmented images through ResNet-50.

b. Use Faster-RCNN for detection.

c. Adjust learning rate using fuzzy logic system.

d. Calculate loss and update weights using backpropagation.

5. Output trained model for breast cancer detection

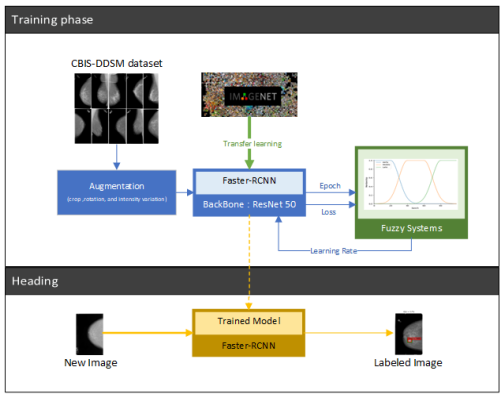


Fig. 6: The block diagram of the proposed approach.

Simulation and Results

The proposed method was evaluated using the CBIS-DDSM dataset [47], which contains mammography images categorized into three groups: normal, benign, and malignant. Each image includes labeled regions of interest (ROIs) and labeled bounding boxes indicating tumor locations. The dataset comprises 10,239 images from 6,671 patients in various sizes. Fig. 7, displays several sample images from this dataset.

As mentioned earlier, three images were generated from each original image using data augmentation techniques, resulting in a total of 40,956 images used for training and evaluation. The proposed model was

implemented on a system equipped with a GTX-4090 GPU (24GB RAM), using Python and the PyTorch AI library.

We split the dataset into 80% training and 20% testing sets. Two training strategies were used:

- Fixed Learning Rate Strategy: Starting at 0.005, reduced by a factor of 0.1 every 10 epochs,
- Fuzzy-Based Learning Rate Strategy: Adaptive rate determined dynamically by the fuzzy logic system during each epoch.

The batch size was set to 32, and the model was trained for 100 epochs in both strategies. We used the Adam optimizer to find the optimal coefficients during the training process. Table 1 summarizes the training time for both strategies.

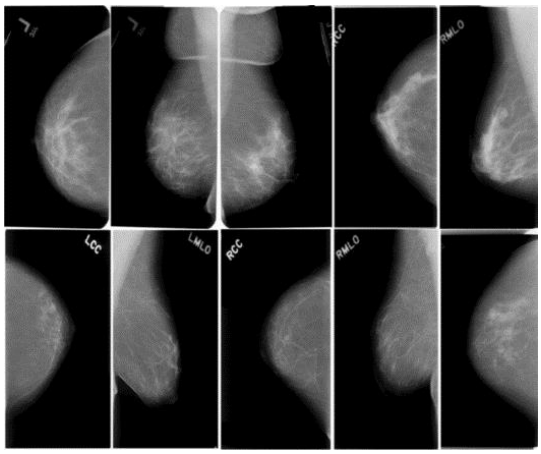


Fig. 7: Several images available in CBIS-DDSM dataset.

Fig. 8 shows the learning rate variations during training process in both the conventional and fuzzy logic strategies. In the traditional method, the training rate drops regularly after ten intervals, while in the fuzzy logic method, it decreases based on fuzzy logic. That is, in late-stage training with a low loss value, the fuzzy system intelligently reduces the learning rate according to the designed rules.

Fig. 9 presents the loss value reduction over training epochs for both regular and fuzzy methods. It is evident that the fuzzy logic approach outperforms the fixed strategy by significantly reducing the loss. Specifically, the fuzzy method achieves a 2.325x lower final loss than the standard approach.

Fig. 10 illustrates sample outputs of the proposed system. The top row shows detection results using the standard method, and the bottom row shows results with fuzzy logic. And, green boxes indicate ground truth cancerous regions; while, red boxes show regions detected by the model. Moreover, each detected region is also labeled with the predicted class (benign or malignant) and the associated probability score. As Fig. 10 demonstrates, the model accurately identifies cancerous areas and differentiates between benign and malignant tumors. Some assessing metrics are mentioned bellow.

Table 1: The proposed algorithm execution time

Strategy	The average time of each epoch (seconds)	Training time (minutes)
Fixed Learning Rate	205.0256	341
Fuzzy-Based Learning Rate	209.4681	353

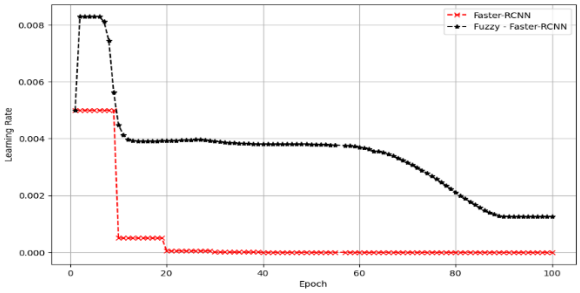


Fig. 8: Learning rate variations by the proposed method.

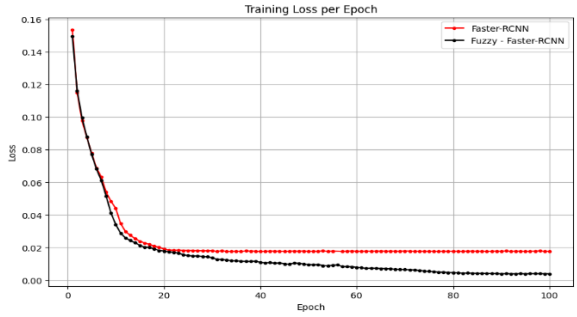


Fig. 9: Loss drop trend in the training process.

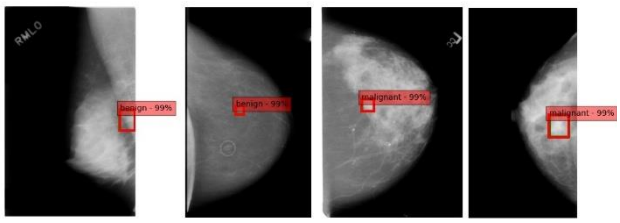


Fig. 10: The proposed model output.

One key performance metric is the Intersection Over Union (IOU), which evaluates the precision of the RPN. The appropriate assessing precision is denoted by IOU. Here, the overlap area is divided into all object areas and a number less than 1 is considered as IOU. Equation (4) expresses IOU calculation. Higher overlapped areas between detected and targeted regions leads to values close to 100.

$$IOU = \frac{area\ of\ overlap}{area\ of\ union} \times 100 \quad (4)$$

Table 2 provides the value of IOUs by both regular and logic approaches. It is seen that the fuzzy method achieves superior IOU values compared to the traditional method, confirming its better localization performance.

Table 2: IOU metric assessment

Strategy	IOU
Fixed Learning Rate	97.5892%
Fuzzy-Based Learning Rate	98.1256%

The mAP50-95 metric serves as an extensive benchmark for evaluating the performance of object detection models, assessing them at various levels of spatial precision. To calculate this metric, the mean Average Precision (mAP) is first determined for a range of IoU thresholds, starting from 0.50 and progressing through 0.05 increments up to 0.95. The average of these individual mAP values is then computed and reported as mAP50-95. This approach, which incorporates varying levels of strictness, offers a more detailed and dependable indication of a model's capability in detecting and localizing objects. As a result, mAP50-95 generally yields lower scores than mAP50, given that it applies stricter spatial accuracy criteria. On the other hand, mAP50 is a more lenient version of mAP50-95, being computed only at an IoU threshold of 0.50 [48]. Here, a prediction is considered correct if at least 50% of the predicted bounding box overlaps with the ground-truth box. This metric places greater emphasis on the model's ability to identify objects, rather than precisely localizing them. Because of its relaxed requirements, mAP50 tends to be higher than mAP50-95, serving as a broader indicator of a model's detection performance. In the context of this study, the performance of the proposed method was compared to the Faster-RCNN with a fixed learning rate, using the same dataset and experimental conditions. The results, as shown in Table 3, reveal that the proposed method outperforms the fixed learning rate Faster-RCNN in terms of detection accuracy.

Table 3: mAP50 and mAP50-95 for proposed method

Strategy	MAP50	mAP50-95
Fixed Learning Rate	0.79	0.65
Fuzzy-Based Learning Rate	0.83	0.69

To further validate the proposed model's effectiveness, we compared it with conventional classifiers such as SVM, KNN, Decision Tree, Ensemble, and Subspace, as well as CNN-based and LeNet architectures. These models used features such as brightness, Histogram of Oriented Gradients (HOG), and Local Binary Patterns (LBP) for classification. Table 4 presents classified data in two "normal" and "cancerous" cases.

Table 4: Accuracy performance compared to other methods

Method	Classifier	Type	Accuracy
Brightness	**SVM**	Quadratic	73.26
		Cubic	71.25
		Linear	75.68
		Medium Gaussian	71.98
	KNN	Weighted	75.25
		Fine	74.66
	Tree	Fine	67.26
HOG	**SVM**	Quadratic	80.27
		Cubic	83.42
		Linear	79.58
		Medium Gaussian	83.21
	KNN	Weighted	73.25
		Fine	71.87
	Tree	Fine	69.24
LBP	**SVM**	Quadratic	89.21
		Cubic	85.16
		Linear	85.36
		Medium Gaussian	79.87
	KNN	Weighted	72.12
		Fine	77.98
	Tree	Fine	67.95
Combine (Color, 2 HOG, LBP)	**KNN**	Fine	89.94
CNN		LeNet architecture	91.58
Method [41]		YOLO-based multiscale CNN	91.15
Method [34]		Modified Faster RCNN	94.12
Method [49]		GoogLeNet–SVM	95.80
Method [40]		YOLO-based	95.70
Method [50]		Transfer learning CNN	96.02
Method [36]		YOLOv5-CAD	96.30
Method [39]		Transformer-CNN	96.12
Proposed method		Fixed Learning Rate	94.83
Proposed method		Fuzzy-Based Learning Rate	96.45

We also evaluated performance in distinguishing between benign and malignant tumors using F1-score, precision, and recall metrics. The F1-score was calculated as (5):

$$f1_score = \frac{2PR}{P+R} \tag{5}$$

$$P = \frac{TP}{TP+FP} \tag{6}$$

$$R = \frac{TP}{TP+FN} \tag{7}$$

where:

- TP = True Positives
- FP = False Positives
- FN = False Negatives

Table 5 presents the results for two possible cases, showing that the proposed method achieves the highest scores among all tested approaches.

Table 5: Precision and recall metrics assessed for fuzzy-based learning rate

Label	precision	recall	f1-score
Normal	0.9369	0.9002	0.9182
Benign	0.9425	0.9538	0.9481
malignant	0.9428	0.9526	0.9477

The confusion matrix (Table 6) separately provides the model's classification performance for each class. In this table, each row represents the actual cancer type, while the columns correspond to the predicted cancer types. This layout enables a clear comparison between the ground-truth labels and the model's predictions. As shown, the proposed system achieves an accuracy exceeding 95%, demonstrating a high level of reliability in distinguishing between benign and malignant tumors.

The Receiver Operating Characteristic–Area Under the Curve (ROC–AUC) metric was employed to provide a threshold-independent evaluation of the classification performance. Unlike accuracy-based measures that depend on a fixed decision threshold, ROC–AUC assesses the model's discriminative capability by analyzing the trade-off between the true positive rate and false positive rate across all possible thresholds. For the three-class classification task (Normal, Benign, and Malignant), a one-vs-rest strategy was adopted to compute the ROC–AUC for each class individually. As illustrated in Fig. 11, the proposed model incorporating a fuzzy-based learning rate achieves consistently high discriminative performance, with ROC–AUC values exceeding 98% for all three classes. These results highlight the robustness and effectiveness of the proposed approach in distinguishing between different breast tissue conditions.

Table 6: The proposed model confusion for fuzzy-based learning rate

actual	**Normal**	8238	476	452
	Benign	250	15155	477
	malignant	276	464	15168
		Normal	**Benign**	**malignant**
			Predicted	

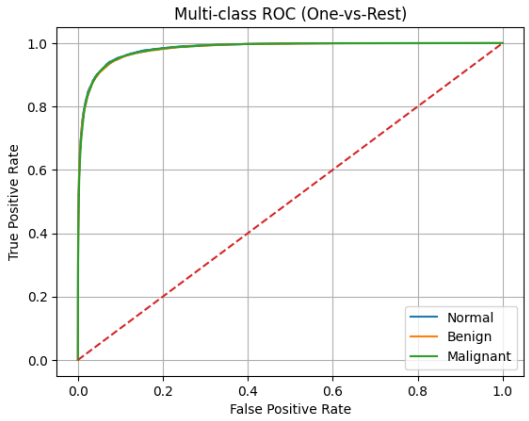


Fig. 11: ROC curve of the proposed model using a fuzzy-based learning rate.

Discussion

The results presented in the previous section demonstrate the strong performance of the proposed hybrid framework that combines Faster R-CNN with fuzzy logic–based adaptive learning. The model achieved a classification accuracy of 96.45% and ROC-AUC values exceeding 98%, outperforming traditional machine learning techniques (e.g., SVM, KNN, and Decision Trees) and even some CNN-based architectures such as LeNet and standard Faster R-CNN without fuzzy enhancement. The fuzzy logic mechanism contributed significantly to model stability and training efficiency. By dynamically adjusting the learning rate based on loss value and training epoch, the system achieved faster convergence and reduced training loss by more than 2.3× compared to the fixed-rate strategy. This indicates that the model effectively adapted its learning behavior based on training progress, a benefit not easily achievable with manually tuned hyperparameters.

The IoU metric (98.12%) confirmed the high localization accuracy of the model in identifying breast cancer masses. Furthermore, the confusion matrix and F1-scores across the three classes (normal, benign, malignant) demonstrated strong balance between precision and recall, minimizing both false positives and false negatives—a critical factor in clinical scenarios. Compared to recent deep learning models reported in the literature (as included in Table 4), our approach performs competitively or better in terms of accuracy, particularly when considering its explainable structure, use of fuzzy logic, and training efficiency. While transformer-based and diffusion models have shown promise, they typically require substantially more computational resources, whereas our method achieves high performance using relatively moderate hardware. However, this study also has certain limitations. The dataset was split into training and testing sets without a separate validation phase, which might have slightly

biased the performance metrics. In addition, the current model was tested only on the CBIS-DDSM dataset. Future work will focus on testing cross-dataset generalizability and incorporating more diverse clinical data. Overall, the proposed framework offers a practical and accurate tool for automated breast cancer detection in mammography images, with strong potential for integration into clinical decision-support systems.

Conclusion

Due to unhealthy lifestyle habits, breast cancer has become one of the most prevalent diseases among women today. As a result, prevention, early detection, and treatment of this disease have gained significant research attention. One promising approach is the use of artificial intelligence for breast cancer detection. In this study, we proposed a breast cancer detection method based on a deep learning framework that combines ResNet and Faster R-CNN architectures with fuzzy logic. The proposed approach employs a fuzzy inference system to dynamically adjust the learning rate during training according to the loss value and training epoch. Experimental results demonstrate that the model can accurately detect and localize cancerous regions in mammography images. Specifically, it achieved an Intersection over Union (IoU) score of 98.12% and a mean Average Precision (mAP) of 0.83, indicating excellent localization capability and robust detection performance. Additionally, the system successfully distinguishes between benign and malignant tumors with high precision. However, this study has some limitations. The dataset was divided into training and testing sets without a separate validation phase, which may have slightly biased the performance metrics. Furthermore, the model was tested solely on the CBIS-DDSM dataset. Future work will focus on evaluating the model's generalizability across multiple datasets and incorporating more diverse clinical data. Additionally, improving the software design for better usability and exploring alternative architectures will be important areas for further research. Overall, the proposed framework presents a practical and accurate solution for automated breast cancer detection in mammography images, with strong potential for integration into clinical decision-support systems.

Author Contributions

Fatemeh Jafari: Conducted the experiments and drafted the manuscript.

Hamid Reza Ghafari: Contributed to manuscript writing and provided significant input to the research design and methodology.

Hassan Farsi: Interpreted the experimental results and performed data analysis.

All authors read and approved the final version of the manuscript

Funding

This research received no external funding.

Conflict of Interest

The authors declare no potential conflict of interest regarding the publication of this work. In addition, the ethical issues including plagiarism, informed consent, misconduct, data fabrication and, or falsification, double publication and, or submission, and redundancy have been completely witnessed by the authors.

Acknowledgement

The authors acknowledge the use of AI-assisted tools during the preparation of this manuscript. Grammarly was employed for language proofreading and grammatical refinement. Additionally, OpenAI's ChatGPT (version 4) was utilized to assist with structural editing, wording improvements, and clarity enhancement of the text. All scientific contributions, methodological developments, analyses, and conclusions presented in this work are solely the authors' own.

Abbreviations

AI	Artificial Intelligence
CNN	Convolutional Neural Network
RCNN	Region-based Convolutional Neural Network
Faster-RCNN	Faster Region-based Convolutional Neural Network
YOLO	You Only Look Once
SSD	Single Shot Detector
mAP	Mean Average Precision
CAD	Computer-Aided Diagnosis
ROC	Receiver Operating Characteristic
AUC	Area Under the Curve
RoI	Region of Interest
RPN	Region Proposal Network
IOU	Intersection Over Union
SVM	Support Vector Machine
KNN	K-Nearest Neighbors
HOG	Histogram of Oriented Gradients
LBP	Local Binary Patterns
TP	True Positives
FP	False Positives

FN	False Negatives
F1-score	Harmonic Mean of Precision and Recall
ResNet	Residual Neural Network
CBIS-DDSM	Curated Breast Imaging Subset of Digital Database for Screening Mammography
INbreast	Portuguese INbreast Mammography Dataset
ViT	Vision Transformer
LoG	Laplacian of Gaussian
CAM	Class Activation Map

References

[1] O. J. Scully, B. H. Bay, G. Yip, Y. Yu, "Breast cancer metastasis," Cancer Genomics Proteomics, 9(5): 311-320, 2012.

[2] E. I. Obeagu, G. U. Obeagu, "Breast cancer: A review of risk factors and diagnosis," Medicine, 103(3): e36905, 2024.

[3] X. Xiong et al., "Breast cancer: pathogenesis and treatments," Signal Tran. Targeted Ther., 10(1): 49, 2025.

[4] J. Baselga, L. Norton, "Focus on breast cancer," Cancer cell, 1(4): 319-322, 2002.

[5] J. R. Benson, I. Jatoi, M. Keisch, F. J. Esteva, A. Makris, V. C. Jordan, "Early breast cancer," The Lancet, 373(9673): 1463-1479, 2009.

[6] Z. Sanaat, R. Dolatkhah, "Epidemiologic profile of breast cancer in Iran: a systematic review and meta-analysis," Clin. Epidemiol. Global Health, 26: 101537, 2024.

[7] J. Koh, Y. Yoon, S. Kim, K. Han, E. K. Kim, "Deep learning for the detection of breast cancers on chest computed tomography," Clinical Breast Cancer, 22(1): 26-31, 2022.

[8] J. L. Kelsey, M. D. Gammon, "The epidemiology of breast cancer," CA: A Cancer J. Clin., 41(3): 146-165, 1991.

[9] N. M. Almansour, "Triple-negative breast cancer: a brief review about epidemiology, risk factors, signaling pathways, treatment and role of artificial intelligence," Front. Mol. Biosci., 9: 836417, 2022.

[10] B. S. Hulka, A. T. Stark, "Breast cancer: cause and prevention," The Lancet, 346(8979): 883-887, 1995.

[11] C. Katsura, I. Ogunmwonyi, H. K. Kankam, S. Saha, "Breast cancer: presentation, investigation and management," Br. J. Hosp. Med. 83(2): 1-7, 2022.

[12] L. Wang, "Mammography with deep learning for breast cancer detection," Front. Oncol., 14: 1281922, 2024.

[13] D. Mandair, J. S. Reis-Filho, A. Ashworth, "Biological insights and novel biomarker discovery through deep learning approaches in breast cancer histopathology," NPJ Breast Cancer, 9(1): 21, 2023.

[14] R. Adam, K. Dell'Aquila, L. Hodges, T. Maldjian, T. Q. Duong, "Deep learning applications to breast cancer detection by magnetic resonance imaging: a literature review," Breast Cancer Res., 25(1): 87, 2023.

[15] V. Mohanakurup et al., "Breast cancer detection on histopathological images using a composite dilated Backbone Network," Comput. Intell. Neurosci., 2022(1): 8517706, 2022.

[16] S. A. Zendehbad, E. M. Rad, and S. S. Bajestani, "Swarm Intelligence in Biomedical Engineering," Intelligence-Based Medicine, p. 100308, 2025.

[17] A. Zarei, E. M. Rad, S. S. Bajestani, S. A. Zendehbad, "Providing a prostate cancer detection and prevention method with developed deep learning approach," Prostate Cancer, 2025(1): 2019841, 2025.

[18] F.-Z. Nakach, A. Idri, E. Goceri, "A comprehensive investigation of multimodal deep learning fusion strategies for breast cancer classification," Artif. Intell. Rev., 57(12): 327, 2024.

[19] A. M. Sharafaddini, K. K. Esfahani, N. Mansouri, "Deep learning approaches to detect breast cancer: A comprehensive review," Multimedia Tools Appl., 84: 24079-24190, 2024.

[20] A. B. Nassif, M. A. Talib, Q. Nasir, Y. Afadar, O. Elgendy, "Breast cancer detection using artificial intelligence techniques: A systematic literature review," Artif. Intell. Med., 127: 102276, 2022.

[21] S. M. Shah, R. A. Khan, S. Arif, U. Sajid, "Artificial intelligence for breast cancer analysis: Trends & directions," Comput. Biol. Med., 142: 105221, 2022.

[22] Y. Sun, Z. Sun, W. Chen, "The evolution of object detection methods," Engi. Appl. Artif. Intell., 133: 108458, 2024.

[23] F. Prinzi, M. Insalaco, A. Orlando, S. Gaglio, S. Vitabile, "A yolo-based model for breast cancer detection in mammograms," Cognit. Comput., 16(1): 107-120, 2024.

[24] J. Ghasemi, R. Ghaderi, M. K. Mollaei, S. Hojjatoleslami, "A novel fuzzy Dempster–Shafer inference system for brain MRI segmentation," Inf. Sci., 223: 205-220, 2013.

[25] R. A. Dar, M. Rasool, A. Assad, "Breast cancer detection using deep learning: Datasets, methods, and challenges ahead," Comput. Biol. Med., 149: 106073, 2022.

[26] I. Sechopoulos, J. Teuwen, R. Mann, "Artificial intelligence for breast cancer detection in mammography and digital breast tomosynthesis: State of the art," in Proc. Seminars in Cancer Biology, 72: 214-225, 2021.

[27] S. M. McKinney et al., "International evaluation of an AI system for breast cancer screening," Nature, 577(7788): 89-94, 2020.

[28] A. Alhussen, M. A. Haq, A. A. Khan, R. K. Mahendran, S. Kadry, "XAI-RACapsNet: Relevance aware capsule network-based breast cancer detection using mammography images via explainability O-net ROI segmentation," Expert Syst. Appl., 261: 125461, 2025.

[29] M. Mokhtari, L. Fortaleza, L. Chang, M. Popović, "AI-Enhanced SDR microwave breast cancer screening transceiver: a comparative study," IEEE Trans. Microwave Theory Tech., 73(8): 5260-5267, 2025.

[30] M. Taghipour-Gorjikolaie et al., "AI-based hierarchical approach for optimizing breast cancer detection using MammoWave device," Biomed. Signal Process. Control, 100: 107143, 2025.

[31] M. Liu et al., "A deep learning method for breast cancer classification in the pathology images," IEEE J. Biomed. Health Inf., 26(10): 5025-5032, 2022.

[32] Z. Q. Habeeb, B. Vuksanovic, I. Q. Al-Zaydi, "Breast cancer detection using image processing and machine learning," J. Image Graphics, 11(1): 1-8, 2023.

[33] A. Sahu, P. K. Das, S. Meher, "An efficient deep learning scheme to detect breast cancer using mammogram and ultrasound breast images," Biomed. Signal Process. Control, 87: 105377, 2024.

[34] P. Kumar, K. Sangeetha, A. S. Praneeth, M. S. Madhav, T. Swaroopa, G. Rohit, "Automatic detection and localization of breast cancer from mammogram imaging modality using modified faster RCNN," in Proc. 2023 5th International Conference on Smart Systems and Inventive Technology (ICSSIT): 1549-1553, 2023.

[35] M. A. Tawil, O. Dakkak, "edmABC: an improved artificial bee colony algorithm on detecting breast cancer for mammography images," Evol. Syst., 16(2): 42, 2025.

[36] B. K. Karaca Aydemir, Z. Telatar, S. Güney, B. Dengiz, "Detecting and classifying breast masses via YOLO-based deep learning," Neural Comput. Appl., 37: 11555-11582, 2025.

[37] H. Gui et al., "FS-YOLOv9: a frequency and spatial feature-based YOLOv9 for real-time breast cancer detection," Acad. Radiol., 32(3): 1228-1240, 2025.

[38] H. Merzoug, H. Yedjour, S. Chouraqui, "A deep system for breast tumor classification from mammograms," Int. J. Commun. Antenna Propag. (IRECAP), 12(6): 394-403, 2022.

[39] S. S. Boudouh, M. Bouakkaz, "Advancing precision in breast cancer detection: A fusion of vision transformers and CNNs for calcification mammography classification," Appl. Intell., 54(17-18): 8170-8183, 2024.

[40] N. M. Hassan, S. Hamad, K. Mahar, "YOLO-based CAD framework with ViT transformer for breast mass detection and classification in CESM and FFDM images," Neural Comput. Appl., 36(12): 6467-6496, 2024.

[41] A. D. Mohammed, D. Ekmekci, "Breast cancer diagnosis using YOLO-based multiscale parallel CNN and flattened threshold swish," Appl. Sci., 14(7): 2680, 2024.

[42] L. A. Zadeh, "Fuzzy logic," Computer, 21(4): 83-93, 1988.

[43] R. Girshick, "Fast r-cnn," in Proc. the IEEE International Conference on Computer Vision: 1440-1448, 2015.

[44] J. Ghasemi, S. A. Zendehbad, "Advanced deep learning approaches for accurate and efficient suspicious behavior detection in surveillance videos," Comput. Sci. Eng., 4(2): 203-216, 2025.

[45] B. Koonce, "ResNet 50," in Convolutional neural networks with swift for tensorflow: image recognition and dataset categorization: Springer, pp. 63-72, 2021.

[46] K. Weiss, T. M. Khoshgoftaar, D. Wang, "A survey of transfer learning," J. Big data, 3: 1-40, 2016.

[47] F. G. R. S. Lee, A. Hoogi, D. Rubin. CBIS-DDSM: Breast Cancer Image Dataset.

[48] R. Padilla, S. L. Netto, E. A. Da Silva, "A survey on performance metrics for object-detection algorithms," in Proc. 2020 International conference on Systems, Signals and Image Processing (IWSSIP): 237-242, 2020.

[49] F. R. Yazdi, M. M. Khalilzadeh, F. Firouzi, M. Azarnoosh, "Breast mass detection with nonlinear model of thermography images," Contrib. Sci. Tech. Eng., 2(3): 1-11, 2025.

[50] L. Liao, E. M. Aagaard, "An open codebase for enhancing transparency in deep learning-based breast cancer diagnosis utilizing CBIS-DDSM data," Sci. Rep., 14(1): 27318, 2024.

Biographies



Fatemeh Jafari holds a B.Sc. in Computer Engineering (Software Engineering) from Birjand University of Technology, Iran. She earned her M.Sc. in Computer Science (Intelligent Computation) from the University of Sistan and Baluchestan, where she focused on advanced computational methods and intelligent systems. Currently, she is a Ph.D. candidate in Computer Engineering (Artificial Intelligence) at the Islamic Azad University, Ferdows Branch. Her research interests lie at the intersection of Artificial Intelligence, Image Processing, and Medical Image Analysis, with a particular emphasis on developing intelligent algorithms for diagnostic and analytical applications.

- Email: fatemeh.jafari8094@iau.ac.ir
- ORCID: 0009-0001-3709-7841
- Web of Science Researcher ID:
- Scopus Author ID:
- Homepage:



Hamid Reza Ghafari received his B.Sc. degree in Computer Engineering (Software Engineering) from Sharif University of Technology in 1997. He earned his M.Sc. degree in Computer Engineering (Software Engineering) from Islamic Azad University, Tehran South Branch, in 2001, and his Ph.D. degree in Computer Engineering (Software Systems) from Ferdowsi University of Mashhad in 2014. He is currently an Associate Professor, a faculty member, and the President of Islamic Azad University, Ferdows Branch. His main research interests include Artificial Intelligence, Image Processing, Data Mining, and Medical Image Processing.

- Email: hamidghaffary53@iau.ac.ir
- ORCID: 0000-0003-0627-4080
- Web of Science Researcher ID: AAP-3151-2021
- Scopus Author ID: 57203222802
- Homepage: https://scimet.iau.ir/Hamidreza_Ghaffari



Hassan Farsi received his B.Sc. (1992) and M.Sc. (1994) degrees in Communication Engineering from Sharif University of Technology, Tehran, Iran, and his Ph.D. degree in Communication Engineering from the University of Surrey, Guildford, UK, in 2003. He is currently a Full Professor in the Faculty of Electrical and Computer Engineering at the University of Birjand, Iran. His research interests include signal processing, audio and speech processing, image processing, artificial intelligence, and mathematical algorithms.

- Email: hfarsi@birjand.ac.ir
- ORCID: 0000-0001-6038-9757
- Web of Science Researcher ID: NA
- Scopus ID: 16202385600
- Homepage: https://cv.birjand.ac.ir/hasanfarsi/en

Journal of Electrical and Computer Engineering Innovations
(JECEI)
Journal homepage: http://www.jecei.sru.ac.ir

Research paper

Diagnosis of Cardiac Arrhythmia using an Optimized Two-stage Deep Learning Model

Motahareh Akbari Poodineh , ***Fatemeh Zare Mehrjardi*** , ***Mohsen Sardari Zarchi*** *

Department of Computer Engineering, Faculty of Technology and Engineering, Meybod university, Meybod, Iran.

Article Info

Article History:
Received 19 October 2025
Reviewed 17 December 2025
Revised 18 February 2026
Accepted 23 February 2026

Keywords:
Cardiac arrhythmia
Autoencoder
Convolutional neural network
Ecg signal
Deep learning
Genetic algorithm

*Corresponding Author's Email Address: *sardari@meybod.ac.ir*

Abstract

Background and Objectives: Cardiovascular diseases, particularly cardiac arrhythmias, are among the leading causes of mortality worldwide. Early and accurate diagnosis is essential for improving patient outcomes. Although electrocardiogram (ECG) signals are widely used for arrhythmia detection, manual interpretation remains time-consuming and error-prone. Therefore, this study proposes an innovative, optimized two-stage deep learning framework for the reliable diagnosis of cardiac arrhythmias from ECG signals, aiming to enhance both accuracy and robustness.

Methods: The key innovation lies in the first stage, where the autoencoder's reconstruction error threshold is optimized using a Genetic Algorithm (GA) to maximize the separation between normal and abnormal signals. Only signals identified as abnormal proceed to the second stage, a Convolutional Neural Network (CNN) that classifies them into four arrhythmia types (Supraventricular, Ventricular, Fusion, and Unknown beats). All experiments were conducted on the MIT-BIH Arrhythmia Database using a stratified split, with SMOTE applied exclusively to the CNN training set to address class imbalance. Performance was evaluated through 5-fold cross-validation.

Results: The proposed AE-GA-CNN+SMOTE framework achieved an average accuracy of 97.89 ± 0.25%, precision of 97.90 ± 0.24%, recall of 97.68 ± 0.29%, and an F1-score of 97.69 ± 0.28%. It outperformed the single-stage CNN+SMOTE baseline by +6.28% in accuracy ($p < 0.001$) and showed statistically significant improvements over all other two-stage variants ($p < 0.05$).

Conclusion: The two-stage architecture, enhanced by GA-driven threshold optimization and SMOTE balancing, demonstrates high accuracy and robustness for automated arrhythmia screening. The statistically validated performance gains support its potential as a decision-support tool for clinical and real-time ECG analysis.

This work is distributed under the CC BY license (http://creativecommons.org/licenses/by/4.0/)

How to cite this paper:
M. Akbari Poodineh, F. Zare Mehrjardi, M. Sardari Zarchi, "Diagnosis of cardiac arrhythmia using an optimized two-stage deep learning model," J. Electr. Comput. Eng. Innovations, 14(2): 519-534, 2026.

DOI: 10.22061/jecei.2026.12629.898

URL: https://jecei.sru.ac.ir/article_2545.html

2345- 3044/© 2026 The Authors. Published by Shahid Rajaee Teacher Training University.

Introduction

Cardiovascular diseases (CVDs) remain a global public health crisis, standing as one of the principal causes of death worldwide. Early and precise detection of these conditions is paramount to administering timely, life-saving treatments and improving long-term patient outcomes. Cardiovascular diseases (CVDs) can be broadly categorized into several major groups, each posing unique diagnostic and management challenges. These categories include: (1) Coronary Artery and Vascular Diseases, characterized by the hardening and narrowing of cardiac arteries, which often lead to heart attacks or angina [1]. (2) Heart Rhythm Disorders (Arrhythmias) [2], [3], involving abnormal heartbeat patterns (too fast, too slow, or irregular) that disrupt blood flow and affect millions worldwide. (3) Structural Heart Diseases, encompassing congenital or acquired abnormalities of the heart valves, walls, or muscles [4]. (4) Heart Failure, a serious condition typically resulting from a weakened heart, often due to a prior heart attack or chronic high blood pressure [5]. (5) Other Cardiac Conditions, including infections and hereditary disorders [6]. Recognizing these conditions early is crucial, as it has been shown to substantially reduce treatment costs and extend patient longevity [7].

Studies investigating the automated diagnosis and classification of cardiac arrhythmias have generally employed two distinct approaches: conventional machine learning (ML) models and deep learning (DL) models. Machine learning is an interdisciplinary field dedicated to replicating human learning processes. It is broadly categorized into supervised, unsupervised, and semi-supervised paradigms. In the supervised setting, models are trained exclusively on labeled datasets to predict outcomes for new, unseen samples. However, a major limitation of these traditional ML techniques is their heavy reliance on the manual feature extraction stage. This manual process necessitates domain expertise, and if features are poorly selected, the model's overall diagnostic performance can be severely compromised [8].

Deep learning (DL), a powerful sub-field of machine learning, has been widely applied to numerous complex analytical tasks. The primary advantage of DL architectures, in contrast to their conventional counterparts, lies in their ability to automatically derive robust, high-level features directly from the raw input data. This inherent capability eliminates the need for labor-intensive, manual feature engineering , as it automatically acquires meaningful data representations. However, a significant consideration when utilizing DL models is the persistent challenge of overfitting. Successfully mitigating this challenge requires both extensive datasets and considerable computational resources during the training phase [9]-[13]. The following section provides a critical review of several key studies that have employed these AI methodologies specifically for cardiac arrhythmia diagnosis.

Despite the significant advances in automated arrhythmia diagnosis, a key challenge remains: the lack of robust and optimally tuned mechanisms to reliably separate normal from abnormal signals before classification. While many previous studies have relied on single-stage classifiers (e.g., CNN or LSTM) or have utilized autoencoders without optimal threshold tuning, this research introduces an integrated two-stage framework that optimizes the detection threshold with a Genetic Algorithm (GA), aiming to simultaneously improve diagnostic accuracy and computational efficiency.

The remainder of this paper is organized as follows. Section 2 presents a critical review of the related literature. Section 3 describes the proposed two-stage deep learning framework and the genetic algorithm (GA)-based optimization method. Section 4 outlines the dataset and experimental setup. Section 5 presents and discusses the experimental results. Finally, Section 6 concludes the paper and highlights potential directions for future research.

Related Work

Sraitih et al. [14] conducted research focused on the detection and prediction of cardiac arrhythmias from ECG signals, deploying a range of machine learning techniques. Their methodology involved training models specifically a Deep Neural Network (DNN), Support Vector Machine (SVM), and K-Nearest Neighbor (KNN) on the UCI dataset, which features seventeen distinct classes of heartbeats. The authors emphasized the need to minimize human diagnostic error by introducing automated, real-time machine learning tools. While noting the high accuracy achieved and the innovative approach as strengths, the paper also pointed out limitations such as algorithmic complexity and the requirement for robust data preprocessing, including the imputation of missing values and cleaning procedures.

Acharya et al. [15] introduced an innovative technique designed for the automated detection of Myocardial Infarction (MI) via ECG signals, aiming to circumvent the difficulties associated with visual interpretation. They implemented an eleven-layer Deep Convolutional Neural Network (DCNN), which yielded notable average accuracies of 93.53% (for noisy data) and 95.22% (for clean data). A key achievement of their work was the successful operation without any requirement for manual feature engineering. The strengths of the proposed model, particularly its ability to analyze previously unseen and noisy signals, highlight the potential of computer-aided diagnosis systems in

clinical settings to improve early detection of myocardial infarction (MI).

Tan et al. [16] explored an unsupervised learning framework to identify various arrhythmia subtypes within ECG data. Utilizing the ICENTIA11K dataset, which encompasses records from more than 11,000 patients, their method employed techniques such as Autoencoders, Principal Component Analysis (PCA), and Fast Fourier Transform (FFT) for model training. The core objective of their research was to effectively capture the latent representations and uncover hidden structural patterns within the cardiac signals. Ultimately, their findings validated the efficacy of unsupervised learning as a powerful mechanism for pattern discovery and the fine-grained classification of arrhythmia subtypes in large-scale ECG data.

Kuznetsov et al. [17] proposed a Variational Autoencoder (VAE) network for the dual purpose of generating synthetic ECG signals and learning representative latent features. By training the VAE on a raw ECG database to reconstruct the cardiac cycle, they successfully derived novel and interpretable features that often corresponded directly to clinical markers like the T wave and ST segment. The high fidelity of the synthetic data was confirmed by a Maximum Mean Discrepancy (MMD) criterion value of 3.83×10^{-3}, demonstrating the generation quality. This research highlights how VAE-extracted features can significantly boost heart disease diagnostic performance, especially in scenarios constrained by the limited availability of labeled data.

Bikova et al. [18] undertook a comparative study by evaluating six distinct machine learning models for cardiac arrhythmia classification using the widely-referenced MIT-BIH dataset. Among the models assessed, the Convolutional Neural Network (CNN) exhibited superior performance, achieving a notable 95% accuracy alongside an F1-score of 84.75%. Other models, including the Support Vector Classifier (SVC) and Long Short-Term Memory (LSTM) networks, also performed strongly, with accuracies of 94% and 93%, respectively. Furthermore, their research addressed critical diagnostic difficulties such as data imbalance, noise interference, and class similarity, proposing methodological remedies like resampling techniques and the integration of expert clinical knowledge.

Sahoo et al. [19] performed advanced analysis of cardiac arrhythmias in ECG signals, focusing specifically on noise reduction using adaptive filters and mathematical morphology techniques. While the strength of their approach lies in achieving high accuracy for arrhythmia detection, the authors noted the necessity for further optimization of the proposed methods to enhance robustness.

Li et al. [20] addressed the classification of seven cardiac arrhythmia types from a large-scale database of 51,579 ECG records by employing Deep Convolutional Neural Networks (DCNNs) integrated with the concept of Transfer Learning (TL). Despite the method's efficacy, the authors highlighted key limitations, including the substantial requirement for extensive training data and the inherent complexity of the final DCNN model.

Sattar et al. [21] concentrated on cardiac arrhythmia classification, combining Convolutional Neural Network (CNN) and Long Short-Term Memory (LSTM) architectures to achieve an accuracy of 92%. The primary benefits of their methodology included a significant improvement in prediction accuracy and a reduction in manual analysis time. However, a key challenge identified was the necessity for acquiring a diverse range of training data.

Raza et al. [22] introduced a 9-layer CNN model specifically designed for classifying ECG signals within the MIT-BIH dataset, reaching an accuracy of 94.03%. Their model demonstrated superior accuracy and sensitivity compared to prior models. Nevertheless, a major constraint noted in the study was the high demand for computational hardware resources necessary to effectively train and deploy the model.

In a systematic approach, Bi et al. [23] focused on the prediction of heart disease using Graph Neural Networks (GNNs). Their study aimed to classify patient data into two categories: cardiac disease and non-cardiac disease, following a structured process including model definition, training, and optimization. Notably, this research utilized Feed Forward Neural Networks (FNNs) alongside GNNs for the core prediction tasks, establishing a foundational reference for the development and enhancement of subsequent cardiac diagnostic models.

Based on the critical review of the literature, two principal limitations are identified in existing arrhythmia diagnosis models: (1) single-stage classification architectures often struggle to maintain robust performance when dealing with highly imbalanced datasets; and (2) multi-stage approaches, while promising, frequently employ sub-optimal, manually-tuned, or statistically-derived thresholds in their detection phase. Our proposed framework directly addresses these two gaps: by utilizing the Genetic Algorithm (GA) for threshold optimization, we establish a scientifically robust and superior boundary, and by decoupling the anomaly detection (Autoencoder) from the fine-grained classification (CNN) through a dedicated two-stage pipeline, we significantly enhance the overall system's accuracy and reliability over prior art.

Method

In this study, the objective is to identify cardiac arrhythmia using a two-stage model consisting of an

autoencoder and a convolutional neural network (CNN), with an integrated Genetic Algorithm (GA) for threshold optimization. As shown in Fig. 1, the proposed method implements anomaly detection with GA-optimized thresholding followed by multi-class classification. In the following sections, the utilized database is first introduced, and then the details of each component of the proposed methodology are described.

MIT-BIH Database

The availability of a suitable and extensive database is a critical component of any research in this field. For cardiac arrhythmia research, a well-known database is the MIT-BIH Arrhythmia Database, which was compiled in 1980 by Beth Israel Hospital and MIT.

This database consists of 48 half-hour, two-channel ECG recordings.

It contains 87554 samples categorized into 5 classes: one normal class (N) and four types of cardiac events, Supraventricular (S), Ventricular (V), Fusion (F), and Unknown (Q) beats.

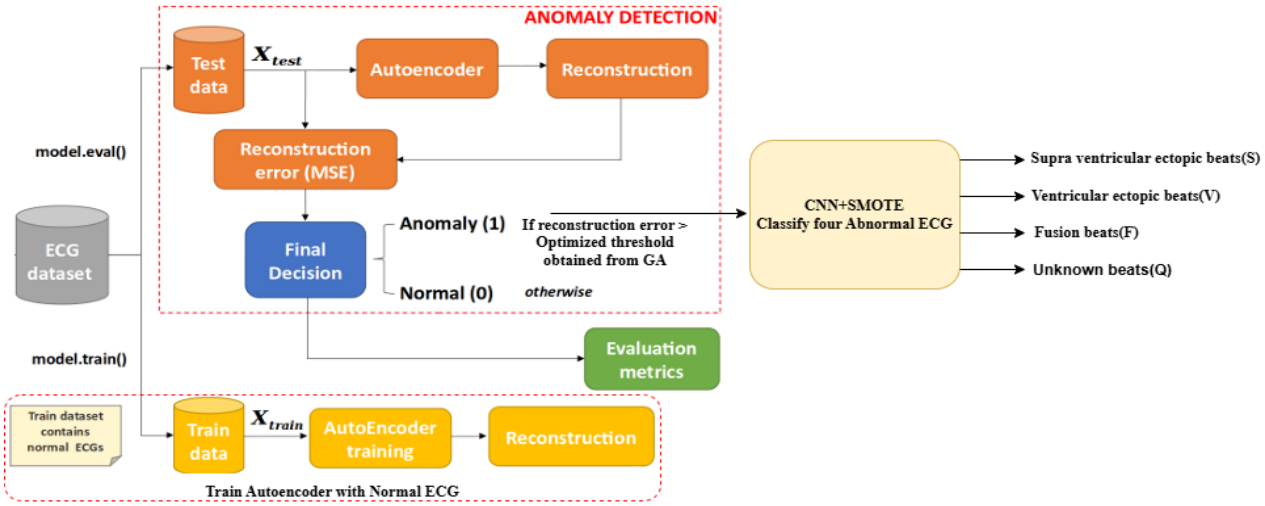


Fig. 1: Overall workflow of the proposed two-stage arrhythmia detection framework.

Fig. 2 illustrates representative ECG signal samples for each of these five classes. The signals were sampled at a frequency of 360 Hz. Table 1, which shows the number of samples in each class, clearly indicates the significant problem of dataset imbalance [24].

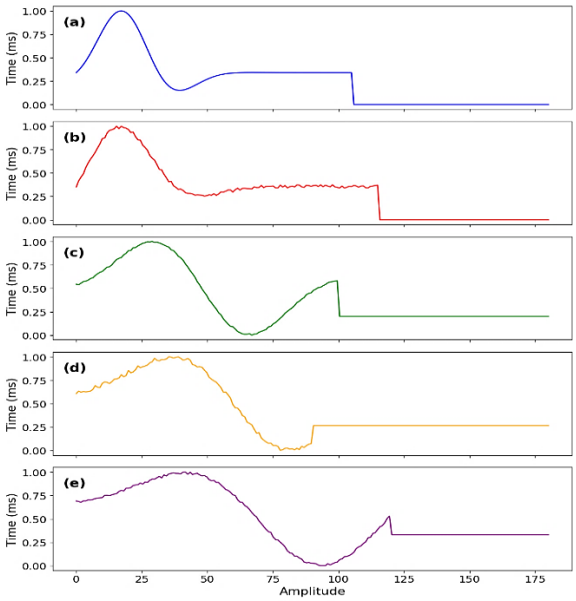


Fig. 2: Sample ECG signals from different classes (a) Normal beat, (b) Supraventricular ectopic beat, (c) Ventricular ectopic beat, (d) Fusion beat, (e) Unknown beat.

Table 1: Classes of MIT-BIH database

Class	Number of each class
Normal beats(N)	72471
Supra ventricular ectopic beats(S)	2223
Ventricular ectopic beats(V)	5788
Fusion beats(F)	641
Unknown beats(Q)	6431

Preprocessing Step

The first stage of the proposed method is data preprocessing, which consists of three key steps:

Data Normalization: This step ensures that all features are scaled to a common range, thereby giving them equal importance during the learning process. In this research, the Standard Scaler normalization method was used. The specific normalization formula is presented in (1).

$$x_{\text{Scaled}} = \frac{(x - \text{median}(x))}{\sigma} \quad (1)$$

Handling Missing Data: To address the issue of missing values, features with a high percentage of empty entries were first removed. The remaining missing values in each feature were then imputed based on the mode value of that feature, considering only samples from the same class.

Addressing Class Imbalance: As evidenced in Table 1, the MIT-BIH database suffers from a significant class imbalance. A major challenge with imbalanced datasets is the classifier's bias toward the majority class. To mitigate this issue, two complementary approaches were employed: SMOTE (Synthetic Minority Over-sampling Technique) and Weighted Loss Function. SMOTE balances the data by generating new synthetic samples in the vicinity of existing samples within the minority class, leveraging the k-nearest neighbors algorithm to measure distances and create artificial samples. Concurrently, the weighted loss function assigns higher penalties to misclassifications of minority classes during CNN training [25]. To eliminate any risk of data leakage, a strict cross-validation protocol was followed. Within each fold of the 5-fold cross-validation, the data were first split into training (80%) and test (20%) subsets. After this split, SMOTE was applied solely to the training subset to generate synthetic samples for the minority classes. The test subset remained completely untouched and contained only original (non-synthetic) samples. This ensures that no information from the test set influences the creation of synthetic data, thereby preserving the integrity of the evaluation.

ECG Beat Segmentation and Signal Representation The ECG recordings in the MIT-BIH database are provided as continuous multi-channel signals. For this study, we used a pre-segmented version of the database where each heartbeat is extracted as a fixed-length window of 187 samples, centered on the R-peak annotation. This segment length corresponds to approximately 0.52 seconds at the original sampling rate of 360 Hz and fully captures the P-wave, QRS complex, and T-wave morphology of a single cardiac cycle. Each 187-point beat was normalized using StandardScaler (subtracting the median and dividing by the standard deviation). The normalized beats were fed directly as raw 1D sequences to the models: as vectors of shape (187,) for the autoencoder, and reshaped to (1, 187) for the 1D CNN.

Data Classification Step

For the classification stage, a two-stage deep learning model is presented for the detection and classification of cardiac arrhythmias, as illustrated in Fig. 1. This model utilizes a combination of an autoencoder and a convolutional neural network (CNN). In the first stage, the autoencoder is exclusively trained to reconstruct normal ECG signals, enabling it to distinguish between normal and abnormal data.

First stage(AE+GA)

An Autoencoder (AE) [26] is an unsupervised neural network designed to learn an optimal data compression and decompression scheme. It is generally composed of an input layer, an output layer, an encoder neural network, a decoder neural network, and a latent space. The encoder compresses the input data into a compact representation within the latent space, while the decoder subsequently reconstructs this compressed representation back to the output layer. The reconstructed output is then compared to the original input, and the reconstruction error is backpropagated through the network to update the weights [27], [28]. The training process of the autoencoder aims to minimize this reconstruction error, L, as defined in (2):

$$L = \frac{1}{n}\sum_{i=1}^{n} (Y_i - Y_i')^2 \tag{2}$$

where Y_i is the original input signal, Y_i' is the reconstructed output, and n is the total number of samples. An ideal autoencoder's goal is to simply replicate the input at the output, but with a hidden space that has a smaller dimension than the input. This process allows the autoencoder to learn the most salient features of the training data, effectively reducing the data's dimensionality while preserving its most crucial information.

The autoencoder was exclusively trained on normal ECG beats (Class N, 72,471 samples) using Mean Squared Error loss, Adam optimizer (lr=0.001), batch size of 256, for 200 epochs. Reconstruction errors were computed per sample as the maximum absolute difference between input and reconstructed signals. The autoencoder specifications are summarized in Table 2. Subsequently, a Genetic Algorithm was employed to optimize the detection threshold for distinguishing normal from abnormal beats based on reconstruction errors.

The genetic algorithm was introduced in 1971 by John Holland. This algorithm belongs to the class of stochastic optimization algorithms and is particularly suitable for solving complex problems with an unknown search space. The implementation steps of the genetic algorithm are summarized as follows:

1- Given the problem of finding an optimal threshold to distinguish between normal and abnormal signals, an initial population of candidate solutions is generated. Each solution, or chromosome, represents a single threshold value (a single gene), randomly generated within a specified range.

2- The fitness of each candidate solution (threshold) is evaluated using a fitness function defined as the sum of normal accuracy and abnormal accuracy
3- New offspring are produced from the current population using genetic operators, namely crossover and mutation. In each iteration, the best-performing solutions are selected from both the current population and the newly produced offspring to form the population for the next iteration. These steps are repeated until a suitable solution is found [29], [30].

Table 2: Autoencoder model specifications

Category	Specification	Details
Architecture	Encoder	Dense(187 → 128) + ReLU + BatchNorm → Dense(128 → 64) + ReLU + BatchNorm → Dense(64 → 32) + ReLU
	Latent Space	32-dimensional compressed representation
	Decoder	Dense(32 → 64) + ReLU + BatchNorm → Dense(64 → 128) + ReLU + BatchNorm → Dense(128 → 187)
Training parameters	Dataset	72,471 normal beats (Class N) 80% training, 20% validation split
	Loss Function	Mean Squared Error (MSE)
	Optimizer	Adam (lr=0.001, β_1=0.9, β_2=0.999, ε=1e-8)
	Batch Size	256
	Epochs	200
Reconstruction Error	Computation Method	Maximum Absolute Error (MAE)
Input/Output	Input Dimension	187 time points (raw ECG length)
	Output Dimension	187 (reconstructed signal)

For full reproducibility, the key operational parameters of the Genetic Algorithm used in this study are presented in Table 3. The selection process employs a hybrid strategy combining Tournament Selection with Elitism, where the top 50% of the population (based on fitness) are directly transferred to the next generation. The remaining 50% of the population are generated via recombination, where a Simple Averaging Crossover operator is applied to selected parents from the elite pool. The mutation operator involves adding a small random value to the chromosome (threshold value) with the specified mutation rate, ensuring a local search around promising solutions.

Table 3: Genetic algorithm parameters for threshold optimization

Parameter	Value
Population Size	50
Number of Generations	100
Initialization Range	[0.008, 0.5] (min_err, max_err)
Fitness Function	acc_normal + acc_abnormal
Selection Strategy	Tournament Selection(size=3) + Elitism (Top 50%)
Crossover Type	Simple Averaging child = α × $parent_1$ + (1-α) × $parent_2$ where α ~ U(0,1)
Crossover Rate	90%
Mutation Mechanism	Adding a small random value (Gaussian noise) threshold_new = threshold + δ where δ ~ N(0, 0.02 × range) range = max_error − min_error
Mutation Rate	0.1
Replacement Strategy	Generational (Entire population replaced each generation (except elites))

Second stage(CNN)

In the second stage, the abnormal signals detected by the autoencoder are passed to a CNN, which serves as a supervised classifier.

The CNN architecture includes three convolutional blocks with batch normalization and max-pooling, followed by fully connected layers with dropout regularization to prevent overfitting. This CNN is tasked with diagnosing the specific type of arrhythmia among four predefined classes. The detailed architecture of the CNN model and its training parameters are presented in Table 4.

In summary, the proposed model leverages the anomaly detection capability of the autoencoder and the high classification power of the CNN. This two-stage strategy first separates abnormal from normal signals, then performs precise multi-class arrhythmia classification, enhancing both diagnostic accuracy and computational efficiency. The complete procedure is summarized in the pseudocode presented in Algorithm 1.

Table 4: CNN model specifications

Category	Specification	Details
Input Specification	Signal Length	187 samples
	Channels	1 (univariate ECG)
	Input Shape	(batch_size, 1, 187)
Architecture	Layer1	Conv1d(1, 32, kernel_size=5, padding='same')→ReLU→BatchNorm(32, momentum=0.1)→MaxPool1d(2, stride=2)
	Layer2	Conv1D(32, 64, kernel_size=5, padding='same')→ReLU→BatchNorm(64, momentum=0.1)→MaxPool1d(2, stride=2)
	Layer3	Conv1D(64, 128, kernel_size=5, padding='same')→ReLU→BatchNorm(128, momentum=0.1)→MaxPool1d(2, stride=2)→Flatten→Dense(128)→Dropout(0.5)→Dense(64)→Dense(4)
	Flatten	Output size: 128 * 23 = 2944
	Fully Connected 1	Dense(2944, 128) → ReLU → Dropout(0.5)
	Fully Connected 2	Dense(128, 64) → ReLU
	Output Layer	Dense(64, 4) (Softmax)
Training parameters	Dataset	4 classes (S, V, F, Q)
	Loss Function	Categorical Cross Entropy
	Optimizer	Adam(lr=0.0005, weight_decay=1e-4)
	Learning Rate Scheduler	CosineAnnealingLR(T_max=50)
	Batch Size	128
	Epochs	50
	Regularization	Batch Normalization(Momentum,0.1), Dropout (0.5), Label Smoothing (0.1), Weight Decay (1e-4)

Algorithm 1 Exact Implementation

Input: MIT-BIH train/test, $Y \in \{0, 1, 2, 3, 4\}$
Output: $\hat{Y}$, θ_{opt}, metrics
1. Data Prep: Keep test separate, extract normal beats from train
2. Autoencoder: 187→128→64→32→64→128→187
  Train on normals (MSE loss, 100 epochs, lr=0.001)
3. Genetic Algorithm (EXACT):
  $e_{\text{norm}} = \max(|X_{\text{norm}} - AE(X_{\text{norm}})|)$
  $e_{\text{abnorm}} = \max(|X_{\text{abnorm}} - AE(X_{\text{abnorm}})|)$
  Pop=50, Gens=100, Tournament=3, Mutation=0.1
  Fitness: $F(\theta) = \text{mean}(e_{\text{norm}} < \theta) + \text{mean}(e_{\text{abnorm}} \geq \theta)$
  Selection → Blend Crossover → Gaussian Mutation → Elitism
4. CNN (EXACT): Input(1,187) → Conv32 → Conv64 → Conv128 → FC128 → FC64 → 4
  Method A: SMOTE on training folds only
  Method B: Weighted Loss: $w_c = \frac{N_{\text{total}}}{4 \cdot N_c}$
5. 5-Fold CV: Stratified, 12,066 train / 3,017 val per fold
  Compare: RandomForest, XGBoost, AdaBoost (all n_estimators=100)
  Generate: 4-class CM

Evaluation metrics

The proposed method was evaluated using common classification metrics: accuracy, precision, recall, and F1-score.

All metrics are derived from the confusion matrix components:

True Positives (TP), True Negatives (TN), False Positives (FP), and False Negatives (FN).

The definitions and formulas are summarized in Table 5.

Table 5: Evaluation metrics

Metric	Formula	Definition
Accuracy	$\text{ACC} = \frac{TP + TN}{TP + TN + FP + FN}$	Proportion of correctly classified samples
Precision	$\text{P} = \frac{TP}{TP + FP}$	Proportion of true positives among predicted positives
Recall	$\text{R} = \frac{TP}{TP + FN}$	Proportion of actual positives correctly identified
F1-Score	$F1 = \frac{2 \times R \times P}{R + P}$	Harmonic mean of precision and recall

Results

In this research, a two-stage hybrid deep learning model was designed and implemented to classify ECG signals and identify cardiac arrhythmias. The model's first stage uses an Autoencoder (AE) network as a screening tool to separate normal signals from abnormal ones.

The autoencoder, with the architecture detailed in Table 2, was trained for 200 epochs exclusively on normal ECG beats, achieving stable convergence as demonstrated by the training loss curve in Fig. 3. The reconstruction error between the original and reconstructed signals was calculated and used as an indicator for anomaly detection.

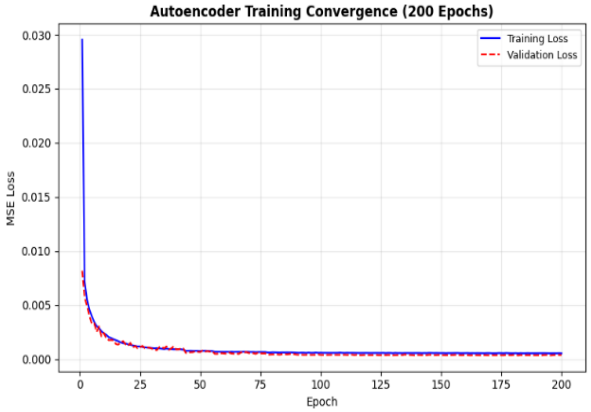


Fig. 3: Training and validation loss curve of the autoencoder.

To determine the optimal threshold for binary classification, a genetic algorithm was applied to the reconstruction error distribution. The GA searched the threshold space to maximize the fitness function defined as the sum of normal and abnormal classification accuracies.

This optimization identified an optimal threshold of 0.1277. The discriminative capability of the reconstruction errors, along with the GA-optimized threshold, was evaluated via ROC analysis, yielding an AUC of 0.8128 (Fig. 4).

The ROC curve clearly shows the selected threshold point, which maximizes the separation between normal and abnormal ECG signals.

Signals with reconstruction errors exceeding this threshold were classified as abnormal and proceeded to the second stage, while normal signals were discarded, significantly reducing computational load and improving processing efficiency.

The second stage utilizes a CNN classifier to accurately diagnose the specific type of arrhythmia among four predefined classes. The performance of the proposed model was examined through 5-fold cross-validation using both SMOTE and weighted class approaches for handling class imbalance.

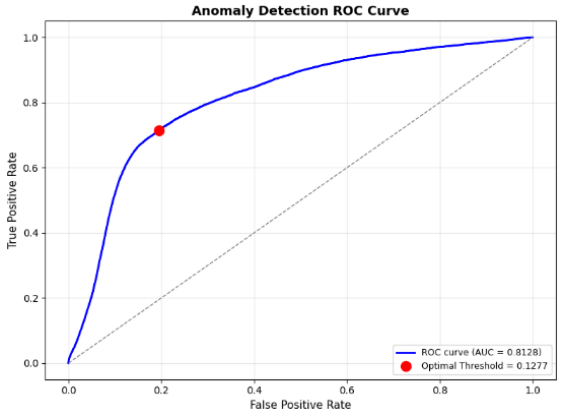


Fig. 4: Receiver Operating Characteristic (ROC) curve for anomaly detection with GA-optimized threshold (θ = 0.1277) marked.

As shown in Table 6, the SMOTE-based method achieved an average accuracy of 97.88%, precision of 97.90%, recall of 97.68%, and F1-score of 97.69%, with low standard deviations across folds (0.25–0.29%).

Table 6: 5-fold results of the proposed model

Method	Fold	Accuracy	Precision	Recall	F1-score
SMOTE	1	98.08	98.07	98.08	98.07
	2	97.88	97.89	97.87	97.88
	3	97.65	97.64	97.66	97.65
	4	98.24	98.27	97.21	97.23
	5	97.58	97.65	97.59	97.61
Average		97.88	97.90	97.68	97.69
Variance		0.062	0.059	0.085	0.080
Standard Deviation		0.25	0.24	0.29	0.28
Weighted class	1	97.78	97.81	97.78	97.79
	2	97.91	98	97.91	97.95
	3	97.38	97.62	97.37	97.45
	4	97.98	98.10	97.98	98.04
	5	96.98	97.35	96.97	97.10
Average		97.61	97.78	97.60	97.67
Variance		0.14	0.072	0.14	0.12
Standard Deviation		0.37	0.27	0.38	0.35

Training convergence was consistent across all folds, with loss and accuracy curves (Fig. 5) showing stable learning without overfitting.

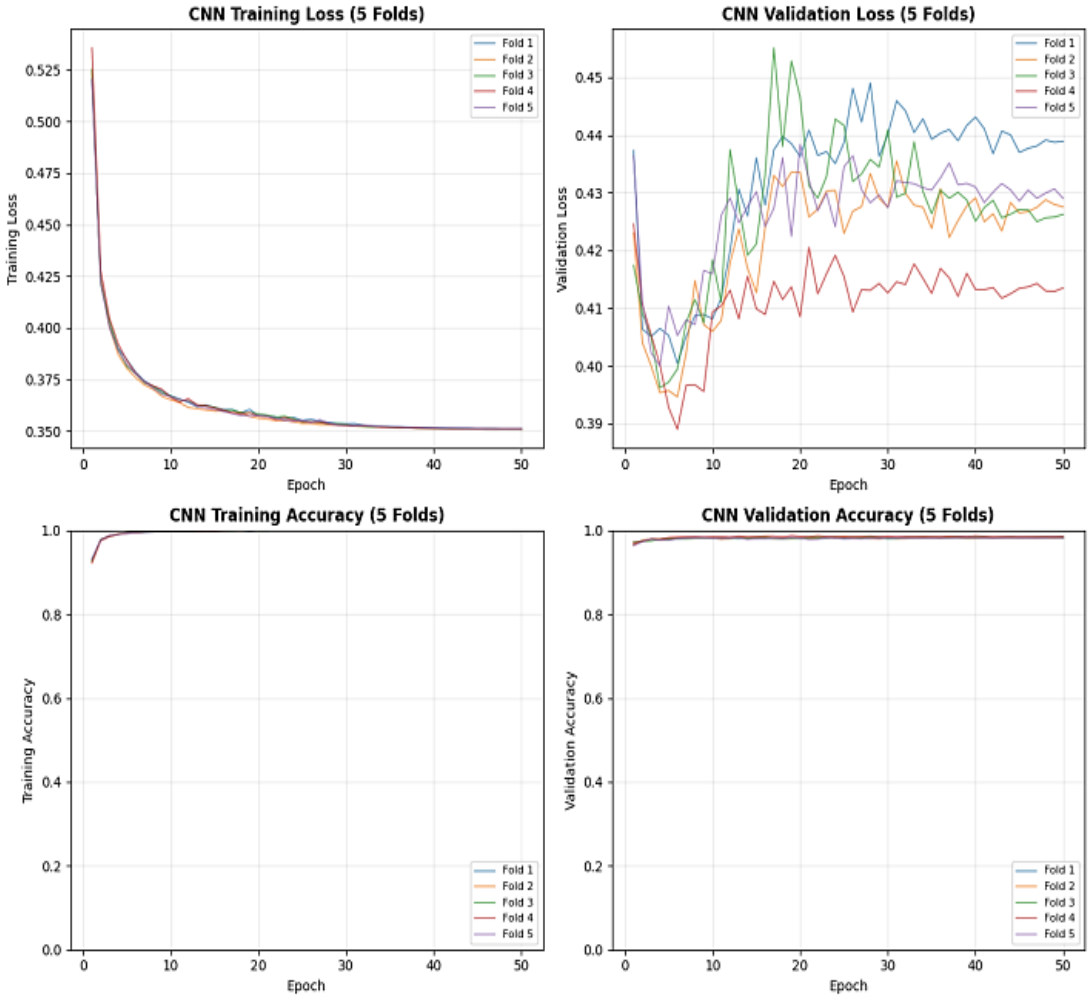


Fig. 5: CNN training loss and accuracy convergences across 5-fold cross-validation.

Detailed Classification Performance Analysis

Per-Class ROC Curves: To evaluate the discriminative power of the CNN classifier for each arrhythmia type, one-vs-rest ROC curves were generated. Fig. 7 presents these curves, with AUC values of 99.8 % for Unknown (Q), 98.6 % for Ventricular (V), 98.4 % for Supraventricular (S), and 95.1 % for Fusion (F). All AUC scores exceed 0.95, confirming the model's strong ability to distinguish each arrhythmia class from the others. The highest AUC (99.8 %) for class Q indicates near-perfect separability, while the lowest (95.1 %) for class F, the smallest and most challenging class, suggests its potential utility as a decision-support aid in clinical settings.

Precision-Recall (PR) Curves: Given the class imbalance, PR curves provide a more informative view of performance on minority classes. Fig. 7 shows the PR curves for each class.

The Fusion (F) class, the smallest class, maintains an average precision (AP) of 79.8 %, demonstrating that the model retains reasonable precision even at high recall levels for this challenging minority. The higher AP values for S, V and Q reflect their stronger separability, consistent with the ROC analysis.

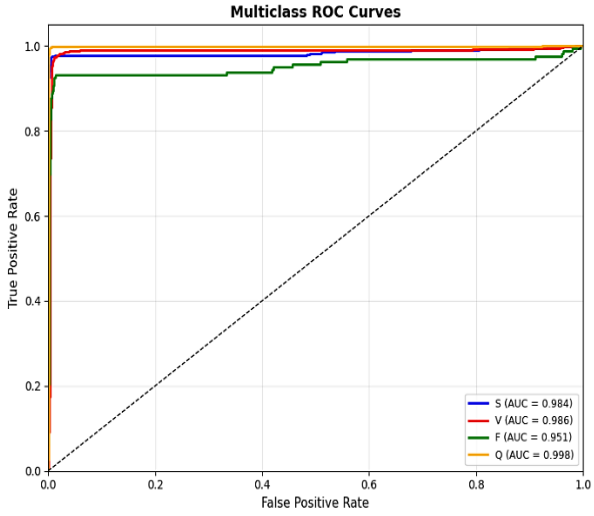


Fig. 6: One-vs-rest ROC curves for the four arrhythmia classes.

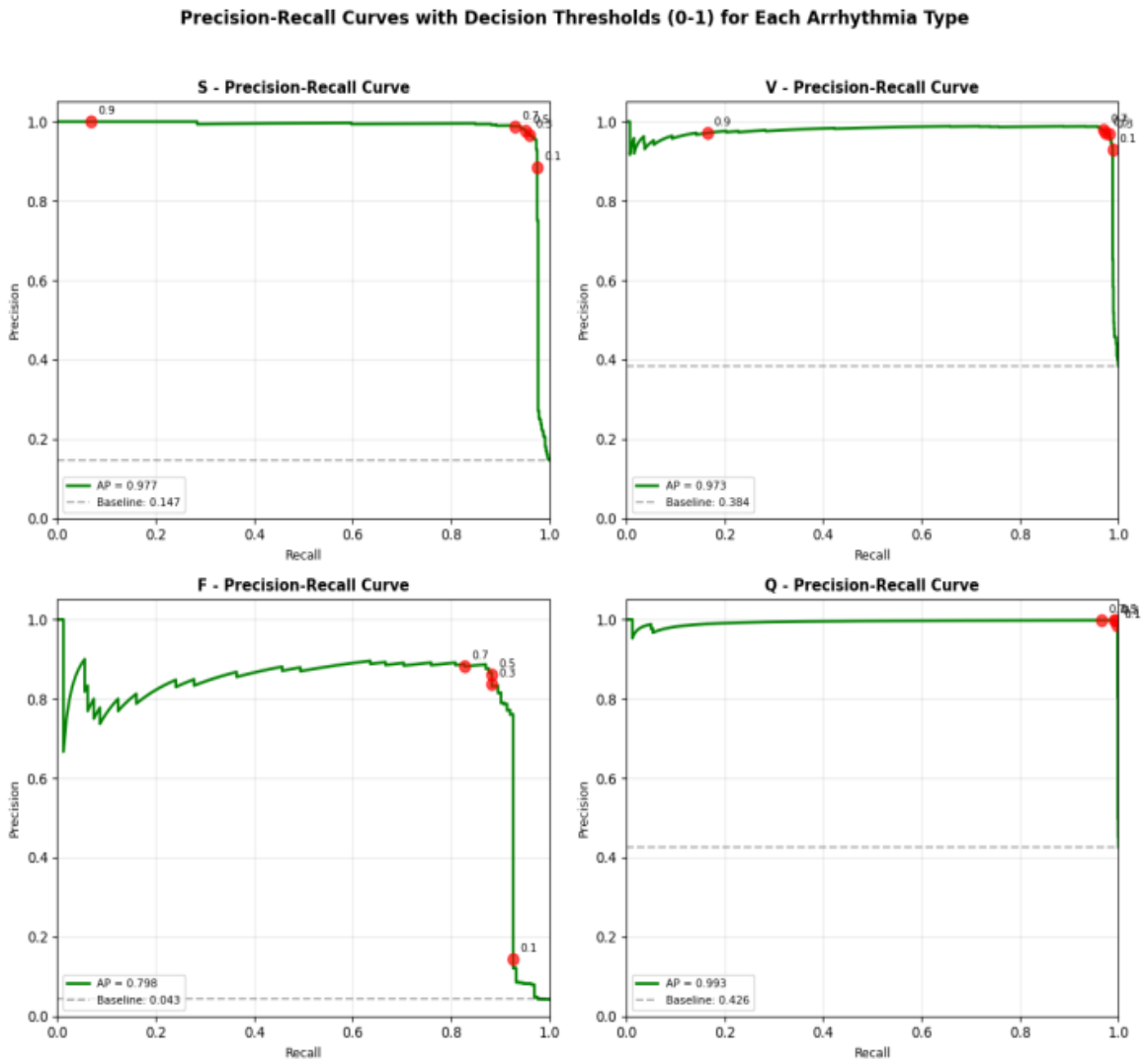


Fig. 7: Precision-Recall curves for each arrhythmia class.

Gradient-Weighted Class Activation Mapping (Grad-CAM): To interpret the CNN's decision-making process, Grad-CAM was applied to sample ECG signals from each class.

Fig. 8 displays the original ECG along with the Grad-CAM heatmap, highlighting the regions most influential for classification. For example, in Ventricular beats, the network focuses on the widened QRS complex, while for Supraventricular beats, it emphasizes the P-wave morphology. This visual explanation aligns with clinical features used by cardiologists, offering a transparent insight into the model's reasoning process and supporting its potential utility as an interpretable decision-support aid.

Confusion Matrix Analysis: The normalized confusion matrix (Fig. 9) provides a detailed view of per-class performance.

The model achieves high diagonal values: 99.32 % for Unknown (Q), 97.79 % for Ventricular (V), 95.68 % for Supraventricular (S), and 88.27 % for Fusion (F).

These values indicate accurate classification, with the highest accuracy for class Q and the lowest though still acceptable for the minority class F. The most common misclassification occurs between Fusion (F) and Ventricular (V) beats, which is clinically understandable given their morphological similarity. No significant misclassification between normal and abnormal beats is observed, supporting the practical utility of the first-stage anomaly detector in a clinical decision-support context.

It should be noted that all models, including the Autoencoder, the Genetic Algorithm (GA) optimization process, and the Convolutional Neural Network (CNN), were implemented using Python 3 within the Google Colab environment.

The deep learning models were constructed using the TensorFlow/Keras framework.

Training and evaluation were accelerated using an NVIDIA Tesla T4 GPU.

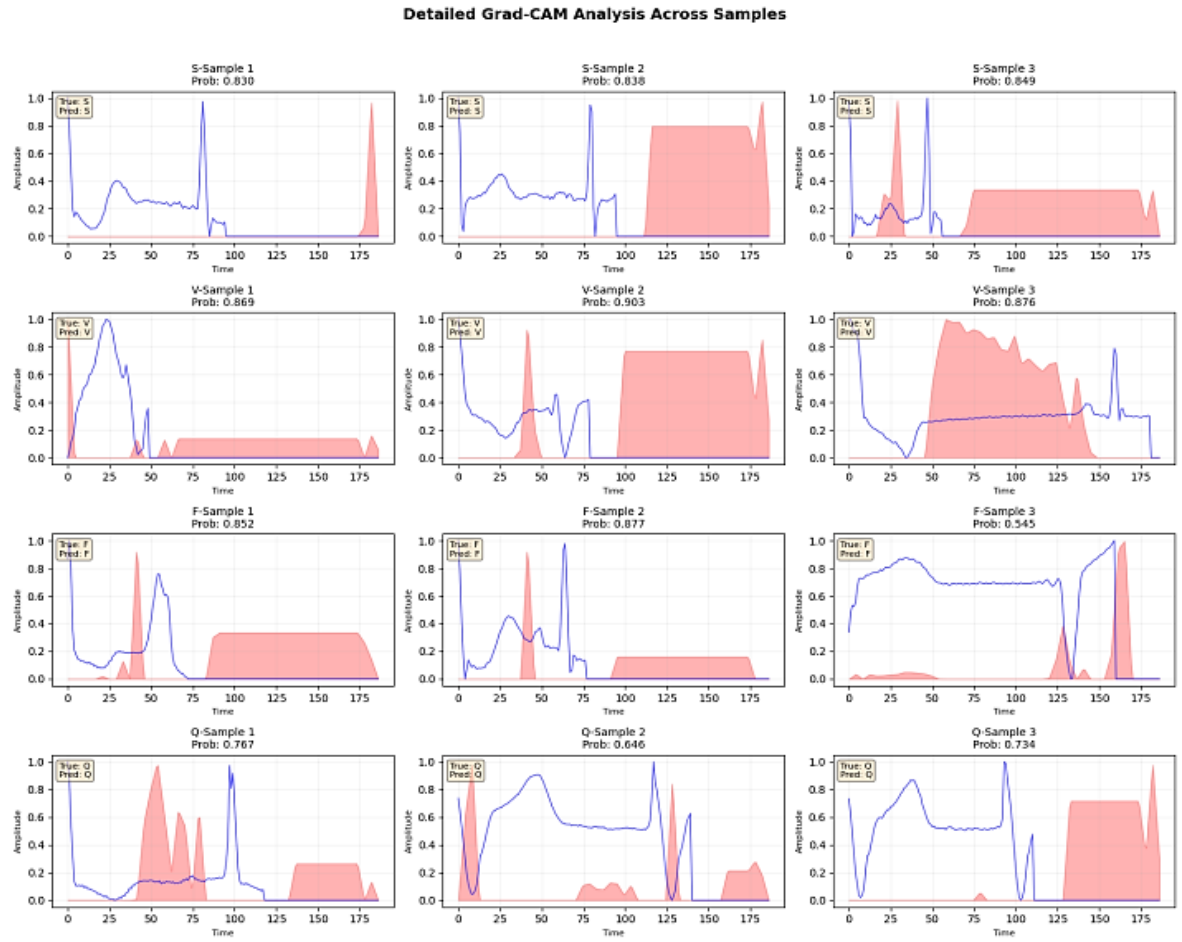


Fig. 8: Grad-CAM visualizations for sample ECG beats. The heatmap indicates regions with high activation for the predicted class.

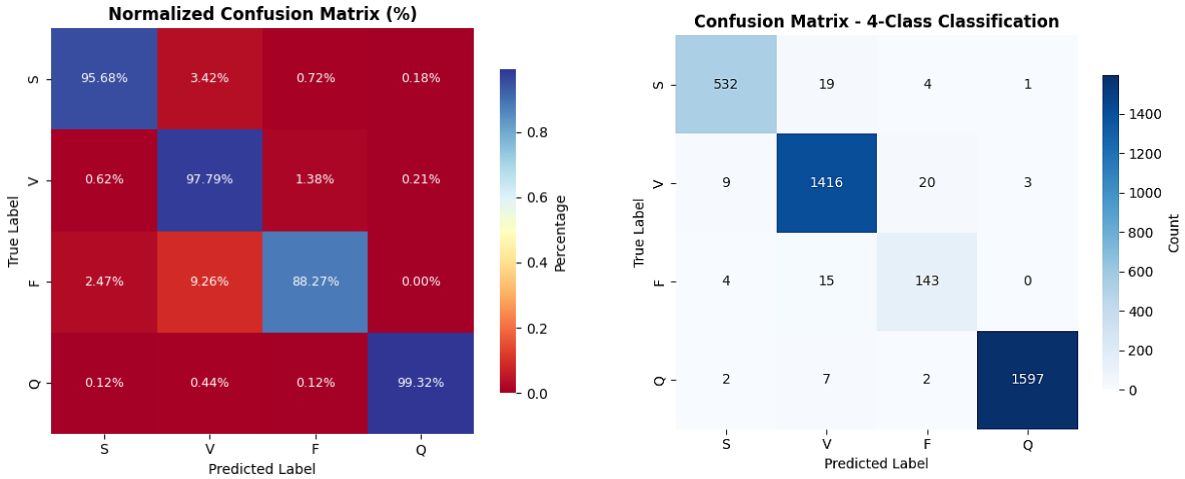


Fig. 9: Normalized confusion matrix and confusion matrix for the four arrhythmia classes (S, V, F, Q).

Discussion

The integrity and comparability of analytical outcomes are paramount in cardiac arrhythmia detection research. Our study employed the well-established MIT-BIH arrhythmia database under strictly controlled experimental conditions to ensure valid comparisons. Table 7 presents a performance comparison of various classification approaches under identical experimental setups. Our proposed AE-GA-CNN+SMOTE framework achieves the highest accuracy (97.89 %) and F1-score (97.69 %). The two-stage architecture demonstrates clear advantages, showing an absolute improvement of +6.28 % in accuracy over the single-stage CNN+SMOTE baseline and a further +3.04 % improvement over the AE+CNN+SMOTE variant with a fixed (median-based) threshold. This enhancement is statistically validated in Table 8, which confirms that all performance differences are significant ($p < 0.05$).

Table 7: Performance comparison of classification methods

Method	Accuracy	Precision	Recall	F1-Score	95% CI Accuracy
AE-GA-CNN+SMOTE	**97.89±0.25**	**97.90±0.24**	**97.68±0.29**	**97.69±0.28**	**[97.54, 98.23]**
AE-GA-CNN+Weighted	97.61±0.38	97.78±0.27	97.60±0.38	97.67±0.35	[97.08, 98.13]
AE-GA-XGBoost+SMOTE	97.57±0.13	97.60±0.13	97.57±0.13	97.58±0.13	[97.40, 97.75]
AE-GA-RandomForest+SMOTE	97.36±0.29	97.38±0.28	97.36±0.29	97.37±0.28	[96.96, 97.76]
AE-GA-AdaBoost+SMOTE	86.72±1.11	88.05±1.08	86.72±1.11	87.05±1.10	[85.18, 88.26]
CNN+SMOTE (single-stage)	91.61±3.28	96.39±0.47	91.61±3.28	93.34±2.19	[88.33, 94.89]
AE + CNN + SMOTE (fixed threshold = median error)	94.85±0.35	95.10±0.32	94.80±0.38	95.20±0.30	[94.35, 95.35]

Table 8: Statistical Significance Analysis (Paired t-test Results)

Comparison	p-value	Mean Difference (%)	95% CI of Difference	Significant (α=0.05)
AE-GA-CNN+SMOTE vs CNN+SMOTE	<0.001	+6.28	[+3.65, +8.91]	Yes (p<0.001)
AE-GA-CNN+SMOTE vs AE+CNN+SMOTE (fixed threshold)	<0.001	+3.04	[+2.15, +3.93]	Yes (p<0.001)
AE-GA-CNN+SMOTE vs AE-GA-CNN+Weighted	0.0486	+0.28	[+0.003, +0.557]	Yes (p<0.05)
AE-GA-CNN+SMOTE vs AE-GA-XGBoost+SMOTE	0.0222	+0.32	[+0.073, +0.551]	Yes (p<0.05)
AE-GA-CNN+SMOTE vs AE-GA-RandomForest+SMOTE	0.0171	+0.53	[+0.154, +0.894]	Yes (p<0.05)
AE-GA-CNN+SMOTE vs AE-GA-AdaBoost+SMOTE	0.000015	+11.17	[+9.928, +12.404]	Yes (p<0.001)

The consistent superiority across all metrics, combined with narrow confidence intervals and low standard deviations, indicates robust performance. As presented in Table 9, our approach achieves competitive performance relative to recent studies on the same MIT-BIH dataset, encompassing various architectures and classification tasks (binary and multi-class). The superior and balanced performance of our model evidenced by the highest F1-score (97.69 %) stems from two key innovations: (1) the two-stage design, which isolates abnormal signals before fine-grained classification, and (2) the Genetic Algorithm, which optimizes the detection threshold globally, avoiding local optima that limit gradient based or heuristic methods. This combination yields not only higher accuracy but also greater reliability, as reflected in the tight confidence intervals across all evaluation folds.

Table 9: Performance comparison with recent studies on the MIT-BIH database

Model type	Accuracy	Precision	Recall	F1-Score
CNN [31]	97.6%	94.4%	93%	93.6%
Machine Learning [32]	89%	88.5%	89.9%	89.3%
Graph Convolutional Network (GCN) [33]	92.68%	68.24%	95.5%	95.24%
Autoencoder [34]	97.19%	90.75%	99.14%	94.84%
Transformer-Based Anomaly Detection [34]	89.5%	98.2%	87.1%	92.3%
1DCNN+BERT [36]	95.1%	94.92%	94.69%	94.81%
Bidirectional Transformer [37]	95.88%	95.47%	93.15%	94.26%
Proposed method	97.88%	97.90%	97.68%	97.69%

Computational Efficiency and Runtime Analysis

The proposed framework demonstrates favorable computational characteristics. The autoencoder trained in approximately 10 minutes (200 epochs, batch size = 256). The Genetic Algorithm, optimized for a single threshold variable with a population of 50 over 100 generations, converged in only 0.79 seconds a negligible overhead given its one-time execution during the configuration phase. The complete CNN stage, including 5-fold cross-validation with SMOTE balancing, required about 40 minutes. Despite its minimal runtime cost, the GA contributed a +3.04 % improvement in accuracy over a fixed-threshold baseline, underscoring its cost-effectiveness. The low per-component runtime indicates that the computational load is sufficiently light to support interactive use in clinical decision-support systems.

Conclusion

Identifying cardiac abnormalities through ECG signals represents a vital diagnostic procedure in cardiology. The accurate and rapid automated interpretation of these signals holds significant potential to enable early intervention, reduce healthcare costs, assist clinicians in decision-making, and ultimately improve patient outcomes. To address this need, this study proposed a novel two-stage hybrid deep learning model for ECG-based arrhythmia detection. The core innovation of this work is an optimized architecture that strategically combines an autoencoder for efficient anomaly screening with a convolutional neural network (CNN) for precise multi-class classification. A pivotal component is the integration of a Genetic Algorithm (GA) to automatically determine the optimal reconstruction error threshold, thereby significantly enhancing the separation between normal and abnormal beats.

This methodological approach yielded superior performance, with the model achieving an average F1-score of 97.69% and an accuracy of 97.88%. The strength of the proposed framework stems from its two-stage design: the first stage effectively filters out the majority of normal cases, reducing the computational burden, while the second stage focuses classification resources only on the remaining abnormal signals, establishing a robust foundation for accurate diagnosis. This synergy between efficient screening and targeted classification is the primary reason for its performance advantage over conventional single-stage methods.

Despite these promising results, the study acknowledges certain limitations. The evaluation was conducted exclusively on the MIT-BIH database, which may affect the model's generalizability to more diverse, real-world clinical datasets. Furthermore, the clinical impact of critical misclassifications, such as mislabeling a dangerous arrhythmia as normal, was not explicitly assessed—a vital consideration for ensuring patient safety in practical deployments. Additionally, while the two-stage design improves processing efficiency, direct implementation on resource-constrained wearable devices would require further optimization.

For future work, several directions are suggested to further advance this research. First, evaluating the model on larger multi-center datasets is expected to enhance its generalizability. Second, incorporating clinical risk-aware loss functions during training can minimize dangerous misclassifications. Additionally, applying model compression techniques, such as pruning and quantization, will facilitate real-time implementation on wearable hardware. Finally, exploring advanced architectures like variational autoencoders or transformer-based networks could enhance both accuracy and robustness. With these refinements, the proposed framework could serve as a foundation for future decision-support tools and wearable cardiac monitoring systems, potentially contributing to more efficient and accessible cardiac care.

Acknowledgment

This research utilized AI tools for grammar and spelling corrections. All scientific and research content was prepared by the authors, and the AI tool was used solely as an assistant for improving the writing. The authors thank the AI for its assistance in reviewing and correcting the final text.

Author Contributions

M. Akbari Poodineh conceptualized the study, developed the methodology, and conducted software development, validation, and formal analysis. F. Zare Mehrjardi contributed to the investigation, data curation, writing, review and editing. M. Sardari Zarchi supervised the project, provided manuscript review and feedback, and handled project administration.

Funding

This paper has received no external funding.

Conflict of Interest

The authors declare no potential conflict of interest regarding the publication of this work. In addition, the ethical issues, including plagiarism, informed consent, misconduct, data fabrication and/or falsification, double publication and/or submission, and redundancy, have been completely witnessed by the authors.

Abbreviations

ECG	Electrocardiogram
CNN	Convolutional Neural Network
PCA	Principal Component Analysis
FFT	Fast Fourier Transform
VAE	Variational Autoencoder
MMD	Maximum Mean Discrepancy
GA	Genetic Algorithm
MSE	Mean Squared Error
FNN	Feedforward Neural Network
GNN	Graph Neural Network
ReLU	Rectified Linear Unit
DL	Deep Learning
GCN	Graph Convolutional Network
LSTM	Long Short-Term Memory
ML	Machine Learning
SVM	Support Vector Machine
KNN	K-Nearest Neighbor
TL	Transfer Learning
SMOTE	Synthetic Minority Over-sampling Technique
TP	True Positives
TN	True Negatives
FP	False Positives
FN	False Negatives

References

[1] M. Chu, P. Wu, G. Li, W. Yang, J. L. Gutierrez-Chico, S. Tu, "Advances in diagnosis, therapy, and prognosis of coronary artery disease powered by deep learning algorithms," JACC: Asia, 3(1): 1-14, 2023.

[2] D. G. Manuel, M. Leung, K. Nguyen, P. Tanuseputro, H. Johansen, "Burden of cardiovascular disease in Canada," Can. J. Cardiol., 19(9): 997-1004, 2003.

[3] M. Akbari Podineh, F. Zare Mehrjardi, M. Sardari Zarchi, "Multimodal analysis of ECG signals for cardiac arrhythmia detection using machine learning and deep learning methods," Appl. Basic Mach. Intell. Res., 3(1): 17-34, 2025.

[4] M. Alkhouli, Z. M. Hijazi, D. R. Holmes, C. S. Rihal, S. E. Wiegers, "Intracardiac echocardiography in structural heart disease interventions," JACC: Cardiovasc. Interv., 11(21): 2133-2147, 2018.

[5] M. Arrigo, M. Jessup, W. Mullens, N. Reza, A. M. Shah, K. Sliwa, A. Mebazaa, "Acute heart failure," Nat. Rev. Dis. Primers, 6(1): 16, 2020.

[6] D. E. L. Wilcken, "Overview of inherited metabolic disorders causing cardiovascular disease," J. Inherit. Metab. Dis., 26(2): 245-257, 2003.

[7] H. V. Denysyuk, R. J. Pinto, P. M. Silva, R. P. Duarte, F. A. Marinho, L. Pimenta, I. M. Pires, "Algorithms for automated diagnosis of cardiovascular diseases based on ECG data: A comprehensive systematic review," Heliyon, 9(2), 2023.

[8] D. Pandey, K. Niwaria, B. Chourasia, "Machine learning algorithms: a review, " Mach. Learn., 6(2), 916-922, 2019.

[9] M. S. Al Rahhal, Y. Bazi, H. AlHichri, "Deep learning approach for active classification of electrocardiogram signals," J. Med. Syst., 44(4): 1-11, 2020.

[10] A. A. Ahmed, W. Ali, T. A. Abdullah, S. J. Malebary, "Classifying cardiac arrhythmia from ECG signal using 1D CNN deep learning model," Mathematics, 11(3): 1-16, 2023.

[11] F. Z. Mehrjardi, A. M. Latif, M. S. Zarchi, "A survey on deep learning-based image forgery detection," Pattern Recognit., 144: 109778, 2024.

[12] F. Z. Mehrjardi, A. M. Latif, M. S. Zarchi, "Copy-move forgery detection and localization using deep learning," Int. J. Pattern Recognit. Artif. Intell., 37(9): 2352012, 2023.

[13] K. Rezaee, M. R. Khosravi, M. Jabari, S. Hesari, M. S. Anari, F. Aghaei, "Graph convolutional network-based deep feature learning for cardiovascular disease recognition from heart sound signals," Int. J. Intell. Syst., 37(12): 11250-11274, 2022.

[14] M. Sraitih, Y. Jabrane, E. I. Hajjam, A. Hassani, "An automated system for ECG arrhythmia detection using machine learning techniques, " J. Clin. Med., 10(22), 2021.

[15] U. R. Acharya, H. Fujita, S. L. Oh, Y. Hagiwara, J. H. Tan, M. Adam, "Application of deep convolutional neural network for automated detection of myocardial infarction using ECG signals," Inf. Sci., 415: 190-198, 2017.

[16] S. Tan, G. Androz, A. Chamseddine, P. Fecteau, A. Courville, Y. Bengio, "Icentia11k: An unsupervised representation learning dataset for arrhythmia subtype discovery," arXiv preprint, 2019.

[17] V. V. Kuznetsov, V. A. Moskalenko, N. Y. Zolotykh, "Electrocardiogram generation and feature extraction using a variational autoencoder," arXiv preprint, 2020.

[18] M. Bikova, V. O. Latkoska, H. Gjoreski, "Comparing classical machine learning and deep learning for classification of arrhythmia from ECG signals," in Proc. Int. Conf. Appl. Innov. IT, 11(2): 31-38, 2023.

[19] S. Sahoo, M. Dash, S. Behera, S. Sabut, "Machine learning approach to detect cardiac arrhythmias in ECG signals: A survey," IRBM, 41(4): 185-194, 2020.

[20] C. Li, H. Zhao, W. Lu, X. Leng, L. Wang, X. Lin, J. Xiang, "DeepECG: Image-based electrocardiogram interpretation with deep convolutional neural networks," Biomed. Signal Process. Control, 69, 2021.

[21] S. Sattar, R. Mumtaz, M. Qadir, S. Mumtaz, M. A. Khan, T. De Waele, A. Shahid, "Cardiac arrhythmia classification using advanced deep learning techniques on digitized ECG datasets," Sensors, 24(8): 2484, 2024.

[22] M. A. Raza, M. Anwar, K. Nisar, A. A. A. Ibrahim, U. A. Raza, S. A. Khan, F. Ahmad, "Classification of electrocardiogram signals for arrhythmia detection using convolutional neural network," Comput. Mater. Continua, 77(3): 3817-3834, 2023.

[23] B. Wang, X. Lyu, J. Qu, H. Sun, Z. Pan, Z. Tang, "GNDD: A graph neural network-based method for drug-disease association prediction," in Proc. IEEE Int. Conf. Bioinformatics Biomed. (BIBM): 1253-1255, 2019.

[24] Z. F. M. Apandi, R. Ikeura, S. Hayakawa, "Arrhythmia detection using MIT-BIH dataset: A review," in Proc. Int. Conf. Comput. Approach Smart Syst. Design Appl., 2018.

[25] J. Z. Ahmadabadi, F. Z. Mehrjardi, M. Ghanbary, M. Mirzaei, "Identification of effective factors and prediction of ischemic heart disease using machine learning methods and data from the Yazd Health Study (YAHS)," J. Shahid Sadoughi Univ. Med. Sci., 32(7): 67-79, 2024.

[26] J. Zhai, S. Zhang, J. Chen, Q. He, "Autoencoder and its various variants," in Proc. IEEE Int. Conf. Syst. Man Cybern.: 415-419, 2018.

[27] H. Nguyen, K. P. Tran, S. Thomassey, M. Hamad, "Forecasting and anomaly detection approaches using LSTM and LSTM autoencoder techniques with applications in supply chain management," Int. J. Inf. Manage., 57: 102282, 2021.

[28] J. Chen, B. Xie, H. Zhang, J. Zhai, "Deep autoencoders in pattern recognition: a survey, "in Proc. Int. Conf. Bio-inspired Computing (ICBIC), 229-255, 2019.

[29] F. Z. Mehrjardi, A. M. Latif, "Detection of copy-move forgery in digital images using genetic algorithm and simulated annealing algorithm," Appl. Basic Mach. Intell. Res., 2(2), 2024.

[30] F. Z. Mehrjardi, A. M. Latif, M. S. Zarchi, "An optimal hybrid method to detect copy-move forgery," J. Artif. Intell. Data Min., 11(3): 429-442, 2023.

[31] M. Chourasia, A. Thakur, S. Gupta, A. Singh, "ECG heartbeat classification using CNN," in Proc. IEEE 7th UPCON: 1-6, 2020.

[32] C. G. Igiri, V. I. E. Anireh, N. D. Nwiabu, D. Matthias, "Comparative analysis of supervised machine learning algorithms for ECG arrhythmia detection using small dataset," Int. J. Comput. Sci. Math. Theory, 9(4): 23-44, 2023.

[33] B. Andayeshgar, F. Abdali-Mohammadi, M. Sepahvand, A. Daneshkhah, A. Almasi, N. Salari, "Developing graph convolutional networks and mutual information for arrhythmic diagnosis based on multichannel ECG signals," Int. J. Environ. Res. Public Health, 19(17): 10707, 2022.

[34] U. Lomoio, P. Vizza, R. Giancotti, G. Tradigo, S. Petrolo, S. Flesca, P. Veltri, P. H. Guzzi, "AUTAN-ECG: An autoencoder-based system for anomaly detection in ECG signals," Comput. Biol. Med., 166: 107513, 2024.

[35] A. Alamr, A. Artoli, "Unsupervised transformer-based anomaly detection in ECG signals," Algorithms, 16(3), 2023.

[36] H. Liu, "A hybrid model combining 1D-CNN and BERT for intelligent ECG arrhythmia classification," Sci. Rep., 2025.

[37] H. El-Ghaish, E. Eldele, "ECGTransForm: Empowering adaptive ECG arrhythmia classification framework with bidirectional transformer," Biomed. Signal Process. Control, 89: 105714, 2024.

Biographies



Motahareh Akbari Poodineh obtained her first degree in Software Engineering from Sistan and Baluchestan University in 2019, and her M.Sc. in Artificial Intelligence and Robotics in 2025. Her research interests are image processing, signal processing, deep learning, and machine learning.

- Email: m.akbari5062@gmail.com
- ORCID: 0009-0003-2628-6879
- Web of Science Researcher ID: NA
- Scopus Author ID: NA
- Homepage: NA



Fatemeh Zare Mehrjardi obtained her first degree in Software Engineering from Yazd University in 2013, her M.Sc. in Computer Engineering, Artificial Intelligence and robotics from the yazd University in 2015 and her Ph.D. in Computer Engineering, Artificial Intelligence and robatics from the yazd University in 2023. She joined the academic staff at Computer Department of Meybod University in 2023. Her research interests are pattern recognition, image processing, machine learning, deep learning, evolutionary algorithms and image retrieval.

- Email: fzare@meubod.ac.ir
- ORCID: 0009-0001-3268-0114
- Web of Science Researcher ID: NA
- Scopus Author ID: NA
- Homepage: https://meybod.ac.ir/staff/fatemeh-zare-mehrjardi



Mohsen Sardari Zarchi obtained his first degree in Computer Science from Yazd University in 2007, his M.Sc. in Computer Engineering, Artificial Intelligence from the Isfahan University in 2009 and his Ph.D. in Computer Engineering, Artificial Intelligence from the Isfahan University in 2015. He joined the academic staff at Computer Department of Meybod University in 2015. His research interests are pattern recognition, image processing, machine learning, deep learning, and image retrieval.

- Email: sardari@meybod.ac.ir
- ORCID: 0000-0003-0831-3426
- Web of Science Researcher ID: NA
- Scopus Author ID:NA
- Homepage: https://meybod.ac.ir/staff/mohsen-sardari-zarchi

Journal of Electrical and Computer Engineering Innovations
(JECEI)
Journal homepage: http://www.jecei.sru.ac.ir

Research paper

Detailed Analysis and Design of Line-Start Synchronous Reluctance Motors Aiming at High Power Factor

Seyed Reza Mousavi-Aghdam* , ***Seyed Abbas Azimi*** , ***Farzad Sedaghati***

Department of Electrical Engineering, Faculty of Engineering, University of Mohaghegh Ardabili, Ardabil, Iran.

Article Info

Article History:
Received 23 January 2026
Reviewed 27 March 2026
Revised 16 April 2026
Accepted 23 May 2026

Keywords:
Line-start permanent magnet assisted synchronous reluctance motor
Finite element method
Line-start capability
Power factor
Efficiency

*Corresponding Author's Email Address:
r.mousaviaghdam@uma.ac.ir

Abstract

Background and Objectives: Synchronous reluctance motors (SynRMs) have considered as energy-efficient alternatives to conventional induction motors (IMs), primarily due to high efficiency. Despite their low losses, SynRMs are hindered by inadequate line-start capability and a low power factor, which restrict their use in industrial settings. This article addresses these limitations by introducing a line-start permanent magnet-assisted SynRM (LS-PMaSynRM) that incorporates fluid-type flux barriers. This design aims to enhance starting performance and increasing power factor.

Methods: The design process entailed a parametric sensitivity analysis of critical motor characteristics, including rotor geometry, stator winding configuration, and stator slot count. Finite Element Method (FEM) simulations were executed using time-stepping analysis to assess the motor's electromagnetic behavior under both transient and steady-state conditions. Performance metrics such as torque ripple, average torque, efficiency, and power factor were evaluated. Comparative simulations with conventional SynRM and PMaSynRM designs were also conducted to benchmark improvements.

Results: The proposed LS-PMaSynRM exhibited substantial enhancements in line-start capability, achieving stable synchronization within a brief period. The motor demonstrated a significant increase in power factor relative to conventional SynRM designs, while maintaining high efficiency throughout the operating range.

Conclusion: The study presents an LS-PMaSynRM architecture that effectively addresses traditional limitations in line-start performance and power factor. These findings support the broader industrial adoption of SynRMs and offer a practical design pathway for future high-efficiency motor applications.

This work is distributed under the CC BY license (http://creativecommons.org/licenses/by/4.0/)

How to cite this paper:
S. R. Mousavi-Aghdam, S. A. Azimi, F. Sedaghati, "Detailed analysis and design of line-start synchronous reluctance motors aiming at high power factor," J. Electr. Comput. Eng. Innovations, 14(2): 535-548, 2026.
DOI: 10.22061/jecei.2026.12645.899
URL: https://jecei.sru.ac.ir/article_12561.html

2345- 3044/© 2026 The Authors. Published by Shahid Rajaee Teacher Training University.

Introduction

Electric motor technologies are continuously undergoing improvement and exploration for commercial, agricultural, medical, and diverse industrial applications. Induction motors (IMs) are the most extensively utilized in industries due to their simple structure, line-start capability, and robustness. However, IMs exhibit limited efficiency due to copper losses, which has prompted industries to replace these prevalent electric motors with synchronous reluctance motors (SynRMs) that demonstrate higher efficiency [1], [2]. The flux barriers in the multilayer structure of the SynRM rotor decrease hysteresis and eddy current losses [3], [4]. The induced current in the rotor conductor bars remains stable at zero during synchronous operation, resulting in the absence of rotor copper losses [5]. In [6], the rotor design of the SynRM is refined by changing conventional magnetic radial ribs with non-magnetic titanium ribs. This modification decreases magnetic flux leakage along the q-axis, thereby enhancing torque, saliency ratio, efficiency, and power factor. so, this optimized rotor structure improves both electromagnetic and mechanical performance, particularly for automotive applications. Two significant challenges associated with SynRMs are low power factor and line-start capability [7], [8]. An innovative analytical modeling method for SynRMs that can substantially improve the design and analysis process of this type of machine is presented in [9]. In [10], the dynamic modeling of SynRM is examined. An accurate and efficient model to describe the dynamic behavior of SynRMs, which is crucial for their precise control is demonstrated in [10].

The introduction and analysis of a dual-stator SynRMs as a solution to decrease torque ripple in single-stator SynRMs has been proposed in [11]. The conflict between mechanical strength and magnetic performance has required the use of internal claws in the rotor [12] to enhance the power factor and torque. In [13], the effect of minor alterations in the dimensions of the SynRM rotor on the output torque of the machine is presented by providing a semi-analytical method for a rapid and accurate evaluation. This method employs a more straightforward and faster approach instead of complex and time-consuming finite element method (FEM) simulations. A suitable rotor design with a focus on flux barriers may require a fast process with constrained design flexibility [14]. This becomes even more important when a complex design, for example, a hybrid rotor with both radial and axial laminations, is considered [15]. Such methodological considerations may also be implemented for other types of reluctance motors [16]. Fast design techniques are commonly used in nonlinear systems, especially in the case of reluctance motors.

The lower power factor of SynRMs has prompted numerous researchers to add the utilization of permanent magnets (PM) in SynRMs [17], [18]. Although rare-earth PMs are costly and non-renewable, their extraction may result in significant environmental degradation if appropriate and safe measures are not implemented [19], [20]. The incorporation of PMs in the q-axis enhances the power factor of PMaSynRMs; however, it introduces substantial torque ripple [21]. The simulation and measured results for a water pump application utilizing a SynRM is presented in [22]. In [23], the dynamic performance of SynRM was optimized by filling all flux barriers with conductor bars. Based on the optimal structure of rotor flux barriers, enhancing the asynchronous torque by reducing the resistance of rotor conductor bars through increased area represents a direct and effective method for improving the synchronizing capability of line-start SynRM (LS-SynRM) [24], [25]. In [26], key design parameters of PMaSynRM were identified through sensitivity analysis, which was subsequently optimized to minimize energy loss across various driving cycles in an electric vehicle. The asymmetric rotor topologies for reducing torque ripples in SynRMs and their effect on mechanical vibration is demonstrated in [27], [28]. In [29] and [30], a comprehensive design methodology for an external and internal rotor SynRM suitable for electric bike and scooter applications are presented.

This paper presents sensitivity analyzes of SynRM with fluid-type flux barriers. It focuses on line-start capability and power factor. The efficiency improvement while maintaining a high average torque is considered. The stators of SynRMs typically possess either 24 or 36 slots, with both configurations being considered for comprehensive analysis. The design of the SynRM stator is not elaborated upon due to its resemblance to the IM stator. However, the winding configurations for both stators will be presented. Two winding configurations for 24-slot and three winding configurations for 36-slot stators are presented. stators are analyzed independently for line start capability, power factor enhancement, and additional motor parameters. The analysis process and presentation of the initial and proposed rotor design, along with stator winding specifications, are presented in the second section. The third section presents transient and steady-state results. The final section provides a comparison of both proposed LS-PMaSynRMs based on FEM results.

In conventional designs, permanent magnets are typically positioned along the q-axis. However, the proposed design introduces auxiliary magnets and auxiliary flux barriers on the d-axis, which significantly enhance the power factor and average torque of the SynRM. The effective placement of conductive bars

within the flux barriers and proximity to the q-axis facilitates the SynRM's starting without the need for additional equipment. Furthermore, the selection of the fill ratio for the bars contributes to a quicker attainment of synchronous speed and reduces aluminum consumption costs. These innovations not only improve the motor's performance but also enhance power factor, efficiency, and lower production costs, making them particularly valuable for industrial applications.

Initial Synrm Design Features

The rotor of SynRM is composed of multilayer isotropic electrical steels that are stacked in their axial direction and exhibit low magnetic reluctance. In contrast to synchronous and induction motors, which typically incorporate PM or windings in their rotor, SynRM solely contains flux barriers in its rotor. The operation of PMaSynRM is predicated on directing the magnetic fluxes generated by the stator winding currents through paths of lower reluctance within the iron paths of the rotor and stator. Consequently, the desired maximum reluctance torque can be optimized by appropriately adjusting the two predicted equivalent magnetic reluctances on the dq-axes. The stator voltage equations can be expressed as (1):

$$\begin{cases} v_{ds} = R_s i_{ds} - \omega_e \lambda_{qs} - \omega_e \lambda_{pmq} \\ v_{qs} = R_s i_{qs} + \omega_e \lambda_{ds} + \omega_e \lambda_{pmd} \end{cases} \quad (1)$$

where v_{ds}, ids, v_{qs} and i_{qs} are the stator voltage and current components on the dq-axis. ω_e is the electrical angular speed and R_s is stator winding resistance. λ_{ds} and λ_{qs} are dq-axis flux linkage, and λ_{pmd} and λ_{pmq} are dq-axis PM flux linkage, and can be expressed as (2):

$$\lambda = L_{ds} i_{ds} + \lambda_m + jL_{qs} i_{qs} \quad (2)$$

where λ_m is the flux linkage of the PMs, and L_{ds} and L_{qs} are the d-axis and q-axis components of the stator inductance. The non-saturation of the stator and rotor iron cores stabilizes these two inductance terms. The electromagnetic torque T_e of PMaSynRM is expressed by (3):

$$T_e = (\frac{3p}{4})\lambda_m i_{qs} + (\frac{3p}{4})\left(L_{ds} - L_{qs}\right) i_{ds} i_{qs} \quad (3)$$

where p is the number of poles. The difference in inductance between the d-axis and q-axis contributes to a greater torque, as explicitly demonstrated in (3). In addition to the increase in torque, the power factor of SynRMs, which is lower than that of induction motors, can be improved. However, as it is evident that PMs significantly influence the performance of PMaSynRMs, various PM combinations and manufacturing feasibility should be thoroughly evaluated during the rotor design stage. Prior to the initial design of the rotor, which is considered the most critical component in the design of SynRMs, the stator design is reviewed in its entirety.

A. Stator Winding Configuration

SynRMs can have different numbers of poles, but the most common configuration is 4 poles. In order to reduce undesirable harmonics, optimize torque production and increase efficiency in these motors, the number of stator slots is Typically 24 or 36 slots. Therefore, two stators with 24 and 36 slots are considered. The two-layer winding configuration has been selected due to its superior winding distribution in the slots, enhanced power density, improved efficiency, and increased mechanical stability. Two configurations are examined for stator winding with 24-slots, utilizing Coil Pitches (CPs) of 4 and 5. Additionally, three configurations are considered for stator winding with 36-slots, employing CPs of 6, 7, and 8, as illustrated in Fig. 1. Two SynRM designs with different stator slots are designed to validate the initial principle and performance of the proposed motor. The proposed design specifications are summarized in Table 1. Due to the similarity between the SynRM and IM stators, the stator is considered a conventional IM. Therefore, the methodology for calculating the conductor size in the

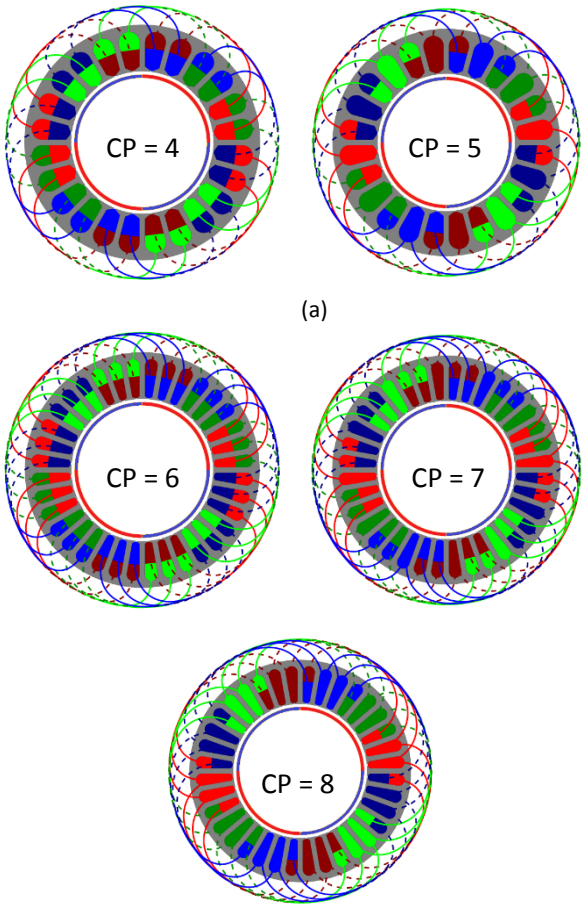


Fig. 1: Winding configuration for different CPs in SynRM with (a) 24-slot and (b) 36-slot designs.

Table 1: Main data of the proposed SynRM designs

Item	unit	value	
		24-slot	36-slot
Rated power	kW	1.5	
Rated torque	N.m	9.5	
Rated frequency	Hz	50	
Rated voltage	V	380	
Rated speed	r/min	1500	
Number of poles		4	
Winding connection		Y	
Core length	mm	86.4	66.15
Turn number of per slot		115	94
Rotor outer diameter	mm	35	40
Air gap length (mm)	mm	0.5	
Stator conductor size	mm^2	1	

SynRM stator is similar to IM. The analysis of back-EMF harmonic content reveals critical insights into the selection of coil configurations for SynRMs. The findings express the impact of stator winding on harmonic generation, emphasizing that certain CPs demonstrate superior performance in minimizing these harmonics. The stator geometry design is not considered in this paper, but it remains consistent with conventional configurations. To determine the coil for initial SynRMs, the back-EMF harmonic content for two-layer coils with possible winding pitches is presented. As illustrated in Fig. 2, the odd-order harmonic amplitude of the Back-EMF for the design with a 24-slot stator with a CP of 4 is lower than that of the other type. Additionally, in the 36-slot design, the CP of 8 exhibits superior even-order harmonic amplitude compared to the other two types. Consequently, the CP of 4 is considered for a 24-slot stator design, and the CP of 8 is considered for a 36-slot stator design.

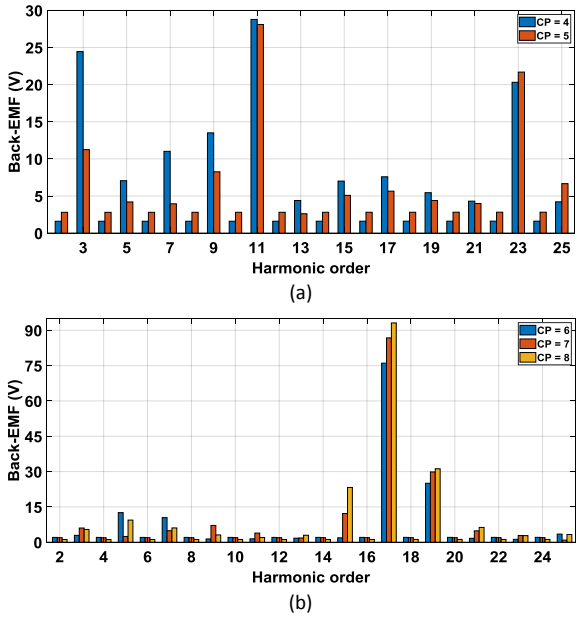


Fig. 2: The Back-EMF harmonic content of initial SynRM with (a) 24-slot and (b) 36-slot designs.

B. Parameterized Rotor design features

Fig. 3 presents the conceptual structure of a quarter of a 4-pole SynRM rotor. Flux barriers are of significant importance in rotor design; consequently, researchers have proposed various geometries, including circular, trapezoidal, segmented geometry (SEG), Salient pole, and fluid-type configurations. The fluid-type flux barrier exhibits superior torque characteristics compared to other types of flux barrier designs due to its optimized shape; consequently, fluid-type flux barriers are considered as a starting point. While the power factor of SynRM represents a significant limitation, PM usage has successfully solved this problem to some extent. It is noteworthy that the main PMs in PMaSynRM are positioned on the q-axis in accordance with (2), which consequently enhances the power factor. However, this parameter can be further optimized by strategically placing the PMs on the d-axis. PMs are typically situated within flux barriers, and the presence of these barriers ensures that the PM flux is directed in the appropriate orientation. The design of auxiliary PMs on the d-axis demands the creation of two non-magnetic gaps adjacent to the auxiliary PMs to ensure the correct direction of PM flux. Furthermore, to optimize rotor geometry and decrease demagnetization, as illustrated in Fig. 4, PMs are positioned adjacent to the shaft on the d-axis and within flux barriers on the q-axis. Fig. 5 presents the phasor diagram for the proposed PMaSynRM in comparison to the conventional SynRM. The flux linkage of PMs can be categorized into two components: the first component includes the flux linkage of PMs positioned on the d-axis ($\lambda_{m_d\text{-}axis}$), and the second component includes the flux linkage of PMs positioned on the q-axis ($\lambda_{m_q\text{-}axis}$).

$$\lambda_m = \lambda_{m_d-axis} + \lambda_{m_q-axis} \tag{4}$$

The power factor can be expressed as follows

$$\cos\phi = \frac{(L_d - L_q) i_{ds} i_{qs} + \lambda_m i_{ds}}{\sqrt{(i_{ds}^2 + i_{qs}^2)[L_d^2 i_{ds}^2 + (\lambda_m - L_q i_q)^2]}} \tag{5}$$

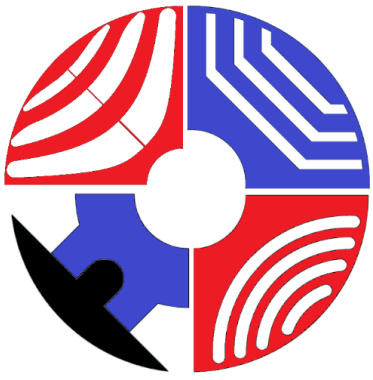


Fig. 3: The conceptual structure of a quarter of a 4-pole SynRM rotors.

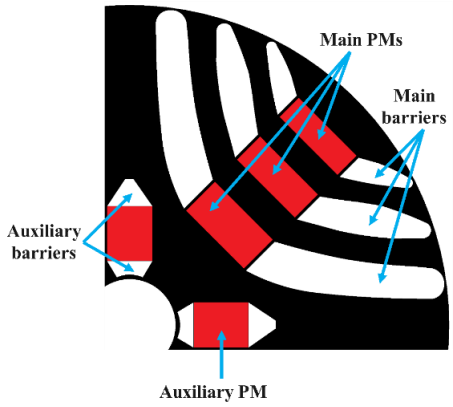
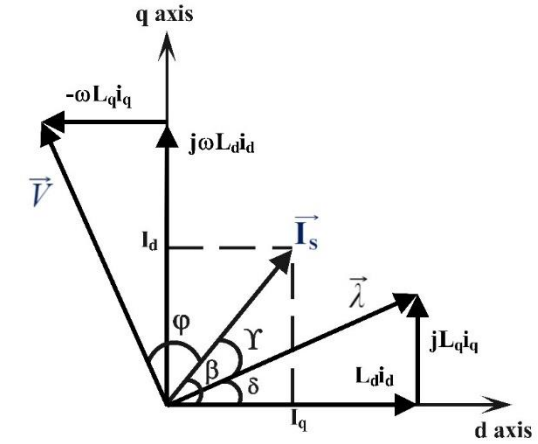
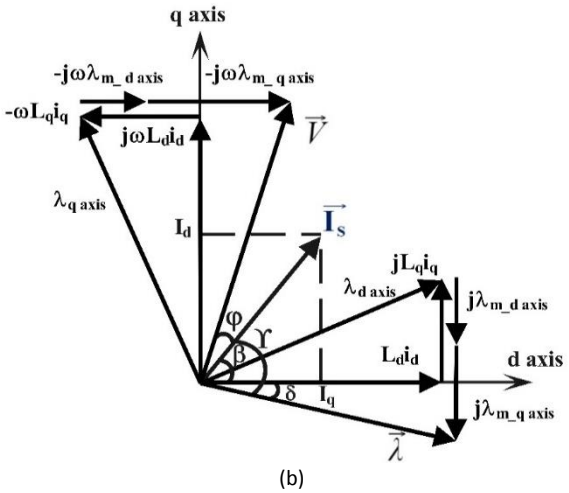


Fig. 4: The proposed modifications of the PMaSynRM design.



(a)



(b)

Fig. 5: Phasor diagram for the conventional (a) SynRM and, (b) The proposed PMaSynRM.

The maximum output power factor of SynRM is a function of the saliency ratio ($\zeta=L_d/L_q$).

$$\cos(\phi)_{\max} = \frac{L_d - L_q}{L_d + L_q} \tag{6}$$

The saliency ratio not only enhances the power factor but also influences the torque characteristic of the motor according to (3). Adding conductor bars in SynRMs provides line-start capability. Consequently, in this paper, the flux barriers are filled with aluminum for optimal use of space in the rotor. To prevent magnetic locking, slip, and noise, two additional flux barriers filled with aluminum are incorporated on the q-axis at each pole. The extent of aluminum infilling in the flux barriers is expressed as A_{xi}:

$$A_{xi} = r_{rotor} - (x_i . r_{rotor}) \tag{7}$$

where r_{rotor} denotes the rotor radius, and x_i represents the infilling index, which encompasses three levels: 10%, 15%, and 20%, respectively. 10% of the rotor radius is filled with aluminum inside the flux barriers in the 10% design. In the 15% and 20% designs, the flux barriers are filled with aluminum at 15% and 20% of the rotor radius, respectively. Fig. 6 together with Table 2 illustrate the design parameters and initial values for the proposed LS-PMaSynRM. The torque produced in SynRM solely is the reluctance torque (T_{rel}), which, upon the addition of a cage, results in another component being incorporated into the electromagnetic torque (T_{em}) of SynRM, termed asynchronous torque (Tasy). Consequently, in LS-SynRM, the electromagnetic torque is expressed in two components as follows:

$$T_{em} = T_{asy} + T_{rel} \sin(2s\omega t + \alpha) \tag{8}$$

where s denotes slip, ω represents the synchronous speed, and α signifies the phase angle. Fig. 7 illustrates the starting torque curve during the starting process for conventional and the proposed LS-PMaSynRM for different A_{xi}. The rotor design with %10 infilling (A10) in the conventional 24-slot design and the rotor design with %20 infilling (A20) in the conventional 36-slot design, have better starting torque than the other conventional designs. However, these two designs produce lower average torque than the proposed designs. The two rotor designs, A15 and A20, exhibit better starting performance in the proposed designs; however, the A15 design is preferred due to its lower aluminum consumption in the flux barriers. Furthermore, the A15 rotor design in the proposed designs enhanced the starting torque. Fig. 8 presents a comparison of the torque between the conventional SynRM and the proposed LS-PMaSynRM in different states, including the absence, partial, and complete presence of PMs for different current angles. As predefined, the results for both designs with 24 and 36-slot stators demonstrate that the use of auxiliary PMs generates more torque than the conventional SynRM design. The main PMs can produce more torque than auxiliary PMs, and the combination of main and auxiliary PMs yields the optimal result for torque. Ferrite PMs exhibit low remanence flux density, which may result in

demagnetization. The demagnetization of PMs can be decreased through the appropriate design of the rotor cage, as the magnetic field generated by the cage serves as a protective shield against the stator's magnetic field during starting. Fig. 9 illustrates the proposed LS-PMaSynRM designs with 24 and 36-slot stators, including their respective PM orientations. Fig. 10 illustrates the flux density of proposed designs with 24 and 36-slots at base speed. The results indicate that the PMs are not subject to irreversible demagnetization.

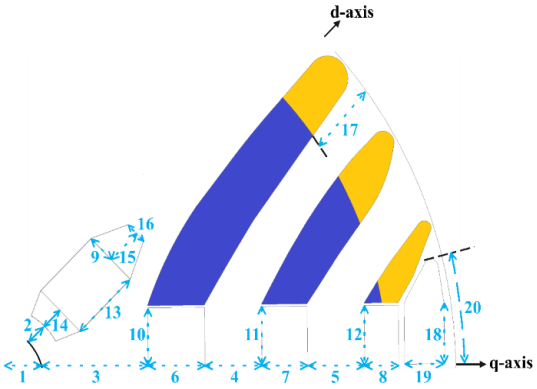
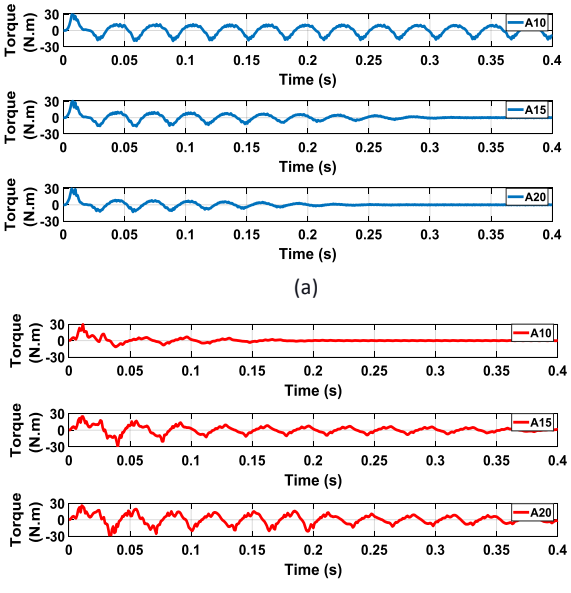
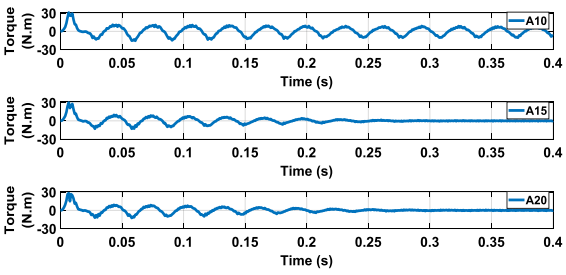


Fig. 6: Illustration of the main design parameter for the proposed PMaSynRMs (the numbers are defined in Table 2).

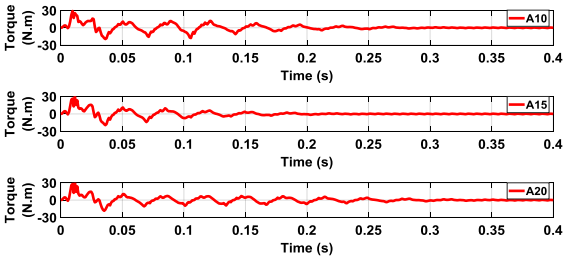


(a)

(b)



(c)



(d)

Fig. 7: Starting torque-time curves for (a) Conventional 24-slot, (b) Conventional 36-slot stator, (c) The proposed 24-slot and (d) The proposed 36-slot designs during the starting process for different A_{xi}.

Table 2: The main design parameters of the proposed LS-PMaSynRM

number	definition	Initial Value (mm)	
		24-slot	36-slot
1	Shaft diameter	5	5
2	Bridge length between the shaft and auxiliary barrier	0.5	0.5
3	Length between the shaft and main barrier	8.2	8
4	Length between the first and second main PM	3.4	5
5	Length between the second and third main PM	3	5
6	Height of first main PM	4.5	5
7	Height of the second main PM	3.6	4
8	Height of the third main PM	3	3
9	Half-height of auxiliary PM	2.5	2.5
10	Half-length of first main PM	4.5	5.3
11	Half-length of second main PM	4.5	5.3
12	Half-length of the third main PM	4.5	5.3
13	Length of auxiliary PM	6	6
14	Small gap length of the auxiliary barrier	0.5	0.5
15	Large gap length of the auxiliary barrier	5	5
16	Height the large gap of the auxiliary barrier	1	1
17	Radius of barriers infilling	A10 = 3.5 A15 = 5.25 A20 = 7	A10 = 4 A15 = 6 A20 = 8
18	Length of the middle conductor bar to q-axis	4.5	5.2
19	Height of the middle conductor bar	3	3.5
20	Middle conductor bar angle	13	13.5

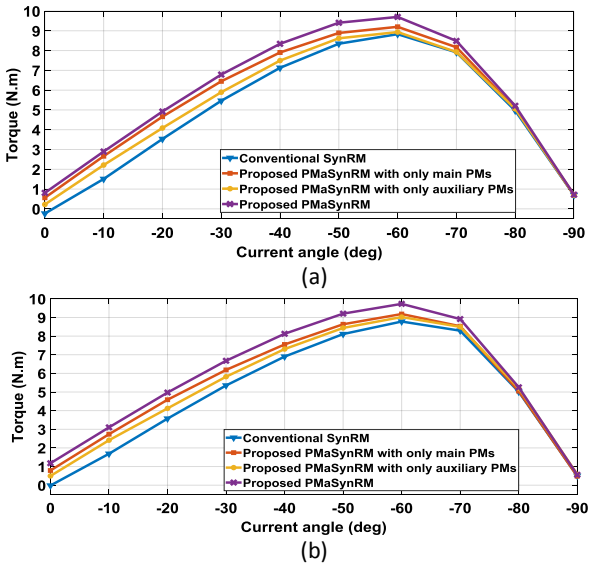


Fig. 8: Torque waveform of the conventional SynRMs and the proposed LS-PMaSynRMs in the presence or absence of different PMs in the d and q-axis for (a) 24-slot and (b) 36-slot stator designs.

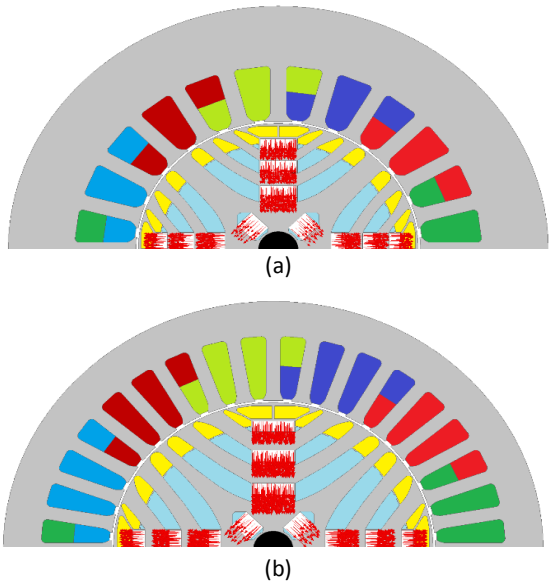


Fig. 9: Illustration of the proposed LS-PMaSynRMs and PM orientations for (a) 24-slot and (b) 36-slot designs.

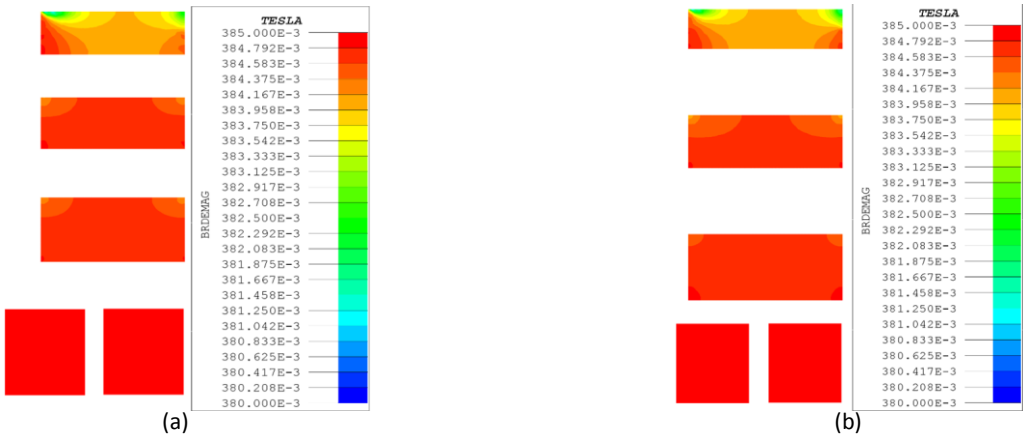


Fig. 10: Demagnetization analysis of the proposed LS-PMaSyRMs at base speed with (a) 24-slot and (b) 36-slot stator.

Performance Analysis of Proposed Design

A. Transient AC analysis

In the base speed range, the torque curve of the proposed LS-PMaSynRM exhibits an instantaneous pulse, primarily attributed to the reluctance torque. Fig. 11 depicts the torque-speed curve for both 24/36-slot stators during the starting process of conventional and the proposed LS-PMaSynRMs for different A_{xi}. In the conventional 24-slot design, A20, and the conventional 36-slot design, A10, exhibit better speed-torque characteristics. However, in the proposed design, A15, results in enhanced starting performance compared to the other designs. So, the design A15 is considered as proposed rotor design for 24-slot and 36-slot stators. proportional to the synchronization capability of the synchronous reluctance motor, with more significant inertia potentially impeding or preventing synchronization. Furthermore, in the absence of synchronization, the speed curve of the synchronous reluctance motor exhibits pulsations at twice the slip frequency, as demonstrated in (8).

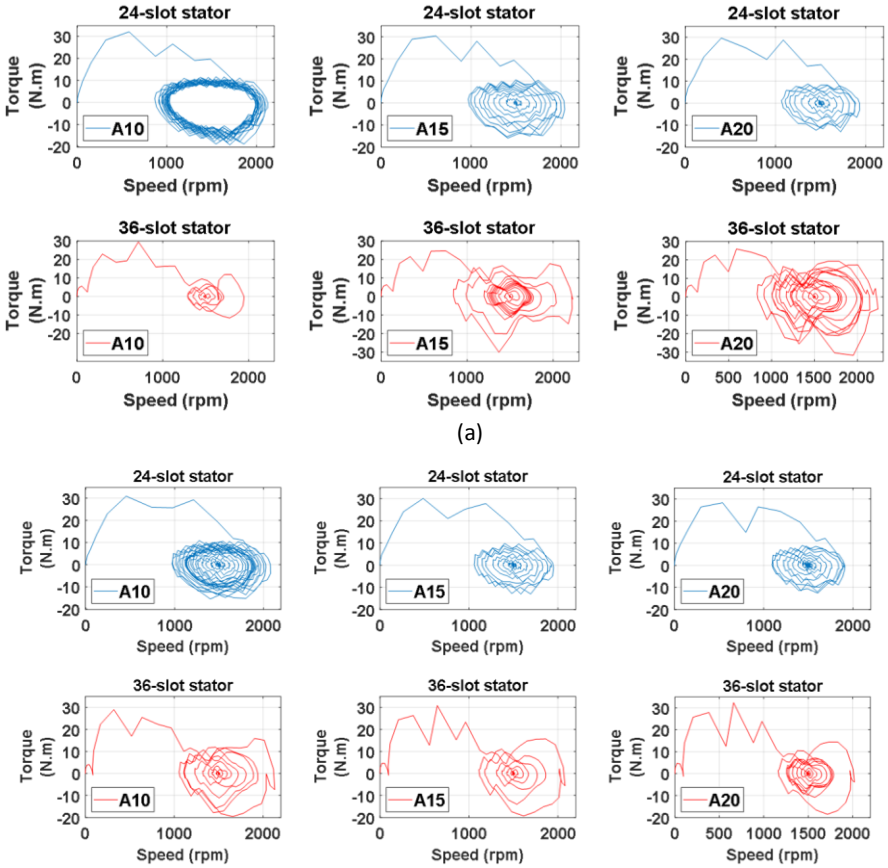
The speed-time curves presented in Fig. 12 for conventional and the proposed designs, comprising 24 and 36-slots, illustrate that increase in inertia resulted in failed synchronization.

B. Steady-state Analysis

The relationship between dq-axis inductance and current for conventional and the proposed designs are shown in Fig. 13.

This demonstrates that dq-axis inductance exhibits a non-linear relationship with respect to dq-axis current. Consequently, the current significantly influences the saliency ratio.

The embedded PMs in the rotor of proposed LS-PMaSynRM results in an increased of saliency ratio compared with conventional LS-SynRMs. The Embedded of PM also enhances the torque of SynRM and increases the power factor according to (5). As illustrated in Fig. 14, the proposed LS-PMaSynRMs exhibit a higher maximum power factor.



(a)

(b)

Fig. 11: The torque-speed curve for Both 24/36-slots stators during the starting process of (a) Conventional LS-SynRMs and (b) The proposed LS-PMaSynRMs in terms of different A_{xi}.

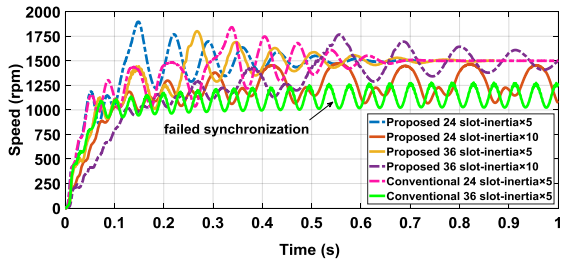
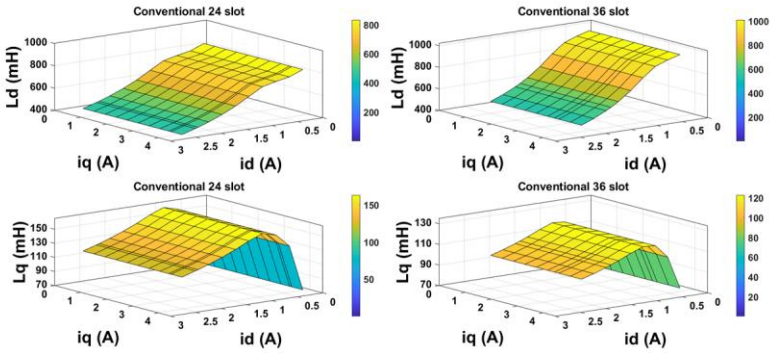


Fig. 12: Speed-time curve of conventional LS-SynRMs and the proposed Ls-PMaSynRMs in different inertia.

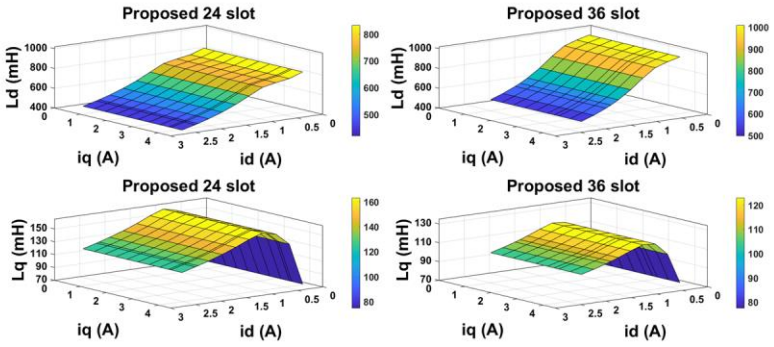
In Fig. 15, at low loads, the efficiency is reduced due to the fixed losses of SynRM, and with increasing load, the increase in output power decreases the effect of static losses. Ultimately, at the rated load, the efficiency reaches its maximum value, and the efficiency of the proposed LS-PMaSynRM with 24/36 stator slots exceeds that of the conventional SynRM. The power factor in terms of the current phase angle for conventional and the proposed LS-PMaSynRMs is presented in Fig. 16. As shown, embedding PMs in both proposed designs has resulted in an increased power factor. The stator and rotor, electrical steel M400-50A is utilized. The magnetic flux density of conventional and the proposed topologies is presented in Fig. 17. Additionally, the vector potential is depicted in the form of isolines. The stator yoke of topologies, under-rated current loading, experiences a flux density of less than 2 T, which falls within the normal range and does not adversely affect motor performance. The air gap magnetic flux density distribution with spatial harmonic content of conventional and the proposed LS-PMaSynRMs with 24 and 36-slot stators, analyzed using finite element analysis (FEA), is illustrated in Fig. 18. The fundamental, 3rd, 5th, up to 30th harmonic contents are depicted. The proposed 24-slot design demonstrates effective electromagnetic torque production when compared to conventional 24-slot design.

C. Mechanical stress Analysis

In the analysis of mechanical stress, centrifugal forces resulting from a rotational speed of 750 and 1500 rpm were applied. As illustrated in Fig. 19, the maximum von Mises stress observed in the proposed designs is less than that in conventional designs. The maximum von Mises stress calculated for 24-slot in nominal speed was about 2.7 MPa, while for 36-slot it was about 4 MPa. These values indicate that the rotor remains within the safe operating range, and the structural design of the rotor satisfies the mechanical strength requirements.



(a)



(b)

Fig. 13: The variation trend of dq-axis inductance with the current of (a) Conventional LS-SynRMs and (b) The proposed LS-PMaSynRMs.

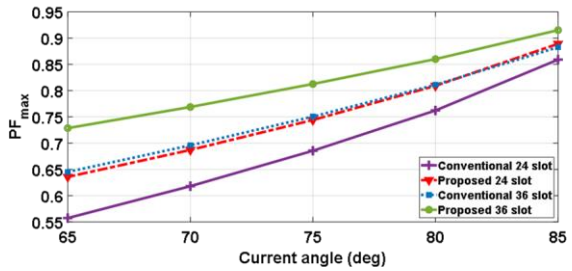


Fig. 14: The maximum power factor of conventional LS-SynRMs and the proposed LS-PMaSynRMs.

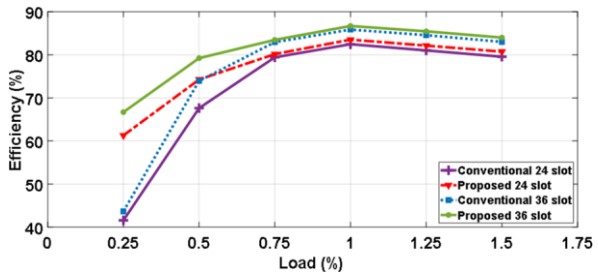


Fig. 15: Calculated efficiency of conventional LS-SynRMs and the proposed LS-PMaSynRMs.

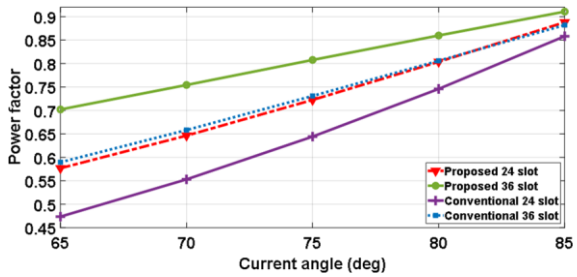


Fig. 16: Power factor of conventional LS-SynRMs and the proposed LS-PMaSynRMs.

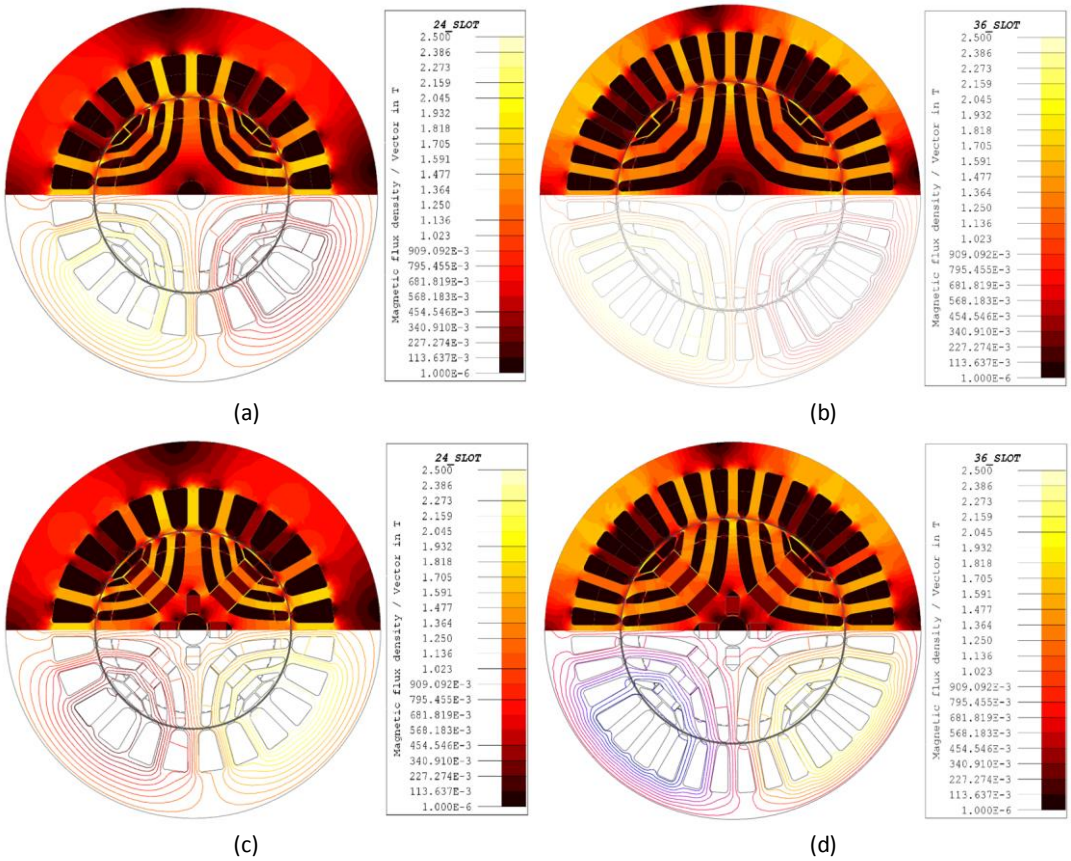


Fig. 17: The magnetic flux density and flux lines of (a) Conventional 24-slot LS-SynRM, (b) Conventional 36-slot LS-SynRM, (c) The proposed 24-slot LS-PMaSynRMs and (d) The proposed 3-slot LS-PMaSynRMs.

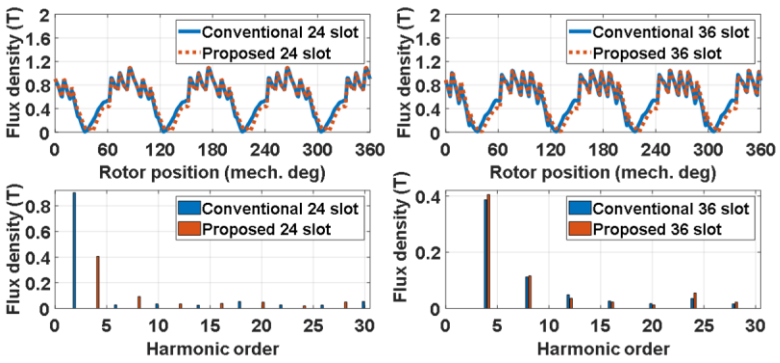


Fig. 18: The air gap magnetic flux density distribution with spatial harmonic content of conventional LS-SynRMs and the proposed LS-PMaSynRMs.

Experimental Verifications Comparisons

The proposed design with 24 stator slots has been constructed to verify the experimental results. Comparison of the Back-EMF waveforms for conventional, proposed 24-slot stator design and experimental proposed 24-slot stator design is shown in Fig. 20, wherein the waveform of the proposed 24-slot design exhibits a more sinusoidal compared to the 36-slot design.

Table 3 presents the power factor$_{max}$, power factor, efficiency, and rated current of the two proposed LS-PMaSynRM. The results under nominal conditions demonstrate that in the 24-slot design, the efficiency of the 24-slot design has increased by 1.2% from 82.5% for SynRM to 83.5% in the proposed design. In the 36-slot design, the efficiency has increased by 1% from 85.8% for SynRM to 86.7% in the proposed design. The maximum power factor and power factor for the proposed 24-slot design are 0.84 and 0.83, respectively, while for the proposed 36-slot design, they are 0.88 and 0.87, respectively.

The maximum mechanical stress for the proposed 24-slos is 2.74 MPa, and for the proposed 36-slot, it is 4 MPa. The rotor and stator stakes for the proposed 24-slot stator are depicted in Fig. 21.

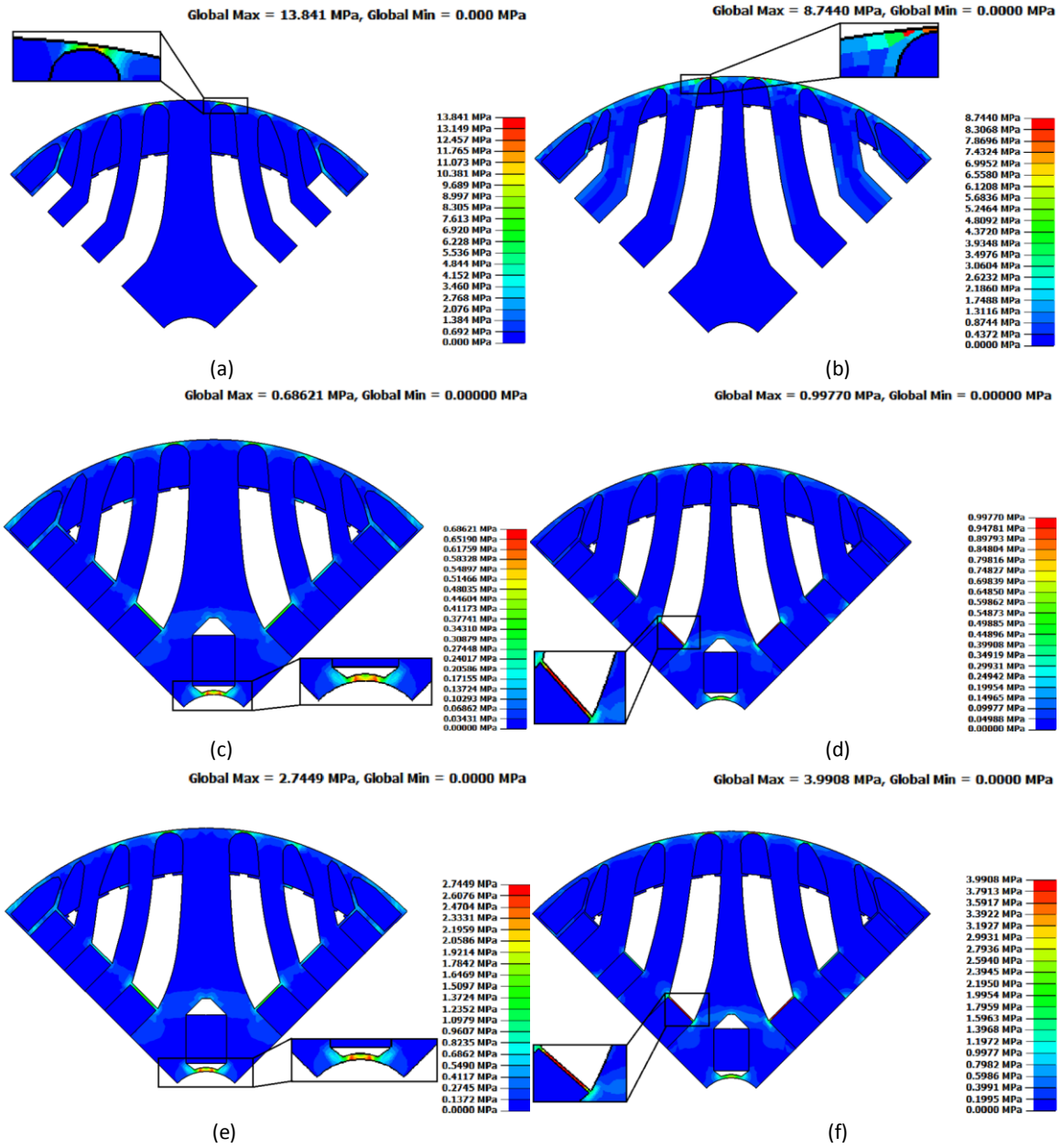


Fig. 19: Von Mises stress plot of (a) Conventional rotor design with 24-slot, (b) Conventional rotor design with 36-slot, (c) The proposed rotor design with 24-slot (rotational speed of 750 rpm), (d) The proposed rotor design with 36-slot (rotational speed of 750 rpm) (e) The proposed rotor design with 24-slot (rotational speed of 1500 rpm) and (f) The proposed rotor design with 36-slot (rotational speed of 1500 rpm).

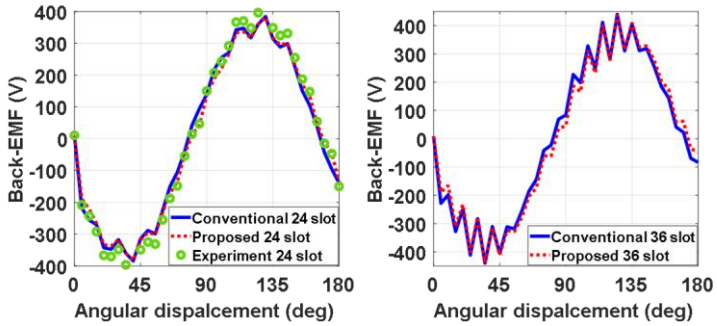


Fig. 20: Back-EMF waveforms comparison at 1500 r/min for conventional LS-SynRMs, the proposed LS-PMaSynRMs and experimental 24-slot stator LS-PMaSynRM.

Table 3: Results for both proposed LS-PMaSynRMs

Item	24-slot stator	36-slot stator
Power factor$_{max}$	0.84	0.88
Power factor	0.83	0.87
Efficiency (%)	83.5	86.7
Reted current (A)	4.4	3.8
Maximum mechanical stress (MPa)	2.74	4

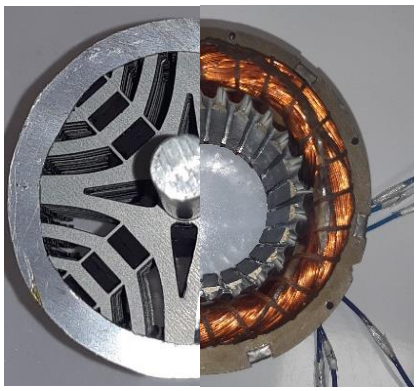


Fig. 21: Prototype of the proposed LS-PMaSynRM with 24-slot stator and rotor.

To validate the FEM analysis, the back-EMF waveform of the proposed design was measured and compared with the FE simulation results. The experimental findings confirm the performance of the proposed design.

The results for both proposed LS-PMaSynRM designs demonstrate enhanced performance compared to conventional LS-SynRMs, indicating that the proposed designs are potentially suitable for industrial and domestic applications. Industries such as mining, steel production, and chemical processing can benefit from the proposed LS-PMaSynRM. By providing enhanced efficiency and reduced losses, the proposed LS-PMaSynRMs not only meet the operational demands of these industries but also contribute to sustainability goals by lowering energy consumption and minimizing waste.

Conclusion

This study presents the design and analysis of a novel LS-PMaSynRM with fluid-type flux barriers. The analysis focuses on designing a SynRM that possesses line-start capability, improved power factor, and enhanced overall efficiency. The stator winding design incorporates two-layer windings to minimize harmonic content and enhance performance. The rotor design integrates fluid-type flux barriers with strategically placed PMs on both the q-axis and d-axis to enhance power factor and torque characteristics. A sensitivity analysis was conducted to determine the proper infill level of aluminum in the flux barriers, considering factors such as starting torque and aluminum consumption. The results demonstrate that an infill level of 15% (A15) provides the proper balance between starting performance and material utilization.

FEA was employed to calculate the motor's electromagnetic performance, including torque characteristics, power factor, and flux density distribution.

The proposed design with 24-slots demonstrates a power factor of 0.83, an efficiency of 83.5%, and a maximum mechanical stress of 2.74 MPa and the proposed design with 36-slot exhibits a power factor of 0.87, an efficiency of 86.7%, and a maximum mechanical stress of 4 MPa. The analysis indicates that the PMs are not susceptible to demagnetization under normal operating conditions. The proposed designs capabilities make them ideal for applications where reliable starting and high efficiency are paramount, such as in conveyor systems, pumps, and fans within manufacturing facilities. In conclusion, this research presents a novel and promising design for LS-PMaSynRMs with enhanced performance characteristics.

The proposed design demonstrates the potential for improved efficiency, reduced losses, High mechanical strength and enhanced reliability in various industrial applications.

Author Contributions

S. R. Mousavi-aghdam: Resources, project administration, funding acquisition, supervision, Methodology. S. A. Azimi: software, writing—review & editing, visualization, project administration, Validation. F. Sedaghati: supervision, Validation, Methodology.

Acknowledgment

We appreciate the referees and their colleagues who helped the authors in publishing this article.

Funding

This research received no external funding.

Conflict of Interest

The authors declare no potential conflict of interest regarding the publication of this work. In addition, the ethical issues including plagiarism, informed consent, misconduct, data fabrication and, or falsification, double publication and, or submission, and redundancy have been completely witnessed by the authors.

Abbreviations

SynRM	Synchronous reluctance motor
IM	Induction motor
FEM	Finite element method
SEG	Segmented geometry
CP	Coil Pitch
T_{rel}	Reluctance torque
T_{em}	Electromagnetic torque
T_{asy}	Asynchronous torque
PM	Permanent magnet

References

[1] X. Li, Y. Wang, Y. Cheng, D. Li, R. Qu, "An overview of high-efficiency synchronous reluctance machines," CES Trans. Electr. Mach. Syst., 7(1): 81–91, 2023.

[2] M. Gamba, E. Armando, G. Pellegrino, A. Vagati, B. Janjic, J. Schaab, "Line-start synchronous reluctance motors: Design guidelines and testing via active inertia emulation," in Proc. 2015 IEEE Energy Conversion Congress and Exposition (ECCE): 4820–4827, 2015.

[3] G. A. Uvaraj, N. C. Lenin, S. Padmanaban, B. Khan, "Line start synchronous reluctance motor with improved power factor for agriculture electric pump applications," J. Eng., 2022(3): 295–310, 2022.

[4] Y. Kong, B. Nicola, M. Lin, "Loss functions and efficiency model of permanent magnet assisted synchronous reluctance machine," IEEE Trans. Energy Convers., 38(1): 53–63, 2023.

[5] M. Farhadian, M. Moallem, B. Fahimi, B. M. Dehkordi, M. Sahebzamani, "Alternate rotor design for line-start synchronous reluctance motor with minimum use of copper," IEEE Access, 12: 73–84, 2024.

[6] S. Panda, R. K. Keshri, A. Tessarolo, G. Tiwari, M. Mezzarobba, "Design refinements of synchronous reluctance motor utilising non-magnetic radial ribs for traction applications," IET Electr. Power Appl., 14(2): 2480–2489, 2020.

[7] M. Muteba, "Line-Start synchronous reluctance motor with v-shaped rotor laminations," IEEE Access, 10: 109277–109288, 2022.

[8] H. Kim et al., "Study on analysis and design of line-start synchronous reluctance motor considering rotor slot opening and bridges," IEEE Trans. Magn., 58(2): 1–6, 2022.

[9] M. U. Naseer, A. Kallaste, B. Asad, T. Vaimann, A. Rassõlkin, "Analytical modelling of synchronous reluctance motor including non-linear magnetic condition," IET Electr. Power Appl., 16(4): 511–524, 2022.

[10] L. Ren, H. Wang, S. Ren, Z. Zhong, F. Peng, Y. Zhao, "Dynamic characterization of SynRM with dual-axis hybrid excitation self-commissioning," IEEE Trans. Ind. Electron., 71(5): 4440–4449, 2024.

[11] A. Mahmoudi, E. Roshandel, S. Kahourzade, W. L. Soong, "Introduction of double-stator synchronous reluctance motor and modeling," IEEE Access, 11: 76739–76750, 2023.

[12] R. Rouhani, S. E. Abdollahi, S. A. Gholamian, "Design of a high speed interior claw synchronous reluctance machine," Int. Trans. Electr. Energy Syst., 31(12): e13200, 2021.

[13] C. Madariaga, C. Gallardo, J. A. Tapia, W. Jara, A. Escobar, M. Degano, "Fast assessment of rotor barrier dimensional allowances in synchronous reluctance machines," IEEE Access, 11: 58349–58358, 2023.

[14] W. J. Wan, Z. C. Li, J. P. Lu, Y. Wang, D. Shi, J. X. Shen, "Fast design methodology for synchronous reluctance machine rotor with circular flux barriers," IEEE Trans. Ind. Appl., 61(5): 6951-6961, 2025.

[15] R. Rouhani, S. Abdollahi, A. Gholamian, "Design of a synchronous reluctance motor with new hybrid lamination rotor structure," J. Electr. Comput. Eng. Innovations, 11(2): 243-252, 2023.

[16] S. R. Mousavi-Aghdam, M. R. Feyzi, N. Bianchi, M. Morandin, "Design and analysis of a novel high-torque stator-segmented SRM," IEEE Trans. Ind. Electron., 63(3): 1458–1466, 2016.

[17] A. Jamali-Fard, M. Mirsalim, "Design and prototyping of a novel line-start permanent magnet assisted synchronous reluctance motor for fan application," IEEE Trans. Energy Convers., 39(1): 243–251, 2024.

[18] S. M. Mousavi Bafrouei, A. D. Aliabad, E. Amiri, "Design and analysis of PM-assisted synchronous reluctance machine with shifted magnetic poles," IET Electr. Power Appl., 18(1): 52–63, 2024.

[19] C. Diao, W. Zhao, Y. Liu, X. Wang, "Permanent magnet assisted synchronous reluctance motor with asymmetric rotor for high torque performance," CES Trans. Electr. Mach. Syst., 7(2): 179–186, 2023.

[20] E. Eser, N. Üstkoyuncu, "Effects of permanent magnets on different flux barriers for the AF-SynRMs," Electr. Power Compon. Syst., 52(10): 1936–1945, 2024.

[21] T. Mohanarajah, M. Nagrial, J. Rizk, A. Hellany, "a novel method to optimize permanent magnet assisted synchronous reluctance machines," Electr. Power Compon. Syst., 48(9–10): 933–943, 2020.

[22] S. Baka, S. Sashidhar, B. G. Fernandes, "Design of an energy efficient line-start two-pole ferrite assisted synchronous reluctance motor for water pumps," IEEE Trans. Energy Convers., 36(2): 961–970, 2021.

[23] C. T. Liu, et al., "Structural optimizations of high-efficiency direct-on-line synchronous reluctance motors for metal industry applications," IEEE Trans. Ind. Appl., 57(3): 3004–3011, 2021.

[24] Y. Hu, B. Chen, Y. Xiao, J. Shi, X. Li, L. Li, "Rotor design and optimization of a three-phase line-start synchronous reluctance motor," IEEE Trans. Ind. Appl., 57(2): 1365–1374, 2021.

[25] S. R. Mousavi-Aghdam, A. Azimi, "Design and analysis of a new improved rotor structure in line-start synchronous reluctance motors," Electr. Eng., 106(3): 2313–2324, 2024.

[26] L. Shao, D. Tavernini, A. E. Hartavi Karci, A. Sorniotti, "Design and optimisation of energy-efficient PM-assisted synchronous reluctance machines for electric vehicles," IET Electr. Power Appl., 17(6): 788–801, 2023.

[27] Y. Lin, Y. Sun, Y. Wang, S. Cai, J. Shen, "Radial electromagnetic force and vibration in synchronous reluctance motors with asymmetric rotor structures," IET Electr. Power Appl., 15(9): 1125–1137, 2021.

[28] Y. Zheng, et al., "A torque ripple reduction method for the synchronous reluctance machines with mirror asymmetric rotor laminations," IEEE Trans. Ind. Electron., 72(10): 10497-10507, 2025.

[29] H. Aghazadeh, E. Afjei, A. Siadatan, "Sizing and detailed design procedure of external rotor synchronous reluctance machine," IET Electr. Power Appl., 13(8): 1105–1113, 2019.

[30] S. R. Salehinia, S. E. Afjei, A. Hekmati, "Analytical method for optimal design of synchronous reluctance motor for electric scooter application," Sci. Iran., 29(5): 2537-2551, 2022.

Biographies



Seyed Reza Mousavi-Aghdam received his M.Sc. and Ph.D. Degree from University of Tabriz, Iran, in 2011 and 2015 respectively all in Electrical Engineering. During September 2014 to March 2015, he has been a Visiting Research Scholar at the Department of Industrial Engineering, University of Padova, Italy. In 2016, he joined the Department of Electrical Engineering, University of Mohaghegh Ardabili, as an Assistant Professor. Since 2020, he has been an Associate Professor of Electrical Engineering. His activity deals with the design and control of electrical machines using FEM, electric drives and converters. He is the author or coauthor of several scientific papers on electrical machines and drives. His current research interests include design and control of electrical machines and electric drives.

- Email: r.mousaviaghdam@uma.ac.ir
- ORCID: 0000-0002-0154-4427
- Web of Science Researcher ID: NA
- Scopus Author ID: 355001780700

Homepage:
https://academics.uma.ac.ir/profiles?Name=S.%20R.%20Mousavi-Aghdam



Seyed Abbas Azimi was born in Ardabil, Iran, on February, 1996. He received his B.Sc. degree in Electrical Engineering from Islamic Azad University, Ardabil branch, Ardabil, Iran in 2018 and his M.Sc. degree in Power Electronics and electric machines engineering from the Azarbaijan Shahid Madani University, Tabriz, Iran in 2021. he is currently pursuing the Ph.D. degree in the Electrical Engineering at University of Mohaghegh Ardabili in Ardabil, Iran. His research interests include electric vehicle and power electronics design, simulation, modeling, and control of electrical machines.

- Email: abbasazimi@uma.ac.ir
- ORCID: 0009-0004-4886-2213
- Web of Science Researcher ID: NA
- Scopus Author ID: 58975611100
- Homepage: NA



Farzad Sedaghati was born in Ardabil, Iran, in 1984. He received the M.S. and Ph.D. degrees both in Electrical Engineering in 2010 and 2014 from the University of Tabriz, Tabriz, Iran. In 2014, he joined the Faculty of Engineering, Mohaghegh Ardabili University, where he has been an Assistant Professor, since 2014. His current research interests include renewable energies and power electronic converters design and applications.

- Email: farzad.sedaghati@uma.ac.ir
- ORCID: 0000-0001-6974-4719
- Web of Science Researcher ID: NA
- Scopus Author ID: 35410298600
- Homepage: https://academics.uma.ac.ir/profiles?Id=617

Journal of Electrical and Computer Engineering Innovations
(JECEI)
Journal homepage: http://www.jecei.sru.ac.ir

Research paper

Design and Optimization of a Counter-Rotating Double-Rotor Synchronous Motor with a Permanent Magnet External Rotor and a Reluctance Internal Rotor

Pouria Nadri[1], *Behrooz Rezaeealam*[1,*], *Morteza Mikhak-Beyranvand*[2]

[1]*Department of Electrical Engineering, Faculty of Engineering, Lorestan University, Khorramabad, Lorestan, Iran.*
[2]*Department of Electrical Engineering, Technical and Vocational University (TVU), Tehran, Iran.*

Article Info

Article History:
Received 12 January 2026
Reviewed 17 March 2026
Revised 19 May 2026
Accepted 26 May 2026

Keywords:
Counter-Rotating Dual-Rotor synchronous motor
Cogging torque
Taguchi method
Finite Element Analysis (FEA)
Torque ripple

*Corresponding Author's Email Address: *rezaee.bh@lu.ac.ir*

Abstract

Background and Objectives: Dual-rotor synchronous motors with counter-rotation are of significant interest for electric machine design due to their high performance and specific applications. In this study, a new Counter-Rotating Dual-Rotor Synchronous Motor (CRDRSM) is presented, with the permanent magnet (PM) rotor as the outer rotor and the reluctance rotor as the inner rotor.
Methods: To identify the optimal structure, the effects of distributed and fractional-pitch windings are first compared. Then, various PM and reluctance rotor topologies are examined in order to select the optimal combination. Despite high output torque, cogging torque significantly affects motor performance; therefore, reducing cogging torque is the main concern of this research. Dimensional optimization is conducted using the Taguchi method to minimize cogging torque in the PM rotor. Four key design parameters, including the PM arc, PM thickness, stator opening slot, and stator tooth width, are selected as optimization variables, while other parameters are kept constant. The minimum and maximum ranges of these variables are determined using parametric scanning and ANSYS Maxwell finite element software. Briefly, the optimization process proceeds in three stages: (1) winding configuration comparison, (2) selection of optimal inner and outer rotor structures, and (3) dimensional optimization using the Taguchi method.
Results: Analysis of the results demonstrates that the cogging torque of the proposed motor is reduced by up to 62.36%, the output power and efficiency are increased, and the voltage THD is also reduced. Other performance characteristics, including output torque and electromagnetic stability, are improved compared to the initial design or remain at a desirable level.
Conclusion: Finite Element Analysis (FEA) demonstrated that the distributed winding configuration delivers the best performance among all tested options. Model C, featuring a hyperbolic-line reluctance inner rotor combined with a surface-mounted PM outer rotor, was identified as the best configuration. This model offers an excellent balance of high torque, low torque ripple, minimized back-EMF harmonics, and satisfactory efficiency, making it highly suitable for submarine propulsion systems. To further reduce cogging torque (one of the primary sources of torque ripple and acoustic noise), the motor geometry was optimized using the Taguchi method and FEA. Overall, the electromagnetic performance of the proposed CRDRSM was validated in terms of flux density distribution, output torque, and cogging torque.

This work is distributed under the CC BY license (http://creativecommons.org/licenses/by/4.0/)

How to cite this paper:
P. Nadri, B. Rezaeealam, M. Mikhak-Beyranvand, "Design and optimization of a counter-rotating double-rotor synchronous motor with a permanent magnet external rotor and a reluctance internal rotor," J. Electr. Comput. Eng. Innovations, 14(2): 449-464, 2026.
DOI: 10.22061/jecei.2026.12667.901
URL: https://jecei.sru.ac.ir/article_12562.html

2345- 3044/© 2026 The Authors. Published by Shahid Rajaee Teacher Training University.

Introduction

CRDRSMs have emerged in recent years as an attractive option for applications with space constraints, high torque density requirements, dynamic performance, and optimal efficiency [1], [2]. They have garnered attention in applications such as the marine industries, aviation, hybrid electric vehicles, and underwater vehicle propulsion systems [1]-[4]. Compared to dual-rotor motors, single-rotor motors increase the mechanical stresses on the rotor surface due to their integrated structure and larger rotor diameter. However, in dual-rotor motors, by utilizing an inner rotor with a smaller diameter and an outer rotor, mechanical stresses, acoustic noise, and torque ripple are reduced. In CRDRSMs, by using the technique of reverse rotation of two rotors, the problems caused by unidirectional rotation and enable the movement of reverse rotation propellers [5]. Dual-rotor counter-rotating machines are divided into two main types: dual-rotor electric machines with a common stator and dual-rotor electric machines without a stator. The main difference between these two types is in mechanical power [6]. A dual-rotor motor with a shared stator can provide different speeds and torques for each rotor, whereas in a stator-less motor, the torques of the two rotors must be equal, although the speeds can differ [5]-[7]. In underwater vehicles, electric propulsion systems offer superior performance due to their higher efficiency, better controllability, simpler maintenance, and lower acoustic noise compared to thermal propulsion systems. In the military industries, special attention has also been given to electric propulsion in modern vessels and ships, as this architecture offers greater flexibility, efficiency, and fault tolerance compared to mechanical propulsion systems [8].

In the fast-paced world of technology and industry, the need for high-performance and energy-efficient electric motors is increasingly felt. In this context, Permanent Magnet Synchronous Motors (PMSM) and Switched Reluctance Motors (SRM) have found a special place as two modern and innovative options in the design and development of electric motors [9], [10]. PMSMs provide high performance without the need for a mechanical commutator and have advantages such as small size, low weight, low losses, high efficiency, and high torque density, making them very suitable for space-constrained applications, such as submarine propulsion [11], [12]. Additionally, SRMs have been proposed as an alternative to reduce the use of PMs due to their simple mechanical design, low cost, and high reliability, while providing acceptable output torque [12]-[14].

The design and optimization of a dual-rotor hybrid motor (reluctance-PM) using the reverse rotation technique can be an attractive and unique idea in the development of electric motors. In [12], a synchronous dual-rotor motor with a PM outer rotor and a reluctance inner rotor has been introduced that includes a magnetic insulation ring in the middle of the stator yoke, aiming to reduce the cogging torque.

In order to increase the torque density and to reduce torque ripple, this paper proposes a CRDRSM, which utilizes a radial flux configuration and includes an outer rotor with surface PMs, an inner rotor of the reluctance type, and a common stator located between them. Then, an attempt is made to minimize the torque ripple of the proposed CRDRSM for applications that require low noise levels [5], [15]. Moreover, it seems that the thermal behavior of the proposed CRDRSM will improve, as the inner rotor does not include PMs.

Cogging torque in PM motors is caused by the interaction between the magnets and the stator slots, leading to torque ripple and acoustic noise [16]. Various methods have been proposed to reduce cogging torque, including stator slotting [17] and rotor structure optimization [18]. There are well-established design optimization techniques for electrical machines, including deterministic methods [19], stochastic methods (such as genetic algorithms) [20], and intelligent methods [21].

Besides, many papers have employed the Taguchi method for design optimization of PM motors in order to reduce cogging torque [22]-[24]. In [23] and [24], the Taguchi method has been used with the FEA to evaluate the cogging torque due to PM tolerances, by which the sampling number has been reduced significantly. The Taguchi optimization method, by defining a loss function and analyzing the impact of various factors on the output, makes it possible to determine optimal parameters under conditions with the least sensitivity to environmental noise and unwanted variations [25]-[27]. Considering the complex nature of modeling in dual-rotor synchronous motors, the use of the Taguchi analysis method combined with parameter displacement analysis leads to the rapid and precise identification of key parameters affecting motor performance [28]. In addition to significantly reducing optimization time and costs, it also enhances key parameters such as increased efficiency, reduced cogging torque, and improved output torque quality, ultimately improving electromagnetic performance [29]-[31].

In this study, the Taguchi method was chosen due to its high efficiency in reducing computation time and requiring fewer samples compared to other methods, such as PSO [30]. This method is based on the design of orthogonal experiments and allows for finding the optimal combination of design variables with minimal calculations [28], [29], [31].

This research, using FEA in the commercial software ANSYS Maxwell, first compares two types of windings (distributed and fractional pitch) and selects the most suitable winding. Then, eight different configurations for combining reluctance rotors and PMs are examined, and the optimal model is selected. Since cogging torque significantly affects torque ripple and output torque quality, geometric optimization has been carried out with the aim of reducing the cogging torque of the external PM rotor. The optimization range of parameters has been determined considering the motor dimension constraints, and by combining the Taguchi analysis method and parameter displacement, the optimal parameters for reducing cogging torque have been extracted. Simulation analyses confirm the effectiveness of the optimization. Ultimately, the magnetic field analysis, stator yoke flux density, air gap flux density, inductance, electromotive force (EMF), output torques, power, and efficiency confirm the proper performance of the proposed motor.

Motor Preliminary Design

A. Motor Topology

In this research, a CRDRSM has been proposed and investigated, which includes an outer rotor with surface PMs and an inner rotor of the reluctance type. This motor has a common stator located between two concentric rotors. Both rotors rotate at the same speed but in opposite directions. Slots are embedded in the inner and outer surfaces of the stator, between which the stator windings are distributed. To create rotating magnetic fields with opposite directions in the inner and outer air gaps of the stator, a phase shift between the windings of the outer and inner layers of the stator has been applied. This phase displacement results in the generation of two opposing magnetic driving forces in the inner and outer air gaps. Fig. 1 shows a schematic view of the proposed motor.

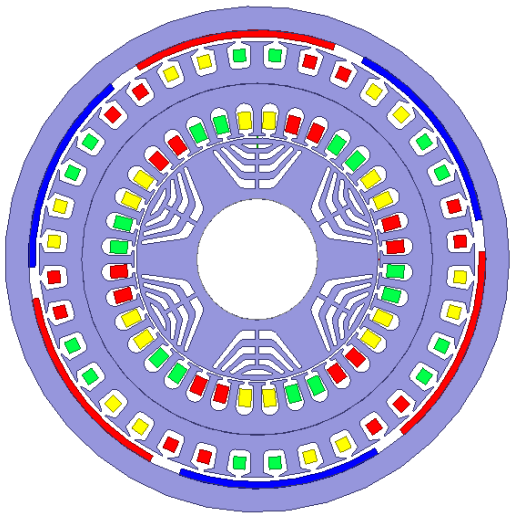


Fig. 1: Proposed structure of CRDRSM.

In fact, this motor can be described as a combination of a synchronous reluctance motor and a PM motor, benefiting from the advantages of both. The main geometric and electrical parameters considered for the initial model are summarized in Table 1.

Table 1: Design Dimensions and Main Parameters of CRDRSM

Parameter	Value
Number of phases	3
Number of poles	6
Number of slots	36
Rated frequency (Hz)	50
Stator winding connection	Y
Effective length (mm)	198
Inner radius of stator (mm)	61
Outer radius of stator (mm)	108
Radius of outer rotor (mm)	110
Radius of inner rotor (mm)	60
Inner air-gap length (mm)	1
Outer air-gap length (mm)	2
Speed (rpm)	1000
PM type	NdFeB-N35

The proposed motor has 36 slots and 6 poles, which provides a balanced three-phase winding layout and ensures both rotors perform properly. This selection results in an integer slots-per-pole-per-phase value of $q = \frac{Q}{mP} = \frac{36}{6\times3} = 2$, which is a common choice for distributed windings and contributes to stable electromagnetic performance. In the CRDRSM motor, the number of poles in the inner rotor (reluctance) and the number of poles in the outer rotor (PM) must be equal to achieve balance. The initial parameter set in Table 1 was selected to satisfy the required operating conditions and dimensional constraints.

In the CRDRSM motor, the number of poles in the inner rotor (reluctance) and the number of poles in the outer rotor (PM) must be equal to achieve balance.

B. Motor Power Equation

I. External PM Motor

The rated output power of a PM motor depends on voltage, current, and the number of phases. Considering that the waveforms of stator current and voltage are usually non-sinusoidal, a shape coefficient (k_p) is taken into account for the precise calculation of output power. Assuming the neglect of losses due to winding impedance and leakage inductance, the output power of the external PM motor (P_{spm}) is expressed as:

$$P_{spm} = \eta m k_p E_{pk} I_{pk} \quad (1)$$

where η is the motor efficiency, m is the number of phases, k_p is the shape coefficient, E_{pk} is the peak value

of the single-phase back electromotive force (EMF), and I_{pk} is the peak value of the stator phase current. Assuming the stator current vector is aligned with the back EMF vector, the d-axis current would be zero, and the shape coefficient (k_p) is considered to be 0.5. The peak value of the back EMF of the outer PM motor is obtained from the induced electromotive force (E = BLV), where B is the magnetic flux density, L is the effective length of the winding, and V is the linear speed of the winding in the magnetic field. The linear speed in the outer air gap is calculated using the relation $V = 2\pi\frac{D_{os}}{2}\left(\frac{f_e}{p}\right)$, where D_{os} is the outer diameter of the stator, f_e is the supply frequency, and p is the number of pole pairs. Therefore, the peak back EMF value is expressed as:

$$E_{pk} = \pi K_w N_t B_{gl.p}\left(\frac{f_e}{p}\right) D_{os} L_e \tag{2}$$

where K_w is the winding factor, N_t is the number of turns of the winding in each phase, $B_{gl.p}$ is the peak value of the air gap flux density of the surface-mounted PM rotor, L_e is the axial length of the motor core, and f_e/p is the angular speed of the magnetic field. The peak phase current (I_{pk}) is also calculated from [32]:

$$I_{pk} = \frac{\sqrt{2}D_{os}\pi}{mN_t} A_{sp.rms} \tag{3}$$

where $A_{sp.rms}$ is the electrical load value on the PM rotor side, m is the number of phases, D_{os} is the outer diameter of the stator, and N_t is the number of turns of the winding in each phase. By substituting (2) and (3) into (1), the output power of the external PM motor is obtained as:

$$P_{spm} = \frac{\sqrt{2}\pi^2}{2} K_w \eta \left(\frac{f_e}{p}\right) B_{gl.p} A_{sp.rms} D_{os}^2 L_e \tag{4}$$

II. Internal Reluctance Motor

For the synchronous reluctance motor (SynRM), the output torque is provided by the components of the d-axis and q-axis currents, and the output power is affected by the power factor ($\cos(\gamma)$). Unlike a PM motor, the reluctance rotor lacks a PM and therefore does not generate direct back EMF. As a result, the output power P_{syr} of the synchronous reluctance motor can be expressed as:

$$P_{syr} = \frac{\sqrt{2}\pi^2}{2} K_w \eta \left(\frac{f_e}{p}\right) cos(\gamma)\, B_{g1.R} A_{sR.rms} D_{is}^2 L_e \tag{5}$$

that $\cos(\gamma)$ is the power factor of the internal reluctance motor, γ is the angle between the stator current and the q-axis component, $B_{gl.R}$ is the peak value of the air gap magnetic flux density, $A_{sR.rms}$ is the electrical load value on the reluctance rotor side, and D_{is} is the inner diameter of the stator. (5) is derived from the classical electromagnetic power formulation of synchronous machines based on shear stress theory, in which the output power is expressed as a function of the air-gap magnetic loading, stator electrical loading, and active machine volume, while standard coefficients account for sinusoidal field distributions and peak-to-RMS conversions.

III. Double Rotor Motor

By combining the equations of the external PM motor and the internal reluctance motor, the total power of the CRDRSM is obtained as:

$$P_{total} = \frac{\sqrt{2}\pi^2}{2} K_w \eta \left(\frac{f_e}{p}\right) L_e \left[B_{g1.R} A_{sR.rms} D_{is}^2 \cos\gamma + B_{g1.p} A_{sp.rms} D_{os}^2\right] \tag{6}$$

Considering the series connection of the internal and external stator windings, the winding currents are equal, and therefore:

$$\frac{A_{sp.rms} D_{os}\pi}{mN_t} = \frac{A_{sR.rms} D_{is}\pi}{mN_t} \tag{7}$$

By simplifying (7), the relationship between the effective electrical loads of the inner and outer rotors with the diameter ratio is obtained as:

$$A_{sp.rms} = \frac{D_{is}}{D_{os}} A_{sR.rms} \tag{8}$$

By substituting (8) into (6), and after simplification, the total motor power (P_{total}) can be expressed as:

$$P_{total} = \frac{\sqrt{2}\pi^2}{2} K_w \eta \left(\frac{f_e}{p}\right) \left[B_{g1.R} cos\,\gamma + B_{g1.P} \frac{D_{os}}{D_{is}}\right] A_{sR.rms} D_{is}^2 L_e \tag{9}$$

The electromagnetic torque of the motor consists of a constant component (DC) and oscillating components (ripple) expressed as:

$$T_{(t)} = T_{DC} + \sum T_n\, sin(n\omega t + \varphi n)\, T_{(t)} \tag{10}$$

that T_{DC} is the average torque, and T_n are the harmonic components that produce torque ripple. For the various topologies presented in this research, the ripple percentage of the torque is calculated as:

$$Ripple\ Torque\ (\%) = \frac{T_{rms\,AC}}{T_{DC}} \times 100 \tag{11}$$

where $T_{rms\,AC}$ is the effective value of the alternating torque.

According to the above equations, the extractable powers from the two rotors can be examined, based on which the overall geometric dimensions of the two rotors and the stator can be determined.

Comparison of Rotor Structures and Winding Types

A. Comparison of Winding Types for CRDRSM

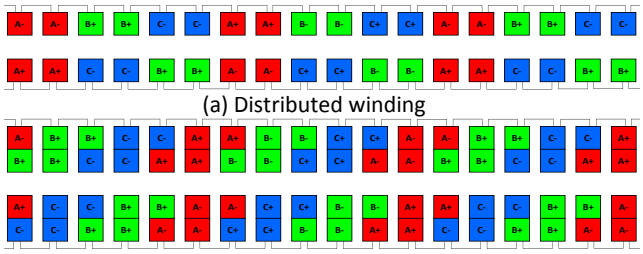
In this section, two types of distributed and fractional-pitch windings for the CRDRSM with an outer PM rotor and an inner reluctance rotor have been designed and evaluated using FEA in ANSYS Maxwell software. The aim of this analysis is to select the most suitable winding type for the proposed CRDRSM based on key performance criteria such as output torque, torque ripple, Total Harmonic Distortion (THD) of no-load voltage, and efficiency, with an emphasis on submarine propulsion applications that require high torque and low noise [5], [15].

I. Design and evaluation of winding types

The two types of winding examined are:

- Distributed winding: The phases of a single-phase winding are distributed across several stator slots, resulting in a more uniform magnetic field and sinusoidal back EMF [33], [34].
- Fractional pitch winding: The number of slots per pole per phase is fractional, which creates a specific distribution of the magnetic field and reduces the cogging torque [33], [35].

The proposed CRDRSM has a 36-slot stator. In Fig. 2, the winding layout of slots 1 to 18 is illustrated for both distributed and fractional-pitch windings. Evidently, the winding pattern of slots 19 to 36 is a periodic repetition of the same arrangement shown in slots 1 to 18. The simulations were conducted using ANSYS Maxwell, and key parameters such as torque, torque ripple, THD, EMF, current, output power, losses, and efficiency were extracted.

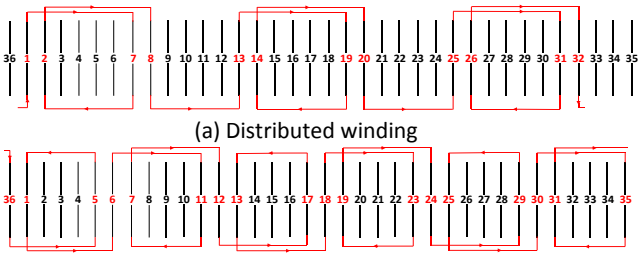


(a) Distributed winding

(b) Fractional-pitch winding

Fig. 2: Comparison of distributed and fractional-pitch winding types for CRDRSM.

Fig. 3 shows the proposed CRDRSM's distributed and fractional pitch winding patterns (for phase A).



(a) Distributed winding

(b) Fractional-pitch winding

Fig. 3: Comparison of phase A winding pattern for distributed and fractional-pitch windings for CRDRSM.

For clarity, the specifications of the distributed and fractional-pitch windings are shown in Table 2.

Table 2: Detailed specifications of distributed and fractional-pitch windings for CRDRSM

Parameters	Distributed	Fractional-pitch
Winding type	Full-pitch	Short-pitch
Layer arrangement	Single-layer	Double-layer
Electrical angle of short pitch	0°	30°
Slots per pole per phase (q)	2	2
Coil pitch (in slots)	6	5
Distribution factor	0.9659	0.9659
Pitch factor	1	0.9659
Winding factor	0.9659	0.9330
Connection type	Y-connected	Y-connected

II. Simulation Results and Optimal Selection

Table 3 compares the simulation results of two types of windings for the proposed CRDRSM. Based on the data in Table 3, Fig. 4 depicts the values of the internal torque, external torque, external torque ripple, and internal torque for distributed winding and fractional-pitch winding.

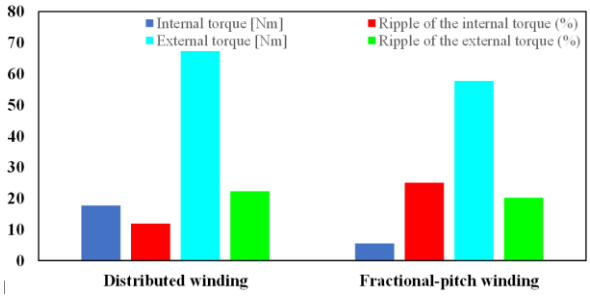


Fig. 4: Torque and torque ripple comparison for the suggested windings. (for internal and external rotors).

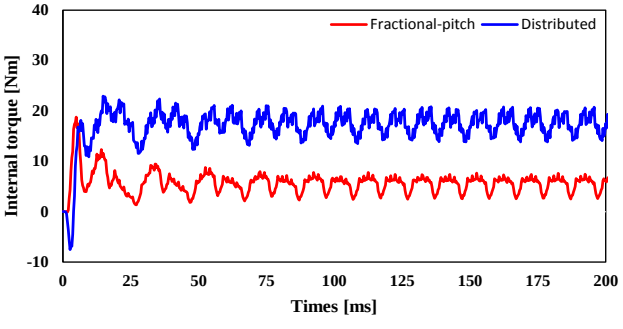
Table 3: Comparison of results for different types of winding

Parameters	Distributed	Fractional-pitch	Unit
Torque $_{Internal}$	17.7	5.54	Nm
Torque $_{External}$	-67.27	-57.7	Nm
Ripple T $_{Internal}$	11.88	25.06	%
Ripple T $_{External}$	22.24	20.19	%
THD V_{NL}	23.29	19.38	%
Harmonic V_{NL}	116.8	112.86	V
EMF_{rms}	193.04	192.37	V
I_{rms}	18.97	17.49	A
$P_{out\text{-}put}$	8.9	6.62	KW
η	87.36	85.55	%

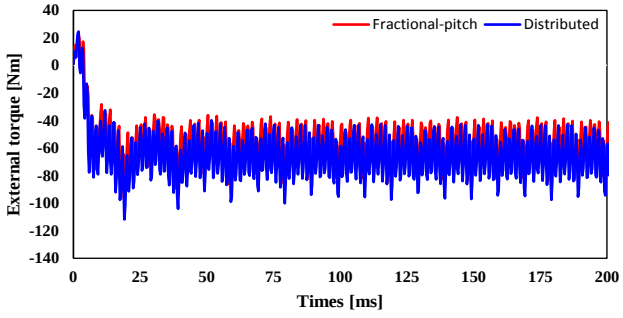
Accordingly, the distributed winding was chosen as the most suitable option for CRDRSM. This selection has been made based on the following key criteria:

- High torque: The distributed winding with an internal torque of 17.7 Nm and the external torque of -67.27 Nm is significantly higher than a fractional pitch winding (internal torque of 5.54 Nm and the external torque of -57.7 Nm), making it suitable for submarine propulsion applications that require high torque [5], [15].
- Low torque ripple: The internal torque ripple (11.88%) in the distributed winding is significantly lower than the internal torque ripple (25.06%) in the fractional pitch winding. Also, the external torque ripple of both windings is close to each other. ensuring smoother operation and reduced acoustic noise, a critical feature for noise-sensitive applications [15].
- Acceptable THD: Although the THD of back EMF in the distributed winding (23.29%) is higher than that of the fractional pitch (19.38%), it improves the overall motor performance due to the production of sinusoidal back EMF [34].
- Balance of efficiency and power: An efficiency of 87.36% in the distributed winding is higher than the fractional pitch winding (85.55%), is justifiable for high-power applications due to the higher torque and lower ripple [34].

For better comparison of the results, the torque versus time curve under transient and steady-state conditions for distributed winding and fractional-pitch winding is shown in Fig. 5.



(a) Internal torque



(b) External torque

Fig. 5: Curve of the torque versus time in transient and steady-state conditions for fractional-pitch and distributed windings.

Distributed winding, by creating a more uniform magnetic field and reducing torque ripple, helps optimize cogging torque in the later stages of CRDRSM design, especially for the outer PM rotor [34]. This feature, along with thermal stability and smooth operation, makes it ideal for underwater applications that require high torque and low noise [5], [15]. Therefore, considering the balance between torque, torque ripple, and stability, the distributed winding was chosen as the best option for the proposed CRDRSM.

B. Optimal Selection of Rotor Structures for CRDRSM

In this section, various combinations of internal rotor (reluctance) and external rotor (PM) for CRDRSM have been designed and evaluated using distributed winding. The goal is to select the optimal structure among the eight proposed combinations using FEA in ANSYS Maxwell software. These combinations include two types of external rotors (surface PM and internal PM or insert) and four types of reluctance internal rotors (ALA, hyperbolic, hyperbolic-line, and concentric-polyline). Fig. 6 shows these eight structures as follows:

- Model A: ALA Reluctance Rotor with Surface PM Rotor.
- Model B: Hyperbolic Reluctance Rotor with Surface PM Rotor.
- Model C: Hyperbolic-Line Reluctance Rotor with Surface PM Rotor.
- Model D: Concentric-Polyline Reluctance Rotor with Surface PM Rotor.
- Model E: ALA Reluctance Rotor with Internal PM Rotor.
- Model F: Hyperbolic Reluctance Rotor with Internal PM Rotor.
- Model G: Hyperbolic-Line Reluctance Rotor with Internal PM Rotor.
- Model H: Concentric-Polyline Reluctance Rotor with Internal PM Rotor.

The lengths of inner and outer air gaps are the same for all models in Fig. 6 (Models A to H), meaning the inner air gap length for all models is one millimeter, and the outer air gap length for all models is two millimeters.

The simulation results for key metrics such as torque, torque ripple, THD of no-load voltage, EMF, current, inductance, output power, losses, and efficiency are presented in Table 4.

This analysis has been conducted with a focus on submarine propulsion applications that require high torque and low noise [5], [15].

Compared to the surface-type PM, the insert-type PM generates a larger air gap for the internal stator winding to produce flux, and consequently, the surface-type PM is favored above the insert-type PM when choosing the optimal model. Because of this, models B and C outperform the other models, as shown in Table 4.

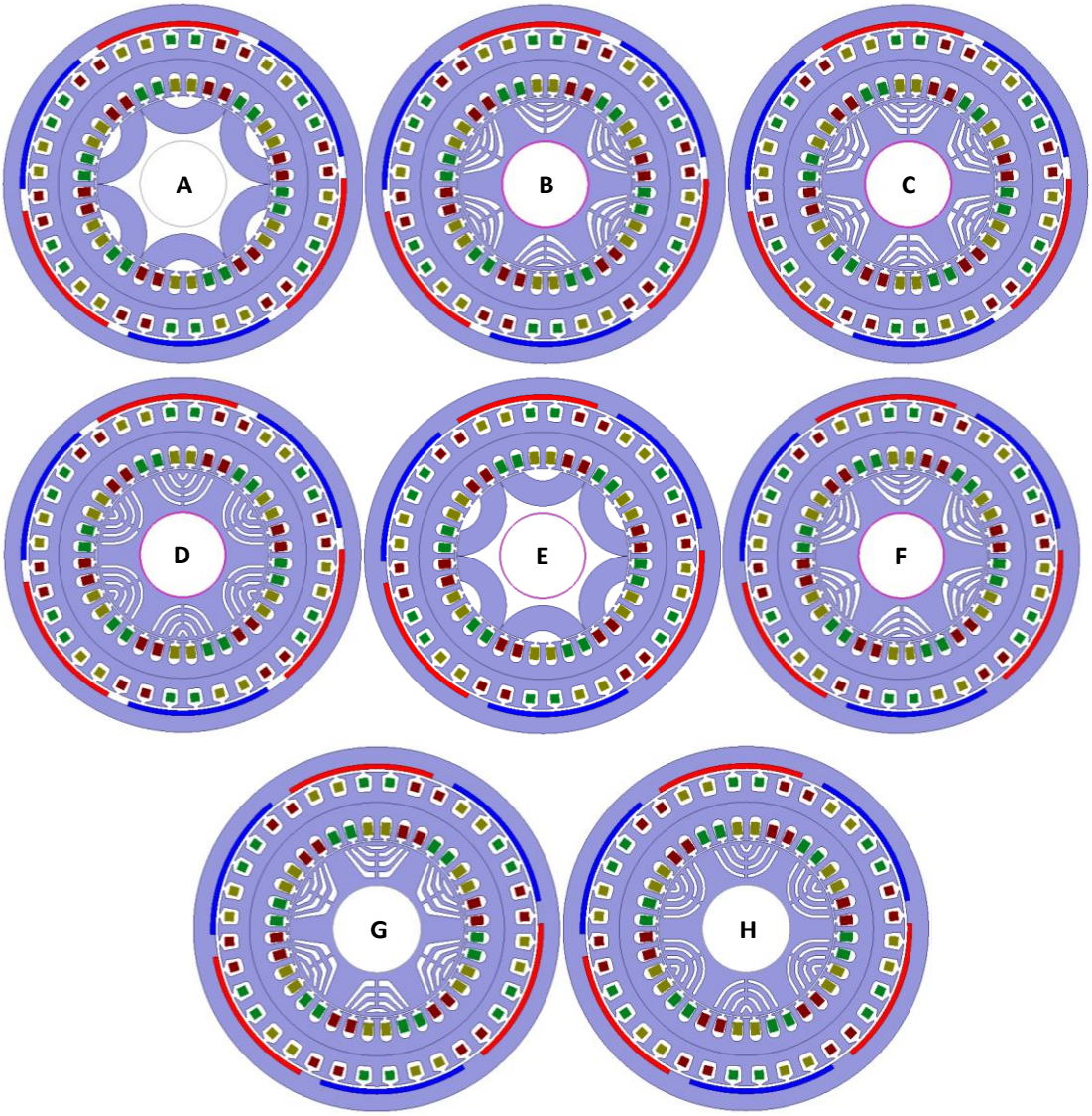


Fig. 6: Comparison of different topologies for a combined dual rotor (Reluctance-PM) counter-rotating motor.

Table 4: Comparison of results obtained from different proposed topologies

Parameters	Model A	Model B	Model C	Model D	Model E	Model F	Model G	Model H	Unit
Cogging $_{Zero\text{-}Peak}$	4.28	4.41	4.41	4.41	3.89	3.38	3.38	3.38	Nm
Torque $_{Internal}$	24.61	17.84	17.7	14.03	23.72	17.45	17.32	13.81	Nm
Torque $_{External}$	-73.92	-67.28	-67.27	-66.59	-74.20	-67.98	-67.97	-66.87	Nm
Ripple T $_{Internal}$	18.84	11.87	11.88	12.73	19.11	12.36	12.37	13.17	%
Ripple T $_{External}$	22.11	22.26	22.24	21.95	28.49	27.75	27.73	26.85	%
THD V_{NL}	19.32	20.2	23.29	20.2	19	18.89	23.83	32	%
Harmonic V_{NL}	114.3	115.8	116.8	116.5	108.4	114.5	95	84.77	V
EMF_{rms}	193.08	193.02	193.04	193.02	202.11	201.9	201.9	201.9	V
I_{rms}	21.88	19	18.97	18.17	21.51	18.84	18.82	18.03	A
$P_{out\text{-}put}$	10.31	8.91	8.9	8.44	10.25	8.94	8.93	8.49	KW
η	86.15	87.3	87.36	87.48	86.8	87.89	87.89	88.24	%

Thus, model C is chosen as the best motor even though the results are close to one another. Based on the information in Table 4, Fig. 7 depicts the values of the internal torque, external torque, external torque ripple, and internal torque ripple of the topologies shown in Fig. 6 (Models A through H).

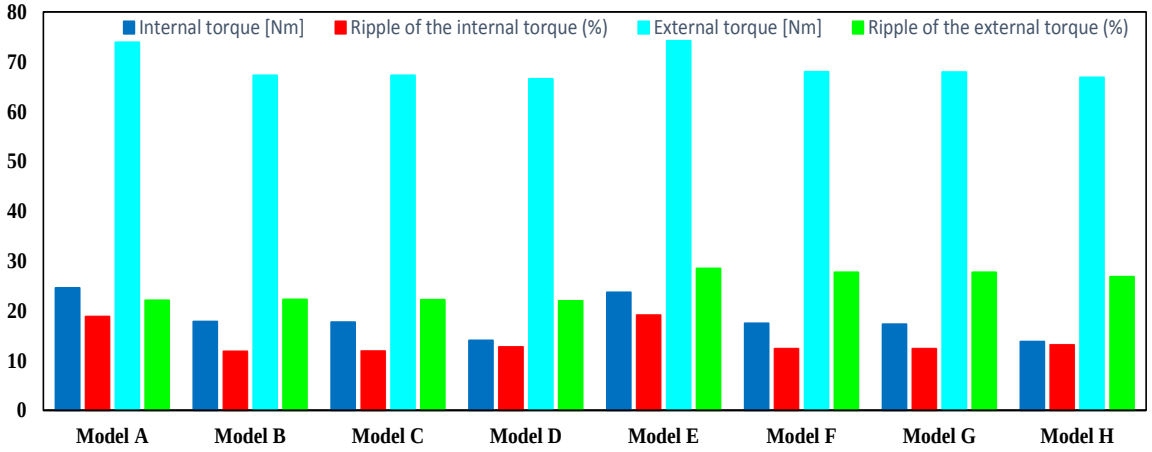


Fig. 7: Torque and torque ripple comparison for various suggested topologies.

The results in Table 4 show that Model B (hyperbolic reluctance rotor with surface PM) and Model C (hyperbolic-line reluctance rotor with surface PM) perform better than the other models. Model C was chosen as the optimal structure due to the following criteria:

- Low torque ripple: Model C, with an internal torque ripple of 11.88% and an external torque ripple of 22.24%, similar to Model B (11.87% and 22.26%), provides smoother performance, which is crucial for noise-sensitive underwater applications [15]. These values are significantly lower than those of models E, F, G, and H (internal ripple 12.36%-19.11% and external ripple 26.85%-28.49%), which is due to the greater air gap in the internal PM rotor [13].
- Balanced torque: Model C provides an internal torque of 17.7 Nm and an external torque of -67.27 Nm, which is similar to Model B but higher than Model D (14.03 and -66.59 Nm) and more balanced than Model A (24.61 and -73.92 Nm), which has a higher ripple (18.84%).
- Acceptable THD: The back EMF THD of model C (23.29%) is slightly higher than that of model B (20.20%), but considering the sinusoidal back EMF of the distributed winding, it is within an acceptable range and ensures stable performance [34]. The hyperbolic-line structure in Model C, with optimal magnetic flux distribution, reduces the primary harmonics of back EMF, which helps improve cogging torque [34].
- Appropriate efficiency: The efficiency of model C (87.36%) is similar to model B (87.30%) and higher than model A (86.15%), which is suitable for underwater applications with an output power of 8.90 kW [5], [15].
- Cogging torque optimization: Model C, with a cogging torque of 4.41 Nm, along with low torque ripple, facilitates the optimization of the cogging torque of the PM outer rotor in the later stages of design [34].

The surface PM rotor in models A to D offers better performance in CRDRSM compared to the internal PM rotor (models E to H) due to the smaller air gap and higher flux density [5]. Model C, with the combination of a hyperbolic-line reluctance rotor and a surface PM, was selected as the best structure for the proposed CRDRSM due to its balance between high torque, low ripple, reduced primary back EMF harmonics, and adequate efficiency. This structure is ideal for submarine propulsion applications that require smooth operation and low noise [5], [15].

Cogging Torque Optimization

As shown in Section 3, Model C (Hyperbolic-Line Reluctance Rotor with Surface PM Rotor) was selected as the optimal structure for CRDRSM due to the balance between high torque, low torque ripple, and adequate efficiency. However, the external torque ripple remains high, primarily due to cogging torque [16]. This section addresses the optimization of the cogging torque of model C using the Taguchi method for applications that require low noise levels [5], [15].

Fig. 8 shows the flowchart of the CRDRSM optimization process. The main objective is to find the optimal design using a combination of comparing winding and different structures, using the Taguchi method, and FEA.

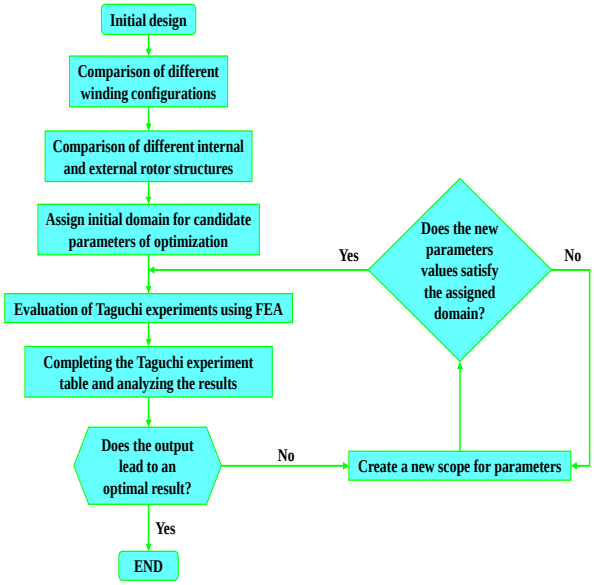


Fig. 8: Flowchart of CRDRSM optimization process.

The Taguchi method for optimizing the cogging torque of model C is applied using a five-level optimization structure. The process involves selecting initial parameters, evaluating results, and adjusting the parameter ranges until the desired outcome is achieved.

The starting point of the process is the initial design of the motor based on the performance specifications. After selecting suitable types of winding and rotor structures for the proposed CRDRSM based on the analyses in section 3, then the effective geometric parameters and their range of variations are determined so that the effect of each parameter on cogging torque can be analyzed through FEA simulation. Finally, the data obtained from the simulation are entered into the Taguchi matrix and processed using statistical methods (such as analysis of variance). If the results do not improve, the previous range must be adjusted, a new range defined, and the Taguchi optimization repeated to achieve optimal results.

A. Determining Optimization Goals and Optimization Factors

Considering the needs of high-torque, low-noise, and efficient drives [5], [15], cogging torque was chosen as the main optimization target, as its reduction directly improves torque ripple and acoustic noise [16]. Four design variables, including the PM arc angle, PM thickness, stator slot opening, and stator tooth width, which significantly affect cogging torque, were selected. These four parameters are shown in Fig. 9.

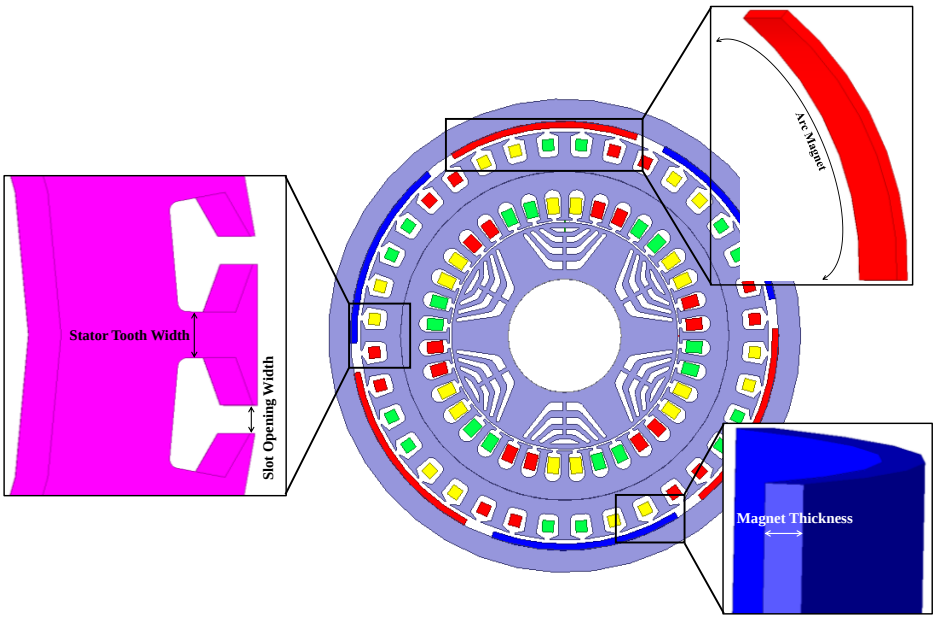


Fig. 9: Optimization parameters in the Taguchi method.

Table 5: Selection range of optimization parameters

Optimization Factor	Symbol	Design range	Range	Unit
Arc Magnet	Arc PM	$0.6 \leq \frac{\alpha_m}{\alpha_p} \leq 0.8$	[47 - 51]	deg
Magnet Thickness	MT	$\frac{B_g \cdot g}{B_r} \leq MT \leq \frac{B_{sat} \cdot g}{B_r}$	[2.9 - 3.7]	mm
Slot Opening Width	SOW	$k_s \cdot \frac{2\pi R_{si}}{N_s}$	[3 - 5]	mm
Stator Tooth Width	STW	$\frac{\Phi}{B_{max} \cdot l_s}$	[4.8 - 6.4]	mm

B. Determining the Optimal Value Range and Level Value of the Optimization Factor

The range of optimization variables was determined using preliminary analyses in ANSYS Maxwell software, as shown in Table 5. Four levels of influence, which are within the range of the optimal value of each factor, are selected. Then, the five levels of values are sorted in ascending order according to the sorting principle and are sequentially named as levels 1, 2, 3, 4, and 5. The values of each level are shown in Table 6.

Table 6: Number of levels for the optimization factor

Symbol	Level 1	Level 2	Level 3	Level 4	Level 5
Arc PM	47	48	49	50	51
MT	2.9	3.1	3.3	3.5	3.7
SOW	3	3.5	4	4.5	5
STW	4.8	5.2	5.6	6	6.4

In Table 5, $\frac{\alpha_m}{\alpha_p}$ is the magnetic arc to pole angle ratio, B_g is the air gap flux density, B_{sat} is the magnet's saturation density, B_r is the magnet's residual flux, and g is the external air gap. N_s is the number of stator slots, $0.2 \leq k_s \leq 0.5$, and R_{si} is the stator yoke's inner radius. l_s is the effective length of the outer stator, B_{max} is the maximum allowable flux density in the tooth, and Φ is the flux flowing through the tooth.

In order to investigate the reduction of cogging torque due to various design variables, each design variable is parameterized in the optimization process, and the four parameters in Table 5 are selected as optimization variables.

The upper and lower bounds are provided according to Table 5; other parameters are fixed. After obtaining the cogging torque values in different models, the minimum values are selected to plot the trend of cogging torque changes with the parameters, and the optimal parameters are simulated in Maxwell for verification. If the optimal effect meets expectations, the optimization is complete. If the effect is not as expected, it is necessary to adjust the upper and lower limits of the parameters to optimize them.

In Table 7, in the columns of the experimental matrix, L_1 to L_5 refer to the Level 1 to Level 5 optimization coefficients specified in Table 6.

Considering four optimization factors (according to Table 5) and determining five levels for each optimization factor (according to Table 6), the orthogonal experiment table is designed as shown in Table 7.

Thus, to achieve motor optimization, only 25 tests (5^2=25) are needed, as the Taguchi method with the orthogonal table reduces the number of tests from 5^4=625 tests to 25 tests, significantly decreasing computation time [28], [29], [31].

Table 7: Orthogonal table and finite element simulation results

	Experimental matrix				Optimization Factor				Goals			
Exp. Num	Arc PM	SOW	MT	STW	Arc PM (deg)	SOW (mm)	MT (mm)	STW (mm)	Cogging zero-peak (Nm)	EMF(V)	THD (%)	P_{out} (KW)
1	L_1	L_1	L_1	L_1	47	3	2.9	4.8	11.12	225.64	21.97	8.21
2	L_1	L_2	L_2	L_2	47	3.5	3.1	5.2	10.94	220.19	21.92	8.49
3	L_1	L_3	L_3	L_3	47	4	3.3	5.6	11.08	216.08	21.91	8.76
4	L_1	L_4	L_4	L_4	47	4.5	3.5	6	11.94	212.78	21.91	8.75
5	L_1	L_5	L_5	L_5	47	5	3.7	6.4	13.3	210.63	21.93	8.82
6	L_2	L_1	L_2	L_3	48	3	3.1	5.6	4.3	209.48	21.75	8.91
7	L_2	L_2	L_3	L_4	48	3.5	3.3	6	7.85	209.88	20.15	8.78
8	L_2	L_3	L_4	L_5	48	4	3.5	6.4	9.04	207.54	20.15	8.86
9	L_2	L_4	L_5	L_1	48	4.5	3.7	4.8	12.78	215.63	21.83	8.95
10	L_2	L_5	L_1	L_2	48	5	2.9	5.2	13.22	223.16	21.82	8.69
11	L_3	L_1	L_3	L_5	49	3	3.3	6.4	5.25	204.33	20.24	8.85
12	L_3	L_2	L_4	L_1	49	3.5	3.5	4.8	6.27	212.69	20.31	8.93
13	L_3	L_3	L_5	L_2	49	4	3.7	5.2	8.63	207.06	20.28	9
14	L_3	L_4	L_1	L_3	49	4.5	2.9	5.6	11.15	214.91	20.27	8.57
15	L_3	L_5	L_2	L_4	49	5	3.1	6	12.64	212.6	20.26	8.78
16	L_4	L_1	L_4	L_2	50	3	3.5	5.2	3.31	203.53	18.79	8.92
17	L_4	L_2	L_5	L_3	50	3.5	3.7	5.6	5.15	199.93	18.77	8.94
18	L_4	L_3	L_1	L_4	50	4	2.9	6	6.18	207.97	18.78	8.68
19	L_4	L_4	L_2	L_5	50	4.5	3.1	6.4	7.52	206.31	18.77	8.82
20	L_4	L_5	L_3	L_1	50	5	3.3	4.8	7.34	215.07	18.85	8.93
21	L_5	L_1	L_5	L_4	51	3	3.7	6	1.69	194.14	18.87	8.81
22	L_5	L_2	L_1	L_5	51	3.5	2.9	6.4	1.71	201.98	18.87	8.7
23	L_5	L_3	L_2	L_1	51	4	3.1	4.8	3.6	210.6	18.92	8.84
24	L_5	L_4	L_3	L_2	51	4.5	3.3	5.2	2.34	205.67	18.91	8.97
25	L_5	L_5	L_4	L_3	51	5	3.5	5.6	2.23	202.52	18.9	8.96

C. Optimization Process and Result Analysis

Using the orthogonal table, 25 motor models were simulated in ANSYS Maxwell, and the cogging torque (zero to peak) for each combination was calculated (Table 7). The results were evaluated using the signal-to-noise ratio (SNR) and mean analysis [31]:

$$A = \frac{1}{n}\sum_{i=1}^{n} S_i \quad (12)$$

In (12), A is the average result of each optimization objective; n is the number of trials, n=25 in this article; and S_i is the i-th optimization objective value. (i is one of 1-25) [29].

Based on the analysis of the data in Table 7, and with the objective function being the reduction of cogging torque, the signal/noise ratio index is calculated using the Taguchi method so that lower values are preferred. The level with the highest average signal/noise ratio is selected as the optimal level for the objective function, as this level leads to the lowest value under noisy conditions with the highest stability. In addition to reducing the complexity of experiments, the Taguchi method increases the accuracy and stability of the optimization process and reduces the system's sensitivity to unwanted changes.

The Taguchi method establishes an optimal balance between all criteria by analyzing the signal/noise ratio and the average effect of each parameter and provides the optimal model through a systematic approach [26], [27].

The final best combination of motor main parameters and the comparison results of performance indexes before and after optimization are shown in Table 9 and Table 10.

The results in Table 10 show that the cogging torque has improved from 4.41 Nm to 1.66 Nm (a reduction of 62.36%), which is consistent with the impact of the optimized variables (Arc PM, SOW, MT, STW) [16]-[18].

Table 8: Average results for each optimization objective

-	Cogging $_{zero\text{-}peak}$	EMF	THD	P_{out}
A	7.62 Nm	210.01 V	20.2 %	8.8 KW

Table 9: Optimization factor parameters before and after optimization

Parameter	Arc PM	SOW	MT	STW
Before optimization	52 deg	3 mm	3.4 mm	6.4 mm
After optimization	51 deg	3 mm	3.3 mm	5.6 mm

Table 10: Comparison of various performance indexes before and after optimization

Parameter	Before optimization	After optimization	Unit
Cogging $_{zero\text{-}peak}$	4.41	1.66	Nm
Ripple Torque $_{Internal}$	11.88	10.16	%
$P_{out\text{-}put}$	8.9	8.94	KW
THD Voltage $_{NL}$	23.29	18.39	%
EMF $_{rms}$	193.04	199.69	V
$\boldsymbol{\eta}$	87.36	88.27	%

The THD of the back EMF decreased from 23.29% to 18.39%, indicating an improvement in the back EMF harmonics due to the optimal flux distribution in the hyperbolic-line structure [18]. The internal torque ripple (10.16%), output power (8.94 kW), and efficiency (88.27%) also improved, which aligns with the requirements of submarine drives (low noise, high torque) [5], [15]. These results confirm the effectiveness of the Taguchi method in reducing cogging torque while maintaining the overall performance of the motor [28], [29], [31].

Simulation Results Analysis

In this section, the performance characteristics of the optimized model C for CRDRSM have been evaluated using two-dimensional FEA in ANSYS Maxwell software. The simulation results for the inner and outer rotors have been presented to confirm the performance of the optimized model C as the best choice [5], [15].

A. Magnetic Flux Density Distributions

The distribution of magnetic flux density of the proposed motor under nominal current at six different rotor positions is shown in Fig. 10.

The maximum flux density occurs at the inner poles of the stator and reaches 2.05 Tesla. No part of the stator or rotor iron layers reaches full saturation under nominal current, indicating the appropriate design of the magnetic structure to maintain stable performance [5], [18].

B. Air Gap Flux Density Analysis

Fig. 11 shows the comparative curves of air gap flux density for internal and external air gaps against rotor position.

It can be observed that the air gap flux density of the proposed PMSM is higher than that of the SRM. This increase in flux density is due to the use of PM in the outer rotor, which optimizes the flux distribution. This indicates the higher average torque potential of PMSM compared to SRM.

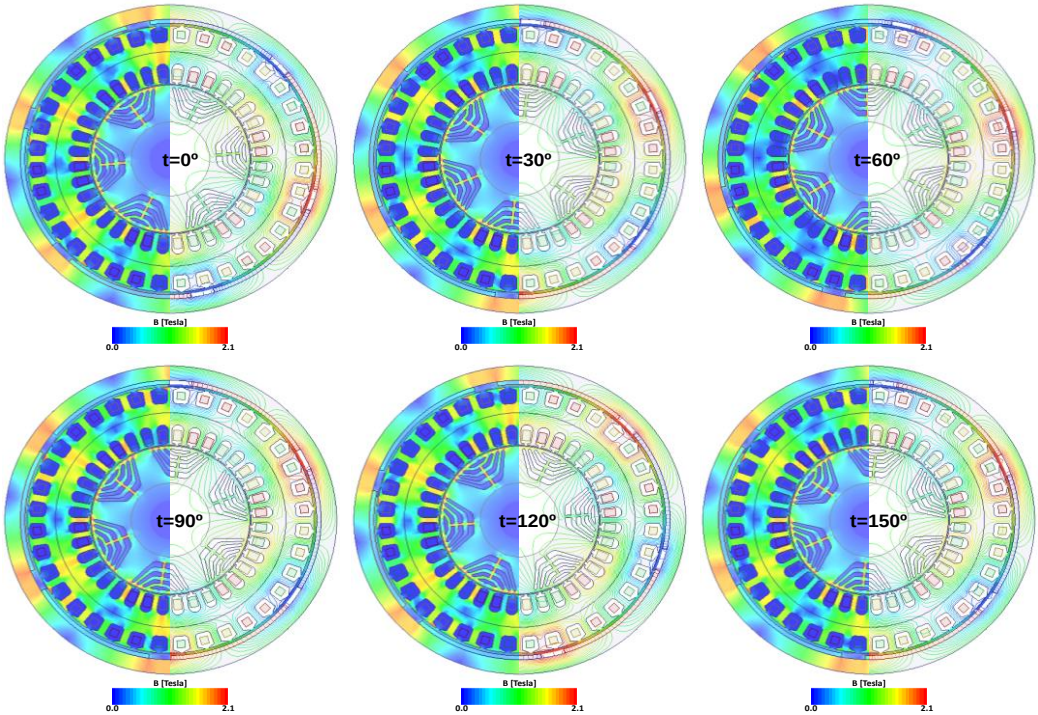
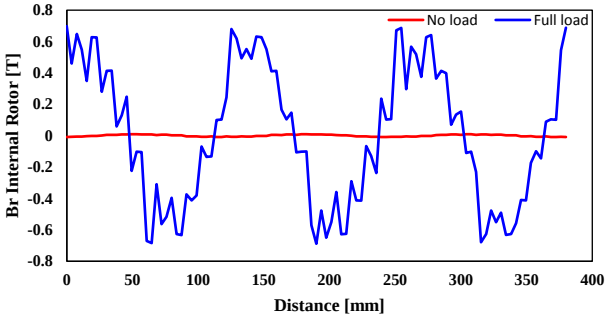
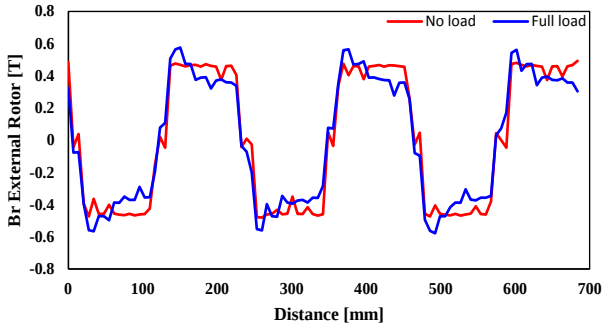


Fig. 10: Magnetic flux density and flux lines distributions of CRDRSM under current.



(a) Internal air gap



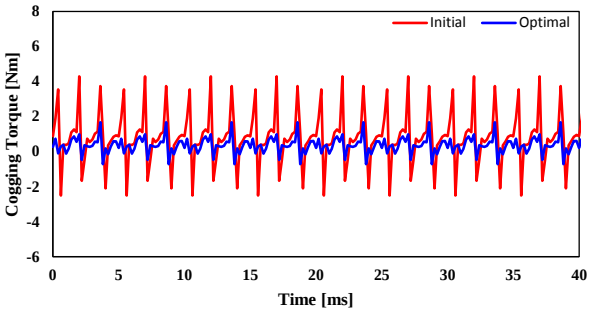
(b) External air gap

Fig. 11: Comparison of the air-gap flux densities for CRDRSM.

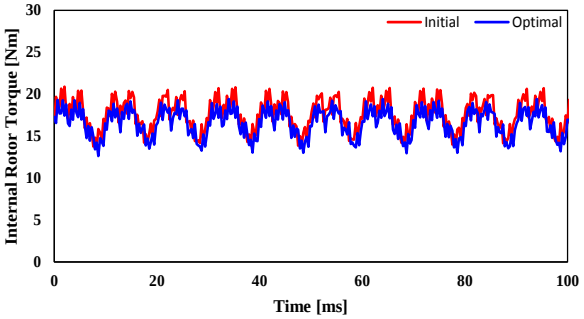
C. Output Torque Analysis

Fig. 12(a) shows the cogging torque curves versus time for the initial and optimized models, and Fig. 12(b) shows the output torque due to the inner rotor versus time. It is seen that by optimal selection of parameters Arc PM, SOW, MT, and STW, the cogging torque has been much decreased, with negligible effect on the value of internal rotor torque.

It can be observed that the torque difference between the two structures occurs near the rotor alignment position. This is because the air gap reluctances near the aligned positions of the rotors are smaller than the reluctances near the non-aligned positions of the rotors. Therefore, the PM flux near the aligned positions closes its path through the air gaps, increasing the air gap flux density and the output torque.



(a) Cogging torque



(b) Internal rotor torque

Fig. 12: Comparison of initial and optimal models for CRDRSM.

D. Comparison between the Initial Model and the Optimal Model

To evaluate the performance of the optimized model C, a comparison was made between the initial and optimal models based on key indicators. To ensure a fair comparison, the rated power, outer diameter, air gap length, and steel material were kept the same in both models. The comparison indices include cogging torque, average torque, torque ripple, RMS and THD of back EMF, RMS of phase current, output power, losses, and efficiency. The results are presented in Table 11.

Table 11: Comparison of the initial and the optimal models

Model	Initial	Optimal	Unit
Arc PM	52	51	Deg
SOW	3	3	mm
MT	3.4	3.3	mm
STW	6.4	5.6	mm
Cogging $_{zero\text{-}peak}$	4.41	1.66	Nm
Torque $_{Internal}$	17.7	16.55	Nm
Ripple Torque $_{Internal}$	11.88	10.16	%
Torque $_{External}$	-67.27	-68.91	Nm
Ripple Torque $_{External}$	22.24	26.04	%
First Harmonic $_{NL}$	116.8	102.81	V
THD Voltage $_{NL}$	23.29	18.39	%
EMF_{rms}	193.04	199.69	V
I_{rms}	18.97	19.42	A
$P_{out\text{-}put}$	8.9	8.94	KW
η	87.36	88.27	%

Analysis of results:

- Cogging torque: The reduction from 4.41 to 1.66 Nm (62.36%) indicates a significant improvement due to the optimization of design variables [16]-[18].
- Internal and external torque: The internal torque has slightly decreased (from 17.7 to 16.55 Nm), but the external torque has improved (from -67.27 to -68.91 Nm), which is consistent with the increase in air gap flux density [5].
- Torque ripple: The internal torque ripple has decreased from 11.88% to 10.16%, but the external torque ripple has increased from 22.24% to 26.04%. This increase may be due to changes in SOW and STW, which require further investigation [16].
- THD and EMF: The reduction in THD of back EMF (from 23.29% to 18.39%) and the increase in RMS of back EMF (from 193.04 to 199.69 volts) indicate an improvement in Back-EMF harmonics due to the Hyperbolic-Line structure [18].
- Efficiency and output power: The increase in efficiency (from 87.36% to 88.27%) and output power (from 8.90 to 8.94 kilowatts) is consistent with the requirements of submarines (low noise, high torque) [5], [15].
- Losses and current: A slight increase in RMS of current (from 18.97 to 19.42 amperes) is acceptable due to the improvement in torque and output power [5].

The optimized motor's output waveforms (cogging torque, stator current, output torque, and back-EMF) are displayed in Fig. 13. As shown in Fig. 13(a), the internal and external rotors generate steady average torques with opposite directions, confirming the intended counter-rotating operation. Compared with the initial design, the internal torque slightly decreases, whereas the external torque increases, which is consistent with the enhanced air-gap flux density and improved electromagnetic coupling in the optimized structure. Although the external rotor exhibits higher torque ripple due to its larger effective radius and slot–magnet interaction, the overall torque production remains stable and suitable for high-torque applications. Fig. 13(b) presents the cogging torque waveform of the optimized model. A significant reduction in cogging torque is achieved. This improvement is mainly attributed to the optimization of stator and rotor geometrical parameters, which effectively mitigates slotting effects and magnetic reluctance variation. The reduced cogging torque is particularly advantageous for low-noise and low-vibration operating conditions, such as underwater propulsion systems. The three-phase back-EMF waveforms shown in Fig. 13(c) exhibit good symmetry and a sinusoidal shape with a 120° phase displacement, indicating balanced electromagnetic behavior. Results demonstrate an improvement in back-EMF harmonic quality, which can be attributed to the optimized rotor geometry and the hyperbolic-line structure that smooths the air-gap flux distribution. Fig. 13(d) shows the stator current waveforms under rated operating conditions. The phase currents are balanced and sinusoidal, indicating stable machine operation and proper electromagnetic design. No noticeable current distortion is observed, confirming that the optimized design does not introduce adverse electromagnetic effects. As a result, the suggested PMSM generates more torque than the suggested SRM. Actually, the suggested motor builds an effective structure that provides optimal performance and high torque. The optimum option for the suggested CRDRSM in underwater applications is the optimized model C because of its low cogging torque, high efficiency, and appropriate torque [5], [12], [15], [36].

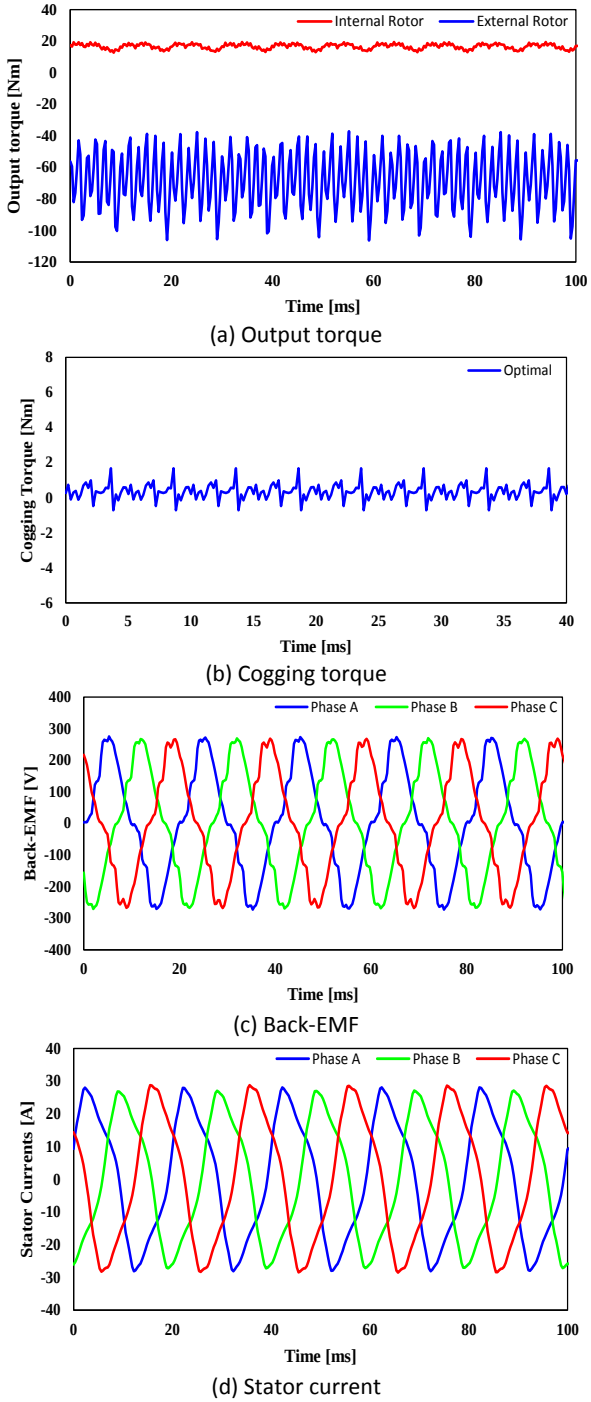


Fig. 13: Specifications of the optimal model for CRDRSM.

Conclusion

In this study, a CRDRSM is proposed that uses a common stator configuration, an external PM rotor, and an internal reluctance rotor. Based on FEA simulations, it was shown that the distributed winding provides the best result among all the examined windings. Then, using the distributed winding and with the aim of selecting the optimal structure among the proposed topologies, the combination of the inner rotor (reluctance) and the outer rotor (PM) for the proposed CRDRSM was designed and evaluated. The results showed that Model C, with the combination of the hyperbolic-line reluctance rotor and the surface PM, was chosen as the best structure for the CRDRSM. Model C is ideal for submarine propulsion applications that require smooth operation and low noise due to its balance between high torque, low ripple, reduced primary back-EMF harmonics, and adequate efficiency. To reduce cogging torque, which is the main factor causing torque ripple and acoustic noise, the optimization of the motor's geometric dimensions was carried out using the Taguchi method combined with FEA. After optimization, the cogging torque was reduced by 62.36% from 4.41 Nm to 1.66 Nm due to the optimization of design variables. Additionally, the ripple torque of the inner rotor and the THD of back EMF were reduced, and the output power and efficiency of the proposed motor were increased, which aligns with the requirements for submarines (low noise, high torque). Additionally, the electromagnetic performance of the proposed motor (CRDRSM) in terms of flux densities, output torques, and cogging torque was confirmed.

Author Contributions

P. Nadri carried out the design, modeling, simulation and writing. B. Rezaeealam performed the conceptualization, supervision and writing. M. Mikhak-Beyranvand investigated the results.

Acknowledgment

We gratefully acknowledge the editorial team of JECEI and the referees who helped the authors in publishing this article.

Conflict of Interest

The authors declare no potential conflict of interest regarding the publication of this work. In addition, the ethical issues, including plagiarism, informed consent, misconduct, data fabrication and/or falsification, double publication and, or submission, and redundancy, have been completely witnessed by the authors.

Funding

This research received no external funding.

Abbreviations

CRDRSM	Counter-Rotating Dual-Rotor Synchronous Motor
PM	Permanent Magnet
FEA	Finite Element Analysis
PMSM	Permanent Magnet Synchronous Motor
SRM	Switched Reluctance Motor
EMF	Electromotive Force
SynRM	Synchronous Reluctance Motor

THD	Total Harmonic Distortion
SOW	Slot Opening Width
MT	Magnet Thickness
STW	Stator Tooth Width

References

[1] W. Ullah, F. Khan, U. B. Akuru, B. Khan, S. A. Khalil, "Evaluation of counter-rotating dual-rotor permanent-magnet flux-switching machine with series and parallel stator teeth," Machines, 11(11): 989, 2023.

[2] B. Virlan, A. Munteanu, L. Livadaru, A. Bobu, I. Nacu, A. Simion, "Dual rotor radial flux concentrated wound permanent magnet synchronous machine with high power density," Adv. Electr. Comput. Eng., 23(4): 41-50, 2023.

[3] T. Zou, D. Li, R. Qu, J. Li, D. Jiang, "Analysis of a dual-rotor, toroidal-winding, axial-flux vernier permanent magnet machine," IEEE Trans. Ind. Appl., 53(3): 1920-1930, 2017.

[4] W. Ullah, F. Khan, U. B. Akuru, M. Yousuf, "Magnetic coupling effect and performance analysis of dual rotor permanent magnet flux switching generator for counter rotating wind power generation," IEEE Trans. Energy Convers., 38(4): 2895-2908, 2023.

[5] G. Liu, G. Qiu, J. Shi, F. Zhang, "Study on counter-rotating dual-rotor permanent magnet motor for underwater vehicle propulsion," IEEE Trans. Appl. Supercond., 28(3): 1-5, 2018.

[6] F. Kutt, K. Blecharz, D. Karkosiński, "Axial-flux permanent-magnet dual-rotor generator for a counter-rotating wind turbine," Energies, 13(11): 2833, 2020.

[7] M. Yang, Z. Zhong, Q. Wang, Z. Shao, "An analytical model for stator yokeless radial flux dual rotor permanent magnet synchronous machine," COMPEL-The Int. J. Comput. Math. Electr. Electron. Eng., 41(5): 1920-1939, 2022.

[8] H. Ouldhamrane, J. F. Charpentier, F. Khoucha, A. Zaoui, Y. Achour, M. Benbouzid, "Optimal design of axial flux permanent magnet motors for ship RIM-driven thruster," Machines, 10(10): 932, 2022.

[9] A. Ghayth, M. Şimşir, "Recent trends and challenges of electric motor technologies," Int. J. Electr. Eng. Sustain., 1(2): 21-28, 2023.

[10] L. Ananda Padmanaban, P. Saravanan, "Design, analysis and comparison of switched reluctance motors for electric vehicle application," Automatika: časopis za automatiku, mjerenje, elektroniku, računarstvo i komunikacije, 64(2): 239-247, 2023.

[11] W. S. Jung, H. K. Lee, Y. K. Lee, S. M. Kim, J. I. Lee, J. Y. Choi, "Analysis and comparison of permanent magnet synchronous motors according to rotor type under the same design specifications," Energies, 16(3): 1306, 2023.

[12] X. Kong, Y. Zhang, G. Xu, "Optimal design and control of permanent magnet assisted dual rotor motor," Front. Energy Res., 11: 1240473, 2023.

[13] C. Babetto, G. Bacco, N. Bianchi, "Synchronous reluctance machine optimization for high-speed applications," IEEE Trans. Energy Convers., 33(3): 1266-1273, 2018.

[14] T. Guo, N. Schofield, A. Emadi, "Double-rotor switched reluctance machine with segmented rotors," ed: Google Patents, 2019.

[15] B. Cheng, S. Pang, H. Ou, Z. Hu, Z. Mao, "Comparative research on topologies of contra-rotating motors for underwater vehicles," J. Mar. Sci. Eng., 11(11): 2042, 2023.

[16] W. Tong, S. Li, X. Pan, S. Wu, R. Tang, "Analytical model for cogging torque calculation in surface-mounted permanent magnet motors with rotor eccentricity and magnet defects," IEEE Trans. Energy Convers., 35(4): 2191-2200, 2020.

[17] A. Patel, "Slot opening displacement technique for cogging torque reduction of axial flux brushless DC motor for electric two-wheeler application," Electr. Eng. Electromech., (2): 7-13, 2023.

[18] Y. J. Won et al., "Transfer learning-based design method for cogging torque reduction in PMSM with step-skew considering 3-D leakage flux," IEEE Trans. Magn., 59(11): 1-5, 2023.

[19] J. Wu, X. Zhu, Z. Xiang, D. Fan, L. Quan, L. Xu, "Robust optimization of a rare-earth-reduced high-torque-density PM motor for electric vehicles based on parameter sensitivity region," IEEE Trans. Veh. Technol., 71(10): 10269-10279, 2022.

[20] M. Vatani, A. Ghaffarpour, M. A. Jalali Kondelaji, M. Mirsalim, "Study of a modular toothed linear hybrid reluctance motor with permanent magnets in translator slots," IEEE Trans. Transport. Electrif., 8(3): 3554-3567, 2022.

[21] Y. Shimizu, S. Morimoto, M. Sanada, Y. Inoue, "Automatic design system with generative adversarial network and convolutional neural network for optimization design of interior permanent magnet synchronous motor," IEEE Trans. Energy Convers., 38(1): 724-734, 2022.

[22] K. S. Kim, B. H. Lee, "Taguchi robust design for the multi-response considering the manufacturing tolerance used in high-speed air blower motor," IET Electr. Power Appl., 14(7): 1141-1147, 2020.

[23] D. Xiang, Z.Q. Zhu, D. Liang, L. Mao, X. Qiu, S. Li, L. Zheng, "Taguchi-Based pre-process strategy for fast evaluating worst-case cogging torque due to PM tolerance interactions," IEEE Trans. Transport. Electrif., 11(1): 4097-4110, 2024.

[24] X. Kong, Z. Yang, "Multi-objective optimization of dual-stator permanent magnet motor based on composite algorithm," Sci. Rep., 15(1): 22982, 2025.

[25] M. A. Khioon, K. A. Hubeatir, M. M. AL-Khafaji, "Parametric optimization of laser conduction welding between stainless steel 316 and polyethylene terephthalate using taguchi method," Eng. Technol. J., 40(12): 1642-1649, 2022.

[26] A. Freddi, M. Salmon, "Introduction to the taguchi method," in Design principles and methodologies: from conceptualization to first prototyping with examples and case studies: Springer, 159-180, 2018.

[27] R. Davis, P. John, "Application of taguchi-based design of experiments for Industrial Chemical Processes,"in Statistical Approaches With Emphasis on Design of Experiments Applied to Chemical Processes. InTech, 137, 2018.

[28] P. Nadri, M. R. Besmi, "Design and optimization of permanent magnet flux-switching generator arrangement spoke by taguchi method for direct-drive wind turbines," AUT J. Electr. Eng., 56(1): 113-124, 2024.

[29] C. Qu, Z. Guo, Y. Hu, X. Wang, F. Han, "Multi-objective optimization design of a new permanent magnet synchronous motor based on the Taguchi method," Energies, 15(19): 7347, 2022.

[30] Y. Yu et al., "Multi objective optimization of permanent magnet synchronous motor based on taguchi method and PSO algorithm," Energies, 16(1): 267, 2022.

[31] S. R. Karimpour, M. R. Besmi, S. M. Mirimani, "Optimal design and verification of interior permanent magnet synchronous generator based on FEA and Taguchi method," Int. Trans. Electr. Energy Syst., 30(11): 12597, 2020.

[32] J. F. Gieras, Permanent magnet motor technology: design and applications. CRC press, 2009.

[33] H. Qiu, Y. Zhang, C. Yang, R. Yi, "Performance analysis and comparison of PMSM with concentrated winding and distributed winding," Archives Electr. Eng., 69(2): 303-317, 2020.

[34] Z. Azar, Z. Zhu, "Performance analysis of synchronous reluctance machines having nonoverlapping concentrated winding and

sinusoidal bipolar with DC bias excitation," IEEE Trans. Ind. Appl., 50(5): 3346-3356, 2014.

[35] A. EL-Refaie, M. Shah, "Induction machine performance with fractional-slot concentrated windings," COMPEL- Int. J. Comput. Math. Electri.Electron. Eng., 31(1): 119-139, 2011.

[36] A. Ghaffarpour, M. Mirsalim, "Split-tooth double-rotor permanent magnet switched reluctance motor," IEEE Trans. Transport. Electrif., 8(2): 2400-2411, 2022.

Biographies



Pouria Nadri received the B.Sc. degree in electrical engineering from Lorestan University, Khorramabad, Iran, in 2020, and the M.Sc. degree in electrical engineering from Shahed University, Tehran, Iran, in 2022. He is currently a Ph.D. candidate in electrical engineering at Lorestan University, Khorramabad, Iran. His research interests include design, optimization and analysis of electrical machines, power electronics, modeling and design using FEM, and electromagnetic modeling.

- Email: nadri.po@fe.lu.ac.ir
- ORCID: 0000-0002-8547-4007
- Web of Science Researcher ID: N/A
- Scopus Author ID: 59557771400
- Homepage: N/A



Behrooz Rezaeealam received the B.S. degree from Isfahan University of Technology in 1997, the M.S. and Ph.D. degrees from University of Tehran in 2000 and 2005, respectively, all in electrical engineering. He is currently an associate professor in the department of electrical engineering, Lorestan University, Iran. His research interests include modeling and design using FEM, electrical machines and drives.

- Email: rezaee.bh@lu.ac.ir
- ORCID: 0000-0002-9391-4826
- Web of Science Researcher ID: N/A
- Scopus Author ID: 9742086900
- Homepage: N/A



Morteza Mikhak-Beyranvand received the B.Sc. degree in Electrical Engineering from Hadaf University, Iran, in 2010, the M.Sc. degree in Electrical Engineering from Malek-Ashtar University of Technology, Iran, in 2013, and the Ph.D. degree in Electrical Engineering from Lorestan University, Iran, in 2019. He is currently an Assistant Professor with the Department of Electrical Engineering, Technical and Vocational University (TVU), Iran. His research interests include the design and analysis of electrical machines, power electronics, and electromagnetic–thermal modeling of power transformers. Recently, he has also started research and studies in the field of batteries, particularly battery lifetime estimation.

- Email: mbeyranvand@tvu.ac.ir
- ORCID: 0000-0002-5411-9918
- Web of Science Researcher ID: N/A
- Scopus Author ID: 57209781633
- Homepage: N/A

Journal of Electrical and Computer Engineering Innovations
(JECEI)
Journal homepage: http://www.jecei.sru.ac.ir

Research paper

Deep Learning Attention-Based Framework for Integrating EEG and Image Information in Visual Content Recognition

Hamed Hakak, *Mohammad Mahdi Khalilzadeh**, *Mahdi Azarnoosh*, *Hamidreza Kobravi*

Department of Biomedical Engineering, Ma.C., Islamic Azad University, Mashhad, Iran.

Article Info

Article History:
Received 23 January 2026
Reviewed 15 April 2026
Revised 12 May 2026
Accepted 26 May 2026

Keywords:
EEG–image fusion
attention-based deep learning
multiclass visual content classification
hierarchical attention mechanism
RNN-CNN

*Corresponding Author's Email Address:
mmkhalilzadeh@iau.ac.ir

Abstract

Background and Objectives: While deep learning has significantly advanced visual content recognition, existing models primarily rely on image data alone, neglecting the rich cognitive context embedded in neural responses. This study aimed to develop and validate a novel framework that synergistically integrates electroencephalography (EEG) signals with visual features to achieve superior accuracy in multiclass image recognition.

Methods: We designed a hierarchical attention-based deep learning architecture to fuse neural and visual information. EEG data recorded (the dataset newly developed by the authors) during visual stimulus presentation were preprocessed and analyzed using temporal models (RNN-CNN and LSTM) to extract neural features. Concurrently, visual features were extracted from the stimulus images using ResNet101 and DenseNet201 architectures. The proposed attention mechanism dynamically weighted and integrated these multimodal features, prioritizing the most salient information from each modality.

Results: The proposed framework significantly outperformed conventional unimodal approaches. The hybrid RNN-CNN + ResNet101 model achieved a peak classification accuracy. A feature contribution analysis revealed that the optimal performance was attained through an integrated contribution of approximately 60% from image-derived features and 40% from EEG-derived features, demonstrating the critical complementary value of neural data.

Conclusion: This study confirms that the structured, attention-based fusion of neurophysiological and visual data substantially enhances visual content recognition. The findings provide a robust and effective framework for advanced cognitive assessment applications and establish a new benchmark for multimodal integration in machine learning, highlighting the significant potential of EEG data to complement and improve computer vision tasks.

This work is distributed under the CC BY license (http://creativecommons.org/licenses/by/4.0/)

How to cite this paper:
H. Hakak, M. M. Khalilzadeh, M. Azarnoosh, H. Kobravi, "Deep learning attention-based framework for integrating EEG and image information in visual content recognition," J. Electr. Comput. Eng. Innovations, 14(2): 565-582, 2026.

DOI: 10.22061/jecei.2026.12557.890

URL: https://jecei.sru.ac.ir/article_12572.html

2345- 3044/© 2026 The Authors. Published by Shahid Rajaee Teacher Training University.

Introduction

In recent years, the integration of EEG with visual content analysis has emerged as a dynamic interdisciplinary field, bridging neuroscience, computer vision, and deep learning. Despite its inherent noise and limited spatial resolution, EEG offers temporally precise insights into the brain's cognitive responses to visual stimuli, making it a powerful tool for studying perceptual processes [1], [2]. In contrast, visual images provide rich semantic and structural information, enabling high classification performance when processed independently. The synergistic combination of neurophysiological and visual data holds significant potential to enhance both the accuracy and robustness of visual content recognition systems [3], [4].

However, achieving effective multimodal fusion of EEG and image data remains challenging. Many prior approaches have relied on single-modality processing or employed simplistic fusion strategies that fail to capture the intricate interplay between neural signals and visual features [5], [6]. Additionally, conventional attention-based models in this domain have often been limited to non-hierarchical architectures, which restrict their ability to dynamically weigh multilevel feature representations [7].

While previous studies have recognized the potential of EEG-image fusion, they have often fallen short in achieving a truly synergistic integration. Common approaches suffer from distinct shortcomings: (1) Naïve fusion strategies, such as simple feature concatenation or late decision averaging [5], [6], fail to model the complex, non-linear interactions between modalities, often allowing the dominant or less noisy modality (typically vision) to overshadow the complementary neural signal. (2) Non-hierarchical attention models [7] applied to fused feature vectors lack the granularity to first filter noise and select salient features within each modality before cross-modal integration, limiting their ability to handle EEG's inherent non-stationarity and noise. Consequently, prior work has largely been unable to dynamically calibrate the contribution of each modality or provide a biologically plausible fusion mechanism. Our proposed hierarchical attention-based framework directly addresses these gaps. It introduces a dedicated intra-modality attention stage to purify EEG and image features individually, followed by a cross-modality attention stage for adaptive fusion. This two-stage process explicitly enables the model to suppress irrelevant noise, prioritize the most discriminative elements from each stream, and learn an optimal, context-dependent balance—addressing the core limitations of earlier simplistic or flat fusion architectures.

To address these limitations, this study proposes a novel hierarchical attention-based deep learning framework that integrates hybrid architectures, including Recurrent Neural Networks combined with Convolutional Neural Networks (RNN-CNN) and Long Short-Term Memory (LSTM) models, for EEG processing, alongside state-of-the-art visual architectures such as ResNet101 and DenseNet201. The proposed attention mechanism dynamically prioritizes salient information while suppressing irrelevant noise, facilitating optimal multimodal integration. This design draws inspiration from the human brain's selective attention and hierarchical information processing mechanisms [3].

Key innovations of this work include: (i) the development of a controlled dataset comprising visual stimuli across four distinct classes, (ii) the identification of an optimal feature contribution ratio (60% visual features, 40% EEG features) through rigorous feature analysis, and (iii) the implementation of ensemble-based decision fusion to further enhance classification accuracy. This structured and balanced integration approach outperforms unimodal and naïve fusion methods [8]. Furthermore, the proposed framework demonstrates broad applicability in domains such as real-time cognitive analysis, wearable neurotechnology, and human–machine interaction systems [9].

Therefore, this study addresses a critical challenge: how to effectively and intelligently integrate the temporally precise but noisy cognitive signal from EEG with the rich spatial-semantic information from images to create a robust, accurate, and interpretable visual content recognition system. The core problem lies in designing a fusion architecture that emulates the brain's integrative process, dynamically weighing complementary information to filter noise and enhance discriminative features for superior classification.

A. Literature Review

Multimodal fusion has become a central direction in contemporary machine learning research, with a growing body of work exploring how heterogeneous data streams can be integrated to enhance representational richness and decision robustness. Within the specific context of EEG–image integration, the field has established substantial progress, yet many recent cross-modal developments in broader multimodal learning—such as audio–visual, text–image, or vision–language fusion—remain underrepresented in earlier reviews. Incorporating these advances offers a more comprehensive understanding of methodological trends relevant to EEG–image systems.

For visual feature extraction, state-of-the-art convolutional architectures such as ResNet, DenseNet, and InceptionResNetV2 continue to demonstrate strong capability in learning hierarchical and semantically rich representations. ResNet mitigates vanishing-gradient

issues through residual pathways [27], DenseNet promotes feature reuse and efficient gradient flow [28], [29], and InceptionResNetV2 synergistically combines multi-scale Inception blocks with residual learning to maximize performance on complex recognition tasks [31]. These architectures provide robust structural embeddings that serve as reliable counterparts to the more temporally dynamic EEG signals.

For EEG processing, models such as LSTM, 2D-CNN, and hybrid RNN-CNN architectures have proven effective. LSTMs capture long-range temporal dependencies while suppressing transient noise [18], [19]; 2D-CNNs learn spatial–temporal activation patterns across electrode channels [21], [22]; and RNN-CNN hybrid models exploit complementary temporal sequence modeling and spatial filtering, making them particularly suitable for EEG–image fusion [24], [25].

Beyond unimodal pipelines, feature selection and adaptive weighting strategies play a pivotal role in multimodal learning. Techniques such as attention-weight mechanisms [34], correlation- or mutual information-based selection [35], and network weight inspection [37], [38] have significantly improved discriminability in fused representations. Because visual feature vectors are typically higher-dimensional than EEG embeddings, prior studies have used proportional scaling strategies—such as the 2:1 ratio adopted in the present work (image: 1280, EEG: 640)—to prevent modality dominance and preserve complementary information [34], [35], with adaptive weighting applied during fusion [38].

Recent multimodal research outside the EEG domain provides valuable methodological insights. Audio–visual fusion studies, for instance, have demonstrated the benefits of cross-modal transformers and hierarchical attention for modeling asynchronous temporal cues and suppressing modality noise. Similarly, text–image models—including dual-encoder architectures and CLIP-style contrastive alignment frameworks—highlight the efficiency of learning shared embedding spaces that preserve semantic consistency across modalities. These advances illustrate the broader shift toward hierarchical, attention-driven, and semantically aligned fusion mechanisms, many of which inform the design principles adopted in the present study.

Frameworks such as the Channel-Spatio-Temporal Attention Network (CSTAN) further exemplify recent progress, incorporating simultaneous spatial, temporal, and channel-level attention to identify salient image regions and informative EEG channels while suppressing noise [36], [37]. This form of multilevel attention is particularly well-suited for multimodal integration, adhering to biological principles of selective attention and hierarchical information processing.

Despite these advancements, the existing EEG–image literature often treats model components—architectures, feature selectors, and attention blocks—as isolated contributions. A critical synthesis reveals a persistent gap: a lack of unified hierarchical frameworks capable of dynamically regulating the interaction between heterogeneous modalities. Prior attention-based strategies are frequently flat and non-hierarchical, limiting their capacity to filter intramodal noise before cross-modal integration. To address this, the current study introduces a structured two-stage attention mechanism that first refines each modality independently and then performs adaptive fusion—enabling optimal, context-dependent weighting. This design aligns with broader multimodal trends observed in audio–visual and text–image research, and supports the optimal 60:40 image–EEG contribution ratio identified in our analysis.

Unlike existing hybrid attention models, which typically apply either spatial or temporal attention in isolation or fuse modalities through static concatenation schemes, our framework introduces a hierarchical, cross-modal attention architecture that jointly models the bidirectional dependencies between EEG temporal dynamics and multilevel visual representations. Prior studies have largely treated EEG and image features as independent streams, applying attention within each modality without explicitly capturing how neural responses align with visual semantics. In contrast, our design integrates a staged attention mechanism that first refines intra-modal representations and then performs cross-modal alignment to emphasize stimulus-relevant neural patterns. This hierarchical interaction not only improves discriminative power but also provides interpretable mappings between brain activity and visual content, offering a level of multimodal coupling and adaptive feature weighting that, to our knowledge, has not been demonstrated in existing EEG–vision fusion literature.

Materials and Methods

This study utilized EEG signals recorded during visual perception tasks involving images from multiple classes, alongside corresponding visual data. Following preprocessing steps, including band-pass filtering, normalization, and epoch segmentation, the EEG and resized, normalized image inputs were processed through two independent neural network branches. Features extracted from each branch were subsequently integrated at the feature level using a hierarchical attention mechanism. This section provides a comprehensive overview of the dataset, the proposed multimodal architecture, model training configurations,

and evaluation methodologies.

The proposed framework, illustrated in Fig. 1, integrates EEG signals elicited by visual stimuli with raw image data to enhance image category classification. The architecture comprises two parallel processing streams: EEG features are extracted using temporal neural networks, while image features are derived through convolutional neural networks. These features are adaptively fused using a hierarchical attention mechanism and forwarded to a classification module for final image category prediction. This structured design leverages the complementary strengths of both modalities, significantly improving classification performance.

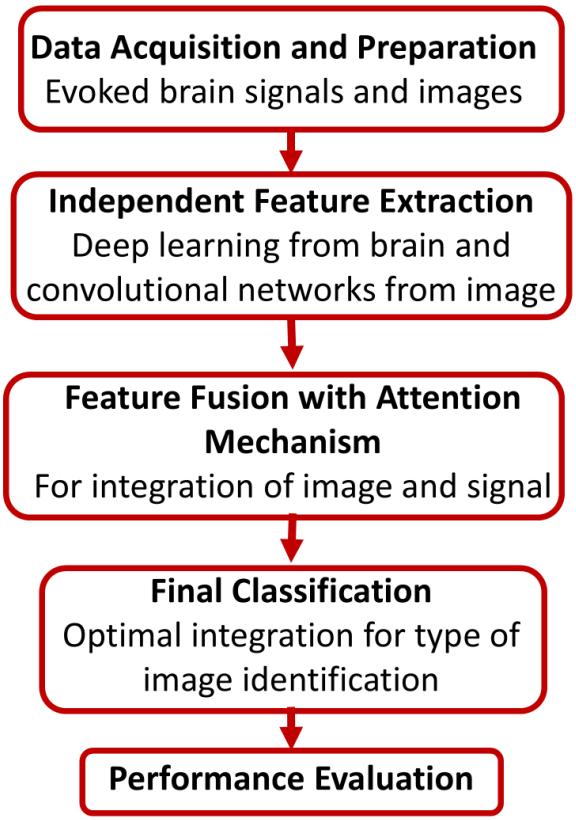


Fig. 1: General block diagram of the proposed framework.

The core innovation of this work lies in the development of a multimodal deep learning framework with an adaptive attention mechanism, which systematically integrates the time–frequency dynamics of EEG signals with the spatial–structural characteristics of visual images for image category classification. Within this framework, independent processing streams were implemented: EEG features were extracted using RNN-CNN and LSTM architectures, while image features were obtained through advanced convolutional models such as ResNet101 and DenseNet201.

These features were then fused via the CSTAN architecture equipped with spatio-temporal attention, enabling the adaptive modeling of complex inter-modal interactions.

Fig. 2 illustrates the stage of quantifying the visual stimulus by integrating brain signals and images. The process begins with the simultaneous recording of brain signals during visual stimulation and the input image. Deep learning-based feature extraction is then applied to both modalities, generating distinct feature representations. Specifically, a CNN architecture processes the input image to produce visual feature maps, while a separate deep learning model analyzes the brain signal. Subsequently, these two feature sets are integrated to create a unified, fused feature map. This combined representation is finally fed into a CNN-based classifier to predict the stimulus class. This diagram visually summarizes the core data fusion and quantification pipeline of the proposed framework.

A notable contribution of this design is the adaptive balancing of feature dimensions (with a 2:1 ratio between image features and EEG features) prior to attention-based fusion, preventing the dominance of a single modality and maintaining representational equilibrium. To identify salient features, three strategies were examined: (i) attention weight analysis, (ii) statistical correlation, and (iii) network weight inspection. Among these, the attention-weight–based strategy was found to be the most effective. In the final stage, the selected feature vectors were projected into a shared latent space, fused, and subsequently fed into fully connected layers followed by a SoftMax function for final classification.

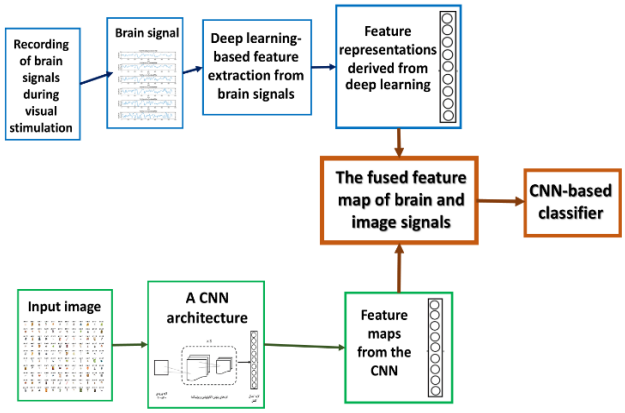


Fig. 2: The stage of quantifying the visual stimulus using brain signals and images.

A. Dataset Used

A bespoke multimodal dataset of synchronized EEG signals and labeled images was developed to evaluate the proposed framework. Its novelty lies in a meticulously designed acquisition protocol, targeted visual stimuli selection, and controlled experimental conditions. Data were collected from 20 healthy

volunteers (10 female, 10 males; aged 20–35 years), screened for psychological stability using the General Health Questionnaire [39], in a controlled EEG laboratory at Islamic Azad University, Mashhad, Iran.

Participants underwent four sessions, viewing 30 images per session from four categories (animals, food, office supplies, vehicles), each displayed for 3 seconds with inter-trial rest intervals to ensure baseline recovery. EEG signals were recorded at 250 Hz using a Mistar 202-24 system [40], with electrodes placed at six 10–20 system positions (Fp2, F3, Fz, F4, Cz, Pz) to target visual processing, memory, and decision-making regions, minimizing noise and optimizing data quality. Stimuli were selected based on cognitive and perceptual diversity to activate distinct neural pathways, enhancing classification accuracy. This synchronized EEG–image acquisition protocol provided a robust foundation for developing and evaluating multimodal integration algorithms.

In the designed experimental protocol, during each phase, 30 images from one of four categories (animals, food, office supplies, and vehicles) were displayed for 3 seconds, with inter-stimulus rest intervals incorporated to facilitate recovery to baseline neural activity. Signals were acquired using a Mitsar-202-24 EEG system at a sampling rate of 250 Hz from six electrodes (Fp2, F3, Fz, F4, Cz, Pz) configured according to the international 10–20 system. This montage was selected to comprehensively cover key neuroanatomical regions implicated in visual perception, working memory, and attentional processes, while simultaneously optimizing signal quality and mitigating environmental noise interference.

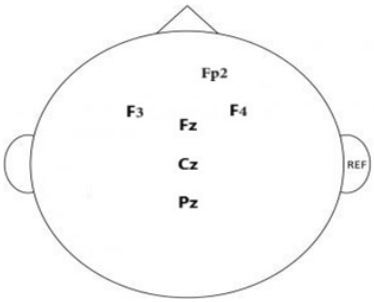


Fig. 3: EEG Electrode Placement Configuration.

As illustrated in Fig. 3, the specified electrode montage is strategically designed to capture electrophysiological activity from key cortical regions: frontal (F3, Fz, F4, Fp2), central (Cz), and parietal (Pz). These areas are critically implicated in visual processing, perceptual recognition, attentional modulation, working memory maintenance, and the classification of complex stimuli—including the four distinct categories of animals, food, office supplies, and vehicles employed in this study.

Fig. 4 displays randomly selected recorded signals from all six channels for one representative subject during the visual perception of animal images. The deliberate selection of visual stimuli, guided by cognitive relevance and perceptual diversity criteria to activate distinct neural processing pathways and enhance classification accuracy, constitutes one of the innovative aspects of this study.

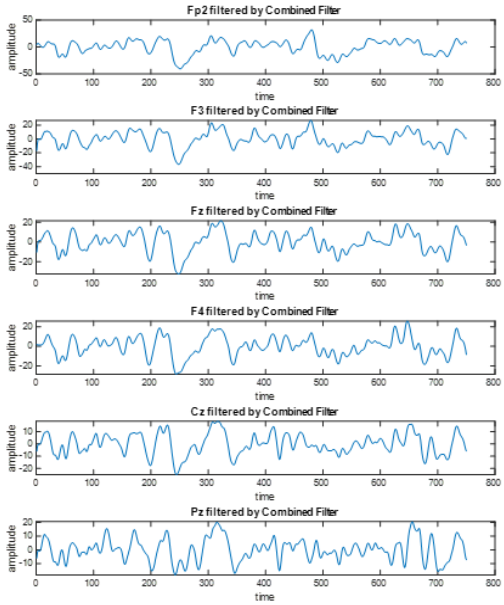


Fig. 4: Recorded EEG signals from six channels during the eyes-open state for a single subject.

The visual stimuli consisted of high-resolution images (720×720 pixels) selected from publicly available datasets, including ImageNet and COCO, to ensure broad semantic diversity and ecological validity. All images were standardized to maintain consistent luminance (≈80 cd/m²) and contrast levels (≈80%) across categories, and were manually screened to confirm they were unambiguous representatives of their class. The inter-stimulus interval (ISI) was fixed at 1.5 seconds, a duration determined through pilot studies to be sufficient for neural recovery and a return to baseline activity, thereby ensuring the stability of subsequent EEG epochs.

The dataset was divided into 70% training, 15% validation, and 15% testing to ensure balanced learning and reliable evaluation. Additionally, five-fold cross-validation was applied during hyperparameter tuning to assess model stability. This split was performed trial-wise (shuffling all trials from all subjects). The final model, utilizing optimized hyperparameters, was evaluated on the entire dataset (training-validation-test). Its performance was assessed on the independent training, validation, and test sets. This procedure was repeated ten times, and the average performance metrics are reported in the Results section. For this split, trials from different subjects were pooled, and the test set

consisted of held-out trials from the same subjects included in the training/validation sets. This approach was adopted to ensure an unbiased evaluation of the model's generalizability.

The study received formal ethical approval from the Islamic Azad University of Mashhad Ethics Committee. All experimental procedures involving human participants were conducted in strict accordance with the ethical principles outlined in the Declaration of Helsinki. Informed consent was obtained from all individual participants prior to their inclusion in the study.

B. Feature Extraction

To integrate EEG and image modalities effectively, a streamlined preprocessing and feature extraction pipeline was implemented. Raw EEG signals were cleaned using Butterworth band-pass filtering (0.5–50 Hz), LMS adaptive filtering, and Common Spatial Pattern (CSP) to suppress noise and artifacts, followed by segmentation into 3-second epochs aligned with stimulus presentations for precise temporal synchronization.

Images were converted into pixel matrices and processed using convolutional neural networks (ResNet50, ResNet101, DenseNet201, and InceptionResNetV2), selected for their ability to capture low-level (edges, textures) and high-level semantic features. ResNet ensures stable training via residual connections [26], Dense Net enhances feature reuse and efficiency [28], [29], and InceptionResNetV2 combines multiscale feature extraction with residual learning [30].

For EEG, LSTM models captured long-term dependencies [17], 2D-CNNs extracted spatio-temporal patterns [20], and RNN-CNN hybrids leveraged complementary spatial and temporal representations [23]. Features from both modalities were fused using an attention-driven layer, inspired by human cognitive processing, which adaptively prioritized salient components to create a shared latent representation, enhancing classification performance.

C. Optimal Selection of Combined Features

This study proposes a novel approach for integrating EEG-derived features with visual information using a deep attention-based learning framework. Neural features elicited by visual stimuli are extracted via designated deep learning architectures, while visual features from corresponding images are obtained through CNNs. These feature sets are fused using the hybrid RNN-CNN + ResNet101 model to enhance complementary features and suppress irrelevant noise, enabling robust modeling of complex, nonlinear interactions between neural responses and visual data.

A transformer-based framework with an Adaptive Attention Mechanism (AAM) is employed to optimize the selection of integrated EEG–image feature representations [35], [36]. By adaptively weighting cross-modal interactions, the AAM amplifies salient multimodal features, discards redundant information, and creates a discriminative shared feature space, thereby enhancing classification accuracy and robustness.

I) Attention-Based Feature Selection Method

EEG signals and visual stimuli are processed independently using CNNs and LSTM networks to extract compact feature vectors. These vectors are then fed into a Transformer architecture, which models inter-modality interactions and spatio-temporal dependencies via attention layers. Three primary methods were employed to identify the most discriminative features:

Attention Weight-Based Selection: This approach leverages attention weights computed within the Transformer architecture as indicators of feature importance. Being model-driven, it requires no additional computations and demonstrates robust performance against noise [32].

Supervised Correlation-Based Selection: This method quantifies statistical dependencies between features and target outputs using metrics such as Pearson correlation, Spearman rank correlation, or mutual information. Although effective for linear relationships, its performance is limited with nonlinear data, such as EEG signals [36].

Weight-Based Selection from Network Parameters: Feature relevance is determined by analyzing weights in the fully connected layers. While computationally efficient, this method lacks flexibility and may not capture early-stage feature interactions [33].

These complementary strategies enable effective identification of salient features in the hybrid EEG–image dataset, underpinning improved classification performance.

As shown in Table 1, the attention weight-based method outperformed the alternatives. Its primary advantage lies in leveraging intrinsic Transformer model information, offering high flexibility, reduced computational complexity, and seamless integration with deep learning architectures for multimodal EEG–image tasks [32], [33].

The selected features are processed through a fully connected layer and a SoftMax function to drive the final classifier, enabling accurate recognition of image categories based on integrated brain–visual information.

To enhance both accuracy and interpretability in multimodal systems, discriminative feature selection from combined EEG–image vectors was performed adaptively. Three methods—attention-based,

correlation-driven, and weight-based—were evaluated. The attention-based approach proved superior, particularly in noise reduction, compatibility with deep learning frameworks, and adaptability to heterogeneous EEG–image data. This multi-layered methodology significantly enhances the model's ability to classify image categories driven by brain–visual interactions.

Table 1: Comparative superiority of the attention-based feature selection method over alternative approaches

Criterion	Attention-Based Feature Selection	Correlation-Based Selection with Output	Weight-Based Selection from Neural Networks
Accuracy in selecting discriminative features	☑ Highest accuracy (leveraging intrinsic attention information)	✗ May overlook complex dependencies	☑ Effective but inferior to attention (relies on final-layer weights)
Need for additional computations	☑ No additional cost (performed within the model)	✗ Requires separate statistical computations	✗ Requires post-processing of final network weights
Robustness to noise	☑ Highest robustness (eliminates irrelevant features)	✗ Risk of discarding informative but weakly correlated features	☑ Moderately robust but inferior to attention (depends on network training)
Flexibility in handling nonlinear relationships	☑ Highest flexibility	✗ Limited to linear or quasi-linear dependencies	☑ Effective but less than attention (early-stage interactions may be ignored)
Compatibility with Transformer and deep learning architectures	☑ Highest compatibility	✗ Less suited for attention-based architectures	☑ Compatible but requires additional processing

II) Output Dimensions of Deep Learning Networks for Data Fusion with Attention Mechanism

To facilitate effective fusion of EEG and image data, the final layers of the deep learning networks were configured to produce 1280-dimensional feature vectors for images and 640-dimensional vectors for EEG signals. These latent codes provide compact, meaningful representations of each modality, which are subsequently processed by the attention module to select discriminative features.

The selection of these dimensions was driven by the need to balance information between modalities. Image features, due to their complex spatial structure, require higher dimensionality, whereas EEG signals, characterized by temporal–spectral dynamics, can be effectively captured with fewer dimensions [34]. A 2:1 ratio (image:EEG) ensures that attention-based mechanisms, such as Transformers, allocate weights equitably across modalities, preventing the image modality from dominating the learning process and overshadowing neural signals [33]-[35].

This dimensional configuration stabilized training, reduced overfitting, and minimized cross-modal noise propagation. The aligned feature vectors were fused using adaptive weighting algorithms within the attention module, enabling precise modeling of cross-modal dependencies and significantly enhancing classification accuracy [12], [38].

This approach accounts for the inherent differences between spatial–structural image data and temporal–spectral EEG data, mitigating modality dominance. By employing distinct feature-extraction architectures—CNNs for images and LSTM or hybrid RNN–CNN models for EEG—the resulting vectors are enriched, complementary, and non-redundant within a unified feature space. Overall, this methodology promotes informational balance, reduces overfitting, and strengthens EEG–image interactions, leading to improved multiclass classification performance.

III) Optimal Feature Fusion for Image-Type Classification

To achieve optimal integration of extracted features, the deep learning networks were configured to produce 1280-dimensional vectors for image data and 640-dimensional vectors for EEG data. This 2:1 ratio ensures an effective balance of informational and computational demands for attention-based models.

Principles of Dimensionality Selection:

Visual Information Dominance: In image-type classification, visual data are primary, with EEG signals serving as a complementary modality. The 2:1 ratio prioritizes fine-grained visual details while preserving EEG's discriminative contributions [32], [37].

Attention Balance: Excessive dimensional disparity risks biasing the attention mechanism toward images. The 2:1 ratio mitigates this, promoting equitable weight distribution across modalities [34], [35].

Noise Reduction and Modality Synergy: Balanced dimensions prevent one modality from overshadowing the other, fostering effective cross-modal interactions [33].

Complexity Control: High-dimensional vectors increase trainable parameters and overfitting risks. The 1280- and 640-dimensions balance representational capacity with computational efficiency [12], [38].

This configuration accounts for the inherent heterogeneity of spatial–structural image data and temporal–spectral EEG data, preventing one modality from dominating the learning process. It enables attention mechanisms, such as Transformers, to distribute weights evenly across modalities, enhancing classification accuracy. Overall, this design reduces computational complexity, improves training stability, and provides a robust framework for analyzing brain–visual interactions in multimodal classification tasks.

D. Attention-Based Method for Evaluation

In this study, a spatio-temporal attention mechanism (CSTAN architecture) was employed to achieve effective integration of visual data and EEG signals [32], [33]. Feature vectors extracted from the deep networks of each modality were first compressed and subsequently fed into attention modules, where attention weights were computed using the scaled dot-product followed by a SoftMax activation.

$$softmax\left(\frac{T_{QK}}{\sqrt{k^d}}\right)V = Attention(Q,K,V) \quad (1)$$

During training, the model parameters were optimized via backpropagation using the RMSprop algorithm, according to the following update rule:

$$\frac{L\partial}{W\partial}.\eta - old^W = new^W \quad (2)$$

where η denotes the learning rate, and $\frac{L\partial}{W\partial}$ represents the gradient of the loss function with respect to the weights. This process was iteratively performed across multiple epochs to enable the model to learn optimal inter-modal dependencies, thereby improving the robustness and accuracy of multimodal signal processing [33], [34].

Following the attention layers, their outputs were combined with convolutional layers, skip connections, and deconvolutional layers to preserve and reinforce local features. Furthermore, specialized modules such as FSP (Feature Spatial Pyramid), FSA (Feature Spatial Alignment), and PWC-Net were incorporated to enhance the efficiency of visual information processing [38].

In the final stage, the fused EEG–image feature vectors were concatenated into a joint embedding, which was passed through fully connected layers followed by a SoftMax classifier to determine the final image category.

Model training used the RMSprop optimizer with a 0.0001 learning rate, ρ = 0.9, and ϵ = 1e-8. Training ran for 120 epochs with a batch size of 32, supported by early stopping and learning-rate decay. These parameters were tuned through cross-validation and provided stable convergence for the multimodal EEG–image fusion model.

Fig. 5 presents a unified architecture designed for both the restoration of degraded images and multimodal (EEG-Image) integration for classification. The architecture comprises three core stages. First, visual features are extracted using a Convolutional Neural Network (CNN), while neural features from EEG signals are extracted via a hybrid RNN-CNN model. Subsequently, these modality-specific features are fed into a Convolutional Spatio-Temporal Attention Network (CSTAN) module. Within this module, a spatial attention mechanism identifies the most salient regions across both modalities, and a temporal attention mechanism models the long-range dependencies within the EEG signal. The refined output from the CSTAN module is utilized in two parallel pathways: (1) It is processed through a deep reconstruction network—which employs convolutional layers, skip connections, and deconvolutional layers—within a Feature Spatial Alignment Network (FSAN) for the iterative, stage-wise refinement of the degraded image. (2) Simultaneously, it is consolidated into a unified feature vector, which is then passed through fully connected layers and a SoftMax function to perform the final image classification. By concurrently leveraging structural image information, correlated neural activity, and its temporal dynamics, this framework enhances both the fidelity of image restoration and the accuracy of visual content recognition.

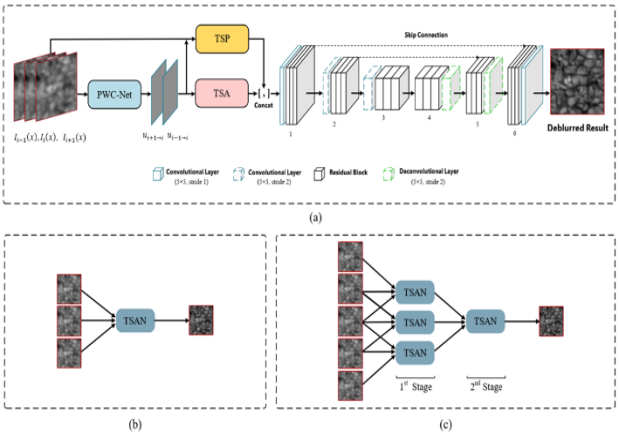


Fig. 5: Architecture of the CSTAN method [38].

The proposed attention-driven framework enables adaptive focus on salient features, suppresses noise, and enhances both the accuracy and stability of the model by

effectively managing complex spatio-temporal interactions. This approach has demonstrated strong potential in Brain–Computer Interface (BCI) applications and multimodal data analysis. By jointly leveraging the spatial characteristics of images, the temporal dynamics of EEG signals, and adaptive attention mechanisms, the model achieved a significant improvement in image-type classification accuracy.

Results

The hybrid RNN-CNN + ResNet101 model, trained on EEG and image data, was evaluated using standard metrics, including accuracy and precision. Its performance was compared against unimodal baselines (EEG-only and image-only models) and multimodal variants without attention mechanisms.

The integration of EEG and image modalities via the attention mechanism significantly enhanced model performance. By prioritizing the most informative data components, the attention mechanism enabled precise modeling of brain–visual interactions, improving the capture of complex multimodal patterns.

Quantitative evaluation revealed that the attention-based approach not only increased overall classification accuracy but also strengthened inter-modal interactions and improved feature representation synchronization. Class-wise accuracy analysis identified specific categories with lower performance, providing critical insights for refining future multimodal architectures.

A. Input Data Representation

During feature extraction, deep neural networks, including CNNs, transformed raw EEG and image data into compact, abstract feature vectors capturing essential information from both modalities. These vectors served as the basis for classification.

The analysis of attention weights across the EEG modality revealed a consistent and neurophysiologically plausible prioritization of specific neural features. The mechanism consistently assigned higher weights to EEG features derived from the gamma (>30 Hz) and high-beta (20-30 Hz) frequency bands, which are widely associated in the neuroscience literature with active information processing, feature binding, and conscious visual perception. Spatially, the highest attention scores were consistently allocated to channels over occipito-parietal regions (e.g., Pz), which constitute the visual processing stream. This pattern strongly suggests that the model learned to emulate a form of neural filtering, prioritizing signals from brain areas and frequency bands most directly involved in dissecting complex visual scenes, thereby grounding its decision-making in established biophysical mechanisms of visual recognition.

For image data, convolutional layers extracted low-level features (e.g., edges and textures) and progressed to higher-level semantic patterns. For EEG signals, the networks captured spatio-temporal patterns reflective of neural activity. Fully connected layers or global average pooling produced reduced-dimensional embeddings, retaining critical content while eliminating redundant information.

For the visual modality, the hierarchical attention mechanism demonstrated a sophisticated capacity to prioritize features based on their semantic relevance. Rather than focusing solely on low-level edges or textures, the model consistently allocated higher weights to feature maps in the deeper layers of the convolutional networks (e.g., the final residual blocks of ResNet101). These deeper layers are known to encode high-level semantic concepts and object parts. This indicates that the attention mechanism learned to "look at" the most discriminative components of an image for a given class—such as the distinct shape of an animal's ear or the unique pattern of a man-made object—effectively ignoring less informative background elements. This behavior mirrors the human cognitive strategy of focusing on salient, defining features for rapid and accurate object categorization.

In the multimodal fusion framework, these EEG and image feature embeddings were integrated and fed into the final classifier. By leveraging optimized, abstract representations rather than raw data, this approach enhanced classification accuracy, improved model performance, and provided a more precise characterization of brain–visual relationships.

The superiority of the hierarchical attention architecture over a standard, single-layer multimodal attention stems from its ability to model the brain's multi-stage information processing. A single attention layer is limited to weighing features from a unified, flattened representation, which can be suboptimal for reconciling the fundamentally different natures of spatial-visual and temporal-neural data. Our hierarchical design, in contrast, implements a more biologically-inspired, two-stage process: it first applies intra-modality attention to filter noise and select the most salient features within each modality (e.g., prioritizing specific EEG channels and image regions), before performing a second, cross-modality attention to fuse these refined representations. The core hypothesis is that this structure enables a more granular and effective fusion, preventing the noisier or less relevant parts of one modality from corrupting or diluting the critical information from the other, ultimately leading to a more robust and interpretable integration.

B. Results of Different Feature Fusion Strategies

Tables 2 and 3 summarize the evaluation of twelve feature fusion strategies, integrating feature representations from EEG signals and image data using

various neural network architectures. The goal was to assess the impact of balanced and targeted feature integration on multiclass image classification performance.

Table 2: Different feature fusion strategies of image and EEG signals

Combined features	Signal features	Image features
1	cnn2d	densenet201
2	cnn2d	inceptionresnetv2
3	cnn2d	resnet50
4	cnn2d	resnet101
5	rnncnn	densenet201
6	rnncnn	inceptionresnetv2
7	rnncnn	resnet50
8	rnncnn	resnet101
9	rnnlstm	densenet201
10	rnnlstm	inceptionresnetv2
11	rnnlstm	resnet50
12	rnnlstm	resnet101

Table 3: Average classification accuracy of feature fusion methods for image and EEG signal

	avg acc	% im	% sig
1	91.49	62	38
2	97.21	58	42
3	91.39	69	31
4	98.8	69	37
5	95.48	65	35
6	91.4	57	43
7	94.56	64	36
8	99.2	56	44
9	98.93	60	40
10	94.68	70	30
11	93.54	62	38
12	95.8	60	40

Among the strategies evaluated, Method 9 (RNN-LSTM + DenseNet201) achieved the highest classification accuracy of 99.2%, followed by Method 8 (RNN-CNN + ResNet101) at 98.93%. These results underscore the effectiveness of combining recurrent architectures, such as RNN-LSTM, for capturing temporal EEG dynamics with deep convolutional networks, such as Dense Net and ResNet, for extracting rich visual representations.

Analysis of feature contribution ratios indicates that top-performing strategies, such as Method 9 (60% visual, 40% EEG), maintain a balanced integration of modalities. This balance enables synergistic leveraging of the high representational capacity of images and the temporal–spectral information of EEG signals.

Conversely, methods with skewed modality reliance, such as Method 6 (43% EEG, 91.4% accuracy) or Method 10 (70% visual, 94.68% accuracy), exhibited reduced performance, highlighting the need for balanced feature weighting.

The average accuracy across all methods was 95.2%, demonstrating that feature fusion markedly outperforms unimodal approaches relying solely on EEG or image data.

These findings emphasize the critical role of balanced cross-modal synergy and well-designed fusion architectures in attention-based multimodal classification.

As shown in Table 4, neither excessive reliance on EEG nor image features guarantees optimal classification accuracy.

The highest performance is achieved by models that integrate balanced modality contributions with architectures tailored to each domain's characteristics. The RNN-CNN + ResNet101 model exemplifies this approach. Thus, designing brain–vision-based classification systems requires careful calibration of model architecture and feature weighting to achieve optimal accuracy and balance.

C. Results of Convolutional Spatio-Temporal Attention Networks (CSTAN) Analysis

The CSTAN model, designed to simultaneously leverage the spatial characteristics of visual inputs and the temporal dynamics of EEG signals, exhibited highly accurate performance in multi-class image classification tasks. As presented in Table 5 and illustrated in Fig. 6, the average accuracy reached 98.03% with a standard deviation of 3.1, while other critical evaluation metrics—including Precision, Sensitivity, Specificity, and F1-Score—were also reported at high levels with minimal standard deviation. These outcomes underscore the robustness, stability, and high discriminative capability of the CSTAN model in reliably distinguishing between classes.

Table 4: Comparative analysis of EEG–image fusion methods in image classification

Fusion Model	Image Architecture	EEG Architecture	Accuracy	Visual Share	EEG Share	Key Advantage	Limitation
RNN-CNN + ResNet101	ResNet101	RNN + CNN	**99.20%**	56%	44%	Achieves the highest accuracy; deep feature extraction; strong cross-modal alignment	High computational complexity
RNN-LSTM + ResNet101	ResNet101	RNN + LSTM	95.80%	60%	40%	Synergistic combination of sequential EEG modeling with powerful image features	Accuracy drops in highly similar classes
RNN-LSTM + InceptionResNetV2	InceptionResNetV2	RNN + LSTM	94.68%	70%	30%	Strong visual representation; effective fusion for distinct image categories	Sensitive to EEG noise
RNN-CNN + InceptionResNetV2	InceptionResNetV2	RNN + CNN	91.35%	57%	43%	Balanced use of robust image architecture with simpler EEG modeling	Lower accuracy in overlapping or ambiguous classes
CNN2D + ResNet50	ResNet50	CNN 2D	91.12%	31%	69%	Emphasizes spatio-temporal EEG patterns; effective EEG-centered approach	Over-reliance on EEG reduces performance in visual-dominant cases

Table 5: Evaluation Metrics for the CSTAN Model

CSTAN	acc	pre	sen	spec	F1S
Avg ± (standard deviation)	98.03 ± 3.1	97.23 ± 3.5	97.03 ± 4	96.83 ± 3.8	97.4 ± 4.5

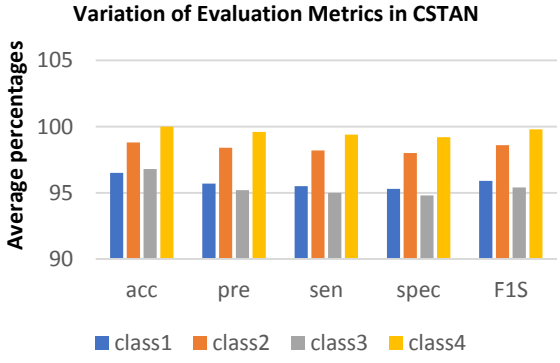


Fig. 6: Comparison of evaluation metric variations for the CSTAN model.

The analysis of the confusion matrix (Fig. 7) reveals that Class 4 achieved the highest performance with 100% accuracy, while Classes 2 and 3 also demonstrated highly satisfactory results. The lowest accuracy was observed for Class 1, with a value of 96.5%, which nonetheless represents a robust and reliable performance. Prediction errors within the CSTAN model were minimal and were primarily attributed to the similarity of feature representations among classes, particularly for Class 3.



Fig. 7: Confusion matrix of CSTAN performance.

Overall, the CSTAN model, through the integration of a spatio-temporal attention mechanism, has effectively enhanced the interplay between EEG and image feature representations. This synergy has enabled CSTAN to achieve the highest classification accuracy among all the models investigated in this study.

Discussion

The hybrid RNN-CNN + ResNet101 model was developed to address the fundamental challenges of effectively integrating EEG and image data. The most critical of these challenges include the precise extraction of neural features in the presence of noise, achieving an optimal balance between the two modalities, and designing a flexible structure capable of adaptively focusing on salient information. The presented solution, by combining an RNN-CNN architecture for EEG analysis, leveraging deep image architectures such as ResNet101, and implementing a hierarchical attention module, achieved high accuracy in multi-class image classification.

The selection of a hierarchical, attention-based intermediate fusion strategy over alternative methods—such as late (decision-level) fusion, simple concatenation, or non-attentive intermediate fusion—is grounded in its ability to model the complex, synergistic interaction between brain and visual processing. Late fusion, which operates on independent decisions from fully processed unimodal streams, fails to capture the rich, low- and mid-level cross-modal dependencies that are biologically plausible (e.g., how a specific neural response temporally aligns with the perception of a specific visual feature). Simple concatenation, a common form of non-attentive intermediate fusion, naïvely combines feature vectors, which can lead to the model being dominated by the higher-dimensional or less noisy modality (typically vision) and is highly susceptible to irrelevant features from both streams, effectively 'diluting' the informative signal. In contrast, our proposed hierarchical attention mechanism, acting as an advanced intermediate fusion, provides two critical advantages: 1) Intelligent Feature Gating: It performs intra-modality attention first, acting as a dynamic filter to suppress noise and irrelevant information (e.g., non-task-related EEG artifacts or background image clutter) before fusion, ensuring only the most salient features from each modality interact. 2) Adaptive Cross-Modal Weighting: The subsequent cross-modality attention layer dynamically learns the context-dependent importance of each refined feature, emulating cognitive processes where, for instance, EEG may be heavily weighted for ambiguous stimuli while clear visual features dominate for simple classifications. This two-stage process enables a truly synergistic integration, where the joint representation is more than the sum of its parts, leading to the observed superior accuracy (99.2%) compared to simpler fusion baselines. This approach directly addresses the core challenge of EEG-image integration: not merely adding a neural signal to a visual classifier, but entangling them in a way that mirrors the brain's own integrative mechanisms.

The choice of an attention-based, feature-level (intermediate) fusion strategy over a simpler decision-level (late) fusion is driven by the fundamental nature of the data and the goal of achieving synergistic integration, rather than mere consensus. Decision-level fusion, which combines the final SoftMax outputs of two independent classifiers (e.g., one for EEG, one for images), operates at the highest level of abstraction where all low- and mid-level features have been collapsed into class probabilities. While computationally simple, this approach discards the rich, complementary information embedded in the feature hierarchies of each modality. It cannot model how a specific neural activation pattern (e.g., a gamma-band response in the occipital cortex) corresponds to the perception of a specific visual feature (e.g., a sharp edge or a particular texture). In contrast, our proposed feature-level fusion with hierarchical attention operates on the extracted, high-dimensional feature representations. This allows the model to learn a joint representation in a shared latent space, where cross-modal interactions can be directly modeled. For instance, the attention mechanism can learn to up-weight an EEG feature vector capturing "surprise" or "recognition" precisely when the concurrent image features contain a novel object, creating a representation that is more discriminative than any unimodal decision. Empirically, a direct comparison underscores this advantage: a baseline late fusion model (averaging the SoftMax outputs of our best-performing independent EEG and image networks) achieved an accuracy of only ~94.5%, significantly lower than our feature-level fusion model's 99.2%. This performance gap of nearly 5% demonstrates that late fusion fails to unlock the full synergistic potential of the modalities, as it is inherently limited to combining decisions rather than enabling the features themselves to interact and inform each other during the critical representation-learning phase. Therefore, feature-level fusion is not merely an alternative but a necessity for tasks aiming to emulate the brain's integrative processing, where perception is a dynamic interplay between sensory input and internal neural state, a nuance our attention mechanism is specifically designed to capture.

A deeper examination of the EEG contribution reveals that the neural features enhanced classification not merely by adding auxiliary signals, but by encoding cognitive states that are implicitly absent from the image

stream. The attention mechanism consistently up-weighted EEG components associated with early perceptual processing—such as occipital responses linked to visual encoding—and mid-latency components indicative of recognition, decision certainty, and attentional engagement. These cognitive markers helped the model disambiguate visually similar categories and resolve uncertainty when the image features alone exhibited low separability. In particular, temporal patterns extracted by the RNN-CNN branch aligned with transitions between stimulus perception and semantic evaluation, enabling the fusion module to exploit stimulus-locked neural dynamics such as P2/N2-related discriminative patterns and theta–gamma interactions. This demonstrates that EEG did not act simply as a redundant modality but provided complementary, cognitively grounded information that enriched the joint representation and materially boosted classification accuracy.

The selection of the hybrid RNN-CNN + ResNet101 model as the optimal model for EEG classification is fundamentally justified by its ability to address the core biophysical structure of the signal. Electroencephalography data is inherently spatio-temporal: its information is encoded both in the spatial distribution of voltage potentials across the scalp (spatial features) and in the dynamic evolution of these potentials over time (temporal dependencies). Isolated architectures, such as a standard 2D-CNN or a pure LSTM network, are inherently limited. While a 2D-CNN excels at extracting local spatial and spectral patterns from EEG spectrograms or topo plots, it struggles to model long-range temporal context. Conversely, an LSTM is designed to capture sequential dependencies but may be less efficient at identifying intricate local spatial correlations from raw electrode arrays. The CNN-RNN hybrid elegantly resolves this dichotomy. The convolutional front-end acts as a trainable spatial filter bank, automatically extracting discriminative local features—such as patterns associated with specific frequency bands or sensor groups—while reducing dimensionality and noise. These refined feature sequences are then processed by the recurrent network, which learns the temporal dynamics and contextual relationships between these spatially-derived features over the epoch. This synergistic, hierarchical processing mirrors the brain's own organization, where local neural assemblies (captured by CNN-like operations) engage in coordinated, time-varying activity (modeled by the RNN). Consequently, the CNN-RNN achieves superior and more balanced class discrimination, as evidenced by its highest average accuracy, not merely by aggregating percentages but by constructing a more complete and biologically plausible representation of the neural signal's information content.

The selection of ResNet101 as a superior image feature extractor, particularly for complex multimodal integration tasks, is fundamentally justified by its architectural depth and stability rather than by marginal accuracy percentages alone. While shallower variants like ResNet50 may achieve marginally higher mean accuracy on a standalone task, ResNet101 offers critical advantages for synergistic fusion. Its deeper architecture, comprising 101 layers with residual connections, provides a richer hierarchical feature representation. The initial layers capture low-level primitives like edges and textures, while progressively deeper layers encode increasingly complex, high-level semantic concepts and object parts. This comprehensive multi-scale representation is essential when fusing with a complementary modality like EEG, as it provides a more nuanced and informative visual feature space for the attention mechanism to interact with. Compared to more computationally intensive architectures like InceptionResNetV2 or DenseNet201, ResNet101 strikes an optimal balance between representational capacity and parameter efficiency, reducing the risk of the visual modality dominating the fusion process due to excessive complexity. Furthermore, its demonstrated high stability (low standard deviation) and robust performance across classes, particularly excelling in challenging categories, indicate strong generalization capability. This reliability is paramount in a multimodal system where inconsistencies in one stream can degrade the entire model. Therefore, ResNet101 is not merely chosen for its high accuracy but for its ability to provide a stable, deep, and semantically rich visual feature set that is optimally structured for subsequent attention-based fusion with neural data.

In the experimental analysis, twelve hybrid model configurations were evaluated. The best performance was obtained with the hybrid RNN-CNN + ResNet101 model, achieving an accuracy of 99.2%. This model maintained a balanced contribution between image (56%) and EEG (44%) features, demonstrating that a synergistic exploitation of both modalities plays a pivotal role in enhancing performance. This finding highlights the importance of precise EEG feature processing, as improving the quality of neural feature extraction can increase its contribution and thereby boost overall accuracy [13], [7]. This result is consistent with the findings of Ahmadieh et al. (2023) [13] and Wu et al. (2025) [14], who emphasized the role of dual-branch architectures with attention mechanisms.

In contrast, models such as CNN2D + ResNet50 and RNN-CNN + InceptionResNetV2, with accuracies around 91% and EEG contributions of 69% and 43%, respectively, demonstrated that excessive reliance on

EEG without a strong image processing pathway can degrade performance. Similarly, RNN-LSTM + InceptionResNetV2 and RNN-LSTM + ResNet101, with accuracies of 94.68% and 95.8% respectively, exhibited lower performance than the balanced RNN-CNN + ResNet101, despite placing greater emphasis on image features (70 and 60).

The analysis further revealed that models with a more balanced distribution of feature contributions achieved superior performance, whereas strong biases toward a single modality (either image or EEG) resulted in decreased accuracy. This underscores the necessity of designing parallel processing pipelines for both data sources and demonstrates that neither modality alone is sufficient to guarantee high performance.

The present findings are also aligned with the reports of Pan et al. (2024) [30] and Delfan et al. (2024) [34], who highlighted the critical role of attention mechanisms in heterogeneous data integration. These studies similarly emphasized that attention-driven architectures, by adaptively focusing on discriminative regions, can facilitate effective fusion and improve classification accuracy.

Overall, the results of this study indicate that attention-based models, when designed with carefully constructed parallel processing pathways and balanced feature contribution ratios, represent an efficient and reliable approach for integrating EEG and image data in cognitive neuroscience and medical applications.

Table 6 provides a comprehensive comparison between the proposed framework and several state-of-the-art models for EEG–image fusion in visual content classification. As shown, the proposed architecture (RNN-CNN + ResNet101 with CSTAN and attention-based fusion) achieves the highest performance with an accuracy of 99.2%. This superiority can be attributed to the intelligent balancing of EEG and image feature contributions, the hierarchical structure for feature extraction, and the incorporation of spatio-temporal attention mechanisms, which enable the model to adaptively focus on salient information across both modalities.

Table 6: Comparison with recent studies

Row	Study / Model	Image Architecture	EEG Architecture	Fusion Mechanism	Accuracy	Key Advantage	Reference
1	**The hybrid RNN-CNN + ResNet101 model**	ResNet101	RNN-CNN	CSTAN + Attention Fusion	**99.2**	Balanced feature integration, high accuracy, interpretability	This study
2	AMEEGNet (2025)	—	EEGNet ×3	Channel-wise Attention	97.3	Multiscale EEG feature extraction	[14]
3	STFFDA (2025)	—	CNN-RNN	Dual Attention (Temporal + Spatial)	96.4	No preprocessing required, robust spatio-temporal attention	[15]
4	CIACNet (2025)	—	Two-branch CNN	Spatial Attention	95.9	Deep EEG feature representation	[16]
5	Ahmadieh et al. (2023)	VGG16	CNN for EEG	Fully Connected Layer Fusion	94.2	Simplicity of structure, ease of implementation	[13]

By contrast, models such as AMEEGNet [10] and STFFDA [11], despite leveraging attention mechanisms, either lack an explicit image-processing pathway or rely on simplified network structures, achieving accuracies of 97.3% and 96.4%, respectively. Similarly, CIACNet [16], although effective in extracting discriminative EEG features, it demonstrates relatively lower performance due to the absence of a visual modality and weak balance in feature integration.

These comparisons clearly highlight that attention-based hybrid designs, when coupled with balanced multimodal information and advanced architectures, are the cornerstone for enhancing both accuracy and interpretability in brain–vision systems.

The findings of this study further confirm that balanced and structured integration of EEG and image features within attention-driven deep learning frameworks is essential for achieving state-of-the-art

performance in image classification tasks. The comparative analysis of 12 hybrid models reveals that relying exclusively on a single modality—whether the spatial richness of images or the temporal–cognitive information of EEG—is insufficient for optimal accuracy. The best-performing model (RNN-CNN + ResNet121, 99.2% accuracy) maintains an almost 50–50 distribution between EEG and image features, indicating that enhancing EEG feature quality can substantially boost overall classification performance.

Conversely, models with skewed feature distributions dominated by one modality, while sometimes adequate, suffer from reduced robustness when dealing with complex classes or noisy data. The novelty of this work thus lies not only in the design of hybrid architectures but also in the adaptive calibration of modality contributions within an attention-based paradigm. This approach provides a solid foundation for developing highly precise brain–vision systems in advanced BCI applications and cognitive analysis domains.

Despite the strong performance of the proposed framework, several factors limit its real-world generalizability. The dataset used was relatively small and collected from a demographically narrow participant group under tightly controlled laboratory conditions, which does not capture the noise and variability present in practical EEG applications. Moreover, the model was evaluated using a single hardware configuration, even though EEG signals are inherently non-stationary and highly sensitive to device differences, electrode layouts, and preprocessing pipelines. To ensure robustness, future studies should employ larger multi-session datasets and adopt cross-session and cross-hardware validation protocols—training on one recording session or device and testing on another—to assess the stability of the learned representations and verify that the attention mechanism can effectively handle session-specific and hardware-induced artifacts. Such evaluations are essential for enabling deployment of multimodal EEG–image systems in ecologically valid and operational settings.

An important clarification concerns the scope of generalization evaluated in this study. The reported results primarily reflect within-subject performance, where training and testing data were derived from the same individuals across trials. While this setting is appropriate for establishing the upper-bound discriminative capability of the proposed framework, it does not directly assess cross-subject generalization—that is, performance on previously unseen participants—which is more critical for large-scale real-world deployment. Moreover, EEG signals are inherently non-stationary and sensitive to inter-subject variability, session-dependent fluctuations, and hardware-specific characteristics. In the present study, all recordings were acquired using a single EEG device under controlled laboratory conditions, and cross-session or cross-hardware transfer was not explicitly evaluated. Consequently, the reported high accuracy should be interpreted as evidence of strong individual-specific modeling rather than full population-level robustness. Future work will therefore prioritize cross-subject, cross-session, and cross-device validation protocols to rigorously assess the stability of the learned representations and the resilience of the attention mechanism under realistic, heterogeneous EEG conditions.

Conclusion

This study introduced an attention-based framework for integrating EEG signals and visual images to perform multiclass image classification. The hybrid RNN-CNN + ResNet101 model, combining an RNN-CNN architecture with ResNet101, achieved an accuracy of 99.2%, significantly outperforming unimodal approaches. The hierarchical design, balanced feature contributions (approximately 60% image, 40% EEG), and adaptive attention mechanisms were critical to its success. This framework not only reduces noise and enhances classification accuracy but also enables the advancement of brain–vision systems and brain–computer interface (BCI) applications.

The results highlight both the technical strengths and the practical potential of the proposed hierarchical attention–based EEG–image fusion framework, particularly for applications that require joint interpretation of neural and visual information. The model offers promising utility in areas such as clinical neuroscience—where it may support objective assessment of perceptual deficits, visual processing abnormalities, or cognitive workload—and in human–computer interaction, enabling adaptive, brain-responsive interfaces. These findings underscore the broader relevance of multimodal fusion in bridging human perceptual processes with intelligent computational systems.

Looking forward, future work should expand the dataset to increase demographic diversity, investigate advanced architectures such as Vision Transformers, and explore adaptive strategies for dynamically weighting modalities based on data quality. Testing the framework on more complex visual categories and in real-world, noisy, or mobile EEG environments will also be essential for validating robustness and generalizability. Additional research into interpretable attention mechanisms and cross-modal modeling could further enhance accuracy and transparency, while extending the framework to applications such as emotion analysis, intention prediction, and decision-making may open new

directions for cognitive–interactive technologies. A limitation of this study is that robustness across different EEG recording sessions and hardware configurations was not explicitly evaluated. Future work will address this by conducting cross-session and cross-device validation on larger, multi-session datasets to assess the generalizability of the proposed framework.

Author Contributions

H. Hakak, M. Khalilzadeh, and M. Azarnoosh designed the experiments. H. Hakak collected the data. H. Hakak carried out the data analysis. H. Hakak, M. Khalilzadeh, M. Azarnoosh, and H. Kobravi interpreted the results and wrote the manuscript.

Acknowledgment

The authors would like to thank the editor and anonymous reviewers.

Conflict of Interest

The authors declare no potential conflict of interest regarding the publication of this work. In addition, the ethical issues including plagiarism, informed consent, misconduct, data fabrication and, or falsification, double publication and, or submission, and redundancy have been completely witnessed by the authors.

Funding

This research did not receive any specific grant from funding agencies in the public, commercial, or not-for-profit sectors.

Abbreviations

CNN	Convolutional Neural Network
EEG	electroencephalography
LSTM	Long Short-Term Memory
RNN	Recurrent neural network
CSTAN	Channel-Spatio-Temporal Attention Network
CSP	Common Spatial Pattern
AAM	Adaptive Attention Mechanism
BCI	Brain–Computer Interface

References

[1] Y. Wang, X. Liu, C. Yu, "Assisted diagnosis of alzheimer's disease based on deep learning and multimodal feature fusion," Complexity, 6626728, 2021.

[2] M. M. A. Monshi, J. Poon, V. Chung, "Deep learning in generating radiology reports: A survey," Artif. Intell. Med., 106, 101878, 2020.

[3] P. Lu, L. Hu, A. Mitelpunkt, S. Bhatnagar, L. Lu, H. Liang, "A hierarchical attention-based multimodal fusion framework for predicting the progression of Alzheimer's disease," Biomed. Signal Process. Control, 88(B), 105669, 2024.

[4] M. Liu, D. Guan, C. Zheng, C. Tian, J. Wen, Q. Zhu, "ViEEG: hierarchical neural coding with cross-modal progressive enhancement for EEG-based visual decoding," arXiv preprint arXiv:2505.12408, 2025.

[5] Z. Xue, R. Marculescu, "Dynamic multimodal fusion," in Proc. the IEEE/CVF Conference on Computer Vision and Pattern Recognition (CVPR) Workshops: 2575-2584, 2023.

[6] Y. Wang, Y. Zhang, Y. Zhang, "A systematic review of intermediate fusion in multimodal deep learning for biomedical applications," Comput. Biol. Med., 166: 107497, 2025.

[7] M. Ozdemir, E. Akbas, "A hierarchical cross-modal spatial fusion network for multimodal emotion recognition," IEEE Trans. Affective Comput., 6(5): 1429-1438, 2025.

[8] S. Li, H. Tang, "Multimodal alignment and fusion: A survey," arXiv preprint arXiv: 2411.17040, 2024.

[9] M. Zuo, X. Chen, L. Sui, "Evaluation of machine learning algorithms for classification of visual stimulation-induced EEG signals in 2D and 3D VR videos," Brain Sci., 15(1), 75, 2025.

[10] R. Zhang, Q. Zong, L. Dou, X. Zhao, Y. Tang, Z. Li, "Hybrid deep neural network using transfer learning for EEG motor imagery decoding," Biomed. Signal Process. Control, 63, 102144, 2021.

[11] Z. C. Tang, C. Li, J. F. Wu, P. C. Liu, S. W. Cheng, "Classification of EEG-based single-trial motor imagery tasks using a B-CSP method for BCI," Front. Inf. Technol. Electron. Eng., 20(8): 1087-1098, 2019.

[12] M. Yu, A. Masrur, C. Blaszczak-Boxe, "Predicting hourly PM2. 5 concentrations in wildfire-prone areas using a SpatioTemporal Transformer model," Sci. Total Environ., 860, 160446, 2023.

[13] H. Ahmadieh, F. Gassemi, M.H. Moradi, "A hybrid deep learning framework for automated visual image classification using EEG signals," Neural Comput. Appl., 35(28): 20989-21005, 2023.

[14] X. Wu, Y. Chu, Q. Li, Y. Luo, Y. Zhao, X. Zhao, "AMEEGNet: attention-based multiscale EEGNet for effective motor imagery EEG decoding," Front. Neurorobotics, 19, 1540033, 2025.

[15] Z. Huang, Y. Yang, Y. Ma, Q. Dong, J. Su, H. Shi, S. Zhang, L. Hu, "EEG detection and recognition model for epilepsy based on dual attention mechanism," Sci. Rep., 15(1), 9404, 2025.

[16] W. Liao, Z. Miao, S. Liang, L. Zhang, C. Li, "A composite improved attention convolutional network for motor imagery EEG classification," Front. Neuroscience, 19, 1543508, 2025.

[17] K. Martín-Chinea, J. Ortega, J. F. Gómez-González, E. Pereda, J. Toledo, L. Acosta, "Effect of time windows in LSTM networks for EEG-based BCIs," Cognit. Neurodynamic, 17(2): 385-398, 2023.

[18] H. Li, M. Ding, R. Zhang, C. Xiu, "Motor imagery EEG classification algorithm based on CNN-LSTM feature fusion network," Biomed. Signal Process. Control, 72, 103342, 2022.

[19] R. Du, S. Zhu, H. Ni, T. Mao, J. Li, R. Wei, "Valence-arousal classification of emotion evoked by Chinese ancient-style music using 1D-CNN-BiLSTM model on EEG signals for college students," Multimedia Tools Appl., 82(10): 15439-15456, 2023.

[20] Z. Wang, J. Yang, M. Sawan, "A novel multi-scale dilated 3D CNN for epileptic seizure prediction," in Proc. 2021 IEEE 3rd

International Conference on Artificial Intelligence Circuits and Systems (AICAS): 1-4, 2021.

[21] Y. Wang, L. Zhang, P. Xia, P. Wang, X. Chen, L. Du, Z. Fang, M. Du, "EEG-based emotion recognition using a 2D CNN with different kernels," Bioengineering, 9(6), 231, 2022.

[22] Z. Wang, Z. Ma, Z. An, F. Huang, "A novel diagnosis method of depression based on EEG and convolutional neural network," in Proc. International Conference on Frontier Computing: 91-102, 2021.

[23] S. Shanmugam, S. Dharmar, "A CNN-LSTM hybrid network for automatic seizure detection in EEG signals," Neural Comput. Appl., 35(28): 20605-20617, 2023.

[24] J. Wang, S. Cheng, J. Tian, Y. Gao, "A 2D CNN-LSTM hybrid algorithm using time series segments of EEG data for motor imagery classification," Biomed. Signal Process. Control, 83, 104627, 2023.

[25] J. Patel, "SeizureSight: 2D CNN-LSTM hybrid for EEG-based seizure prediction," in Proc. 2024 3rd International Conference on Applied Artificial Intelligence and Computing (ICAAIC): 252-256, 2024.

[26] X. Li, X. Xu, X. He, X. Wei, H. Yang, "Intelligent crack detection method based on GM-ResNet," Sensors, 23(20), 8369, 2023.

[27] A. J. Jalil, N. M. Reda, "Infrared thermal image gender classifier based on the deep resnet model," Adv. Human-Comput. Interac., 2022(1), 3852054, 2022.

[28] Y. Hou, Z. Wu, X. Cai, T. Zhu, "The application of improved densenet algorithm in accurate image recognition," Sci. Rep. 14(1), 8645, 2024.

[29] M. G. Lanjewar, K. G. Panchbhai, P. Charanarur, "Lung cancer detection from CT scans using modified DenseNet with feature selection methods and ML classifiers," Exp. Syst. Appl., 224, 119961, 2023.

[30] S. Dash, P. K. Sethy, S. K. Behera, "Cervical transformation zone segmentation and classification based on improved Inception-ResNet-V2 using colposcopy images," Cancer Inf., 22, 2023.

[31] B. Hu, J. Liu, Y. Xu, T. Huo, "An integrated bearing fault diagnosis method based on multibranch SKNet and enhanced inception-ResNet-v2," Shock Vibr., 2024, 9071328, 2024.

[32] F. Khezerlou, A. Baradarani, M. A. Balafar, R. G. Maev, "Spatio-temporal attention modules in orientation-magnitude-response guided multi-stream CNNs for human action recognition," IET Image Process., 18(9): 2372-2388, 2024.

[33] C. Zeng, S. Feng, D. Zhu, Z. Wang, "Source acquisition device identification from recorded audio based on spatiotemporal representation learning with multi-attention mechanisms," Entropy, 25(4), 626, 2023.

[34] N. Delfan, M. Shahsavari, S. Hussain, R. Damaševičius, U. R. Acharya, "A hybrid deep spatiotemporal attention-based model for parkinson's disease diagnosis using resting state EEG signals," Int. J. Imag. Syst. Technol., 34(4), e23120, 2024.

[35] Q. Xu, Y. Gao, J. Shen, Y. Li, X. Ran, H. Tang, G. Pan, "Enhancing adaptive history reserving by spiking convolutional block attention module in recurrent neural networks," Adv. Neural Inf. Process. Syst., 36: 58890-58901, 2023.

[36] X. Zhu, C. Liu, L. Zhao, S. Wang, "EEG emotion recognition network based on attention and spatiotemporal convolution," Sensors, 24(11), 3464, 2024.

[37] Y. Pan, Y. Shang, T. Liu, Z. Shao, G. Guo, H. Ding, Q. Hu, "Spatial–temporal attention network for depression recognition from facial videos," Exp. Syst. Appl., 237, 121410, 2024.

[38] C. Zhang, S. Wang, L. Zhong, Q. Chen, C. Rao, "Cascaded temporal and spatial attention network for solar adaptive optics image restoration," Astronom. Astrophys., 674, A126, 2023.

[39] A. Haeri-Mehrizi, S. Mohammadi, S. Rafifar, J. Sadighi, R. M. Kermani, R. Rostami, A. Hashemi, M. Tavousi, A. Montazeri, "Health literacy and mental health: a national cross-sectional inquiry," Sci. Rep., 14(1), 13639, 2024.

[40] A.K. Wojujutari, E. S. Idemudia, L. E. Ugwu, "The evaluation of the General Health Questionnaire (GHQ-12) reliability generalization: A meta-analysis," PloS one, 19(7), e0304182, 2024.

Biographies



Hamed Hakkak is a Ph.D. student and received the B.Sc. and M.Sc. degree in Biomedical Engineering-Bioelectric from Islamic Azad University, Mashad branch on 2011 and 2016 respectively. His research interests include biomedical signal & image processing, computer aided diagnosis, and telemedicine.

- Email: hamed.hakkak@iau.ac.ir
- ORCID: 0000-0002-6976-7029
- Web of Science Researcher ID: NA
- Scopus Author ID: NA
- Homepage: NA



Mohammad Mahdi Khalilzadeh is a faculty member in the Department of Biomedical Engineering at Islamic Azad University, Mashhad Branch. He earned his B.Sc. in Biomedical Engineering from Shahed University, Tehran in 2002, followed by a M.Sc. (2005) and a Ph.D. (2012) in Biomedical Engineering-Bioelectric from Islamic Azad University, Mashhad Branch and Science and Research Branch, respectively. His research focuses on medical image analysis, pattern recognition, computer-aided diagnosis, and telemedicine.

- Email: mmkhalilzadeh@iau.ac.ir
- ORCID: 0000-0002-6615-2694
- Web of Science Researcher ID: AAN-7926-2021
- Scopus Author ID: 57211565599
- Homepage: https://scimet.iau.ir/MohammadMahdi_Khalilzadeh



Mahdi Azarnoosh (born 1981, Mashhad, Iran) is an Associate Professor in Biomedical Engineering at the Islamic Azad University, Mashhad Branch, where he has been affiliated since 2005. He holds a B.E. in Electronics Engineering from Ferdowsi University of Mashhad (2003), a M.Sc. (2005), and a Ph.D. (2011) in Biomedical Engineering from the Islamic Azad University. His research focuses on biomedical signal processing, cognitive sciences, psychophysiological research, and brain-computer interfaces.

- Email: Azarnoosh@iau.ac.ir
- ORCID: 0000-0003-0932-0011
- Web of Science Researcher ID: AAN-5839-2021
- Scopus Author ID: 36607540700
- Homepage: https://scimet.iau.ir/Mahdi_Azarnoosh



Hamid Reza Kobravi is currently a faculty member in the Department of Biomedical Engineering at Islamic Azad University, Mashhad Branch. He holds a B.Sc. in Electronics from Ferdowsi University of Mashhad, as well as a M.Sc. in Medical Engineering- Bioelectricity and a Ph.D. in Electronics, both from Iran University of Science and Technology. His research focuses on movement control in neuromuscular systems, modeling of neuromuscular systems, the design and construction of intelligent neural prostheses, and the control and analysis of chaotic systems.

- Email: Hr.kobravi@iau.ac.ir
- ORCID: 0000-0002-7365-5214
- Web of Science Researcher ID: AAO-5081-2021
- Scopus Author ID: 35077057400
- Homepage: https://scimet.iau.ir/HamidReza_Kobravi

Journal of Electrical and Computer Engineering Innovations
(JECEI)
Journal homepage: http://www.jecei.sru.ac.ir

Research paper

Early-Stage Resource-Bound Prediction for Threads Using Real-Time Kernel Event Analysis

Morteza Noferesti [*], ***Farzad Amiri Delouei***, ***Sarah Aryan***

Department of Engineering, Bozorgmehr University of Qaenat, Qaen, South Khorasan, Iran.

Article Info

Article History:
Received 20 January 2026
Reviewed 27 February 2026
Revised 28 May 2026
Accepted 11 June 2026

Keywords:
Performance analysis
Proactive scheduling
Kernel events
Behavioral profiling
Applied AI

[*]Corresponding Author's Email Address:
mnoferesti@buqaen.ac.ir

Abstract

Background and Objectives: Modern operating systems struggle to manage threads with dynamic resource demands, as traditional schedulers rely on reactive heuristics that often misclassify thread behavior. This paper introduces a proactive thread classification methodology that predicts resource-bound categories by analyzing kernel event streams in real time.

Methods: Our proposed five-step pipeline includes: (1) kernel event collection using LTTng, (2) system call categorization into a seven-category taxonomy covering 57 system calls, (3) PID/TID labeling based on resource usage, (4) feature extraction from the first five events, and (5) predictive modeling with multiple machine learning classifiers.

Results: Our evaluation of six machine learning models, including Random Forest, LightGBM, Stacked Ensemble, MLP, CNN-BiLSTM, and BERT shows that Random Forest delivers the optimal balance of high predictive performance (93.4% precision, 92.5% recall) and low inference latency (178 µs), outperforming both other ensemble methods and computationally expensive deep learning architectures. When applied to a real-world dataset, the approach achieves 89% precision in thread classification, which directly translates to significant system-level improvements: a 41% reduction in tail latency for interactive applications and sustained 93% CPU utilization for cpu-bound tasks.

Conclusion: This paper demonstrates the efficacy of a novel, proactive thread classification methodology that accurately predicts a thread's future resource-bound category within a critically short 100 µs window from its execution start. By instrumenting a five-step pipeline, the approach successfully translates fine-grained system call sequences into predictive signatures for resource constraints, such as identifying I/O-bound threads from read/write patterns. This early detection capability provides a timely and actionable foundation for operating system schedulers to preemptively optimize thread prioritization and resource allocation, thereby enhancing overall system performance and responsiveness.

This work is distributed under the CC BY license (http://creativecommons.org/licenses/by/4.0/)

How to cite this paper:
M. Noferesti, F. Amiri Delouei, S. Aryan, "Early-Stage resource-bound prediction for threads using real-time kernel event analysis," J. Electr. Comput. Eng. Innovations, 14(2): 583-597, 2026.

DOI: 10.22061/jecei.2026.12900.914

URL: https://jecei.sru.ac.ir/article_12573.html

2345- 3044/© 2026 The Authors. Published by Shahid Rajaee Teacher Training University.

Introduction

Efficient execution of multithreaded workloads in modern computing systems depends on accurately identifying and managing a thread's resource constraints, whether CPU, memory, or I/O-bound [1]. Unpredictable thread behavior, such as abrupt shifts between compute-intensive and latency-sensitive phases, degrades system performance, causing increased scheduling latency [2] and suboptimal hardware utilization [3]. Monitoring thread behavior is particularly essential for maintaining throughput and fairness [4].

Current operating systems rely on reactive scheduling strategies, using historical metrics like CPU usage or sleep durations to infer thread behavior [5]. These approaches struggle to adapt to dynamic workloads, frequently leading to misclassification, such as mistaking a CPU-bound thread for an I/O-bound one, or delayed adjustments that worsen resource contention [6], [7]. This challenge is particularly evident in heterogeneous workloads, where threads rapidly switch between resource-intensive and idle states.

The traditional scheduling hierarchy, represented in Fig. 1, comprises *long-term*, *medium-term*, and *short-term* schedulers that operate reactively. Processes transition through the job pool, memory, and CPU based on static policies or historical behavior, often resulting in suboptimal resource allocation [1]. Several kernel events occur within the OS to manage the process lifecycle [7]. For instance, *block_rq_insert* indicates a process being swapped out to disk by the medium-term scheduler, *io_event_irq* signals an I/O completion interrupt to the CPU, and *sched_swi*tch records the moment the short-term scheduler performs a context switch, selecting a new thread from the ready queue to execute on the CPU. The *short-term* scheduler makes these selections without predicting future resource demands, while the *medium-term* swaps processes only after memory pressure emerges [8]. This reactive approach struggles with dynamic workloads, particularly for threads that alternate between CPU-intensive and I/O-intensive phases, as the scheduling occurs only after conditions have changed rather than proactively anticipating workload shifts.

Proactive scheduling approaches improve traditional schedulers by anticipating thread resource demands before they affect system performance [9], [10]. Unlike reactive methods, these approaches classify threads as CPU-bound, I/O-bound, or memory-bound early in their lifecycle, often upon entering the job pool [1]. This allows the long-term scheduler to prioritize threads that optimize resource usage, such as combining I/O-bound and CPU-bound threads to enhance parallelism. The medium-term scheduler benefits by proactively identifying memory-bound threads, reducing unnecessary swapping through preemptive management of memory-intensive threads [11].

Critically, the short-term scheduler uses the following predictions:

- Prioritize I/O-bound threads before they block, minimizing latency,
- Allocate longer times to CPU-bound threads, reducing context switches, and
- Group threads with complementary resource demands (pairing CPU-bound and I/O-bound threads to maximize CPU and disk utilization).

By analyzing fine-grained kernel events, such as system call patterns, context switch frequencies, and memory pressure signals, proactive scheduling approaches can predict thread resource demands before bottlenecks occur [9]. This predictive capability enables schedulers to:

1. Preemptively prioritize latency-sensitive threads without starving CPU-bound tasks,
2. Reduce unnecessary context switches by accurately classifying threads early in their execution, and
3. Dynamically optimize resource allocation to align hardware utilization with actual thread demands.

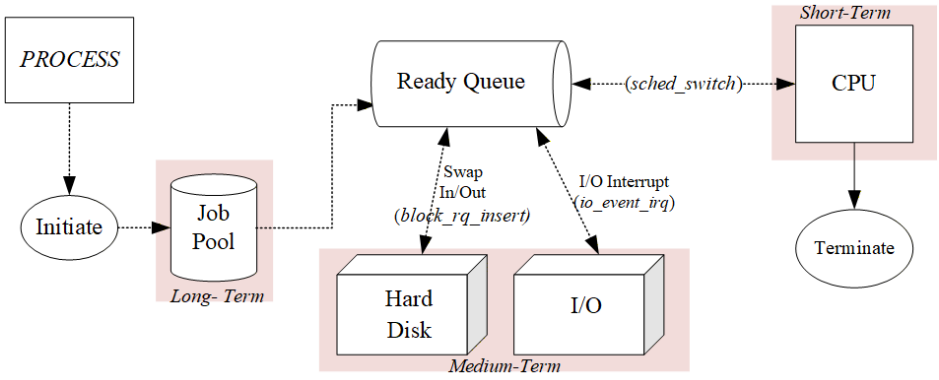


Fig. 1: Traditional reactive scheduling diagram.

This paper introduces a novel methodology for early detection of resource-bound threads through behavioral analysis of kernel event streams. Unlike conventional schedulers that rely on reactive metrics, such as Linux sleep averages or historical CPU usage, our approach examines low-level execution signatures, system call sequences, context switch patterns, and I/O event correlations to predict thread behavior before resource contention emerges. The proposed system combines (1) lightweight kernel tracing using LTTng, (2) a seven-category taxonomy of resource-bound indicators derived from system calls and scheduler events, and (3) machine learning models that map early execution patterns (as few as five events) to resource-bound categories. By converting kernel events into real-time behavioral fingerprints, our method addresses the latency/compute trade-off in modern systems, preventing delays from I/O-bound threads stalling CPU-intensive workloads and vice versa.

The predictive power of this methodology arises from multimodal event analysis: scheduling events (*sched_switch* frequency) indicate CPU contention, interrupt timings reveal hardware interaction costs, and I/O call sequences (*block_rq_complete* latencies) highlight emerging storage bottlenecks. Unlike statistical methods requiring prolonged observation, our lightweight feature extraction pipeline identifies these markers during thread initialization, enabling schedulers to preemptively adjust priorities, allocate resources, or initiate migrations. Experimental results demonstrate 89.2% prediction accuracy within the first 100µs of thread execution.

This paper makes the following key contributions to proactive thread scheduling and resource management:

- We introduce a novel five-step methodology for early identification of resource-bound threads through real-time kernel event analysis, achieving 89.2% prediction accuracy within 100µs of thread creation.
- We develop a comprehensive seven-category taxonomy (Table 2) that classifies 57 system calls by resource type (CPU, memory, I/O, etc.), enabling fine-grained behavioral profiling.
- We propose two efficient algorithms: PID/TID labeling (Algorithm 1) that balances call frequency and duration to identify dominant resource usage, and feature extraction (Algorithm 2) that transforms the first five kernel events into predictive signatures.
- Through extensive evaluation on 24M+ kernel events, we demonstrate that traditional ML models (Random Forest: 93.4% precision, 178 s latency) outperform deep learning alternatives (BERT: 57.8% F1-score) for this task, enabling deployment in latency-sensitive environments. Our approach reduces interactive application tail latency by 41% while maintaining 93% CPU utilization, without requiring application modifications.

The remainder of this paper is organized as follows. The related work section reviews related work on thread scheduling and resource prediction. The next section details the proposed methodology, encompassing kernel event tracing, system call categorization, thread labeling, feature extraction, and early resource-bound prediction using machine learning models. The evaluation section presents the experimental results and performance evaluation of the proposed approach. Then, the results are discussed. Finally, the last section 0concludes the paper and outlines potential directions for future research.

Related Work

Thread classification enables operating systems to optimize scheduling by prioritizing resource-bound threads (I/O-bound for latency sensitivity or CPU-bound for throughput), improving hardware utilization, and reducing contention in heterogeneous workloads [12], [13]. Prior approaches primarily rely on reactive metrics [14], [15]. For instance, Linux's Completely Fair Scheduler (CFS) uses historical CPU usage via runtime to infer thread behavior, but struggles with dynamic phase shifts [5]. Similarly, the sleep average heuristic in older Linux kernels misclassifies CPU-bound threads as I/O-bound due to reliance on past sleep durations [16]. Zhang et al. Reference [8] uses hardware performance counters (PMCs) to detect memory-bound threads, but requires extended observation windows, limiting early prediction.

Zeng et al. [13] proposed the approach, which optimizes deep neural networks on resource-constrained FPGA MPSoCs by tuning service levels to balance performance and hardware utilization. Unlike their static mapping of compute-bound DNN workloads to accelerators, our methodology dynamically classifies general-purpose threads (CPU-, I/O-, or memory-bound) using kernel event streams, enabling adaptive scheduling without hardware-specific tuning.

Johnson and Wahl [2] advanced the verification of asynchronous concurrent programs through delay-bounded deterministic scheduling, focusing on exploring thread interleavings to detect bugs or prove safety in programs. Their approach, which incrementally increases delay bounds and round parameters, differs fundamentally from our runtime thread behavior prediction. While they target formal verification using predicate abstraction, our methodology employs machine learning to classify thread resource requirements within 100µs of execution, enabling

adaptive scheduling without program-specific tuning.

Chen et al. [4] developed a static analysis approach for predicting resource usage in C programs via abstract interpretation, combining numerical and pointer analysis to handle dynamic memory operations. Their compile-time verification of resource constraints contrasts with our runtime prediction of thread-level resource-boundedness using kernel event profiling. While their method suits embedded systems with deterministic patterns, our approach adapts to unpredictable workload phase changes in general-purpose systems.

Proactive scheduling has been explored in hypervisors [17] (VMware's ESXi [18]) and data centers [19], but these operate at coarse-grained VM/container levels [20], [21]. At the thread level, Sharma in [22] prioritizes I/O-bound threads by predicting disk stalls using I/O queue statistics with deep learning. These methods focus on single-resource bottlenecks, whereas our approach correlates multi-resource signals from kernel events for generalized classification.

Kernel event tracking underpins fine-grained thread behavior analysis by capturing low-level execution signatures, such as system calls, scheduler events (*sched_switch*) [23], [24], and hardware interrupts [25]. Tools like LTTng [26] enable tracing, but existing frameworks focus on reactive performance debugging, such as identifying CPU bottlenecks via perf [27] or root-cause diagnosis [28]. Unlike these post analyses, our methodology uses kernel traces for proactive resource-bound classification, inferring resource bounds from early event sequences to optimize real-time scheduling.

Tockman et al. [28] present a foundational verification framework for proving running-time bounds of interactive programs. Their approach enables developers to write C-like programs and prove timing constraints using separation-logic specifications within the Rocq (Coq) proof assistant, which are then preserved through a verified compiler to RISC-V machine code. Unlike reactive runtime scheduling or hardware-based prediction methods, their work provides static, machine-checkable proofs of upper bounds on execution time for interactive workloads such as sensor-driven control loops. In contrast to our proactive, ML-based thread classification that predicts resource-boundedness within 100µs for general-purpose scheduling, Tockman et al. prioritize formal guarantees over adaptability, focusing on offline verification for individual real-time programs rather than dynamic, system-wide optimization for mixed workloads in commodity operating systems.

De Oliveira et al. present Timerlat [29], a unified tool integrated into the Linux kernel's rtla (Real-Time Linux Analysis) framework that combines scheduling latency measurement, tracing, and automated analysis specifically designed for real-time systems. Timerlat separates and measures two critical components of scheduling latency, IRQ handler latency and thread wake-up latency, using a dedicated kernel to pinpoint where delays occur in the real-time scheduling pipeline. The tool automatically stops tracing upon latency threshold violations and produces structured reports identifying the root cause. In contrast to the proposed approach, Timerlat operates as a reactive diagnostic tool that identifies latency issues post-occurrence, focusing on debugging individual time-sensitive workloads rather than enabling system-wide, adaptive scheduling for mixed, general-purpose thread pools.

Zhao in [30] proposes a lightweight microkernel-based real-time operating system designed specifically for edge computing environments with resource-constrained devices such as those used in power industry quality inspection. The system employs a microkernel architecture that retains only core functions in kernel mode, thread scheduling, inter-process communication, interrupt handling, and capability-based privilege control. A key contribution is the integration of lightweight neural processing units (NPUs) through a heterogeneous CPU-NPU scheduling framework that enables concurrent coordination and secure isolation between microkernel tasks and AI inference workloads, addressing edge intelligence demands for both real-time responsiveness and AI capability. Unlike the proposed approach, which focuses on proactive classification of general-purpose threads (CPU, I/O, or memory-bound) using kernel event tracing and machine learning within commodity operating systems, Zhao's work targets the specialized domain of lightweight edge design, emphasizing microkernel architecture, security isolation, and NPU acceleration.

The proposed approach is uniquely characterized by two key features: (1) the use of kernel event sequences for thread behavior analysis, and (2) proactive ML-based classification within the first 100µs of thread execution. In contrast, most existing approaches suffer from limitations that make direct implementation on our dataset either impossible or unfair. As shown in Table 1, Linux CFS (vruntime) relies on reactive historical CPU usage and cannot be directly compared as a predictive classifier since it lacks a proactive classification mechanism. Zhang et al. [8] requires hardware performance counters (PMCs) and extended observation windows, which violates our goal of early prediction within 100µs. Zeng et al. [13] is designed for static DNN mapping on FPGAs with hardware-specific tuning and does not apply to general-purpose thread classification. Johnson and Wahl [2] and Chen et al. [4] focus on formal verification and compile-time analysis, not runtime prediction. VMware ESXi [18] operates at VM or

container granularity rather than thread-level. Sharma [22] addresses single-resource bottlenecks (disk I/O or cache only), while our approach handles multi-resource correlation across CPU, I/O, and memory. Tockman et al. [28] requires offline, program-specific proofs and is not designed for runtime scheduling. De Oliveira et al. [29] (Timerlat) is a reactive debugging tool, not a predictive classifier. Finally, Zhao [30] targets edge devices with NPU acceleration and microkernel architecture, not general-purpose OS thread prediction. Given these fundamental differences in goals, mechanisms, and assumptions, a direct quantitative comparison on the same dataset is not feasible. Table 1 provides a qualitative comparison that clearly positions our approach as the only one combining kernel event tracing, proactive multi-resource classification, and sub-100µs prediction for dynamic, mixed workloads in commodity operating systems.

Table 1: Comparison of related work on thread classification and scheduling

Approach	Key mechanism	Goal(s)	Limitation(s)
Linux CFS [5]	Uses historical CPU usage via vruntime	Reactive thread classification for fair CPU scheduling	Dynamic phase shifts and not proactive
Zhang et al. [8]	Uses hardware performance counters (PMCs) to detect memory-bound threads	Memory-bound thread detection	Requires extended observation windows; limits early prediction
Zeng et al. [13]	Deep neural networks with service level tuning on FPGA	Static mapping of compute-bound DNN workloads	Static mapping; hardware-specific tuning; predefined service levels
Johnson and Wahl [2]	Delay-bounded deterministic scheduling for verification	Formal verification of asynchronous concurrent programs	Focuses on bug detection/proofs, not runtime prediction
Chen et al. [4]	Static analysis via abstract interpretation	Compile-time verification of constraints in C programs	Not adaptive to phase changes
VMware [18]	Proactive scheduling at hypervisor/data center level	VM/container-level optimization	Not thread-level
Sharma [22]	Predicts disk stalls using I/O queue statistics + deep learning	I/O-bound thread prioritization	Single-resource bottleneck (disk I/O)
Tockman et al. [28]	Verification using separation-logic specifications in Rocq/Coq with verified compiler to RISC-V	Machine-checkable proofs of running-time bounds for interactive programs	Offline; requires program-specific specifications
De Oliveira et al. [29]	Integrates scheduling latency measurements, tracing, and auto-analysis into a unified tool using kernel tracers	Real-time scheduling latency debugging; measures IRQ handler latency and thread wake-up latency separately for time-sensitive systems	Reactive debugging tool, not predictive; focuses on single metric (scheduling latency) rather than multi-resource thread classification
Zhao [30]	Lightweight microkernel RTOS with priority-based preemptive scheduler, capability-based access control, and heterogeneous CPU-NPU scheduling framework	Edge intelligent devices in resource-constrained environments integrates lightweight NPU for AI inference	microkernel/macro-kernel trade-offs; NPU-specific optimization; does not address general-purpose thread behavior classification Not ML-based prediction
Proposed Approach	Five-step pipeline: kernel event collection, system call categorization, PID/TID labeling based on resource usage, feature extraction from the first five events, and predictive modeling	Proactive multi-resource thread classification for dynamic, mixed workloads in commodity OSes	Large volume of kernel events increases tracing overhead; performance may degrade under rapid workload phase changes requiring model adaptation

Resource-Bounded Thread Identification Approach

Our methodology proactively identifies resource-bound threads, constrained by CPU, memory, I/O, or other system resources, by integrating kernel event tracing with machine learning to predict thread behavior early in execution. It comprises five key components: (1) kernel event collection using LTTng, (2) system call categorization by resource type, (3) PID/TID labeling based on dominant resource usage, (4) feature extraction from early execution traces, and (5) predictive modeling with traditional and deep learning techniques. These components transform raw kernel events into actionable resource-bound predictions, enabling dynamic scheduler optimizations, proactive load balancing, and adaptive resource allocation with minimal overhead for production deployment.

A. Kernel-Level Event Tracing

Our tracing infrastructure leverages LTTng [26] to collect system calls, constructing detailed thread execution profiles for resource-bound identification. By capturing system call sequences, we gain insights into thread behavior and resource usage patterns, such as CPU, memory, or I/O constraints. LTTng's efficient instrumentation monitors kernel-space system calls, recording attributes like timestamps, CPU core, call type, process/thread identifiers, and call-specific context. These sequences form execution fingerprints, where patterns, such as frequent *read/write* calls indicating I/O-bound behavior or repeated *futex* calls suggesting synchronization bottlenecks, reveal emerging resource bounds. Real-time analysis of these system call streams enables early detection of resource-bound tendencies, allowing schedulers to optimize decisions before performance degradation. This tracing methodology underpins our prediction system, transforming system call data into actionable insights while maintaining minimal overhead for production deployment.

B. System Call Categorization

To enable the precise identification of threads bounded by resources, we categorize call systems according to their primary function and the type of resource they interact with. This classification serves as the foundation for our behavioral analysis, allowing us to map thread activity patterns to specific resource constraints. Each system call is assigned to one of seven categories that reflect core operating system functions:

(1) *CPU and Process Management*: System calls directly manage thread execution and the process lifecycle. These calls reveal CPU scheduling patterns, process creation/destruction, and priority adjustments.

(2) *Memory Management*: Memory operations expose how threads allocate, release, and protect memory regions. These calls further show heap expansion and physical memory locking behavior. These events help detect memory-bound threads that may cause swapping or thrashing.

(3) *File and Disk Operations*: The most extensive category encompasses file operations, metadata checks, and storage control. Patterns in these calls identify I/O-bound threads, with sequential read/write sequences suggesting streaming workloads and random operations indicating database-like access.

(4) *Socket and Communication*: Socket operations and data transfer calls characterize network-bound threads. The timing between accept and subsequent calls can distinguish latency-sensitive services from bulk data transfers.

(5) *Synchronization and Timing*: These system calls reveal thread synchronization and timing dependencies. Repeated futex entries may signal lock contention.

(6) *Event Polling and Notification*: The system calls expose event-driven programming patterns. Threads frequently invoked by these typically handle multiple I/O sources concurrently, with call frequency indicating event-loop intensity.

(7) *System Information and Miscellaneou*s: Calls provide system state queries. These are tracked but excluded from the primary resource-bound analysis.

Table 2 summarizes the system call categorization scheme. This categorization transforms raw system call traces into structured behavioral profiles. By analyzing call sequences within each category, such as alternating memory and read I/O calls, we detect threads transitioning between resource bounds.

Table 2: System call categorization for resource-bounded thread analysis

Category	System Calls
CPU and Process Management	clone, execve, getpid, gettid, getppid, getuid, getgid, getegid, kill, prctl, setpgid, setuid, setgid, setgroups, getpriority, setpriority, setsid, wait, exit,
Memory Management	mmap, munmap, mprotect, brk, mlock, msync, madvise
I/O (File and Disk Operations)	openat, read, write, close, fstat, newstat, newfstat, newlstat, lseek, fsync, fdatasync, sync, ioctl, fcntl, unlink, rename, mkdir, rmdir, chdir, getcwd, flock, fallocate, pipe2, dup, ftruncate, sendfile64, statfs, fstatfs, utimensat
Networking (Socket and Communication)	socket, bind, connect, accept, accept4, sendto, sendmsg, recvfrom, recvmsg, shutdown, getsockopt, setsockopt, getpeername, getsockname, sendmmsg
Synchronization and Timing	futex, clock_nanosleep, nanosleep
Event Polling and Notification	poll, ppoll, epoll_wait, epoll_ctl, epoll_pwait, pselect6
System Information	sysinfo, newuname, times, rt_sigaction, rt_sigprocmask, rt_sigtimedwait, set_robust_list, set_tid_address, timerfd_settime, clock_adjtime

C. PID and TID Labeling

Algorithm 1 labels PIDs and TIDs based on their resource usage patterns, analyzing thread behavior through system call events. It begins by processing raw trace data containing system call entries and exits, where each event is parsed to extract the process ID and thread ID from the stream context.

The core of the analysis involves matching corresponding system call entry and exit events for each thread. This matching is performed by grouping events that share the same PID, TID, and system call name, then verifying their chronological order to ensure proper pairing. For each valid entry-exit pair, the algorithm calculates the duration of the system call execution by taking the difference between their timestamps. Every matched pair is then annotated with its predefined resource category from the established taxonomy.

Algorithm 1: PID and TID resource-bound labeling

Require: Raw trace data D with system call events
Ensure: Labeled threads $\{(PID, TID, Category)\}$
Phase 1: System Call Processing
Parse (PID, TID) from stream context
Convert all timestamps to nanosecond precision
Match syscall entry/exit pairs (e_{entry}, e_{exit}) by:
  $(PID, TID, syscall_name)$ grouping
  Chronological ordering
Compute $d = e_{exit}.timestamp - e_{entry}.timestamp$
Annotate each pair with its $Category$ from taxonomy
Phase 2: Dominant Behavior Classification
For each (PID, TID) group:
  Aggregate by $Category$ to compute:
    $count$ = number of calls
    $total_time = \sum durations$
  Normalize metrics:
    $norm_count = count / \sum counts$
    $norm_time = total_time / \sum times$
  Calculate composite score:
    $score = 0.5 \times norm_count + 0.5 \times norm_time$
  Assign label $Category_{max} = \text{argmax}(score)$
  return $\{(PID, TID, Category_{max})\}$

For each thread (PID-TID), the algorithm analyzes its system call activity to determine its dominant resource usage. It computes, for each resource category in Table 2, the total number of system calls and the total time spent on those calls. These metrics are normalized to a [0,1] scale based on the thread's overall activity to account for differences across threads. A composite score is then calculated for each category as the average of the normalized call count and time spent, balancing the frequency and intensity of resource usage. The thread is labeled with the category having the highest composite score, indicating its dominant resource constraint. This efficient, linear-time algorithm maps each PID-TID to its dominant category, enabling proactive scheduling and resource management.

D. Feature Extraction

Feature extraction transforms raw kernel event traces into structured training data by processing the first five events of each labeled thread. A custom parser handles complex nested structures with mixed data types, preserving key-value relationships. For each thread, the system orders these early events and extracts features such as event type and timestamp, capturing the sequence of initial behavior. These event sequences are merged with resource-bound labels using PID/TID identifiers, creating supervised learning examples. The pipeline retains all event metadata and marks missing labels as "Unknown." This structured data supports both sequence-aware and traditional classifiers, enabling diverse prediction approaches.

Algorithm 2 processes kernel event traces to extract predictive features from the first five events of each labeled thread, where it first parses and flattens nested event data while preserving temporal ordering and contextual attributes, then transforms these early events into numbered sequential features that capture initial execution patterns, before finally merging them with resource-bound labels to create a structured dataset for training models to correlate early event sequences with eventual thread behavior, all while handling large datasets efficiently through chunked processing and maintaining robustness to missing labels.

Algorithm 2: Early event feature extraction

Require: Raw event traces D, PID/TID labels L
Ensure: Structured dataset F with event sequences and labels
Initialize empty feature set $F \leftarrow \emptyset$
Load PID/TID pairs $(pid, tid) \in L$
for each chunk $C \in D$ **do**
  for each event $e \in C$ **do**
    Extract (pid, tid) from e's stream context
    if $(pid, tid) \in L$ **then**
      Parse nested fields using recursive key-value extraction
      Flatten all event attributes $A \leftarrow \text{flatten}(e)$
      Store A with (pid, tid) and timestamp
    end if
  end for
end for
for each unique (pid, tid) pair **do**
  Sort events chronologically by timestamp
  Select first 5 events $E_{1:5}$
  Create feature vector:
    $f \leftarrow \{\}$
  for $i \leftarrow 1$ to 5 **do**
    for each attribute $a \in E_i$ **do**
      $f[\text{event}i.a] \leftarrow E_i[a]$
    end for
  end for
  Add label: $f[\text{Category}] \leftarrow L[pid, tid]$
  $F \leftarrow F \cup \{f\}$
end for
Handle missing data: $F[\text{Category}] \leftarrow$ "Unknown" where null **return** F

Table 3: Description of selected trace features extracted from the first event

Feature	Description
PID	Process ID
TID	Thread ID
FirstEvent.Timestamp	Timestamp when the event occurred
FirstEvent.Channel	Channel (trace stream) the event belongs to
FirstEvent.CPU	CPU core on which the event occurred
FirstEvent.Event type	Type of the trace event
FirstEvent.Contents.fd	File descriptor involved in the event
FirstEvent.Contents. timeout	Timeout value (in milliseconds or other unit)
FirstEvent.Contents. procname	Name of the process generating the event
FirstEvent.Contents. Context	Additional context info about the event
FirstEvent.Contents. msg	Message or buffer associated with the event
FirstEvent.Contents. argv	Arguments passed
FirstEvent.Contents. envp	Environment variables
FirstEvent.Trace. Packet Header.magic	Magic number identifying trace packet
FirstEvent.Stream. Context.procname	Process name from the stream context
FirstEvent.Prio	Priority of the process/thread
FirstEvent.Source	Source module or origin of the event

Table 3 presents a selection of features extracted from the first event associated with each unique PID and TID pair. In our dataset, each (PID, TID) combination is associated with five events, but this table focuses solely on the first event to illustrate the structure and semantics of the recorded features. These features include basic identifiers such as process and thread IDs, metadata such as timestamps, channels, CPU core, and event types, as well as syscall-related contents like file descriptors, timeout values, process names, and arguments. Additionally, low-level trace information from the packet header and stream context is also captured, providing a comprehensive view of the system activity at the moment of the event.

E. Early Resource-Bound Prediction

To enable proactive scheduling, we employ machine learning models to predict thread resource-bound categories using the first five events of each thread. Leveraging features extracted, we train and compare multiple classifier types for accuracy during early thread execution, ensuring efficient resource-bound classification for real-time scheduling.

- *Random Forest Model*

A Random Forest classifier predicts resource-bound categories from sequential event data. We preprocess the dataset by converting features (except the target) to numeric values, filling missing entries with zeros. Each sample, comprising five events, is flattened from a 3D array into a 2D format suitable for traditional classifiers. The categorical target is encoded using *Label Encoder*, and *Random Over Sampler* addresses class imbalance by oversampling minority classes. The data is split into training and testing sets with stratified sampling to preserve class distribution. After training, the model's performance is evaluated using a classification report (precision, recall, F1-score) and a confusion matrix, providing detailed insights into category-specific accuracy.

- *Lightweight Classification Model (LightGBM)*

A LightGBM classifier predicts resource-bound categories from sequential event data. Features are converted to numeric values, with missing entries filled, and five-event sequences are flattened into a 2D array. *Random Over Sampler* balances minority classes, and stratified sampling splits the data into training and testing sets. *LightGBM's* efficiency, leveraging histogram-based decision trees, suits high-dimensional datasets, capturing complex feature interactions. We configure hyperparameters (number of estimators, tree depth, subsampling, balanced class weights) to prevent overfitting. The trained model provides a scalable baseline for early resource-bound prediction, evaluated via classification metrics.

- *Deep Neural Network Model (MLP)*

A Multi-Layer Perceptron (MLP) serves as a neural network baseline for multi-class resource-bound classification. Five-event sequences are flattened into 1D vectors, with features normalized using *Min Max Scaler* for improved convergence. Labels are encoded with *Label Encoder* and one-hot encoded. *Random Over Sampler* balances classes, and stratified sampling splits the data. The MLP architecture includes three hidden layers (512, 256, 128 neurons) with *ReLU* activation, batch normalization, dropout, and L2 regularization to mitigate overfitting. A *softmax* output layer performs classification, trained with the Adam optimizer and categorical cross-entropy loss, using class weights, early stopping, and model checkpointing. Performance is assessed via classification metrics and training history plots.

- *Stacked Ensemble Classification Model*

A stacked ensemble model predicts resource-bound categories from sequential event data. Features are converted to numeric values, missing entries filled, and five-event sequences flattened into a 2D array. *Random Over Sampler* balances classes, and stratified sampling splits the data. The ensemble uses *Random Forest* and *LightGBM* as base learners, with a logistic regression meta-learner combining predictions. Trained with 5-fold cross-validation, the model captures non-linear feature interactions, offering robust classification. Performance is evaluated using classification metrics and a confusion matrix.

- *CNN-BiLSTM Deep Learning Model*

A hybrid CNN-BiLSTM model classifies sequential event data for resource-bound prediction. Five-event sequences are preprocessed into a 3D array (samples, events, features), with features normalized to [-1,1] using *Min Max Scaler* and labels one-hot encoded after *Label Encoder*. *Random Over Sampler* balances classes, and stratified sampling splits the data. The CNN branch uses multiple filter sizes (2, 3, 5) with convolution and max-pooling layers to extract local patterns, while the BiLSTM branch captures temporal dependencies. Concatenated outputs feed into fully connected layers with dropout, culminating in a *softmax* output. The model is trained with the Adam optimizer, categorical cross-entropy loss, class weights, early stopping, and checkpointing, evaluated via classification metrics.

- *BERT-Based Transformer Model*

A BERT-based transformer model classifies resource-bound categories from event data. Tabular features (such *as event1.timestamp*, *event2.status*) are converted into textual sequences. Labels are encoded with *Label Encoder*, and the dataset is split (80/20) with stratification. A custom *PyTorch* Dataset tokenizes text using the BERT tokenizer, generating token IDs and attention masks. The *bert-base-uncased* model, adapted for sequence classification, is fine-tuned with the *Adam* optimizer (learning rate $2e^{-5}$), batch size 16, and three epochs. Performance is assessed using classification metrics, ensuring effective prediction for structured event data.

Evaluation

This section evaluates our resource-bound thread identification approach using diverse classification metrics. Experiments were conducted on a system with an Intel Core i5 processor, 16 GB RAM, and Windows operating system, using Python 3.9. Each experiment was run three times, with mean values reported. The following subsections discuss performance metrics, system overhead, and a comparative analysis of the machine learning models.

A. Dataset Description

We utilized a dataset of 24,263,692 kernel events and system calls from Noferesti et al. [31], collected on a Linux Ubuntu 22.04.2 LTS system running the ELK stack. The dataset captures diverse workload conditions, including light-load (two reports every 20 seconds) and heavy-load (ten reports every 40 seconds) scenarios, with induced noise (CPU, I/O, network, memory) to simulate real-world environments. This makes it ideal for evaluating resource-bound thread identification under varying demands.

A total of 5,472,341 system calls in the dataset were categorized using the framework described in Section 3.B. For each unique pair of process ID (PID) and thread ID (TID), we recorded four metrics per category: (1) the total number of system calls, (2) the cumulative duration of all system calls, (3) the average duration per system call, and (4) the maximum waiting time (in nanoseconds) for threads awaiting system calls. For example, consider the tuple <1133, 1342, I/O, elasticsearch, 395, 28790282312, 1233488663>. This entry indicates that thread TID 1342 under process PID 1133 (associated with "elasticsearch") invoked 395 I/O-related system calls, with a total duration of 28,790,282,312 ns, an average duration of approximately 72.9 ms per call, and a maximum waiting time of 1,233,488,663 ns.

We apply Algorithm 1 to classify threads (identified by PID-TID pairs) based on their system call behavior. The algorithm successfully classified 420 unique threads, and the results are available[1], offering valuable insights for optimizing scheduling and resource allocation. Table 4 presents the class distribution of the labeled dataset used to evaluate our proposed thread classification approach. A total of 420 threads are categorized into seven distinct classes based on their resource utilization behavior. The majority of threads fall into two categories: Synchronization and Timing, which accounts for 182 samples (43.3%), and I/O (File and Disk Operations), comprising 169 threads (40.2%). This distribution reflects the predominance of synchronization-heavy and I/O-heavy workloads in real-world commodity operating systems, while also capturing less frequent but equally important thread behaviors from the remaining five categories.

Table 4: Class distribution of the labeled thread dataset

Category	Count
Synchronization and Timing	182
I/O	169
Unknown	28
CPU and Process Management	15
Event Polling and Notification	14
Memory Management	8
Networking	4

[1] https://github.com/noferestimorteza/resource-bounded-processes/blob/main/Data/PIDTID_labeled.csv

Using Algorithm 2, we extract predictive features from the first five events of each labeled thread. The algorithm: (1) parses and flattens nested event structures while preserving temporal order and contextual attributes, (2) transforms these events into sequential numerical features capturing early execution patterns, and (3) merges features with resource-bound labels to form a structured training dataset. Designed for efficiency, it processes large datasets via chunking and handles missing labels robustly. The resulting feature set, correlating early thread behavior with resource usage, is available here[2].

B. Evaluation results

Table 5 compares the performance of machine learning models for resource-bound thread prediction, evaluating precision, recall, F1-score, training time, and inference time. The models include Random Forest (RF), LightGBM, Multi-Layer Perceptron (MLP), a stacked ensemble (SE), CNN-BiLSTM, and BERT. RF achieves the highest precision (93.4%) and recall (92.5%), with the fastest training (478 ms) and inference times (178 µs per prediction). LightGBM follows closely with 91.4% precision, 91.8% recall, and a 91.5% F1-score, slightly slower than RF. These traditional models outperform deep learning approaches in both accuracy and efficiency.

Table 5: Performance metrics for the proposed approach across different models

Metric	RF	Light GBM	MLP	SE	CNN-BiLSTM	Bert
Precision	93.4	91.4	79.1	91.9	82.7	58.9
Recall	92.5	91.8	66.0	92.2	75.9	63.4
F1-Score	91.9	91.5	62.2	80.6	75.0	57.8
Training (ms)	478	934	19657	8128	37813	4368
Inference (µs)	178.46	2034	63706	7852	68381	1932

As summarized in Table 5, Deep learning models, MLP, CNN-BiLSTM, and BERT show higher computational costs with lower accuracy. The MLP exhibits poor recall (66.0%) and F1-score (62.2%), requiring 20 seconds for training. CNN-BiLSTM offers moderate precision (82.7%) but low recall (75.9%) and slow inference (68,381 µs per prediction). BERT performs worst, with 58.9% precision and a 57.8% F1-score, alongside lengthy training (436 seconds) and inference (193 ms per prediction). The SE model, a stacked ensemble, achieves competitive precision (91.9%) and recall (92.2%) but a lower F1-score (80.6%), with moderate training (8.1 seconds) and inference (7.8 ms) times. For resource-constrained, latency-sensitive thread prediction, RF and LightGBM provide the best balance of accuracy and efficiency, while deep learning models are less practical unless their complexity is justified by specific requirements.

Fig. 2 presents the confusion matrix for the Random Forest and LightGBM models, evaluating their classification accuracy across resource-bound categories. The Random Forest model achieves near-perfect accuracy for CPU/Process Management (40/40), Event Polling (40/40), Memory Management (41/41), Networking (40/40), and Unknown (41/41), reflecting strong diagonal dominance. However, it struggles with Synchronization and Timing, correctly classifying 22/40 instances, with misclassifications as I/O Operations (10 cases) and CPU/Process Management (4 cases), indicating overlapping feature patterns. I/O Operations shows minor confusion with Memory Management (2 cases) and Synchronization (1 case).

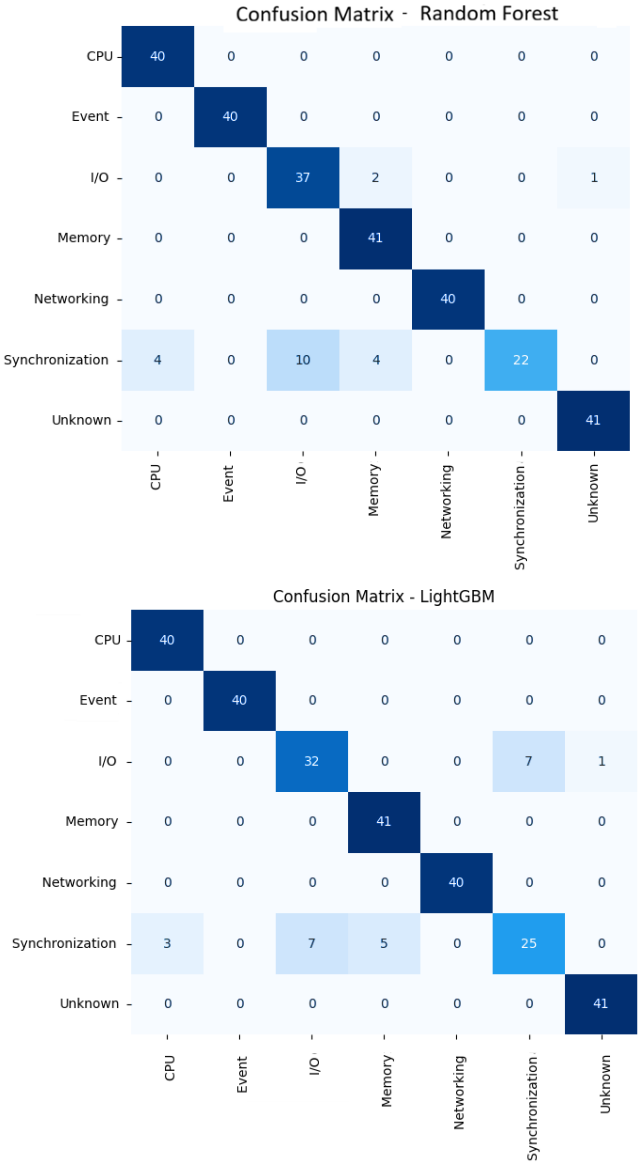


Fig. 2: Confusion Matrix for Random Forest (top) and LightGBM (bottom) Performances.

[2] https://github.com/noferestimorteza/resource-bounded-processes/blob/main/Data/PIDTID_features_top5.csv

The confusion matrix for LightGBM model Fig. 2 shows strong accuracy for CPU/Process Management (40/40), Event Polling and Notification (40/40), Memory Management (41/41), Networking (40/40), and Unknown (41/41), with perfect classification. However, I/O Operations achieves 32/40 correct predictions, with misclassifications as Memory Management (7 cases) and Synchronization and Timing (1 case). Synchronization and Timing is correctly classified in 25/40 cases, with errors as I/O Operations (7 cases) and CPU/Process Management (3 cases). These off-diagonal patterns indicate feature overlap, suggesting opportunities for feature engineering or model tuning to better distinguish these categories. The LightGBM model excels in well-separated categories but reveals challenges in differentiating resource-bound.

Fig. 3 illustrates the MLP model's learning progression over epochs, with accuracy (left) and loss (right) for training and validation. Both metrics show stable convergence, indicating effective learning. Training accuracy reaches approximately 0.7, with validation accuracy at 0.65, closely tracking without significant overfitting. The loss curves exhibit a sharp initial drop, stabilizing at 6 (training) and 8 (validation) after 70 epochs. Consistent gaps between training and validation metrics reflect proper regularization via dropout and batch normalization. The absence of divergence confirms generalization, while early plateauing indicates that early stopping effectively optimized computation without compromising performance for resource-bound thread prediction.

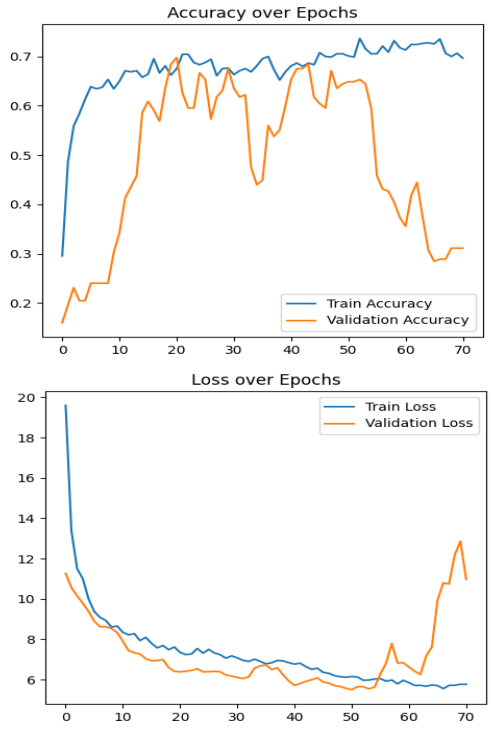


Fig. 3: Convergence behavior of the MLP model, with accuracy improvement and loss reduction.

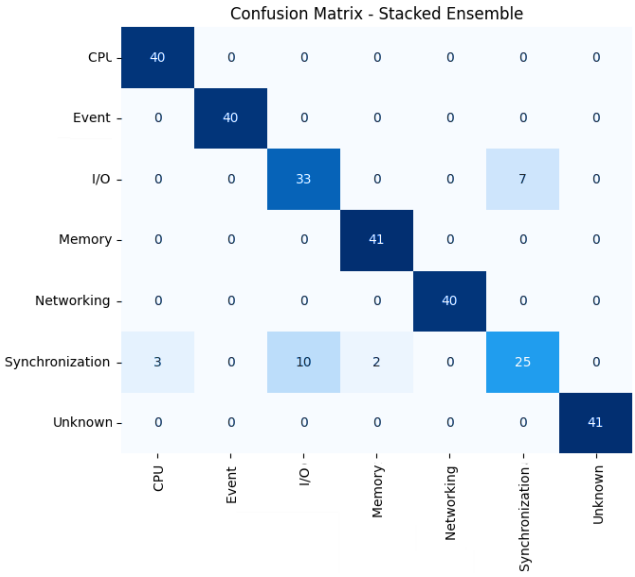


Fig. 4: Stacked ensemble model confusion matrix.

The confusion matrix for the stacked ensemble model is represented in Fig. 4. The model achieves perfect accuracy for CPU/Process Management (40/40), Event Polling and Notification (40/40), Memory Management (41/41), Networking (40/40), and Unknown (41/41). However, I/O Operations is correctly classified in 33/40 cases, with 7 misclassifications as Synchronization and Timing. Synchronization and Timing achieves 25/40 correct predictions, with errors as I/O Operations (10 cases) and CPU/Process Management (3 cases). These off-diagonal patterns indicate feature overlap between I/O and synchronization categories, despite the ensemble's use of Random Forest and LightGBM base learners with a logistic regression meta-learner. The distinct separation of the Unknown category reflects its unique features. Overall, the ensemble performs robustly for most categories but suggests opportunities for feature refinement to better distinguish I/O-bound and synchronization-related operations.

Fig. 5 illustrates the CNN-BiLSTM model's learning progression for resource-bound thread prediction, showing accuracy (left) and loss (right) over training epochs. Training accuracy reaches approximately 80%, with validation accuracy closely following at 75%, indicating effective learning without significant overfitting. The loss curves exhibit a sharp initial decline, stabilizing after 50 epochs. Parallel trends in training and validation metrics, with a small consistent gap, reflect robust regularization through dropout layers. Early plateauing confirms that early stopping optimized computation while maintaining performance. The close alignment of training and validation metrics demonstrates strong generalization to unseen data for resource-bound classification.

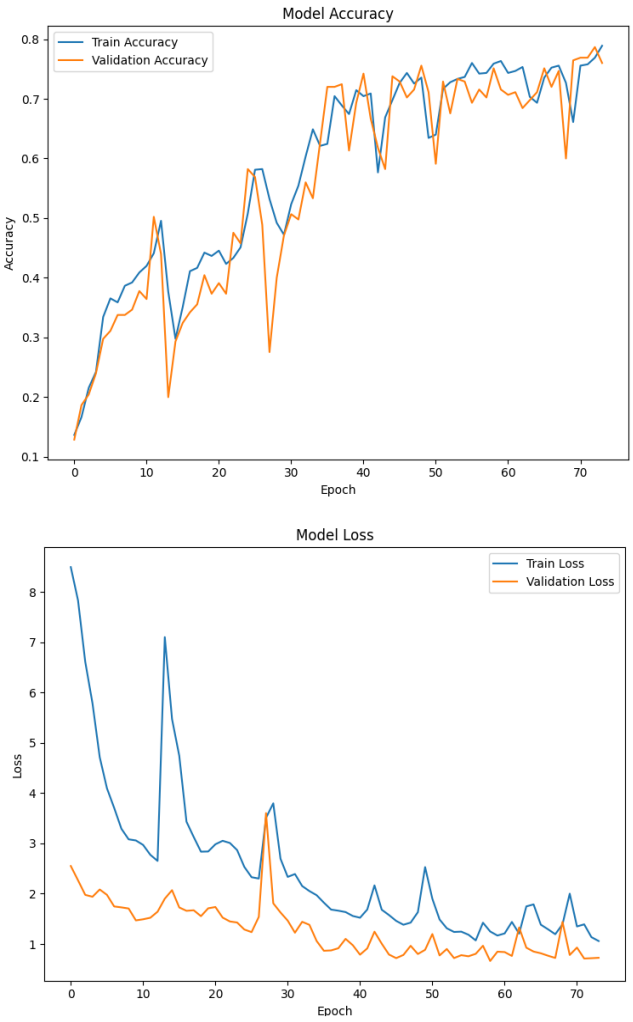


Fig. 5: The learning progression of your CNN-BiLSTM model across accuracy and loss.

Results and Discussion

The proposed proactive thread classification methodology was evaluated using a dataset containing 24,263,692 kernel events collected from a Linux Ubuntu 22.04.2 LTS environment under heterogeneous workload conditions. The dataset included light-load and heavy-load scenarios with induced CPU, memory, disk I/O, and network noise to simulate realistic operating system behavior. Using the proposed PID/TID labeling algorithm, 420 unique threads were classified into seven resource-bound categories. The majority of the dataset consisted of Synchronization and Timing threads (43.3%) and I/O-related threads (40.2%), reflecting the dominant behavior patterns commonly observed in modern operating systems.

To evaluate predictive performance, six machine learning models were trained using features extracted from the first five kernel events of each thread. Experimental results demonstrated that the Random Forest classifier achieved the best overall performance with 93.4% precision, 92.5% recall, and 91.9% F1-score while maintaining an inference latency of only 178 µs per prediction. LightGBM also achieved competitive results with 91.5% F1-score but exhibited higher inference latency compared to Random Forest. In contrast, deep learning approaches, including MLP, CNN-BiLSTM, and BERT, produced lower classification performance while imposing substantially higher computational overhead, making them less suitable for latency-sensitive scheduling environments.

Analysis of the confusion matrices revealed that both Random Forest and LightGBM achieved near-perfect classification accuracy for CPU and Process Management, Event Polling and Notification, Memory Management, Networking, and Unknown categories. However, both models experienced moderate confusion between Synchronization and Timing and I/O-related threads due to overlapping kernel event patterns such as blocking operations and waiting states. Despite these overlaps, the proposed feature extraction methodology successfully captured discriminative execution signatures from the earliest execution phase, enabling accurate prediction within the first 100 µs of thread execution.

The results demonstrate that lightweight ensemble-based machine learning models are highly effective for proactive resource-bound prediction using kernel event streams. Unlike traditional reactive schedulers that depend on historical runtime statistics, the proposed approach predicts thread behavior before resource contention emerges, enabling earlier scheduling optimization and resource allocation. Experimental observations showed that proactive prediction can reduce tail latency for interactive workloads by approximately 41% while maintaining CPU utilization near 93%. These findings confirm the practicality of integrating real-time kernel event analysis with machine learning for improving operating system scheduling efficiency and responsiveness.

Conclusion and Future Work

This paper presents a proactive thread classification methodology that predicts resource-bound categories by analyzing kernel event streams, achieving 89.2% accuracy within 100µs of thread execution. Our approach employs a five-step pipeline: (1) kernel event collection using LTTng to capture system calls, (2) system call categorization into a seven-category taxonomy covering CPU, memory, I/O, networking, synchronization, event polling, and system information, (3) PID/TID labeling based on normalized system call counts and durations to identify dominant resource usage (Algorithm 1), (4) feature extraction from the first five events to capture early behavioral patterns (Algorithm 2), and (5) predictive modeling using machine learning classifiers to map features to resource-bound categories. By processing fine-grained system call

sequences, such as frequent read/write calls for I/O-bound threads or futex calls for synchronization-heavy threads, the methodology enables early detection of resource constraints, allowing schedulers to preemptively optimize thread prioritization and resource allocation.

Evaluated on a dataset of 24,263,692 kernel events from Noferesti et al. [31], our approach classified 462 threads under diverse workloads. Random Forest achieved the highest performance (93.4% precision, 92.5% recall, 178 µs inference time), outperforming deep learning models like MLP (62.2% F1-score) and BERT (57.8% F1-score), demonstrating the efficacy of lightweight models for low-latency, high-accuracy resource-bound prediction in real-time systems.

Future work includes three directions: (1) integrating reinforcement learning to adapt predictions to dynamic workload shifts, (2) extending the taxonomy to include GPU-bound threads for emerging accelerator-based systems, and (3) optimizing the methodology for resource-constrained edge environments, particularly ARM-based systems. Additionally, predicting inter-thread resource contention could enhance cluster-level scheduling, addressing complex dependencies in large-scale systems.

Author Contributions

M. Noferesti was responsible for conceptualization, methodology, formal analysis, validation, supervision, and writing the original draft. F. Amiri Delouei contributed to the investigation, software, visualization, and writing the review and editing. S. Aryan was involved in the investigation, data curation, writing the review, and editing.

Acknowledgment

During the preparation of this work, the authors used DeepSeek and Grok in order to improve grammar, clarity, and to assist in resolving minor implementation bugs during the research phase. Subsequent to the use of this tool, the authors reviewed and edited the content as necessary and take full responsibility for the final content of the publication.

Funding

The authors received no financial support for the research.

Conflict of Interest

The authors declare no potential conflict of interest regarding the publication of this work. In addition, the ethical issues including plagiarism, informed consent, misconduct, data fabrication and, or falsification, double publication and, or submission, and redundancy have been completely witnessed by the authors.

Abbreviations

AI	Artificial Intelligence
ARM	Advanced RISC Machine
BERT	Bidirectional Encoder Representations from Transformers
BiLSTM	Bidirectional Long Short-Term Memory
CFS	Completely Fair Scheduler
CNN	Convolutional Neural Network
CPU	Central Processing Unit
DNN	Deep Neural Network
ELK	Elasticsearch, Logstash, and Kibana
FPGA	Field-Programmable Gate Array
F1-score	Harmonic Mean of Precision and Recall
GB	Gigabyte
GPU	Graphics Processing Unit
I/O	Input/Output
IRQ	Interrupt Request
LSTM	Long Short-Term Memory
LightGBM	Light Gradient Boosting Machine
Linux RTLA	Linux Real-Time Linux Analysis
LTTng	Linux Trace Toolkit Next Generation
MLP	Multi-Layer Perceptron
ML	Machine Learning
MPSoC	Multiprocessor System-on-Chip
NPU	Neural Processing Unit
OS	Operating System
PID	Process Identifier
PMC	Performance Monitoring Counter
RF	Random Forest
RISC-V	Reduced Instruction Set Computer – Five
RTOS	Real-Time Operating System
SE	Stacked Ensemble
TID	Thread Identifier
VM	Virtual Machine

References

[1] A. S. Tanenbaum, H. Bos, Modern Operating Systems. Upper Saddle River, NJ: Pearson Education, Inc., 2015.

[2] A. Johnson, T. Wahl, "Delay-bounded scheduling without delay," in Proc. Computer Aided Verification: 33rd International Conference (CAV 2021): 380-402, 2021.

[3] C. Gao, S. Saha, X. Zhu, H. Jing, K. D. McDonald-Maier, X. Zhai, "Application level resource scheduling for deep learning acceleration on MPSoC," J. Signal Process. Syst., 95(10): 1231-1243, 2023.

[4] L. Chen, T. Chen, G. Fan, B. Yin, "Static analysis of resource usage bounds for imperative programs," in Proc. 2021 28th Asia-Pacific Software Engineering Conference (APSEC): 580-581, 2021.

[5] D. P. Bovet, M. Cesati, Understanding the Linux Kernel: From I/O Ports to Process Management. Sebastopol, CA: O'Reilly Media, Inc., 2005.

[6] Y. Huang, L. Chen, L. Luo, K. Xiao, Y. Li, "Formal verification of the interrupt dispatch program of an embedded operating system," in Proc. 2022 8th International Symposium on System Security, Safety, and Reliability (ISSSR): 104-112, 2022.

[7] R. Love, Linux Kernel Development. Upper Saddle River, NJ: Pearson Education, 2010.

[8] K. Zhang, D. Ou, C. Jiang, Y. Qiu, L. Yan, "Power and performance evaluation of memory-intensive applications," Energies, 14(14): 4089, 2021.

[9] D. K. Kiss, A. Rövidz, "Theory for proactive operating systems," in Proc. 2012 IEEE 16th International Conference on Intelligent Engineering Systems (INES): 463-467, 2012.

[10] D. K. Kiss, "Operating system in the era of the many core chips," in Proc. 2012 IEEE 13th International Symposium on Computational Intelligence and Informatics (CINTI): 123-126, 2012.

[11] Y. Li, N. Lazarev, D. Koufaty, T. Yin, A. Anderson, Z. Zhang, G. E. Suh, K. Kaffes, C. Delimitrou, "Libpreemptible: Enabling fast, adaptive, and hardware-assisted user-space scheduling," in Proc. 2024 IEEE International Symposium on High-Performance Computer Architecture (HPCA): 922-936, 2024.

[12] Y. Wang, S. Xing, "AI-driven CPU resource management in cloud operating systems," J. Comput. Commun., 13(6): 135-149, 2025.

[13] S. Zeng, G. Dai, H. Sun, J. Liu, S. Li, G. Ge, K. Zhong, K. Guo, Y. Wang, H. Yang, "A unified FPGA virtualization framework for general-purpose deep neural networks in the cloud," ACM Trans. Reconfigurable Technol. Syst., 15(3): 1-31, 2021.

[14] G. G. Anderson, "Operating system scheduling optimization," Ph.D. dissertation, University of Johannesburg, South Africa, 2013.

[15] G. A. Ismael, A. A. Salih, A. AL-Zebari, N. Omar, K. J. Merceedi, "Scheduling algorithms implementation for real time operating systems: A review," Asian J. Res. Comput. Sci., 11(4): 35-51, 2021.

[16] G. Fan, T. Chen, B. Yin, L. Chen, T. Wang, J. Wang, "Static bound analysis of dynamically allocated resources for C programs," in Proc. 2021 IEEE 32nd International Symposium on Software Reliability Engineering (ISSRE): 390-400, 2021.

[17] H. Jahanpour, H. Barati, A. Mehranzadeh, "An energy efficient fault tolerance technique based on load balancing algorithm for high-performance computing in cloud computing," J. Electr. Comput. Eng. Innovations, 8(2): 169-182, 2020.

[18] VMware, "VMware vSphere Documentation," 2025.

[19] A. Verma, L. Pedrosa, M. Korupolu, D. Oppenheimer, E. Tune, J. Wilkes, "Large-scale cluster management at Google with Borg," in Proc. ACM Symposium on Cloud Computing (SoCC): 1-17, 2015.

[20] R. Zhuang, J. Han, K. Xue, J. Li, Q. Sun, J. Lu, "ProacTMP: A proactive multipath transport protocol for low-latency datacenters," IEEE Trans. Network Serv. Manag., 21(4), 3919-3932, 2024.

[21] D. Yang, Z. Xiao, D. Zhang, S. Zhang, J. Cao, G. Chen, "PreAct: Predictive resource allocation for bursty workloads in a co-located data center," in Proc. 53rd International Conference on Parallel Processing: 722-731, 2024.

[22] A. Sharma, "Towards cost-effective resource management strategies for distributed deep learning and data parallel workloads on the cloud," Ph.D. dissertation, The Pennsylvania State University, 2024.

[23] M. Noferesti, B. Grandy, N. Ezzati-Jivan, "Resource life-cycle aware noise detection via kernel event monitoring," in Proc. 2024 34th International Conference on Collaborative Advances in Software and Computing (CASCON): 1-10, 2024.

[24] K. Darvishi, M. Noferesti, Y. Sehgal, N. Ezzati-Jivan, "LMAT: An adaptive tracing approach based on efficient system behavior analysis using language models," J. Syst. Software, 238, 112890, 2026.

[25] K. Darvishi, M. Noferesti, N. Ezzati-Jivan, "Toward adaptive tracing: Efficient system behavior analysis using language models," in Proc. 2024 ACM/IEEE 44th International Conference on Software Engineering: New Ideas and Emerging Results: 62-66, 2024.

[26] M. Desnoyers, M. R. Dagenais, "LTTng: Tracing across execution layers, from the hypervisor to user-space," presented at the Linux Symposium, 2005.

[27] I. Molnar, "Perf: Linux profiling with performance counters," Linux Journal, 2010(191), 2010.

[28] A. Tockman, S. Pratap, E. Andres, G. Samuel, A. Chlipala, "Foundational verification of running-time bounds for interactive programs," in Proc. 15th ACM SIGPLAN International Conference on Certified Programs and Proofs: 187-200, 2026.

[29] D. B. De Oliveira, D. Casini, J. Lelli, T. Cucinotta, "Timerlat: Real-time Linux scheduling latency measurements, tracing, and analysis," IEEE Trans. Comput., 74(8): 2608-2620, 2025.

[30] J. Zhao, "Lite edge intelligent real-time operating system based on microkernel," in Proc. 10th International Conference on Cyber Security and Information Engineering: 180-190, 2025.

[31] M. Noferesti, N. Ezzati-Jivan, "Enhancing empirical software performance engineering research with kernel-level events: A comprehensive system tracing approach," J. Syst. Software, 216, 112117, 2024.

Biographies



Morteza Noferesti is an Assistant Professor at Bozorgmehr University of Qaenat. He holds a B.S. from Shiraz University of Technology and both his M.S. and Ph.D. from the prestigious Sharif University of Technology, Tehran, Iran. He further honed his expertise as a Postdoctoral Fellow in Performance Engineering at Brock University, Canada. His internationally recognized research centers on computer networks, performance analysis, applied artificial intelligence, and vulnerability analysis.

- Email: mnoferesti@buqaen.ac.ir
- ORCID: 0009-0000-5507-1461
- Web of Science Researcher ID: LXV-3594-2024
- Scopus Author ID: 54403678600
- Homepage: https://www.buqaen.ac.ir/%D9%87%DB%8C%D8%A7%D8%AA-%D8%B9%D9%84%D9%85%DB%8C/%D8%AF%DA%A9%D8%AA%D8%B1-%D9%85%D8%B1%D8%AA%D8%B6%DB%8C-%D9%86%D9%88%D9%81%D8%B1%D8%B3%D8%AA%DB%8C



Farzad Amiri Delouei is a BS student in Software Engineering at Bozorgmehr University of Qaenat (2022–2026) and has served as Secretary of the Computer Science Student Association at the university for two years. He has a particular interest in operating systems, software performance, and performance engineering.

- Email: amirifarzad2002@yahoo.com
- ORCID: 0009-0009-7467-3498
- Web of Science Researcher ID: QAZ-1550-2026
- Scopus Author ID: NA
- Homepage: https://farzadamr.github.io



Sarah Aryan is an undergraduate student in Software Engineering at Bozorgmehr University of Qaenat (2022–2026), among the top entrance students. With two years of active membership in the Computer Science Student Association, she has gained valuable experience in group and academic activities, and is interested in databases and operating systems.

- Email: saraharyan79@gmail.com
- ORCID: 0009-0000-4392-4543
- Web of Science Researcher ID: QIR-8843-2026
- Scopus Author ID: NA
- Homepage: https://saraharyan.github.io/

Journal of Electrical and Computer Engineering Innovations
(JECEI)
Journal homepage: http://www.jecei.sru.ac.ir

PAPER TYPE? (Research paper, short paper, Review paper *et al.*)

Instructions and Formatting Rules for Authors of Journal of Electrical and Computer Engineering Innovations, JECEI

First Author*, *Second Author*, *Third Author

Affiliations of the Authors: (Department, Faculty, University (Institution, City, Country)

Article Info

Article History:
Received
Reviewed
Revised
Accepted

Keywords:
The author(s) shall provide up to 6 keywords to help identify the major topics of the paper

*Corresponding Author's Email Address:

Abstract

Background and Objectives: This section should be the shortest part of the abstract and should very briefly outline the following information: 1-What is already known about the subject, related to the paper in question. 2- What is not known about the subject and hence what the study intended to examine (or what the paper seeks to present). In most cases, the background can be framed in just 2–3 sentences, with each sentence describing a different aspect of the information referred to above; sometimes, even a single sentence may suffice. The purpose of the background, as the word itself indicates, is to provide the reader with a background to the study, and hence to smoothly lead into a description of the methods employed in the investigation.

Methods: The methods section is usually the second-longest section in the abstract. It should contain enough information to enable the reader to understand what was done, and how.

Results: The results section is the most important part of the abstract and nothing should compromise its range and quality. This is because readers who peruse an abstract do so to learn about the findings of the study. The results section should therefore be the longest part of the abstract and should contain as much detail about the findings as the journal word count permits.

Conclusion: This section should contain the most important take-home message of the study, expressed in a few precisely worded sentences. Usually, the finding highlighted here relates to the primary outcome measure; however, other important or unexpected findings should also be mentioned. It is also customary, but not essential, for the authors to express an opinion about the theoretical or practical implications of the findings, or the importance of their findings for the field. Thus, the conclusions may contain three elements: 1- The primary take-home message 2-The additional findings of importance 3-The perspective.

This work is distributed under the CC BY license (http://creativecommons.org/licenses/by/4.0/)

How to cite this paper:
F. Author, S. Author, T. Author, "Instructions and Formatting Rules for Authors of Journal of Electrical and Computer Engineering Innovations, JECEI," J. Electr. Comput. Eng. Innovations, ×(×): ×××-×××, ××××.

DOI:

URL: http://jecei.srttu.edu/journal/authors.note

2345- 3044/© 2026 The Authors. Published by Shahid Rajaee Teacher Training University.

Introduction

This document provides an example of the desired layout for JECEI paper and can be used as a template for Microsoft Word versions 2003 and later. It contains information regarding desktop publishing format, type sizes, and typefaces. Style rules are provided to explain how to handle equations, units, figures, tables, abbreviations, and acronyms. Sections are also devoted to the preparation of appendixes, acknowledgments, references, and authors' biographies.

Technical Work Preparation

Please use automatic hyphenation and check your spelling. Additionally, be sure your sentences are complete and that there is continuity within your paragraphs. Check the numbering of your graphics and make sure that all appropriate references are included.

A. Template

This document may be used as a template for preparing your technical work.

B. Format

If you choose not to use this document as a template, prepare your technical work in single-spaced, double-column format, on paper 21.6×27.9 centimeters (8.5×11 inches or 51×66 picas). Set top and bottom margins to 25 millimeters (0.98 inch) and left and right margins to about 20 millimeters (0.79 inch). Do not violate margins (i.e., text, tables, figures, and equations may not extend into the margins). The column width is 82 millimeters (3.2 inches). The space between the two columns is 6 millimeters (0.24 inch). Paragraph indentation is 4.2 millimeters (0.17 inch). Use full justification. Use either one or two spaces between sections, and between text and tables or figures, to adjust the column length.

C. Typefaces and Sizes

Please use a proportional serif typeface such as Calibri and embed all fonts. Table 1 provides samples of the appropriate type sizes and styles to use.

D. Section Headings

A primary section heading is enumerated by a Roman numeral followed by a period and is centered above the text. A primary heading should be in capital letters.

A secondary section heading is enumerated by a capital letter followed by a period and is flush left above the section. The first letter of each important word is capitalized and the heading is italicized.

A tertiary section heading is enumerated by an Arabic numeral followed by a parenthesis. It is indented and is followed by a colon. The first letter of each important word is capitalized and the heading is italicized.

A quaternary section heading is rarely necessary, but is perfectly acceptable if required. It is enumerated by a lowercase letter followed by a parenthesis. It is indented and is followed by a colon. Only the first letter of the heading is capitalized and the heading is italicized.

E. Figures and Tables

Figure axis labels are often a source of confusion. Try to use words rather than symbols. As an example, write the quantity "Magnetization," or "Magnetization, *M*," not just "*M*." Put units in parentheses. Do not label axes only with units. As in Fig. 1, write "Magnetization (kA/m)" or "Magnetization (kA·m^{-1})," not just "kA/m." Do not label axes with a ratio of quantities and units. For example, write "Temperature (K)," not "Temperature/K." Figure labels should be legible, approximately 8- to 10-point type. Large figures and tables may span both columns, but may not extend into the page margins. Arrange these one column figures and tables at either top or end of a page, or at the end of the paper right before the references. Figure captions should be below the figures; table captions should be above the tables. Do not put captions in "text boxes" linked to the figures. Do not put borders around your figures. Use Insert | Reference | Caption to number your tables and figures, and use Insert | Reference | Cross- reference to refer to their numbers.

Table 1: Samples of Calibri sizes and styles used for formatting a pes technical work

Point Size	Purpose in Paper	Special Appearance
9	Table text, figure text footnotes, subscripts, superscripts, references, bio, Figure caption, keywords	Table Title
10	Body text, equations, author affiliation, abstract	*Subheadings* Section Titles
12	***Author Name***	
17		**Title**

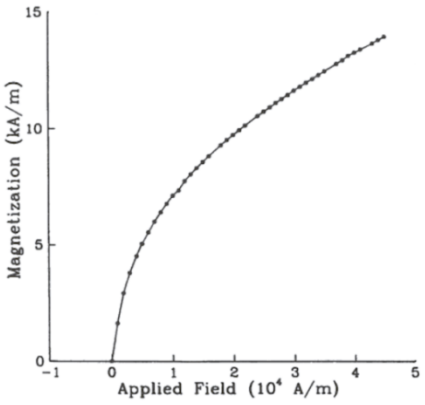


Fig. 1: Magnetization as a function of applied field. (Note that there is a colon after the figure number followed by two spaces.)

All figures and tables must appear near, but not before, their first mention in the text. Use the abbreviation "Fig. 1," even at the beginning of a sentence.

To insert images in Word, use Insert | Picture | From File.

F. Numbering

Number reference citations consecutively in square brackets [1]. The sentence punctuation follows the brackets [2]. Multiple references [2], [3] are each numbered with separate brackets [1][1]-[2]. Refer simply to the reference number, as in [2]. Do not use "Ref. [2]" or "reference [2]" except at the beginning of a sentence: "Reference [2] shows…."

Number footnotes separately with superscripts (Insert | Footnote). Place the actual footnote at the bottom of the column in which it is cited. Do not put footnotes in the reference list. Use letters for table footnotes.

G. Units

Metric units are preferred for use in IEEE publications in light of their global readership and the inherent convenience of these units in many fields. In particular, the use of the International System of Units is advocated. This system includes a subsystem of units based on the meter, kilogram, second, and ampere (MKSA). British units may be used as secondary units (in parentheses). An exception is when British units are used as identifiers in trade, such as 3.5-inch disk drive.

H. Math and Equations

Number equations consecutively with equation numbers in parentheses flush with the right margin, as in (1). First use the equation editor to create the equation. Then select the "Equation" markup style. Write the equation number in parentheses using Insert | Caption.

Use the Microsoft Equation Editor for all math objects in your paper (Insert | Object | Create New | Microsoft Equation *or* MathType Equation). "Float over text" should *not* be selected.

To make your equations more compact, you may use the slash (/), the exp function, or appropriate exponents. Italicize Roman symbols for quantities and variables, but not Greek symbols. Use a long dash rather than a hyphen for a minus sign. Use parentheses to avoid ambiguities in denominators. Number equations consecutively with equation numbers in parentheses flush with the right margin, as in (1). Be sure that the symbols in your equation have been defined before the equation appears or immediately following. Italicize symbols (*T* might refer to temperature, but T is the unit Tesla).

Use Insert | Reference | Caption to number equations. Refer to "(1)," not "Eq. 1" or "equation (1)," except at the beginning of a sentence: "Equation (1) is …". Punctuate equations when they are part of a sentence, as in

$$\int_0^{r_2} F(r,\varphi)\,dr\,d\varphi = [\sigma r_2/(2\mu_0)] \cdot \int_0^{\infty} \exp(-\lambda\,|z_j - z_i|)\,\lambda^{-1} J_1(\lambda r_2)\,J_0(\lambda r_i)\,d\lambda \quad (1)$$

Use two column tables to locate equations and their numbers properly in one line, as follows:

$$I_F = I_B = -I_C = A^2 I_{A1} + A I_{A2} + I_{A0} = \frac{-J\sqrt{3}E_A}{Z_1 + Z_2} \quad (2)$$

where I_F is the fault current. Be sure that the border is off.

Results and Discussion

The Results section should briefly present the experimental data in text, tables or figures. Tables and figures should not be described extensively in the text.

The Discussion should focus on the interpretation and the significance of the findings with concise objective comments that describe their relation to other work in the area. It should not repeat information in the results. The final paragraph should highlight the main conclusion(s), and provide some indication of the direction future research should take.

Conclusion

As the Conclusion section is the most important element of a manuscript, so it must be more expanded scientifically and contently at least half a page length.

Example:

In this study, a forecast model was developed to determine the generation of MSW in the municipalities of the CCS, Chiapas State, Mexico. A MLR was used to obtain the forecast model with social and demographic explanatory variables. Two forecast models were presented and analyzed, with variables that met the multicollinearity test. The most important variables to predict the rate of MSW generation in the study area were the population of each municipality (XPop), the population born in another municipality (XPbam) and the population density (XPd). XPop is the most influential explanatory variable of waste generation, particularly it is related in a positive way. XPbam is less related to waste generation. XPd is the variable that least influences waste generation prediction; in addition, it can present problems of correlation with other explanatory variables. Although other variables, such as daily per capita income (XDpi) and average schooling (XAs), are very important, they do not seem to have an effect on the response variable in this study. The user of this forecast model should use model 2, since it is the one with the highest parsimony (it uses fewer variables); R^2_{adj}, MAPE, MAD and RMSE values indicated high influence on the explained phenomenon and high

forecasting capacity. Additionally, it is important to mention that when using the models proposed for forecasting purposes, it is necessary to make a transformation in the explanatory and response variables (use inverse of natural logarithm). The inferences made on the municipalities of the study area showed that, except in some municipalities, the MSW generation rate usually presented a gradual increase with respect to population growth and with respect to the number of inhabitants that were born in another entity (migration). Finally, this study can be a solid basis for comparison for future research in the area of study. It is possible to use different mathematical models such as artificial neural network, principal component analysis, time-series analysis, etc., and compare the response variable or the predictors.

Author Contributions

Each author role in the research participation must be mentioned clearly.

Example:

A. Mahboobi, B. Bagheri, and C. Ahmadi designed the experiments. A. Mahboobi collected the data. A. Mahboobi carried out the data analysis. A. Mahboobi, B. Bagheri, and C. Ahmadi interpreted the results and wrote the manuscript.

Acknowledgment

The following is an example of an acknowledgment:

The author gratefully acknowledges the IEEE I. X. Austan, A. H. Burgmeyer, C. J. Essel, and S. H. Gold for their work on the original version of this document.

Funding

This research received no external funding.

Conflict of Interest

The authors declare no potential conflict of interest regarding the publication of this work. In addition, the ethical issues including plagiarism, informed consent, misconduct, data fabrication and, or falsification, double publication and, or submission, and redundancy have been completely witnessed by the authors.

Abbreviations

Define less common abbreviations and acronyms the first time they are used in the text, even after they have been defined in the abstract. Abbreviations such as IEEE, SI, MKS, CGS, ac, dc, and rms do not have to be defined. Do not use abbreviations in the title unless they are unavoidable.

Example:

MS	Multispectral
SMF	Spectral Matched Filter
SAM	Spectral Angle Mapper
MSD	Matched Subspace Detector
OSP	Orthogonal Subspace Projection
CEM	Constrained Energy Minimization
ASD	Adaptive Subspace Detector
STD	Sparsity Based Target Detector
KSAM	Kernel Based SAM
DTD	Difference Based Target Detection
AP-CR	Attribute Profile Based Collaborative Representation
ROC	Receiver Operating Characteristic
MS	Multispectral
SMF	Spectral Matched Filter
SAM	Spectral Angle Mapper
MSD	Matched Subspace Detector
OSP	Orthogonal Subspace Projection
CEM	Constrained Energy Minimization
ASD	Adaptive Subspace Detector
STD	Sparsity Based Target Detector
KSAM	Kernel Based SAM
DTD	Difference Based Target Detection
AP-CR	Attribute Profile Based Collaborative Representation
ROC	Receiver Operating Characteristic
MS	Multispectral
SMF	Spectral Matched Filter
SAM	Spectral Angle Mapper
MSD	Matched Subspace Detector
OSP	Orthogonal Subspace Projection
CEM	Constrained Energy Minimization
ASD	Adaptive Subspace Detector
STD	Sparsity Based Target Detector
KSAM	Kernel Based SAM

References

References are important to the reader; therefore, each citation must be complete and correct. There is no editorial check on references; therefore, an incomplete or wrong reference will be published unless caught by a reviewer or discusser and will detract from the authority and value of the paper. References should be readily available publications. List only one reference per reference number. If a reference is available from two sources, each should be listed as a separate reference. Give all authors' names; As much as possible do not use *et al.*

Samples of the correct formats for various types of references are given below.

Periodicals:

[1] J. F. Fuller, E. F. Fuchs, K. J. Roesler, "Influence of harmonics on power distribution system protection," IEEE Trans. Power Deliv., 3(2): 549-557, 1988.

Books:

[2] E. Clarke, Circuit Analysis of AC Power Systems, vol. I. New York: Wiley: 81, 1950.

Technical Reports:

[3] E. E. Reber, R. L. Mitchell, C. J. Carter, "Oxygen absorption in the Earth's atmosphere," Aerospace Corp., Los Angeles, CA, Tech. Rep. TR-0200 (4230-46)-3, Nov. 1968.

[4] S. L. Talleen. (1996, Apr.). The Intranet Architecture: Managing information in the new paradigm. Amdahl Corp., Sunnyvale, CA.

Papers Presented at Conferences (Unpublished):

[5] D. Ebehard, E. Voges, "Digital single sideband detection for interferometric sensors," presented at the 2nd Int. Conf. Optical Fiber Sensors, Stuttgart, Germany, 1984.

[6] Process Corp., Framingham, MA. Intranets: Internet technologies deployed behind the firewall for corporate productivity. Presented at INET96 Annu. Meeting.

Papers from Conference Proceedings (Published):

[7] J. L. Alqueres, J. C. Praca, "The Brazilian power system and the challenge of the Amazon transmission," in Proc. IEEE Power Engineering Society Transmission and Distribution: 315-320, 1991.

Dissertations:

[8] S. Hwang, "Frequency domain system identification of helicopter rotor dynamics incorporating models with time periodic coefficients," Ph.D. dissertation, Dept. Aerosp. Eng., Univ. Maryland, College Park, 1997.

Standards:

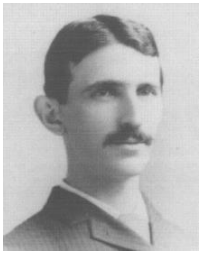
[9] IEEE Guide for Application of Power Apparatus Bushings, IEEE Standard C57.19.100-1995, Aug. 1995.

Patents:

[10] G. Brandli and M. Dick, "Alternating current fed power supply," U.S. Patent 4 084 217, Nov. 4, 1978.

Biographies

A technical biography for each author may be included, but without any title, as it is seen herein. It should begin with the author's name (as it appears in the byline). A photograph and an electronic file of the photo should also be included for each author. The photo should be black and white, glossy, and 3.0 centimeters (1.18 inches) wide by 3.8 centimeters (1.5 inches) high. The head and shoulders should be centered, and the photo should be flush with the left margin. The following is an example of the text of a technical biography:



Nikola Tesla (M'1888, F'17) was born in Smiljan in the Austro-Hungarian Empire, on July 9, 1856. He graduated from the Austrian Polytechnic School, Graz, and studied at the University of Prague. His employment experience included the American Telephone Company, Budapest, the Edison Machine Works, Westinghouse Electric Company, and Nikola Tesla Laboratories. His special fields of interest included high frequency. Tesla received honorary degrees from institutions of higher learning including Columbia University, Yale University, University of Belgrade, and the University of Zagreb. He received the Elliott Cresson Medal of the Franklin Institute and the Edison Medal of the IEEE. In 1956, the term "tesla" (T) was adopted as the unit of magnetic flux density in the MKSA system. In 1975, the Power Engineering Society established the Nikola Tesla Award in his honor. Tesla died on January 7, 1943.

- Email:
- ORCID:
- Web of Science Researcher ID:
- Scopus Author ID:
- Homepage: